Earth Systems Data and Models

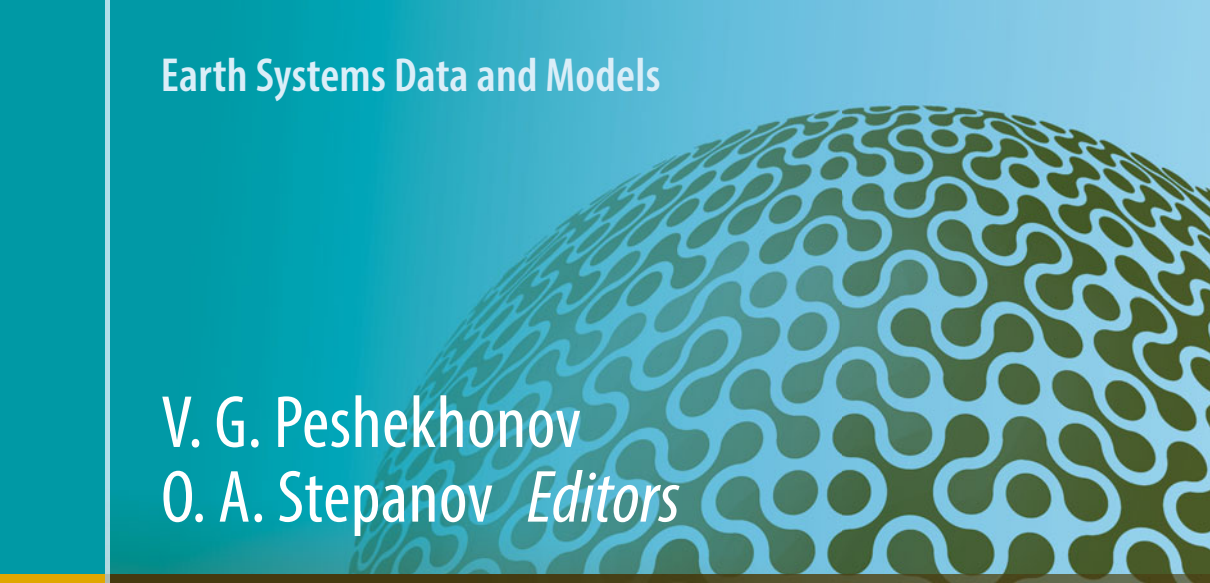

V. G. Peshekhonov
O. A. Stepanov *Editors*

Methods and Technologies for Measuring the Earth's Gravity Field Parameters

Springer

Earth Systems Data and Models

Volume 5

The book series Earth Systems Data & Models publishes state-of-the-art research and technologies aimed at understanding processes and interactions in the earth system. A special emphasis is given to theory, methods, and tools used in earth, planetary and environmental sciences for: modeling, observation and analysis; data generation, assimilation and visualization; forecasting and simulation; and optimization. Topics in the series include but are not limited to: numerical, data-driven and agent-based modeling of the earth system; uncertainty analysis of models; geodynamic simulations, climate change, weather forecasting, hydroinformatics, and complex ecological models; model evaluation for decision-making processes and other earth science applications; and remote sensing and GIS technology. The series publishes monographs, edited volumes and selected conference proceedings addressing an interdisciplinary audience, which not only includes geologists, hydrologists, meteorologists, chemists, biologists and ecologists but also physicists, engineers and applied mathematicians, as well as policy makers who use model outputs as the basis of decision-making processes.

V. G. Peshekhonov · O. A. Stepanov
Editors

Methods and Technologies for Measuring the Earth's Gravity Field Parameters

Springer

Editors
V. G. Peshekhonov
Concern CSRI Elektropribor
St. Petersburg, Russia

ITMO University
St. Petersburg, Russia

O. A. Stepanov
Concern CSRI Elektropribor
St. Petersburg, Russia

ITMO University
St. Petersburg, Russia

ISSN 2364-5830 ISSN 2364-5849 (electronic)
Earth Systems Data and Models
ISBN 978-3-031-11157-0 ISBN 978-3-031-11158-7 (eBook)
https://doi.org/10.1007/978-3-031-11158-7

This Springer imprint is published by the registered company Springer Nature Switzerland AG
The registered company address is: Gewerbestrasse 11, 6330 Cham, Switzerland

Preface

Knowledge of the Earth's gravity field (EGF) is essential in a wide range of fundamental and applied research areas. They include, for instance, offshore hydrocarbon exploration, for which marine gravimetric surveys are regularly conducted by geophysical companies. The quantum leap in INS/GNSS technology has opened the possibilities for airborne gravimetry along with shipborne surveys. Now the accuracy of airborne gravimetry is about 0.5–1 mGal and higher at a spatial resolution of less than 5–10 km. However, in a variety of problems related to the study of the Earth's figure, high-precision navigation, and geodesy, the requirements for accuracy, spatial resolution, and efficiency of gravimetric surveys are becoming more stringent in recent years. This, in turn, generates a need for improved accuracy of onboard EGF measurements against the background of vertical disturbing accelerations, the magnitude of which is hundreds of thousands times greater than the useful signal.

Recently, marine and airborne gravimetric surveys in remote Arctic regions have assumed a new urgency, which is associated with the studies of the continental shelf. The lack of data on the polar regions also impedes further improvement of the model for the Earth's figure.

To solve the problems of high-precision navigation and geodesy, it is necessary to know the absolute value of the gravity (free-fall) acceleration at the object location. Therefore, high-precision measurement of the total gravity acceleration onboard dynamic vehicles is one of the key challenges in modern gravimetry.

Considerable progress has been made in all the above areas since the late 1980s, but the recent results have not been adequately reported in the literature so far. In this regard, the publication of this monograph on modern methods and technologies for measuring the EGF parameters is particularly relevant.

The book is written by a team of well-known researchers in the field of EGF measurements from prominent Russian organizations, chief designers, and leading developers of widely applied gravimeters. This book provides the most relevant descriptions of designs and principles of operation of modern gravimeters, as well as the data processing methods used. It is neither a training manual nor a methodical guide. Therefore, the book does not claim to be comprehensive or to cover the

above topics in full; it is rather a description of the authors' personal experiences in the development and research of methods and technologies for measuring the EGF parameters.

This book is an adapted translation of the Russian book *Sovremennye metody i sredstva izmerenya parametrov gravitatsionnogo polya Zemli* published in 2017 by Concern CSRI Elektropribor, St. Petersburg, Russia.

Compared to the Russian version of the book published in 2017, some changes have been introduced regarding the composition of the sections, reference list, etc. Additional international references have been included, and references to Russian scientific journals have been substituted with the English versions published by Springer and other international publishers. Information about the contributors, including their academic degrees and publications, has also been updated.

The book contains six chapters.

Chapter 1 describes modern equipment used for gravity measurements. It gives an overview of absolute ballistic gravimeters and analyzes the design features of two types of relative gravimeters manufactured in Russia, mobile Chekan-AM gravimeters and airborne/marine GT-2 gravimeters, widely used for onboard gravity measurements.

Chapter 2 analyzes data processing methods for onboard gravity anomaly measurements, implemented in Chekan-AM and GT-2 gravimeters, and discusses various approaches to improving the accuracy of onboard gravity field measurements. In particular, consideration is given to the experience of using optimal and adaptive filtering and smoothing methods, as well as the application of spherical wavelet expansion to combine airborne gravimetry data and global EGF models.

Chapter 3 provides an overview of the methods to determine and calculate deflections of the vertical (DOV) on a moving base. They include the gravimetric method based on gravity anomaly measurements, the astrogeodetic method based on the comparison of astronomical and geodetic coordinates, and the inertial-geodetic method based on high-precision inertial system data. The chapter considers the technologies implementing the DOV determination methods and improving their effectiveness, such as the automated zenith telescope recently developed by Concern CSRI Elektropribor. Improved data processing algorithms enhancing the accuracy of DOV determination methods are also covered.

Chapter 4 focuses on the studies of the gravity field in hard-to-reach areas of the Earth. It discusses the current knowledge of the Arctic gravity field, analyzes the experience of using the Chekan-AM gravimeter in remote areas, and considers the polar versions of GT-2 gravimeters capable of operating in all latitudes.

Chapter 5 presents some advanced methods for studying the Earth's gravity field. Airborne vector gravimetry based on strapdown inertial navigation systems is described. Possible approaches to gravity anomaly determination using this method are addressed. The state and prospects for the development of instruments for onboard measurements of the second derivatives of geopotential are discussed. Basic physical principles of cold-atom gravimeters and the outlook for their further development are also considered.

Chapter 6 deals with the construction of EGF models and their applications. Special attention is given to the estimation of their accuracy. These models are especially important in monitoring the quality of relative measurements (depending on the proper operation of equipment and the physical factors affecting it, such as zero-point drift), map-aided navigation, and estimation of the measurements navigation informativity.

St. Petersburg, Russia

V. G. Peshekhonov
O. A. Stepanov

About the Book

The book provides an overview of the main modern methods and technologies for measuring the Earth's gravity field parameters. It presents a variety of gravity measurement instruments, including ground-based, marine, airborne, and space equipment.

The book addresses data processing methods applied to onboard gravity anomaly measurements. The optimal filtering and smoothing problem is formulated and solved in general form. The problem of structural and parametric identification of the anomaly models and errors of the measuring instruments is formulated. The proposed identification algorithm is described, based on nonlinear filtering methods and actually making the estimation process and algorithms adaptive.

Considerable attention is given to the methods for determining the deflections of the vertical. Their features are covered, and a qualitative comparative analysis is carried out.

The book covers the studies of the Earth's gravity field in remote areas. All-latitude modifications of instruments and software are considered. The results of gravimetric surveys in hard-to-reach regions are presented.

Promising methods for studying the gravity field, including simultaneous determination of the gravity anomaly and deflections of the vertical (vector gravimetry), are described and analyzed. The state of the art in cutting-edge technologies such as gravity gradiometers and cold-atom gravimeters is considered.

Modern models of the Earth's gravity field are compared, and their use in various applied problems such as map-aided navigation is discussed.

The book is written for engineers and researchers in gravimetry-related spheres. It will be also useful to the specialists in development and application of navigation systems, including designers of gravimetric instruments and navigation officers.

Contents

Abbreviations

ABG	Absolute ballistic gravimeter
AI	Atomic interferometer
AZT	Automated zenith telescope
BIPM	International Bureau of Weights and Measures
CCD	Charge-coupled device
CHAMP	Challenging Minisatellite Payload
CID	Control and indication device
CIPM	International Committee of Weights and Measures
CPU	Central processing unit
DOV	Deflections of the vertical
DTG	Dynamically tuned gyroscope
EGF	Earth's gravity field
EGG	Exploration gravity gradiometer
FFA	Free-fall acceleration
FOG	Fiber-optic gyroscope
FTG	Full tensor gradiometer
GA	Gravity anomaly
GES	Gravimeter elastic system
GG	Gravity gradiometer
GNSS	Global Navigation Satellite System
GOCE	Gravity Field and Steady-State Ocean Circulation Explorer
GD	Gravity disturbance
GP	Gyro platform
GRACE	Gravity Recovery and Climate Experiment
GRS	Gravity reference station
GSE	Gravimeter sensing element
IAG	International Association of Geodesy
ICAG	International Comparison of Absolute Gravimeters
IF	Interference fringes
INS	Inertial navigation system
KF	Kalman filter

LHM	Local harmonic modeling
LPF	Low-pass filter
LSM	Least squares method
MOT	Magneto-optical trap
OEC	Optoelectronic converter
OI	Optical interferometer
OSF	Optimal smoothing filter
PDD	Proximate decomposition and decorrelation
PDF	Probability density function
PSD	Power spectral density
SC	Scaling coefficient
SDGP	Second derivatives of the geopotential
SGSF	Suboptimal gravimetric smoothing filter
SIMU	Strapdown inertial measurement unit
SINS	Strapdown inertial navigation system
SWC	Spherical wavelet coefficient
TF	Transfer function
UKF	Unscented Kalman filter
VCT	Vertical component transformation
ZUPT	Zero velocity update

Chapter 1
Instruments for Measuring Gravity

L. Vitushkin, L. Elinson, A. Krasnov, V. G. Peshekhonov, A. Sokolov, Yu. Smoller, and S. Yurist

Abstract This chapter describes technical instrumentation for gravity measurements. Various types of absolute ballistic gravimeters intended for ground-based measurements of the absolute free-fall acceleration are described. The focus is on the most recently used laser-interferometric absolute gravimeters. Regular international comparisons of absolute gravimeters are considered. Applications of ground-based absolute gravimetry using ballistic gravimeters for the national and international geodetic projects such as the Global Geodetic Observing System of the International Association of Geodesy are described. Development and operation of the Russian Chekan and GT-2 series mobile gravimeters are addressed.

Keywords Absolute ballistic gravimeters · International comparisons of absolute gravimeters · Relative gravimeters · Gravimeter Chekan · Gravimeter GT-2A

Introduction

This chapter is devoted to the description of the technical instrumentation for gravity measurement. It contains three sections.

L. Elinson—Deceased

L. Vitushkin
Mendeleyev Institute for Metrology, St. Petersburg, Russia

L. Elinson · A. Krasnov (✉) · V. G. Peshekhonov · A. Sokolov
Concern CSRI Elektropribor, St. Petersburg, Russia
e-mail: anton-krasnov@mail.ru

V. G. Peshekhonov
e-mail: onti@eprib.ru

A. Krasnov · V. G. Peshekhonov · A. Sokolov
ITMO University, St. Petersburg, Russia

Yu. Smoller · S. Yurist
Gravimetric Technologies, Moscow, Russia

V. G. Peshekhonov and O. A. Stepanov (eds.), *Methods and Technologies for Measuring the Earth's Gravity Field Parameters*, Earth Systems Data and Models 5,
https://doi.org/10.1007/978-3-031-11158-7_1

Section 1.1 describes the principle of operation, structure, and design features of various types of modern absolute ballistic gravimeters (ABG) intended for ground-based measurements of the absolute values of the free-fall acceleration (FFA). The focus is on the most recently used laser-interferometric ABGs, which determine FFA based on measurements—conducted with a laser displacement interferometer—of the travel path of a macroscopic test body (MTB) and the time intervals during its free fall in a gravitational field. The sources of uncertainties in FFA measurements using the ABGs are analyzed. The chapter provides an analysis of the modern metrological assurance system for absolute gravimeters. It is pointed out that, in order to determine ABG metrological characteristics belonging to national metrological institutes, regular international comparisons under the auspices of the International Committee of Weights and Measures and regional international comparisons are held under the authority of regional metrological organizations. The results of these comparisons are briefly described, also given is the information on the international database of absolute FFA measurements, developed by the Institute of Geodesy of the German Federal Agency for Cartography and Geodesy (BKG). Applications of ground-based absolute gravimetry using ABGs for the implementation of national and international projects in modern geodesy such as the Global Geodetic Observing System of the International Association of Geodesy are described. The section points out the current trend of research aimed at determining whether it is possible to carry out absolute FFA measurements using ABGs on moving platforms in marine and airborne gravimetry.

Sections 1.2 **and** 1.3 describe the features of the development and operation of the Russian Chekan series (Sect. 1.2) and GT-2 series (Sect. 1.3) mobile gravimeters. These systems belong to the class of relative gravimeters, i.e., those designed to measure gravity increments. They are widely used for high-precision measurements of the Earth's gravitational field from sea vessels and aircraft, including measurements in hard-to-reach Arctic and Antarctic areas.

Each section provides brief information on the development history of the instruments, describes design features of gravimeter sensing elements along with their block diagrams, and gives a detailed description of the main technical solutions implemented when building the latest versions of gravimeters. Mathematical models of gravity sensors and inertial sensing elements used are provided. The main structural features and the sources of uncertainties of stabilization and correction circuits for gyrostabilized platforms are analyzed.

1.1 Absolute Gravimeters

Absolute measurements of the free-fall acceleration (gravity) are the basis for the determination of the Earth's gravitational field (EGF). In absolute measurements, the measurement result is represented by the absolute FFA value, in contrast to relative measurements, the result of which is represented by the difference between FFA values at the stations where the measurements were taken.

At the initial stages of the development of instruments for measuring the gravitational field, the number of absolute FFA measurements was insignificant, and the uncertainties in measurements were relatively large.

From 1909 to 1971, all gravitational field measurements were performed in the framework of the Potsdam Gravimetric System. At the initial gravimetric site, absolute measurements were taken using reversible pendulums, and their uncertainty was 3 mGal (1 Gal = 1 cm/s^2) (Cook 1965).

IGSN-1971, the gravimetric system that combines gravitational field measurements throughout the world, was adopted by the General Assembly of the International Union of Geodesy and Geophysics in Moscow in 1971, Russia (Resolution 16).

IGSN-71 was originally based on 10 absolute measurements at 8 gravimetric sites with an FFA measurement uncertainty of 1 mGal.

In the 1970s, IGSN-1971 was expanded to 471 sites with 24,000 links measured using relative gravimeters and with 1200 absolute measurements using pendulum gravimeters. The uncertainty in the FFA determination was 0.1 mGal.

In 1986, G. Boedeker and T. Fritzer proposed a new International Absolute Gravity Basestation Network (IAGBN) within which the monitoring of variations in the gravitational field was to be carried out, but the intended set of sites was not implemented.

The emergence of transportable absolute ballistic gravimeters in the 1970s resulted in a significant increase in the accuracy of absolute FFA measurements, increasing their number, and made it possible to build a new global system of absolute gravimetric sites with an uncertainty in measuring absolute FFA values not exceeding 10 μGal.

It should be noted that the modern international database of absolute measurements AGrav developed and supported jointly by the German Federal Agency of Cartography and Geodesy and the International Gravimetric Bureau (BGI) (France) presents the results of more than 3300 absolute measurements by 50 absolute gravimeters with 1100 gravimetric sites (http://agrav.bkg.bund.de).

1.1.1 Types and Designs of Absolute Ballistic Gravimeters

At present, absolute FFA values can be measured by ABGs, in which laser interferometers measure the fall path of an MTB with an optical interferometer reflector attached to it or with cold atom interferometers for which the test objects are the clouds of cold atoms. The term “ballistic” is associated with the type of the free-fall path of the test body in a gravimeter. In such gravimeters, the free motion of the test body in the gravitational field is used, and the FFA is calculated from the measured path and time intervals from the test body ballistic motion equation (Cook 1965).

ABGs use two types of the test body trajectories: symmetric (a rise-and-fall trajectory such that the test body is thrown up and then falls down) and asymmetric (a free-fall trajectory such that the test body falls down freely). An example of a gravimeter with a symmetric trajectory is the device developed by the Italian National Institute of

Metrological Research (INRIM) (Germak et al. 2002). However, most of the modern ABGs have an asymmetric trajectory (please see Niebauer et al. 1995; Arnautov et al. 1974; Vitouchkine and Faller 2002; Vitushkin and Orlov 2014).

Figure 1.1 shows a schematic of a laser-interferometric ABG, which is implemented in various designs of gravimeters with an MTB, where a displacement laser interferometer is used to measure the free-fall trajectory.

At present, the relative uncertainty of the absolute FFA measurements using ABGs is about 10^{-9} (several microgal in absolute units). However, it should be noted that such a measurement uncertainty cannot be obtained in a single throw of the proof mass but is obtained in comparably long series of throws.

ABGs with an MTB normally include:

- a vacuum chamber with a ballistic unit, test body, and a vacuum system;
- a laser interferometer to measure the displacement of the test body in its free motion, passive or active vibration isolation system for the reference reflector, against which the laser interferometer measures the test body displacement;
- a frequency-stabilized laser of the laser interferometer;
- a path and time interval recording system, a reference rubidium frequency oscillator for the path and time interval recording system;

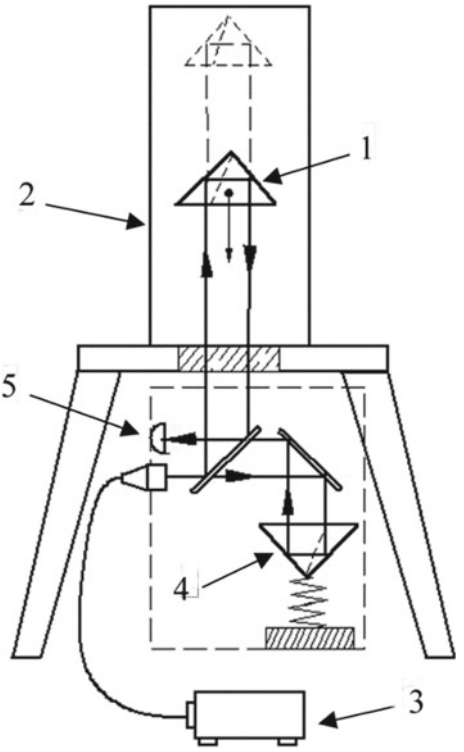

Fig. 1.1 A schematic of a laser-interferometric ABG with a macroscopic test body. *1*—test body with an integrated optical reflector in the measuring arm of the interferometer; *2*—vacuum chamber; *3*—laser; *4*—reflector placed on a vibroprotective (active or passive) suspension in the reference arm of the interferometer; *5*—optical interference signal photoreceiver

- a computer with software for processing the measured data and calculating the measured FFA value with the introduction of necessary instrumental and geophysical corrections;
- additional equipment that ensures ABG functioning.

The test body falls in vacuum chambers to eliminate or reduce air (residual gas) resistance.

In ABGs with an MTB, the laser interferometer measures the displacement of the test body, and the small time interval measuring system measures time intervals.

In ABG designs known, the length of the test body trajectory is from 2 to 50 cm, the time of the test body fall is approximately from 0.02 to 0.32 s.

The vacuum chamber contains a ballistic unit carrying out the entire cycle of the test body motion, including its free motion along a symmetric or asymmetric trajectory and catch of the test body at the end of the trajectory.

In rise-and-fall ABGs, the test body is thrown by a special catapult (for example, see Germak et al. 2002). In almost any design, there is an inevitable effect of mechanical recoil which is the source of undesirable mechanical oscillations of the reference reflector of the laser interferometer, with respect to which the intervals of the path traveled by the test body are measured.

In some free-fall ABGs (for example, in all gravimeters manufactured by Micro-g LaCoste, Inc., USA), in the ballistic unit of the gravimeter, the test body fall is accompanied by a simultaneous motion of the carriage on which the test body rests before the throw and which, having accelerated enough for the test body separation, then moves ahead of the test body during its fall (Niebauer et al. 1994). Such motion of the carriage causes parasitic mechanical excitations.

In the design of the GABL gravimeter of the Institute of Automation and Electrometry of the Siberian Branch of the Russian Academy of Sciences, the test body is held in its initial upper position with an electromagnet and brought to a fall by switching the electromagnet off (Arnautov et al. 1988); there are no mechanical excitations during the test body fall, but the effect of the residual magnetic field remains at the initial segment of the fall path.

In the design of the ABG-VNIIM-1 gravimeter (Vitushkin and Orlov 2011), the test body is held in the initial upper position with a special piezoceramics-based clamp, while there are no mechanical excitations or residual magnetic fields during the free fall of the test body.

The time interval between individual throws in some ABGs with MTB can be quite small: it does not exceed 0.3 s in an eccentric gravimeter (Vitouchkine and Faller 2002).

The equation for the test body motion that does not take into account the vertical gradient of the gravitational field is quite simple:

$$L = L_0 + V_0 T + \frac{gT^2}{2}, \tag{1.1.1}$$

where g is the free-fall acceleration, L is the path interval traveled by the free-falling test body during the time T, L_0 and V_0 are the test body coordinate and speed at the initial moment of time $T = 0$.

If $L_0 = 0$ and $V_0 = 0$, the following measurement equation can be used:

$$g = \frac{2L}{T^2}. \tag{1.1.2}$$

This expression gives simple estimates of the level of measurement uncertainties included in Eq. (1.1.2) path intervals L and time T needed to achieve the relative uncertainty 1×10^{-9} when calculating the absolute value of FFA g. It follows from formula (1.1.2) that the relative uncertainty of path interval measurements should not exceed 1×10^{-9}, and the relative uncertainty in measuring time intervals of the test body fall should not exceed 5×10^{-10}.

These values of uncertainties also define the requirements for the laser radiation wavelength (frequency) uncertainty and for the uncertainty in detecting interference fringes (IF) in the interferometer.

The inhomogeneity of the Earth's gravitational field (the presence of the vertical gradient W_{zz}, i.e., the second derivative of the gravitational potential W in the vertical coordinate z) complicates the equation of motion for a free-falling test body in a gravitational field with a vertical gradient:

$$\ddot{z} = g_{top} + W_{zz} z, \tag{1.1.3}$$

where g_{top} is the FFA at $z = 0$, W_{zz} is the vertical gradient of the gravitational potential W:

$$W_{zz} = \frac{(\partial^2 W)}{\partial z^2}.$$

The approximate solution of Eq. (1.1.3) for $W_{ZZ} \ll 1$ is as follows:

$$z(t) = z_0\left(1 + \frac{t^2}{2}\right) + v_0\left(t + \frac{W_{zz}t^3}{6}\right) + \frac{g_{top}}{2}\left(t^2 + \frac{W_{zz}t^4}{12}\right), \tag{1.1.4}$$

where z_0 and v_0 are the vertical coordinate and speed of the test body at $t = 0$.

In practice, based on Eq. (1.1.4) derived from Eq. (1.1.3), a vertical gradient correction is calculated for the solution of Eq. (1.1.1) when calculating the FFA value measured with an absolute ballistic gravimeter using the least squares method from the "path/time interval" pairs measured during a free fall of the test body.

The vertical gradient is usually measured using a relative gravimeter installed at various heights above the pedestal of the gravimetric site.

The vertical gradient correction is also used in reducing the measured FFA value g_{top} to a specified height above the pedestal. For a more accurate calculation of such

a correction, the FFA vertical distribution is measured with a relative gravimeter and approximated by a second-order polynomial.

The reduction of measurement results of various gravimeters with different heights inherent in their designs, where g_{top} is measured, is necessary; in particular, for the analysis of their measurement results during the comparison of absolute gravimeters.

It should be noted that, when measuring the accelerated fall of a test body with an interferometer, the frequency of IF counting rapidly changes from almost zero to several megahertz during the fall in tenths of a second, which requires high-speed recording of such signals with almost linear frequency modulation.

In ABGs, laser interferometers most commonly use helium–neon frequency-stabilized lasers at a wavelength of 633 nm (red region of the visible spectrum) and, more recently, solid-state lasers at a wavelength of 532 nm (for example, see Orlov and Vitushkin 2010).

Solid-state lasers have the following advantages:

(a) a shorter wavelength (which improves the measurement resolution, since the wavelength sets the displacement measurement scale increment: the smaller the increment (scale division), the greater the resolution);
(b) a higher radiation power (which also increases the resolution when measuring displacements due to an increase in the signal-to-noise ratio of the interference signal);
(c) a lower level of frequency noise, i.e., greater frequency stability at short time intervals (which is important when measuring an interference signal with a rapidly changing frequency).

For example, when measuring the free-fall path of a test body with a length of 10 cm (as in the gravimeter described in Vitushkin and Orlov 2014), the path length measuring uncertainty should not exceed 0.1 nm to provide a relative uncertainty of 10^{-9} when measuring the FFA.

In ABGs with an MTB, various versions of two-beam laser interferometers are commonly used (in particular, see Vitushkin et al. 2012). There is also a known case of using a multibeam interferometer in an ABG (Canuteson and Zumberge 1996).

In two-beam interferometers, the length of one of the arms (referred to as the reference arm) is constant; the length of the other measuring arm changes with the motion of the reflector attached to the falling test body. The test body motion is measured with respect to any element in the optical layout (Vitushkin et al. 2012) which represents the origin of a quasi-inertial coordinate system. Such a reference reflector is usually suspended using a passive (usually a long-period seismometer) or active (Niebauer et al. 1994, 1995) vibration isolation system to reduce undesirable vibrations caused by microseismic vibrations of the base.

Over a relatively short time while the test body is falling (tenths of a second), the IF recording system of a laser interferometer records hundreds of thousands of IFs. For example, in the ABG-VNIIM-1 gravimeter, about 350 thousand IFs are recorded within 0.1 s, each of which corresponds to a test body displacement for half the wavelength $\lambda = 532$ nm of the laser radiation Nd:YVO_4/KTP/I_2 of the laser.

This number of fringes is recorded in groups of scaled fringes (for example, 1024 IFs each) and, together with the recorded time intervals, they are used to calculate the measured FFA value using the least-squares method (LSM). Thus, hundreds of data pairs are used in the calculations with the use of the LSM.

Along with laser-interferometric ABGs with MTBs containing built-in optical reflectors, cold-atom ABGs (Bordé 2002; Peters et al. 2001; Merlet et al. 2009; Gillot et al. 2014) using matter wave interferometry (de Broglie wave interferometry) were developed. The latter are discussed in detail in Sect. 5.3. Cold, i.e. slowed by laser pulses, cesium or rubidium atoms controlled by laser pulses, when absorbing or emitting photons, split or merge while forming equivalents of beam splitters of a classical interferometer, where atomic waves are split or recombine. When propagating in the gravitational field in two arms of an atomic interferometer, atomic waves in one of the arms of the interferometer gain an additional phase shift proportional to the FFA value and the propagation time squared. The interference fringes of such an interferometer can be recorded by measuring the relative population of the states of two recombined atomic beams using induced laser fluorescence.

1.1.2 Sources of Uncertainties and Corrections in Measurements with Absolute Ballistic Gravimeters

When calculating the FFA from measured pairs of path and time intervals, instrumental and geophysical corrections to the measurement results (common to almost all designs of such ABGs) should be introduced in ABGs with an MTB.

Instrumental corrections currently known and common to all types of ABGs include corrections for the following factors:

- deceleration of the test body by residual gases in the vacuum chamber;
- interaction of the falling test body with the gravitational field of the ABG itself;
- interaction of the falling test body with the gradient of the geomagnetic field and the magnetic field of the ion pump (if used in the design);
- effects associated with the finite speed of light;
- diffraction effects during the propagation of a laser beam in the interferometer.

Geophysical corrections are made for the Earth's gravitational tides, the oceanic load and the motion of the Earth's poles.

The following components are taken into account when calculating the total instrumental uncertainty of an ABG:

- uncertainty of the wavelength (frequency) of laser radiation;
- uncertainty of the frequency of the reference rubidium oscillator for the path and time interval measuring system;
- uncertainty due to the choice of the initial and final reference interval of the path from the array of all measured intervals for calculating the FFA using the LSM method;

- uncertainty due to phase delays in electronics;
- uncertainty of the reference height, for which the FFA value is measured;
- uncertainty of the laser beam verticality in the measuring arm of the interferometer;
- uncertainty due to atmospheric pressure variations when determining the correction for the deviation from the nominal value of atmospheric pressure at a gravimetric site;
- uncertainties in the calculation of the above instrumental corrections.

In rise-and-fall ABGs, the influence of such sources of uncertainty as resistance of the residual gas is significantly reduced, and this was used in the initial development of gravimeters when it was impossible to achieve a sufficient degree of vacuum. Later, when ABGs were developed, asymmetric trajectory designs were used, which made it possible to avoid the recoil effect when the test body was thrown up with special catapults.

As examples, we note that the extended (i.e., ensuring a given interval of values with a probability of 95%) total instrumental uncertainty of the ABG-VNIIM-1 gravimeter (Vitushkin and Orlov 2014) and the value of uncertainty reported on the company website for the FG5 gravimeter manufactured by Micro-g LaCoste, Inc., do not exceed 2 μGal. The experimental standard deviation of the measurement result depends on the microseismic conditions at the gravimetric site.

1.1.3 Metrological Assurance of Absolute Gravimeters

ABGs measure the free-fall acceleration. Acceleration is a derivative physical quantity; and an absolute gravimeter should be basically supplied with units of length and time in the respective measurement ranges, which can be done by calibrating the interferometer of the gravimeter with respect to the displacement and the frequency of the laser and the reference frequency oscillator.

In practice, a displacement laser interferometer integrated into an ABG is not calibrated in terms of length unit, like ordinary industrial displacement laser interferometers. Designs of gravimeters with laser interferometers that take measurements in vacuum are not suitable for direct calibration of these interferometers.

The interferometer laser is normally calibrated by frequency (wavelength). However, a unit of length is realized with a laser interferometer rather than with a laser, which is only a source of radiation for the interferometer and generates an infinite traveling electromagnetic wave. Without going into details, it is only worth mentioning that without additional elements (mirrors, photodetectors, etc.), such a wave cannot realize a unit of length in accordance with its definition, i.e. indicate two material points in space between which there is a unit of length or a part of it or two successive positions of a material point as it moves, similar to what, for example, occurs in a gravimeter interferometer that measures the motion of a falling reflector.

As for the calibration of the time interval measurement system, in practice, only the rubidium frequency generator (the reference oscillator for the time interval measurement system) is calibrated by frequency. Such calibration confirms the required level of 5×10^{-10} of the rubidium generator relative frequency uncertainty but not in the entire frequency range of interest. This calibration is normally done at time intervals of tens of minutes, and the question of the metrological characteristics of the measurement system for small (millisecond and microsecond) time intervals for the passage of the above reference path intervals remains open.

Calibration of the laser frequency (wavelength) and the rubidium oscillator frequency is necessary but not sufficient to determine the metrological characteristics of an ABG.

Thus, to determine the metrological characteristics of an ABG when measuring the FFA, it is required to calibrate or verify ABGs using standards in gravimetry as in the case of any other measuring instruments.

ABGs, as well as gravimetric sites and gravimetric networks can be standards in gravimetry. In this case, the FFA values at gravimetric sites and in gravimetric networks should be measured in advance. In some cases, the FFA values at gravimetric sites and in gravimetric networks vary with time as they experience non-tidal changes in the gravitational field.

ABGs, which are, in fact, the measurement standards of the acceleration unit in gravimetry, have the highest metrological characteristics.

Note that a gravimetric site is referred to as the "gravity standard" and an ABG as the "measurement standard in gravimetry" (Vitushkin 2011).

The ABG with the studied metrological characteristics belonging to a National Metrological Institute (NMI) is the officially recognized national primary standard. It is these standards that are involved in the international ABG comparisons organized by the International Committee of Weights and Measures (CIPM) or regional metrological organizations (RMO).

In the Russian Federation, the national primary special standard for the acceleration unit in gravimetry GET190-2011 was created and is used in D. I. Mendeleev All-Russian Research Institute for Metrology (Vitushkin, Orlov 2014).

1.1.4 International Comparisons of Absolute Gravimeters

The first international comparisons of absolute gravimeters were organized following the Recommendation adopted at the XVII General Assembly of the International Union of Geodesy and Geophysics in Canberra (December 1979).

Comparisons of six ABGs built by the International Bureau of Weights and Measures (BIPM), as well as in China, Japan, Russia, and the USA, were organized by the BIPM and the President of Special Research Group 3.40 of the International Association of Geodesy (IAG), associate member of the USSR Academy of Science, Yu. D. Boulanger and conducted in Sèvres (France) in 1980–1981.

Later on, such comparisons were carried out by the BIPM almost every four years. A total of 22 absolute gravimeters were used during the 8th International Comparison of Absolute Gravimeters (ICAG) in 2009.

The organization of ICAGs was improving in the course of time; a technical protocol describing the order of their organization, admission criteria for instruments to participate in comparisons, the procedure for measuring and processing their results, as well as the rules for publishing the results of comparisons were developed and refined. Since 2001, ICAGs have been conducted in accordance with the rules for the organization of comparisons recommended by the international Mutual Recognition Arrangement (MRA) for calibration certificates and measurement results signed by 101 national metrology institutes and organizations responsible for the metrological assurance of any kinds of measurement.

Until 2009, almost all organizations that had ABGs were allowed to participate in the ICAG, and the results of measurements with all gravimeters were used in calculating the result of comparisons (the average FFA values obtained with all gravimeters at gravimetric sites where measurements were taken, the uncertainties of those average values, as well as the degree of equivalence of the gravimeters used which was measured by their deviations from the average values obtained by all gravimeters).

More than 90% of ABGs used in the world are commercial; all of them are produced by one company in the USA. These gravimeters do not have any calibration certificates; therefore, the organizations that had them sought to take part in the ICAG, as well as in comparisons organized in the underground laboratory in Walferdange (Luxembourg) (Jiang et al. 2012) in order to determine metrological characteristics of their instruments.

Due to the increase in the number of ABGs in the world, it will be almost impossible to conduct their simultaneous comparisons in one laboratory in the future; therefore, it is necessary to use a conventional practice in metrology: to recognize national standards and arrange calibrations of ABGs. It should be noted that such a system in the field of absolute gravimetry has not been organized until recently.

In 2009, ICAGs were organized as key comparisons according to the MRA rules (see CIPM MRA-D-05 "Measurement Comparisons in CIPM MRA" at http://www.bipm.org/en/cipm-mra/cipm-mra-documents/), according to which only gravimeters belonging to the NMI are allowed to be compared. As an exception, comparisons of ABGs from other organizations were carried out as pilot studies in parallel with the key comparisons in the BIPM. Meanwhile, only the results of 11 NMI gravimeters were used when calculating the official results of comparisons. These results were published in the official key comparison database on the BIPM website (http://www.kcdb.bipm.org).

The results of pilot studies can be published in scientific journals, but they cannot serve as grounds for issuing calibration certificates. All the results of the ICAG 2009 were published in Jiang et al. (2012).

The increasing IAG requirements for the reliability of absolute measurements of the gravitational field led to the development and adoption of the "Strategy of the Consultative Committee for Mass and Related Quantities and IAG in Metrology in

Absolute Gravimetry" (published in IAG Proceedings of the 2011–2015 (Travaux of the IAG 2011–2015)). The purpose of this document is to draw the attention of geodetic and geophysical communities to the need to develop a system of metrological assurance for absolute gravimeters according to the classical hierarchical procedure with primary standards, calibrations and verifications of ABGs. Various ABG calibration procedures are considered: direct comparison with the primary ABG standard or by measuring the FFA using the gravimeter being calibrated at a gravimetric site where the FFA value was previously measured using the ABG standard, and comparing the measurements using the gravimeter being calibrated with the result obtained with the ABG standard. The highest reliability of this calibration method for the previously measured FFA value can be ensured by continuous monitoring of the FFA time variations using an additional gravitational field measurement tool—a relative superconducting gravimeter (SG) (see an example of using a cryogenic gravimeter during ABG comparisons in Francis et al. 2014). Relative SGs allow for continuous measurements of variations in the gravitational field with a resolution of one hundredth of a microgal over many months and years. SGs are used to measure time variations of the FFA.

1.1.5 Comparisons of Absolute Gravimeters: The Results

A clear understanding of metrological characteristics of modern ABGs is provided by the results of key comparisons organized by the CIPM and key regional comparisons organized by RMOs (EURAMET—Europe RMO, NORAMET—North America RMO, APMP—Asia–Pacific RMO, etc.). The results of the 2009 key ABG comparisons (BIPM) and the 2013 key comparisons (Walferdange), as well as the results of the 2013 key European comparisons (Walferdange) will be presented here.

It should be noted that after ICAG-2009, the BIPM decided to stop the organization of comparisons of absolute gravimeters in the bureau itself because the procedure for organizing comparisons had been well-elaborated and they could now be organized by other NMIs. In 2013, the key ABG comparisons organized by CIPM along with ABG pilot studies took place in the underground laboratory in Walferdange. Comparisons were also held in China in the laboratory of the National Metrology Institute in the Changping campus in 2017.

Figure 1.2 presents the results of key comparisons of CCM.G-K1 ABGs (Jiang et al. 2012; Arias et al. 2012). Note that the reports of all key comparisons are available online in the key comparison database on the BIPM website.

Figure 1.3 shows the results of the key comparisons of CCM.G-K2 ABGs (Francis et al. 2015). Figure 1.4 shows the results of the key European comparisons of ABGs conducted under the authority of the regional metrological organization EURAMET (Francis et al. 2014).

In all the figures, the uncertainty bars represent the extended total uncertainty of each result.

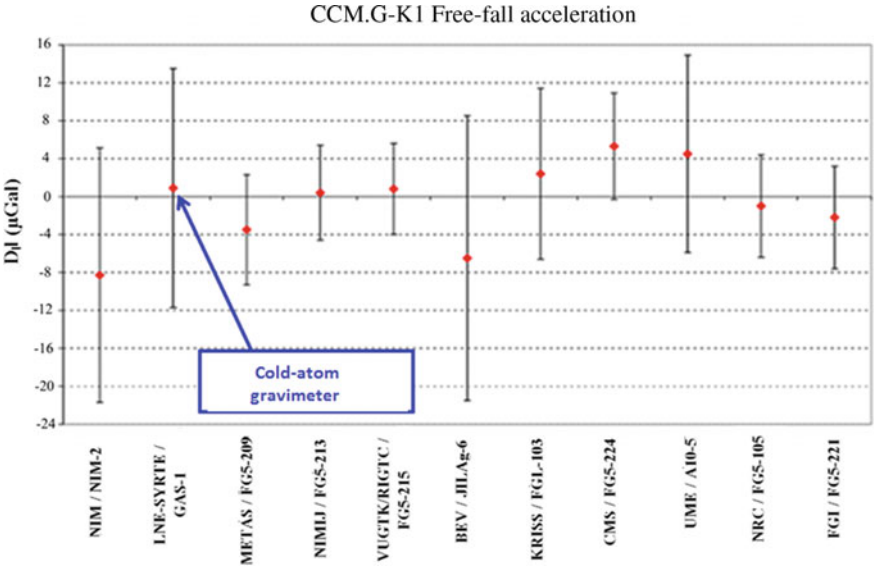

Fig. 1.2 The results of the key comparisons of CCM.G-K1 absolute gravimeters (2009, BIPM, Sèvres, France). The vertical axis shows the deviations from the key comparison reference value (in micrograls) for the result of each gravimeter; the horizontal axis shows the type and number of the gravimeter and the organization to which it belongs

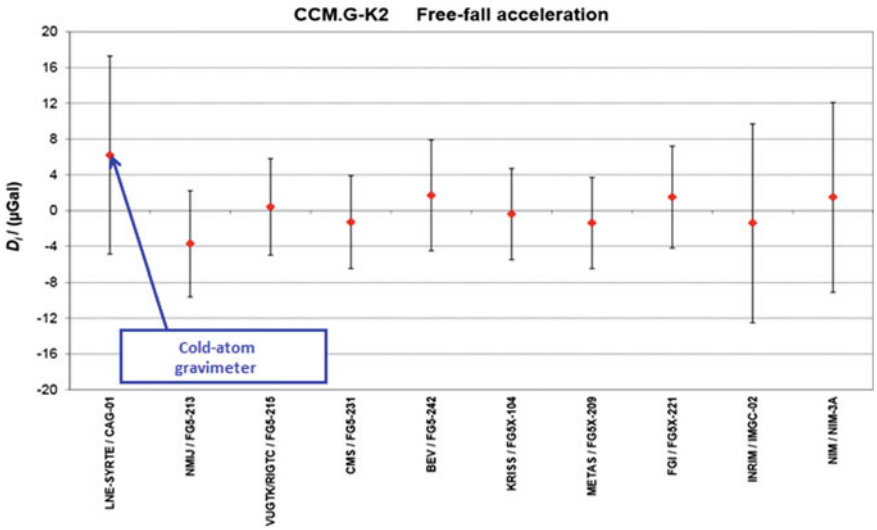

Fig. 1.3 The results of the key comparisons of CCM.G-K2 absolute gravimeters (2013, Walferdange, Luxembourg). The vertical axis shows the deviations from the key comparison reference value in micrograls for the result of each gravimeter; the horizontal axis shows the type and number of the gravimeter and the organization to which it belongs

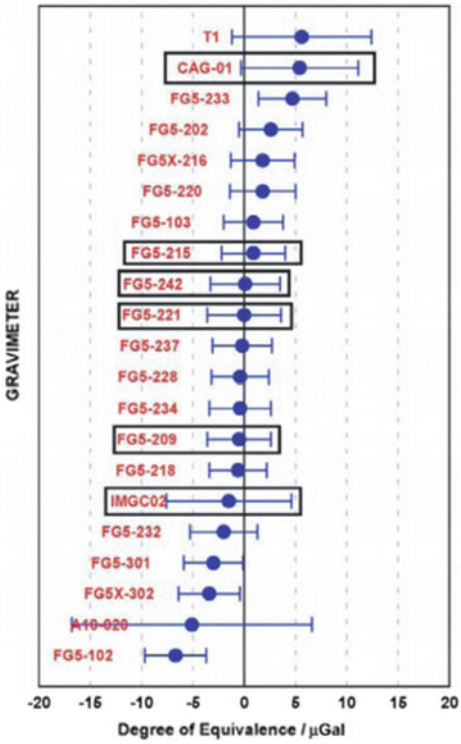

Fig. 1.4 The results of the regional European comparisons of ECAG-2011 absolute gravimeters (2011, Walferdange, Luxembourg). The vertical axis shows the type and number of the gravimeter; the horizontal axis shows the degree of equivalence of the results of each gravimeter in microgals with the reference value of comparisons. The names of the NMI gravimeters used in the key comparisons are shown in frames. The remaining gravimeters were used in pilot studies as part of the general comparison campaign

As can be seen from the figures, the comparisons were carried out mainly for FG5 and A10 gravimeters, both manufactured by Micro-g LaCoste, Inc. There were only three gravimeters from other organizations: the IMGC gravimeter (Italy), the CAG-1 cold atom gravimeter (France), and the T1 gravimeter (China).

Note that the uncertainty of FFA measurements with the use of a cold-atom gravimeter is currently slightly greater than the uncertainty of the best laser-interferometric ABGs with MTB. The A10 gravimeter is designed for field measurements and has a greater uncertainty than the FG5-type gravimeters.

1.1.6 Practical Applications of Absolute Free-Fall Acceleration Measurements

Currently, at least two hundred transportable ABGs are used in the world. Most of them were manufactured by Micro-g LaCoste, Inc.

ABG allows measuring the FFA in any place with no reference to any sites of gravimetric networks. Of course, the accuracy of measurements depends on the level

of microseismic conditions at the gravimetric site which determines the random component of the uncertainty.

The emergence of a significant number of such ABGs allowed changing the measuring strategy of gravimetric networks and their use (for example, see Boedecker 2002).

Transportable ABGs made it possible not only to measure the FFA at different gravimetric sites when creating gravimetric networks, but also take repeated measurements to monitor temporal variations of the gravitational field.

The combination of an ABG and an SG allows for almost continuous monitoring of the gravitational field. Starting in 1997, about 30 gravimetric sites on Earth, including the Antarctic Syowa station, conducted monitoring of the gravitational field variations using an ABG and an SG in the framework of the IAG International Global Geodynamic Project. This project has currently been reformed into the permanent IAG IGETS service and continues developing.

Transportable ABGs are used, for example, in hydrogeology for prospecting and monitoring of water reserves, as well as in engineering geology.

Studies are conducted on the possibility of using laser-interferometric ABGs and cold-atom ABGs on moving bases in airborne and marine gravimetry (Baumann et al. 2012; Sokolov et al. 2017).

The concept of joint use of absolute and relative gravimeters installed on a gyrostabilized platform for marine gravimetry was proposed in the early 2000s. It is not necessary to conduct continuous FFA measurement using ABGs. ABGs can be used for periodic calibration of relative gravimeters when the vessel stops at a pier or on a calm sea. It should be noted that an eccentric-type gravimeter with a short free-fall path of the test body of about 2 cm allowing for 200 drops per minute can be successfully used in airborne and marine gravimetry (Vitouchkine and Faller 2002).

1.1.7 Conclusions

Ground-based absolute gravimetry is finding increasing use for national and international projects in modern geodesy such as the Global Geodetic Observing System of the International Association of Geodesy.

In international comparisons of absolute gravimeters, the uncertainties in measuring absolute FFA values may not exceed 1 μGal at gravimetric sites where many ABGs are compared and a great number of measurement series are carried out (for example, more than 60 12-h series of measurements at 5 gravimetric stations of a gravimetric site in comparisons in BIPM in 2009 (Jiang et al. 2012)). The FFA values and their uncertainties obtained in such comparisons are most reliable. This circumstance, as well as the increasing number of absolute gravimeters, the development of their metrological assurance system, and the distribution of comparisons to other continents (North America, Asia) provided the basis for creating a new global system of absolute gravimetric sites outlined, in particular, in Crossley et al. (2013).

Key comparisons of gravimeters were carried out in Europe; regional comparisons of gravimeters were carried out in North America and China. Gravimetric sites where comparisons are made will be used as the basis for a new global system.

In 2015, the International Association of Geodesy held the 26th General Assembly of the International Union of Geodesy and Geophysics in Prague, where they adopted Resolution 2 "For the Establishment of a Global Absolute Gravity Reference System", specifying the FFA value measurement uncertainty not higher than 10 μGal for the reference sites of the system, i.e., 10 times less than in the IGSN-1971 system.

The development of absolute gravimetry in the Russian Federation requires the development of new ABGs, including field gravimeters and ABGs adapted to measurements on moving bases.

Both types of absolute gravimeters—MTB laser interferometer gravimeters and cold-atom gravimeters—will certainly find their applications; besides, they can be improved to reduce their overall dimensions, increase their reliability and reduce their measurement uncertainty.

1.2 Chekan-Series Relative Gravimeters

For more than 50 years, Concern CSRI Elektropribor has been working on creation of gravimetric systems for measuring gravity from moving carriers. This work started in 1967 with the creation of GAL-M, a gravimeter with a photo-recording system, at the Schmidt Institute of Physics of the Earth under supervision of E.I. Popov. At the same time, the Cheta gyro platform was developed at CSRI Elektropribor for stabilization of this gravimeter on surface ships (Popov 1959). On the basis of these developments, the MGF gravimeter was created and adopted for the Navy supply by order of the Navigation and Oceanography Department of the Russian Ministry of Defense. That was the first Russian gravimetric system intended for marine gravity surveys in the open ocean in 1970–1980.

Cheta-AGG, the first automated marine gravimetric system (chief designer A.D. Bereza) with a specialized digital computer, was created by order of the Navy in 1982 and was produced in series (Zheleznyak and Popov 1982). This system was installed on more than ten research vessels. For many years, it was the main means of route and areal gravity surveys and was used until the beginning of the twenty-first century both on Navy ships and on civilian vessels. Under the World Gravity Survey Program, the Cheta-AGG system was used to take a large amount of measurements in the Atlantic, Indian, and Pacific Oceans, the Black and Barents Seas (Zheleznyak et al. 1983).

The development of the Skalkochnik, the third-generation system (chief designer L.P. Nesenyuk (Pamyati professora L.P. Nesenyuka 2010)), was aimed at improving the performance characteristics through the use of the latest computing aids of the day. It was the first to use a personal computer both for data acquisition and office processing of marine survey results. In 1994, the system passed the Navy tests and was put into operation. Unfortunately, the difficult economic situation in the country at the end of the twentieth century did not allow for full-scale production of the

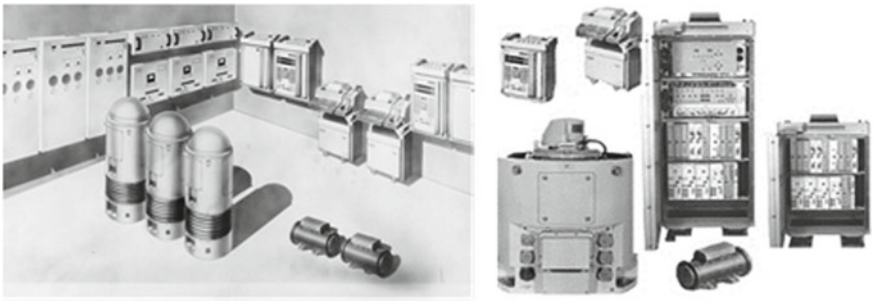

Fig. 1.5 General view of the second- and third-generation systems

Skalochnik system. Only a prototype model was made which was upgraded in 2001 and used by the Navy hydrographic service until 2006 (Nesenyuk and Elinson 1995; Bikeeva et al. 2007). A general view of the Cheta-AGG and Skalochnik systems is shown in Fig. 1.5.

The work on the construction of the fourth-generation system began in the late 1990s, when the Chekan-A prototype system was made in 1998 and its marine tests were carried out in 1999 combined with a commercial marine geophysical survey conducted by the Norwegian company NOPEC (Sokolov et al. 2000). The success in the accomplishment of this work allowed CSRI Elektropribor to fulfill the research on design and development of a mobile gravimeter (chief designer L.S.Elinson). As a result, the fourth-generation Chekan-AM system was developed in 2001 (Sokolov 2003).

Today, the Chekan-AM mobile gravimeter is one of the main instruments used to measure gravity from sea vessels and aircraft (Kovrizhnykh and Shagirov 2013; Atakov et al. 2010; Lygin 2010; Forsberg et al. 2013; Barthelmes et al. 2013; Peshekhonov et al. 2020). More than 50 gravimeters have been manufactured at CSRI Elektropribor and delivered to Russian and international organizations. Table 1.1 shows how the global geophysical equipment market has been developing: from marine surveys abroad to airborne gravity surveys in Russia.

The geography of the gravity surveys carried out with the Chekan-AM mobile gravimeter shown in Fig. 1.6 covers the waters of all oceans and shelf zones in all continents. Chekan-AM has been used in geophysical surveys from the Antarctic to the North Pole (Krasnov et al. 2014a).

In 2013, a new system Shelf-E was developed (chief designer A.V. Sokolov) on the basis of the Chekan-AM mobile gravimeter (Krasnov et al. 2014b). The system has improved accuracy and performance characteristics. Its serial production started in 2015, so that these systems are supposed to replace Chekan-AM mobile gravimeters in the near future. This chapter is devoted to the description of the principle of operation, design features, and technical characteristics of the Chekan-AM and Shelf-E systems.

Table 1.1 Development of the global geophysical equipment market

Country	Years in operation
Marine gravity surveys	
Norway	1999 up to the present
Great Britain	2003–2012
Russia	2005 up to the present
China	2007 up to the present
USA	2008 up to the present
Kazakhstan	2010–2011
Airborne gravity surveys	
Germany	2007 up to the present
Norway	2007–2011
Russia	2007 up to the present

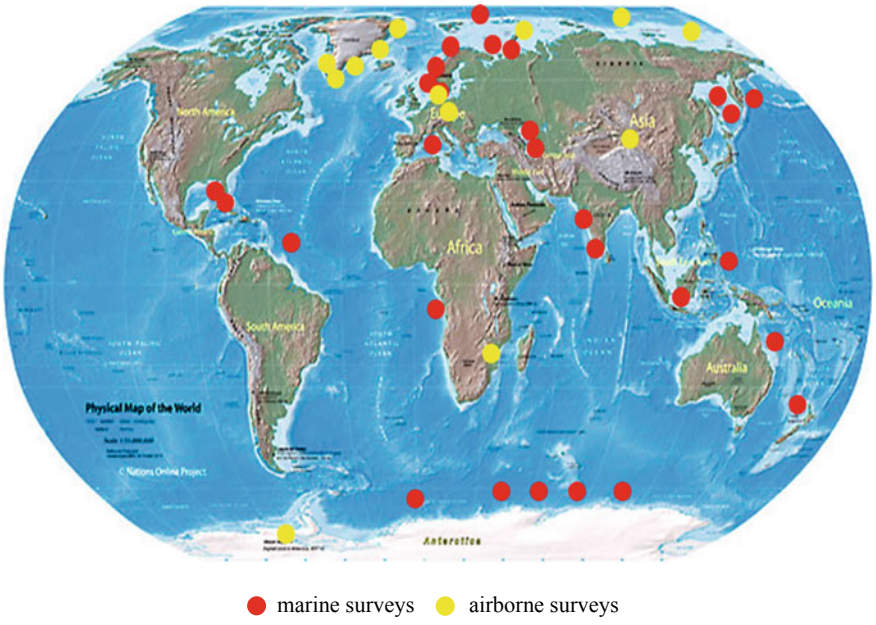

Fig. 1.6 Geography of the gravity surveys carried out with the Chekan-AM mobile gravimeter

1.2.1 Gravimeter Parts

The main distinction of the Chekan-AM mobile gravimeter from the systems of previous generations is its higher accuracy and performance characteristics along with a multifold decrease in its weight and overall dimensions (Blazhnov et al. 2002). The development of electronic components made it possible to combine the

Fig. 1.7 Chekan-AM gravimeter

gravimeter sensing element (GSE), a biaxial gyro platform, and a control device based on microcontrollers in a single device.

The structure of the Chekan-AM mobile gravimeter is shown in Fig. 1.7. The basis of the system is a gravity sensor (GS) with a double quartz torsion-type elastic system installed in a two-axis gyro platform (GP) designed to keep its sensitive axis in the vertical direction on a moving carrier.

A thermostabilization device (TD) is placed in the upper part of the GP housing in order to maintain a constant temperature inside it. The TD is controlled by the UMT unit external to it.

The delivery set of the Chekan-AM gravimeter also includes an industrial-grade personal computer with real-time data acquisition and primary processing software and programs for diagnosing the parts of the system. The system is powered by a voltage of 27 VDC generated by AC/DC converter from an onboard mains of 220 V/50 Hz via a SMART-UPS uninterruptible power supply.

Figure 1.8 shows a block diagram of a mobile gravimeter for marine and airborne versions of the system. The main difference between these versions is real-time software since continuous correction of GP is necessary when taking measurements from aircraft. GP correction is carried out with the use of external information on the speed and position of the carrier; therefore, when conducting airborne gravity surveys, it is necessary to ensure data reception from a GNSS receiver which is not included in the system.

Another feature of airborne gravity surveys is the absence of a standard 220 V/50 Hz mains onboard aircraft. Therefore, for the airborne version of the

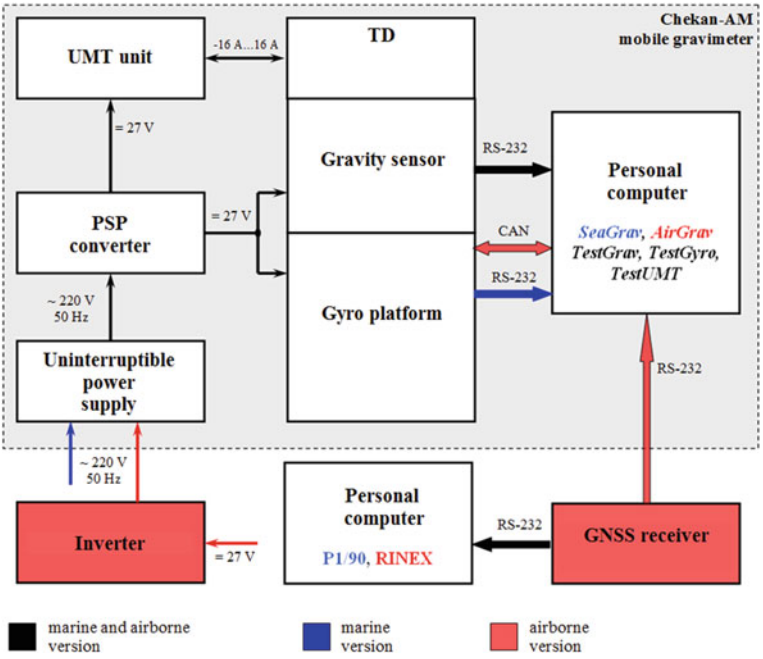

Fig. 1.8 Block diagram of the Chekan-AM gravimeter

system, an additional inverter is required, which is not included in the gravimeter instrumentation.

Navigation data recorded by the GNSS equipment is used for the office processing of marine and airborne gravity measurements. For this purpose, the navigation and gravimetric data are synchronized on a time scale.

The structure of the Shelf-E gravimeter is even more simplified: there are no secondary power supply and no GP thermal regulation system. It has just a gyro platform with a gravity sensor and a laptop. The system is connected with one cable; data can be transmitted via a wireless communication channel based on Wi-Fi technology (Peshekhonov et al. 2015).

1.2.2 Gravimeter Sensing Element

The gravimeter sensing elements used in the CSRI Elektropribor systems were created on the basis of a double quartz elastic system of the gravimeter (GES). Its principles of construction and first designs were developed by the Schmidt Institute of Physics of the Earth of the Russian Academy of Sciences (Zheleznyak and Popov 1984). Later on, the GES design and manufacturing technology were improved jointly by both enterprises and in parallel with the construction of new gravimetric

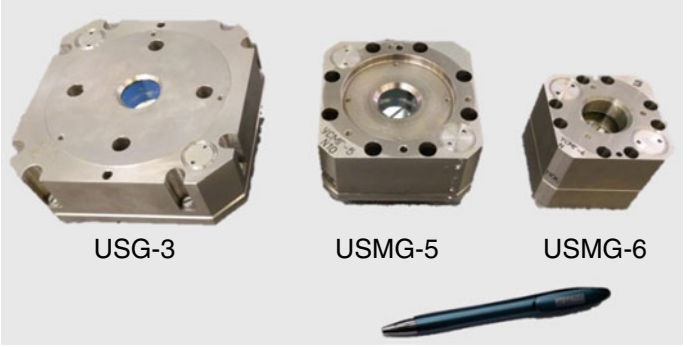

Fig. 1.9 Gravimeter elastic systems

systems. Figure 1.9 shows the GESes installed in the third- and fourth-generation systems: USG-3 (Skalnochnik), USMG-5 (Chekan-AM), and USMG-6 (Shelf-E).

Structurally, the gravimeter elastic system consists of two torsion systems made of very-high-purity quartz glass contained in a common housing. The torsion systems are turned 180° in a horizontal plane relative to each other. The housing of the elastic system is filled with polymethylsiloxane fluid to provide its damping, thermal compensation, and pressure isolation. As a material, quartz has a number of advantages: it is manufacturable; under deformation, it follows the Hooke law until it fractures; and it has a positive thermoelastic coefficient, which allows ensuring thermal compensation due to the use of simple construction.

The elastic systems of the Chekan-AM and Shelf-E gravimeters are designed as all-welded structures. They have no adjusting elements, owing to which its reliability is significantly increased. The advanced technology for fabrication of elastic systems provides a high degree of quartz system identity both in sensitivity and in damping. Nonidentity of the two systems does not exceed 0.2%, which almost completely eliminates the error caused by the cross-coupling effect, which is due to the mutual influence of vertical and horizontal accelerations and is less than 0.2 mGal for a double system when rolling-induced accelerations are up to 1 m/s^2. The elimination of the cross-coupling effect is an important advantage of the GES as compared with other types of gravimeter torsion sensing elements (Panteleev 1983).

Throughout these years, it has been possible to make the elastic system completely sealed, reduce its overall dimensions by several times, simplify the manufacturing technology, and start its manufacturing at CSRI Elektropribor (Sokolov et al. 2021).

GSE principle of operation is shown in Fig. 1.10. The output value of the elastic system is the angle of rotation ϕ of the pendulum lever which changes by the magnitude of the torsional angle $\Delta\phi$ in the presence of gravity increment δg in accordance with the following expression:

$$\Delta\phi = k_1 \cdot \delta g, \tag{1.2.1}$$

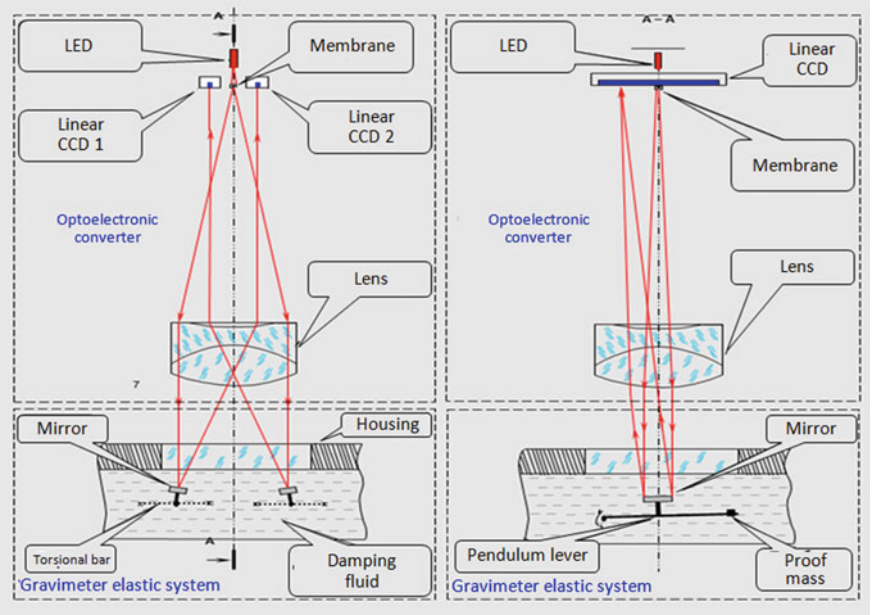

Fig. 1.10 GSE principle of operation

where k_1 is a coefficient defining sensitivity of the elastic system.

To measure the angle of rotation of the pendulums, the latter have mirrors welded to them. Their planes are parallel to the axes of the pendulums and turned at a small angle in the opposite direction. Protective glass with two pairs of optical wedges on it is installed in the upper part of the housing. An optoelectronic converter (OEC) is located above the GES housing. It includes a light source, an autocollimation mark placed in the focal plane of the lens, and two light receivers whose function is performed by linear-type charge-coupled devices (CCD) (Bronstein et al. 2000).

Structurally, the CCDs are separated by a distance corresponding to the angle of rotation of the pendulum mirrors in the direction perpendicular to the scanning. The light source provided by a pulsed LED with the maximum spectral brightness at a wavelength of $\lambda = 626\ \mu$m is placed on the optical axis of the lens between the CCD arrays.

Using the OEC, the pendulum angle of rotation is converted into a linear displacement of the luminous mark along the light-sensitive area of the CCD array. The CCD arrays are directed along the displacement of the slot autocollimation image, and their housings are turned 180° relative to each other. The change in the ΔL position of autocollimation images is proportional to the change in the torsional angle according to the formula:

$$\Delta L = 2nf\Delta\phi, \tag{1.2.2}$$

where n is the refraction index of the damping fluid; f is the focal length of the lens.

The signals from CCD arrays are processed using a video signal to code converter, on which they are directly mounted. The control inputs of both CCDs are connected to a single control signal shaper connected via an optical coupler with an external sync pulse receiver. The signal shaper is also connected to a control signal frequency synthesizer which is connected to a frequency reference oscillator.

The current position of the autocollimation image is calculated based on the energy center using programmable logic devices. Readings m_1, m_2 representing the numerical equivalent of the angle of rotation of the GES pendulum are transmitted via a serial interface to a personal computer with a frequency of 10 Hz (Sokolov 2004).

To maintain a constant temperature, the GES is installed in a thermostat. The temperature inside the thermostat is stabilized by controlling four pairs of thermoelectric converters mounted on the side walls of the thermostat housing made of an aluminum alloy with high thermal conductivity.

Thermoelectric converters are based on the Peltier effect, and the temperature point can be adjusted in the range from +30 to +35 °C. The output power of the thermostat control board is 20 W, which makes it possible to stabilize the GES temperature when the ambient temperature changes relative to the specified temperature point in the range of ±15 °C with an error of 0.01 °C in the steady state. Despite its high accuracy, the GSE thermal regulation system of the Chekan-AM gravimeter has two disadvantages such as a high temperature of thermostabilization and a considerable transient process when the ambient temperature changes.

The main research on modernization of the gravity sensor for the Shelf-E system was aimed at reducing its instrumental error (Krasnov et al. 2014c; Sokolov et al. 2008). This required the development of a new GES and led to a substantial redesign of the gravity sensor (Fig. 1.11). The overall dimensions of the new GES were made 1.5 times smaller than those of the Chekan-AM gravimeter. The dimensions of the quartz frames, torsional bars, pendulums, and other elements of the quartz system were significantly reduced. To extend the range of disturbing accelerations, the polymethylsilixane fluid with a viscosity of 65,000 cPs, which is more than 3 times higher than that of the fluid in the sensing element of the Chekan-AM gravimeter was used to damp the pendulum motion in the new elastic system.

The information about the angular position of the GES pendulums is also obtained using the OEC, but the new OEC uses a specialized 5-megapixel black and white CMOS camera as a photoreceiver. To reduce the size of the gravity sensor, the focal length of the new optoelectronic converter was made half that of the Chekan-AM gravimeter. This did not lead to deterioration in the autocollimator resolution because the pixel size of the CMOS sensor used is only one-third that of the previously used CCD array (Berezin et al. 2004).

A fundamentally important design feature of the new gravity sensor in comparison with all previous versions is that the GES with the OEC are placed in a single thermostat. This made it possible to significantly reduce the effect of changes in the ambient temperature on the gravimeter readings. Another important advantage of the new thermostat is a substantial reduction of the stabilization temperature

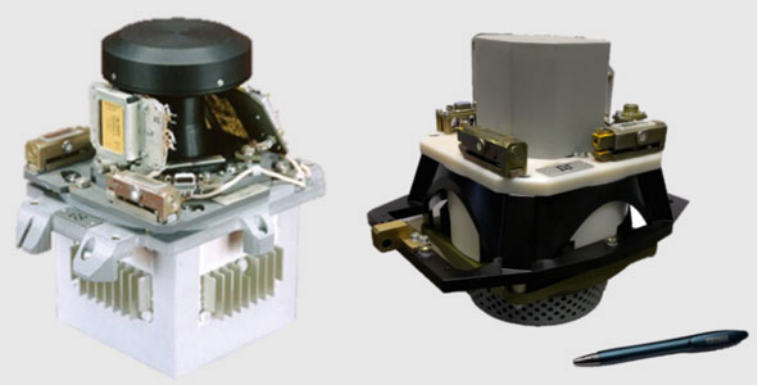

Fig. 1.11 General view of Chekan-AM and Shelf-E gravity sensors

of the sensing element from +35 to +15 °C. As a result, the drift of the Shelf-E gravimeter was reduced several times below that of the Chekan-AM gravimeter. Also, for the first time, the new elastic system and optoelectronic converter are fixed rigidly together without any additional adjustment elements, which made the gravity sensor assembly and adjustment much simpler and increased long-term stability of the gravimeter sensitive axis.

1.2.3 Biaxial Gyro Platform of the Gravimeter

According to its principle of operation, the gyro platform is a biaxial gyrostabilizer with accelerometric correction of the gyroscope rotor positions (Chelpanov et al. 1978). The GP operation is explained by the schematic presented in Fig. 1.12, which shows a biaxial gimbal suspension consisting of outer and inner rings. The orientation of the axes of the gimbal suspension on a vehicle is set in such a way that rolling of the vehicle (θ_K) is compensated for by the outer ring axis, and its pitching (ψ) is compensated for by the inner ring axis. The gravity sensor is installed on the inner ring of the GP together with the sensing elements of the stabilization system: two floated one-degree-of-freedom gyroscopes, two AK10/4 accelerometers, and an azimuth fiber optic gyroscope (FOG).

The sensitive axis of the gravity sensor is kept in the vertical direction using a gearless servo drive and an accelerometer correction system of the gyroscopes. The gearless servo drive on each axis is made on the basis of MK-BSS single-channel microcontrollers that control the position of the outer and inner rings, compensating for the mismatch between the gyro pick-off and its housing.

The accelerometer correction system in the MK-FG microcontrollers is designed to bring the gyroscope precession axes to the vertical. The sensors of the correction system are accelerometers whose sensitive axes are parallel to the axes of the

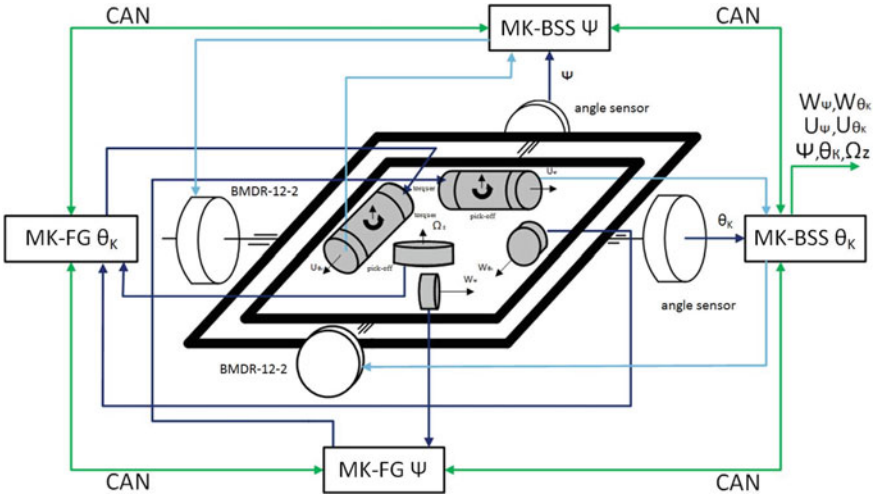

Fig. 1.12 Schematic of the gyro platform

gimbal suspension. Owing to this arrangement, each accelerometer corrects the position of the gyroscope along one of the stabilization axes. During airborne gravity surveys, satellite navigation data are additionally used in the accelerometer correction system, which significantly reduces stabilization errors during the aircraft maneuvers (Krasnov and Sokolov 2009).

To ensure the GP start-up and operation on a moving base, it has different operation modes: electric caging, rough and precision stabilization. In the electric caging mode, the position of the axes of the gimbal rings is matched with the position of the GP housing. In this mode, the servo drive is operated by signals from angle sensors located along the suspension axes.

In the rough stabilization mode, the gimbal rings are stabilized in the horizon plane by the signals coming directly from the accelerometers. This mode is necessary for the gyro spin-up.

After the gyro spin-up, the GP switches to the precision stabilization mode, in which the gyro pick-offs become sensing elements of the servo drive, and the positions of their rotors are controlled by the accelerometer correction system. The ring caging is carried out using a retractable mechanical stopper, and the start and stop of the GP using two buttons mounted on the GP housing which also contains LED indicators that show the current operation mode of the GP. The weight of the GP with a gravity sensor and the thermostabilization device does not exceed 67 kg, and the overall dimensions are Ø 430 × 638 mm. The principle of the GP operation and its design features do not require any additional adjustment operations during commissioning. Owing to these features, the gravimeter can be installed onboard the carrier by one operator.

In the course of the Shelf-E gravimeter design, the GP construction underwent significant changes. All its sensing elements, as well as the MK-FG microcontrollers,

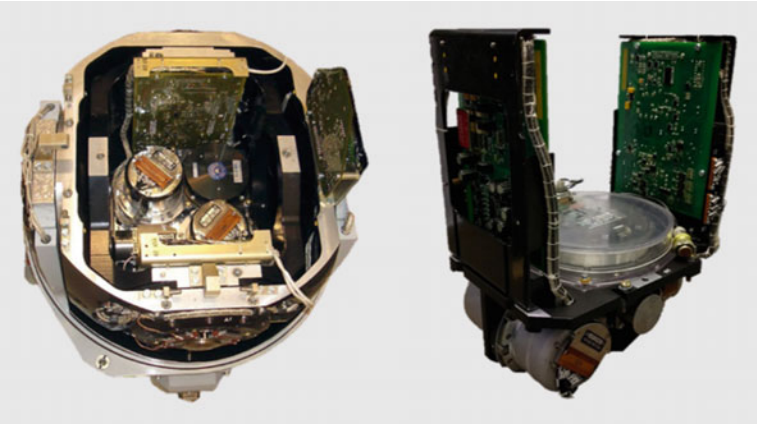

Fig. 1.13 General view of the gyro platform and the gyro unit

are arranged on a single bracket (Fig. 1.13). The gyro unit is easy to remove and install on the GP inner ring.

The gearless servo drive microcontrollers are put into the GP base. This has increased the possible pitch angle of the inner ring by a factor of 1.5 and, thus, removed the restriction on the value of the aircraft pitch angle at takeoff. The advanced design of the gravity sensor has made it possible to omit the GP thermal regulation system, which has reduced the gravimeter total power consumption by three times as compared with the Chekan-AM gravimeter.

An MK-BPR microcontroller is contained in the GP base. It integrates the data from the gravity sensor, its thermal regulation system, and the gyro platform into a single information flow. The data from the MK-BPR microcontroller can be transmitted to the computer either via the RS-232 serial interface or via the Wi-Fi channel.

1.2.4 Mathematical Model of the Gravimeter Sensing Element

The GES principle of operation is explained in the diagram shown in Fig. 1.14. The GES torsional bars are pretwisted in such a way that the pendulum is in a position close to horizontal. In the case of changes in gravity and under the action of inertial accelerations, the pendulum deviates from the horizon and forms the angle $\Delta\phi$.

The sensitive axis of the elastic system described is a straight line which is perpendicular to the pendulum axis and passes through the center of mass of the sensing element. Thus, in the case of changes in gravity and under the action of inertial accelerations, the sensitive axis changes its direction, even if the position of the instrument housing remains unchanged. This is a fundamental difference between a torsional

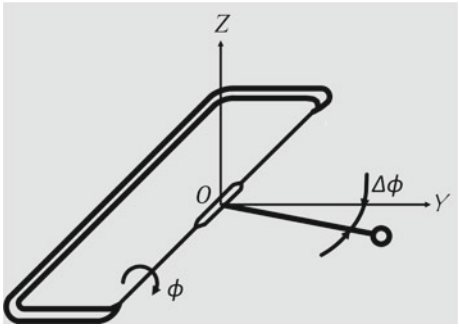

Fig. 1.14 Torsional-type elastic system: principle of operation

system and a linear one. And, as was shown in Eq. (1.2.1), the increment of the torsional angle $\Delta\phi$ corresponds to the increment of gravity δg. In view of the above, the differential equation of motion for the torsional-type GES can be represented as follows (Zheleznyak and Popov 1984):

$$k(T\Delta\phi' + \Delta\phi) = \Delta g - Z'' - (g - Z'')(\alpha^2 + \beta^2 + \Delta\phi^2 + 2\beta\Delta\phi)/2 + X''\alpha + Y''(\beta + \Delta\phi), \tag{1.2.3}$$

where X'', Y'', Z'' are inertial accelerations acting on the gravimeter; α, β are GSE stabilization errors.

In the static state, when there is no inertial acceleration and the GSE is in the horizon, Eq. (1.2.3) has the following form:

$$\delta g = \Delta\phi(k + g \cdot \Delta\phi/2), \tag{1.2.4}$$

where g is the value of gravity.

From expression (1.2.4), it follows that to convert the angle of rotation of the pendulum into readings, it is necessary to use the calibration characteristic which is a function of readings rather than a constant coefficient. In accordance with (1.2.4), there is a gravity increment from the point where the pendulum is in the horizon in the instrument readings. For a torsional-type elastic system during rolling, in addition to the errors due to the tilts of the base discussed above, there are additional components of measurement errors:

$$\varepsilon_{\delta g} = g\beta\Delta\tilde{\phi} + Y''\Delta\tilde{\phi}. \tag{1.2.5}$$

The values of β and $\Delta\tilde{\phi}$ are variable functions of the horizontal and vertical accelerations, respectively. At a certain ratio of their phases, constant errors may appear in the gravimeter readings. This error, which can reach the first tens of milligals, is known as the cross-coupling effect. A double elastic system consisting of two identical systems turned in a horizontal plane at 180° relative to each other is used

to reduce it. In this case, the total effect of disturbing accelerations on the double elastic system can be written as:

$$\varepsilon_{\delta g} = g\beta\left(\Delta\tilde{\phi}_1 - \Delta\tilde{\phi}_2\right) + Y''\left(\Delta\tilde{\phi}_1 - \Delta\tilde{\phi}_2\right), \tag{1.2.6}$$

where $\Delta\tilde{\phi}_1$, $\Delta\tilde{\phi}_2$ are the variable components of the change of the torsional angle of the 1st and 2nd GES pendulums, respectively.

As can be seen from expression (1.2.6), for a double elastic system, the error decreases to a difference effect and is defined by the identity of the two systems included in the double system. For modern systems, their difference in sensitivity does not exceed 0.1%, and in terms of response time, 1.5%, which makes it possible to almost completely eliminate the cross-coupling effect on the double quartz elastic system.

Taking into account the fact that the GSE output signal is the readings formed by two CCD photoreceivers in accordance with expression (1.2.2), the calibration characteristic of the GSE to be determined is a quadratic function of the OEC readings:

$$\delta g = b(m - m_0) + a(m - m_0)^2, \tag{1.2.7}$$

where b, a are the linear and quadratic coefficients of the gravimeter calibration characteristic, m_0 is the reading of the CCD photoreceiver at which the coefficients b, a were determined.

Due to damping fluid, the GSE model contains a first-order aperiodic link which has smoothing properties. Amplitude and phase distortions of the signal to be measured can be excluded by using a recovery filter of the following structure (Blazhnov et al. 1994):

$$W(p) = T_g p + 1, \tag{1.2.8}$$

where T_g is the gravimeter response time, p is the Laplace operator.

Due to the creep of the quartz glass elastic element, the gravimeter readings change with time. Therefore, the GSE model also includes the linear element which describes the quartz GES drift in accordance with the formula:

$$\Delta g_C = C(t - T_0), \tag{1.2.9}$$

where C is the drift value, t is the current time, T_0 is the time of reference measurements.

The drift value is determined from the results of reference measurements and can be refined during the office processing upon completion of the survey.

1.2.5 Algorithms for Gyro Platform Correction

Figure 1.15 is a block diagram of one of the two identical channels of gyro platform accelerometric correction (Krasnov 2007). Control is formed by the integrated correction circuit that implements a short-period gyro vertical based on accelerometer signals. Besides, external information from the GNSS receiver is additionally used in order to eliminate stabilization errors caused by aircraft maneuvering.

The following symbols are used in Fig. 1.15: FT1, FT 2 are frame transformers; K is the heading; R is the average radius of the Earth; $\Omega\cos\varphi$ is the horizontal component of the Earth's angular rate; g is gravity; w is horizontal acceleration; V_E is the horizontal speed produced by the inertial method; V_E^{GNSS} is the horizontal speed coming from the GNSS receiver; ΔV_E is the speed mismatch; ε is the angular rate of the gyroscope drift; α is the stabilization error.

The dashed line in Fig. 1.15 shows the physical connections determining the measuring signals of the GP sensing elements.

The transfer function of the filter $F(p)$ has the following form:

$$F(p) = \frac{n^2}{2} \cdot \frac{2.6Tp + 1}{0.5Tp + 1},\ n = \frac{T_{Sch}}{T}, \tag{1.2.10}$$

where $T_{Sch} \approx 13.4$ min is the Schuler time constant, T is the response time of the gyro vertical.

In this scheme, the dynamic stabilization error during a maneuver is eliminated by subtracting the speed value received from the GNSS from the signal coming to the input of the filter $F(p)$. In addition, control signals equal to the projections of the Earth's angular rate on their sensitive axes are fed to the gyroscope torquers. At the same time, the difference between the speed components coming from the

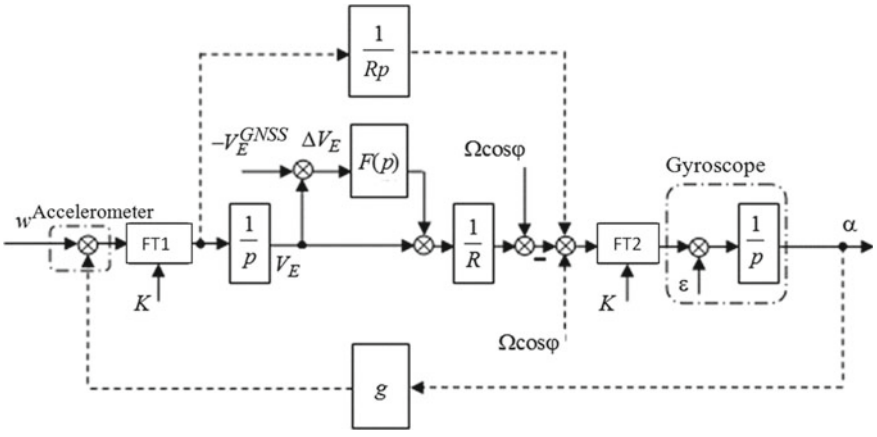

Fig. 1.15 Block diagram of the 'eastern' channel of the gyro vertical

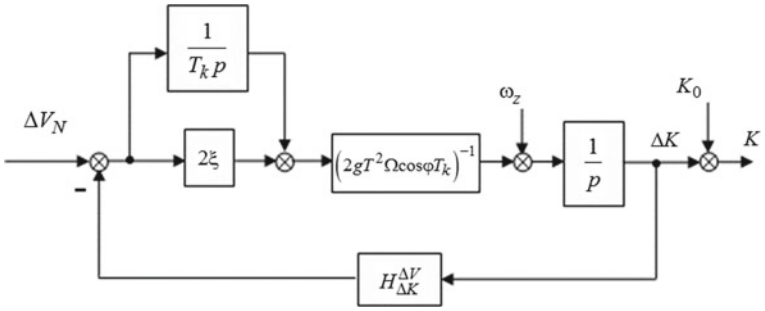

Fig. 1.16 Block diagram of the heading channel

GNSS receiver and those produced by the inertial method is formed in the axes of the geographic trihedron (FT1), and the control signals to the gyroscope torquers are formed in the instrument coordinate system (FT2). Thus, in the gyro vertical channels, the coordinates are converted twice based on the current values of the heading. The heading value can come from an external source or be generated autonomously based on the information from the fiber-optic angular rate sensor installed on the gyro platform and the angular rate error in the northern channel of the gyro vertical.

The analytical generation of heading is based on the gyrocompassing method using, in addition, the information from the azimuth FOG (Krasnov 2007). The block diagram of the heading channel is shown in Fig. 1.16.

The following symbols are used in the figure: T_k is the response time of the heading channel; ξ is the damping coefficient; ΔV_N is the mismatch of the northern component of the speed; ω_Z is the vertical angular velocity of the carrier according to FOG data; $H_{\Delta K}^{\Delta V}$ is the transfer function of the gyro vertical from the heading error to the speed mismatch; ΔK is the correction to the current heading value in the frame transformers.

Before the vehicle begins to move, the initial heading value K_0 is calculated and the FOG zero drift is specified. The heading is determined according to the formula:

$$K = \arctan \frac{\omega_y}{\omega_x}, \tag{1.2.11}$$

where ω_y, ω_x are the signals from the torquers of the floated gyroscope satisfying the following relations:

$$\begin{aligned} \omega_y &= \Omega \cos\varphi \sin K, \\ \omega_x &= \Omega \cos\varphi \cos K. \end{aligned} \tag{1.2.12}$$

In accordance with the principle of gyrocompassing, the feedback comes from the "northern" channel of the gyro vertical. The correction ΔK is formed by two signals, the mismatch of the northern speed component and the vertical angular rate from the FOG. The response time of the heading channel T_k is chosen at least an

order of magnitude greater than that of the gyro vertical T so that the gyro vertical errors will not participate in the formation of correction ΔK.

1.2.6 Calibration and Verification of the Chekan-AM Gravimeter

Calibration of the Chekan-AM gravimeter is performed during the manufacturing process. It includes the determination of the coefficients of the GSE calibration characteristic, its response time, and the value of the initial drift. The following GP parameters are also determined during calibration: scale factors and gyroscope drifts and accelerometer zero offsets, servo drive coefficients, and non-orthogonality of the floated gyroscope axes.

Since the Chekan-AM gravimeter is a certified measuring instrument, it also undergoes primary and periodic calibrations. The error components due to the influence of inertial accelerations and temperature are determined during the calibration.

Figure 1.17 shows a GSE calibration characteristic of a Chekan-AM mobile gravimeter. As Eq. (1.2.7) shows, it is a quadratic function whose coefficients are determined experimentally by the tilting method (Sokolov et al. 2015). The main feature of the method is the possibility to determine the coefficients only in the direction of decreasing gravity due to the GSE tilt. At the same time, the GSE is tilted by an angle of up to 5° with an error of less than 2 arcsec, which allows the device to be calibrated in the range of 0–4 Gal with the required accuracy. As can be seen from Fig. 1.17, the error due to the nonlinearity of the calibration characteristic does not exceed 0.2 mGal.

The next main parameter determined during the GSE calibration is the drift value. Taking into account the fact that the drift of the newly manufactured GES can reach from 3 mGal/day (the Chekan-AM gravimeter) to 1 mGal/day (the Shelf-E gravimeter), this step of calibration takes at least one month and is performed in

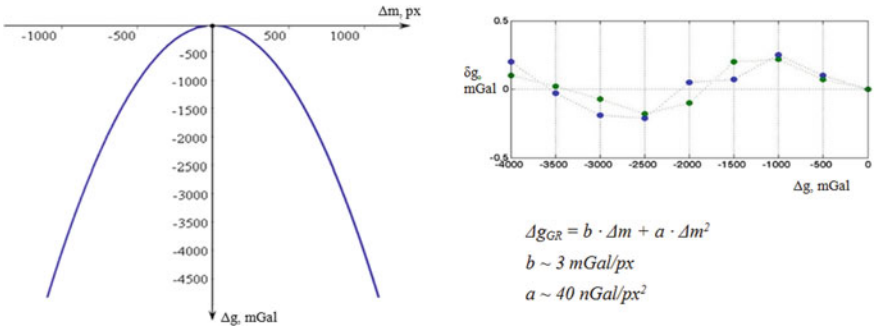

Fig. 1.17 Calibration characteristic and the error of its determination

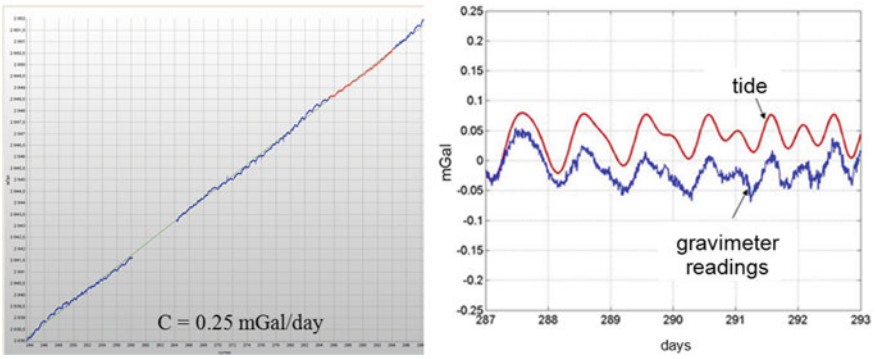

Fig. 1.18 GSE measurements on a fixed base

parallel with all types of tests. Figure 1.18 shows the curve of the Shelf-E drift two years after the GSE manufacture. It is obvious that in addition to a high degree of the drift linearity, its value is 0.25 mGal/day, which is almost 5 times lower than the initial value and is close to the similar parameters of the GT-2 and L&R gravimeters.

Removing the linear drift from the gravimeter readings, it is possible to qualitatively estimate its instrumental accuracy on a static base. An illustrative example of this is also given in Fig. 1.18 which shows that it is possible to observe lunar-solar tides whose influence on the change in gravity is less than 0.1 mGal.

Figure 1.19 shows the results of bench tests of the Chekan-AM and Shelf-E gravimeters when they were exposed to vertical accelerations in the range of periods from 14 to 100 s. The curves shown for the residual errors of the gravimeter readings were obtained after correction for the vertical acceleration, which was calculated based on the readings from the vertical displacement test bench, and data processing using a low-pass filter with a cutoff frequency of 0.006 Hz. The upper part of the figure shows the values of the amplitude and period of the vertical accelerations set for all modes of rocking. From the experimental data, it follows that the standard deviation of random error component of gravimeters in a wide range of frequencies of vertical accelerations does not exceed 0.2 mGal.

However, a systematic error, which may reach 1.5 mGal for the Chekan-AM gravimeter, is observed at high frequencies. For the Shelf-E gravimeter, this systematic error is three times lower. The reduction of the systematic error in the high-frequency range of vertical disturbing accelerations is due to a higher level of damping of the gravimeter sensing element. Owing to the digital filter used to recover the input signal, the increase in the damping level does not affect the final resolution of measurement results.

The effect of the ambient temperature variation on the Shelf-E gravimeter readings is shown in Fig. 1.20. It is obvious that in the operating temperature range between +5 to +35 °C, a 5° change in temperature results in a transient process with amplitude of up to 1 mGal, which lasts about 4 h. Besides, the steady-state systematic component of the error is significantly lower for the Shelf-E gravimeter than that for the Chekan-AM

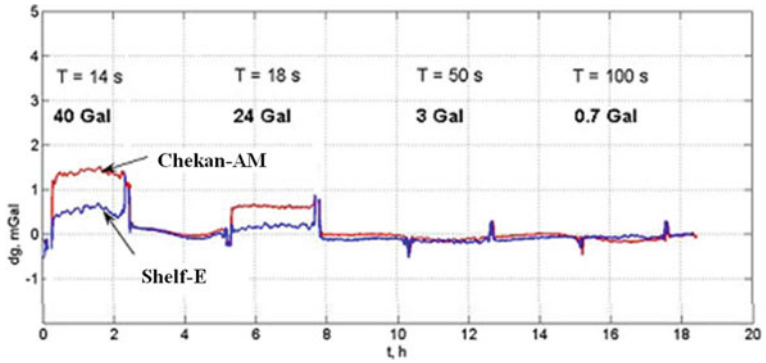

Fig. 1.19 Gravity measurements under the action of vertical accelerations

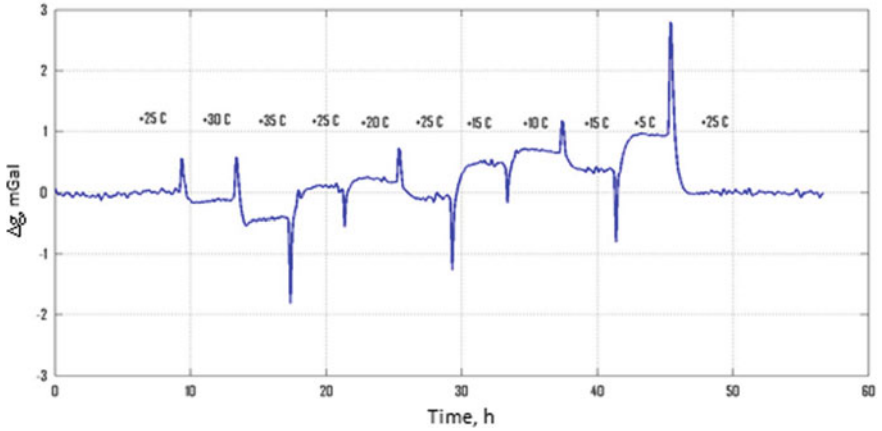

Fig. 1.20 Shelf-E gravimeter measurement error under the changes of ambient temperature

gravimeter. This is very important when conducting airborne gravity measurements, where daily external temperature differences may reach tens of degrees.

1.2.7 Conclusions

The main technical solutions implemented in the Chekan-AM mobile gravimeter, which is the fourth-generation system, have been described.

The main parts of the gravimeter, its structure, and the differences between the marine and airborne versions have been discussed.

The gravimeter sensing element and the gyro platform have been considered in detail, including the principle of operation, design features, mathematical models and operation algorithms.

The features of the Chekan-AM mobile gravimeter calibration have been discussed, and the main results of the bench tests are presented.

The advantages of the new Shelf-E system have been analyzed by comparison with the Chekan-AM gravimeter.

Gravimetric data processing methods and examples of the practical use of Chekan-AM in hard-to-reach areas of the Earth are given in the subsequent chapters.

1.3 GT-2 Relative Gravimeters

Gravimeters of the GT-2 series (GT-2A and GT-2 M are the codes for airborne and marine gravimeters, correspondingly) manufactured by NTP Gravimetric Technologies are widely used in gravity surveys aboard sea vessels and aircraft. More than 40 gravimeters of this series are used in gravity surveys of Russian and international companies on all continents of the Earth, including the Arctic and Antarctic regions (Richter et al. 2013; Berzhitsky et al. 2002; Kovrizhnykh et al. 2013a, b, 2016; Kovrizhnykh and Shagirov 2013; Smoller et al. 2013; Drobyshev et al. 2011; Mogilevsky et al. 2015a). Aerogeophysica Geophysical Scientific and Production Enterprise (Mogilevsky et al. 2010, 2015b; Kontarovich and Babayants 2011; Mogilevsky and Kontarovich 2011; Kontarovich 2015) and the Schmidt Institute of Physics of the Earth of the Russian Academy of Sciences (Koneshov et al. 2013; Drobyshev et al. 2011) that conduct a great number of airborne gravity surveys throughout Russia are the main Russian users of these airborne gravimeters. The GT-2 gravimeter was developed by a group of scientists and engineers at Gravimetric Technologies. The main designers of the company, who had been engaged in research and development at the Dolphin Central Research Institute for more than thirty years, specialized in developing inertial gravimetric systems and gyroscopic systems for the Russian Navy. Five technical solutions implemented in the gravimeter are recognized as inventions and protected by patents of the Russian Federation (Berzhitsky et al. 1999, 2000; Ilyin et al. 1993). The software for post-processing of airborne measurements for GT-2 gravimeters was developed in the Laboratory of Control and Navigation of the Lomonosov Moscow State University (Koneshov et al. 2013b). The first model of the GT-2 gravimeter was manufactured in 2001. It was tested aboard an AN-30 aircraft in Kubinka and in the vicinity of the Cherepovets airport. In 2002, the first commercial gravimeter was manufactured. With the financial support of Canadian Micro Gravity, it was put to extended tests in Australia on a plane, car, and helicopter, the results of which were considered positive. In February 2003, a long-term agreement was signed with Canadian Micro Gravity on the commercialization and supply of GT-2 gravimeters. Gravimeters of this series are manufactured in cooperation with the Ramensky Instrument-Making

Plant. At the stage of development, the plant carried out substantial work on preproduction engineering and revision of the documentation for the gravimeter central device to comply with the series-produced elementary base.

Gravimeters of this series are continuously improved. The first gravimeters, codenamed GT-1A, had a dynamic measuring range of ±0.5 g. In 2007, gravimeter versions with an extended dynamic range of ±1 g were created. They were assigned the codes of GT-2A, GT-2 M. The GT-2A, GT-2 M gravimeters allow conducting surveys in harsh conditions of strong turbulence and sea waves, which significantly increases the performance of survey. Actually, all gravimeters produced earlier were upgraded to this version.

In 2012, another version of the gravimeter with an extended latitude range of ±89° was created (a gravimeter with standard specifications has a latitude range of ±75°). The new gravimeter was equipped with a multi-antenna GNSS receiver. This version was assigned the code GT-2AP. It allows conducting surveys in high latitudes (Smoller et al. 2013; Drobyshev et al. 2011). In 2015, a version of the GT-2AQ gravimeter was created using quasi-coordinates.

This version has no restrictions on latitudes in its application. It retains its operability even directly at the points of geographic poles (Smoller et al. 2016). At present, three international companies—the University of Texas (USA), the Wagner Institute (Germany), and the Polar Research Institute of China—are conducting gravity surveys in the Antarctic using polar versions of the GT-2A gravimeter.

GT-2A gravimeters have high measurement accuracy. For the airborne version, it is between 0.5 and 0.7 mGal with an averaging time of 100 s, which, at an aircraft speed of 200–400 km/h, corresponds to the spatial resolution of half the anomaly length of 2.5 km to 5 km; for the marine version, 0.3 mGal with an averaging time of 600 s, which at a vessel speed of 5 kn corresponds to a spatial resolution of half the anomaly length of 0.75 km.

The higher averaging time for the marine version of the gravimeter as compared with the airborne version is due to the fact that the level of noise in the marine version is caused by sea swell and is significantly higher than that in the airborne version, which is caused by the GNSS error (for more details, see Sect. 2.4).

However, despite this, the resolution in the marine version is higher than that in the airborne version because of relatively low speeds of vessels.

1.3.1 Gravimeter Parts

The structure of the GT-2 gravimeter is shown in Fig. 1.21.

The gravimeter uses real-time information from a GNSS receiver operating in the standard mode.

Schematic of the GT-2 gravimeter is shown in Fig. 1.22.

The gravimeter includes a gyrostabilized platform in a triaxial gimbal suspension with an external azimuth axis (the motor of the azimuth axis is not shown).

The following equipment is installed on the platform:

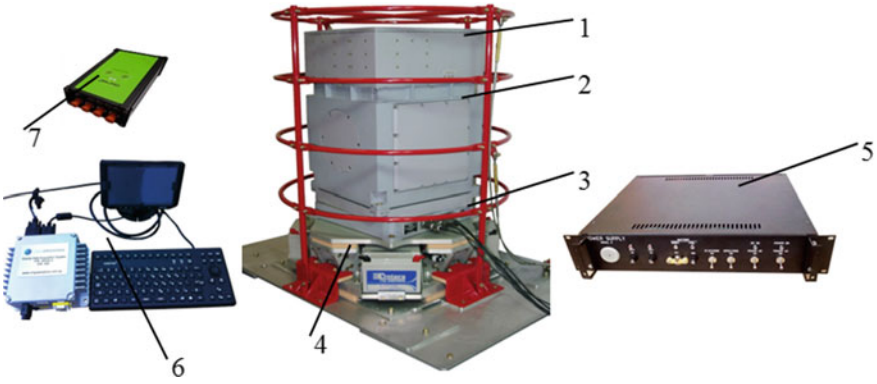

Fig. 1.21 Gravimeter structure: *1*—electronics module; *2*—central (gyro) module; *3*—rotary table; *4*—shock-absorber; *5*—power supply device; *6*—control and indication device (CID); *7*—GNSS receiver

- a GVK-18 dynamically tuned gyroscope (DTG) (Matveev et al. 2005) with a vertical orientation of the angular momentum, developed by Ramenskoye Instrument Design Bureau; the drift instability is 0.01–0.02°/h;
- two horizontal quartz pendulum-type accelerometers QAx, QAy of the A15 type developed by Ramenskoye Instrument Design Bureau with a zero signal instability of $5 \cdot 10^{-4}$ m/s^2;
- gravity sensing element (GSE);
- medium-grade FOG (Logozinsky, Solomatin 1996) developed by Fizoptika with a vertical sensitive axis, the drift instability of which during the entire period of operation without a thermal regulation system is 3°/h. Its short-term (within 5 to 10 days) drift instability in the gravimeter is 0.6°/h.

The output signals of accelerometers (W_x, W_y), GSEs (W_z), DTG angle sensors (β, γ), and FOGs (Ω_Z) are fed through the analog-to-digital converter (ADC) to the central processing unit (CPU) of the micro PC 5066 type. The DTG control signals (p_x, q_y) generated in the CPU by the gyro platform position correction system are fed through digital-to-analog converters (DAC) to the DTG torquers.

The control signals M_x, M_y of the servo drives generated in the CPU are fed through a DAC to the torque motors TM_x, TM_y of the servo drives.

The azimuthal stabilization motor control signal generated in the CPU according to the gyro platform heading information is fed to an azimuth stabilization motor (not shown in the figure), which ensures the platform stabilization in the geodetic reference frame.

GSE output signals are formed by an ADC with a range of +/–1 g.

To measure the angles of pitch, roll, and heading of the vehicle, angle sensors AS_x, AS_y, AS_z are installed on the axes of the gimbal suspension and on the vertical axis of the rotary table.

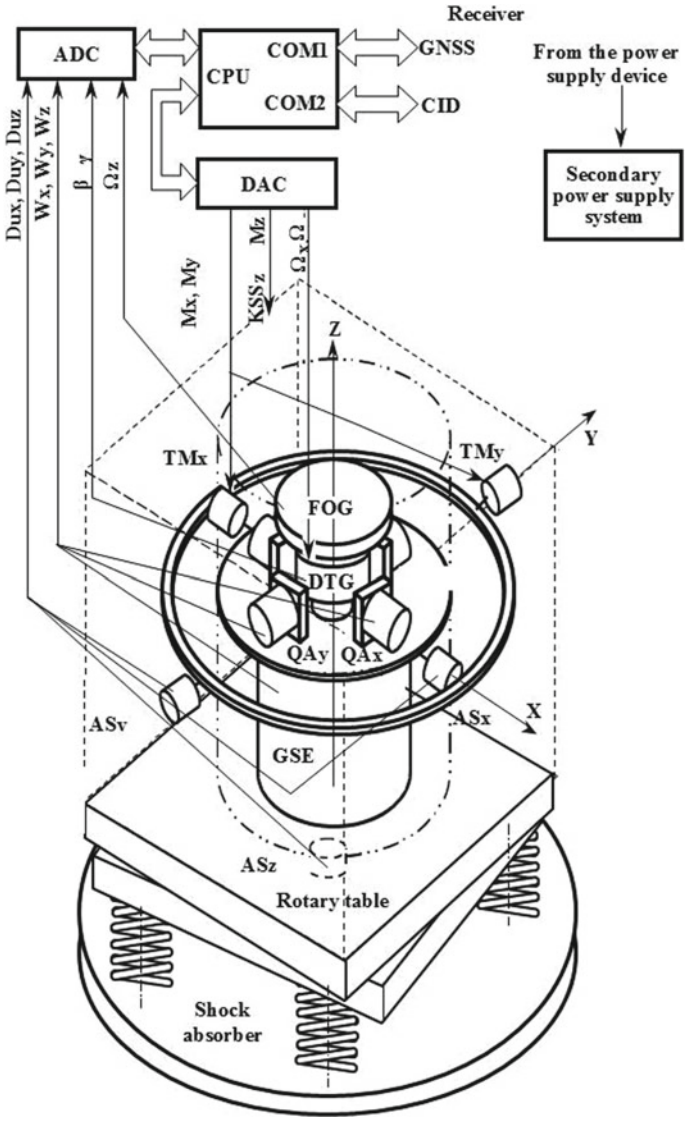

Fig. 1.22 Schematic of the GT-2 gravimeter

To ensure a constant temperature of the sensing elements, the code-to-current converter (CCC) for controlling the DTG torquers during fluctuations in the ambient temperature, the thermal regulation systems (TRS) include:

- single-circuit TRS of the CCC;
- single-circuit TRS of the inertial module with DTGs, FOGs, and accelerometers;
- dual-circuit GSE TRS.

The TRS actuating elements are controlled by the CPU using thermal bridge signals that are fed to the DAC via analog-to-digital converters.

1.3.2 Gravimeter Sensing Element

The sensing element of the GT-2 gravimeter is of the axial type with a magnetoelectric feedback. Its block diagram is presented in Fig. 1.23.

Proof mass (about 37 g) is suspended on flat metal springs with a thickness of about 50 μm. The measuring winding placed in a permanent magnet field is wound on the proof mass. The GSE includes an optical position sensor consisting of light and photo diodes. The sensor measures the proof mass displacement relative to the housing, and hence its displacement in the magnetic field of permanent magnets. The signal from the photo diode passes through a correction amplifier with a transfer function $F(s)$ that provides stable feedback and changes the current in the measuring winding. A precision reference resistor R is connected in series with the winding. The current in the measuring winding, and hence the voltage across the resistor R, is a measure of the specific force projection onto the GSE sensitive axis (W_z). The signal proportional to the voltage on the reference resistor, as well as the output signal of the position sensor enter the CPU via analog-to-digital converters.

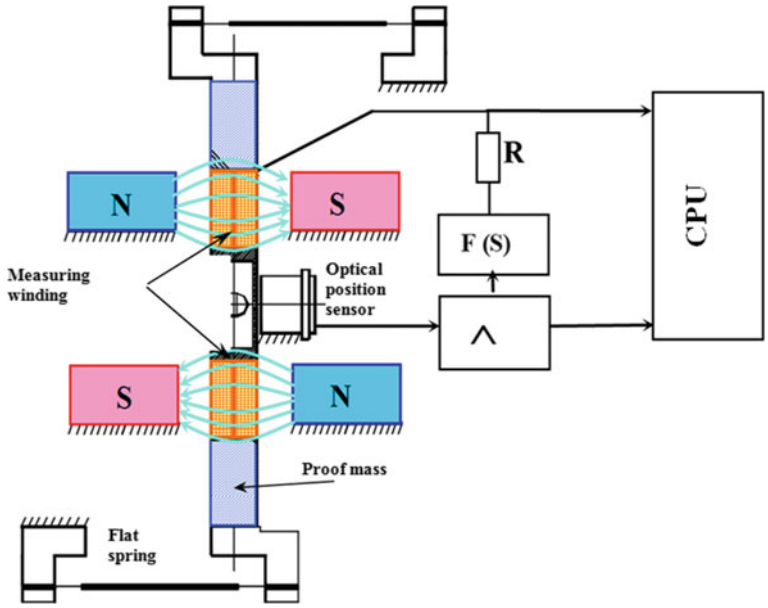

Fig. 1.23 Block diagram of the gravimeter sensing element

The feedback, which stabilizes the proof mass position relative to the housing, is based on an analog circuit. When there is no vibration, the proof mass is practically immobile relative to the GSE housing, and hence, relative to the magnetic field generated by the magnetic system. Under vibration, the proof mass moves relative to the magnetic field. The averaged data of the GSE have an error proportional to the square of the proof mass deviation from zero, which is due to the nonlinearity of the magnetic field mainly caused by the error in the geometry of the permanent magnets and the displacement of the initial position of the proof mass relative to the magnets The proportionality coefficient K_{ps} is determined at the manufacturing plant when the gravimeter is calibrated on a vibration table and is used in the mathematical software of the gravimeter to compensate for the effect of the proof mass deviation on the GSE readings.

The block diagram of an axial-type GSE has an advantage over a pendulum-type GSE: it has no cross-coupling effect error (Dehlinger 1978). However, due to the finite longitudinal rigidity of the spring plane, the averaged data of the GSE have an error proportional to the square of the horizontal acceleration. The proportionality coefficients $K w_x(y)$ are determined at the manufacturing plant when the gravimeter is calibrated on a horizontal acceleration test bench and are used in the firmware of the gravimeter to compensate for the GSE error caused by the square of the horizontal accelerations.

GSE bandwidth is from 0 to 100 Hz. The measuring range is ±1 g. The drift is ±3 mGal/month. The standard deviation of the noise component in the test bench conditions is ±0.1 mGal to 0.2 mGal with an averaging time of 60 s.

1.3.3 Circuit for Integrated Correction of the Gyro Platform Position

The gravimeter has a Schuler-type circuit for integrated correction of the gyro platform position.

A block diagram of one channel of the correction circuit is shown in Fig. 1.24. The dead reckoning equations are integrated in the azimuth-free coordinate system. The azimuth-free coordinate system is determined by the *XaYaZa* frame-of-reference (Fig. 1.25) obtained from the local geodetic reference frame *ENZ* by turning around the vertical axis *Z* and having a zero component of the absolute angular rate with respect to the vertical axis *Za.*

The following symbols are used in the figure:

a_y is a projection of the horizontal specific force of the aircraft on the instrument axis Y (see Fig. 1.25);

W_x, W_y are readings of the accelerometers *X* and *Y*, respectively;

$\widehat{dw}_x$, $\widehat{dw}_y$ are estimates of biases of the transducer accelerometers (see Fig. 1.27); scale-factor errors are not taken into consideration;

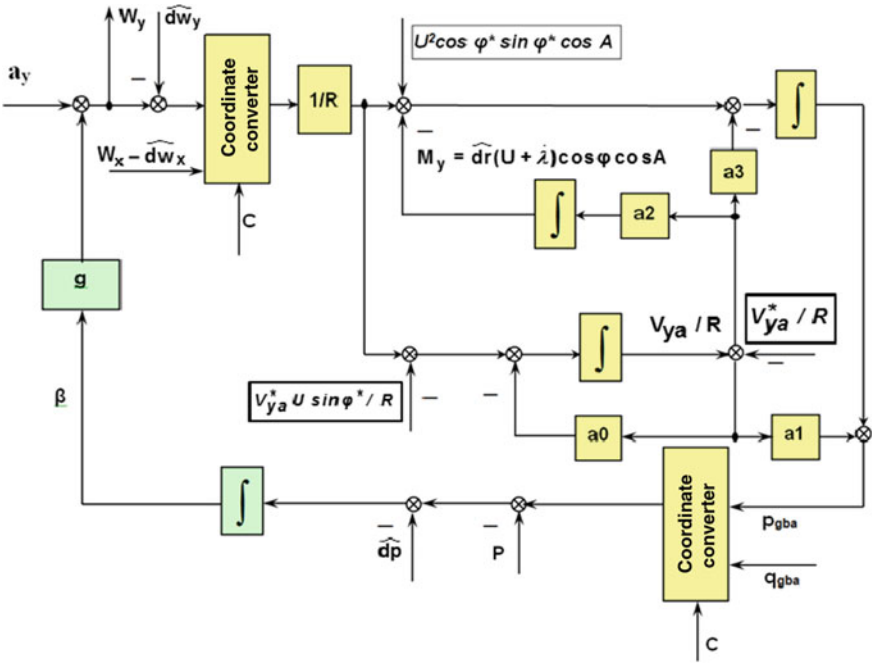

Fig. 1.24 One channel of the circuit for integrated correction of the gyro platform position

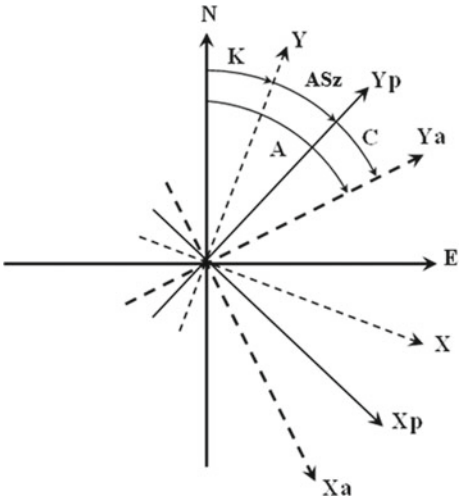

Fig. 1.25 Coordinate systems

C is the angle between the platform coordinate system and the azimuth-free coordinate system (see Fig. 1.25);

g is the absolute value of gravity on the flight path;

$\widehat{dr}$ is an estimate of the angular rate of the FOG drift;

R is the mean Earth radius;

φ is the geographical latitude of a point;

$\dot{\lambda}$ is the longitude derivative;

U is the absolute value of the Earth's angular rate;

β is the misalignment error of the gyro platform around the X axis;

A is the heading of the azimuth-free coordinate system (see Fig. 1.25);

p_{gba}, q_{gba} are the signals applied to the DTG torquers, in projections on the Xa and Ya axes of the azimuth-free coordinate system (see Fig. 1.25);

P is the projection of the absolute angular rate of the gyro platform on the X_p axis of reference frame whose azimuthal orientation is determined by the angle of the platform heading (see Fig. 1.25);

$\widehat{dp}$ is an estimate of the drift angular rate of the DTG and the transducer around the X axis (see Fig. 1.29), errors of the scale factors are not considered;

V_{xa}, V_{ya} are projections of the relative velocity of the vehicle on the Xa and Ya axes of the azimuth-free coordinate system (see Fig. 1.25);

$a0 - a3$ are the coefficients of gyro platform oscillation damping algorithm:

$$\begin{aligned} a0 &= 2.613/T_{gg}; \\ a1 &= 1 - 3.414/\upsilon^2; \\ a2 &= \frac{-1}{\upsilon^2 T_{gg}^4}; \\ a3 &= a0\left(1 - \frac{1}{\upsilon^2 T_{gg}^2}\right); \end{aligned} \tag{1.3.1}$$

υ is the Schuler frequency;

T_{gg} is a parameter corresponding to the time constant of the gyro platform position correction system.

The Schuler-type integrated correction circuit of the gyro platform nondisturbed by the vehicle motion (Seleznev 1967) was synthesized based on the equations of the stationary Kalman filter (KF). The following simplifications were accepted for the relevant algorithmic solutions: channel-by-channel models of the INS error equations are used; the FOG drift is considered as the integral of white noise; and white noise is considered as a statistical approximation of the error in the GNSS-derived velocity (Smoller 2002). This led to an easy-to-operate and easy-to-customize one-parameter algorithmic structure, the parameters $a0$, $a1$, $a2$, $a3$ of which—the damping coefficients (1.3.1)—are a function of one parameter, T_{gg}. Application of the algorithm for damping gyro platform angular oscillations using the GNSS-derived velocity made it possible to ensure the value of the misalignment errors in the instrument leveling during the flight at a level of 1–2 arcmin. The misalignment errors of the instrument

leveling are estimated at the stage of integrated postprocessing of airborne gravimetric data using the GTNAV software (see Sect. 1.2.2). In the GTNAV software, estimation of misalignment errors is carried out with the use of the smoothing KF, which is based on sufficiently complete models of INS error equations and models of instrumental errors of inertial sensors. Measurements are formed with the use of GNSS differential carrier phase solutions. This allowed providing the level of 10–15 arcsec for errors in estimating the misalignment errors of the vertical, which is confirmed by the experience in processing experimental data.

In Fig. 1.24, the formulas that use aiding information are shown in italic and are framed for clarity. Symbol * indicates trajectory parameters provided by the GNSS. The upper formula is a compensation for the gyro platform misalignment error due to the centripetal acceleration caused by the Earth's rotation, the lower one is a compensation for the Coriolis acceleration projection on the vertical axis, and the right one is the aiding data used to damp gyro platform oscillations. The GNSS receiver delivers the values of the aircraft velocity vector components in projections on the axes of the geographic coordinate system with the axes oriented according to the sides of the world (east, north) and upwards (*ENZ*). To implement the damping algorithm, it is required to have external information about the vehicle velocity on the axis of the azimuth-free geographical coordinate system. When calculating the velocity projections, it is necessary to know the heading angle. Significant errors in external information can result from the heading errors.

Coordinate Systems. Main Formulas. Figure 1.25 shows the main coordinate systems used in the gravimeter software.

For simplicity, let us assume that the roll and pitch of the aircraft are equal to zero and the gyro platform is not disturbed. Figure 1.25 shows the horizontal axes of the four coordinate systems. The vertical axes of all the coordinate systems considered are directed perpendicular to the plane of the drawing to the observer.

The following symbols are used in the figure:

E, N are the axes of the geographic reference frame;

X, Y are the aircraft body frame axes;

Xp, Yp are the gyro platform axes;

Xa, Ya are the axes of the azimuth-free coordinate system;

K is the vehicle heading;

A is the heading of the azimuth-free coordinate system;

AS_z is the readings of the angle sensor of the gimbal suspension external axis;

C is the angle between the platform coordinate system and the azimuth-free coordinate system calculated by integrating the FOG readings (r):

$$C = \int r dt. \tag{1.3.2}$$

The standard-configuration GT-2 gravimeter uses the data from a single-antenna GNSS receiver for damping of the gyro platform. The GNSS receiver (both single-antenna and multi-antenna) initially determines the coordinates and projections of the relative velocity vector in the Greenwich coordinate system, then recalculates them

into the geodetic reference frame *ENZ* (for more details, see Sect. 4.3). The single-antenna GNSS receiver provides the geographic coordinates (latitude and longitude), the aircraft relative velocity vector projection V^* onto the local horizon plane and the track angle TA*, which is the angle between the projection of the above-mentioned vector onto the horizon plane and the north direction.

In the standard configuration, heading A of the azimuth-free coordinate system, as well as the velocity projections V_{xa}^*, V_{ya}^*, necessary for damping of gyro platform oscillations (see the formulas given in italics and framed in Fig. 1.24), are calculated in the GT-2 gravimeter software based on the following formulas:

$$\begin{aligned} U_{xa} &= p_{gba} - V_{ya}^*/R; \\ U_{ya} &= q_{gba} - V_{xa}^*/R; \end{aligned} \tag{1.3.3}$$

$$A = arctg\left(U_{xa}/U_{ya}\right); \tag{1.3.4}$$

$$V_N^* = V^* \cos TA^* + V^* \sin TA^*; \tag{1.3.5}$$

$$V_{ya}^* = V_N^* \cos A + V_E^* \sin A; \tag{1.3.6}$$

$$V_{xa}^* = V_E^* \cos A - V_N^* \sin A. \tag{1.3.7}$$

In formulas 1.3.3, U_{xa}, U_{ya} represent the calculated values of the Earth's angular rate projections onto the corresponding axes in the azimuth-free coordinate system. The heading calculated from formulas (1.3.3, 1.3.4) is called a compass heading. As is known (Smoller et al. 2015), the error in the calculation of the compass heading is expressed by the following formula:

$$dA = \frac{dp_E + \dot{\beta}_E}{\left(U + \dot{\lambda}\right)\cos\varphi}, \tag{1.3.8}$$

where dp_E is the east drift of the DTG;
$\dot{\beta}_E$ is the dynamic error rate of the gyro horizon around the eastern axis;
$\dot{\lambda}$ is the longitude derivative.
Analysis of formula (1.3.8) allows for the following conclusions:

1. As latitudes φ become higher, heading error A in the single-antenna configuration of the gravimeter, and hence, relevant induced errors in determining the relative velocity components V_{xa}^*, V_{ya}^* required for damping increase in (1.3.6, 1.3.7). When approaching the pole, the value dA tends to infinity. This makes it impossible to use the GT-2A gravimeter at latitudes higher than $\pm$ 75°.
2. Flights in the eastward direction in terms of the heading error, when the value $\dot{\lambda}$ is positive, are preferable to flights in the westward direction, when the value

$\dot{\lambda}$ is negative. This effect is particularly significant at high latitudes, where the value $\dot{\lambda}$ becomes commensurate with the angular rate of Earth's rotation U.

3. The heading error dA in the standard single-antenna gravimeter configuration depends on the instability of the instrumental errors of the inertial gravimeter sensing elements, which cause misalignment errors of the gyro platform and on the constant eastern drift of the DTG. The compass heading error does not depend on the constant component of the FOG drift.

An alternative to the compass heading in the GT-2A gravimeter could be the inertial heading A_i calculated by the formula:

$$A_i = \int (r - (U + V_E^*/R\cos\varphi^*)dt + A_i(0). \tag{1.3.9}$$

By varying this relation under the assumption that the FOG drift dr is a constant and neglecting the GNSS errors, we obtain

$$dA = dr \cdot t. \tag{1.3.10}$$

The comparison of the compass heading error (1.3.8) with the inertial one (1.3.10) allows for the following conclusion: the inertial heading has no distinguishing features at high latitudes, but it cannot be used in the GT-2 gravimeter because of the medium-grade FOG. As mentioned in Sect. 1.3.1, its short-term instability is 0.6°/h, which in 5 to 10 h flights can lead to an unacceptable inertial heading error of (3–6)°, while the GT-2 gravimeter compass heading error does not exceed 0.5–1°. To eliminate the features of the compass heading, it was proposed to use a multi-antenna GNSS receiver. The main idea of its use is that the multi-antenna GNSS receiver generates the value of the carrier heading in addition to navigation information, in particular, the relative velocity and the local coordinates. The heading obtained in this way has no drawbacks that are inherent in the compass heading obtained in the standard configuration of the GT-2A gravimeter. Thus, by using the readings from the angle sensors of gravimeter gimbal suspension, it becomes possible to determine the projections of the carrier relative velocity vector on the gyro platform axes, needed to damp oscillations of the gyro platform. This circumstance, as well as the use of quasi-coordinates in the software of the gravimeter and GNSS receiver, made it possible to create an all-latitude version of the GT-2AQ gravimeter. Creating an all-latitude version of the gravimeter is discussed in Sect. 4.3.

1.3.4 Mathematical Models of the Channels of Inertial Sensing Elements

The term 'channels' of the GSE, FOG, and horizontal accelerometer is used to mean the mathematical model of these inertial sensing elements with an integrating ADC and a sequence of computations in the CPU for the purpose of compensation for systematic instrumental errors and digitization of the output signal in the appropriate dimension. The concept of the DTG channel is defined below.

Gyro Platform Channel of the Gravity Sensing Element

Figure 1.26 on the left shows the adopted mathematical model of a GSE with an ADC; on the right, mathematical calculations implemented in the CPU.

The following symbols are used in Fig. 1.26:

W_z is the vertical specific force (for simplicity, it is assumed that the QA sensitive axis coincides with vertical);

Kw_z is the scale factor error of a transducer GSE;

dw_z is the zero signal drift of a transducer GSE;

$\widehat{Kw}_z$ is an estimate of the error of the scale factor of a transducer GSE;

$\widehat{dw}_z$ is an estimate of the zero signal drift of a transducer GSE;

T_e is the anti-alias filter time constant;

$\mathrm{W_{zout}}$ is the GSE channel output data.

The GSE signal is read out at a frequency of 300 Hz by an integrating ADC, at the output of which the average value of acceleration is in the range of 1/300 s. After the scale factor error $\widehat{Kw}_z$ compensation and the zero signal drift $\widehat{dw}_z$, the data obtained is passed through an anti-aliasing filter (aperiodic link with the time constant $T_e = 2$ s). Its output is averaged over 16 readings. The values $\mathrm{W_{zout}}\, W_{zout}$ with a frequency of about 18 Hz (more precisely, 300/16 Hz) are recorded in the G file and fed to the input of the vertical channel generating gravity anomalies in the GT-2 M marine gravimeter. In the GT-2A airborne version, the output data of the vertical channel are used when the aircraft is for functional diagnostics at the airdrome.

It is easy to show that the impact of vibration on a gravimeter with a frequency close to the sampling frequency $\mathrm{W_{zout}}$ in the G file (approximately 18 Hz) leads to the effect of frequency masking and, consequently, to an undesirable low frequency in the output data of the GSE channel, which will be perceived as a false anomaly. The task of the anti-aliasing filter operating at 300 Hz frequency is designed to suppress

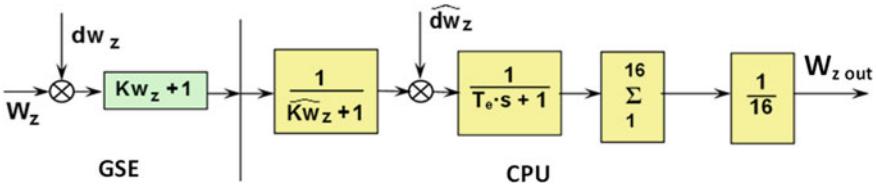

Fig. 1.26 Mathematical model of the GSE channel

the amplitudes of signals with frequencies close to 18 Hz. The use of an aperiodic link with the time constant $T_e = 2$ s as an anti-aliasing filter attenuates the amplitudes of the harmonics with frequencies close to 18 Hz by more than 200 times, which almost completely eliminates the effect of frequency masking. The anti-aliasing filter leads to a delay in the output data for a fixed time of 2 s, which is taken into account during postprocessing.

The value of the scale factor error for a transducer GSE is determined only at the instrument making plant during the manufacture of the gravimeter by the tilting method on a precision tilt meter device with a relative error not exceeding several 10^{-4}. More than a decade-long experience with operating gravimeters has shown that the value Kw_z remains stable with the specified accuracy throughout the entire period of operation.

Horizontal Accelerometer Channel

The following symbols are used in Fig. 1.27:

W is the horizontal specific force of the vehicle (for simplicity, it is assumed that the GSE sensitive axis coincides with vertical);

Kw is the scale factor error of a transducer accelerometer;

dw is the zero signal drift of a transducer accelerometer channel;

$\widehat{Kw}$ is the estimate of the scale factor error of a transducer accelerometer;

$\widehat{dw}$ is the estimate of the zero signal drift of a transducer accelerometer;

$\mathrm{W_{out}}\,W_{out}$ is the output signal of the accelerometer channel.

Figure 1.27 on the left shows the adopted mathematical model of a transducer accelerometer. The figure on the right shows the mathematical operations used to compensate for the factory-defined values Kw and dw. Obviously, in the ideal case of ($\widehat{Kw} = Kw, \widehat{dw} = dw$), the output signal of the accelerometer channel $\mathrm{W_{out}}\,W_{out}$ will be equal to the input acceleration W. The analog signal of the accelerometer with a frequency of 300 Hz is converted into a code by an integrating ADC. Thus, the CPU receives a code proportional to the mean value of specific force (specific velocity increment) over an interval of 1/300 s.

Practice has shown that Kw remains unchanged during operation with sufficient relative accuracy (not worse than 10^{-3}). The values $\widehat{Kw}_x$, $\widehat{Kw}_y$ are defined by the "Calibration" procedure (see Sect. 1.3.6) at the instrument making plant during the gravimeter manufacturing process. The values $\widehat{dw}_x$, $\widehat{dw}_y$ are also defined only at the instrument making plant during the gravimeter manufacturing as described in Sect. 1.3.5. The values $\widehat{Kw}_x(y)$ and $\widehat{dw}_x(y)$ discussed above are entered into the gravimeter database and remain unchanged during the entire period of operation.

FOG Channel

The following symbols are used in Fig. 1.28:

r is the vertical angular rate of the gyro platform;

Kr is the scale factor error of a transducer FOG;

dr is the zero signal drift of a transducer FOG channel;

$\widehat{Kr}$ is an estimate of the error of the scale factor of a transducer GSE;

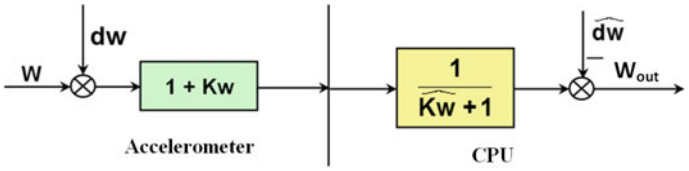

Fig. 1.27 Mathematical model of the accelerometer channel

$\widehat{dr}$ is an estimate of the zero signal drift of a transducer accelerometer;
r_{out} is the FOG channel output signal.

Figure 1.28 on the left shows the adopted mathematical model a transducer FOG. On the right, the figure shows the mathematical operations to compensate for the factory-defined values Kr and dr. It is obvious that in the ideal case ($\widehat{Kr} = Kr$, $\widehat{dr} = dr$) the output value of the FOG channel r_{out} r_{out} will be equal to the input angular rate r. The analog signal of the FOG with a frequency of 300 Hz is converted into a code by an integrating ADC. Thus, the CPU receives a code proportional to the average value on an interval of 1/300 with the vertical angular rate of the gyro platform.

Practice has shown that the Kr value with sufficient relative accuracy (not worse than 10^{-3}) remains unchanged during operation. Therefore, Kr is determined by turning the platform of the gravimeter at a fixed angle using a rotary table and comparing the integral of r_{out} r_{out} with its value. The dr value is determined occasionally, once every 10–15 days and after each cold start of the gravimeter during operation, using the automatic 'Autocalibration' procedure integrated in the gravimeter software (see Sect. 1.3.6).

The DTG, which is a free gyroscope, contains two torquers—X and Y—that provide precession movement of the gyro platform around horizontal axes. The input of the gyroscope is the magnitude of the current supplied by the code-to-current converter (CCC) to its torquer sensor winding, its output is the precession rate of its rotor, and hence the gyro platform, around the corresponding horizontal axis.

The DTG channel will be understood as a mathematical model of the DTG with a CCC and a sequence of computations in the CPU to compensate for systematic instrumental errors.

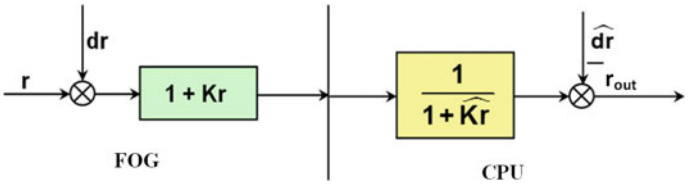

Fig. 1.28 Mathematical model of the FOG channel

One Channel of a Dynamically Tuned Gyroscope

The following symbols are used in Fig. 1.29:

p_{out} is the actual angular rate of the gyro platform around the X axis (for clarity, one of the identical X channels of the DTG is considered);

p is the angular rate of the gyro platform around the X axis fed to the input of the CCC (calculated by the correction system);

Kp is the scale factor error of the DTG and the converter;

dp is the angular rate component of the gyroscope drift around the X axis;

$\widehat{Kp}$ is an estimate of the scale factor error of the DTG and the converter;

$\widehat{dp}$ is an estimate of the angular rate of the DTG and transducer around the X axis.

Figure 1.29 on the right shows a mathematical model of the DTG and the CCC. On the left, the figure shows mathematical operations to compensate for the $\widehat{Kp}$ and $\widehat{dp}$ values determined during calibration. Obviously, in the ideal case ($\widehat{Kp} = Kp$, $\widehat{dp} = dp$), the actual angular rate of the platform p_{out} will have the design value of p.

Practice has shown that the Kp value remains unchanged during operation with sufficient relative accuracy (not worse than 10^{-3}). The values $\widehat{Kp}$ and $\widehat{dp}$ are defined at the instrument making plant in the process of gravimeter manufacturing by turning the gravimeter platform placed on a rotary table by four rhumbs relative to the meridian. The dp value is determined occasionally, once every 10–15 days and after each cold start of the gravimeter during operation, using the "Autocalibration" procedure integrated in the gravimeter software.

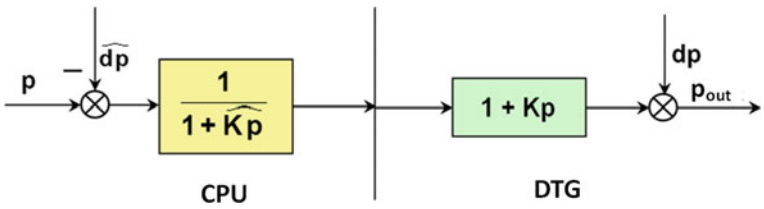

Fig. 1.29 DTG mathematical model and channel

1.3.5 Analysis of the Gravimeter Main Errors

Below is the main gravimetric equation which represents the GSE readings taking into account the gyro platform misalignment errors, geometry errors, and the instrumental errors taking into consideration the specific design features of the GT-2 gravimeter:

$$W_z = \left(\Delta g + g_0 + \Delta g_E + \ddot{Z}\right)\cos(\beta_Z + \alpha_1)\cos(\gamma_Z + \alpha_2) - W_y(\beta_Z + \alpha_1) + \\ + W_x(\gamma_Z + \alpha_2) + K_{PS} \cdot PS^2 + Kw_x \times Wx^2 + Kw_y \times Wy^2 + \upsilon,$$
$$g_0 = g_e - Wzz \cdot h, \tag{1.3.11}$$

where

W_z is the vertical specific force measured by a GSE;

Δg is the gravity anomaly;

g_0 is the normal gravity on the flight lines;

g_e is the normal gravity on the surface of the Earth's ellipsoid;

Δg_E is the Eötvös correction term;

$\ddot{Z}$ is the second derivative of the flight altitude;

β_Z is misalignment of the GSE sensitive axis of the gyro platform plane, which corresponds to the rotation around the *X*-axis;

γ_Z is misalignment of the GSE sensitive axis of the gyro platform plane, which corresponds to the rotation around the *Y*-axis;

α_1 is the misalignment of the platform caused by its disturbed state, which corresponds to the the rotation around the *X*- axis of the gyro platform;

α_2 is misalignment of the platform caused by its disturbed state, which corresponds to the the rotation around the *Y*-axis of the gyro platform;

W_x, W_y is the horizontal specific force of the carrier in projections on the *X* and *Y* axes, respectively measured by horizontal accelerometers;

K_{PS} is the coefficient of influence of the proof mass displacement relative to GSE housing caused by vibration on the GSE error;

PS is the readings of the GSE proof mass position sensor (see Fig. 1.3.3);

Kw_x, Kw_y are coefficients of influence of the horizontal projections of the vehicle acceleration in projections on the *X* and *Y* axes of the gyro platform, respectively, on the GSE error;

υ is random noise;

W_{ZZ} is the vertical gravitational gradient;

h is the flight altitude.

The plane of the gyro platform is a conditional concept defined by accelerometer signals. Let us assume that the plane of the platform coincides with the plane of the local horizon, when the accelerometer signals are equal to zero. Therefore, in the case of biases of the horizontal accelerometers, the values of β_Z, γ_Z will change.

As mentioned in Sect. 1.3.2, the influence coefficients of the proof-mass displacement relative to the GSE housing caused by vibration, and the influence coefficients of horizontal accelerations K_{PS}, $Kw_x(y)$ are determined at the manufacturing plant. They are entered into the gravimeter database and taken into account in real

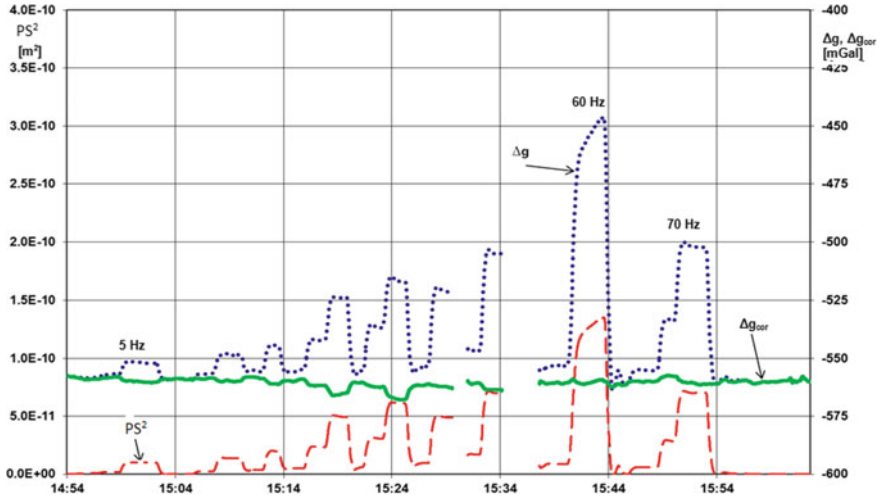

Fig. 1.30 Determination of K_{PS} on a vibration table

time to form corrections in accordance with the fourth, fifth, and sixth terms of formula (1.3.11), which practically eliminates the effect of vibration and horizontal accelerations of the vehicle on the gravimeter error.

Figure 1.30 shows an example of determination of the influence coefficient K_{PS} on a vibration table.

To identify the effect of the GSE proof-mass displacement during gravimeter calibration, vibration is set in the range from 5 to 70 Hz with amplitudes (0.2–0.3) g that are significantly higher than the vibration amplitudes acting on the gravimeter during the flight. The square of the deviation of the proof mass PS^2 [m^2] is shown by the dashed curve, the GSE readings are shown by the dotted curve. From these results, coefficient K_{PS} was determined as the ratio of the data of the dotted curve to those of the dashed curve. The result after the compensation is represented by the solid curve. From the curves presented, it follows that after the compensation, the effect of vibration decreased by more than 20 times.

Requirements for the accuracy of flight altitude determination. For simplicity, consider the following example.

Assume that the aircraft or, more precisely, a GSE proof mass is making vertical harmonic motion with an amplitude of $A = 1$ mm and a period $T = 100$ s (typical averaging time used in postprocessing of the GT-2A gravimeter measurements). The angular frequency $\omega \approx 0.061/s$. Assume that the GNSS receiver does not measure this displacement.

Then, in accordance with the first term of formula 1.3.11, there arises an error in the gravity anomaly generation with amplitude $d\Delta g$ equal to $\Delta g = \ddot{Z}_{max} = A\omega^2 =$ 0.4 mGal will appear. It follows that the accuracy of measuring the altitude of the GSE location should be approximately 1 mm (average for 100 s). As the experience with the operation of the GT-2A gravimeter has shown, this accuracy is achieved due

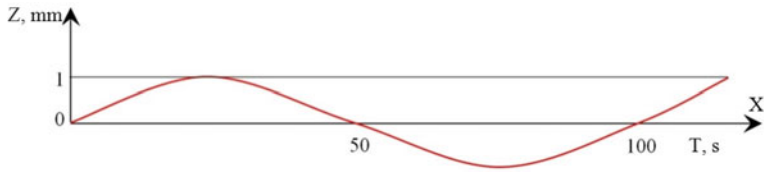

Fig. 1.31 The aircraft flight path leading to an error of 0.4 mGal

to the use of dual-frequency carrier phase GNSS receiver operating in the differential mode and with compensation of antenna lever arm effect using the readings from the angle sensors of the gravimeter gimbal suspension (Fig. 1.31).

Requirements for data synchronization accuracy. During the gravity survey, the data obtained from the GSE are recorded in the measuring file of the gravimeter. The GNSS data file obtained after taking into account the differential correction from the base station (hence, after the flight) is used to remove inertial perturbation from the GSE data. The data provided by GT-2 instrument should be time-synchronized. Let us estimate the requirement for data synchronization accuracy requirement using a simple example.

Assume that the aircraft is performing harmonic motion in the vertical plane ("GSE motion" curve in Fig. 1.32) with an amplitude $A = 1$ m and a period of 100 s (angular frequency $\omega \approx 0.061/s.$). Suppose that the GSE measurements ("GSE data" curve in Fig. 1.32) are ideal and the vertical acceleration is ideally determined using GNSS data ("GNSS" curve in Fig. 1.32), but the files have time lag relative to each other by $dt = 0.01$ s.

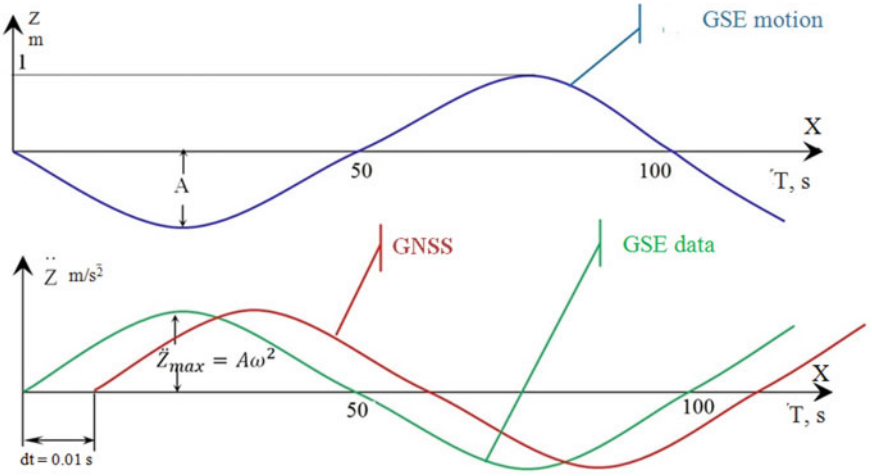

Fig. 1.32 Inaccuracy in synchronization between the GNSS and GSE data streams leads to an error of 0.2 mGal

It is easy to show that in this case, there will be an error in the gravity anomaly measurement with amplitude $d\Delta g$ equal to $d\Delta g = A\omega^3 dt \approx 0.2$ mGal .

It follows that the synchronization accuracy for the files should be at a level of 0.01–0.02 s (10– 20 ms).

In the GT-2A gravimeter, these requirements can be fulfilled owing to the following technical solutions:

1. Almost inertialess GSE with a bandwidth of 100 Hz is used, which corresponds to a GSE time constant of approximately 1 ms. Therefore, the GSE constant time and its instability during operation may be neglected.
2. GNSS-derived PPS signal, associated with the beginning of the Greenwich second, makes it possible to synchronise GSE measurements to an almost perfect accuracy of 0.00003 s (0.03 ms). For this purpose, the lag time of each individual GSE measurement from the PPS is recorded in the GSE file.

Requirements for the accuracy of the GSE-sensitive axis verticalization. There are two components of the GSE sensitive axis misalignment from vertical (the error in knowing the angle between the GSE sensitive axis and the vertical) that cause error in the gravity anomaly estimation. The first one is defined by the first term of formula 1.3.11. This error has a cosine (quadratic for small stabilization error angles) nature and does not impose any strict requirements on the accuracy of keeping the GSE sensitive axis vertical. It is easy to show that in this case, the error in keeping the GSE sensitive axis vertical equal to 4.5 arcmin leads to an error in the gravity anomaly estimation equal to 1 mGal. Much stricter requirements for the GSE sensitive axis vertical alignment are imposed by the effect of horizontal accelerations on the GSE sensitive axis, defined by the second and third terms of formula (1.3.11). Let us estimate the influence of this error component on the gravimeter error. Assume that the aircraft or, more precisely, the place where the GSE proof mass is located on it, performs harmonic motion in the horizontal plane with amplitude of 25 m and a period of 100 s. Let the error in keeping misalignment errors of GSE sensitive axis be 10 arcsec. Then it is easy to show that the amplitude of the gravity anomaly generation error due to the projection of the horizontal acceleration onto the GSE sensitivity axis will be 0.5 mGal. Therefore, the requirement for the error in keeping the GSE sensitive axis vertical in airborne gravimetry is from 10 to 15 arcsec.

A similar result was also obtained using real data of horizontal accelerations from ten survey lines in different flight conditions. For this purpose, horizontal accelerations were scaled and passed through a filter with an averaging time of 100 s. The following conclusion was made based on the calculation results: the accuracy required to maintain (know) the GSE sensitive axis vertical deflection angles for airborne gravimetry of the 0.5 mGal level is from 10 arcsec in favorable flight conditions to 6 arcsec in adverse flight conditions.

The error in keeping the GSE sensitive axis vertical depends on two components: instability of the angles β_Z, γ_Z between the GSE sensitive axis and the normal to the plane of the platform due to the instability of zero drifts of horizontal accelerometers (see the explanations for formula 1.3.1) and errors in determining the gyro platform angles α_1, α_2 during the flight.

To reduce the influence of the first component of the error, the "Autocalibration" procedure was introduced in the software of the GT-2A gravimeter which helps occasionally, once every 10–15 days and after each cold start of the gravimeter, determine the estimates $\hat{\beta}_Z$, $\hat{\gamma}_Z$. Certain values $\hat{\beta}_Z$, $\hat{\gamma}_Z$ are entered into the database of the gravimeter and taken into account in real time to form corrections in accordance with the second and third terms of formula 1.3.11. The second component of α_1, α_2 is determined during postprocessing in the GTNAV software (see Sect. 1.2.2). Errors in determining the sum of the components $\beta_Z + \alpha_1$, $\gamma_Z + \alpha_2$ are additionally estimated by the correlation method at the postprocessing stage in the GTRAV software. These solutions provide the required accuracy of keeping the GSE sensitive axis vertical.

Nonorthogonality of the DTG angular momentum with respect to the gyro platform plane. Consider a simple example (Fig. 1.33) explaining the disturbance of a gyro platform placed in a biaxial gimbal suspension during its azimuthal turn.

Figure 1.33 represents one axis of a biaxial gyrostabilizer. As mentioned above, the plane of the platform is a conventional concept; it is defined by accelerometer signals. The top part of the figure shows the gyro platform with its plane in the horizontal position, an accelerometer signal, which is conventionally represented as a spring ball and has zero readings. If the gravimeter is quickly rotated by 180° around its vertical axis, the position of the angular momentum in the inertial space will remain unchanged at the first moment of time (it can be assumed that under

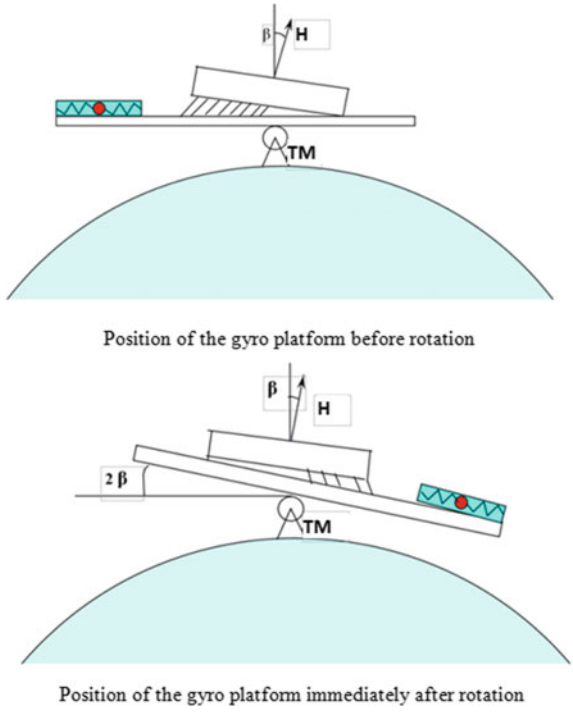

Fig. 1.33 The error in the alignment of the DTG angular momentum orthogonally to the platform plane

the influence of the correction system, the gyroscope precession can be neglected). As a result, at the first moment, the platform will deviate from the horizon plane by an angle of 2 β, which will be measured by the accelerometer, where β is the nonorthogonality angle of the gyroscope angular momentum to the platform plane.

This effect served as a basis for the method of determining nonorthogonality of the DTG angular momentum vector of the platform plane at the manufacturing instrument making plant. After determining the angles β (rotation around the X axis) and γ (rotation around the Y axis), the angular momentum vector is vertically aligned by adding the constants $\widehat{dw}_x = g\beta$ and $\widehat{dw}_y = -g\gamma$ to the signals of the accelerometers X and Y, respectively.

During operation, the DTG angular momentum deviates from the normal to the platform plane due to the instability of the accelerometer zero signals (for A15 accelerometers used in the gravimeter, the instability of zero signals is estimated at a level of ±10 arcsec). To ensure that this error does not cause the platform deviation from the horizon plane during the vehicle maneuvers, the third external azimuthal axis is used to stabilize the gravimeter (platform) position in the geographic coordinate system. Thus, the use of the third azimuthal axis completely eliminates the gravimeter error caused by the nonorthogonality of the DTG angular momentum of the gyro platform plane.

It is easy to show that the use of the third axis, which allows gyro platform stabilization in the geographic reference frame, also eliminates the effect of the constant components of the estimation errors of the scale factors and drifts of the DTG channels on the angular errors of the gyro platform.

1.3.6 Main Tasks of the Gravimeter Central Processing Unit

The central device is designed to generate preliminary (raw) gravimetric data. Its CPU executes the following relevant tasks.

Gravimeter startup. After the gravimeter is switched on, relevant gravimeter systems start their operation automatically according to the time diagram.

Generation of input data. At a frequency of 300 Hz, the data acquisition system forms information read out from the DTG angle sensors, GSE, accelerometers QAx, QAy, the FOG, and the GSE position sensor. GSE readings are corrected for the Harisson effect (according to signals from the DTG angle sensors), nonorthogonality of the GSE sensitive axis to the platform plane (according to the QAx, QAy readings), and the influence of the squares of horizontal accelerations.

Control of stabilization servo drives. The task generates the signals applied to the torque sensors DM_x, DM_y of the horizontal axes of the gimbal suspension and the azimuth stabilization motor. The task of horizontal stabilization servo drives implemented as a discrete Kalman filter operates at a frequency of 300 Hz. The input data are signals from QA accelerometers (to provide an intermediate stage for gravimeter startup) or from DTG angle sensors read out in the normal operation

mode. The input data for the control of the azimuth servo drive is the generated value of the compass heading of the gyro platform.

Systems for correcting gyro platform attitude. The task provides a proportional correction in the gravimeter startup mode and a Schuler-type integral correction in the operating mode. The input data for the task are the signals of the QAx, QAy accelerometers, the FOG, and data on the latitude and the vehicle vector velocity from the GNSS receiver.

Calculation of the compass heading of the gyro platform. The task calculates the geographical heading of the gyro platform, which is the input for the task of control of the gravimeter azimuthal servo system. The task input data are the values of the absolute angular rates of the platform obtained in the previous task, as well as the data on the GNSS-derived velocity.

Generation of the vehicle attitude angles. The task generates the heading, the angles of roll and pitch of the aircraft based on the data obtained from the previous task, as well as the readings of the stabilization angle sensors. The angles of roll and pitch are used in postprocessing to recalculate the coordinates of the GNSS antenna to the GSE location.

Gravimetric data generation. The task generates three suboptimal estimates of the gravity anomalies with various averaging times in real time (for more details, see Sect. 2.4). In addition, in the marine version, the task generates a mean value of the vertical specific acceleration per second which, at the customer's request, can be transferred to their data acquisition system. In the airborne version of the gravimeter, the generated value of the gravity anomaly is used to control the GSE on a fixed platform and to estimate the noise level of the output information of the gravimeter.

Thermal regulation. The task ensures generation of signals for the triggering the thermal regulation system (heaters and fans). The task input is signals from the thermal sensors.

Reception of commands and data output. The task ensures interaction of the computing unit of the central device with the computing unit of the control and indication device (CID). In the airborne version, during a gravity survey, the task ensures the generation of data for two so-called S- and G-files. The S-file contains information on the dynamics of the gravimeter gyro horizon; it is recorded on the CID hard disk with a frequency of 3 Hz, and serves as input information for the optimal filter implemented in the GTNAV software, which evaluates the disturbed state of the gravimeter gyro horizon in postprocessing. The G-file contains information with a frequency of 18 Hz on the measured values of the vertical and horizontal specific forces; it is recorded on the CID hard disk and used in the postprocessing task of GTGRAV software to generate gravity anomalies on the aircraft flight trajectory. For details, see Sect. 2.2.

In the marine version, the CID receives data on the three gravity anomaly values with various averaging times from the CPU in real time and records them into the G file on the hard disk once every 10 s.

Autocalibration. The task is executed occasionally during the gravimeter operation. It determines the estimates of the deviation angles $\hat{\beta}_Z$, $\hat{\gamma}_Z$ of the GSE sensitive axis from the normal to the plane of the platform by the method of successive tilts

of the platform around the X, Y axes at known fixed angles determined by QAs. At the same time, estimates of the FOG drift $\widehat{dr}$ and the drift components of the DTG gyroscope $\widehat{dp}$, $\widehat{dq}$ are determined by the method of successive rotation of the platform at 0° and 270° rhumbs. After the task is completed, the resulting parameter values are entered into the gravimeter database in order to enter corrections in real time. The task runs 5.5 h.

Calibration. Calibration is performed at the instrument making plant during the gravimeter manufacturing. It automatically determines the estimates of the deviation angles $\hat{\beta}_Z$, $\hat{\gamma}_Z$ of the GSE sensitive axis from the normal to the plane of the platform by the method of successive tilts of the platform around the X, Y axes at known fixed angles determined by QAs. At the same time, the thickness of leveling shims for the GSE base is calculated to eliminate the specified deviation. The duration of this task is 3 h.

Monitoring of the gravimeter state. The extensive monitoring system allows efficient diagnostics and timely detection of faults arising during operation. The task forms two generalized criteria of the state (readiness of the gravimeter):

- the gravimeter is serviceable (yes/no): hardware serviceability;
- g is reliable (yes/no): the reliability of measurements.

The gravimeter hardware serviceability criterion is generated as a logical sum of twenty fault criteria of elements and systems recorded in a special CID control frame.

The display of the CID monitor shows fault symptoms from the first fault detection until the operator issues the Fault Accepted command. If a fault symptom is not removed, that means that it is present at the time of issuing the command. Thus, no short-term fault goes unnoticed by the operator.

The criterion of the reliability of measurements is formed as a logical sum of six criteria such as the increased turbulence, the lack of information from the GNSS for more than 10 min during which the damping of the gyro platform oscillations is disabled, and other such criteria. In the CID frame, the operator observes the generalized criteria of the gravimeter state, and only if the gravimeter fault or unreliable measurements are detected, he turns to monitoring to find out the reasons.

Based on the results of the monitoring, a status word is generated which is recorded to the output G- and S-files.

To make fault diagnostics easier, the CPU forms diagnostic data during the operation of the gravimeter, and the CID records the so-called diagnostic file on its hard disk, which allows for remote fault diagnostics.

Noise level assessment. The task assesses the quality of the gravimeter operation on a fixed base. The task input is the output of the task on generation of gravimetric information. The task of assessing the noise level simulates the initial and final reference measurements with a length of 15 min and a flight with a length of 3 h. According to the results of the reference measurements, the simulated flight measurements are adjusted and the standard deviations of measurement errors are calculated. The result is displayed on the CID monitor.

1.3.7 Conclusions

The features of the GT-2 gravimeters have been considered both in terms of their design and software. Extremely stringent accuracy requirements for subsystems of the airborne gravimeter have been formulated; the proposed hardware, firmware, and software solutions have made it possible to satisfy the above requirements. The accuracy parameters, as well as the operational features including, in particular, the presence of a gyro platform which remains undisturbed during vehicle maneuvers, a wide dynamic measurement range (± 1 g) and a small GSE drift (3 mGal/month) have determined a great interest of Russian and international companies in gravimeters of this series.

References

Arias F, Jiang Z, Robertsson L, Vitushkin L et al (2012) Final report of key comparison CCM. G-K1: International comparison of absolute gravimeters ICAG2009. Metrologia 49(1A), Tech Suppl 07011

Arnautov GP, Gik LD, Kalish EN, Koronkevich VP, Malyshev IS, Nesterikhin YuE, Stus YuF, Tarasov GG (1974) High-precision laser gravimeter. Appl Opt 13(2):310–313

Arnautov GP, Kalish EN, Smirnov MG, Stus YuF, Tarasyuk VG (1988) Ballistic gravimeter. Author's Certificate SSSR SU 1563432, G 01 V 7/14, 01/08/1988

Atakov AI, Lokshin BS, Prudnikov AN, Shkatov MY (2010) Results of integrated geophysical survey at the Ushakovsko-Novosemel'skaya prospective area in the Kara Sea. In: IAG symposium on terrestrial gravimetry: static and mobile measurements (TG-SMM2010). Elektropribor, St. Petersburg, pp 33–35

Barthelmes F, Petrovic S, Pflug H (2013) First experiences with the GFZ new mobile gravimeter Chekan-AM, Paper abstracts of IAG symposium on terrestrial gravimetry: static and mobile measurements (TG-SMM2013). Elektropribor, St. Petersburg, p 18

Baumann H, Klingele EE, Marson I (2012) Absolute airborne gravimetry: a feasibility study. Geophysical prospecting, March 2012, pp 361–372

Berezin VB, Berezin VV, Tsitsulin AK, Sokolov AV (2004) Adaptive image reading in an astronomical system on a matrix CCD. Izvestiya vysshykh uchebnykh zavedenii, Radioelektronika 4:36–45

Berzhitsky VN, Ilyin VN, Smoller YL, Yurist SS (1999) Analog-to-digital converter. Patent of the Russian Federation no. 2168269 dated 12/23/1999

Berzhitsky VN, Ilyin VN, Smoller YL, Cherepanov VA, Yurist SS (2000) Three-axis gyrostabilizer. Patent of the Russian Federation no. 2157966 dated 01/17/2000

Berzhitsky VN, Bolotin YV, Golovan AA, Iljin VN, Parusnikov NA, Smoller YL, Yurist SS (2002) GT-1A inertial gravimeter system. Results of flight tests. Center of Applied Research Publishing House, Faculty of mechanics and mathematics, Moscow State University, Moscow

Bikeeva MM, Smirnova LA, Sokolov AV (2007) Features of the geophysical studies using a marine gravimetric system. In: 8 konferentsiya molodykh uchenykh Navigatsiya i upravlenie dvizheniem (8th Conference of Young Scientists Navigation and Motion Control). Elektropribor, St. Petersburg, pp 162–167

Blazhnov BA, Nesenyuk LP, Elinson LS (1994) Eliminating the effect of gravitational field smoothing in processing the readings of a damped airborne gravimeter. In: Proceedings of the international conference shipborne and airborne gravimetry 94, St. Petersburg

Blazhnov BA, Nesenyuk LP, Peshekhonov VG, Sokolov AV, Elinson LS, Zheleznyak LK (2002) Integrated mobile gravimetric system: development and test results. In: Volfson GB, Peshekhonov VG (eds), Primenenie graviinertsial'nykh tekhnologii v geofizike (Application of Graviinertial Technologies in Geophysics), St. Petersburg, pp 33–44

Boedecker G (2002) World gravity standards—present status and future challenges. Metrologia 39(5):429–433

Bordé CJ (2002) Atomic clocks and inertial sensors. Metrologia 39(5):435–463

Bronshtein IG, Livshits IL, Elinson LS, Gerasimova NL, Sokolov AV (2001) Quartz Gravimeter: Patent no. 2171481 of the Russian Federation: MPK G01V7/02/ appl 03.02.2000; pub 27/07/2001

Canuteson EL, Zumberge MA (1996) Fiber-optic extrinsic Fabry-Perot vibration isolated interferometer for use in absolute gravity meters. Appl Opt 35(19):3500–3505

Chelpanov IB, Nesenyuk LP, Braginsky MV (1978) Raschet kharakteristik navigatsionnykh giropriborov (Calculation of Characteristics of Navigation Gyrodevices). Sudostroenie, Leningrad

Cook AH (1965) The absolute determination of the acceleration due to gravity. Metrologia 1(3):84–114

Crossley D, Vitushkin LF, Wilmes H (2013) Global reference system for determination of the Earth gravity field: from the Potsdam system to the Global Geodynamics Project and further to the international system of fundamental absolute gravity stations. Trudy Instituta Prikladnoi Astronomii RAN 27:333–338

Dehlinger P (1978) Marine gravity, Amsterdam

Drobyshev NV, Koneshov VN, Koneshov IV, Solov'ev VN (2011) Development of an aircraft laboratory and a procedure for airborne gravimetric surveys in Arctic conditions, Vestnik Permskogo universiteta, Geologiya Series, no 3, pp 37–50

Forsberg R, Olesen A, Einarsson I (2013) Airborne gravimetry for geoid determination with Lacoste Romberg and Chekan gravimeters. In: IAG symposium on terrestrial gravimetry: static and mobile measurements (TG-SMM2013). Elektropribor, St. Petersburg, pp 22–28

Francis O, Baumann H, Volarik T, Rothleitner C (2014) The European comparison of absolute gravimeters 2011 (ECAG-2011) in Walferdange, Luxembourg: Results and recommendations. Metrologia 50(3):257–268

Francis O, Baumann H, Ullrich C et al (2015) CCM. G-K2 key comparison. Metrologia 52(1A) Tech Suppl 07009

Germak A, Desogus S, Origlia C (2002) Interferometer for the IMGC rise-and-fall absolute gravimeter. Metrologia 39(5):471–475

Gillot P, Francis O, Landragin A, Pereira Dos Santos F, Merlet S (2014) Stability comparison of two gravimeters: optical versus atomic interferometers. Metrologia 51(5):L15–L17

Ilyin VN, Volnyansky VN, Nikitin VP, Smoller YL, Yurist SS (1993) Gravimeter for measuring gravity from moving vehicles. Patent of the Russian Federation No. 2056643 dated 07/09/1993

Jiang Z, Pálinkáš V, Arias FE, Liard J, Meriet S, Vitushkin L et al (2012) The 8th international comparison of absolute gravimeters 2009: The first key comparison (CCM.GK1) in the field of absolute gravimetry. Metrologia 49(6):666–684

Koneshov VN, Bolotin YV, Golovan AA, Smoller YL, Yurist SS, Fedorova IP, Hevison W, Richter T, Greenbaum J, Young D, Blankenship D (2013a) Using airborne gravimeter GT-2A in polar areas. In: IAG symposium on terrestrial gravimetry: static and mobile measurements (TG-SMM2013a). Elektropribor, St. Petersburg, pp 36–40

Koneshov VN, Koneshov IV, Klevtsov VV, Makushin AV, Smoller YL, Yurist SS, Bolotin YV, Golovan AA (2013b) An approach to refined mapping of the anomalous gravity field in the Earth's polar caps. Izvestiya, Phys Solid Earth 49(1)):77–79

Koneshov VN, Nepoklonov VB, Sermyagin RA, Lidovskaya EA (2013c) Modern global Earth's gravity field models and their errors. Gyroscopy Navig 4(3):147–155

Kontarovich RS (2015) Aerogeophysica Inc Company: 45 years in service of the national geology. Razvedka i okhrana nedr 12:3–6

Kontarovich RS, Babayants PS (2011) Airborne geophysics: An effective tool to solve geological prospecting problems. Razvedka i okhrana nedr 7:3–7

Kovrizhnykh PN, Shagirov BB (2013) Marine gravity survey of the Kazakhstan sector of the Caspian Sea. In: IAG symposium on terrestrial gravimetry: static and mobile measurements (TG-SMM2013). Elektropribor, St. Petersburg, pp 59–62

Kovrizhnykh PN, Shagirov BB, Zhunusov IE, Saurykov ZZ (2013a) Gravity surveys in the Caspian Sea Kazakhstan transition zone. In: IAG symposium on terrestrial gravimetry: static and mobile measurements (TG-SMM2013). Elektropribor, St. Petersburg, pp 73–76

Kovrizhnykh PN, Shagirov BB, Yurist SS, Bolotin YV, Saurykov Z, Karsenov T et al. (2013b) Marine surveys in the Caspian Sea using GT-2M, Chekan-AM and LR gravimeters: accuracy comparison. Geol Protect Mineral Resour 4:58–62

Kovrizhnykh PN, Saurykov ZZ, Shagirov BB, Paydin MO (2016) Experience of airborne gravimetric surveys in Kazakhstan upland conditions. In: 4th IAG symposium on terrestrial gravimetry: static and mobile measurements (TG-SMM2016). Elektropribor, St. Petersburg, pp 44–52

Krasnov AA (2007) Results of bench and field tests of the airborne gravimeter gyrostabilizer. In: 9 konferentsiya molodykh uchenykh "Navigatsiya i upravlenie dvizheniem" (9th Conference of Young Scientists "Navigation and Motion Control"). Elektropribor, St. Petersburg, pp 26–33

Krasnov AA, Sokolov AV (2009) Development and implementation of airborne gravimetric measurement processing methods. In: Materialy X konferentsii molodykh uchenykh "Navigatsiya i upravlenie dvizheniem" (10th Conference of Young Scientists "Navigation and Motion Control"). Concern CSRI Elektropribor, St. Petersburg

Krasnov AA, Odintsov AA, Semenov IV (2010) Gyro stabilization system of a gravimeter. Gyroscopy and Navigation 1:191–200

Krasnov AA, Sokolov AV, Elinson LS (2014a) Operational experience with the Chekan-AM gravimeters. Gyroscopy Navig 5(3):179–183

Krasnov AA, Sokolov AV, Elinson LS (2014b) A new air-sea shelf gravimeter of the Chekan series. Gyroscopy Navig 5(3):129–135

Krasnov AA, Sokolov AV, Evstifeev MI, Starosel'tseva IM, Elinson LS, Zheleznyak LK, Koneshov VN (2014c) A new generation of gravimetric sensors. Meas Tech 57(9):967–972

Lygin VA (2010) Gravity surveys in transition zones with the use of hovercraft. In: IAG symposium on terrestrial gravimetry: static and mobile measurements (TG-SMM2010). Elektropribor, St. Petersburg, pp 47–49

Logozinsky VN, Solomatin VA (1996) Fiber-optic gyroscopes for industrial use. Giroskopiya i Navigatsiya 4:27–31

Matveev VA, Podchezertsev VP, Fateev VV (2005) Giroskopicheskie stabilizatory na dinamicheski nastraivaemykh giroskopakh (Gyroscopic Stabilizers on Dynamically Tuned Gyroscopes). MGTU im. N.E. Baumana, Moscow

Merlet S, Gouët JL, Bodart Q, Clairon A, Landragin A, Pereira dos Santos F, Rouchon P (2009) Operating an atom interferometer beyond its linear range. Metrologia 46(1):87–94

Mogilevsky VE, Kontarovich OR (2011) Airborne gravimetry: an innovative technology in geophysics. Razvedka i okhrana nedr 7:7–10

Mogilevsky VE, Kaplun DV, Kontarovich OR, Pavlov SA (2010) Airborne gravity surveys in Aerogeophysica Inc. In: IAG symposium on terrestrial gravimetry: static and mobile measurements (TG-SMM2010). Elektropribor, St. Petersburg, pp 42–46

Mogilevsky VE, Pavlov SA, Kontarovich OR, Brovkin GI (2015a) Features of airborne geophysical surveys in high latitudes. Razvedka i okhrana nedr 12:6–10

Mogilevsky VE, Brovkin GI, Kontarovich OR (2015b) Accomplishments, features, and problems of airborne gravimetry. Razvedka i okhrana nedr 12:16–25

Nesenyuk LP, Elinson LS (1995) The experience in carrying out a detailed marine gravimetric survey. Giroskopiya i Navigatsiya 4:60–67

Niebauer TM, Hollander WJ, Faller JE (1994) Absolute gravity in-line measuring apparatus incorporating improved operating features, United States Patent #5,351,122, Sept 27, 1994

Niebauer TM, Sasagawa GS, Faller JE, Hilt R, Klopping F (1995) A new generation of absolute gravimeters. Metrologia 32(3):159–180

Orlov OA, Vitushkin LF (2010) A compact green laser for absolute ballistic gravimeter. In: IAG symposium on terrestrial gravimetry: static and mobile measurements (TG-SMM2010). Elektropribor, St. Petersburg

Panteleev VL (1983) Osnovy morskoi gravimetrii (Fundamentals of Marine Gravimetry). Nedra, Moscow

Pamyati professora L.P. Nesenyuka (2010) Izbrannye trudy i vospominaniya (In Memory of Professor L.P. Nesenyuk. Selected Papers and Memoirs). CSRI Elektropribor, St. Petersburg

Peshekhonov VG, Sokolov AV, Elinson LS, Krasnov AA (2015) A new air-sea gravimeter: development and test results. In: 12th St. Petersburg international conference on integrated navigation systems. Elektropribor, St. Petersburg, pp 173–179

Peshekhonov VG, Sokolov AV, Zheleznyak LK, Bereza AD, Krasnov AA (2020) Role of navigation technologies in mobile gravimeters development. Gyroscopy Navig 11(1):2–12

Peters A, Chung KY, Chu S (2001) High-precision gravity measurements using atom interferometry. Metrologia 38:25–61

Popov EI (1959) Quartz gravimeter for marine observations. Trudy IFZ AN SSSR (Trans of the Institute of Physics of the Earth of The Russian Academy of Sciences) 8:32–41

Richter TG, Greenbaum JS, Young DA, Blankenship DD, Hewison WQ, Tuckett H (2013) University of Texas airborne gravimetry in Antarctica, 2008 to 2013. In: Paper abstracts of IAG symposium on terrestrial gravimetry: static and mobile measurements (TG-SMM2013). Elektropribor, St. Petersburg, p 13

Seleznev VP (1967) Navigatsionnye ustroistva (Navigation Devices). Oborongiz, Moscow

Smoller YL (2002) Mechanics, control and processing algorithms in the inertial-gravimetric aerial complex. Cand Sci Dissertation, Moscow

Smoller YL, Yurist SS, Fedorova IP, Bolotin YV, Golovan AA, Koneshov VN, Hevison W, Richter T, Greenbaum J, Young D, Blankenship D (2013) Using airborne gravimeter GT-2A in polar areas. In: IAG symposium on terrestrial gravimetry: static and mobile measurements (TG-SMM2013). Elektropribor, St. Petersburg, pp 36–40

Smoller YL, Yurist SS, Golovan AA, Yakushik LY (2015) Using a multiantenna GPS receiver in the airborne gravimeter GT-2a for surveys in polar areas. Gyroscopy Navig 6(4):299–304

Smoller YL, Yurist SS, Golovan AA, Iakushyk LY, Hewison YW (2016) Using quasicoordinates in software of multi-antenna GPS receivers and airborne gravimeter GT-2A for surveys in Polar Areas, In: 4th IAG symposium on terrestrial gravimetry: static and mobile measurements (TG-SMM2016). Elektropribor, St. Petersburg

Sokolov AV (2003) Mobile gravimeter. Prib Tekh Eksp 46(1):165–166

Sokolov AV, Usov SV, Elinson LS (2000) The experience of conducting gravity surveys in the conditions of marine seismic operations. Giroskopiya I navigatsiya 1:39–50

Sokolov AV (2004) Evaluating the position of the optical signal of a known shape. In: 6 konferentsiya molodykh uchenykh "Navigatsiya i upravlenie dvizheniem" (6th Conference of Young Scientists "Navigation and Motion Control"). Elektropribor, St. Petersburg, pp 248–254

Sokolov AV, Krasnov AA, Elinson LS, Vasil'ev VA, Zheleznyak LK (2015) Calibration of the Chekan-AM gravimeter by a tilting method. Gyroscopy Navig 6(4):288–293

Sokolov AV, Krasnov AA, Alekseenko AS, Stus YF, Nazarov EO, Sizikov IS (2017) Measuring absolute gravity aboard moving vehicles. Gyroscopy Navig 8(4):287–294

Sokolov AV, Staroseltseva IM, Elinson LS (2008) Gravity measurement device: Pat. No. 2377611 Russian Federation: IPC G01V7/00/appl. 04/22/2008; pub. 12/27/2009

Sokolov AV, Krasnov AA, Konovalov AB (2021) Automation of mobile gravimeter quartz elastic system manufacturing technology. Gyroscopy Navig 12(2):138–146

Vitouchkine AL, Faller JE (2002) Measurement results with a small cam-driven absolute gravimeter. Metrologia 39(2):465–469

Vitushkin LF (2011) Measurement standards in gravimetry. Gyroscopy Navig 2(3):184–191

Vitushkin LF, Orlov OA (2011) Absolute ballistic gravimeter. Patent for invention no. 2475786, May 06, 2011

Vitushkin LF, Orlov OA (2014) Absolute ballistic gravimeter ABG-VNIIM-1 developed at D.I. Mendeleev Research Institute for Metrology. Giroskopiya i navigatsiya 2:95–100

Vitushkin LF, Orlov OA, Germak A, D'Agostino G (2012) Laser displacement interferometers with subnanometer resolution in absolute ballistic gravimeters. Meas Tech 55(3):221–228

Zheleznyak LK, Popov EI (1982) Principles of construction and optimal design of a modern marine gravimeter. In: Fiziko-tekhnicheskaya gravimetriya (Physical and Technical Gravimetry). Nauka, Moscow, pp 43–60

Zheleznyak LK, Popov EI (1984) Uprugaya sistema tipa USG. Pribory i metody obrabotki gravi-inertsial'nykh izmerenii (Elastic system of the gravimeter. Devices and methods for processing graviinertial measurements). IFZ, AN SSSR, Moscow, pp 54–66

Zheleznyak LK, Markov GS, Romanishin PA (1983) Experimental production gravimetric survey in the Black Sea. In: Graviinertsial'nye issledovaniya (Gravi-Inertial Studies). IFZ AN SSSR, Moscow, pp 35–42

Chapter 2
Data Processing Methods for Onboard Gravity Anomaly Measurements

A. Krasnov, A. Sokolov, Yu. Bolotin, A. Golovan, N. Parusnikov, A. Motorin, A. Nosov, O. A. Stepanov, S. Yurist, and V. Vyazmin

Abstract This Chapter gives an overview of data processing methods used in measuring gravity anomalies on a moving base. Data processing and software of Russian mobile relative gravimeters Chekan and GT-2 are described. Information is given on optimal and suboptimal filtering and smoothing algorithms for estimation of gravity anomalies, and the methods used to identify the models needed for the algorithm design. The method of designing suboptimal smoothing algorithms with a constant delay is considered as applied to marine gravity measurements. Fusion of airborne gravimetric data and the global EGF models by multiscale representation of an anomalous gravity field using wavelet expansion on the sphere is addressed.

Keywords Gravimeter Chekan · Gravimeter GT-2A · Optimal and suboptimal filtering algorithms · Optimal and suboptimal smoothing algorithms · Earth's gravity field models

A. Krasnov · A. Sokolov · A. Motorin · O. A. Stepanov (✉)
Concern CSRI Elektropribor, St. Petersburg, Russia
e-mail: soalax@mail.ru

A. Krasnov
e-mail: anton-krasnov@mail.ru

Yu. Bolotin · A. Golovan · N. Parusnikov · V. Vyazmin
Lomonosov Moscow State University, Moscow, Russia

A. Sokolov · A. Motorin · A. Nosov · O. A. Stepanov
ITMO University, St. Petersburg, Russia

A. Nosov
Luxoft Professional LLC, Moscow, Russia

S. Yurist
Gravimetric Technologies, Moscow, Russia

V. G. Peshekhonov and O. A. Stepanov (eds.), *Methods and Technologies for Measuring the Earth's Gravity Field Parameters*, Earth Systems Data and Models 5,
https://doi.org/10.1007/978-3-031-11158-7_2

Introduction

This chapter gives a comprehensive overview of data processing methods used in measuring gravity anomalies (GA) on a moving base. The chapter contains five sections.

Sections 2.1 and 2.2 describe the features of data processing and software of Russian mobile relative gravimeters of the Chekan series (Sect. 2.1) and GT-2 series (Sect. 2.2) that are widely used for taking high-precision measurements of the Earth's gravitational field from marine vessels and aircraft, including measurements in remote areas of the Arctic and the Antarctic.

Each section provides a description of the technology for acquisition, onboard quality control, postprocessing, and subsequent geophysical interpretation of marine and airborne gravity survey data. Algorithms and mathematical software used for acquisition and postprocessing of gravimetric data obtained using gravimeters of these series are discussed.

Section 2.3 focuses on the design of optimal and suboptimal filtering and smoothing algorithms for estimation of gravity anomalies, and the methods used to identify the models needed for the algorithm design.

The optimal filtering and smoothing problem is considered in general form within the Bayesian approach; an example is given to illustrate the design of optimal algorithms as applied to GA estimation. Within this approach, the potential estimation accuracy can be calculated with the specified models of the anomalies and the errors of the measuring instruments, which allows objective estimation of the efficiency of various suboptimal algorithms. Further, the practical stationary algorithms based on the Butterworth filter and the two-stage estimation procedure are discussed, and their efficiency is analyzed. The importance of structural and parametric identification of the models is emphasized, which provides the required information on the models when implementing optimal algorithms. An identification algorithm is proposed, which is based on nonlinear filtering methods and actually makes the GA estimation process and the algorithms adaptive. The results of real data processing using the proposed algorithm are given in Conclusions.

Section 2.4 describes the method of designing suboptimal smoothing algorithms with a constant delay applied to the problem of marine gravity measurements.

A theoretical justification of the proposed method is given, and a methodical example is used to compare the proposed suboptimal algorithm with optimal filtering and smoothing algorithms. The section describes the smoothing algorithm for marine gravity surveys which is designed using the method under consideration and implemented in the GT-2M gravimeter software. The results of survey data processing using the proposed algorithm are presented.

Section 2.5 discusses the problem of combining airborne gravimetric data and the data from the global models of the Earth's gravitational field. The problem is solved by applying multiscale representation of an anomalous gravity field in the area of an airborne gravimetric survey using wavelet expansion on the sphere. The algorithm for data integration obtained by this method is described and the results of its work are discussed.

2.1 Chekan-Series Gravimeter Data Acquisition and Processing Software

High-precision gravity surveying from moving vehicles remains the most common and promising method for studying the Earth's gravitational field. The development of gravimetric equipment involves intense research based on high technology and profound knowledge base. An important aspect on which the final quality of geophysical data depends is functionality and efficiency of mathematical software.

A distinctive feature of marine and airborne gravity surveys is that the data is processed in successive steps that include data acquisition, onboard quality control, postprocessing, and subsequent geophysical interpretation of measurement results. Inadequacy of software at any of these steps can result in a significant deterioration in the quality of the survey results or even complete loss of the material, which is unacceptable for hard-to-reach areas of the Earth.

Choosing an adequate mathematical model that takes into account the design features of the gravimeter used and its calibration parameters, the possibility of applying various corrections and changing the coefficients and structure of the digital filter is of vital importance in postprocessing of gravity data.

Section 2.1 considers algorithms and mathematical software used in the acquisition and postprocessing of the gravimetric data obtained using the Chekan gravimeters described in detail in Sect. 1.2. All processing steps are described, including calibration and diagnostics of the system equipment that are carried out before the survey starts, real-time data acquisition, processing of the marine and airborne gravimetric profiles and final postprocessing of the survey results (Krasnov and Sokolov 2015). The structure of the software for various stages and types of gravity surveys is shown in Table 2.1.

2.1.1 Calibration and Diagnostics of the Gravimeter Equipment

Periodic calibration of the sensing element is a mandatory procedure for any type of gravimeter. In addition, during marine and especially airborne gravity surveys, it is necessary to calibrate sensing elements of the gyro stabilization system. In order to automate the setup procedures for the gravity sensor (GS), gyro platform (GP), and UMT unit at the manufacturer's plant and provide for their field diagnostics, a special software was developed that comprises 3 programs: TestGrav, TestGyro, and TestUMT.

The GS is adjusted with the TestGrav program, which provides for the following basic operations:

- adjustment of the optoelectronic converter, including its alignment, setup of the intensity and shape of autocollimation images (Fig. 2.1);

Table 2.1 Structure of the software for Chekan gravimeters

Type of operations	Marine gravity survey	Airborne gravity survey
Preparatory work	GS setup: TestGrav GP setup: TestGyro Thermal stabilization system setup: TestUMT GS calibration: Calibr	
Survey execution	Data acquisition: SeaGrav	Data acquisition: AirGrav
	Field data control: Chekan_PP	Field data control: Grav_PP_A
	GS diagnostics: TestGrav GP diagnostics: TestGyro Thermal stabilization system diagnostics: TestUMT	
Postprocessing	Profile processing: Chekan_PP	Profile processing: Grav_PP_A
	Processing of survey results, assessment of measurement accuracy: Chekan_PP	

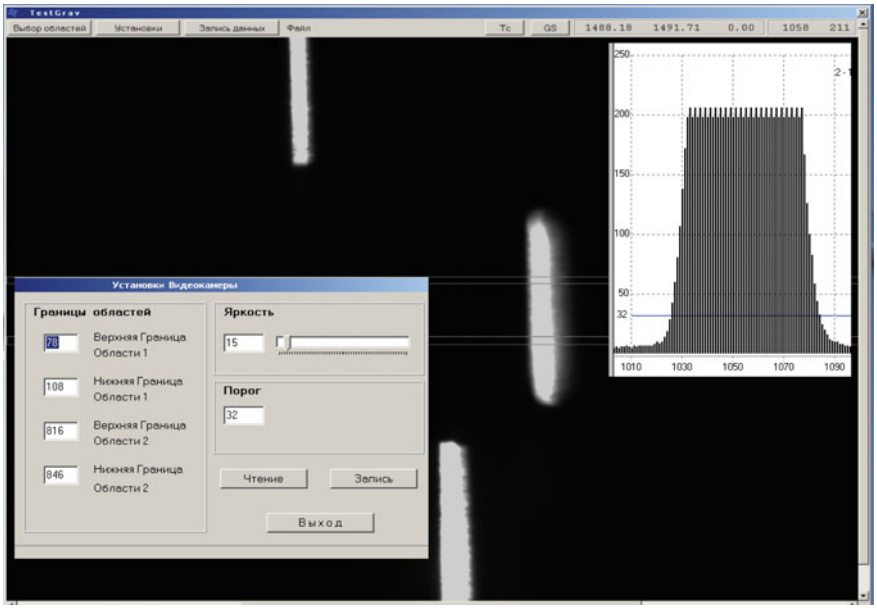

Fig. 2.1 Screen of the TestGrav program during the setup of intensity and shape of autocollimation images

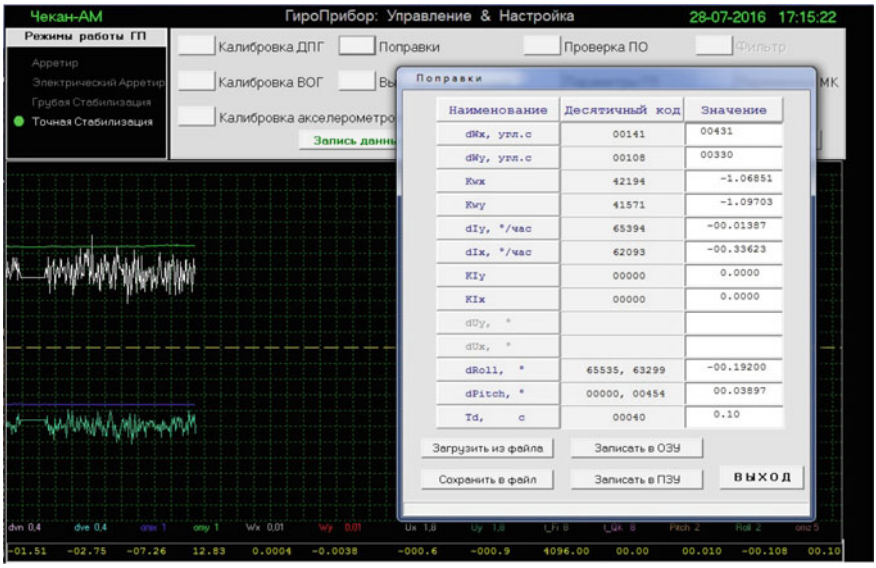

Fig. 2.2 Screen of the TestGyro program during calibration of gyroscopes

- adjustment of the GS digital thermal stabilization system;
- determination of the gravimeter elastic system (GES) response time;
- in-depth diagnostics of the GS hardware.

The TestGyro program is intended to solve similar problems of GP setup; it has the following main functions:

- automatic adjustment of the gearless servo drive in all modes of the GP operation;
- calibration of zero drifts and scale factors of floated one-degree-of-freedom gyroscopes (Fig. 2.2);
- calibration of zero drifts and scale factors of horizontal accelerometers;
- calibration of zero drift and the scale factor of azimuthal FOG;
- in-depth diagnostics of all the GP hardware.

The results of the GP primary setup are stored in the ROMs of microcontrollers and can be refined during operation.

GS calibration is traditionally done by tilting, wherein the known gravity decrements are set by changing the position of the GS measuring axis relative to the local vertical (Zheleznyak and Elinson 1982). Setting and determining tilting angles should be made using high-precision tilt-rotary benches. A special technology for GS calibration was developed and implemented in Chekan-AM and Shelf-E, in which the gyro platform is used to set and determine the gravimeter tilting angles. This technology eliminates the need for high-precision and expensive bench test equipment; and GS calibration can be done in the field (Sokolov et al. 2015).

A special program Calibr was developed to calibrate the GS using a gyro platform. The program provides both for automatic tilting of the GS at specified angles and certain intervals and processing of measurement results (Dudevich et al. 2014).

During the entire measurement cycle, the current readings of the gravimeter and GP tilting angles are recorded in a file (Fig. 2.3). The measurement for each tilting angle of the platform lasts 30 min. The entire calibration period does not exceed 9 h.

The results of data processing are available as a program operation protocol including the values of the following parameters:

- quadratic coefficient a and linear coefficients b_1, b_2 of the calibration characteristic of each quartz gravimeter system;
- specified decrements of gravity acceleration Δa_{eti} and the results of measuring Δg_i for each GP tilting angle;
- deviations δg_i of the Δg_i measurement results from the specified values of Δa_{eti};
- the fiducial error of the gravimeter calibration characteristic which is taken as the ratio of the absolute maximum of the obtained values of δg_i to the upper limit of the gravimeter measurement range;
- the margin for the gravimeter measurement range.

The protocol generated by the program is a requisite document sufficient to prepare verification certificates for Chekan-AM and Shelf-E gravimeters as measuring instruments.

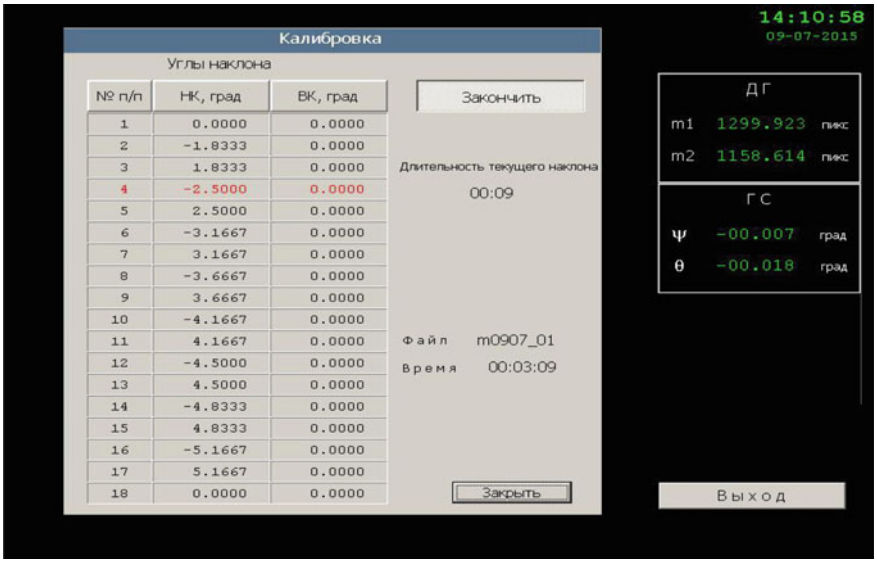

Fig. 2.3 Screen of the Calibr program

2.1.2 Real-Time Algorithms and Software

The main purpose of the real-time software is synchronous recording of the original gravimetric and navigation data at a frequency of 10 Hz in the course of measurements on survey lines. Taking into account the fundamental differences in marine and airborne gravity surveys, real-time data acquisition software comprises two different programs, SeaGrav and AirGrav, both of which provide for the following operations (Demyanenkov et al. 2014; Dudevich et al. 2007):

- GS, GP, and UMT data acquisition;
- reception of navigation information from GNSS equipment and synchronization of the gravimeter data;
- recording of raw data on the hard disk at a frequency of 10 Hz;
- linearization of the GS scale in accordance with formula (1.2.7);
- introduction of the gravimeter drift correction in accordance with formula (1.2.9);
- calculation and filtering of the gravity increment with respect to the initial gravity reference station (GRS) (this data is used for display and can also be used for onboard quality control);
- graphic display of the recorded parameters and recording of output data on the hard disk at a frequency of 1 Hz.

Additionally, the AirGrav program provides for the correction of the carrier motion effect on the gravimeter gyro platform with the use of GNSS data and the generation of current heading values, the algorithm block diagrams of which are presented, respectively, in Figs. 1.15 and 1.16 of Chap. 1.

The SeaGrav and AirGrav programs are designed to work under the Windows operating systems. The exchange of information with the GS, GP, and UMT is carried out using the RS-232 serial interface. Any modern laptop with standard USB/COM interface adapters can be used to operate the gravimeter.

Signals received from the gravimeter equipment are displayed on the screen in graphic and digital form (Fig. 2.4). The interface of SeaGrav and AirGrav provides wide capabilities for zoom control and the choice of colors for the charts. The software is adapted for two languages: Russian and English.

An essential feature of real-time programs is the availability of built-in diagnostics for the basic systems of the gravimeter, which provides for an integral test of the gravimeter operation and reliability of its readings. These diagnostic capabilities greatly simplify the operator's work, especially in airborne gravimetric surveys.

The output data of the real-time gravity data acquisition software is text files, the main content of which is presented in Table 2.2, as well as protocols of the software.

Symbol "*" in the table indicates a unique file name generated automatically. The main output files of data acquisition software are G*.RAW files, in which the readings of the gravity sensor m_1, m_2 and time t are recorded with a frequency of 10 Hz. In the G*.RAW files generated by the SeaGrav program, additional signals are recorded that can be used to calculate dynamic corrections, such as the readings

Fig. 2.4 Screen of the real-time data acquisition software in the reference observation mode

Table 2.2 Text files

File type	SeaGrav	AirGrav
G*.RAW	t, m_1, m_2, W_ψ, W_θ, U_ψ, U_θ, ψ, θ, T	t, m_1, m_2
G*.NAV	t, φ, λ	t, φ, λ, H
G*.DAT R*.DAT	t, Δg	
T*.DAT	–	t, W_ψ, W_θ, U_ψ, U_θ, Ω_z, ω_ψ, ω_θ, K, TOG, V_N, V_E, ΔV_N, ΔV_E, ψ, θ, $W_{cor\psi}$, $W_{cor\theta}$, $\Omega\cos\varphi$, T

of the horizontal accelerometers of the gyro platform W_ψ, W_θ, the floated gyro pick-offs U_ψ, U_θ, pitch angles ψ and roll angles θ, temperature T (GS temperature for the Shelf-E gravimeter or the temperature inside the GP for the Chekan-AM gravimeter).

For the same purpose, the AirGrav program generates a separate T*.DAT output file which, in addition to the signals listed, contains the FOG readings Ω_z, the control signals of the gyroscope torquers ψ, ω_θ and also some calculated corrections and derivatives of the GNSS signals received: heading K, track over ground TOG, north and east speed components V_N, V_E, speed mismatch ΔV_N, ΔV_E, corrections for the horizontal components of Coriolis acceleration $W_{cor\psi}$, $W_{cor\theta}$, and the Earth rate horizontal component $\Omega\cos\varphi$.

Both programs record G*.NAV navigation data files containing the values of latitude φ and longitude λ received from GNSS. The values of height H are additionally recorded in the AirGrav program files. It should be noted that the AirGrav G*.NAV program files are used only for real-time control of survey data; however, satellite

information refined during office processing is used for postprocessing of gravimetric data.

The SeaGrav and AirGrav programs work in two modes: reference observations and gravimetric surveys. The mode of reference observations is necessary to calculate the reference g_{r0} of the gravimeter at the GRS; the time of reference observations T_0, and the drift rate of gravimeter C based on current measurements in accordance with the formulas obtained using the least squares method:

$$g_{r0} = \frac{\sum_{i=1}^{n} g_{ri}}{n}, \tag{2.1.1}$$

$$T_0 = \frac{\sum_{i=1}^{n} t_i}{n}, \tag{2.1.2}$$

$$C = \frac{\sum_{i=1}^{n} g_{ri} \cdot \sum_{i=1}^{n} t_i - n \cdot \sum_{i=1}^{n} g_{ri} \cdot t_i}{\left(\sum_{i=1}^{n} t_i\right)^2 - n \cdot \sum_{i=1}^{n} t_i^2}, \tag{2.1.3}$$

where g_{ri} are the current measurements of the gravimeter calculated in accordance with (1.2.7), t is the measurement time, and n is the number of measurements.

In the gravimetric survey mode, the current values of the gravity increment are calculated relative to the reference at the GRS, taking into account the gravimeter drift according to formula:

$$\delta g = g_r - g_{r0} - C \cdot (t - T_0). \tag{2.1.4}$$

Gravity increments smoothed by the low-pass filter (LPF) described below are stored in the G*.DAT or R*.DAT files, depending on the mode of operation. When conducting a marine survey, G*.DAT files can be used for quality control of gravity data. R*.DAT files are used to calculate the gravimeter readings at the GRS and refine the gravimeter drift.

2.1.3 Marine Gravity Measurement Processing

Figure 2.5 shows a block diagram of marine gravimetric line data processing. As described above, the data for the postprocessing of the line are formed from the following files: G*.RAW for gravimetric data, and G*.NAV for navigation data.

Processing of the line data begins with the conversion of the GS readings into acceleration units using the coefficients of the gravimeter calibration characteristic in accordance with formula (1.2.7). The current values of the gravity increment are calculated and the gravimeter drift correction is accounted for in accordance with formula (2.1.4).

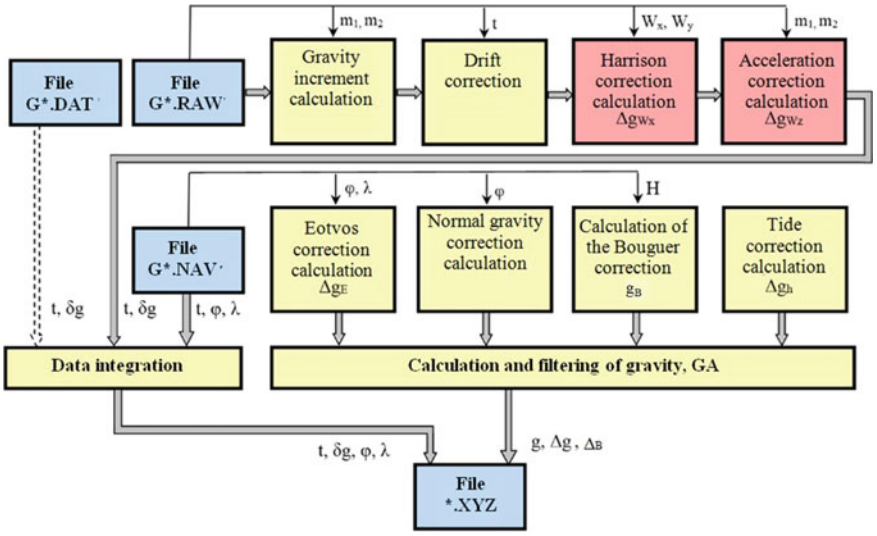

Fig. 2.5 Block diagram of marine gravity line data processing

To calculate the values of gravity and its anomalies on a line, it is necessary to combine gravimetric and navigation data and calculate at least two corrections, namely, the Eotvos correction and the normal gravity correction.

For marine gravimetric surveys, the Eotvos correction, which eliminates the effect of the Coriolis and centripetal accelerations, is calculated using the following simplified formula:

$$\Delta g_E = 7.502 \cos^2 \varphi \cdot d\lambda/dt + 0.0041 \cdot V^2, \tag{2.1.5}$$

where V is the vessel speed, kn; $d\lambda/dt$ is the longitude rate, arcmin/h; φ is the latitude, rad.

Figure 2.6 gives an example how the Eotvos correction changes the systematic component of the gravimeter signal and compensates for the accelerations caused by minor changes in the heading and speed of the carrier on the survey line.

Normal gravity correction γ is usually calculated by the Helmert formula.

The value of gravity at a marine gravimetric station is calculated using the following formula:

$$g = g_0 + \delta g + \Delta g_E, \tag{2.1.6}$$

where g_0 is the value of gravity at the GRS relative to which the survey was conducted.

The GA value in free air Δg is defined as the difference of gravity at the marine station and the normal value of gravity:

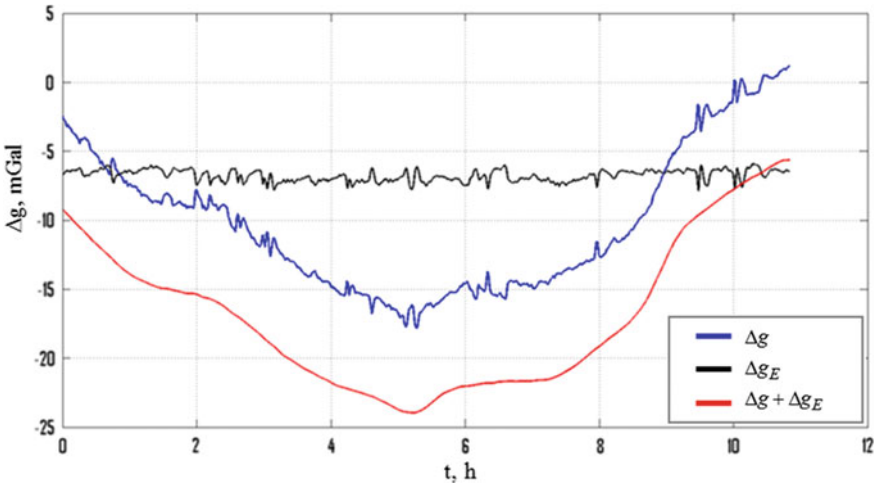

Fig. 2.6 Introducing the Eotvos correction Δg_E to gravity readings

$$\Delta g = g - \gamma. \tag{2.1.7}$$

If depth data is available, the gravity anomaly is calculated in the Bouguer reduction taking into account the gravity of the layer between the gravity station and the sea level in accordance with the following formula (Torge 1989):

$$\Delta g_B = g - \gamma + g_B, \tag{2.1.8}$$

where $g_B = 0.0419 \cdot H \cdot (\sigma_1 - \sigma_2)$ is the Bouguer correction, H is the sea depth, m; σ_1 is the density of seabed rocks; $\sigma_2 = 1.03$ g/cm^3 is the density of sea water.

The effect of vertical accelerations is eliminated from the measurement results using a low-pass filter, to which the value of the gravity increment is input after taking into account all the corrections. For marine surveys, the use of a low-pass filter is fully justified since the power spectral densities (PSDs) of the useful signal and the disturbing acceleration are separated in the frequency domain. For processing the data from Chekan gravimeters, it is recommended to use a combined digital filter which consists of the 1st order aperiodic filter with the time constant T_a and the 4th order Butterworth filter with the time constant T_b.

The data processing using the combined digital filter is conducted in two stages. During the first stage, the readings of the gravimeter are passed through the filter in the forward time mode. After that, the time is inverted, and the gravimeter readings are processed by the same filter in reversed time. As mentioned in Sect. 2.3, the data processing technology in the forward and reversed time modes agrees with the solution of the smoothing problem and allows, among other things, eliminating the phase distortions of signals introduced by the filtering procedure.

Figure 2.7 shows the amplitude-frequency characteristics of the low-pass filter described for various values of the time constants T_a and T_b. The advantage of data processing by survey lines is that it is possible to vary these parameters for various sea states in order to ensure maximum spatial resolution. Table 2.3 presents the recommended values of T_a and T_b, the cutoff frequency f_c of the LPF and their corresponding spatial resolution L/2 at a speed of 5 kn for various sea states obtained empirically so that the root-mean-square deviation (RMSD) of the residual error for the vertical acceleration is less than 0.1 mGal.

Additional corrections Δg_{Wz} and Δg_{Wx} may be introduced in the readings of Chekan gravimeters in order to improve the final accuracy of marine gravimetric surveys, as shown in Fig. 2.5. This is especially relevant for marine surveys with significant sea waves or even in stormy weather (Zheleznyak et al. 2010). As described in Chap. 1, under vertical accelerations above 50 Gal, the readings of

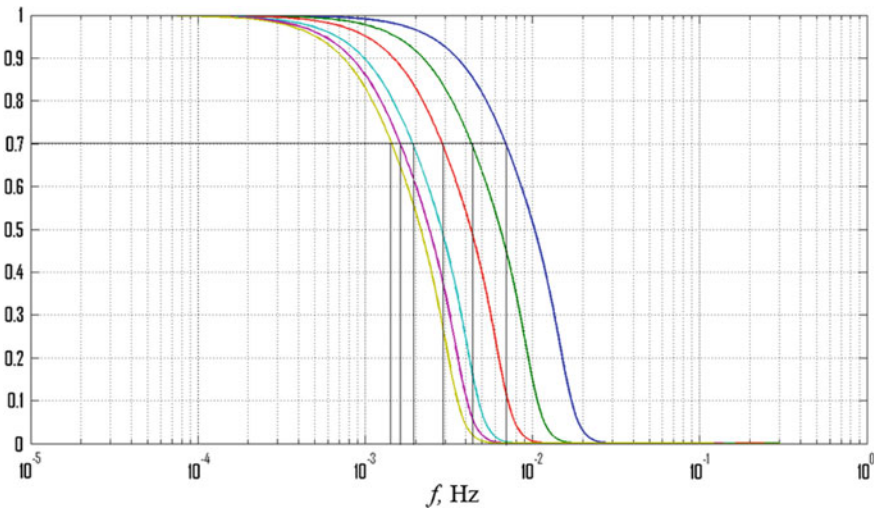

Fig. 2.7 Amplitude-frequency response of the filter

Table 2.3 Filter parameters

Sea state		Filter parameters			Spatial resolution $L/2$, m
Wave height, m	Parameter, points	T_a, s	T_b, s	f_c, Hz	
0–0.25	0–1	15	10	0.0069	190
0.25–0.75	2	24	16	0.0043	300
0.75–1.25	3	36	24	0.0029	440
1.25–2.0	4	54	36	0.0019	680
2.0–3.5	5	64	42	0.0016	800
3.5–6.0	6	72	48	0.0015	860

Chekan-AM gravimeters may include a systematic error δW_z caused by the nonlaminar nature of the fluid damping of GES pendulums. The value of the error δW_z is quadratic in nature; it largely depends on the degree of the GES damping and is substantially lower in the Shelf-E gravimeter. Nevertheless, it is possible to introduce the Δg_{Wz} correction into gravimeter readings in accordance with the algorithm shown in Fig. 2.8.

The values of specific force W_z acting on the pendulums are determined from formula (2.1.4) and are input into the scheme for calculation of Δg_{Wz} correction. In order to eliminate the gravitational component from the values of specific force, the scheme includes negative feedback on the current gravity increments δg generated by a filter of the 3rd order with the time constant $T = 60$ s. As it is, Δg_{Wz} correction is determined using the following formula:

$$\Delta g_{Wz} = k_{Wz} \cdot \tilde{W}_z^2, \tag{2.1.9}$$

where k_{Wz} is a coefficient determined empirically during the gravimeter testing on a vertical displacement test bench. The Δg_{Wz} correction is calculated in real time.

An example of improving the measurement accuracy in stormy weather owing to the Δg_{Wz} correction is shown in Fig. 2.9. It is clear that not only the systematic component but also the high-frequency component of the δW_z error are compensated for, which makes it possible to increase the spatial resolution $L/2$ of the measurements by using an LPF with a higher cutoff frequency f_c. In addition, in the case of a significant change in sea state on the line, the error δW_z cannot be taken into account by the tie methods of the survey but, as can be seen from Fig. 2.9, can be compensated for by introducing the correction Δg_{Wz}.

Another correction shown in Fig. 2.10 is introduced to compensate for the effect of the joint action of horizontal accelerations and residual GP tilting, which is referred to

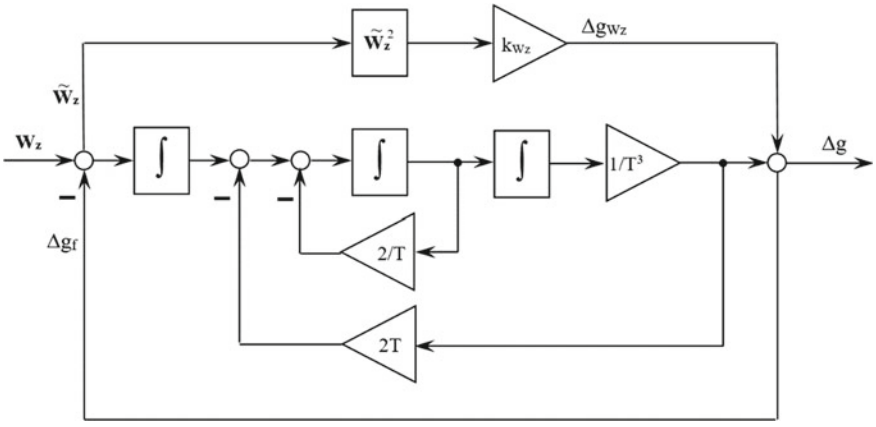

Fig. 2.8 Calculation of the vertical acceleration correction Δg_{Wz}

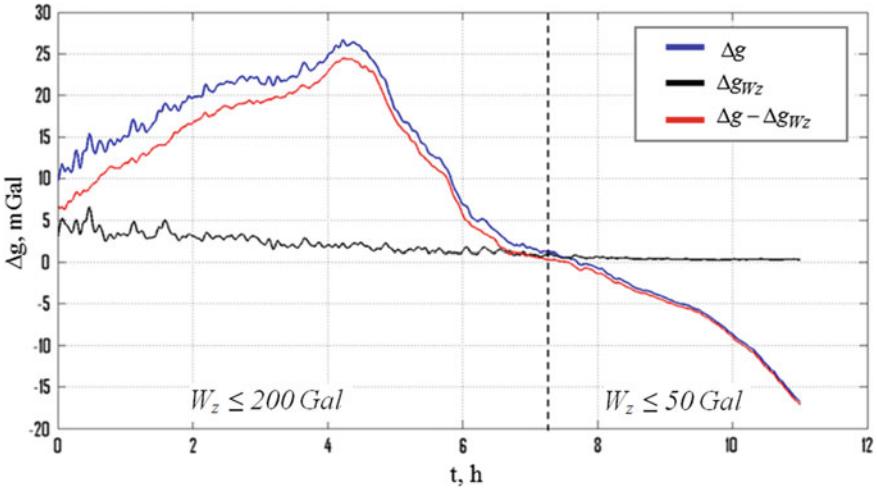

Fig. 2.9 Introduction of the correction for vertical accelerations on a marine line

as the Harrison effect. The Harrison effect correction can be represented as (Panteleev 1983):

$$\Delta g_{Wx} = W_X \alpha + W_Y \beta, \tag{2.1.10}$$

where W_X, W_Y are the longitudinal and transverse horizontal accelerations, respectively; α, β are the gyro vertical tilting angles about the respective stabilization axes.

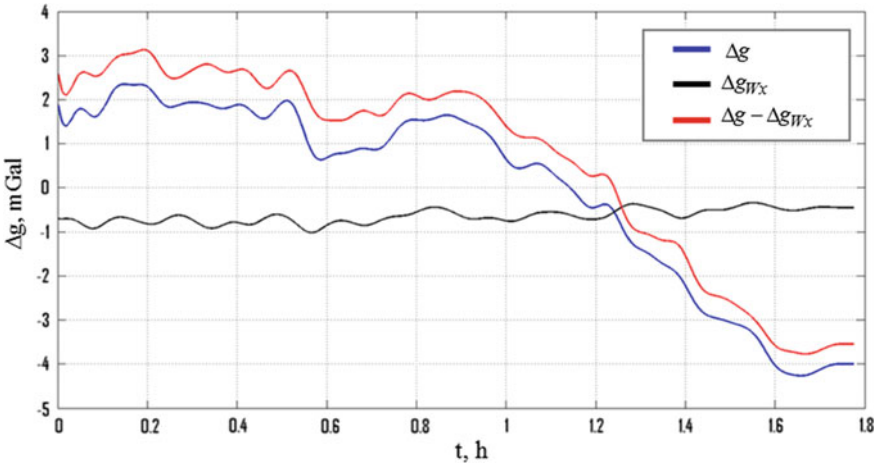

Fig. 2.10 Introduction of the Harrison correction

The tilting angles of the gyro vertical due to the errors of the gearless gyro servo drive do not exceed 15 arcsec, that is, they do not affect the gravimeter accuracy. Therefore, while calculating the Harrison correction, it is necessary to take into account only the errors of the gyroscope accelerometric correction system, which was discussed in Sect. 1.2. Angles α, β are calculated by multiplying the horizontal accelerations obtained from the recordings of accelerometer signals by the transfer function of the gyro vertical which, according to the block diagram presented in Fig. 1.15, takes the form:

$$H_w^{\alpha}(p) = \frac{\frac{1}{R}F(p)}{p^2 + \frac{g}{R}F(p)}, \tag{2.1.11}$$

where $F(p)$ is the transfer function of the filter (1.2.10), and R is the average radius of the Earth.

Figure 2.11 shows the introduction of the Harrison correction on a gravimetric survey line at high sea. The Harrison correction is mainly systematic, and its value for Chekan gravimeters does not usually exceed 1–1.5 mGal.

All the above procedures for processing of gravimetric survey lines are implemented in the Chekan_PP program, which is designed for comprehensive office processing of marine gravimetric survey data (Zamakhov et al. 2013). The

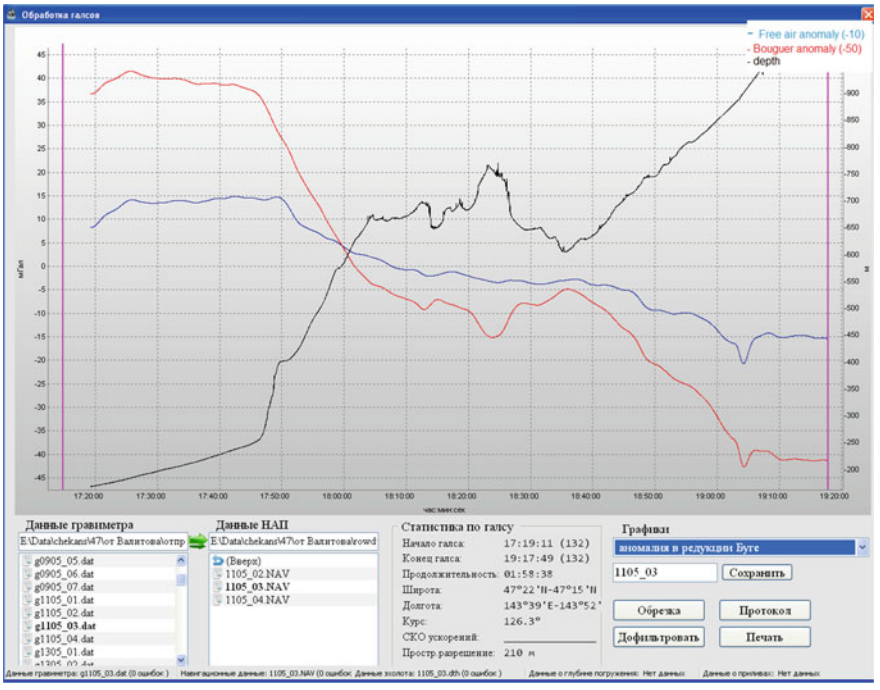

Fig. 2.11 Screen of the Chekan_PP program during the processing of a marine survey line

Chekan_PP program is designed to work under the Windows operating systems and can be used both for office processing of survey data and onboard data quality control. The program interface is quite convenient and clear; all intermediate and final results are presented to the operator in digital and graphical forms.

Logical data control in the *.DAT, *.RAW, *.NAV source files and elimination of minor data gaps are also automatically performed during survey line processing. In the case of low-quality gravimetric data on the survey line, the latter can be divided into several parts. At the user's request, a filtering procedure can also be carried out, which is implemented not only by selecting the values of T_a and T_b but also by sequential repeated use of the LPF. In addition, the cutoff frequency f_c and the spatial resolution $L/2$ on the survey line are calculated automatically. The results of survey line processing are saved in text files of the *.XYZ type and the calculation and filtering parameters are recorded in the program operation protocols.

2.1.4 Airborne Gravity Measurement Processing

Measurements of gravity onboard aircraft are taken against the background of carrier-induced vertical accelerations which not only exceed the "useful" signal by several orders of magnitude but they also overlap in the frequency domain. Figure 2.12 shows a block diagram of processing of an airborne gravimetric survey line. Vertical accelerations in gravimeter readings are partially compensated for during postprocessing using altitude information from GNSS data. However, due to the significant background noise, the final detection of the "useful" signal is also performed using filtering and smoothing (Krasnov and Sokolov 2013).

For the processing of airborne gravimetric survey lines, gravimeter readings are converted into acceleration units (just like it was with marine gravimetric survey lines); GAs are calculated, and corrections are introduced for the gravimeter drift, the normal value of gravity, and the Eotvos effect.

Since the response time of a heavily damped Chekan gravimeter ranges from 40 to 100 s, it is necessary to determine the real value of specific force during the processing of airborne gravimetric measurements. To do this, the smoothed gravimeter signal is passed through a digital recovery filter, in which the aperiodic element of the first order is used as a model of fluid damping, and the transfer function of the recovery filter has the form of formula (1.2.8).

The vertical acceleration of the carrier has the predominant effect on the GS in airborne surveys. It is taken into account based on the results of flight altitude measured by GNSS equipment operating in the differential mode. In the absence of base stations, ephemerides corrections are used to refine the navigation data.

The offset of the GNSS receiver antenna relative to the GS location is calculated in accordance with the following formula:

$$H = H_{GNSS} - (R_X \sin\psi + R_Y \sin\theta + R_Z(\cos\psi - 1) + R_Z(\cos\theta - 1)), \tag{2.1.12}$$

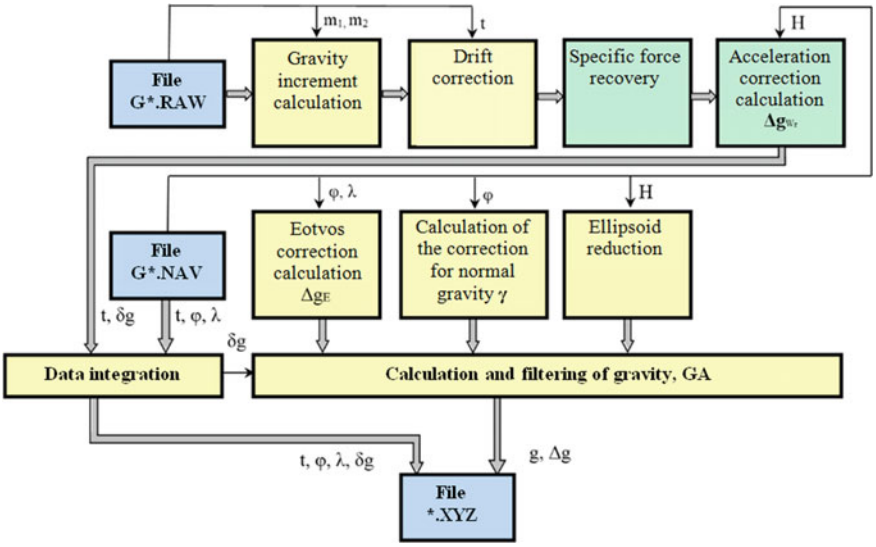

Fig. 2.12 Block diagram of airborne gravimetric survey line data processing

where H_{GNSS} is the altitude value measured at the GNSS receiver antenna location; H is the altitude value at the GS location; R_X, R_Y, R_Z are the offsets of the GNSS receiver antenna relative to the GS measured by the operator in three planes; ψ, θ are the angles of pitch and roll according to the readings of the gravimeter GP angle sensors.

The Eotvos correction in the processing of airborne gravimetric measurements is calculated using the formula that takes into account the nonspherical nature of the Earth and flight altitude variations:

$$\Delta g_E = 15V_E\cos\varphi + \left(\frac{V_N^2}{R}\left(1+\frac{H}{R}-0.5e^2\left(2-3\sin^2\varphi\right)\right)\right.$$
$$\left.+\frac{V_E^2}{R}\left(1+\frac{H}{R}-0.5e^2\sin^2\varphi\right)\right)\cdot 10^5, \qquad (2.1.13)$$

where φ is the latitude; V_N, V_E are the north and east components of the linear speed; R, e are the parameters of the WGS84 common reference ellipsoid. Formula (2.1.13) shall be used in processing of extended survey lines when the nonspherical nature of the Earth cannot be neglected.

Another requisite operation is the reduction of measurement results to the surface of the reference ellipsoid, which is carried out in accordance with the formula that takes into account the normal vertical gradient of gravity:

$$\Delta g = \Delta g_h + 0.3086H, \qquad (2.1.14)$$

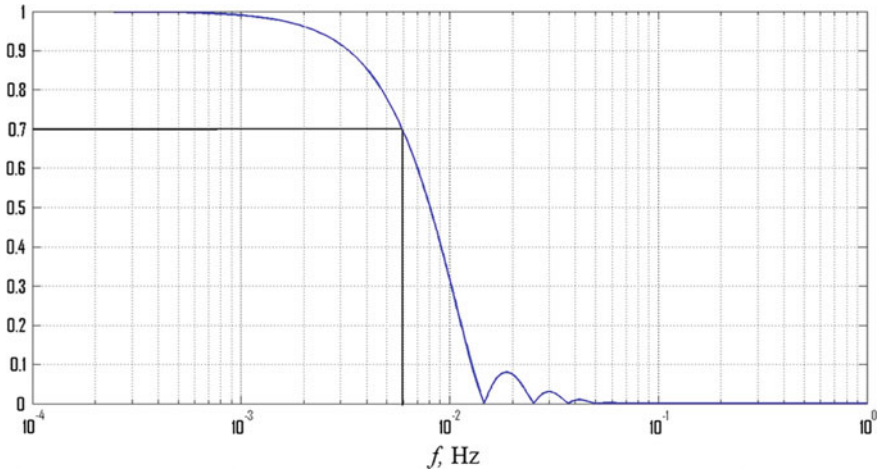

Fig. 2.13 Amplitude-frequency response of the filter at a cut-off frequency of 0.006 Hz

where Δg_h is the GA at altitude H; Δg is the GA reduced to the surface of the ellipsoid.

Even in the case that all the known corrections are thoroughly taken into account, the gravimeter signal remains noisy. Filtering and smoothing are applied in order to identify the useful component. The software of Chekan gravimeters offers a two-stage procedure, which, at the first stage, uses a finite impulse response filter with a trapezoidal Tukey weight function in the time domain (Krasnov and Sokolov 2013). This filter has a finite impulse response, resulting in a constant shift of all the harmonics of the input signal, which is easy to take into account during processing. The amplitude-frequency response of the filter is shown in Fig. 2.13.

The result of processing is a signal, the noise level of which is a few mGal. Next, at the second stage, a smoothing operation is performed, wherein a fast Fourier transform is used to transform the signal into the frequency domain; high-frequency harmonics of the signal are truncated, after which a reverse transition into the time domain is performed. When choosing the required number of harmonics in the final signal, this procedure does not deteriorate the spatial resolution, nor does it cause negative edge effects, provided that the duration of the realization is not decreasing (Fig. 2.14).

In the conditions of airborne gravimetric surveys, of extreme importance is not only postprocessing of the survey line but also onboard quality control of measurements to identify unreliable data. The Grav_PP_A program, operating under the Windows operating system, was developed to solve these two problems.

The purpose of onboard quality control is to detect survey lines or some parts of lines with poor data quality and identify the causes of quality deterioration. The primary analysis of the initial gravimetric and navigation information is aimed at detecting equipment failures. In addition, the program provides for comparison of the measured gravity profile with independent sources of gravimetric data; for example,

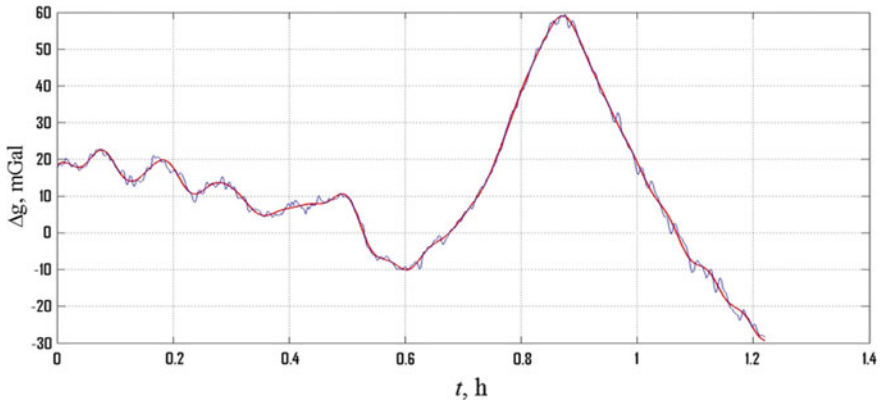

Fig. 2.14 An example of gravimetric measurement smoothing

the results of previous surveys made in this area, the global models of the Earth's gravitational field, and gravity databases, such as the Arctic gravimetric project, ArcGP (Forsberg and Kenyon 2004).

Grav_PP_A program also provides for estimation of the functioning criteria of all gravimeter systems, as well as the conditions for measurements (Fig. 2.15). The presence of such criteria allows effective identification of possible causes of data quality deterioration. The following parameters are analyzed for this purpose:

- gravity sensor: the difference between the readings of quartz systems;
- gyro stabilization system: stabilization errors and heading error;
- satellite receiver: no failures in data reception;

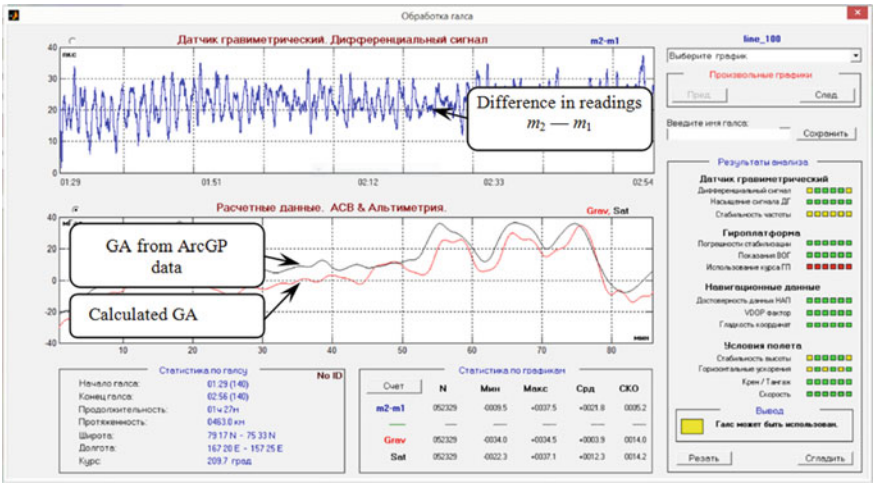

Fig. 2.15 Screen of the Grav_PP_A program with data control

- flight conditions: stable altitude, vertical and horizontal accelerations, the constancy of pitch and roll angles, and constancy of the ground speed.

Similarly to the Chekan_PP program, the results of the airborne gravity line processing are stored in *.XYZ text files used for the subsequent office processing of the survey results.

2.1.5 Postprocessing of Gravimetric Survey Data

The final processing of the results of both marine and airborne gravimetric surveys carried out by Chekan gravimeters is performed with the use of the previously mentioned Chekan_PP program. The results of measurements on lines are loaded into the survey database. The program automatically calculates the statistical parameters of the survey, including the lengths of survey lines, the number of cross points, survey RMS errors and RMS deviations.

The survey RMS error is calculated using the formula:

$$\sigma_{RMS} = \sqrt{\sigma_{CP}^2 + \sigma_{interp}^2}. \tag{2.1.15}$$

The RMS error of a single GA determination at cross points σ_{CP} is calculated using the formula:

$$\sigma_{CP} = \sqrt{\frac{\Sigma d^2}{2n}}, \tag{2.1.16}$$

where d is the difference in measuring gravity anomaly at cross points; n is the number of cross points.

An essential feature is that the survey RMS error also takes into account the interpolation error σ_{interp} in the measurement results between the survey lines:

$$\sigma_{\text{interp}} = \sqrt{\frac{\sum_{\text{i=1}}^{\text{N}} [\Delta g_{\kappa} - (g_{\text{c1}} + g_{c2})/2]_i^2}{N}}, \tag{2.1.17}$$

where Δg_k is the value of the gravity anomaly on the tie line at point K located midway between the survey lines; g_{c1} and g_{c2} are the values of the gravity anomaly on the adjacent survey lines, between which point K is located, at the points of intersection with the tie lines; N is the number of points K in the survey.

The RMSD of the survey error does not take into account systematic difference in the measurement results at cross points; it has the following form:

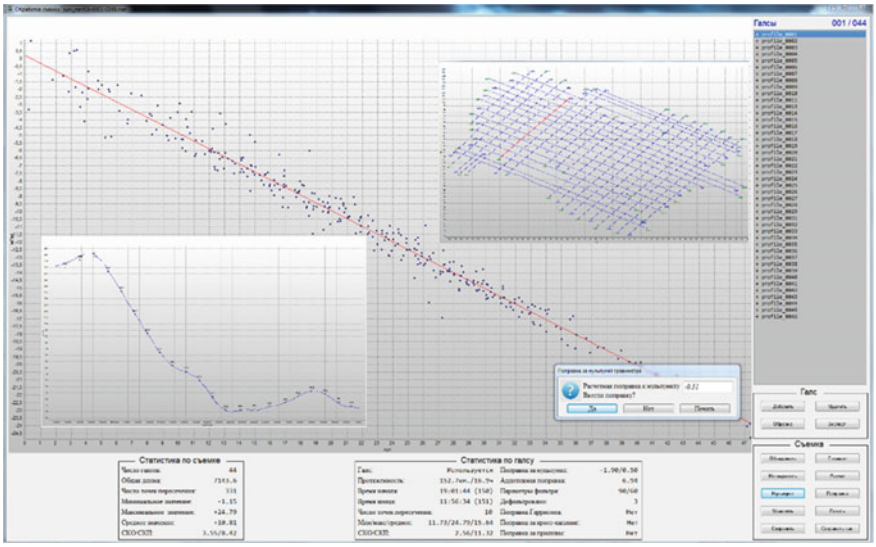

Fig. 2.16 Screen of the Chekan_PP program during processing of survey results

$$\sigma_{RMSD} = \sqrt{\frac{\Sigma(d-r)^2}{2(n-1)}}, \tag{2.1.18}$$

where $r = \frac{\sum d}{n}$.

Since marine geophysical surveys are often conducted without final reference measurements, but initial reference measurements are not long enough to obtain a reliable estimate of the gravimeter drift C, a significant feature is the calculation and introduction of the correction ΔC using the difference between GA measurements at the cross points of the lines (Fig. 2.16).

In the case of multiple reference observations at the same airport, they can also be compiled into an appropriate database to refine the gravimeter drift using all the data obtained.

Another important procedure is tying of survey results, in which averages of discrepancies at cross points are calculated and added into each survey line.

The values of all corrections introduced during data processing are stored along with processing parameters in the program protocols generated automatically.

The results of the survey processing can be exported for further processing in the text format *XYZ* suitable for loading into most of the modern geophysical data processing packages.

2.1.6 Conclusion

Features of data acquisition and processing using gravimeters of the Chekan series have been described.

The design, structure, and functionality of the software used at each stage of acquisition, processing, and analysis of marine and airborne gravimetric data are presented.

Some examples are given to illustrate the improvement of measurement accuracy owing to the introduction of dynamic corrections.

2.2 Data Processing in GT-2 Airborne Gravimeters

In 2000, the Laboratory of Control and Navigation of Lomonosov Moscow State University started developing software for data postprocessing in the first-generation GT-1A airborne gravimeters designed by the Gravimetric Technologies (Russia) (the second-generation gravimeters are known as the GT-2 series). At the same time, preparations began for the first test of the prototype MAG-1 (the first commercial name of the GT-1A airborne gravimeter) aboard an AN-30 aircraft. The tests were carried out in 2001 (Berzhitsky et al. 2002). Earlier, the Laboratory created software for two other Russian airborne gravimeters (Bolotin et al. 2002):

- the airborne gravimeter Graviton-M developed by VNIIGeofizika, Moscow Institute of Electromechanics and Automation (MIEA), and Bauman Moscow State Technical University. The first flight tests (3 flights) of this system were conducted aboard an MI-8 helicopter in December 1995 and January 1996. In July and August 1999, for the first time in Russia, a full-scale areal surveying was carried out aboard an AN-26 aircraft not far from Kaluga. Later on, this system was used by GNPP Aerogeophysica;
- the airborne gravimetric system developed by MIEA. The project, which started in 1996, was financed by the World GeoScience Corporation (Australia). Three series of flight tests were conducted: (1) 3 flights in December 1997; (2) 2 flights in May 1998 aboard an AN-26 aircraft flying near Vologda; (3) a flight in July 1999 aboard an L-410 aircraft, Brno, the Czech Republic.

The flight tests of these gravimeters were attended by experts from The Schmidt Institute of Physics of the Earth of the Russian Academy of Sciences.

Thus, by the time the Laboratory of Control and Navigation started joint work with the Gravimetric Technologies, the Laboratory had already gained considerable experience in processing airborne gravimetric data from Graviton-M and the MIEA system so that it was easy to formulate the objectives of postprocessing and the design philosophy of the software.

The first stage of postprocessing software is quality control (QC) of experimental data. It is very important for a survey operator to be able to quickly answer the question about the quality of the recorded experimental data:

(1) measurements of the gravimeter sensing element (GSE);
(2) data of the GNSS receivers on the aircraft and at base stations;
(3) data of the INS responsible for the GSE vertical orientation;
(4) data from the recording and information-flow-synchronization systems of the gravimetric system.

The main document for the development of the express diagnostic software was The Information Exchange Protocol in the Airborne Gravimetric System which was developed jointly by the Gravimetric Technologies and the Laboratory of Control and Navigation of Moscow State University. The exchange protocol describes the formats of raw data files as well as the formats of output files. The latter contain all relevant information for quality control.

In general, the software for GT-2 airborne gravimeters consists of the two main parts: the GTNAV and GTGRAV modules. The first part includes algorithms for developing satellite navigation parameters and integration of INS and GNSS data; the second part presents the solution to the airborne gravimetry problem based on GSE measurements and navigation data prepared by the GTNAV module.

In addition, for the purposes of quality control, the GTNAV module provides for the analysis of the following parameters:

- correct synchronization of information flows from the INS and GNSS. INS data are recorded with a frequency of about 3 Hz, the GNSS data are recorded at 1, 2, 5, 10, and 20 Hz sampling rates. Synchronization of flows is carried out using the 1PPS (pulse per second) mechanism, recording of the INS and GNSS time scales and their relative biases;
- data integrity (gaps);
- occurrence of events indicative of the gravimeter malfunctioning. For example, such events as ‘GSE not normal’, ‘abnormal ARS drift’, etc. The list of possible events is described in the data exchange protocol;
- correctness of the base station coordinates, its immobility;
- the level of misalignment error estimates of the instrument (gyro platform), levels of DTG and FOG drift estimates.

It is very important that quality control software should be easy to use because operators conducting surveys may be well trained in gravimetry, less competent in satellite navigation, and totally incompetent in inertial navigation. All they need is to enter raw data filenames—INS, GNSS (aircraft and/or base station(s))—as initial information for the GTNAV module, and then run the program. The program can work separately with INS and GNSS data or with their various combinations. Many years of experience in using this software by various companies, both Russian and international, have shown its effectiveness for the purposes of quality control.

GTGRAV program is responsible for processing of the GSE measurements, GTNAV output data, as well as GA determination. Like GTNAV, this program (to

be more exact, its auxiliary module GTQC) performs additional preliminary verification of GSE measurements integrity and synchronizes information flows. Unlike GTNAV, GTGRAV has an advanced graphical interface. The need for an interface is associated with the "creative" nature of the GA determination problem, where customizable processing parameters are often found by the trial-and-error method.

2.2.1 Airborne Gravimetry Software

Let us briefly describe the airborne gravimetry problem from the point of view of theoretical mechanics (a more detailed description can be found in Sect. 1.1) and write down the main gravimetric equation in the form convenient for further consideration. In Sects. 2.2.3, 2.2.4, this equation is specified for the case of the GT-2A gravimeter with a leveled platform.

The problem of gravimetry is the inverse problem of mechanics: to determine force from motion. It should be recalled that force, as a vector quantity, is characterized by magnitude and direction. However, in classical, "scalar" gravimetry, the direction of GA action is not usually specified. This is partly due to the fact that the difference between the magnitude of the gravity vector and the value of its vertical component was, until recently, an order of magnitude lower than the available measurement accuracy. At present, vector gravimetry methods are actively developing (see Sect. 5.2) so that they make it possible to determine three components of the gravity disturbance vector, and thereby, eliminate the above uncertainty.

It should also be noted that, from the mathematical point of view, the problem of GA determination belongs to the class of ill-posed problems since it is solved by differentiation (Tikhonov and Arsenin 1979).

The main equations of airborne scalar gravimetry are Newton's equations that describe the vertical motion of a material point of a unit mass in the field of the Earth's gravitational force under the action of an external force that is accessible for measurement (Torge 1989; Bolotin et al. 1999):

$$\ddot{h} = \dot{V}_3 = \Delta g_E - \gamma_0 - \delta\gamma + f_3 + \Delta g,\ \ \Delta g_E = \left(\frac{V_E^2}{R_E} + \frac{V_N^2}{R_N} + 2\Omega V_E \cos\varphi \right). \tag{2.2.1}$$

The equation uses the following notation: h is the flight altitude above the reference ellipsoid (Torge 1989); V_3 is the vertical velocity; V_E, V_N are the Eastern and Northern components of the relative velocity of the carrier; R_E, R_N are the radii of curvature of the longitudinal and latitudinal cross-sections; Ω is the modulus of the angular rate of the Earth rotation; φ is the geographical latitude; γ_0 is the magnitude of the normal gravity on the reference ellipsoid; $\delta\gamma$ is the correction of the normal gravity value for the flight altitude above the reference ellipsoid; f_3 is the projection

of the specific force on the geographic vertical; Δg is the GA to be found. The term Δg_E is due to the motion of the aircraft; it is called the Eotvos correction.

The goal of the airborne scalar gravimetry problem is to determine (estimate) the values of GA Δg based on model (2.2.1) from the other measured or calculated terms.

The equipment used for information support of the airborne gravimetry problem is directly determined from the main gravimetric Eq. (2.2.1), from which it follows that any airborne gravimetric system with a leveled platform should include:

- a GSE to measure the value of f_3 as a specific force acting on its sensitive mass;
- a navigation system to provide high-accuracy information about the altitude h, coordinates, and the vector of the linear velocity of the vehicle on which the gravimetric system is installed. Currently, such a system is a Global Satellite Navigation System operating in differential carrier phase mode;
- a navigation system providing the vertical orientation of the GSE sensitive axis. An example is a gimbaled INS which, using a gyrostabilized platform, physically simulates the geodetic reference frame, with the GSE sensitive axis rigidly attached to its vertical axis.

The basis for the solution of gravimetric Eq. (2.2.1) with respect to Δg is GSE measurement f_3', measurements of the INS horizontal accelerometers f_1', f_2', and altitude measurements h' from the GNSS. In the linear approximation, the measurement equations can be written as follows:

$$h' = h + \Delta h^{gps}, \tag{2.2.2}$$

$$\begin{aligned} f_3'(t - \tau_3) &= f_{z3} + \kappa_3 f_{z3} + \Delta f_3^0 + \Delta f_3^s + \kappa_2 f_{z1} - \kappa_1 f_{z2}, \\ f_{z3} &= f_3 + \alpha_2 f_{z1} - \alpha_1 f_{z2}, \end{aligned} \tag{2.2.3}$$

$$f_1'(t) = f_{z1} + \Delta f_1^s,\ f_2'(t) = f_{z2} + \Delta f_2^s. \tag{2.2.4}$$

The equations use the following notation: f_{z3} is the projection of the specific force of the proof mass on the instrument axis; κ_3 is the error of the GSE scale factor, Δf_3^0 is the GSE bias; Δf_3^s is the noise component of the measurement error; κ_1, κ_2 are the angular errors of the installation of the GSE sensitive axis to the platform; f_{z1}, f_{z2} are the horizontal (in the platform axes) components of the specific force; α_1, α_2 are the misalignment errors of the instrument vertical; t is the absolute time; τ_3 is the time constant of the GSE clock skew, Δh^{GNSS} is the error in the GNSS altitude determination.

Parameters Δf_{z3}^0, $\kappa_1, \kappa_2, \kappa_3, \alpha_1$, α_2, τ_3 are unknown and should be determined (estimated) during the solution of the airborne gravimetry problem. It should be noted that coefficients $\kappa_1, \kappa_2, \kappa_3$ are normally determined during laboratory and prestart calibrations and are used to adjust GSE readings. However, the experience of data processing has shown that it is advisable to determine and control these coefficients

during postprocessing from airborne measurements. Parameter τ_3 is used to refine data synchronization.

The sources of information for determining coordinates and velocities are GNSS positional and velocity solutions obtained by processing the raw GNSS measurements: code pseudo-ranges, Doppler pseudo-range rates, and carrier phase measurements. The source of information for determining α_1, α_2 is solution of the INS/GNSS integration problem. This is what defines the scope of tasks for the postprocessing software.

2.2.2 Software for GNSS Solutions

The software for GNSS solutions implemented in the GTNAV module provides for different options of calculations depending on the following circumstances:

- the data used can be received from several (one, two, three) GNSS base stations. The software must be able to maintain solutions for different combinations of base stations;
- GNSS receivers may have different data sampling rates; for example, 1, 2, 5, 10, 20 Hz. The software must be able to maintain solutions at a common frequency;
- the carrier phase receivers used can be of multi-frequency type (at present, dual-frequency); accordingly, solutions should be provided both for the $L1$ frequency and for combinations of carrier phases free of ionospheric delays;
- the software must be able to maintain solutions when data are provided by single- and/or dual-frequency receivers;
- velocity solutions should be obtained not only by processing Doppler measurements but also based on carrier phases.

These features are implemented in the GTNAV software.

All of the above requires the solutions of numerous auxiliary problems such as the ephemeris problem to determine the coordinates and vector velocity of navigation satellites, estimation of the integer ambiguities of carrier phases, detection and elimination of satellite measurement failures. In reference (Vavilova et al. 2009), the authors show basic models of the problems of raw GNSS data processing for the standard (autonomous) mode of operation of GNSS receivers, on the basis of which the satellite navigation software was developed.

Described below in general terms is only one problem of velocity determination using raw carrier phases; its solution usually provides the highest accuracy.

The model of carrier phases Z_ϕ looks as follows:

$$Z_\phi = \rho/\lambda + f_\phi(\Delta\tau - \Delta T) + N + \delta\phi_{ion} + \delta\phi_{trop} + \delta\phi^s, \tag{2.2.5}$$

where ρ is the range between the vehicle and the satellite; f_ϕ is the frequency of the radio signal; λ is the wavelength of a frequency; N is an unknown number, an integer

ambiguity of the carrier phase measurement; $\delta\phi_{ion}$, $\delta\phi_{trop}$ are the ionospheric and tropospheric delays, respectively; $\delta\phi^s$ is a random component of the carrier phase error.

The single ∇Z_{ϕ_i}, ΔZ_{ϕ_i} and double $\nabla\Delta Z_{\phi_i}$ differences of carrier phase are defined by the following formulas:

$$\nabla Z_{\phi_i} = Z_{\phi_i} - Z_{\phi_z}, \Delta Z_{\phi_i} = Z^b_{\phi_i} - Z^M_{\phi_i}, \nabla\Delta Z_{\phi_i} = \left(Z^b_{\phi_i} - Z^M_{\phi_i}\right) - \left(Z^b_{\phi_z} - Z^M_{\phi_z}\right), \tag{2.2.6}$$

where $Z^b_{\phi_i}$ is the carrier phase measurement of the base station; $Z^M_{\phi_i}$ is the similar measurement of the aircraft receiver, hereinafter referred as to rover; indices i, z correspond to the measurements obtained from the satellites with the corresponding numbers; z is usually used for the number of the zenith satellite. Taking into account (2.2.6), measurement (2.2.5) takes the form:

$$\nabla\Delta Z_{\phi_i} = \nabla\Delta\rho_i/\lambda + \nabla\Delta N_i + \nabla\Delta\phi_{ion_i} + \nabla\Delta\phi_{trop_i} + \nabla\Delta\phi^s_i,$$

where

$$\begin{aligned}
\nabla\Delta\rho_i &= \left(\rho^b_i - \rho^M_i\right) - \left(\rho^b_z - \rho^M_z\right);\\
\nabla\Delta N_i &= \left(N^b_i - N^M_i\right) - \left(N^b_z - N^M_z\right);\\
\nabla\Delta\phi_{(***)_i} &= \left(\delta\phi^b_{(***)_i} - \delta\phi^M_{(***)_i}\right) - \left(\delta\phi^b_{(***)_z} - \delta\phi^M_{(***)_z}\right).
\end{aligned} \tag{2.2.7}$$

The useful signal in measurement (2.2.7) is the value $\nabla\Delta\rho_i/\lambda$. The residual errors in (2.2.7) are double differences $\nabla\Delta\phi_{ion_i}$, $\nabla\Delta\phi_{trop_i}$, $\nabla\Delta\phi^s_i$ of the ionospheric, tropospheric, and random measurement errors (marked as (***) in the last Eq. (2.2.7)).

The main property of measurement (2.2.7) is the absence of instrumental errors of the receiver and satellites and the errors of their clocks in the model, as well as the decrease in the level of residual errors $\nabla\Delta\phi_{ion_i}$, $\nabla\Delta\phi_{trop_i}$ of the ionosphere and troposphere; note that the smaller are the distances between the bases and rover and the differences in their altitudes, the smaller is the level of the above residual errors.

The value $\nabla\Delta N_i$ is the integer ambiguity of the double differences of carrier phases, which is not fundamentally compensated in this method of phase measurement formation.

Consider the numerical derivative

$$\nabla\Delta Z^*_{V_{\rho_i}}\left(t_j\right) = \lambda\frac{\nabla\Delta Z_{\phi_i}\left(t_{j+1}\right) - \nabla\Delta Z_{\phi_i}\left(t_{j-1}\right)}{t_{j+1} - t_{j-1}} \tag{2.2.8}$$

of the differential carrier phases $\nabla\Delta Z_{\phi_i}\left(t_j\right)$. The result of (2.2.8) is the estimate of the double differences $\nabla\Delta V_{\rho_i} = \left(V_{\rho^b_i} - V_{\rho^M_i}\right) - \left(V_{\rho^b_z} - V_{\rho^M_z}\right)$ of the radial velocities

of the receivers relative to the satellites at time t_j:

$$\nabla\Delta Z^*_{V_{\rho_i}}(t_j) \cong \frac{\nabla\Delta\rho_i(t_{j+1}) - \nabla\Delta\rho_i(t_{j-1})}{t_{j+1} - t_{j-1}} \cong \nabla\Delta V_{\rho_i}.$$

On the other hand, the satellite radial velocity $V_{\rho_i^b}$ relative to the base station (which is stationary) for each i-th satellite can be calculated according to Vavilova et al. (2009):

$$V_{\rho_i^b} = \frac{\left(R_\eta^{sat_i} - R_\eta^b\right)^T}{\rho_i^b} V_\eta^{sat_i},$$

where $R_\eta^{sat_i} = \begin{bmatrix} R_{\eta 1}^{sat_i} & R_{\eta 2}^{sat_i} & R_{\eta 3}^{sat_i} \end{bmatrix}^T$ is the vector of the Cartesian coordinates of the i-th satellite; R_η^b is the vector of the Cartesian coordinates of the base station; $V_\eta^{sat_i}$ is the vector of the relative velocity of the i-th navigation satellite. Symbol η means that the corresponding vectors are defined in the geocentric coordinate system associated with the Earth (Greenwich, rotating), also referred to as ECEF (Earth Centered Earth Fixed). The radial speed of the satellite relative to the vehicle is defined by a similar formula which takes into account both the vector of the vehicle coordinates R_η^M and the vector of its own velocity V_η^M:

$$V_{\rho_i^M} = V^{(1)}_{\rho_i^M} + V^{(2)}_{\rho_i^M};\ V^{(1)}_{\rho_i^M} = \frac{\left(R_\eta^{sat_i} - R_\eta^M\right)^T}{\rho_i^M} V_\eta^{sat_i};\ V^{(2)}_{\rho_i^M} = \frac{\left(R_\eta^{sat_i} - R_\eta^M\right)^T}{\rho_i^M} V_\eta^M.$$

The component $V^{(1)}_{\rho_i^M}$ is explicitly calculated from the known information on the coordinates and vector velocities of navigation satellites, the vehicle coordinates. The component $V^{(2)}_{\rho_i^M}$ contains information on the vehicle's vector velocity V_η^M. Let us form measurement equations in linear approximation:

$$\nabla\Delta Z_{V_{\rho_i}} = \nabla\Delta Z^*_{V_{\rho_i}}(t_j) - \left[\left(V_{\rho_i^b} - V^{(1)}_{\rho_i^M}\right) - \left(V_{\rho_z^b} - V^{(1)}_{\rho_z^M}\right)\right]. \tag{2.2.9}$$

Thus,

$$\nabla\Delta Z_{V_{\rho_i}} = -\left(V^{(2)}_{\rho_i^M} - V^{(2)}_{\rho_z^M}\right) + \nabla\Delta V_{ion_i} + \nabla\Delta V_{trop_i} + \nabla\Delta V_i^s = h^{\mathrm{T}}_{(i)} V_\eta^M + \nabla\Delta r_{\dot{\rho}_i}. \tag{2.2.10}$$

The following notation is used here:

$$h^T_{(i)} = \left(\frac{R_\eta^{sat_i} - R_\eta^M}{\rho_i^M} - \frac{R_\eta^{sat_z} - R_\eta^M}{\rho_z^M}\right)^T,\ \nabla\Delta r_{\dot{\rho}_i} = \nabla\Delta V_{ion_i} + \nabla\Delta V_{trop_i} + \nabla\Delta V_i^s,$$

where $\nabla\Delta r_{\dot{\rho}_i}$ is the residual error of the triple differences of carrier phases. As a result, using the vector form of the equations, we can write:

$$\nabla\Delta\mathbf{Z}_{V_\rho} = \begin{bmatrix} \nabla\Delta z_{V_{\rho_1}} \\ \nabla\Delta z_{V_{\rho_2}} \\ \vdots \\ \nabla\Delta z_{V_{\rho_{N-1}}} \end{bmatrix} = \begin{bmatrix} h^T_{(1)} \\ h^T_{(2)} \\ \vdots \\ h^T_{(N-1)} \end{bmatrix} V^M_\eta + \begin{bmatrix} \nabla\Delta r_{\dot{\rho}_1} \\ \nabla\Delta r_{\dot{\rho}_2} \\ \vdots \\ \nabla\Delta r_{\dot{\rho}_{N-1}} \end{bmatrix} = \mathbf{H}_{(\eta)} V^M_\eta + \nabla\Delta\mathbf{r}_{\dot{\rho}} \tag{2.2.11}$$

The solution to (2.2.11) by the least-squares method (with postulation of the corresponding hypotheses about error $\nabla\Delta r_{\dot{\rho}_i}$) is as follows:

$$\tilde{V}^M_\eta = \left(\mathbf{H}^T_{(\eta)}\Sigma^{-1}\mathbf{H}_{(\eta)}\right)^{-1}\mathbf{H}^T_{(\eta)}\Sigma^{-1}\nabla\Delta\mathbf{Z}_{V_\rho}. \tag{2.2.12}$$

Here, Σ is the covariance matrix of errors $\nabla\Delta r_{\dot{\rho}_i}$. The elevation angles of navigation satellites are usually used for parameterization of matrix Σ (2.2.12) (Vavilova et al. 2009).

We need to make the following comments.

(1) The described algorithm assumes that the velocities $V^{sat_i}_\eta$ of the navigation satellites are known. In this case, GNSS users need to supplement the standard algorithm used to determine coordinates of navigation satellites with an algorithm to calculate their relative velocities.
(2) When forming differential combinations of carrier phases, it is necessary to solve the problem of mutual synchronization of measurements since they are obtained from two receivers operating in their own time scales.
(3) The central part of the algorithm is numerical differentiation of the double differences of phase measurements. Correct implementation of this procedure assumes the absence of cycle slips in carrier phases (changes in the values of uncertainties $\{\nabla\Delta N_i\}$) in the differentiation interval. Therefore, the algorithms of detection and compensation for possible faults in carrier phases is a requisite element of the problem. The Doppler velocity solution is useful additional information in this case. In addition, the problem (2.2.12) can also be solved with the use of L1-optimization since it allows eliminating "bad" satellites (Mudrov and Kushko 1971; Akimov et al. 2012).
(4) In the case of double-frequency receivers, in differentiation, it is possible to use combinations of carrier phases free from the ionospheric error.

For the quality control of satellite navigation solutions, the GTNAV software generates a number of parameters that allow the operator to decide on the normal or problematic functioning of GNSS receivers. Such parameters include data gaps, the number of visible satellites, PDOP values, baseline lengths, solution accuracies, statistical characteristics of solutions based on the analysis of residuals of raw measurements, etc.

The software was adjusted in terms of GNSS solutions based on the processing of a great amount of experimental data obtained during commercial gravimetric surveys in various regions of the Earth, using GNSS equipment produced by various manufacturers and with various characteristics, under various conditions of piloting the carrier of the gravimetric system, etc.

The software supports the following formats of raw data files: Javad's *.jps format, Ashtech's format (e-, b-files), which were used in the first version of the software, the format using the Waypoint GrafNav software (epp, gpb-files). Satellite data processing can be carried out both for a single file (aircraft receiver or base station) and for data from several receivers.

The source data for the software are the names of data files containing raw GNSS measurement records and ephemeris information, calculation time limits and the minimum set of control parameters such as coordinates of the base stations used, satellite mask angle, satellite number with a corresponding time interval which is forced out of processing.

In other words, the software is maximally focused both on the operator of the gravimetric survey, who conducts quality control of satellite data, and on obtaining satellite navigation solutions specific to the airborne gravimetry problem.

Below is the list of options of the GTNAV software.

1. Differential mode (different combinations of base stations):
   - determination of coordinates using carrier phase measurements;
   - determination of coordinates using code measurements;
   - determination of velocity using Doppler measurements;
   - determination of velocity using phase measurements;
   - determination of acceleration using carrier phase measurements.
2. Standard (autonomous) mode:
   - determination of coordinates using carrier phase measurements;
   - determination of coordinates using code measurements;
   - determination of velocity using Doppler measurements;
   - determination of velocity using carrier phase measurements;
   - determination of acceleration using carrier phase measurements.

2.2.3 Software for INS/GNSS Integration

First of all, it should be noted once again that the GTNAV module provides for the following functions: data integrity check, check for synchronization of inertial data recording with GNSS data, check for warning messages about any failure or malfunction of gravimeter sensors.

The GTNAV module also provides INS/GNSS integration solutions, which are used for quality control and solution of the GA estimation problem. The magnitudes of vertical misalignment errors, azimuth (heading) error, and constant components of the gyro drifts are important for quality control. Thus, if the magnitudes of the misalignment errors are within ±4 arcmin, the GT-2A leveling system operates normally. Otherwise, it may be indicative of the DTG and/or FOG malfunctioning.

For the GA estimation problem, the estimates of misalignment errors are input parameters (see (2.2.3)). Estimation of misalignment errors in the GT-1A, GT-2A airborne gravimeters was a nontrivial problem to solve. The key points of the above problem are given below:

- the GT-2A uses GNSS-derived position and velocity to damp Schuler oscillations in real time. Therefore, it was necessary to record real-time damping signals for postprocessing, which is reflected in the data exchange protocol;
- the damping algorithm is based on a simplified channel-by-channel model of the INS error equations;
- INS dead-reckoning algorithms use the model of the so-called compass heading, based on the GNSS-derived velocity;
- the model of the dead-reckoning algorithm uses relative and absolute angular rates of the geodetic reference frame, which caused certain difficulties in the integration problem given below.

Let us describe this problem. The mechanization equations of the two-component INS with the leveled platform (Golovan and Parusnikov 2012) of GT-series airborne gravimeters are as follows (Bolotin and Golovan 2013):

$$
\begin{aligned}
\dot{v}'_1 &= \Omega^2 R_E \sin\varphi^{GNSS} \cos\varphi^{GNSS} \sin A' + f'_1 - a_3 Z_{V_1} - \tilde{\nu}_3^{(1)},\\
\dot{v}'_2 &= \Omega^2 R_E \sin\varphi^{GNSS} \cos\varphi^{GNSS} \cos A' + f'_2 - a_3 Z_{V_2} - \tilde{\nu}_3^{(2)},\\
\dot{V}'_1 &= \Omega \sin\varphi^{GNSS} V_{a2}^{GNSS} + f'_1 - a_0 Z_{V_1},\\
\dot{V}'_2 &= -\Omega \sin\varphi^{GNSS} V_{a1}^{GNSS} + f'_2 - a_0 Z_{V_2},\\
\dot{\tilde{\nu}}_3^{(1)} &= a_2 Z_{V_1},\\
\dot{\tilde{\nu}}_3^{(2)} &= a_2 Z_{V_2},\\
\omega'_1 &= -\frac{v'_2}{R_E} - \frac{V_N^{GNSS}}{R_E}\left(1 - \frac{R_N}{R_E}\right)\cos A' + a_1 \frac{Z_{V_2}}{R_E},\\
\omega'_2 &= -\frac{v'_1}{R_E} - \frac{V_N^{GNSS}}{R_E}\left(1 - \frac{R_N}{R_E}\right)\sin A' - a_1 \frac{Z_{V_1}}{R_E}.
\end{aligned}
\tag{2.2.13}
$$

Equations (2.2.13) use the following notation: v'_1, v'_2, V'_1, V'_2 are the horizontal components of the absolute and relative velocities of the vehicle motion; ω'_1, ω'_2 are the gyro platform leveling signals; Ω is the Earth angular rate; R_E is the radius of curvature of prime vertical, a, e^2 are the semi-major axis and the square of the first eccentricity of the Earth's model ellipsoid; h^{GNSS}, φ^{GNSS}, V_E^{GNSS}, V_N^{GNSS} are the altitude, geographic latitude, eastern and northern components of velocity; the

superscript 'GNSS' hereinafter means that the values of such quantities are taken from the navigation satellite system during calculations; A' is the azimuth angle defined as:

$$A' = arctg\left(-\frac{v_2' - V_2^{GNSS}}{v_1' - V_1^{GNSS}}\right);$$

$V_1^{GNSS} = V_E^{GNSS}\cos A' + V_N^{GNSS}\sin A'$, $V_2^{GNSS} = -V_E^{GNSS}\sin A' + V_N^{GNSS}\cos A'$ are the transformed components of the relative velocity f_1', f_2' are the readings of the horizontal accelerometers; $Z_{V_1} = V_1' - V_1^{GNSS}$, $Z_{V_2} = V_2' - V_2^{GNSS}$ are velocity aiding measurements; a_1, a_2, a_3, a_4 are the gain (damping) coefficients calculated as a function of parameter T_{gg} (this refers to the characteristic time of the transition process).

The corresponding equations of the INS errors are the following:

$$\begin{aligned}
\delta\dot{v}_1 &= -\vartheta_3 v_2^{GNSS} - \alpha_2\left(g + \Omega^2 R_E\cos^2\varphi^{GNSS}\right) + \Delta f_1 \\
&\quad - \left(\frac{\delta v_1\sin A' + \delta v_2\cos A' - \Delta V_N^{GNSS}}{v_E^{GNSS}}\right)\Omega^2 R_E\sin\varphi^{GNSS}\cos\varphi^{GNSS}\cos A' \\
&\quad - a_3 Z_{V_1} - \tilde{\nu}_3^{(1)}, \\
\delta\dot{v}_2 &= \vartheta_3 v_1^{GNSS} + \alpha_1\left(g + \Omega^2 R_E\cos^2\varphi^{GNSS}\right) + \Delta f_2 \\
&\quad + \left(\frac{\delta v_1\sin A' + \delta v_2\cos A' - \Delta V_N^{GNSS}}{v_E^{GNSS}}\right)\Omega^2 R_E\sin\varphi^{GNSS}\cos\varphi^{GNSS}\sin A' \\
&\quad - a_3 Z_{V_2} - \tilde{\nu}_3^{(2)},
\end{aligned}$$

$$\begin{aligned}
\dot{\alpha}_1 &= -\frac{\delta v_1}{R_E} + \vartheta_1 - \frac{\Delta V_N^{GNSS}}{R_E}\left(1 - \frac{R_N}{R_E}\right)\cos A' \\
&\quad - \left(\frac{\delta v_1\sin A' + \delta v_2\cos A' - \Delta V_N^{GNSS}}{v_E^{GNSS}}\right)\frac{V_N^{GNSS}}{R_E}\left(1 - \frac{R_N}{R_E}\right)\sin A' + a_1\frac{Z_{V_2}}{R_E}, \\
\dot{\alpha}_2 &= \frac{\delta v_2}{R_E} + \vartheta_2 + \frac{\Delta V_N^{GNSS}}{R_E}\left(1 - \frac{R_N}{R_E}\right)\sin A' \\
&\quad - \left(\frac{\delta v_1\sin A' + \delta v_2\cos A' - \Delta V_N^{GNSS}}{v_E^{GNSS}}\right)\frac{V_N^{GNSS}}{R_E}\left(1 - \frac{R_N}{R_E}\right)\cos A' - a_1\frac{Z_{V_1}}{R_E},
\end{aligned}$$

$$\begin{aligned}
\delta\dot{V}_1 &= -\vartheta_3 V_2^{GNSS} - \alpha_2 g + \Delta f_1 + \Delta V_2^{GNSS}\Omega\sin\varphi^{GNSS} \\
&\quad + \left(\frac{\delta v_1\sin A' + \delta v_2\cos A' - \Delta V_N^{GNSS}}{v_E^{GNSS}}\right)\Omega\sin\varphi^{GNSS} V_1^{GNSS} - a_0 Z_{V_1}, \\
\delta\dot{V}_2 &= \vartheta_3 V_1^{GNSS} + \alpha_1 g + \Delta f_2 - \Delta V_2^{GNSS}\Omega\sin\varphi^{GNSS} \\
&\quad + \left(\frac{\delta v_1\sin A' + \delta v_2\cos A' - \Delta V_N^{GNSS}}{v_E^{GNSS}}\right)\Omega\sin\varphi^{GNSS} V_2^{GNSS} - a_0 Z_{V_2}.
\end{aligned}$$

Here,

$$
\begin{aligned}
v_1^{GNSS} &= \left(V_E^{GNSS} + \Omega R_E \cos\varphi^{GNSS}\right)\cos A' + V_N^{GNSS}\sin A',\\
v_2^{GNSS} &= -\left(V_E^{GNSS} + \Omega R_E \cos\varphi^{GNSS}\right)\sin A' + V_N^{GNSS}\cos A',\\
\Delta V_1^{GNSS} &= \Delta V_E^{GNSS}\cos A' + \Delta V_E^{GNSS}\sin A',\\
\Delta V_2^{GNSS} &= -\Delta V_E^{GNSS}\sin A' + \Delta V_E^{GNSS}\cos A',
\end{aligned}
$$

δv_1, δv_2, δV_1, δV_2 are the dynamic errors in the determination of the absolute and relative velocities; α_1, α_2 are the misalignment angular errors of the instrument vertical; Δf_1, Δf_2 are the accelerometer errors; $\vartheta = \left[\vartheta_1,\ \vartheta_2,\ \vartheta_3\right]^T$ is the vector of the gyro platform drift, each component of which is described by the Wiener process; g is the gravity assumed to be 9.81 m/s^2.

The aiding measurement model takes the form:

$$
\begin{aligned}
Z_{V_E} &= V_1'\cos A' - V_2'\sin A' V_E' - V_E^{GNSS} = V_1\cos A' - \delta V_2\sin A'\\
&\quad - \delta A\cdot V_N^{GNSS} - \Delta V_E^{GNSS},\\
Z_{V_N} &= V_1'\sin A' + V_2'\cos A' - V_N^{GNSS} = \delta V_1\sin A' + \delta V_2\cos A'\\
&\quad + \delta A\cdot V_E^{GNSS} - \Delta V_N^{GNSS},\\
Z_{v_E} &= v_1'\cos A' - v_2'\sin A' - \left(V_E^{GNSS} + \Omega R_E\cos\varphi^{GNSS}\right)\\
&= \delta v_{a1}\cos A' - \delta v_{a2}\sin A' - \delta A\cdot V_N^{GNSS} - \Delta V_E^{GNSS},\\
\delta A &= -\frac{\delta v_1\sin A' + \delta v_2\cos A' - \Delta V_N^{GNSS}}{v_E^{GNSS}}.
\end{aligned}
\tag{2.2.14}
$$

Here, ΔV_E^{GNSS}, ΔV_N^{GNSS} are the errors of GNSS velocity solutions.

Thus, the behavior of INS errors is described by a general model of the form $\dot{x} = Ax + Bu + w$, where the state vector x includes the inertial system errors and the errors of the inertial sensors; w is a zero-mean white noise; u is the vector of known control signals.

Further, to solve the estimation problem, i.e., to estimate the state vector x using measurements Z_{V_E}, Z_{V_N}, Z_{v_E}, smoothing algorithms are used in the postprocessing mode (see Vavilova et al. (2009) and Sect. 2.3).

The GTNAV software provides the algorithms to solve the described problem. Note that calculations can be carried out using both differential GNSS solutions and GNSS solutions in autonomous mode. The latter is especially important for quality control because in this case it is possible to solve the integration problem without data from base stations, i.e., immediately after the aircraft has landed.

No additional external settings of the integration algorithm are required, which makes the operator's work easier.

The INS/GNSS software makes the work of the gravimetric survey operator simpler from the viewpoint of quality control.

2.2.4 Software for the Solution of the Basic Gravimetry Equation

Based on the results of the GTNAV software operation, the so-called V-files, containing GNSS positional and velocity solutions, and I-files, containing the description of the gyro platform misalignment angles, are generated. Along with the S-files and G-files generated by the GT-2A gravimeter, these data are used during the final processing in the GTQC20 and GTGRAV modules to form a GA estimate on the trajectory recorded in the G3-file.

The GTQC20 module is responsible for monitoring the data quality in the binary files generated by the GT-2A gravimeter. It checks the synchronization of data with the GNSS clock pulse and gaps in processing cycles, makes a conclusion about the data quality and, if possible, restores the omissions and records the refined and synchronized data into text files. The GTGRAV module generates the GA estimate.

Let us briefly discuss the mathematical part of processing. Consider a "model" basic gravimetric equation that differs from (2.2.1) in the absence of GAs and the substitution of measurements instead of the true values of variables (Bolotin et al. 2002):

$$\begin{aligned} \ddot{h}' &= \dot{V}_3', \\ \dot{V}_3' &= \Delta f_E' - \gamma_0' - \delta\gamma' + f_3'. \end{aligned}$$

Subtracting this equation from (2.2.1), denoting $\Delta h = h - h'$, $\Delta W = V_3 - V_3' - \tau_3 f_3'$, $q_f = \Delta f_3^s$ and taking into account the measurement Eqs. (2.2.2)–(2.2.4), we obtain the equations for the vertical channel errors:

$$\begin{aligned} \Delta\dot{h} &= \Delta W + \tau_3 f_3', \\ \Delta\dot{W} &= \kappa_3 f_3' + q_f + (\kappa_2 + \alpha_2) f_1' - (\kappa_1 + \alpha_1) f_2' + \Delta g. \end{aligned} \tag{2.2.15}$$

The zero drift of the GSE is not taken into account here since it is compensated for during the reference measurements.

Depending on the situation, GNSS measurements can be used in carrier phase (standard or differential) or Doppler modes (Wei et al. 1991; Stepanov et al. 2002). The GNSS altitude increment serves as positional measurements when using GNSS carrier phase measurements (Bolotin et al. 2002):

$$\Delta h^* = \int_{t_0}^{t} V_3^{GNSS} dt - h', \;\; \Delta h^* = \Delta h + q_h^s + q_h^i. \tag{2.2.16}$$

Here, q_h^s is the random error of the altitude increment caused by the noise of the GNSS and GSE raw data, and q_h^i is an intermittent error caused by the cycle slip in the carrier phases.

When using GNSS Doppler measurements, we have (Bolotin et al. 2002):

$$\Delta V_3^* = V_3^{GNSS} - W_3', \ \Delta V_3^* = \Delta W_3 + q_v^s. \tag{2.2.17}$$

Here, q_v^s is a random error of the altitude increment caused by the noises of the GNSS and GSE raw data.

Equation (2.2.15) are supplemented with the calibration parameters vs time model (Bolotin and Golovan 2013):

$$\dot{\tau}_3 = q_\tau, \ \dot{\kappa}_3 = q_{\kappa 3}, \ \dot{\kappa}_1 = q_{\kappa 1}, \ \dot{\kappa}_2 = q_{\kappa 2}, \tag{2.2.18}$$

By combining (2.2.15)–(2.2.18) and introducing the vector $q_p = (q_\tau, q_{\kappa 3}, q_{\kappa 1}, q_{\kappa 2})$ of parameters drifts, we obtain the model of the vertical channel in the matrix form:

$$\begin{aligned} \dot{x}_g &= A_g x_g + B_f q_f + B_p q_p + B_{\Delta g} \Delta g, \\ z &= C_g x_g + q_h^s + q_h^i. \end{aligned} \tag{2.2.19}$$

A GA stochastic model is used for solution of (2.2.19) (Bolotin and Popelensky 2007). The GA is assumed to be a stationary (time-invariant) random process with a given PSD $S_{\Delta g}(\omega)$ represented as an output of a finite-dimensional shaping filter with white noise at the input (in the GTGRAV software, the parameters of the first- or second-order model are selected by the user):

$$\begin{aligned} \dot{x}_a &= A_a x_a + B_a q_a, \\ \Delta g &= C_a x_a. \end{aligned} \tag{2.2.20}$$

Equations (2.2.19), (2.2.20) are used to determine GA on the trajectory with the use of the smoothing filter. Here, it is worth pointing out the following features.

- The filter takes into account the nonstationary (time-varying) nature of the noise; in particular, possible cycle slips q_h^i, changes in the number of visible satellites and GSE saturation caused by abnormal vertical accelerations. Both phenomena are simulated by increasing the corresponding noise-variance matrices, which leads to a reduction in the weight of the corresponding measurement when the estimate is calculated. The filter may have several iterations, where noise variances increase with greater values of the residuals. It should be noted that this heuristic technique makes the filter nonlinear.
- The filter automatically takes into account the turns between the survey lines by increasing the value of noise covariance matrices on the turns. This makes it possible to significantly reduce the duration of transient processes at the ends of survey lines.
- The filter provides estimates of the gravimeter calibration parameters, which are used for additional control of data quality.

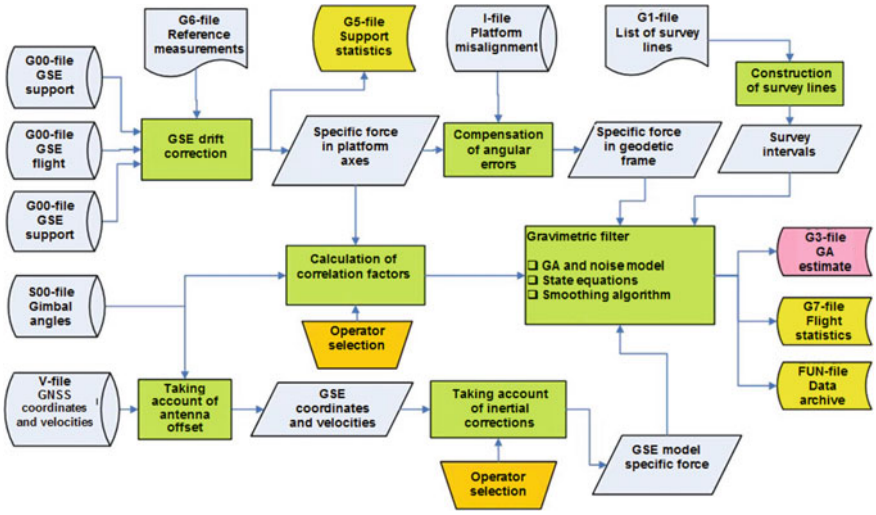

Fig. 2.17 Block diagram of data flows in the GTGRAV software modules

- The filter allows for the state vector expansion in order to take into account additional correlations caused by angular motions of the aircraft.
- The GA is usually determined in two stages. At the first stage, the model includes the maximum number of external factors to verify data quality. At the second stage, the factors whose values do not reach the reliability threshold are removed from the model.
- The software developed allows survey data to be processed in the drape flight mode. This mode requires very high accuracy of the GSE scale factor κ_3 estimation, which makes it necessary to carry out the so-called calibration maneuver. After that, κ_3 is determined using the algorithms described above.
- Adaptive modification of the filtering algorithm is possible, wherein GA is described by a nonstationary Markov process (Bolotin and Doroshin 2011).

A block diagram of the GTGRAV software data flows is shown in Fig. 2.17.

A general block diagram of the data flows in the GT-2A gravimeter and postprocessing software modules is shown in Fig. 2.18.

2.2.5 Conclusion

The features and methods of GT-2 data postprocessing have been discussed. The stages of integrated data postprocessing provided by data acquisition system, GNSS receivers on the aircraft and those at the base stations, inertial navigation system, and

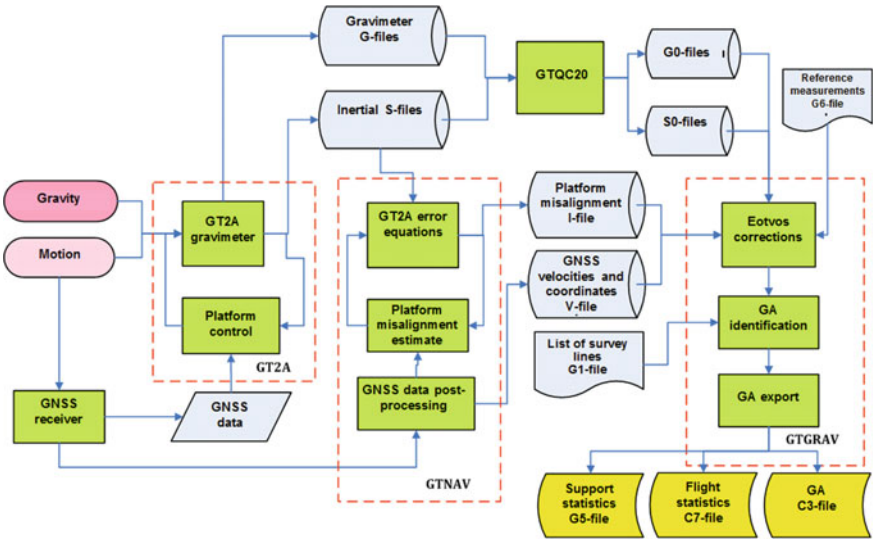

Fig. 2.18 General block diagram of the GT-2A gravimeter and postprocessing software data flows

the GSE have been considered. They include processing of GNSS raw data, estimation of the gyro platform misalignment errors, and solution of the basic gravimetric equation. The data flows in the postprocessing software have been described.

2.3 Optimal and Adaptive Filtering and Smoothing Methods for Onboard Gravity Anomaly Measurements

The previous sections of this Chapter describe the processing algorithms used in the Chekan and GT series gravimeters. When developing the algorithms, a question often arises if the accuracy of gravimetric surveys can be enhanced by improving the processing algorithms. This question is, generally speaking, still open. In our opinion, it can be answered by applying the Bayesian approach. It offers great advantages by helping not only to formalize the problem of designing the estimation algorithms, including optimal ones, but also to obtain their accuracy characteristics in the form of calculated (conditional) and unconditional covariance matrices. The ability to obtain an unconditional covariance matrix of optimal estimation errors, in turn, makes it possible to calculate the potential accuracy with the given models and thus to objectively estimate the performance of various suboptimal algorithms. However, a significant disadvantage of the Bayesian approach is the necessity for the stochastic description (modeling) of the sensor errors and estimated values. This need for the knowledge of consistent (adequate) models hinders the application of optimal estimation methods. Nevertheless, the progress in computer technology and identification

methods used to build the required models provides a new potential for improving the processing methods applied to onboard gravity anomaly measurements.

The present section is devoted to the synthesis of optimal Bayesian algorithms and identification methods, which provide the required models.

2.3.1 General Formulation and Solution of Optimal Filtering and Smoothing Problems

First, let us formulate the problem of optimal Bayesian estimation of gravity anomaly onboard a vehicle, assuming that the models of errors of the measuring instruments and of GA to be estimated are known. For this purpose, let us first formulate the filtering and smoothing problems in the general form and briefly describe the algorithms used to solve them (Meditch 1969; Stepanov 2017b).

Suppose an n-dimensional Markov process is given,

$$\dot{x}(t) = F(t)x(t) + G(t)w(t), x(t_0) = x_0 \tag{2.3.1}$$

and m-dimensional measurements are taken

$$y(t) = H(t)x(t) + v(t), \tag{2.3.2}$$

where $F(t), G(t), H(t)$ are the generally known time-dependent $n \times n, n \times p, m \times n$ matrices; x_0 is the zero-mean vector of initial conditions with covariance matrix P_0; $w(t)$, $v(t)$ are p- and m-dimensional vectors of zero-mean white noises with a given PSD, which are noncorrelated with each other and have the initial conditions x_0, i.e.:

$$E\left\{x_0 w^T(t)\right\} = 0; E\left\{w(t)v^T(t)\right\} = 0; E\left\{x_0 v^T(t)\right\} = 0; \tag{2.3.3}$$

$$E\left\{w(t)w^T(\tau)\right\} = Q(t)\delta(t-\tau), Q(t) \geq 0; \tag{2.3.4}$$

$$E\left\{v(t)v^T(\tau)\right\} = R(t)\delta(t-\tau), R(t) > 0. \tag{2.3.5}$$

The filtering problem is formulated as follows. Using the measurements (2.3.2) $Y(t) = \{y(\tau) : \tau \in [0, t]\}$ accumulated over the interval $[0, t]$, it is needed to obtain the linear mean-square optimal estimate $\hat{x}(t)$ of vector $x(t)$ at time t, which minimizes the criterion

$$r^B(t) = E\left\{\left(x(t) - \hat{x}(t)\right)^T \left(x(t) - \hat{x}(t)\right)\right\}. \tag{2.3.6}$$

It is well known that the estimate $\hat{x}(t)$ and its error covariance matrix $P(t)$ are determined using the following formulas for the Kalman-Bucy filter (Kalman and Bucy 1961; Meditch 1969):

$$\dot{\hat{x}}(t) = F(t)\hat{x}(t) + K(t)\big(y(t) - H(t)\hat{x}(t)\big); \tag{2.3.7}$$

$$K(t) = P(t)H(t)^T R^{-1}(t); \tag{2.3.8}$$

$$\begin{aligned}\dot{P}(t) = {} & P(t)F(t)^T + F(t)P(t) - P(t)H(t)^T R^{-1}(t)H(t)P(t) \\ & + G(t)Q(t)G^T(t).\end{aligned} \tag{2.3.9}$$

In practice, the estimate is calculated using the discrete form of the filter (Kalman 1960; Meditch 1969):

$$\hat{x}_i = \hat{x}_{i/i-1} + K_i\big(y_i - H_i\hat{x}_{i/i-1}\big); \tag{2.3.10}$$

$$\hat{x}_{i/i-1} = \Phi_i\hat{x}_{i-1},\ P_{i/i-1} = \Phi_i P_{i-1}\Phi_i^T + \Gamma_i Q_i \Gamma_i^T; \tag{2.3.11}$$

$$K_i = P_i H_i^T R_i^{-1},\ P_i = \left(P_{i/i-1}^{-1} + H_i^T R_i^{-1} H_i\right)^{-1}; \tag{2.3.12}$$

where $\Phi_i = \Phi(t_i; t_i - \Delta t)$ is the transition matrix of the system (2.3.1) between times $t_i - \Delta t$ and t_i (Δt is the sample interval); Γ_i and Q_i are the matrices chosen so as to satisfy the formula

$$\Gamma_i Q_i \Gamma_i^T \approx G(t_i)Q(t_i)G^T(t_i)\Delta t,$$

corresponding to the condition of stochastic equivalence of the continuous process $x(t)$ and the discrete sequence x_i (Stepanov 2017b), the matrix $R_i = R(t_i)/\Delta t$, and $H_i = H(t_i)$. Note that here Eq. (2.3.11) generate the optimal prediction $\hat{x}_{i/i-1}$ and the corresponding covariance matrix $P_{i/i-1}$ at time t_i.

The smoothing problem is formulated as follows. Using the measurements (2.3.2) $Y(t_1) = \{y(\tau) : \tau \in [t_0, t_1]\}$ accumulated over the interval $[t_0, t_1]$ at time t, it is required to obtain a linear mean-square optimal estimate $\hat{x}^s(t)$ of the vector $x(t)$ at time $t < t_1$, which minimizes the criterion

$$r^B(t) = E\left\{\big(x(t) - \hat{x}^s(t)\big)^T\big(x(t) - \hat{x}^s(t)\big)\right\}.$$

There are three types of smoothing problems: fixed-interval smoothing, constant delay smoothing, and fixed-point smoothing (Meditch 1969; Stepanov 2017b).

Focus on a possible algorithm for solving the problem over a fixed interval, which is used in this study. This algorithm is based on preliminary solution of the filtering problem over the entire time interval $[t_0, t_1]$, resulting in the generation of estimates and their covariance matrices. Further the filtering estimates are denoted by $\hat{x}^f(t)$, $P^f(t)$ and smoothing estimates, by $\hat{x}^s(t)$, $P^s(t)$. Assume that $P^f(t)$ is nonsingular and the inverse matrix $\left(P^f(t)\right)^{-1}$ exists. In this case, the smoothing solution in the form of the optimal estimate $\hat{x}^s(t)$ and the corresponding covariance matrix $P^s(t)$ can be defined by the following equations (Meditch 1969):

$$\dot{\hat{x}}^s(t) = F(t)\hat{x}^s(t) + K^s(t)\left(\hat{x}^s(t) - \hat{x}^f(t)\right); \tag{2.3.13}$$

$$K^s(t) = G(t)Q(t)G(t)^T\left(P^f(t)\right)^{-1}; \tag{2.3.14}$$

$$\dot{P}^s(t) = \left[F(t) + K^s(t)\right]P^s(t) + P^s(t)\left[F(t) + K^s(t)\right]^T - G(t)Q(t)G^{\mathrm{T}}(t). \tag{2.3.15}$$

These equations determine the solution of a continuous optimal smoothing problem over a fixed interval. It is clear that for time $t = t_1$, the formulation and, hence, the solution of the smoothing problem coincide with the formulation and solution of the filtering problem. It should be noted that the residual $\hat{x}^s(t) - \hat{x}^f(t)$ in (2.3.13) has dimension n coinciding with the dimension of the state vector.

The algorithm (2.3.13)–(2.3.15) in the discrete form is referred to as the Rauch-Tung-Striebel (RTS) smoothing algorithm (Rauch et al. 1965) or simply as the optimal smoothing filter (OSF). At the first step, similarly to filtering problem, the conventional Kalman filter (KF) (2.3.10)–(2.3.12) is used to obtain the optimal estimates $\hat{x}_i^f$ and P_i^f. At the second step, a modified filter is used with account for the obtained values, where the filtering estimate is used instead of the predicted estimate, and the residual is the difference between the estimate smoothed at the previous step and the predicted estimate (Simon 2006; Stepanov 2017a):

$$\begin{aligned}
\hat{x}_i^s &= x_i^f + K_i^s\left(\hat{x}_{i+1}^s - \hat{x}_{i+1/i}^f\right),\\
K_i^s &= P_i^f\Phi_i^T\left(P_{i+1/i}^f\right)^{-1},\\
P_i^s &= P_i^f + K_i^s\left(P_{i+1}^s - P_{i+1/i}^f\right)\left(K_i^s\right)^T.
\end{aligned} \tag{2.3.16}$$

It is important that the filter (2.3.16) runs in inverse time, since the smoothed estimate at time t_i depends on the similar estimate at time $t_i + \Delta t$. It also follows from the Eq. (2.3.16) that it is not needed to calculate the smoothing error covariance matrix P^s to obtain the estimate. However, it can be used as a characteristic of estimation accuracy. The analysis of the above equations also shows that to obtain a smoothed estimate, it is necessary to save the estimates, the predicted estimates, and

their error covariance matrices obtained during filtering. Obviously, this increases the requirements for the computer memory when solving the smoothing problem.

2.3.2 Optimal Filtering and Smoothing Algorithms for Onboard Gravity Anomaly Measurements

Let us specify the above problem formulations as applied to the gravity anomaly measurements. As a rule, by the filtering stage the most corrections such as the normal gravity correction, Eotvos correction, altitude correction, etc., have already been introduced in gravimeter measurements. Thus, the gravimeter measurements $g_{GR}(t)$ can be represented as follows:

$$g_{GR}(t) = \Delta g(t) + a_o(t) + w_{GR}(t), \tag{2.3.17}$$

where $\Delta g(t)$ is the GA in free air; $a_o(t)$ is the vertical acceleration of the vehicle; $w_{GR}(t)$ are the total random measurement errors of the gravimeter. Based on the measurements (2.3.17), to apply the optimal filtering and smoothing algorithms it is needed to determine the shaping filter of the form (2.3.1) for GA $\Delta g(t)$ and the vertical accelerations $a_o(t)$.

The gravity anomaly can be described with the Jordan model, the Schwarz model (Jordan 1972) and other models, along with their approximations as the integrals of white noise (Bolotin et al. 2002). Here, let us consider the Jordan model corresponding to the stationary third-order Markov process with the correlation function (Jordan 1972):

$$K_{\Delta g}(\rho) = \sigma_{\Delta g}^2 \left(1 + \alpha\rho - \frac{(\alpha\rho)^2}{2}\right) e^{-\alpha\rho}, \tag{2.3.18}$$

where $\sigma_{\Delta g}^2$ is the GA variance; α is the inverse correlation interval; ρ is the length of a rectilinear trajectory. To transform (2.3.18) to the time domain, use the formula $\rho = Vt$, where V is the vehicle speed. Note that the process with the correlation function (2.3.18) is differentiable and the variance of its derivative can be defined as follows:

$$\sigma_{\partial\Delta g/\partial\rho}^2 = -\frac{d^2}{d\rho^2} K_{\Delta g}(\rho)\Big|_{\rho=0} = 2\alpha^2\sigma_{\Delta g}^2.$$

It should also be noted that $\sigma_{\partial\Delta g/\partial\,\rho}$ characterizes the spatial variability of GA. Further, for simplicity, we will call this quantity the gradient of the gravitational field. PSD of the function (2.3.18) is defined as follows:

$$S_{\Delta g}(\omega) = 2\alpha^3 \cdot \sigma_{\Delta g}^2 \cdot \frac{5 \cdot \omega^2 + \alpha^2}{\left(\omega^2 + \alpha^2\right)^3}, \tag{2.3.19}$$

where ω is the analogue of the circular frequency for the process depending on the length of the straight section. The PSD can be represented as

$$S_{\Delta g}(\omega) = 2\alpha^3 \cdot \sigma_{\Delta g}^2 \cdot \frac{\left(\alpha + \sqrt{5} j\omega\right)\left(\alpha - \sqrt{5} j\omega\right)}{(\alpha + j\omega)^3 (\alpha - j\omega)^3}, \tag{2.3.20}$$

so it is easy to show that $\Delta g(t)$ samples corresponding to this PSD can be generated using the components of the third-order Markov process (Stepanov 2017b):

$$\begin{cases} \dot{b}_1 = -\beta b_1 + b_2; \\ \dot{b}_2 = -\beta b_2 + b_3; \\ \dot{b}_3 = -\beta b_3 + w_{GA}, \end{cases} \tag{2.3.21}$$

where $\beta = V\alpha$; V is the vehicle speed; w_{GA} is the generating white noise with the PSD $q_w = 10\beta^3\sigma_{\Delta g}^2$. In this case, GA Δg is defined as

$$\Delta g = -\beta\vartheta b_1 + b_2, \text{ where } \vartheta = \frac{\sqrt{5} - 1}{\sqrt{5}}. \tag{2.3.22}$$

The vehicle vertical acceleration $a_o(t)$ can also be generally described as a random process. Clearly, its frequency properties significantly depend on the vehicle type.

In marine gravimetry, the frequency properties of the processes $\Delta g(t)$ and $a_o(t)$ greatly differ, so the acceptable accuracy of $\Delta g(t)$ estimation can be achieved without using additional data on vertical accelerations $a_o(t)$. In practice, stationary filtering and smoothing algorithms described in Sect. 2.3.3 are often applied to such problems.

In airborne gravimetry, due to the high speed of the vehicle, the PSDs of $\Delta g(t)$ and $a_o(t)$ substantially overlap in the frequency domain. Therefore, vertical displacements $h_o(t)$ should be applied to achieve the required accuracy of $\Delta g(t)$ estimation. As follows from the previous sections, these data can be obtained using high-precision GNSS measurements of altitude $h_s(t)$ in the differential phase mode. By presenting them as

$$h_s(t) = h_o(t) + v_s(t), \tag{2.3.23}$$

where $h_o(t)$ is the vehicle altitude; $v_s(t)$ are GNSS measurement errors, formulate the problem of GA optimal estimation as the problem of estimating the state vector $x = [h_o, V_o, a_o, b_1, b_2, b_3,]^T$ specified by the following equations:

$$\begin{cases} \dot{h}_o = V_o; \\ \dot{V}_o = a_o; \\ \dot{b}_1 = -\beta b_1 + b_2; \\ \dot{b}_2 = -\beta b_2 + b_3; \\ \dot{b}_3 = -\beta b_3 + w_{GA}; \end{cases} \tag{2.3.24}$$

by measurements (2.3.17), (2.3.23). However, such a formulation requires the description of vehicle accelerations a_o using a shaping filter in the state space. A common way to avoid this in practice is to proceed to the formulation not requiring the introduction of the model of vehicle vertical accelerations (Nesenyuk and Khodorkovsky 2010). By double integration of the gravimeter readings (2.3.17), we obtain

$$\begin{cases} \dot{h}_{GR} = V_{GR}; \\ \dot{V}_{GR} = \Delta g + a_o + w_{GR}, \end{cases} \tag{2.3.25}$$

where $h_{GR} = h_o + \Delta h_{GR}$, $V_{GR} = V_o + \Delta V_{GR}$ are the increments of altitude and speed obtained by integrating the gravimeter readings. Considering (2.3.24), (2.3.25) and the fact that $\Delta g = -\beta\vartheta b_1 + b_2$, we obtain the following formulas:

$$\begin{cases} \Delta\dot{h}_{GR} = \Delta V_{GR}; \\ \Delta\dot{V}_{GR} = -\beta\,\vartheta b_1 + b_2 + w_{GR}; \\ \dot{b}_1 = -\beta b_1 + b_2; \\ \dot{b}_2 = -\beta b_2 + b_3; \\ \dot{b}_3 = -\beta b_3 + w_{GA}. \end{cases} \tag{2.3.26}$$

Forming the differential measurements as

$$y = h_{GR}(t) - h_s(t) = \Delta h_{GR}(t) + v_s(t), \tag{2.3.27}$$

the problem of GA optimal estimation by GNSS and gravimeter data can be formulated as the problem of estimating the state vector $x = [\Delta h_{GR}, \Delta V_{GR}, b_1, b_2, b_3]^T$ described by Eq. (2.3.26) using measurements (2.3.27). Obviously, the above formulation of the problem is invariant to vertical accelerations due to the use of differential measurements (2.3.27). This technique is often applied to process redundant measurements, especially in navigation applications (Groves 2013; Stepanov 2016). However, it should be noted that the above formulation is not invariant to GA: its description is required and in this case specified using the Jordan model (2.3.21), (2.3.22). For more information on invariant and non-invariant algorithms, see Brown and Hwang (1977), Dmitriev and Stepanov (2000), Stepanov (2016).

For example, let us specify the problem formulation by introducing the random error models of gravimeter readings $w_{GR}(t)$ and measurements $v_s(t)$. Following

(Stepanov et al. 2002), describe them for simplicity by white-noise random processes with the known PSD R_{GR} and Q_{SNS}, respectively. In this case, the problem is a linear estimation problem, and its solution is reduced to the optimal KF or the smoothing filter described in the previous subsection, and the corresponding models (2.3.1), (2.3.2) with the following matrices included in them:

$$F = \begin{bmatrix} 0 & 1 & 0 & 0 & 0 \\ 0 & 0 & -\beta\vartheta & 1 & 0 \\ 0 & 0 & -\beta & 1 & 0 \\ 0 & 0 & 0 & -\beta & 0 \\ 0 & 0 & 0 & 0 & -\beta \end{bmatrix}, G = \begin{bmatrix} 0 & 0 \\ \sqrt{R_{GR}} & 0 \\ 0 & 0 \\ 0 & 0 \\ 0 & q_w \end{bmatrix}, H = \begin{bmatrix} 1 & 0 & 0 & 0 & 0 \end{bmatrix}.$$

To implement the algorithms, the initial covariance matrix P_0 is required, which, as can be easily seen, has a block-diagonal form due to the structure of the system (2.3.26).

2.3.3 *Stationary Estimation Algorithms and Their Performance Analysis*

As follows from the previous sections, stationary filtering and smoothing algorithms, which, unlike the optimal algorithms, minimize the error variance only in the steady state, are applied to simplify the processing algorithms in GA estimation (Stepanov 2017b).

One of the methods to construct such filters is based on using the filtering and smoothing solution in the state space for a steady state. Discuss this method in more detail as applied to fixed-interval smoothing assuming that the matrices in (2.3.1), (2.3.2) do not depend on time. It is thought that there exists a steady-state solution for the filtering problem. To simplify the formula, let us put here that the PSD of the generating noise is an identity matrix. Present the solution of the steady-state smoothing problem by the algorithm (2.3.13)–(2.3.15) discussed in Sect. 2.3.2 using the transfer functions (TF). To do this, first obtain the filtering estimate using a conventional steady-state KF

$$\dot{\hat{x}}^f_\infty(t) = \left(F - K^f_\infty H\right)\hat{x}^f_\infty(t) + K^f_\infty y(t), \tag{2.3.28}$$

where

$$K^f_\infty = P^f_\infty H^T R^{-1}, \tag{2.3.29}$$

and then find the smoothed estimate by processing $\hat{x}^f(t)$ with the filter

$$\dot{\hat{x}}^s_\infty(t) = F\hat{x}^s_\infty(t) + K^s_\infty\left(\hat{x}^s_\infty(t) - \hat{x}^f_\infty(t)\right) \tag{2.3.30}$$

with

$$K^s_\infty = Q\left(P^f_\infty\right)^{-1}, \tag{2.3.31}$$

where

$$Q = GG^T. \tag{2.3.32}$$

The matrix P^f_∞ included in these formulas corresponds to the solution of the covariance equation (2.3.9) for the steady state. The solution is sought for the steady state, so the TF matrix can be found for the optimal KF:

$$W^f_x(p) = \left(pE - F + K^f_\infty H\right)^{-1} K^f_\infty. \tag{2.3.33}$$

Considering that $\hat{x}^f_\infty(p) = W^f_x(p)y(p)$, we get the following to estimate smoothing:

$$\begin{aligned}\hat{x}^s_\infty(p) &= \left(-pE + F + Q\left(P^f_\infty\right)^{-1}\right)^{-1} Q\left(P^f_\infty\right)^{-1}\hat{x}^f_f(p)\\ &= \left(-pE + F + Q\left(P^f_\infty\right)^{-1}\right)^{-1} Q\left(P^f_\infty\right)^{-1} W^f_x(p)y(p),\end{aligned}$$

where $W^f_x(p)$ is given by (2.3.33).

It follows that the TF matrix for a smoothing filter, providing the estimation of all state vector components, is defined as

$$W^s_x(p) = \left(-pE + F + Q\left(P^f_\infty\right)^{-1}\right)^{-1} Q\left(P^f_\infty\right)^{-1} W^f_x(p). \tag{2.3.34}$$

A number of methods have been developed to find the required filter TF $W^f_x(p)$, including approximate ones, such as the method of PSD local approximation (Loparev et al. 2012; Stepanov et al. 2014). It constructs the PSDs of the useful signal and noise and searches for their intersection point, where the PSDs are equal. To obtain this intersection point, the PSDs in its vicinity are approximated by linear functions. The found frequency is taken to be the cutoff frequency of the filter, and the TF order is determined by the steepness of the linear approximation slope. It follows from the above that with this method, the parameters of the TF significantly depend only on the properties of the PSDs in the vicinity of the found point. Thus, simpler models can be applied to describe the error and the value to be estimated: for example, the GA model can be specified as the second or third integral of white noise instead of the Jordan model. The studies (Stepanov et al. 2002; Koshaev and

Stepanov 2010) show that with the GA model specified as the second integral of white noise, for the models described in 2.3.2 the TF of the stationary smoothing filter can be represented with a certain degree of approximation using the fourth-order Butterworth filter TF:

$$w_{B_4}(p) = \frac{\mu^4}{p^4 + \gamma p^3 \mu + \frac{\gamma^2}{2} p^2 \mu^2 + \gamma p \mu^3 + \mu^4}, \tag{2.3.35}$$

where $\mu = \left(q_{\ddot{g}}^{\ddot{}} / R_h\right)^{1/8}$ is the filter cutoff frequency; $q_{\ddot{g}}^{\ddot{}} = \sigma^2_{\partial \ddot{g}/\partial \rho} 3V^3/\rho$; V is the vehicle speed; R_h is the standard deviation of altitude error; ρ is the trajectory length; and $\gamma = \sqrt{2\left(2+\sqrt{2}\right)}$ is a dimensionless coefficient.

In the design of smoothing algorithms, various techniques are also applied to reduce their computational complexity. For example, it is known (Stepanov 2017b) that in a particular estimation of a scalar process with a fractional-rational PSD against the white noise background, the TF in the smoothing problem for the measured scalar component $z = Hx$ can be represented as follows:

$$W_z^s(p) = W_*(-p) W_*(p) = |W_*(p)|^2, \tag{2.3.36}$$

where the function $W_*(p)$ is defined as $W_*(p) = rG^T (P_\infty^f)^{-1} W_x^f(p)$ with $r = \sqrt{R}$.

This implies that if the measured and estimated components coincide, a computationally inexpensive algorithm can be employed to obtain the optimal smoothing estimate. It includes the following steps (Stepanov 2017b):

- generation of the estimate vector $\hat{x}^f(t)$ using the KF, which generally estimates the n-dimensional state vector by the scalar measurement $y(t) = z(t) + v(t) = Hx(t) + v(t)$;
- generation and saving of the scalar sample $\hat{\tilde{z}}(t) = T\hat{x}^f(t)$ using the row matrix $T = rG^T\left(P_\infty^f\right)^{-1}$, where $r = \sqrt{R}$;
- generation of the n-dimensional estimate vector $\hat{x}^s(t)$ by processing the scalar $\hat{\tilde{z}}(t)$ in the inverse time in the same Kalman-type filter.

The idea of this modified smoothing algorithm is that it requires saving only the scalar estimates obtained in the filtering mode.

When using this algorithm, as applied to the considered example with the models described in Sect. 2.3.2 and the GA model specified as the second integral of white noise, it can be shown that processing is reduced to differentiating the measurements and applying the Butterworth filters in the forward and inverse time:

$$W_h^c(p) = w_{B_4}(p) w_{B_4}(-p) \begin{pmatrix} 1 \\ p \\ p^2 \\ p^3 \end{pmatrix}. \tag{2.3.37}$$

The study (Stepanov et al. 2002) shows that despite the simplified specification of the anomaly model in the local approximation method, the resulting algorithm is close to the optimal in the steady-state mode for the models described above, including the Jordan model for GA.

Another modification of a suboptimal smoothing algorithm is discussed in Sect. 2.4.

In practice, finite impulse response (FIR) filters are also applied to process airborne gravimetry data. For example, in the two-stage procedure of processing the Chekan gravimeter data described in Sect. 2.1.3, the first stage uses a FIR filter with a trapezoidal Tukey weight function. The use of such a filter with a fixed window width decreases the estimation interval by half the window width on both ends of the trajectory; besides, sometimes the filter fails to achieve the acceptable estimation accuracy. Therefore, a second stage is provided, where the received signal is transferred to the frequency domain, where high-frequency harmonics are reduced by Fourier transformation. This procedure smoothes the resulting estimate but does not reduce the spatial resolution of the survey. The transfer back to the time domain is performed at the final stage. A diagram of this procedure is shown in Fig. 2.19.

The processing algorithm is tuned by selecting the width of Tukey window and the number of harmonics in Fourier transformation. It should be noted that, due to the heuristic nature of this algorithm, there exists no formalized tuning sequence for it. In practice, its parameters are selected so that the resulting estimate is typical of GA. Spectral analysis of the resulting estimate can additionally be used. The estimate is verified by comparison with the known rough map of the gravitational field with the marked characteristic points (GA minima and maxima). The performance of the estimation algorithm is assessed based on the coincidence of the anomalies at these points. Thus, when processing real data using such a procedure, the accuracy

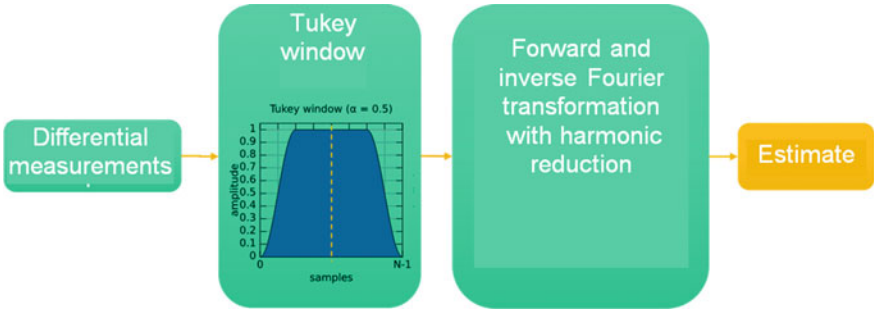

Fig. 2.19 Two-stage processing procedure

of GA estimation largely depends on the experience of the engineer processing the measurements.

As noted in Introduction of this chapter, the Bayesian approach offers the advantage of calculating the potential accuracy of the specified models. This creates a good basis for objective estimation of the efficiency of various simplified algorithms in simulation studies. The results of such a study for the models described in 2.3.2 are presented in Figs. 2.20, 2.21 and 2.22 showing the actual RMS errors (RMSE) for the optimal smoothing algorithm, the stationary Butterworth filter (2.3.35), and the two-stage estimation procedure.

Stationary suboptimal algorithms do not generate the estimation accuracy characteristic during the operation, so the corresponding RMSEs are obtained by statistical testing as described, for example, in Stepanov (2017b). It is also important to note that the true GA was generated in accordance with the Jordan model in all cases.

The simulation results generally confirm that stationary suboptimal algorithms in steady-state mode are close to the optimal algorithm, but suffer from large errors (up to hundreds of mGal) at the boundaries of the intervals. In this case, the transient process recalculated to the trajectory length lasts for up to 25 km.

The transient process of a two-stage procedure generally features somewhat smaller RMSE and a longer time to reach the steady state compared with the stationary algorithm. However, due to the nature of the Fourier transformation, it is accompanied by significant fluctuations up to 50 km long. To prevent this effect, the authors of the algorithm proposed to increase the observation interval by extrapolating the measurements outside the trajectory with high-frequency harmonics (Krasnov and Sokolov 2013).

The advantages of stationary algorithms include low computational complexity and easy implementation. Such algorithms, in some cases, require no explicit models for GA anomalies and the errors of the measuring instruments. However, they suffer

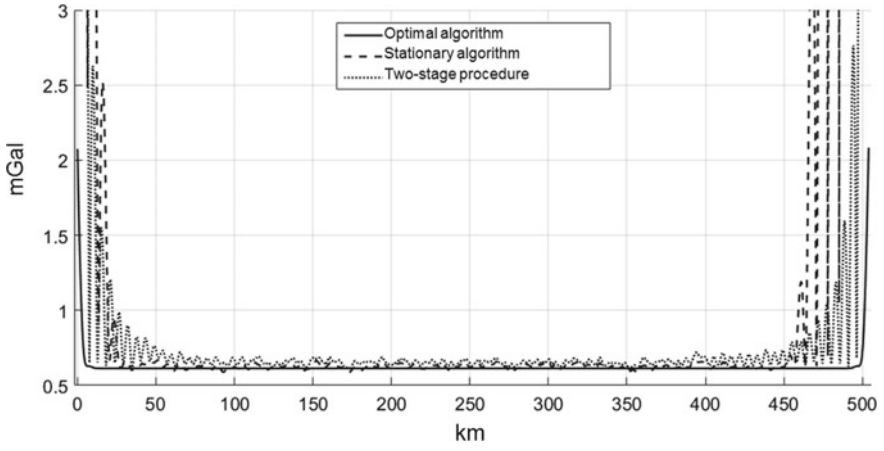

Fig. 2.20 GA estimation RMSE

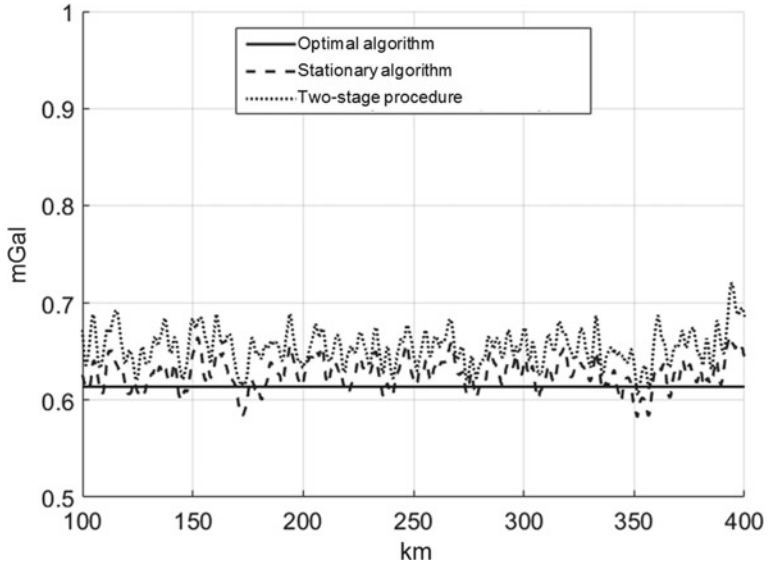

Fig. 2.21 Steady RMSE of GA estimation

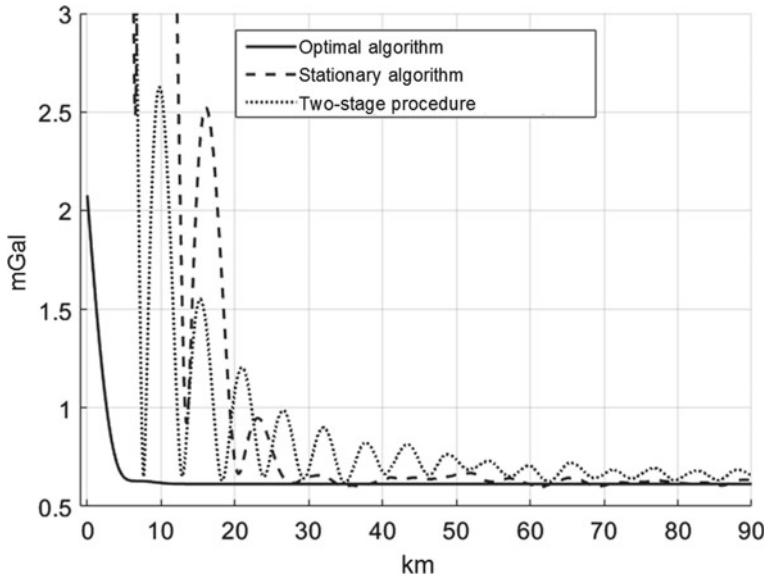

Fig. 2.22 Transient process for GA estimation RMSE

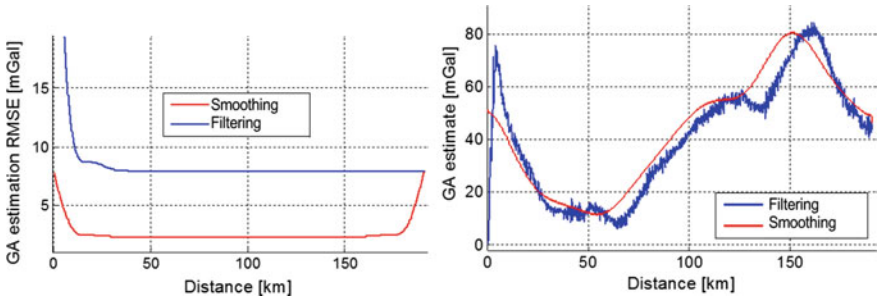

Fig. 2.23 GA estimation RMSE in filtering and smoothing modes (*left*); the obtained GA estimates (*right*)

from the pronounced boundary effects at the trajectory ends and are able neither to assess the estimation accuracy during the transient process nor to account for the varying motion parameters of the aircraft.

It should also be emphasized that the smoothing mode provides a much better GA estimation accuracy as compared to the filtering mode. Figure 2.23 shows GA estimates and their RMSEs in various modes during the processing of airborne gravimetric data.

It can be seen that the estimate obtained in the filtering mode has a non-typical high-frequency component, as well as the phase shift. The use of smoothing procedures eliminates these negative effects. As noted in Sect. 2.3.1, the RMSE of filtering and smoothing coincide at the end of the interval, thus, the minimum filtering RMSE corresponds to the maximum smoothing RMSE. In general, the use of all measurements in the smoothing process increases the accuracy 2–3 times in the steady state. It should be noted that the FIR filter described in the analysis of the two-stage estimation procedure, strictly speaking, also solves the smoothing problem, since it obtains an estimate for the middle of the window, i.e., uses the measurements obtained both before and after the estimation.

2.3.4 Model and Parametric Identification of Gravity Anomaly and Measurement Errors Using Onboard Gravity Measurements

As follows from the previous material, the design of optimal estimation algorithms requires stochastic models of the GA and errors of the measuring instruments. Note that attempts to process real data using optimal filtering and smoothing algorithms for the model (2.3.26), (2.3.27) have failed (Sokolov et al. 2016). It should also be said that the parameters of the GA model (2.3.21), (2.3.22) may vary depending on the survey area: the field gradient may be within 0.5–3 mGal/km in a flat terrain and reach 10 mGal/km and more in a mountainous terrain. Simulation has shown

(Stepanov et al. 2015; Motorin and Nosov 2019) that inaccurate setting of this value can critically reduce the GA estimation RMSE. If the used models differ from the actual ones, the calculated accuracy characteristic in the form of diagonal elements of the covariance matrix does not match the actual estimation accuracy (Stepanov and Koshaev 2011). All this proves the importance of structural and parametric identification of models used in GA measurements. Next, let us discuss the algorithm proposed for identification.

Note that the model used to design the optimal algorithm within the Bayesian approach can generally be represented as a shaping filter:

$$\begin{aligned} x_i^k &= \Phi_i^k\left(\theta^k\right)x_{i-1}^k + \Gamma_i^k\left(\theta^k\right)w_i^k, \\ \theta_i^k &= \theta_{i-1}^k = \theta^k, \end{aligned} \tag{2.3.38}$$

$$y_i = H_i^k\left(\theta^k\right)x_i^k + \Psi_i^k\left(\theta^k\right)v_i^k, \tag{2.3.39}$$

where x_i^k is the state vector; $\Phi_i^k\left(\theta^k\right)$, $\Gamma_i^k\left(\theta^k\right)$, $H_i^k\left(\theta^k\right)$, $\Psi_i^k\left(\theta^k\right)$ are the shaping filter matrices characterizing the error model, whose elements generally nonlinearly depend on the parameter vector θ^k; w_i^k and v_i^k are the p^k- and m^k-dimensional white-noise Gaussian sequences with identity covariance matrices; k is the number of a candidate model used to describe the errors. The structure of the model described by the number k and dimensions of the vectors θ^k and x_i^k(different for different k) included in Eqs. (2.3.38), (2.3.39) may be unknown.

Considering the above equations and introducing the hypotheses for the model number k, the problem of structural and parametric identification can be formulated (Dmitriev and Stepanov 2004; Motorin and Stepanov 2015; Toropov et al. 2016; Stepanov and Motorin 2019). It consists in determining the number of the hypothesis k, which best fits the vector of all measurements obtained by the time i $Y_i = \left[\, y_1 \ \ldots \ y_i \,\right]^T$, and obtaining the estimates of the parameter vector θ^k and the state vector x_i^k corresponding to this hypothesis.

Let us interpret the set of suggested hypotheses as a random variable H, which takes the values h_k, where $k = \overline{1 \ldots K}$, K is the total number of hypotheses. The probability density function (PDF) of H can be represented as follows (Dmitriev and Stepanov 2004):

$$f_{\mathrm{H}}(\mathrm{H}) = \sum_{k=1}^{K} \Pr(\mathrm{H} = h_k)\delta(\mathrm{H} - h_k), \tag{2.3.40}$$

where $\Pr(\mathrm{H} = h_k)$ is the probability that the hypothesis for the model $\mathrm{H} = h_k$ is true, and $\sum_{k=1}^{K} \Pr(\mathrm{H} = h_k) = 1$. The value of h_k is selected such that to maximize the conditional probability $\Pr(\mathrm{H} = h_k / Y_i)$ or, which is the same, to maximize the a posteriori (conditional) PDF $f_{\mathrm{H}}(\mathrm{H}/Y_i)$:

$$h_k^* = \arg\max_{h_k} f_{\mathrm{H}}(\mathrm{H}/Y_i). \tag{2.3.41}$$

With a fixed value of the hypothesis, the estimates of the vectors θ^k and x_i^k are found as the Bayesian optimal estimates, i.e.:

$$\hat{\theta}_i^k(Y_i) = \int \theta^k f_{\theta^k}\left(\theta^k/Y_i, \mathrm{H} = h_k\right) d\theta^k, \hat{x}_i^k(Y_i) = \int x_i^k f_{x_i^k}\left(x_i^k/Y_i, \mathrm{H} = h_k\right) dx_i^k, \tag{2.3.42}$$

where $f_{\theta^k}\left(\theta^k/Y_i, \mathrm{H} = h_k\right)$ and $f_{x_i^k}\left(x_i^k/Y_i, \mathrm{H} = h_k\right)$ are a posteriori PDFs of vectors θ^k and x_i^k, respectively, with a fixed hypothesis about the error model $\mathrm{H} = h_k$. Thus, the problem of identifying the model (2.3.28), (2.3.39) and estimating its parameters is reduced to finding the PDF $f_{\mathrm{H}}(\mathrm{H}/Y_i)$, $f_{\theta^k}\left(\theta^k/Y_i, \mathrm{H} = h_k\right)$, $f_{x_i^k}\left(x_i^k/Y_i, \mathrm{H} = h_k\right)$ and calculating the integrals (2.3.42). These integrals are normally calculated using numerical methods based on various techniques for approximating a posteriori density. In the general case, the dimension of these integrals is determined by the dimension of the vectors θ^k and x_i^k.

Using the Bayesian formulas, we get:

$$\Pr(\mathrm{H} = h_k/Y_i) = \frac{f(y_i/Y_{i-1}, \mathrm{H} = h_k) f_{\mathrm{H}}(\mathrm{H} = h_k/Y_{i-1})}{\sum_{k=1}^{K} f(y_i/Y_{i-1}, \mathrm{H} = h_k) f_{\mathrm{H}}(\mathrm{H} = h_k/Y_{i-1})}, \tag{2.3.43}$$

where $f(y_i/Y_{i-1}, \mathrm{H} = h_k)$ is the measurement likelihood function at step i for a fixed hypothesis; it can be represented as follows:

$$f(y_i/Y_{i-1}, \mathrm{H} = h_k) = \int f_{y_i}\left(y_i/Y_{i-1}, \mathrm{H} = h_k, \theta^k\right) f_{\theta^k}\left(\theta^k/Y_{i-1}, \mathrm{H} = h_k\right) d\theta^k. \tag{2.3.44}$$

In this formula, $f_{y_i}\left(y_i/Y_{i-1}, \mathrm{H} = h_k, \theta^k\right)$ is the measurement likelihood function at the step i for the fixed hypothesis and the parameter vector θ^k, $f_{\theta^k}\left(\theta^k/Y_{i-1}, \mathrm{H} = h_k\right)$ is a posteriori PDF at the step $i-1$. For the PDF of the state vector x_i^k, the following is also true:

$$f_{x_i^k}\left(x_i^k/Y_i, \mathrm{H} = h_k\right) = \int f_{x_i^k}\left(x_i^k/Y_i, \mathrm{H} = h_k, \theta^k\right) f_{\theta^k}\left(\theta^k/Y_i, \mathrm{H} = h_k\right) d\theta^k. \tag{2.3.45}$$

The peculiar feature of the problem is that the model (2.3.38), (2.3.39) describes the problem of linear Gaussian filtering for fixed values of the hypothesis and the parameter vector θ^k. Let θ^{kj}, $j = \overline{1 \ldots M_k}$ be the grid of the vectors θ^k for the fixed hypothesis h_k. Under these conditions, the likelihood functions $f_{y_i}\left(y_i/Y_{i-1}, \mathrm{H} = h_k, \theta^k = \theta^{kj}\right)$ and a posteriori PDF $f_{x_i^k}\left(x_i^k/Y_i, \mathrm{H} = h_k, \theta^k = \theta^{kj}\right)$

are Gaussian, i.e.:

$$f_{y_i}\left(y_i/Y_{i-1}, H = h_k, \theta^k = \theta^{kj}\right) = N\left(y_i; H_i^{kj}\hat{x}_{i/i-1}^{kj}, \Lambda_i^{kj}\right),$$
$$f_{x_i^k}\left(x_i^k/Y_i, H = h_k, \theta^k = \theta^{kj}\right) = N\left(x_i^k; \hat{x}_i^{kj}, P_i^{kj}\right), \tag{2.3.46}$$

where $\Lambda_i^{kj} = H_i^{kj}P_{i/i-1}^{kj}(H_i^{kj})^T + \Psi_i^{kj}(\Psi_i^{kj})^T$; and $\hat{x}_i^{kj}$, P_i^{kj} and $\hat{x}_{i/i-1}^{kj}$, $P_{i/i-1}^{kj}$ are the optimal estimate with the covariance matrix and the optimal prediction for the step *i,* respectively, which can be obtained using the KF bank. Thus, to calculate the integrals (2.3.42), approximation should be introduced only for the PDF $f_{\theta^k}\left(\theta^k/Y_{i-1}, \mathrm{H} = h_k\right)$, and the dimension of the integrals will be determined only by the dimension of the vector θ^k. The technique reducing the dimension of the integrals to be found numerically is referred to as the partitioning method (Lainiotis 1976; Stepanov 1998; Beloglazov and Kazarin 1998), the method of analytical integration over a part of variables, or Rao-Blackwellization procedure (Doucet et al. 2001).

In order to calculate the estimates, approximate the PDF for vector θ^k as follows:

$$f_{\theta^k}\left(\theta^k/Y_i, \mathrm{H} = h_k\right) = \sum_{j=1}^{M_k}\mu_i^{kj}\delta\left(\theta^k - \theta^{kj}\right),\ f_{\theta^k}\left(\theta^k/\mathrm{H} = h_k\right)$$
$$= \sum_{j=1}^{M_k}\mu_0^{kj}\delta\left(\theta^k - \theta^{kj}\right), \tag{2.3.47}$$

According to Bayesian theorem, with this approximation, the recursive formula is valid for the coefficients μ_i^{kj}:

$$\mu_i^{kj} = \frac{\mu_{i-1}^{kj}\cdot f_{y_i}\left(y_i/Y_{i-1}, \mathrm{H} = h_k, \theta^k = \theta^{kj}\right)}{\sum_{j=1}^{L}\mu_{i-1}^{kj}f_{y_i}\left(y_i/Y_{i-1}, \mathrm{H} = h_k, \theta^k = \theta^{kj}\right)}. \tag{2.3.48}$$

Thus, the sought integrals (2.3.42) for the estimates of the parameter vector and the state vector, as well as the probability (2.3.43) can be calculated using the following formula:

$$\hat{\theta}_i^k(Y_i) \approx \sum_{j=1}^{M_k}\mu_i^{kj}\theta^{kj},\ \hat{x}_i^k(Y_i) \approx \sum_{j=1}^{M_k}\mu_i^{kj}\hat{x}_i^{kj}, \tag{2.3.49}$$

$$\Pr(\mathrm{H} = h_k/Y_i)$$
$$\approx \frac{\left[\sum_{j=1}^{M_k}\mu_{i-1}^{kj}N\left(y_i; H_i^{kj}\hat{x}_{i/i-1}^{kj}; \Lambda_i^{kj}\right)\right]\Pr(\mathrm{H} = h_k/Y_{i-1})}{\sum_{k=1}^{K}\left[\left[\sum_{j=1}^{M_k}\mu_{i-1}^{kj}N\left(y_i; H_i^{kj}\hat{x}_{i/i-1}^{kj}; \Lambda_i^{kj}\right)\right]\Pr(\mathrm{H} = h_k/Y_{i-1})\right]}. \tag{2.3.50}$$

An important advantage of the considered approach is that the accuracy characteristic can be obtained in the form of covariance matrices for the estimates (2.3.49):

$$P_i^{\theta k}(Y_i) \approx \sum_{j=1}^{M_k} \mu_i^{kj} \theta^{kj} \left(\theta^{kj}\right)^T - \hat{\theta}_i^k \left(\hat{\theta}_i^k\right)^T,$$

$$P_i^{xk}(Y_i) \approx \sum_{j=1}^{M_k} \left[\mu_i^{kj} \left(\hat{x}_i^{kj} \left(\hat{x}_i^{kj}\right)^T + P_i^{kj} \right) \right] - \hat{x}_i^k \left(\hat{x}_i^k\right)^T. \tag{2.3.51}$$

Since the parameter vector θ^k does not change with time, its estimate obtained in the filtering mode over the entire set of measurements will coincide with the estimate in the smoothing mode. Considering this and the linearity of the filtering problem (2.3.28), (2.3.29) with the known models and the fixed parameter vector, the smoothed estimate of the state vector x and, as a result, the smoothed GA can be obtained using the above optimal linear smoothing algorithms tuned for the identified model. It can be easily seen that the use of the described approach actually makes the estimation process and the filtering and smoothing algorithms adaptive.

2.3.5 *The Results of Using Adaptive Filtering and Smoothing Algorithms in Airborne Gravity Anomaly Measurements*

Let us illustrate the application of the above algorithms to processing the experimental airborne geophysical survey data. They were obtained onboard an L-410 aircraft on March 6, 2015, near the town of Stupino about 150 km south of Moscow, Russia. The Chekan-AM mobile gravimeter manufactured by Concern CSRI Elektropribor (Peshekhonov et al. 2015) was installed onboard an aircraft. A NovAtel SE-D-RT2-G-J-Z dual-frequency GLONASS/GPS onboard receiver with an IMU and a GPS-702 GG antenna was applied to obtain the velocity and coordinates. A NovAtel DL-V3-L1L2-G receiver with a GPS-702 GGL antenna was installed at the reference point to enable the differential correction mode. The maximum distance between the vehicle and the base station during the flight was about 150 km. During the flight, a return survey line about 170 km long was completed with general headings of 170° and 350°. The gravimeter and GNSS receiver data were recorded and processed in the offline mode.

To identify the errors of the measuring instruments and to refine the parameter $\sigma^2_{\partial\Delta g/\partial\rho}$ in the GA model, the general model (2.3.26), (2.3.27) was supplemented with the error component z described by the first-order Markov process with unknown standard deviation σ_m and the correlation interval $\tau_m = 1/\alpha_m$. Two hypotheses were suggested: the first for an additional error in differential measurements, which can

be caused, for example, by inaccurate synchronization of the GNSS receiver and the gravimeter; the second for an additional error component directly in the gravimeter measurements. The shaping filters and measurement equations for the models of these hypotheses can be written as follows:

$$\begin{cases} \Delta\dot{h}_{GR} = \Delta V_{GR}; \\ \Delta\dot{V}_{GR} = -\beta\,\vartheta b_1 + b_2 + w_{GR}; \\ \dot{b}_1 = -\beta b_1 + b_2; \\ \dot{b}_2 = -\beta b_2 + b_3; \\ \dot{b}_3 = -\beta b_3 + w_{GA}; \\ \dot{z} = -a_m z + \sigma_m\sqrt{2\alpha_m}w_m; \end{cases} \quad k = 1,$$
$$y = \Delta h_{GR} + z + v_s. \tag{2.3.52}$$

$$\begin{cases} \Delta\dot{h}_{GR} = \Delta V_{GR}; \\ \Delta\dot{V}_{GR} = -\beta\,\vartheta b_1 + b_2 + z + w_{GR}; \\ \dot{b}_1 = -\beta b_1 + b_2; \\ \dot{b}_2 = -\beta b_2 + b_3; \\ \dot{b}_3 = -\beta b_3 + w_{GA}; \\ \dot{z} = -a_m z + \sigma_m\sqrt{2\alpha_m}w_m; \end{cases} \quad k = 2,$$
$$y = \Delta h_{GR} + v_s. \tag{2.3.53}$$

Thus, the problem of structural identification of the error model (2.3.52), (2.3.53) with the vector of unknown parameters

$$\theta = \left[\,\tau_m\ \sigma_m\ \sigma_{\partial\Delta g/\partial\rho}\,\right]^T$$

and the estimated vector $x(t) = \left[\,\Delta h_{GR}\ \Delta V_{GR}\ b_1\ b_2\ b_3\ z\,\right]^T$ was solved. The GA estimate was generated using the ratio (2.3.22).

Application of the adaptive algorithm with the models introduced above to process the data of the experimental airborne geophysical survey has shown that the hypothesis (2.3.52) for the model with additional error in differential measurements proved to be most likely. The diagrams illustrating the dependence of parameter estimates on time are shown in Fig. 2.24. The estimates of the components of the parameter vector θ on the forward and inverse survey lines converge to approximately the same values.

Figure 2.25 presents the smoothing estimates for GA obtained using the adaptive algorithm and the two-stage estimation procedure described in 2.3.3. The discrepancy between the GA estimates obtained on mutually inverse trajectories using the proposed algorithm complies with the desired accuracy characteristics (RMSE)

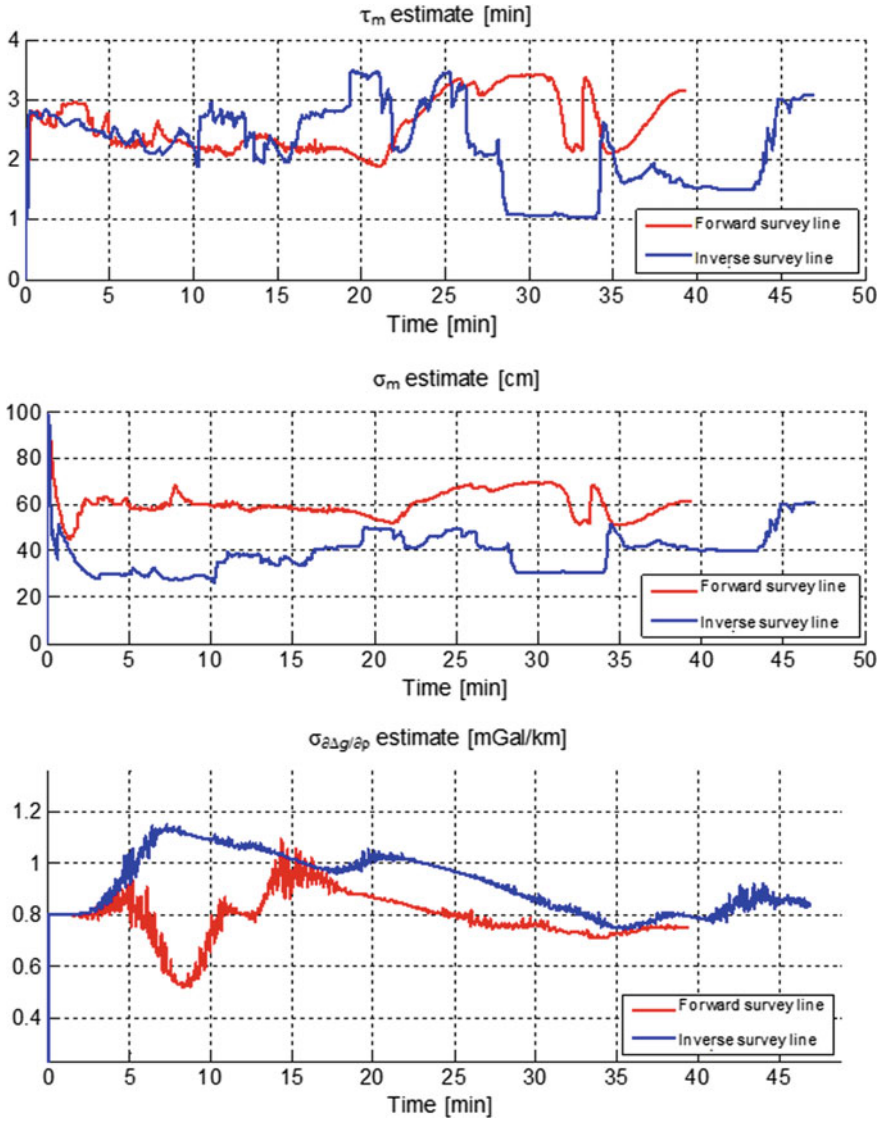

Fig. 2.24 Estimates of model parameters on the forward and inverse survey lines

calculated using the diagonal elements of the covariance matrix obtained by the algorithm (Fig. 2.26).

Thus, it can be stated that the proposed adaptive algorithm provides the expected GA estimation accuracy. Its undoubted advantages include its rigorous approach to the estimation problem, higher accuracy in the transient mode and, most importantly, the ability to obtain consistent characteristics of the estimation accuracy.

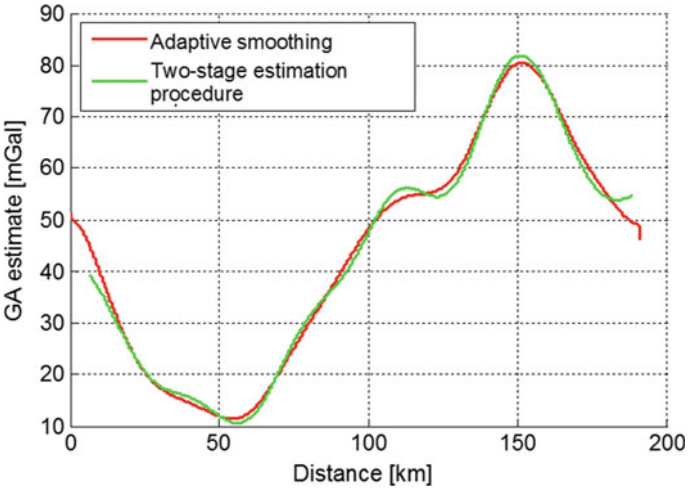

Fig. 2.25 GA estimates obtained using the adaptive algorithm and the two-stage procedure

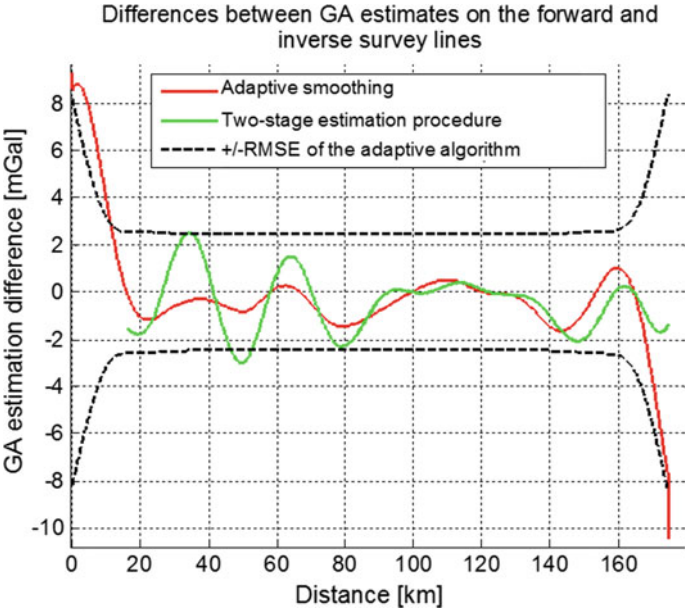

Fig. 2.26 Difference between GA estimates on the forward and inverse survey lines for the adaptive algorithm and the two-stage procedure

The described algorithm was also tested on data obtained in the area of the Arctic Ocean. Ten intersecting survey lines shown in Fig. 2.27 were processed.

The estimates of the parameters determining the properties of the additional error z for various survey lines are shown in Fig. 2.28: the correlation interval of the additional error during data processing was 1.5–2.5 min and the standard deviation was 6–12 cm.

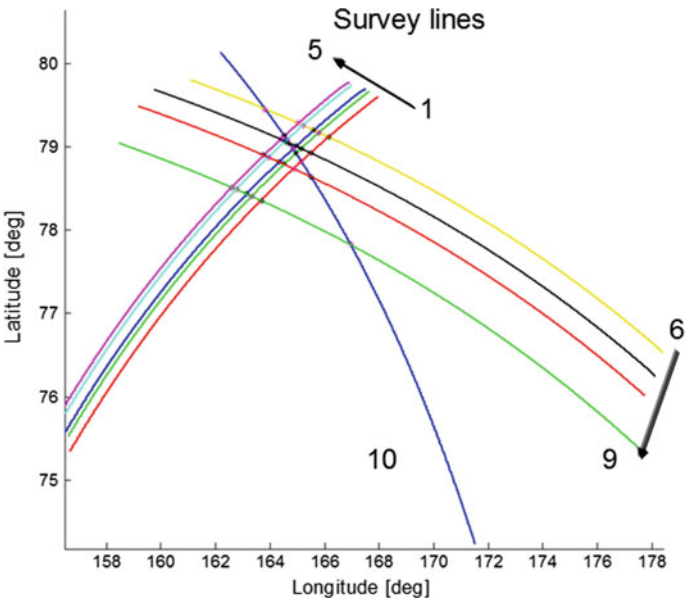

Fig. 2.27 Location of survey lines in the area of the Arctic Ocean

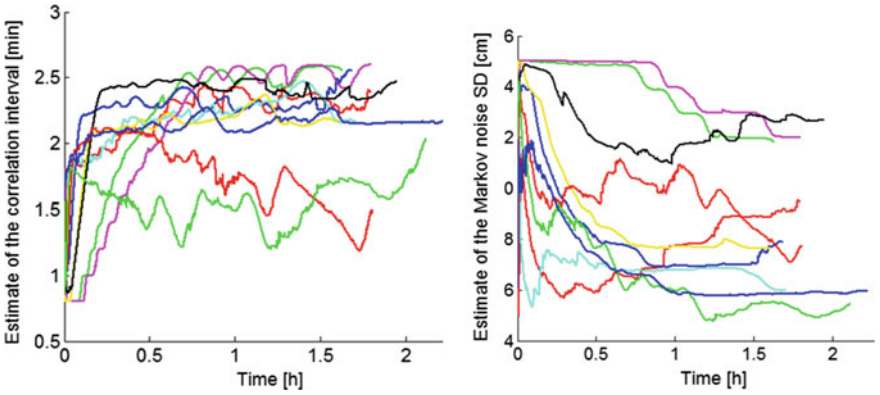

Fig. 2.28 Estimation of the correlation interval and the additional error standard deviation for 10 survey lines

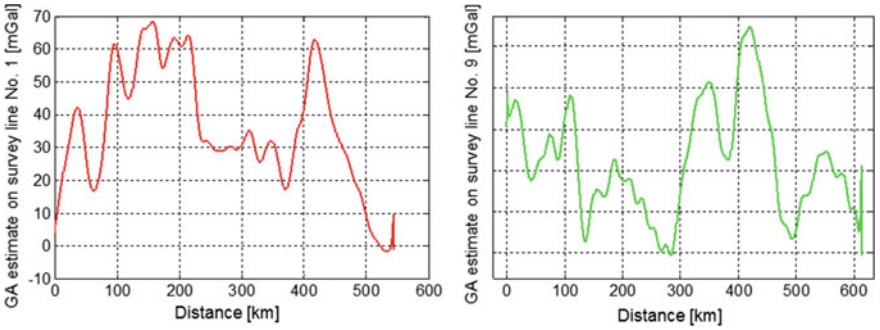

Fig. 2.29 Examples of GA estimates for two survey lines

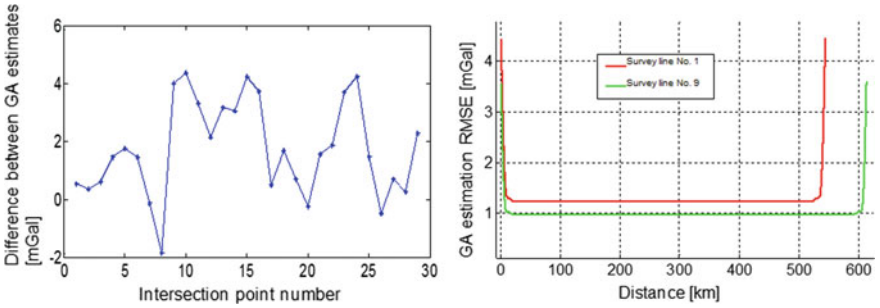

Fig. 2.30 Difference of GA estimates at survey line intersection points (*left*); the calculated RMSE of GA estimates in the smoothing mode on various survey lines (*right*)

Examples of GA estimates for two survey lines are shown in Fig. 2.29. Figure 2.30 presents the RMSE of the obtained estimates and the difference of estimates at the line intersection points. As can be seen, the difference is 1–4 mGal at these points. This suggests that the RMSE of GA estimation is at the level of 1–2 mGal, which agrees with the calculations.

The results confirm the efficiency of the proposed algorithms for GA estimation. Their main advantages include (a) the ability to identify both the GA model and the error model, which reduces the survey time, since there is no need for empirical tuning of filter parameters and manual processing of each survey line; (b) the ability to estimate the accuracy during the calculation; and (c) the reduction of the transient estimation process.

2.3.6 Conclusion

An optimal estimation problem in general form has been formulated within the Bayesian approach, and an example of designing optimal nonstationary filtering

and smoothing algorithms for GA estimation has been considered. The features of designing stationary filtering and smoothing algorithms have been analyzed.

It is noted that a significant advantage of the Bayesian approach lies in its ability to calculate the potential estimation accuracy for the given models of anomalies and the errors of the measuring instruments. This allows objective estimation of the efficiency of various suboptimal algorithms. The applied stationary algorithms based on the Butterworth filter and the two-stage estimation procedure have been compared, and their performance has been analyzed.

The section emphasizes the importance of the model structural and parametric identification, providing the required data on the models for implementing the optimal algorithms, and describes the proposed identification algorithm based on nonlinear filtering methods and actually making the estimation process and algorithms adaptive. The results of real data processing using the proposed algorithm in gravity anomaly estimation are provided, which confirm the algorithm efficiency.

2.4 Suboptimal Smoothing in Marine Gravimetric Surveys Using GT-2M Gravimeters

It was stated earlier that in airborne gravimetry, the PSDs of perturbing accelerations and the GA to be measured overlap because of high carrier speeds (Hein 1995; Koshaev and Stepanov 2010). In this regard, in order to extract gravity anomalies from the GSE readings, one needs precise external information about the flight altitude usually provided by the GNSS operating in the differential phase mode (Koshaev and Stepanov 2010; Bolotin et al. 2002). In marine gravimetry, due to low speeds of vessels, the PSDs of perturbing accelerations lie in a higher frequency range than those of the anomaly components being measured. Therefore, the problem of identifying GAs in GSE readings can be solved, at least in the case of surface vessels, using filtering without precise external information (Panteleev 1983; Krasnov et al. 2014). However, given the fact that the level of noise is five to six orders of magnitude higher than the level of the useful signal, rather stringent requirements may be imposed on the gravimetric filter in terms of its effectiveness when used in real time.

In postprocessing, it is possible to use optimal smoothing algorithms on a fixed interval. As noted in Sect. 2.3, they provide higher estimation accuracy compared with the KF but such algorithms are much more difficult to implement, one of the reasons being the necessity to store a significant amount of data. In this regard, the development of suboptimal smoothing algorithms is relevant.

Design of such algorithms with regard to marine vessels is what this section is devoted to.

2.4.1 Constant-Delay Optimal and Suboptimal Smoothers for Continuous-Time Systems

The search for an algorithm that combines the simplicity of the KF and the quality of the optimal smoothing on a fixed interval is of interest both for the problem of marine gravimetry and other applications. Constant-delay smoothing may be a compromise solution in this case, which, however, imposes an additional restriction: the algorithm should have a filter structure with an infinite impulse response of the same order as the original system.

The proposed algorithm of suboptimal smoothing is designed in relation to the problem (2.3.1), (2.3.2) under the assumption that the system noise is neglected at the smoothing stage, i.e., $Q = 0$. In this case, it is easy to show that the algorithm for generating a suboptimal smoothed estimate is reduced to the 'inversed' extrapolation of the last current optimal estimate of the KF using the transient state matrix, i.e., $\hat{x}_s(t|t_1) = \Phi(t, t_1)\hat{x}(t_1|t_1)$, where $\Phi(t, t_1)$ is the transient matrix of the system. Thus, the suboptimal smoothing algorithm is simpler than the optimal algorithm and does not require repeated filtering of the estimates obtained at the first stage.

In this case, the equations for the suboptimal smoothing error covariance matrix P_s can be written as follows (Meditch 1969):

$$\begin{aligned}\dot{P}_s(t|t_1) &= FP_s(t|t_1) + P_s(t|t_1)F^T + \Phi(t, t_1)\Phi_{F-KH}(t_1, t)GQG^T \\ &+ GQG^T\Phi^T_{F-KH}(t_1, t)\Phi^T(t, t_1) - GQG^T,\end{aligned} \tag{2.4.1}$$

where $\Phi_{F-KH}(t_1, t)$ is the linear system state transient matrix $\dot{x} = (F - KH)x$. Equation (2.4.1) is solved in the inverse time with the boundary condition $P_s(t_1|t_1) = P(t_\infty)$, where $P(t_\infty)$ is the steady-state value of the KF error covariance matrix. The algorithm for finding the suboptimal smoothing estimate with a constant delay τ is determined by solving the following differential equation (Meditch 1969):

$$\frac{d}{dt}\hat{x}_s(t|t+\tau) = F\hat{x}_s(t|t+\tau) + L(t)\big[y(t+\tau) - H\Phi(t, t+\tau)\hat{x}_s(t|t+\tau)\big], \tag{2.4.2}$$

where $L(t) = \Phi(t, t+\tau)^{-1}K(t)$ is the feedback coefficient of the smoothing filter, and $K(t) = P(t+\tau|t+\tau)H^TR^{-1}$ is the KF feedback ratio.

Obviously, the variance of the optimal smoothed estimate with a constant delay is a non-increasing function of interval τ. Due to the methodic error caused by the neglect of the generating noise of the system, the suboptimal smoothed estimate has an error variance greater than the optimal smoothing error variance and does not necessarily decrease with time. Thus, the effective use of suboptimal smoothing is only possible on a limited interval due to the increase in the above-mentioned methodic error with the increase in the interval length.

In order to discuss the effectiveness of the proposed suboptimal smoothing filter and to estimate the interval on which suboptimal smoothing is appropriate to implement, consider the following methodic example. Assume that it is required to estimate the state of a scalar system with a scalar measurement:

$$\begin{aligned} \dot{x}(t) &= w(t), \\ y(t) &= x(t) + v(t), \end{aligned} \tag{2.4.3}$$

where $w(t)$ and $v(t)$ are stationary uncorrelated white noises with intensities Q and R, respectively.

Assume that for some $t_0 > 0$, the KF, generating a current estimate of the system state (2.4.3), is in a steady state, and it is required to obtain a smoothed state estimate on a fixed interval $[t_0, t_1]$. To compare the accuracy of the optimal and suboptimal smoothing algorithms, let us solve the problem in the optimal and suboptimal problem statements. For (2.4.3), it is easy to obtain analytical solutions of the covariance equations for the KF, the optimal and suboptimal smoothing filters on a fixed interval. For this case, $F = 0$, $H = 1$, $\Phi(t_1, t) = 1$. The steady-state values of the variance of the optimal filtering error and the KF gain coefficient are determined by the following formulas: $P(t_\infty) = \sqrt{QR}$, $K = \sqrt{Q/R}$ (Meditch 1969; Stepanov 2017b). The formula for the error variance of the optimal smoothing filter on a fixed interval takes the form:

$$\dot{P}(t|t_1) = -2\sqrt{\frac{Q}{R}}P(t|t_1) + Q.$$

By integrating the last equation in the inverse time with the initial condition $P(t_1|t_1) = P(t_\infty) = \sqrt{QR}$ and considering that $\tau = t_1 - t$, we get:

$$P(t|t+\tau) = \frac{\sqrt{RQ}}{2}\left(1 + e^{-2\frac{\tau}{T_0}}\right), \tag{2.4.4}$$

where $T_0 = 1/K = \sqrt{R/Q}$ is the KF time constant. It can be seen that for $\tau \to \infty$, the variance $P(t|t+\tau)$ tends to the fixed value $P(\tau_\infty) = \sqrt{RQ}/2$.

Now, consider the suboptimal smoothing problem. Since in the case under consideration $\Phi(t, t_1) = 1$, the equation of the suboptimal smoothing filter becomes the following relation: $\hat{x}_s(t|t_1) = \hat{x}(t_1|t_1)$. Thus, for this example, suboptimal smoothing is reduced to a shift back on the time scale of the current KF estimate. In accordance with (2.4.1), we obtain the equation that determines the suboptimal smoothing error variance:

$$\dot{P}_s(t|t_1) = -2e^{-K\tau}Q + Q,$$

which should be solved in the inverse time with the boundary condition at the right end of the interval $P_s(t_1|t_1) = \sqrt{QR}$. After solving the equation, we obtain:

$$P_s(t|t+\tau) = 2\sqrt{RQ}e^{-\frac{\tau}{T_0}} + Q \cdot \tau - \sqrt{RQ}. \tag{2.4.5}$$

In order to find the parameter τ of the suboptimal smoother, for which the minimum of the estimate error variance is feasible, we differentiate (2.4.5) with respect to τ and equate the derivative to zero:

$$\frac{dP_s(t|t+\tau)}{d\tau} = -2Qe^{-\frac{\tau}{T}} + Q = 0.$$

Hence, the optimal value of the suboptimal smoothing interval length is determined by the formula $\tau^* = T_0 \ln 2 \cong 0.7\ T_0$. Substituting the value τ^* and T_0 into (2.4.5), we derive $P_s^* = 0.7\sqrt{RQ} > 0.5\sqrt{RQ} = P(\tau_\infty)$.

The RMSD values of filtering errors, for the optimal and suboptimal smoothers, depending on the length of the smoothing interval, are presented in Fig. 2.31.

Analyzing the curves, it is pertinent to note that the ratio of the RMSDs of the optimal and suboptimal smoothers for $\tau \leq 0.7\,T$ does not exceed the value of $\sigma_s/\sigma < 1.05$, and the ratio of the minimum RMSD of the suboptimal smoothing to the minimum attainable error of the optimal smoothing is $\sigma_s^*/\sigma^* < 1.18$. We can state that, in the example under consideration, the accuracy of the suboptimal smoothing algorithm on an optimally selected delay interval is only 5% lower than that of the optimal smoothing with a constant delay and 18% lower than the potential accuracy of the optimal smoothing on a fixed interval. Thus, it appears that the proposed method for the synthesis of suboptimal smoothing algorithms may be successfully applied in practice.

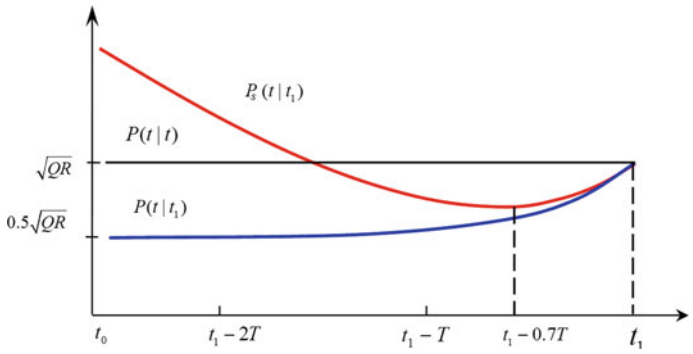

Fig. 2.31 RMSD versus delay time

2.4.2 Suboptimal Gravimetric Filter

Let us solve the problem of suboptimal filter design for the problem of marine gravimetry. Consider a gravimeter with a non-damped (non-inertial) GSE with a vertical sensitive axis, installed on a gyro-stabilized platform. Denote the GSE measurement (vertical specific force) as g_{GR}. Now, subtract the normal gravity value g_0 from the GSE readings, take into account the Eotvos correction Δg_E and the altitude correction $g^0_{ZZ}h_o$, where φ is the latitude, V is the relative velocity vector, g^0_{ZZ} is the normal value of the gravity gradient, h_s is the external altitude information delivered by, for example, the GNSS. Let us integrate the result twice and compare it with the external altitude information (Fig. 2.32).

The mechanization equations corresponding to the structure shown in Fig. 2.32 are written as follows:

$$\begin{aligned} \dot{h}_{GR} &= V_{GR}, \\ \dot{V}_{GR} &= g_{GR} + \Delta g_E - g_0 - g^0_{ZZ}h_o, \\ y &= h_s - h_{GR}. \end{aligned} \tag{2.4.6}$$

Note that these equations are similar to (2.3.25), (2.3.27).

Earlier in Sect. 2.3, it was noted that when designing a stationary filter without significant loss in accuracy, the Jordan model can be approximated by models in the form of integrals of white noise. Other fractionally rational PSDs of the gravity anomaly, for example, the Schwartz model, are also well approximated by this model (Bolotin et al. 2002). Therefore, we will describe the gravity anomaly using the model in the form of the third integral of white noise w_{GA}. Considering errors v_s in the altitude measurements $h_s = h_0 + v_s$ as white noise and neglecting the generating noise in the GA model, we will write the equations of the system state in the deviations $\Delta h = h_0 - h_{GR}$, $\Delta V = V_0 - V_{GR}$ similar to (2.3.26) in the following form:

$$\begin{aligned} \Delta\dot{h} &= \Delta V, \ \dot{b}_1 = b_2, \\ \Delta\dot{V} &= \Delta g, \ \dot{b}_2 = w_{GA}, \end{aligned}$$

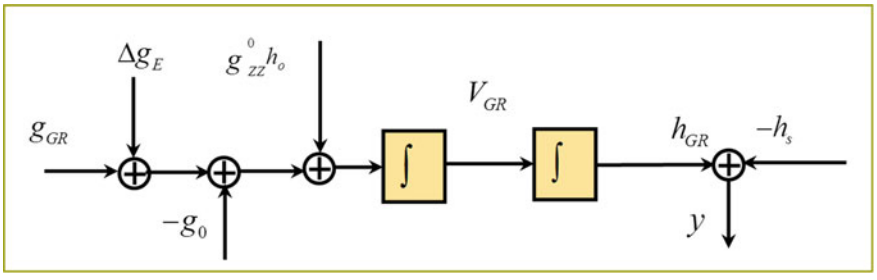

Fig. 2.32 Schematic of GSE data preprocessing

$$\Delta\dot{g} = b_1,\ \ y = \Delta h + v_s, \tag{2.4.7}$$

where w_{GA} and v_s are white noises with intensities Q and R, respectively, and $\Delta g, b_1, b_2$ describe the GA model. By introducing the state vector $x = [\Delta h\ \ \Delta V\ \ \Delta g\ \ b_1\ \ b_2]^T$, it is also possible to reduce (2.4.7) to the matrix form.

The KF equations for (2.4.7) become:

$$\begin{aligned}
\Delta\dot{\hat{h}} &= \Delta\hat{V} + k_1\left(y - \Delta\hat{h}\right),\\
\Delta\dot{\hat{V}} &= \Delta\hat{g} + k_2\left(y - \Delta\hat{h}\right),\\
\Delta\dot{\hat{g}} &= \hat{b}_1 + k_3\left(y - \Delta\hat{h}\right),\\
\dot{\hat{b}}_1 &= \hat{b}_2 + k_4\left(y - \Delta\hat{h}\right),\\
\dot{\hat{b}}_2 &= k_5\left(y - \Delta\hat{h}\right).
\end{aligned} \tag{2.4.8}$$

The values of the KF gain vector $k_1 \ldots k_5$ can be obtained through the analytical solution of the Riccati equation and are given by the following formulas:

$$\begin{aligned}
&k_1 = \mu(Q/R)^{1/10},\ \ k_2 = (\mu+2)(Q/R)^{2/10}\\
&k_3 = (\mu+2)(Q/R)^{3/10},\ \ k_4 = (\mu+2)(Q/R)^{4/10},\\
&k_5 = (Q/R)^{5/10},\ \ \mu = 1 + \sqrt{5} \cong 3.24.
\end{aligned}$$

Introduce parameter $T = (R/Q)^{1/10}$, characterizing the filter time constant. Thus,

$$\begin{aligned}
&k_1 = \frac{\mu}{T} \approx \frac{3.24}{T}, k_2 = \frac{\mu+2}{T^2} \approx \frac{5.24}{T^2}, k_3 = \frac{\mu+2}{T^3} \approx \frac{5.24}{T^3},\\
&k_4 = \frac{\mu}{T^4} \approx \frac{3.24}{T^4}, k_5 = \frac{1}{T^5}.
\end{aligned} \tag{2.4.9}$$

Write the equations of the suboptimal smoothing filter with the delay τ for the system under consideration:

$$\begin{aligned}
&\Delta\dot{\hat{h}}_s = \Delta\hat{V}_s + l_1(y - \Delta\hat{h}),\ \ \dot{\hat{b}}_{1s} = \hat{b}_{2s} + l_4(y - \Delta\hat{h}),\\
&\Delta\dot{\hat{V}}_s = \Delta\hat{g}_s + l_2(y - \Delta\hat{h}),\ \ \dot{\hat{b}}_{2s} = l_5(y - \Delta\hat{h}),\\
&\Delta\dot{\hat{g}}_s = \hat{b}_{1s} + l_3(y - \Delta\hat{h}),\ \ \Delta\hat{h} = \Delta\hat{h}_s - \tau\Delta\hat{V}_s - \frac{\tau^2}{2}\Delta\hat{g}_s - \frac{\tau^3}{6}\hat{b}_{1s} - \frac{\tau^4}{24}\hat{b}_{2s}.
\end{aligned} \tag{2.4.10}$$

Here, we use the following notation:

$$
\begin{aligned}
l_1 &= k_1 - \tau k_2 + \frac{\tau^2}{2}k_3 - \frac{\tau^3}{6}k_4 + \frac{\tau^4}{24}k_5,\\
l_2 &= k_2 - \tau k_3 + \frac{\tau^2}{2}k_4 - \frac{\tau^3}{6}k_5,\\
l_3 &= k_3 - \tau k_4 + \frac{\tau^2}{2}k_5,\\
l_4 &= k_4 - \tau k_5,\\
l_5 &= k_5.
\end{aligned}
\tag{2.4.11}
$$

The estimate of the suboptimal smoothing filter with the constant delay τ is associated with the KF estimate by the backward-in-time extrapolation formula $\hat{x}_c = \Phi(t-\tau, t)^{-1} \cdot \hat{x}$ or, which is the same, $\hat{x} = \Phi(t-\tau, t)\hat{x}_c$. Write down the latter equation in the scalar form:

$$
\begin{aligned}
\Delta\hat{h} &= \Delta\hat{h}_s + \tau\Delta\hat{V}_s + \frac{\tau^2}{2}\Delta\hat{g}_s + \frac{\tau^3}{6}\hat{b}_{1s} + \frac{\tau^4}{24}\hat{b}_{2s},\\
\Delta\hat{V} &= \Delta\hat{V}_s + \tau\Delta\hat{g}_s + \frac{\tau^2}{2}\hat{b}_{1s} + \frac{\tau^3}{6}\hat{b}_{2s},\\
\Delta\hat{g} &= \Delta\hat{g}_s + \tau\hat{b}_{1s} + \frac{\tau^2}{2}\hat{b}_{2s},\\
\hat{b}_1 &= \hat{b}_{1s} + \tau\hat{b}_{2s},\\
\hat{b}_2 &= \hat{b}_{2s}.
\end{aligned}
\tag{2.4.12}
$$

Taking into account the formulas for $\Delta\hat{h}$ from (2.4.7), as well as the fact that $\hat{h} = h_{GR} - \Delta\hat{h}$, Eq. (2.4.10) can be written as follows:

$$
\begin{aligned}
\Delta\dot{\hat{h}}_s &= \Delta\hat{V}_s + l_1\left(\hat{h} - h_o\right),\\
\Delta\dot{\hat{V}}_s &= \Delta\hat{g}_s + l_2\left(\hat{h} - h_o\right),\\
\Delta\dot{\hat{g}}_s &= \hat{b}_{1s} + l_3\left(\hat{h} - h_o\right),\\
\dot{\hat{b}}_{1s} &= \hat{b}_{2s} + l_4\left(\hat{h} - h_o\right),\\
\dot{\hat{b}}_{2s} &= l_5\left(\hat{h} - h_o\right).
\end{aligned}
\tag{2.4.13}
$$

By multiplying the fifth equation in (2.4.13) by $\tau^4/24$, the fourth one by $\tau^3/6$, the third one by $\tau^2/2$, the second one by τ, and adding it to the first one, and also by multiplying the fifth equation by $\tau^3/6$, the fourth one by $\tau^2/2$, the third one by τ, and adding it to the second one, taking into account (2.4.11), we obtain:

$$
\Delta\dot{\hat{h}} = \Delta\hat{V}_s + k_1\left(\hat{h} - h_o\right),
$$

$$\begin{aligned}
\Delta\dot{\hat{V}} &= \Delta\hat{g}_s + \tau\hat{b}_{1s} + \frac{\tau^2}{2}\hat{b}_{2s} + k_2\Big(\hat{h} - h_o\Big),\\
\Delta\dot{\hat{g}}_s &= \hat{b}_{1s} + (k_3 - \tau k_4 + \tau k_5)\Big(\hat{h} - h_o\Big),\\
\dot{\hat{b}}_{1s} &= \hat{b}_{2s} + (k_4 + \tau k_5)\Big(\hat{h} - h_o\Big),\\
\dot{\hat{b}}_{2s} &= k_5\Big(\hat{h} - h_o\Big).
\end{aligned} \tag{2.4.14}$$

By subtracting the first two equations of (2.4.14) from the first two equations of (2.4.6) and taking into account that $\hat{h}_{GR} = h_{GR} - \Delta\hat{h}$, $\hat{V}_{GR} = V_{GR} - \Delta\hat{V}$, we finally derive the vertical channel equations:

$$\begin{aligned}
\dot{\hat{h}}_{GR} &= \hat{V}_{GR} - k_1\Big(\hat{h} - h_o\Big),\\
\dot{\hat{V}}_{GR} &= g_{GR} - g^{\circ}_{zz}h^* - g_0 + \Delta g_E - \Delta\hat{g}_s - \tau\hat{b}_{1s} - \frac{\tau^2}{2}\hat{b}_{2s} - k_2\Big(\hat{h} - h_o\Big),\\
\Delta\dot{\hat{g}}_s &= \hat{b}_{1s} + l_3\Big(\hat{h} - h_o\Big),\\
\dot{\hat{b}}_{1s} &= \hat{b}_{2s} + l_4\Big(\hat{h} - h_o\Big),\\
\dot{\hat{b}}_{2s} &= k_5\Big(\hat{h} - h_o\Big).
\end{aligned} \tag{2.4.15}$$

These are the equations of the suboptimal gravimetric smoothing filter (SGSF) which generates an optimal filtering estimate for the current time of the flight altitude h_{GR}, the vertical velocity V_{GR} and the suboptimal smoothed estimate with the constant delay τ of the gravity anomaly $\Delta\hat{g}_s$. It is easy to show that the current KF estimate can be calculated using the formula:

$$\Delta\hat{g} = \Delta\hat{g}_s + \tau\hat{b}_{1s} + \frac{\tau^2}{2}\hat{b}_{2s}. \tag{2.4.16}$$

The SGSF block diagram for the vertical channel is shown in Fig. 2.33.

To complete the design of the filter, it is necessary to choose the time delay τ. The studies conducted by numerical solution of the covariance equation for the estimate of the form (2.4.10) of the suboptimal fifth-order smoothing gravimetric filter show that the optimal time of the constant delay is very close to $\tau^* = k_4/k_5$. Taking into account (2.4.9), $\tau^* = \mu T \approx 3.24\,T$. As follows from (2.4.11), the coefficients l_3, l_4 in (2.4.15) become equal to zero.

Of great importance for practice is the filter resolution in time—the averaging time T_a. In space, it usually corresponds to half-wavelength L_s passed through the filter. These parameters are related as $L_s = T_a V/2$, where V is the horizontal speed of the vessel. For the given optimal delay time τ^*, we have:

$$T = \frac{\tau^*}{1+\sqrt{5}},\ T_a = 2\pi T \approx 1.94\,\tau^*,\ L_s \approx 0.97\,\tau^* V.$$

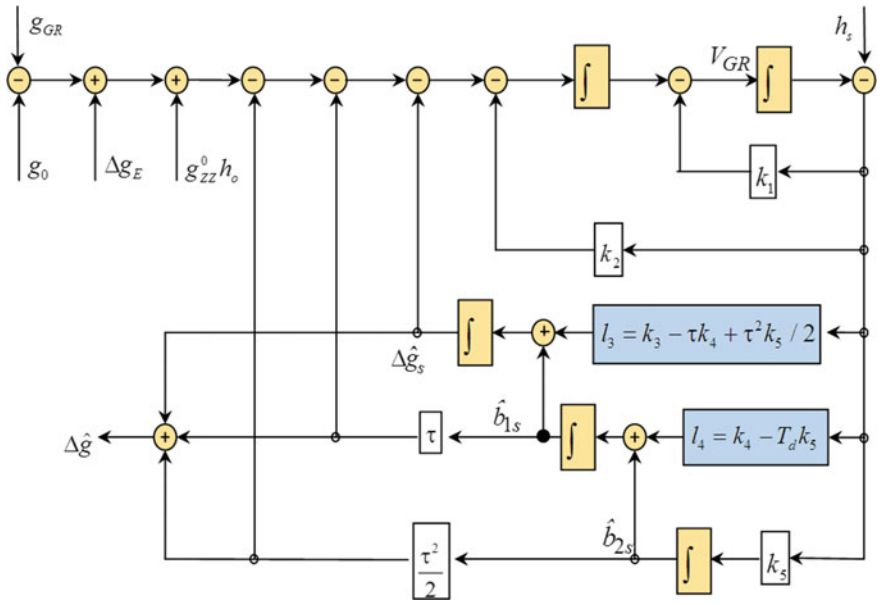

Fig. 2.33 SGSF block diagram for the vertical channel

2.4.3 *Frequency Properties of the Suboptimal Gravimetric Filter*

In the frequency domain, the amplitude response of the SGSF anomaly estimate $\Delta\hat{g}_s(\&)$ can be written as follows:

$$|\Delta\hat{g}_s(\omega)| = \sqrt{|v(\omega)|^2 \cdot \omega^4 + |\Delta g(\omega)|^2} \frac{\sqrt{\frac{1}{4}(\mu T - \tau)^4\omega^4 + 1}}{\sqrt{1 + T^{10}\omega^{10}}}, \tag{2.4.17}$$

where $v(\&)$ is the Fourier transform of the error in the external altitude information, $\Delta g(\&)$ is the Fourier transform of GA as a function of time, & is the angular frequency. When the delay time is zero, the output amplitude coincides with the KF output amplitude defined by the following formula:

$$|\Delta\hat{g}_s(\omega)| = \sqrt{|v(\omega)|^2 \cdot \omega^4 + |\Delta g(\omega)|^2} \frac{\sqrt{\frac{1}{4}(\mu T)^4\omega^4 + 1}}{\sqrt{1 + T^{10}\omega^{10}}}. \tag{2.4.18}$$

With the optimal delay $\tau^* = \mu T \approx 3.24\,T$, the amplitude of the SGSF output is equal to the amplitude of the 5th order Butterworth filter output with the same inputs:

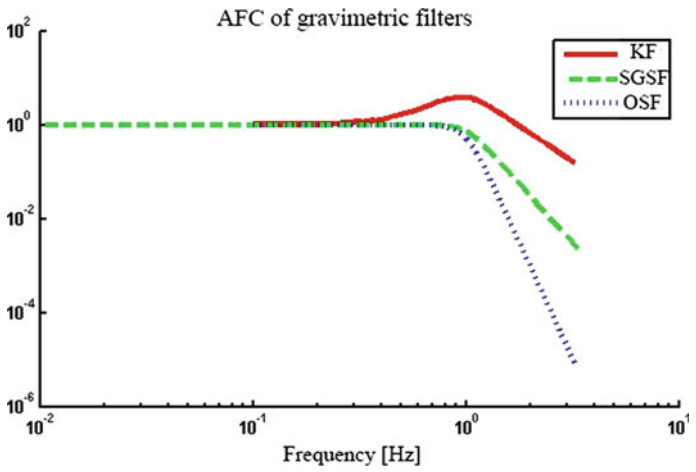

Fig. 2.34 Amplitude-frequency characteristics (AFC) of the GA estimate for KF, OSF, and SGSF. The filter averaging time is 100 s

$$|\Delta\hat{g}_s(\omega)| = \sqrt{|v(\omega)|^2 \cdot \omega^4 + |\Delta g(\omega)|^2}\frac{1}{\sqrt{1 + T^{10}\omega^{10}}}. \tag{2.4.19}$$

The main difference between the Butterworth filter and the SGSF is the behavior of the phase characteristics.

The output amplitude of the optimal smoothing filter (OSF) is defined by the formula:

$$|\Delta\hat{g}_s(\omega)| = \sqrt{|v(\omega)|^2 \cdot \omega^4 + |\Delta g(\omega)|^2}\frac{1}{1 + T^{10}\omega^{10}}. \tag{2.4.20}$$

The relevant plots of the amplitude-frequency and phase-frequency characteristics of the anomaly estimates for different algorithms (2.4.18)–(2.4.20) are shown in Figs. 2.34 and 2.35. The delay interval for smoothing algorithms was 100 s.

2.4.4 Results of the Experimental Data Processing

The GT-2M gravimeter has three parallel vertical channels operating in accordance with the algorithm described above with different operator-defined time constants. These channels generate three suboptimal smoothed GA estimates in real time, which allow the operator, in the process of the anomaly map generation, to choose the number of the vertical channel output, depending on the sea state. Typically, the averaging time T_a varies from 300 to 800 s in order to provide the error RMSD within 0.2–0.3 mGal with the best filter resolution.

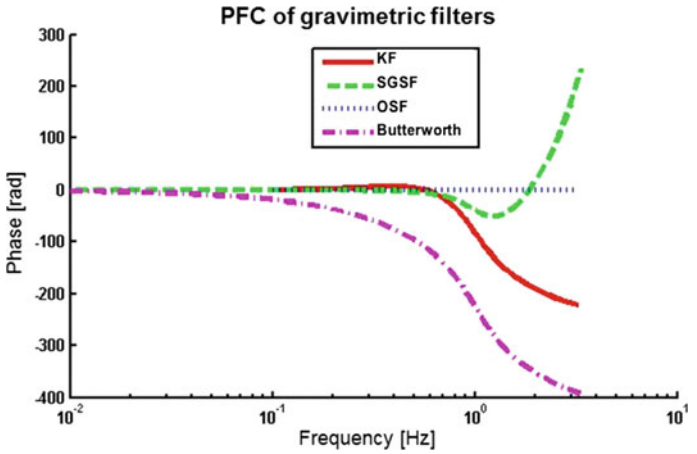

Fig. 2.35 Phase-frequency characteristics (PFC) of the GA estimate for KF, OSF, SGSF, and Butterworth filter

Figures 2.36 and 2.37 show GA estimation plots obtained using the GTGRAV software for processing the GT-2A gravimeter data and the GA estimation error as a function of time for OSF and SGSF for various averaging times. Figure 2.36 shows anomaly estimation plots; Fig. 2.37 shows anomaly estimation errors. The red curve in Fig. 2.36 corresponds to the averaging time of 800 s, which is taken to be a true anomaly during the analysis since there are no independent data to compare with sufficient resolution. Noisier plots correspond to an averaging time of 300 s. The smoothing error RMSD is estimated as 0.28 mGal for SGSF and 0.24 mGal for OSF. Note that the sea was rather rough (the blue dots in both figures indicate the moments of time when the vertical acceleration exceeded 0.5 g). This somewhat reduced the accuracy of the estimation. An important fact is that the OSF calculation took about a minute in the GTGRAV software, and the SGSF calculation took less than a second.

2.4.5 Conclusion

The design of a constant-delay suboptimal smoothing filter has been described. Its feature is the neglect of the generating noise in the shaping filter equations for the state vector being estimated. For a linear stochastic system, the estimation equations and the covariance equation are given for the suboptimal smoothing filter in continuous time. A methodic example is used to compare such a filter with the optimal smoothing filter and the Kalman filter. For this example, it is shown that, as compared with the optimal smoothing filter, the suboptimal filter does not require any additional computation and memory. At the same time, it is close to the optimal filter in accuracy. Using the proposed method, we have synthesized a suboptimal smoothing gravimetric filter corresponding to the steady state under the assumption

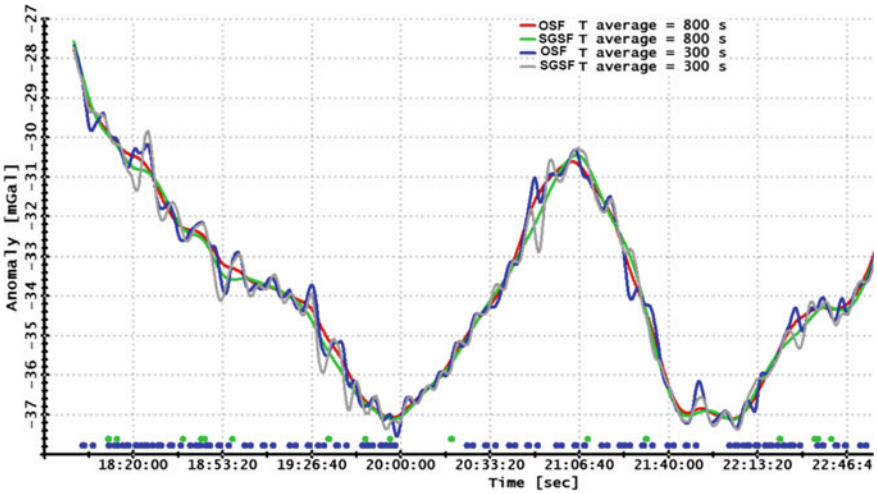

Fig. 2.36 GA estimation plots for OSF and SGSF at averaging times of 800 and 300 s

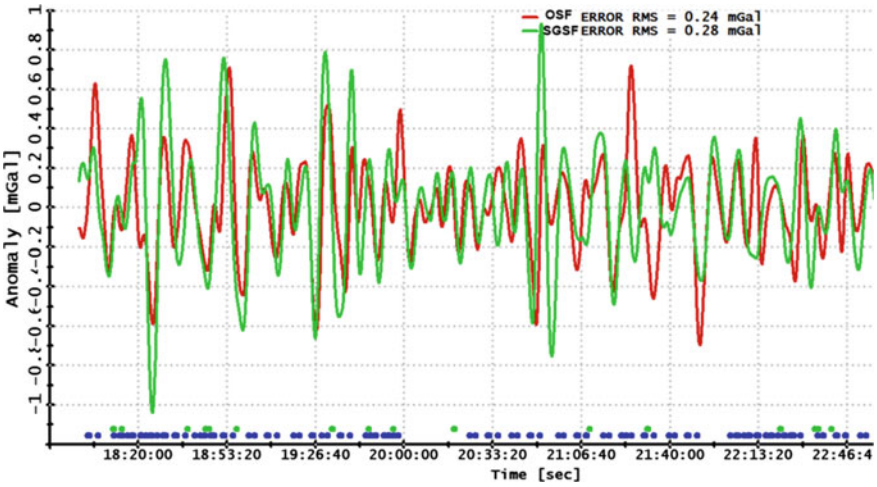

Fig. 2.37 GA estimation error plots for OSF and SGSF with an averaging time of 300 s. The estimate with an averaging of 800 s is used as a reference

that GAs are described as the third integral of white noise and its parameters are defined. It is noted that such a gravimetric filter is integrated in the GT-2M marine gravimeter (Bolotin and Yurist 2011), mass-produced by Gravimetric Technologies. Using data from a real marine gravimetric survey, it is shown that the errors of the suboptimal smoothing gravimetric filter do not differ significantly from the errors of the optimal smoothing filter. At the same time, the designed gravimetric filter shows high accuracy, even at rough seas.

2.5 Using Spherical Wavelet Expansion to Combine Airborne Gravimetry Data and Global Gravity Field Model Data

In airborne gravimetry, the problem of gravity anomaly (GA) determination includes the stages of along-line anomaly estimation and construction of anomaly maps in the survey area. The latter often includes GA transformations (downward continuation, calculation of deflections of the vertical, etc.). Correct transformations require the use of nonlocal information about the gravity field, therefore, airborne gravimetry data are usually combined with gravity data provided by a global EGF model (EGM2008, EIGEN-6C2, etc.), given in terms of coefficients of the spherical harmonic expansion (Kern et al. 2003). The use of such an expansion in the problem under consideration is often technically difficult since working with a full set of coefficients is required. Another well-known approach, the collocation method (Kern et al. 2003), is based on a priori stochastic gravity models, the reliability of which, however, is often questionable. Relatively new approaches to the local GA determination are based on expansions of the gravity field using a system (complete system in a Hilbert space) of spherical radial basis functions that have the spatial localization property (Schmidt et al. 2007). One of such expansions is based on the use of spherical scaling and wavelet functions; it can be found in (Freeden and Michel 2004). In addition to localization in space, in the opinion of the authors of this section, an important feature of this approach is multiscale representation of gravity data, which is a framework for combining airborne gravimetry data and gravity data from a global gravitational field model. The combination is based on selecting a common spherical harmonic bandwidth in both gravity datasets.

Section 2.5 describes the method developed for GA determination in a local area of the airborne gravimetric survey based on joint processing of airborne gravity data and the global EGF model data using the multiscale analysis on the sphere. An algorithm for combining airborne gravity data and global gravity data was developed based on the least squares method.

Section 2.5 is organized as follows. First, the multiscale analysis based on the Abel–Poisson spherical wavelets is briefly described; next, the stages of the local anomaly determination technique developed by the authors of this section are described, one of which solves the problem of combining the wavelet coefficients obtained from airborne gravimetry data and the global EGF model. In the problem, the errors of the wavelet coefficients are assumed to be random values with the known statistical characteristics obtained from the airborne and global gravity data. The problem of gravity data combination (through wavelet coefficients) is formulated as a problem of determining a linear nonbiased estimate optimal under the criterion of the minimum mean square error and is solved by the least squares method (LSM) in the covariance form. The section concludes with the discussion of the results of the experimental data processing using the algorithms developed for the GA local determination.

2.5.1 Spherical Wavelet Expansion and Multiscale Representation of the Anomalous Gravity Field

Let us elucidate the basics of the multiscale analysis on the sphere (Freeden and Michel 2004). The gravity anomaly Δg is assumed to be a function defined in the outer space of the Bjerhammer sphere and square integrable on this sphere. Further, the GA is represented as a convolution of the radial derivative of the scaling function $\Phi_J(x, y_s)$ and the scaling coefficient (SC) $a_J(y_s)$ of a certain resolution level J (Freeden and Michel 2004; Bolotin and Vyazmin 2015):

$$\Delta g(x) = \sum_s \omega_s a_J(y_s) \frac{\partial \Phi_J(x, y_s)}{\partial |x|}, \tag{2.5.1}$$

where y_s are the nodes of an equiangular grid on the Bjerhammer sphere Ω_R of radius R, ω_s are the integration weights, $x \in \mathrm{R}^3$, $|x| = \left(x^T x\right)^{1/2} \geq R$. Due to the normalization of the scaling functions, SCs have the dimension of the potential. The resolution level J (where $J = 0, 1, 2\ldots$) is chosen according to the required spatial resolution of the GA map. The spherical scaling function of the resolution level J is defined by the following formula (Freeden and Michel 2004):

$$\Phi_J(x, y) = \sum_{n=0}^{\infty} \phi_J(n) \left(\frac{R}{|x|}\right)^{n+1} \frac{2n+1}{4\pi R^2} P_n\left(\xi^T \eta\right),$$

where $\varphi_J(n)$ is the so-called scaling function symbol, $P_n\left(\xi^T \eta\right)$ is the Legendre polynomial of the degree n, $\xi = x/|x|$, $\eta = y/|y|$. The scaling function has the following properties:

(1) axisymmetry, i.e., it depends only on the spherical distance between x, y with fixed values of $|x|$, $|y|$; it decreases as the spherical distance between x, y increases;
(2) harmonic in the outer space of the sphere;
(3) it tends to the Dirac delta function on the sphere as $J \to \infty$ in the norm of the Hilbert space $L^2(\Omega_R)$ of the functions quadratically integrated on the sphere.

In this work, the Abel–Poisson scaling function with the symbol $\phi_J(n) = \exp\left(-2^{-J} n\right)$ is chosen, which rapidly decreases in the spatial and spherical harmonic domain and can be represented as an elementary function (Fig. 2.38):

$$\Phi_J(x, y) = \frac{1}{4\pi R} \frac{|x|^2 - R^2 b_J^2}{\left(|x|^2 + R^2 b_J^2 - 2 b_J x^T y\right)^{3/2}}, b_J = \exp\left(-2^{-J}\right). \tag{2.5.2}$$

The expansion in the scaling functions (2.5.1) is performed at the finest resolution level. To solve the gravity data combination problem, however, it is convenient to

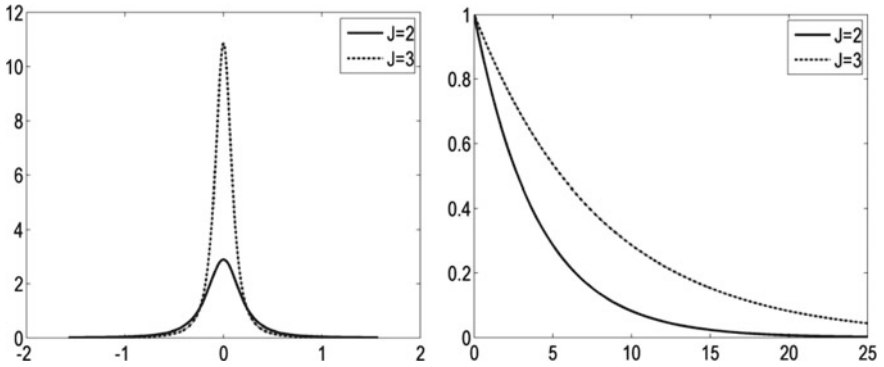

Fig. 2.38 The Abel–Poisson scaling function $\Phi_J(x, y)$ (cross-section) on a sphere with a unit radius at $J = 2, 3$, depending on the angle (rad) between x, y (*left*), and its symbol $\varphi_J(n)$ (*right*)

make an expansion into the components of different resolution levels called the multiscale representation.

The multiscale representation of the GA includes the spherical wavelet decomposition and wavelet reconstruction procedures. GA wavelet decomposition is the calculation of the spherical wavelet coefficients (SWC) at various resolution levels $j \le J$. The SWC contains information about the anomaly within a certain spherical harmonic bandwidth and is determined using the following formulas (Freeden and Michel 2004):

$$c_J(y_s) = a_J(y_s) - \sum_m \omega_m \Phi_J(y_s, y_m) a_J(y_m), \tag{2.5.3}$$

$$c_j(y_{sj}) = \sum_m \omega_m \Psi_j(y_{sj}, y_m) a_J(y_m), \quad j = j_0, \ldots, J-1, \tag{2.5.4}$$

where $c_j(y_{sj})$ is the SWC at the node y_{sj} of the equiangular grid at the resolution level j, $\Psi_j(y_{sj}, y_m)$ is the Abel–Poisson spherical wavelet function of the resolution level j defined by the formula:

$$\Psi_j(y_{sj}, y_m) = \Phi_{j+1}(y_{sj}, y_m) - \Phi_j(y_{sj}, y_m).$$

The Abel–Poisson wavelet function and its symbol $\psi_j(n) = \varphi_{j+1}(\mathrm{n}) - \varphi_j(\mathrm{n})$ are shown in Fig. 2.39.

The reconstruction of the anomaly from the calculated SWC is defined by the formula (Freeden and Michel 2004):

$$\Delta\tilde{g}(x) = \sum_{j=j_0}^{J} \Delta g_j(x), \tag{2.5.5}$$

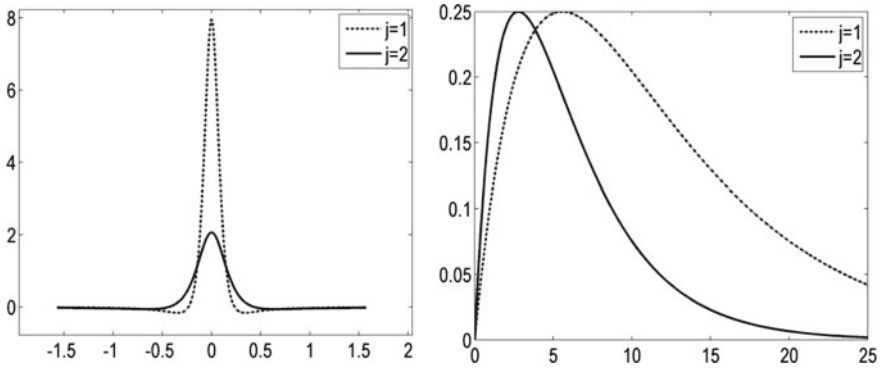

Fig. 2.39 Abel–Poisson wavelet $\Psi_j(x, y)$ (cross-section) on a sphere of a unit radius when $j = 1$, 2, depending on the angle (rad) between x, y (*left*), and its symbol (*right*)

where $\Delta g_j(x)$ is the detailing component of the anomaly at the resolution level j calculated using the convolution formulas (in the discrete form):

$$\Delta g_j(x) = \sum_s \omega_{sj} c_j(y_{sj}) \frac{\partial \Psi_j^d(x, y_{sj})}{\partial |x|}, \quad j = j_0, \ldots, J-1, \tag{2.5.6}$$

$$\Delta g_J(x) = \sum_s \omega_s c_J(y_s) \frac{\partial \Phi_J(x, y_s)}{\partial |x|}. \tag{2.5.7}$$

Here, $\Delta \tilde{g}$ is the result of GA reconstruction, $\Psi_j^d(x, y_s)$ is the dual wavelet function defined by the following formula (Freeden and Michel 2004):

$$\Psi_j^d(x, y_s) = \Phi_{j+1}(x, y_s) + \Phi_j(x, y_s).$$

The result of wavelet reconstruction (2.5.5) coincides with the representation of the anomaly in the form of (2.5.1) with an accuracy of the error of the quadrature formulas of the convolutions (2.5.3), (2.5.4).

Note that the Abel–Poisson wavelet functions at various resolution levels are not orthogonal in the space of functions square integrable on the sphere. Therefore, in the deterministic case, the detailing components of the anomalies Δg_j, Δg_m of various resolution levels $j \neq m$ cannot be calculated independently; and in the stochastic sense, i.e., if there are independent random errors in the SWC, these components are correlated, and the weighted LSM should be used for estimation. Also noteworthy as one of the advantages of the technique is that, similarly to (2.5.5), other functionals of the anomalous field, such as the geoid height, deflections of the vertical, etc., can be calculated from SWC. For this, instead of the wavelet function in (2.5.6)–(2.5.7), one should use the result of its convolution with the kernel of the corresponding transformation.

2.5.2 *Technique of Local Gravity Anomaly Determination from Airborne Gravimetry Data and Global Gravity Field Model Data Using Multiscale Representation*

Figure 2.40 describes the methodology for the local GA determination from airborne gravity data and the global EGF model data.

The developed technique includes the following stages:

(1) estimation of the GA SCs using the Abel–Poisson scaling functions at the finest resolution level J corresponding to the desirable spatial resolution of the GA map based on the results of airborne measurements at survey lines. The recurrent LSM is used in the information form (the covariance form is not suitable since the covariance matrices may be ill-conditioned at initial iterations) with the survey line number as the recursion step; regularization of the information matrix of the SC estimates is used at the last recursion step due to the ill-conditioning of the problem;
(2) SWC calculation at various resolution levels $j \leq J$ based on the SCs estimated at the first stage;
(3) calculation of the anomaly SWC based on the global model of the Earth's gravitational field at various resolution levels $j \leq J_{glob}$, where the J_{glob} value is determined by the resolution of the global EGF model;
(4) combination of the SWCs obtained from airborne measurements and the global model data at common resolution levels;
(5) reconstruction of the anomaly estimate (and other functionals of the gravitational field) from the SWC combining results.

Let us describe these stages in more detail.

At **the first stage** of the technique, the input data in the problem being solved are GAs at survey lines obtained from airborne measurements and smoothed using the gravimetric filter (Stepanov et al. 2015; Bolotin and Yurist 2011) and recorded at the discrete moments of time t_{ik}, i = 1…M_k, where k, k = 1…K, is the survey line

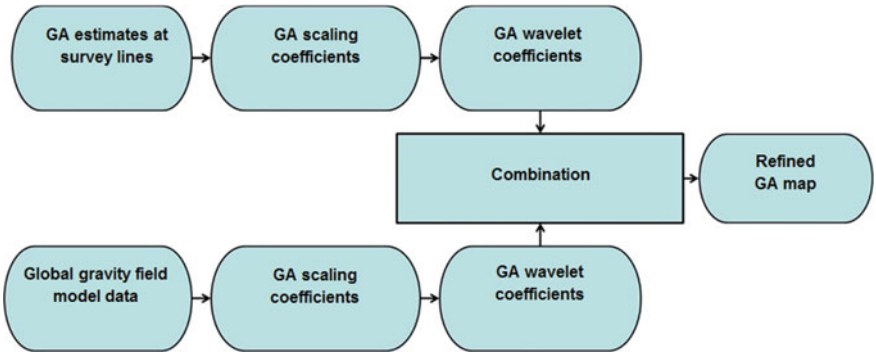

Fig. 2.40 Data flow diagram of airborne and global gravity data processing

number, M_k is the number of measurements at the kth survey line. The filter, assumed here to be stationary for simplicity, is characterized in time by the impulse response function $h_f(t_{ik} - t_{mk})$. The filter support, i.e., the number of moments t_{mk}, for which $h_f(t_{ik} - t_{mk}) \neq 0$, is assumed to be finite and equal to $2M + 1$. The resolution of the filter in time is characterized by the cutoff frequency ω_{cut}. The resolution in space is defined as half-wavelength $L = 2\pi V/\omega_{cut}$, where V is the speed of the aircraft. The model of the smoothed airborne GA data $\Delta g'_k(t_{ik})$ at the kth survey line at the moment of time t_{ik} can be represented as follows:

$$\Delta g'_k(t_{ik}) = \sum_{m=i-M}^{i+M} h_f(t_{ik} - t_{mk}) \Delta g(x(t_{mk})) + \delta g_k(t_{ik}), \tag{2.5.8}$$

where Δg is the true free air GA, $x(t_{mk}) \in \mathrm{R}^3$ are the coordinates of the measurement point at the kth survey line in the geocentric coordinate system, $\delta g_k(t_{ik})$ is the measurement error. It is assumed that

- the coordinates of the measurement points are known exactly from GNSS data;
- the measurement error $\delta g_k(t)$ is a random process with a zero mean and known correlation function defined by the measurement errors of the gravimeter sensing element, the GNSS and the properties of the gravimetric filter;
- measurement errors at different flight lines are uncorrelated.

By replacing Δg in (2.5.8) with representation (2.5.1), we obtain:

$$\Delta g'_k(t_{ik}) = \sum_{m=i-M}^{i+M} h_f(t_{ik} - t_{mk}) \sum_s \omega_s a_J(y_s) \frac{\partial \Phi_J(x(t_{mk}), y_s)}{\partial |x|} + \delta g_k(t_{ik}), \tag{2.5.9}$$

where $i = 1, \ldots, M_k$, $k = 1, \ldots, K$. The resolution level J is determined based on the desired spatial resolution of the map as indicated above. The SC nodes y_s in (2.5.9) are defined on the sphere Ω_R, the radius R of which will be chosen equal to the minimum distance from the center of the Earth to the measurement points at the survey lines. Due to the fast attenuation property of the scaling function, in (2.5.9), it is sufficient to take into account only the nodes y_s from a certain neighborhood of point $x(t_{mk})$. The size of the neighborhood is chosen based on the attenuation rate of the scaling function and the required accuracy of the map. An example of a set of SC nodes defined by the survey lines is shown in Fig. 2.41.

Rewrite the model of the smoothed airborne measurements at the kth survey line (2.5.9) in the vector form:

$$\Delta g'_k = H_k a_{kJ} + \delta g_k, \quad k = 1 \ldots K, \tag{2.5.10}$$

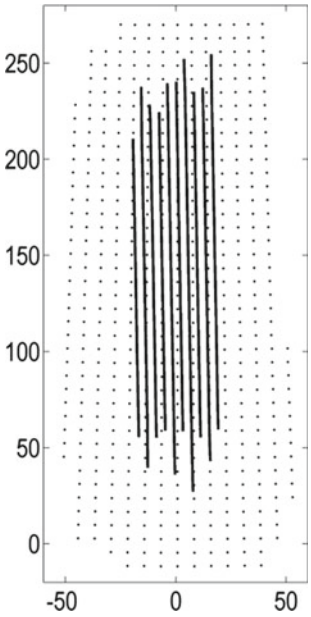

Fig. 2.41 A set of nodes of the scaling coefficients (*dots*) defined by survey lines (*solid lines*) on the longitude–spherical latitude plane (km × km)

where $\Delta g'_k = \left(\Delta g'_k(t_{1k}), \ldots, \Delta g'_k\left(t_{M_k k}\right)\right)^T$ and $\delta g_k = \left(\delta g_k(t_{1k}), \ldots, \delta g_k\left(t_{M_k k}\right)\right)^T$ are $M_k \times 1$ vectors of measurements and their errors, a_{kJ} is the $N_k \times 1$ vector of unknown SCs $a_J(y_s)$ in the nodes y_s corresponding to the kth survey line. H_k denotes the $M_k \times N_k$ matrix consisting of the sum of the products of the filter impulse response function in (2.5.9), the weights ω_s and the values of the scaling function derivative at the nodes y_s:

$$H_k = \begin{pmatrix} w_1(t_{1k}) & \ldots & w_{N_k}(t_{1k}) \\ \vdots & \ddots & \vdots \\ w_1\left(t_{M_k k}\right) & \ldots & w_{N_k}\left(t_{M_k k}\right) \end{pmatrix},$$

$$w_s(t_{ik}) = \omega_s \sum_{m=i-M}^{i+M} h_f(t_{ik} - t_{mk}) \Phi_J(x(t_{mk}), y_s).$$

Introduce the covariance matrix $R_k = E\left[\delta g_k \delta g_k^T\right]$ which is determined from the assumed known correlation function of the airborne gravimetric measurement errors. It should be recalled that $E\left[\delta g_k \delta g_m^T\right] = 0, \quad k \neq m$. Let us solve the problem of estimating the scaling coefficients a_{kJ} based on measurements (2.5.9) using the generalized least squares method with the following criterion:

$$\sum_{k=1}^{K} \left\| \Delta g'_k - H_k a_{kJ} \right\|^2_{R_k^{-1}}$$

$$= \sum_{k=1}^{K} \left(\Delta g'_k - H_k a_{kJ}\right)^T R_k^{-1} \left(\Delta g'_k - H_k a_{kJ}\right) \to \min_{a_{kJ} \in R^{N_k}} \tag{2.5.11}$$

Problem (2.5.11) is essentially the problem of the downward continuation of the gravity field (Freeden and Michel 2004), since the nodes y_s of the SCs of interest are given on the underlying sphere Ω_R. Thus, the problem belongs to the class of inverse ill-posed problems (Tikhonov and Arsenin 1979). Solution (2.5.11) is determined using the recurrent LSM in the information form with the survey line number k as a recursion step (Kailath et al. 2000):

$$Q_k = Q_{k-1} + I_k^T H_k^T R_k^{-1} H_k I_k, \quad k = 1 \ldots K, \tag{2.5.12}$$

$$b_k = b_{k-1} + I_k^T H_k^T R_k^{-1} \Delta g'_k, \tag{2.5.13}$$

with the initial conditions $Q_0 = 0$, $b_0 = 0$, where Q_k is the information $N \times N$ matrix of the vector $a_J \in \mathrm{R}^N$ consisting of the SCs defined by all the K survey lines; b_k is the information estimate of the vector a_J, I_k is the $N_k \times N$ matrix specifying the projection of the vector a_J onto a subset of the SCs correlated only with the kth survey line: $\mathrm{I_k} a_J = a_{kJ}$.

Algorithm (2.5.12)–(2.5.13) is written in the form for a given set of K survey lines and, therefore, for the state vector of the known and constant dimension. However, the form of the algorithm, in which the dimension of the vector of the estimated SCs automatically increases when a new survey line is added to the processing, is practically more convenient. The algorithm in this form is as follows:

$$Q_{(k)} = \begin{pmatrix} Q_{(k-1)} & 0 \\ 0 & 0 \end{pmatrix} + \mathrm{I}_{(k)}^T H_k^T R_k^{-1} H_k \mathrm{I}_{(k)}, \quad k = 1, 2 \ldots \tag{2.5.14}$$

$$b_{(k)} = \begin{pmatrix} b_{(k-1)} \\ 0 \end{pmatrix} + \mathrm{I}_{(k)}^T H_k^T R_k^{-1} \Delta g'_k, \tag{2.5.15}$$

with the initial conditions $Q_{(0)} = 0$, $b_{(0)} = 0$. Here, $Q_{(k)}$ is the information $N_{(k)} \times N_{(k)}$ matrix of the SC vector defined by k survey lines; $b_{(k)}$ is the informational estimate of the SC vector, $I_{(\mathrm{k})}$ is the $N_k \times N_{(k)}$ matrix that specifies the projection of the vector of SCs defined by k survey lines onto a subset of the SCs correlated only with the kth survey line.

The estimate of the $N_{(K)} \times 1$-SC vector $\mathrm{a_J}$ after the Kth recursion step is determined based on the solution of the equation: $b_{(K)} = Q_{(K)} a_J$. The estimate error covariance matrix is calculated using the information matrix $Q_{(K)}$. The $Q_{(K)}$ matrix may be ill-conditioned. Let us define the estimate of the covariance matrix of the SC estimate errors $\tilde{P}_{\delta a_J}$ as the inverse of the regularized information matrix:

$$\tilde{P}_{\delta a_J} = \left(Q_{(K)} + \mu^2 \mathrm{I}\right)^{-1}, \tag{2.5.16}$$

where I is the unit $N_{(K)} \times N_{(K)}$ matrix, μ is a regularization parameter. The estimate of the SC vector is

$$\tilde{a}_J = \tilde{P}_{\delta a_J} b_{(K)}. \tag{2.5.17}$$

The selection of the regularization parameter is discussed below.

The second stage of the technique is the wavelet decomposition (Freeden and Michel 2004) of airborne gravimetry data which includes the calculation of the wavelet coefficients at various resolution levels $j \le J$ based on the SC estimates $\tilde{a}_J(y_s)$ found. The need for this stage is due to the fact that the data of airborne gravimetry and the global EGF model have different spatial resolutions (in terms of the multiscale analysis: different maximum resolution levels). Wavelet decomposition makes it possible to combine SWC estimates of airborne gravimetry data and global EGF model data at common resolution levels. Note that SWCs can be treated as the results of bandpass filtering of anomaly data.

Let us denote the SWCs calculated at various resolution levels $j = j_0 \ldots J$ as $\tilde{c}_j(y_{sj})$ from the SC estimates $\tilde{a}_J(y_s)$ according to formulas (2.5.3), (2.5.4). Denote the $\mathrm{N}_j \times 1$ vector of the SWCs as $\tilde{c}_j$ and represent (2.5.3), (2.5.4) in the vector form $\tilde{c}_j = U_j \tilde{a}_J$. U_j is an $\mathrm{N}_j \times \mathrm{N}_j$ matrix composed of products of the integration weights and the wavelet function values at the nodes of the grid. The covariance matrix for the SWC vector estimation error obtained from airborne gravimetry data is determined from the covariance matrix for the SC estimation error by the following formula:

$$\tilde{P}_j = U_j \tilde{P}_{\delta a_J} U_j^T \quad j = j_0 \ldots J. \tag{2.5.18}$$

The third stage of the technique is the wavelet decomposition of the global model of the gravitational field, namely, the SWC c_j^{glob} of anomalies and the covariance matrices of their errors P_j^{glob} are calculated at various resolution levels $j = j_0 \ldots J_{glob}$ using formulas (2.5.3), (2.5.4), where the SCs $a_{J_{glob}}(y_s)$ are calculated using the scaling expansion formula:

$$a_{J_{glob}}(y_s) = \sum_p \omega_p \Phi_{J glob}(y_s, y_p) \Delta g_{glob}(y_p), \tag{2.5.19}$$

and y_s, y_p are the grid nodes from (2.5.1), J_{glob} is the maximum resolution level of the global model determined from the spatial resolution of the global data, $\Delta g_{glob}(y_p) = g_{glob}(y_p) - g_0(y_p)$ is the GA for which the gravity g_{glob} is calculated from the spherical harmonic coefficients of the global model, and g_0 is calculated using the normal gravity formula used in the GA estimation on survey lines based on airborne gravimetric measurements. Note that the maximum resolution level of the global model is lower than the maximum level of the airborne gravimetry data.

The covariance matrices P_j^{glob} are calculated from the covariance matrix of the global gravity data errors $E[\delta g_{glob}\delta g_{glob}{}^{\mathrm{T}}]$ calculated from the estimates of RMS errors of the spherical harmonics coefficients provided by the developers of the global model.

The **fourth** stage of the technique is devoted to the combination of multiscale representations of airborne gravimetry data and the global EGF model at common resolution levels and is discussed in detail below.

At **the** final **fifth stage** of the technique, the reconstruction of the anomaly estimate (and other functionals of the gravitational field) is performed based on the combination results.

2.5.3 *Multiscale Representation of Gravity Anomaly Based on Combination of Airborne Gravimetry Data and Global Gravity Field Model Data*

The following is the algorithm for combining airborne gravimetry data and the global EGF model in a multiscale representation in the terms of SWCs based on the specific statistical assumptions mentioned below.

Consider the resolution level j, $j = j_0 \ldots J$. Let us pose the problem of refining the estimates of the $\mathrm{N}_j \times 1$ vectors of SWCs $\tilde{c}_j$ and the covariance matrices of their errors obtained from airborne gravimetric measurements by the global model data. Let us represent the obtained above estimate of the SWC vector as $\tilde{c}_j = c_j + \delta c_j$, where c_j is the vector of the true SWCs, δc_j is a random SWC error vector with zero mean and the covariance matrix $\tilde{P}_j = E\left[\delta c_j \delta c_j^T\right]$ determined from airborne gravimetric data using formula (2.5.18).

Assume that c_j^{glob} and P_j^{glob} are the $\mathrm{N_j} \times 1$ SWC vector of the anomaly and the $N_j \times N_j$ matrix of the covariances of their errors calculated from the global model data at the resolution levels $j = j_0 \ldots J_{glob}$. Since the spatial resolution of airborne gravimetry data is usually higher than that of global data, the corresponding maximum resolution levels of the data satisfy the inequality $J_{glob} \leq J$. Let us represent the SWC vector of global data in the form $c_j^{glob} = c_j + \delta c_j^{glob}$ assuming that δc_j^{glob} is a random vector with zero mean and the covariance matrix $P_j^{glob} = E\left[\delta c_j^{glob}(\delta c_j^{glob})^T\right]$. Let us assume the positive definiteness of the matrix $\tilde{P}_j + P_j^{glob}$ and the lack of correlation of the SWC errors of both airborne gravity data and global data at various resolution levels. Let us specify the problem of refining the estimate $\tilde{c}_j$ of the vector c_j by c_j^{glob} at the common resolution levels $j = j_0 \ldots J_{glob}$ as a problem of the SWC vector optimal estimation c_j in the class of linear estimates of the form $F_{1j}\tilde{c}_j + F_{2j}c_j^{glob}$, where F_{1j}, F_{2j} are arbitrary $N_j \times N_j$ matrices. As a criterion, let us use the minimum for all $F_{1\mathrm{j}}, F_{2\mathrm{j}}$ of the guaranteed value for the second moment of the estimation error:

$$\sup_{c_j \in R^{N_j}} E\left[\left\| c_j - F_{1j}\tilde{c}_j - F_{2j}c_j^{glob} \right\|^2\right] \to \min_{F_{1j},F_{2j}}, \quad j = j_0 \ldots J_{glob}. \tag{2.5.20}$$

The unknown vector c_j is assumed to be deterministic. By transforming the formula for the second moment of the estimation error, it is easy to show that (2.5.20) is reduced to a problem of the form:

$$tr\left(F_{1j}\tilde{P}_j F_{1j}^T + F_{2j}P_j^{glob}F_{2j}^T\right) \to \min_{F_{1j}+F_{2j}=I_j}, \tag{2.5.21}$$

where tr is the trace of the matrix, I_j is a unit $N_j \times N_j$ matrix. Solution (2.5.21) and the optimal estimate of the vector c_j are determined by the LSM algorithm in the covariance form (Kailath et al. 2000):

$$\begin{aligned}
\tilde{c}_j^+ &= \left(I - \tilde{F}_{2j}\right)\tilde{c}_j + \tilde{F}_{2j}c_j^{glob}, \\
\tilde{P}_j^+ &= \left(I - \tilde{F}_{2j}\right)\tilde{P}_j, \\
\tilde{F}_{2j} &= \tilde{P}_j\left(\tilde{P}_j + P_j^{glob}\right)^{-1},
\end{aligned} \tag{2.5.22}$$

with $j = j_0 \ldots J_{glob}$, where $\tilde{c}_j^+$, $\tilde{P}_j^+$ denote the result of vector c_j estimation and the estimation error covariance matrix. It should be noted that problem (2.5.20) is actually the least squares collocation problem but it is posed in the space of wavelet coefficients and does not require a priori stochastic hypotheses about GA.

2.5.4 Results of the Real Data Processing

The developed local GA determination technique using the combination algorithm (2.5.22) was applied to the airborne gravimetric data from a survey in the Arctic (Smoller et al. 2013). The airborne measurements were collected using the GT-1A gravimeter. Note that at the same time, the Chekan-AM gravimeter was also used in this onboard survey (Krasnov et al. 2014; Peshekhonov et al. 2015). The spatial resolution of the gravimetric filter of GT-1A was 5 km. Its output data frequency was 18 Hz. The prefiltered measurement errors roughly correspond to the white noise model at the frequency of 1 Hz with the RMS of 50 mGal. The geographical latitude of the survey area varies from 73 to 77°. The average flight altitude is 3700 m. The Helmert formula for the normal gravity was used in calculations (Golovan and Parusnikov 2012). Airborne gravimetric measurements were used to estimate the SC a_J of the gravity anomaly based on algorithm (2.5.14)–(2.5.15) at the maximum resolution level $J = 11$ approximately corresponding to the filter resolution (the first

stage of the developed technique). The airborne data at forty survey lines (north–south) with the line spacing of 1 km were processed. The scaling coefficients were estimated at nodes of 1.0 km × 1.4 km grid on the sphere with the radius $R = 6358$ km. The radius of the area of the SC computation (2.5.9) was chosen to be 20 km. The regularization parameter μ of the information matrix $Q_{(K)}$ in (2.5.16) was selected according to the criterion of the proximity of the anomaly estimate reconstructed at survey lines from the SC estimates $\tilde{a}_J$ (2.5.17) using formula (2.5.1) to the original airborne gravimetric data with the RMS value for the discrepancy not greater than 0.5 mGal.

At the second stage of the technique for SC estimation $\tilde{a}_J$, SWC estimates $\tilde{c}_j$ and the covariance matrices of their errors were calculated using formulas (2.5.3)–(2.5.4) and (2.5.18) at the levels of $j = 9, 10, 11$. The value of the wavelet reconstruction RMS error (2.5.5) of the SWC anomaly $\tilde{c}_j$ on survey lines is 0.65 mGal.

For combining, the EGM2008 global EGF model was used up to the spherical harmonic degree and order of 1800 (the maximum spherical harmonic degree of the model is 2190, the nominal spatial resolution at the equator is 9.3 km × 9.3 km). Based on EGM2008 data, the SWCs c_j^{glob} and the covariance matrices of their errors were calculated at the levels $j = 9, 10$ (the third stage of the technique). The RMS error values of the SWCs of the global EGM2008 model and SWCs of airborne gravimetric data are given in Table 2.4.

The integration of SWCs $\tilde{c}_j$ and c_j^{glob} (the fourth stage) is performed by the LSM algorithm (2.5.22).

At the final (fifth) stage of the technique, the SWC estimates were used to calculate the free air GA estimates at the 1.5 km × 1.5 km grid nodes on the reference ellipsoid surface in the survey area.

The GA maps (Fig. 2.42) and GA along a survey line are shown in Fig. 2.43. The GA based on SC estimates obtained from airborne gravimetric data and the GA resulting from the data combination are oversmoothed in the east–west direction as the distance between the survey lines is smaller than the spatial resolution of the gravimetric filter.

The RMS value of the difference between the GAs obtained from the SCs $\tilde{a}_J$ estimated from airborne gravimetric data and the GAs obtained from data combination is 5.4 mGal.

Table 2.4 RMS errors of global and airborne SWCs

Resolution level j	SWC RMS error, mGal		
	Global data	Airborne data (inside the survey area)	Airborne data (the entire survey area)
9	6.3	3.0	30.0
10	13.0	11.0	70.0

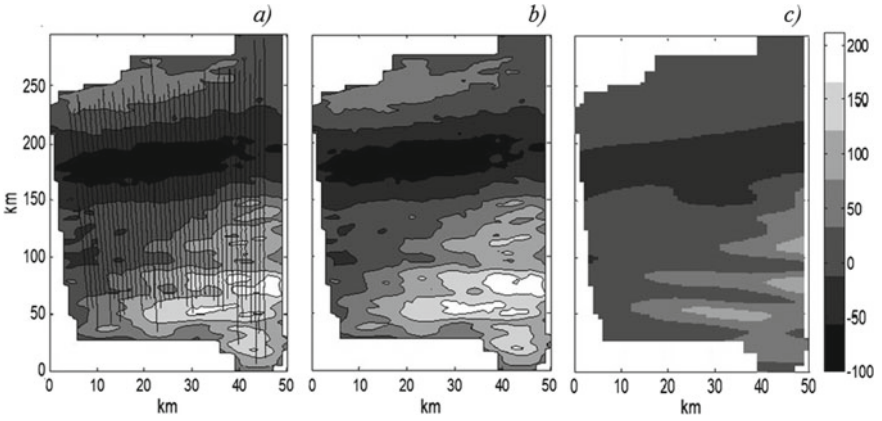

Fig. 2.42 Free air GA at 1.5 km × 1.5 km grid nodes on the surface of the reference ellipsoid in the survey area (mGal): **a** is the anomaly based on the SC estimates obtained from airborne gravity data, at the maximum level $J = 11$, and survey lines; **b** is the anomaly based on the combined SWCs; **c** is the anomaly based on the EGM2008 model

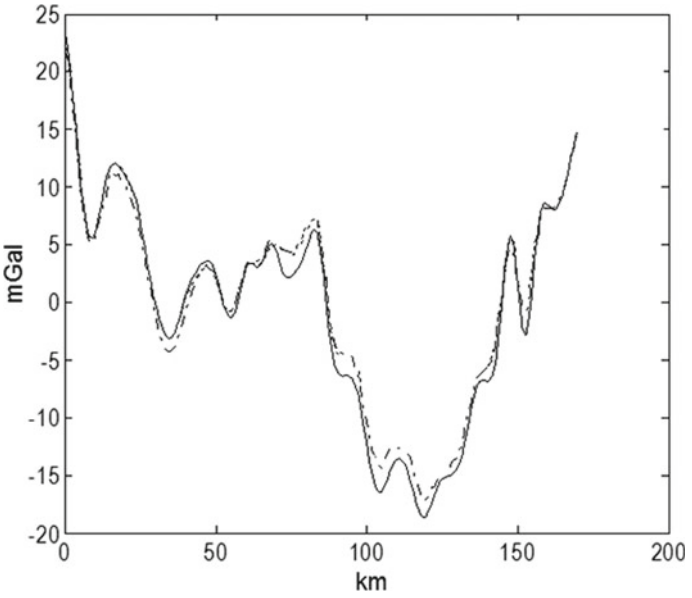

Fig. 2.43 Free air GAs along the survey line (mGal): *solid line*: anomaly from the original airborne gravimetric data; *dash-dotted line*: anomaly based on the SWCs resulting from data combination

2.5.5 Conclusion

The multiscale representation method based on spherical wavelet expansion was applied to the problem of local determination of the anomalous gravity field from the airborne gravimetric data and gravity data from a global model of the Earth's gravitational field. A method for this problem solution was developed and applied to real airborne data and global gravity data (EGM2008). The LSM-based algorithm for combining airborne gravimetric and global data was developed and tested. The gravity anomaly estimate obtained from the data weighted combination is slightly oversmoothed in the east–west direction, which is due to the fact that the spatial resolution of the gravimetric filter (north–south direction) is coarser than the data spatial resolution in the east–west direction defined by the line spacing.

The proposed algorithms make it possible to deal with the inverse ill-posed problem of local gravity determination on the reference ellipsoid surface from airborne gravimetric measurements of GAs at the flight altitude. It is shown that the RMS error of the gravity anomaly reconstruction from the airborne wavelet coefficients did not exceed 0.7 mGal. The proposed algorithms have certain advantages as compared with the algorithms that are often used to combine different types of gravity data and based on the collocation method, since the presented algorithms do not require any statistical hypotheses about GA.

Acknowledgements The research activities described in Sections 2.1 and 2.3 were supported by the Russian Science Foundation (project № 18-19-00627, https://rscf.ru/project/18-19-00627/).

References

Akimov PA, Derevyankin AV, Matasov AI (2012) Garantiruyushchii podhod i L1-approksimatsiya v zadachakh otsenivaniya parametrov BINS pri stendovykh ispytaniyakh (Guaranteed approach and L1-norm approximation in estimation of SINS parameters in bench tests). Moscow State University, Moscow

Beloglazov IN, Kazarin SN (1998) Joint optimal estimation, identification, and hypothesis testing in discrete dynamic systems. J Comput Syst Sci Int 37(4):534–550

Berzhitsky VN, Bolotin YV, Golovan AA, Iljin VN, Parusnikov NA, Smoller YL, Yurist SS (2002) GT-1A inertial gravimeter system. Results of flight tests. Center of Applied Research Publishing House, Faculty of Mechanics and Mathematics, MSU, Moscow

Bolotin YV, Doroshin DR (2011) Adaptive filtering in airborne gravimetry with hidden Markov chains. In: Proceedings 18th IFAC world congress, Milan, Italy, pp 9996–10001

Bolotin YuV, Golovan AA (2013) Methods of inertial gravimetry. Moscow Univ Mech Bull 68(5):117–125

Bolotin YV, Popelensky MY (2007) Accuracy analysis of airborne gravity when gravimeter parameters are identified in flight. J Math Sci 146(3):5911–5919

Bolotin YV, Vyazmin VS (2015) Gravity anomaly estimation by airborne gravimetry data using LSE and minimax optimization and spherical wavelet expansion. Gyrosc Navig 6(4):310–317

Bolotin YV, Yurist SS (2011) Suboptimal smoothing filter for the marine gravimeter GT-2M. Gyrosc Navig 2(3):152–155

Bolotin YV, Golovan AA, Kruchinin PA et al (1999) Airborne gravimetry problem. Some test results, Vestnik Moskovskogo universiteta. Seriya 1: Matematika. Mekhanika 2:36–41
Bolotin YV, Golovan AA, Parusnikov NA (2002) Uravneniya aerogravimetrii. Algoritmy i rezul'taty ispytanii (Airborne gravimetry equations. Test algorithms and results). Publishing House of the Faculty of Mechanics and Mathematics of the Moscow State University, Moscow
Brown RG, Hwang PYC (1977) Introduction to random signals and applied Kalman filtering with MatLab exercises and solutions, 3rd edn. Wiley & Sons, New York
Demyanenkov VV, Krasnov AA, Sokolov AV, Elinson LS (2014) Real-time gravimetric and navigation data acquisition and processing software. Certificate of State Registration of Computer Software No. 2014617747
Dmitriev SP, Stepanov OA (2000) Noninvariant algorithms for inertial navigation system data processing. Giroskopiya i Navigatsiya 1(28):24–38
Dmitriev SP, Stepanov OA (2004) Multiple model filtering for navigation problems of information processing. Radiotekhnika 7:11–17
Doucet A, de Freitas N, Gordon NJ (2001) Sequential Monte Carlo methods in practice. Springer-Verlag, New York
Dudevich NA, Krasnov AA, Sokolov AV, Elinson LS (2007) AIRGRAV computer software. Certificate of State Registration of Computer Software No. 2007610458
Dudevich NA, Krasnov AA, Sokolov AV, Elinson LS (2014) Gravimetric data acquisition and processing software in gravimeter calibration mode. Certificate of State Registration of Computer Software No. 2014617784
Forsberg R, Kenyon S (2004) Gravity and geoid in the Arctic region—The northern gap now filled. In: Proceedings of the Second International GOCE user workshop, Italy
Freeden W, Michel V (2004) Multiscale potential theory (with applications to geoscience). Birkhäuser Verlag
Golovan AA, Parusnikov NA (2012) Matematicheskie osnovy navigatsionnykh sistem (Mathematical foundations of navigation systems), Part 2. Maks Press, Moscow
Groves PD (2013) Principles of GNSS, inertial, and multisensor integrated navigation systems, 2nd edn. Artech House
Hein G (1995) Progress in airborne gravimetry: solved, open and critical problems. In: Proceedings IAG Symposium on airborne gravity field determination, Calgary, August 1995
Jordan SK (1972) Self-consistent statistical models for gravity anomaly and undulation of the geoid. J Geophys Res 77(20):3660–3670
Kailath T, Sayed AH, Hassibi B (2000) Linear estimation. Prentice-Hall
Kalman RE (1960) A new approach to linear filtering and prediction problems. Trans ASME—J Basic Eng 82:34–45
Kalman RE, Bucy RS (1961) New results in linear filtering and prediction theory. Trans ASME—J Basic Eng 83:95–107
Kern M, Schwarz KP, Sneeuw N (2003) A study on the combination of satellite, airborne, and terrestrial gravity data. J Geodesy 77:217–225
Koshaev DA, Stepanov OA (2010) Analysis of filtering and smoothing techniques as applied to aerogravimetry. Gyrosc Navig 1(1):19–25
Krasnov AA, Sokolov AV (2013) Methods and software for office processing of airborne gravity measurements. Trudy Instituta prikladnoi astronomii RAN 27
Krasnov AA, Sokolov AV (2015) A modern software system of a mobile Chekan-AM gravimeter. Gyrosc Navig 6(4):278–287
Krasnov AA, Sokolov AV, Elinson LS (2014) A new air-sea shelf gravimeter of the Chekan series. Gyrosc Navig 3:131–137
Lainiotis DG (1976) Partitioning: A unifying framework for adaptive systems. I: Estimation, II: Control. IEEE Trans 64(8), I. Estimation, pp 1126–1140, II. Control, pp 1182–1198
Loparev AV, Stepanov OA, Chelpanov IB (2012) Using frequency approach to time-variant filtering for processing of navigation information. Gyrosc Navig 3(1):9–19
Meditch J (1969) Stochastic optimal linear estimation and control. McGraw-Hill Inc

Motorin AV, Nosov AS (2019) Accuracy and sensitivity analysis for marine gravimetry algorithms in dependence of survey conditions. In: 2019 IEEE conference of Russian young researchers in electrical and electronic engineering (EIConRus), St. Petersburg and Moscow, Russia. IEEE, pp 1210–1215

Motorin AV, Stepanov OA (2015) Designing an error model for navigation sensors using Bayesian approach. In: Proceedings 2015 IEEE International conference on Multisensor fusion and integration, pp 54–58

Mudrov VI, Kushko VL (1971) Metod naimen'shikh modulei (Least absolute deviations method). Znaniye, Moscow

Nesenyuk LP, Khodorkovsky YI (2010) Synthesis of the structure and parameters of the submarine meter of submergence depth, vertical speed, and vertical acceleration, Pamyati professora L.P. Nesenyuka. Izbrannye trudy i vospominaniya (In memory of Professor L.P. Nesenyuk. Selected papers and memoirs), Concern CSRI Elektropribor, JSC, St. Petersburg, pp 42–50

Panteleev VL (1983) Osnovy morskoi gravimetrii (Fundamentals of marine gravimetry). Nedra, Moscow

Peshekhonov VG, Sokolov AV, Elinson LS, Krasnov AA (2015) A new air-sea gravimeter: Development and test results. In: 22nd St. Petersburg International conference on integrated navigation systems, St. Petersburg: Elektropribor

Rauch HE, Tung F, Striebel CT (1965) Maximum likelihood estimates of linear dynamic systems. AIAA J 3(8):1445–1450

Schmidt M, Fengler M, Mayer-Gurr T, Eicker A, Kusche J, Sanchez L, Han S-C (2007) Regional gravity modeling in terms of spherical base functions. J Geodesy 81(1):17–38

Simon D (2006) Optimal state estimation: Kalman, H-infinity, and nonlinear approaches. John Wiley & Sons Inc., New York

Smoller YL, Yurist SS, Fedorova IP, Bolotin YV, Golovan AA, Koneshov VN et al (2013) Using airborne gravimeter GT2A in polar areas. In: Proceedings of IAG Symposium on terrestrial gravimetry: Static and mobile measurements, TG-SMM 2013, St. Petersburg, Russia

Sokolov AV, Krasnov AA, Elinson LS, Vasil'ev VA, Zheleznyak LK (2015) Calibration of the Chekan-AM gravimeter by a tilting method. Gyrosc Navig 6(4):288–293

Sokolov AV, Stepanov OA, Krasnov AA, Motorin AV, Koshaev DA (2016) Comparison of stationary and nonstationary adaptive filtering and smoothing algorithms for gravity anomaly estimation on board the aircraft. In: Proceedings of 4th IAG Symposium on terrestrial gravimetry: Static and mobile measurements, TG-SMM 2016, St. Petersburg, Russia, pp 53–60

Stepanov OA (1998) Primenenie teorii nelineinoi fil'tratsii v zadachakh obrabotki navigatsionnoi informatsii (Application of nonlinear filtering theory to navigation data processing). CSRI Elektropribor, St. Petersburg

Stepanov OA (2016) Optimal and suboptimal filtering in integrated navigation systems. In: Nebylov A, Watson J (eds) Aerospace navigation systems. Wiley

Stepanov OA (2017a) Osnovy teorii otsenivaniya s prilozheniyami k zadacham obrabotki navigatsionnoi informatsii (Fundamentals of the estimation theory with applications to the problems of navigation information processing). Part 1, Vvedenie v teoriyu otsenivaniya (Introduction to the estimation theory). Concern CSRI Elektropribor, St. Petersburg

Stepanov OA (2017b) Osnovy teorii otsenivaniya s prilozheniyami k zadacham obrabotki navigatsionnoi informatsii (Fundamentals of the estimation theory with applications to the problems of navigation information processing). Part 2, Vvedenie v teoriyu fil'tratsii (Introduction to the filtering theory). Concern CSRI Elektropribor, St. Petersburg

Stepanov OA, Koshaev DA (2011) A program for designing linear filtering algorithms for integrated navigation systems. IFAC Proc Vol (IFAC-PapersOnline) 44:4256–4259

Stepanov OA, Motorin AV (2019) Performance criteria for the identification of inertial sensor error models. Sensors 19(9):1997

Stepanov OA, Blazhnov BA, Koshaev DA (2002) Studying the effectiveness of using satellite measurements in airborne gravity determination. Giroskopiya i Navigatsiya 3(38):33–47

Stepanov OA, Loparev AV, Chelpanov IB (2014) Time-and-frequency approach to navigation information processing. Autom Remote Control 75(6):1090–1108

Stepanov OA, Koshaev DA, Motorin AV (2015) Identification of gravity anomaly model parameters in airborne gravimetry problems using nonlinear filtering methods. Gyrosc Navig 6(4):318–323

Tikhonov AN, Arsenin VY (1979) Metody resheniya nekorrektnykh zadach (Methods for solving ill-posed problems). Nauka, Moscow

Torge W (1989) Gravimetry. de Gruyter, Berlin

Toropov AB, Motorin AV, Stepanov OA, Vasiliev VA (2016) Identification of total errors of digital maps and sensors of geophysical fields. In: Proceedings of 4th IAG Symposium on terrestrial gravimetry: Static and mobile measurements, TG-SMM 2016, St. Petersburg, Russia, pp 213–216

Vavilova NB, Golovan AA, Parusnikov NA, Trubnikov SA (2009) Matematicheskie modeli i algoritmy obrabotki izmerenii sputnikovoi navigatsionnoi sistemy GPS. Standartnyi regim (Mathematical models and processing algorithms for GPS satellite navigation system measurements. Standard mode). MSU Publishing House, Moscow

Wei M, Ferguson S, Schwarz KP (1991) Accuracy of GPS-derived acceleration from moving platform tests. Proc IAG Symp 110:235–249

Zamakhov EY, Krasnov AA, Sokolov AV, Elinson LS (2013) Gravimetric data office processing software. Certificate of State Registration of Computer Software No. 2013660223

Zheleznyak LK, Elinson LS (1982) Calibration of gravimeter with two torsion-type elastic systems using the tilting method. In: Fiziko-tekhnicheskaya gravimetriya (Physical-technical gravimetry). Nauka, Moscow, pp 110–124

Zheleznyak LK, Krasnov AA, Sokolov AV (2010) Effect of the inertial accelerations on the accuracy of the CHEKAN-AM gravimeter. Izvestiya. Phys Solid Earth 46(7):580–583

Chapter 3
Methods for Determination and Calculation of Deflections of the Vertical

I. Chelpanov, M. Evstifeev, V. Koneshov, O. Yashnikova, S. Gaivoronskii, V. Tsodokova, B. Blazhnov, G. Emel'yantsev, and A. Stepanov

Abstract This Chapter is devoted to determination of deflections of the vertical (DOV). A general overview of DOV determination methods on a moving base is provided. The methods addressed include the gravimetric method, astrogeodetic method, and inertial-geodetic method. Also considered are gravity gradiometry, satellite or aircraft altimetry, satellite-to-satellite tracking and other satellite missions using the Earth's gravity models, as well as combinations of these methods. The automated zenith telescope developed by Concern CSRI Elektropribor, which determines DOV components by field observations of the near-zenith part of the stellar sky, is described. Findings from field studies are presented proving the efficiency of the proposed technical solutions. The integrated system comprising a precision inertial measurement unit and a GNSS compass developed by Concern CSRI Elektropribor is presented.

Keywords Determination of deflection of the vertical · Automated zenith telescope · GNSS compass

Introduction

This chapter is devoted to the methods for determining and calculating deflections of the vertical. It includes three sections.

I. Chelpanov–Deceased

I. Chelpanov · M. Evstifeev · O. Yashnikova (✉) · S. Gaivoronskii · V. Tsodokova · B. Blazhnov · G. Emel'yantsev · A. Stepanov
Concern CSRI Elektropribor, St. Petersburg, Russia
e-mail: olga_evstifeeva@mail.ru

M. Evstifeev · O. Yashnikova · V. Tsodokova · A. Stepanov
ITMO University, St. Petersburg, Russia

V. Koneshov
Schmidt Institute of Physics of the Earth, The Russian Academy of Sciences (IPE RAS), Moscow, Russia

V. G. Peshekhonov and O. A. Stepanov (eds.), *Methods and Technologies for Measuring the Earth's Gravity Field Parameters*, Earth Systems Data and Models 5,
https://doi.org/10.1007/978-3-031-11158-7_3

Section 3.1 presents a general overview of the methods used to determine deflections of the vertical (DOV) on a moving base. Special attention is given to the gravimetric method, which is based on gravity anomaly measurements, the astrogeodetic method, involving comparison of astronomical and geodetic coordinates, and its version, the inertial-geodetic method. Also considered are gravity gradiometry, based on measuring the second derivatives of gravity potential, satellite or aircraft altimetry, based on trajectory altitude measurements, satellite-to-satellite tracking and other satellite missions using the Earth's gravity models, as well as combinations of these methods (for example, astrogravimetric method). The classification criteria for DOV determination methods are proposed, and their comparative qualitative analysis is carried out.

Section 3.2 is devoted to the determination of DOV components by the astrogeodetic method. The focus here is on the description of an automated zenith telescope developed by Concern CSRI Elektropribor, intended for real-time determination of DOV components by field observations of the near-zenith part of the stellar sky. The principle of operation, basic parameters of the components, algorithms for processing the observation results and accuracy characteristics of the zenith telescope are discussed. The results of field studies are presented proving the efficiency of the proposed technical solutions and processing algorithms, and the suitability of the automated zenith telescope for high-precision DOV determination.

And finally, **Sect.** 3.3 describes the inertial-geodetic method for DOV determination. The general idea and features of the method are discussed, with special attention given to the potential for its implementation in high latitudes. The proposed solution is creation of a specialized integrated system comprising a precision inertial measurement unit and a GNSS compass, which is a two-antenna receiving system with a 6 m long antenna baseline. Algorithms for the problem solution are described. The accuracy of the integrated system is estimated based on the simulation and the results of sea trials of the GNSS compass developed by Concern CSRI Elektropribor.

3.1 DOV Determination on a Moving Base

Both high-precision navigation and geodetic surveying require the knowledge of the Earth's gravity field (EGF) parameters. These parameters traditionally include quasi-geoid height ζ, gravity anomaly Δg (GA), and DOV. Deflections of the vertical provide more detailed information on the Earth's figure and nonuniform mass distribution under its surface, help to solve reduction problems of higher geodesy and improve the positioning accuracy achieved by high-precision marine navigation instruments.

Due to the complicated nature of the Earth's surface and its internal structure, the direction of the actual gravity vector (vertical) does not coincide with the direction of the normal gravity vector at the points of the Earth's physical surface. This difference is referred to as the deflection of the vertical, or plumb line deflection. A distinction is made between astrogeodetic and gravimetric DOVs (Ogorodova 2006). Deflections

of the vertical are usually specified by a set of two deflection angles in the meridian plane ξ and the plane of prime vertical η, respectively (Shimbirev 1975).

DOV values close to the Earth's surface are within several angular seconds and may come up to one angular minute. For high-precision navigation, it is required to measure the DOV components with errors not exceeding 0.5–1 arcsec. This is feasible on a fixed base, but causes significant technical difficulties onboard moving vehicles (Peshekhonov et al. 1989; Anuchin 1992).

Currently, a wide variety of methods aided with specialized hardware have been developed to determine DOV. To study and comparatively estimate these methods, their specific use on a moving base should be taken into account. Then it should be remembered that all DOV measurements are taken by indirect methods, and the values are calculated in real time or during postprocessing. It is very important to provide stable operating conditions for the measuring equipment and to apply various error reduction methods, both hardware and software.

For the analysis and combination and optimization synthesis of various algorithms while developing the software and well-founded schemes and engineering solutions, diverse DOV determination methods should be represented in the form of classification diagrams based on the selected criteria. Consideration of possible designs of measurement systems with account for various combinations of classification criteria allows covering a wide range of design and technical solutions, as well as stimulating the development of new options using new combinations of components.

This Section gives a comparative analysis of various methods for DOV determination on a moving base taking into account the selected classification criteria.

3.1.1 Basic Methods for DOV Determination

In higher geodesy, the methods for studying the Earth's figure and gravitational field are traditionally classified into geometric and physical (gravimetric) ones, which are subdivided in accordance with the characteristics of the measured quantities (Shimbirev 1975; Torge 2001; Ogorodova 2006). In geometric methods, primary measurements are measurements of lengths and angles, whereas in gravimetric methods, they are gravity measurements. DOV determination methods can also be divided into physical and geometric methods. However, when determining DOV on a moving base (satellites, airplanes, ships, etc.), other features should be taken into account such as the vehicle's dynamic performance, information processing algorithms used, etc.

The main available methods to determine DOV include

- gravimetric method based on gravity anomaly measurements;
- astrogeodetic method based on the comparison of astronomical and geodetic coordinates;
- inertial-geodetic method based on the use of output signals of a precision inertial navigation system (INS) and GNSS;

- gravity gradiometry method based on the measurement of second derivatives of the geopotential;
- satellite or aircraft altimetry method based on measuring the altitude of the trajectory of a moving vehicle;
- method using EGF global models based on satellite-to-satellite tracking, as well as combinations of these methods (e.g., astrogravimetric method). In addition to the above listed, the collocation method may also be mentioned based on the use of known correlations between various EGF components.

The **gravimetric method** based on the acquisition and processing of data arrays on gravity anomalies is one of the main methods for determining DOV at sea. A gravimetric survey was first carried out by F. A. Vening-Meinesz in 1923 onboard a submarine. This method is traditionally practiced in the Russian Federation for trajectory or aerial surveys (Bolshakov 1997; Drobyshev et al. 2006; Nepoklonov 2010; Koneshov et al. 2015, 2016b). It is based on the numerical solution of the Laplace equation for the disturbing gravity potential in explicit form and requires postprocessing of large arrays of primary measurement data. DOV values are obtained by applying Vening-Meinesz' formulas (3.1.1) given in Table 3.1 to the gravimetric survey data. The initial data for DOV calculation are the measured gravity anomaly values Δg with their corresponding geodetic coordinates *B, L*. Airborne gravimetry is more efficient as compared to marine measurements, although the observed wavelength of the measured gravity anomalies is somewhat longer and the dependencies are more smoothed.

The **astrogeodetic method** is based on measuring astronomical and geodetic coordinates at given points along a path or over an area (Peshekhonov et al. 1995; Kudrys 2009; Hirt et al. 2010; Tsodokova et al. 2014). The angles generated by the systems measuring the astronomical coordinates are continuously compared with the readings of geodetic instruments: formula (3.1.2) in Table 3.1. As for the accurate measurement of geodetic coordinates on a moving base, there is virtually no alternative to the GNSS. Astronomical coordinates can be measured by precision systems such as an astronavigation system, or a zenith telescope. These systems implement the astronomic positioning method.

This method has some limitations, for example, when applied at sea, the required accuracy can only be provided at very low speeds (the vessel drift cannot exceed 2 km over the measurement time of about 20 min); another requirement is that near-zenith stars be continuously observed, hence, the sky should be only slightly cloudy and the system should be highly sensitive to faint stars (Vasiliev et al. 1991a). To ensure the desired DOV accuracy, the spatial angular stabilization of the astronomical system is required. Therefore, the best results can be obtained on an inherently non-mobile platform (such as drifting ice) (Troitskii 1994). This ensures the high accuracy of angular measurements and determination of the geodetic zenith with minimal error.

The advantage of the astronavigation system and zenith telescope is that the errors in modeling the inertial frame are limited and practically do not depend on the duration of continuous operation. Their key strong point consists in the ability to determine the full DOV values.

Table 3.1 Analytical dependencies of DOV parameters on measured parameters for various methods

Analytical expressions		Measured parameters
Gravimetric method (Ogorodova 2006)		
$\xi = -\frac{1}{2\pi}\int_0^{\pi}\int_0^{2\pi} \Delta g\, Q(\psi)\cos A\, d\psi\, dA,$ $\eta = -\frac{1}{2\pi}\int_0^{\pi}\int_0^{2\pi} \Delta g\, Q(\psi)\sin A\, d\psi\, dA$	(3.1.1)	Δg, B, L
Astrogeodetic method (Ogorodova 2006)		
$\xi = \varphi - B,$ $\eta = (\lambda - L)\cos\phi$	(3.1.2)	B, L, φ, λ
Gravity gradiometry (Anuchin 1992)		
$\xi = \xi_0 - 1/\gamma(T_{xx}\Delta x + T_{xy}\Delta y + T_{xz}\Delta z),$ $\eta = \eta_0 - 1/\gamma(T_{xy}\Delta x + T_{yy}\Delta y + T_{yz}\Delta z)$	(3.1.3)	T_{xx}, T_{yy}, T_{xy}, T_{xz}, T_{yz}, Δx, Δy, Δz
Altimetry (Shimbirev 1975)		
$\xi = -(1/R)(\partial\zeta/\partial B),$ $\eta = -(1/R\cos B)(\partial\zeta/\partial L)$	(3.1.4)	ζ, B, L
Global EGF models (Satellite missions) (Koneshov et al. 2012)		
$\xi = -\frac{fM_{\oplus}}{\gamma r^2}\sum_{n=2}^{N}\left(\frac{a}{r}\right)^n \sum_{m=0}^{n}\frac{d\overline{P}_{nm}(\sin\varphi)}{d\varphi}(\overline{C}_{nm}\cos m\lambda + \overline{S}_{nm}\sin m\lambda),$ $\eta = -\frac{fM_{\oplus}}{\gamma r^2\cos\varphi}\sum_{n=2}^{N}\left(\frac{a}{r}\right)^n \sum_{m=0}^{n} m\overline{P}_{nm}(\sin\varphi)(\overline{S}_{nm}\cos m\lambda - \overline{C}_{nm}\sin m\lambda)$	(3.1.5)	φ, λ, r

where ξ, η are DOV components in the meridian plane and the prime vertical plane; B, L are geodetic latitude and longitude; ζ is the quasi-geoid height; φ, λ are astronomical latitude and longitude; T_{ij} are components of tensor of geopotential second derivatives ($i, j = x, y, z$); Δx, Δy, Δz are increments of the vehicle coordinates; $Q(\psi)$ is the Vening-Meinesz function; ψ is the spherical distance from the studied point to the current point; A is the geodetic azimuth of the current point; $\Delta g = (g - \gamma)$ is the gravity anomaly measured with a gravimeter; g, γ are the real and normal gravitational accelerations at the reference point; R is the average radius of the Earth; a is the semi-major axis of the common Earth ellipsoid; φ, λ, r are the spherical geocentric coordinates (latitude, longitude, radius vector) of the point; $fM_{\oplus}$ is the product of the gravitational constant by the Earth mass; $\overline{P}_{nm}$ are the normalized Legendre functions; $\overline{C}_{nm}$, $\overline{S}_{nm}$ are the normalized expansion coefficients

The **inertial-geodetic method** utilizes a precision INS and rests on the dependence of errors in its output navigation parameters on the anomalies. This method is described in detail in (Schultz and Winokur 1969; Nesenyuk et al. 1980; Dmitriev 1997; Li and Jekeli 2008; Timochkin 2013), and in Sect. 3.3. Analysis and consideration of the INS error, actually a methodical one, makes it principally possible to directly determine DOV increments with respect to the reference value at a reference point by filtering or smoothing using the differences in the INS and GNSS measurements. It is important that the INS should be a precision one so that in constructing the inertial vertical, the methodical errors caused by the disagreement between the actual EGF and its calculated model used in INS algorithms prevail over instrumental errors of inertial sensors—gyroscopes and accelerometers (Emel'yantsev et al. 2015). In contrast to the astronavigation system, the inertial coordinate system in the INS is based on the readings of gyroscopes and accelerometers, and the errors in the inertial frame simulation are determined by the gyro drift. It should be noted that due to the accumulation of the INS longitude error, the full DOV value in the prime vertical plane cannot be determined during the correction even with perfectly known longitude, i.e., this component is not completely observable (Emel'yantsev et al. 2015).

On the other hand, the advantage of INS as compared to astronavigation system is its independence from weather conditions and time of day. In principle, the inertial-geodetic method can be considered as a type of astrogeodetic method where the astronomical coordinates are generated using a precision INS (Dmitriev 1991; Emel'yantsev et al. 2015). It should be emphasized that, unlike the conventional astrogeodetic method, in the inertial-geodetic method the INS generates both astronomical coordinates and their derivatives.

DOV determination by **gravity gradiometry** uses a device measuring all the components of the tensor of the geopotential second derivatives, the so-called full tensor gradiometer (FTG). This method involves the implementation of an algorithm where the readings of gyroscopes, accelerometers, and FTGs are integrated in real time to determine the vehicle position and gravity vector increments along the motion path with account for the base angular position (Peshekhonov et al. 1989; Evstifeev 2017). To provide for accurate operation of such a system during DOV determination, it is critically important to ensure accurate angular stabilization of the FTG in the Earth-fixed coordinate system and to know the initial conditions of the integration, which are specified by other methods and means. To measure DOV accurate to about 1 arcsec, the permissible FTG error should be 1 Eo, and the error in FTG spacial angular stabilization should be max 1 arcsec without using analytical methods to calculate the stabilizer errors (Staroseltsev 1995; Semenov 2012). The material relating to gravity gradiometers is presented in more detail in Sect. 5.2.

Altimetry method of DOV determination is based on the application of quasi-geoid height models. The accuracy of the method depends on the accuracy of determining the coordinates of the vehicle (satellite or airplane) and the accuracy of measuring the altitude above the Earth's surface and the sea level. DOV values are determined using the G. Moritz formulas—formulas (3.1.4) in Table 3.1 (Moritz 1980). The observed wavelength of anomalies determined by the altimetry method

is within the range between 30 and 300 km (LaCoste et al. 1982; Watts et al. 1984; Medvedev et al. 2010).

The use of **global EGF models** based on the results of satellite missions has provided an enormous amount of data about the EGF. The data received from the CHAMP, GRACE, and GOCE satellite missions were used to derive global models of the EGF anomalies that actually can be used to calculate and display the distribution of DOV components all over the Earth's surface (Jekeli 1999; Hirt 2010; Koneshov et al. 2012; Karpik et al. 2015). It would take several tens or even hundreds of years to solve this global problem by gravimetric or other methods. In this sense, methods based on satellite data are beyond competition. The CHAMP and GRACE missions use satellite-to-satellite tracking. In the CHAMP mission, in the high-low satellite mode the low-orbit satellites are tracked from high-orbit satellites, thus allowing the gravity vector to be measured as the first derivative of the geopotential. In this case, DOV parameters can be determined by the gravimetric method.

The satellite-to-satellite tracking in low-low mode was implemented in the GRACE project employing two twin satellites separated by 220 km at the orbit altitude of about 500 km. The distance between satellites is determined with very high accuracy (about 10 μm) using a precise K-band microwave ranging system (Albertella et al. 2002; Kima and Tapley 2002). Each of the satellites within the system is also tracked from high-orbit satellites. In this system, differences between gravitational accelerations are calculated on a long base as if it were a giant gradiometer measuring some components of the tensor of the geopotential second derivatives. The data obtained for determining DOV smoothed parameters are more informative than in the previous case.

In GOCE mission, an FTG was installed in a satellite. It was designed as a set of three pairs of orthogonal high-precision accelerometers with three sensitive axes spaced 50 cm apart. This resulted in significant progress in determining the distribution of the EGF anomaly parameters (Albertella et al. 2002).

Using global EGF models based on satellite data to determine the DOV variability in a local area (with a short resolvable wavelength) is limited because of rather high speeds and altitudes of satellites above the Earth's surface. Lower orbits are impracticable for satellites due to atmospheric drag.

Global EGF models constructed by the mission data can be found in Sect. 6.1.

Table 3.1 gives the analytical equations used to calculate DOV by the results of direct measurements of other physical quantities using the above methods.

Potential accuracies of DOV determination methods are determined based on the measured parameters and performance of modern equipment.

3.1.2 Features of DOV Determination on a Moving Base

Specific features of DOV determination on a moving base are as follows:

- the need to measure small physical forces and accelerations against the background of large noise, mostly formed by the forces of inertia;
- impossibility, in most cases, to stop a vehicle to make corrections;
- high accuracy requirements for measuring the system orientation angles or compensation for angle variation;
- high speeds of the vehicle relative to the Earth's surface and large distance between the measuring equipment and the Earth (in case of airborne or satellite measurements);
- the need to strictly follow the programmed linear paths during motion to reduce disturbing effects on the instrumentation during turns;
- the need to occasionally update measurements and introduce corrections at preformed zero (reference) points to obtain the corrected DOV values.

The observed DOV variability along the path can be conventionally defined by the wavelengths of anomalies. That is, the shorter the wavelength of the anomaly measureable by a certain method, the more accurately the DOV variability is determined. For example, at a high altitude above the Earth's surface and at a high speed, the instrumentation smoothes short waves while neglecting minor DOV variations. In accordance with the available information, Fig. 3.1 clearly compares the capabilities of various methods to determine the DOV depending on the wavelength of the gravitational field anomalies and the achievable measurement error (Peshekhonov et al. 1989; Anuchin 1992; Li et al. 2001; Albertella et al. 2002; Seeber 2003; Volgyesi 2005; Tse and Baki Iz 2006; Hirt and Seeber 2008; Ceylan 2009; Featherstone and Lichti 2009; Kudrys 2009; Hirt 2010; Jekeli 2011, 2012; Smith et al. 2013; Guo et al. 2014; Rezo et al. 2014; Šprlák and Novák 2014; Koneshov et al. 2014, 2016a). In DOV determination, the minimum observable wavelength and measurement error are different depending on the kind of vehicle.

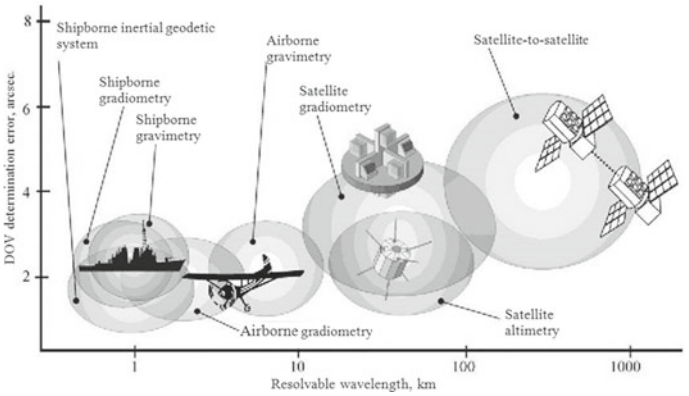

Fig. 3.1 Capabilities of different DOV determination methods

The advance in modern technology has opened up new possibilities that make researchers reconsider the application and feasibility of various methods for DOV determination.

It was shown that DOV can be measured onboard accurate to 1 arcmin if the errors of the applied gravity gradiometers, accelerometers, and gyroscopes do not exceed 1 Eo, $2 \cdot 10^{-5}$ ms^{-2} (2 μg), $5 \cdot 10^{-4}$°/h, respectively (Peshekhonov et al. 1989). As for the inertial-geodetic method, the positioning error of geodetic measurements should not exceed 5–10 m. It was noted that such accuracies were unattainable in 1989 (Peshekhonov et al. 1989).

The new results obtained in modern engineering include the following:

1. GPS and GLONASS positioning accuracy (using open channels) is 1–2 m; it is expected to be improved to a few tens of centimeters (Revnivykh 2012; Mikhailov 2014).
2. High-precision gyroscopes such as electrostatic gyroscopes and systems based on them have been developed. It has become feasible to design strapdown INS on fiber-optic gyroscopes with drifts of about 1 nm per month ($2 \cdot 10^{-5}$°/h) (Peshekhonov 2003, 2011; Paturel et al. 2014).
3. Prototypes of gravity gradiometers, operating and keeping high accuracy on a moving base, have been developed. The studies starting from the 1970–1980s resulted in the creation of devices that have successfully passed the tests aboard satellites, planes, and vessels (Gerber 1978; Murphy 2004; Mumaw 2004; Richeson 2008; DiFrancesco et al. 2009; Soroka 2010; Rummel et al. 2011; McBarnet 2013). Currently available are Lockheed Martin, Bell Geospace, and ARKeX FTGs, with errors of about 1–5 Eo, used aboard aircraft and vessels mainly for mineral exploration (DiFrancesco et al. 2009). Studies were conducted to design cryogenic gravity gradiometers with drifts of about 0.02–1 Eo (DiFrancesco 2007; Richeson 2008; Soroka 2010; Carraz et al. 2014). The FTG used in the GOCE space mission was configured as a set of three pairs of orthogonal high-precision electrostatic accelerometers with noise levels of about 0.003 Eo/$\sqrt{\text{Hz}}$ in the measurement range of 0.005–0.1 Hz (Rummel et al. 2011). The current state of development of gravity gradiometers is described in Sect. 5.2.
4. Mechanical PIGA-type accelerometers with a drift stability of 0.1–1 μg have been developed, and accelerometers based on cold atom interferometry with a resolution of 10^{-5} μg are emerging (Yole Development Report 2012).
5. New generation gravity sensors have been created, including those on cold atoms, for mobile gravimeters. Their sensitivity thresholds are about a few hundredths of fractions of mGal. The accuracies of modern gravity sensors are comparable with those of ground-based devices, which allows their unrestricted application in marine and airborne gravimetric surveys to improve both the accuracy and spatial resolution of surveys (Krasnov et al. 2014; Peshekhonov et al. 2015; Forsberg et al. 2015; Menoret et al. 2016; Zahzam et al. 2016). The principal feasibility of using absolute gravimeters on a moving base has been validated

(Peshekhonov et al. 2016; Vitushkin 2015). More details on the state of development of gravimetric instruments, including absolute gravimeters, can be found in Chap. 1.

6. CHAMP, GRACE, and GOCE satellite missions have been implemented (Sugaipova 2015) and global models of the Earth's gravitational field have been refined based on the mission data. This made it possible to generate geopotential models with the maximum number of spherical harmonics and to obtain digital models of average DOV values for standard geographical 5×5 arcmin trapezoids. DOV errors using EGM2008 model (up to degree 2190) are on average about 1–2 arcsec, which can be compared with DOV accuracy by the astrogeodetic method (Rummel et al. 2002; Nepoklonov 2009; Pavlis 2010; Koneshov et al. 2013). Global EGF models based on the data obtained in satellite missions can be found in Sect. 6.1.

Thus, the modern instrument engineering creates a potential to determine DOV parameters on a moving base with sufficiently high accuracy.

3.1.3 Classification Criteria of DOV Determination Methods

The methods to determine the parameters of EGF anomalies at sea using INS were classified based on individual criteria by Anuchin (1992): the methods are divided into direct, integral, indirect, and combined. In accordance with the terminology accepted in Russian metrology (RMG 29-2013), direct methods directly determine the required physical quantities, and in indirect methods the results of direct measurements of the quantities functionally related to the sought quantity are mathematically transformed to determine it.

The analysis of the existing methods shows that it is impossible to directly measure DOV as angles between the normal to the ellipsoid and the vertical direction (determination of astrogeodetic DOV) or angles between the directions of the vectors of the real and normal gravity fields (determination of gravimetric DOV).

All DOV measurements are performed by indirect methods with subsequent calculation of the sought values. Even the idea of the geometric method measuring DOV as an angular misalignment between the two coordinate systems (Maslov 1983) requires the separate construction of the geodetic and astronomic verticals using different instruments; therefore, it cannot be considered a direct method.

Analysis of the available methods for determining DOV on a moving base as a set of techniques helps to define the following important classification criteria that seriously affect the structure and composition of a measurement system and are used by the authors as the basic criteria for classification schemes:

1. Real-time or a posteriori DOV determination procedures.
2. Methods to improve the DOV determination accuracy.
3. Conditions of the practical application of DOV determination methods.

The first of the main classification criteria is the DOV determination procedure. Based on the measurement processing method, such procedures can be reasonably divided into those providing real-time calculations directly during the vehicle motion and those allowing only posteriori calculation of the sought DOV parameters using the postprocessing of full data arrays (Fig. 3.2).

Strictly speaking, the algorithms used to determine DOV in real time can also be used a posteriori. However, since the real-time operation is one of the most important factors in determining DOV, this criterion is represented as a separate subdivision in this classification.

Figure 3.2 shows the collocation procedure not described above (Moritz 1980; Volfson 1997). This method has not found wide use, however, it is included in the classification criteria to provide a comprehensive overview of available procedures. The collocation method uses covariance relations between different components of the measured and estimated processes (Moritz 1980). It determines DOV components based on primary data from type 1 or type 2 gravitational variometers without direct measurements of the vertical gradient, which considerably simplifies the hardware implementation of such a measurement system (Volfson 1997; Bouman 2012).

Another significant classification criterion concerns the methods to improve the DOV determination accuracy (Fig. 3.3). These methods are grouped as instrumental, algorithmic, and combined methods. Instrumental methods employ the systems protecting the equipment against various external effects (forces and moments of inertia in translational motion, vibrations and angular oscillations of the platform, electromagnetic fields, and temperature) or decreasing these effects. For example, the thermal stabilization system protects equipment from variations of the ambient

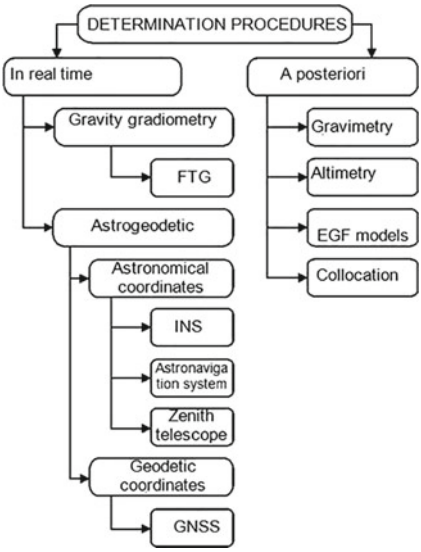

Fig. 3.2 Classification of DOV determination methods based on measurement processing procedure

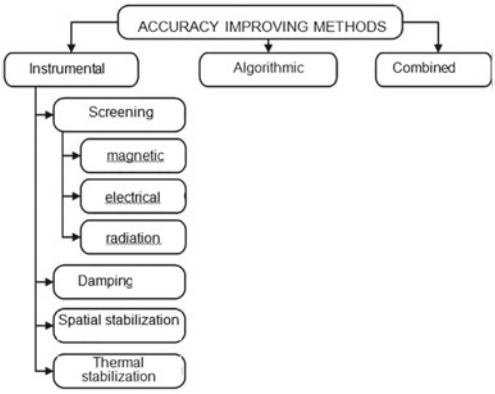

Fig. 3.3 Classification of DOV determination methods based on accuracy improving methods

temperature and maintains the preset operating temperature. The spatial shock-absorbing system reduces the effect of vibration acceleration. It is necessary to have an angular stabilization system that allows keeping the angular position of the measuring device in a specified coordinate system with small errors. ARKeX demonstrates an FTG on shock absorbers with a thermal insulation protector on its website (ARKeX 2013).

Algorithmic methods refer to the methods of data processing. The principles of signal processing influence the selection of procedures for processing data arrays and the possibility of obtaining results in real time or a posteriori. The filters and algorithms used are chosen empirically, or their structures and characteristics are determined by applying various optimization procedures. If at least plausible descriptions of the properties of useful signals and noise as random processes are available, optimization for steady-state (stationary) modes is carried out in real time based on spectral densities by Wiener method (Chelpanov et al. 1978; Dmitriev 1991; Loparev and Yashnikova 2012; Stepanov 2012) (using local approximation procedures); and for non-stationary modes, including the initial stages (with account for deterministic components), by Kalman method (Dmitriev 1991; Loparev et al. 2012a, b; Loparev and Yashnikova 2012; Stepanov 2012; Stepanov et al. 2014; Sokolov et al. 2016).

The combined methods utilize various measuring devices and algorithmic methods to obtain more comprehensive information on DOV components in different wavelength ranges. In Zheleznyak and Koneshov (2007), it was noted that marine and airborne surveys are required to determine DOV in the short-wavelength ranges, and satellite altimetry data are needed for long-wavelength measurements. For marine measurements, the best results in determining DOV over the entire wavelength range are provided by an integrated system including INS, GNSS, astronavigation system, and a velocity sensor (Anuchin 1992).

When considering general classification criteria of DOV determination methods, the conditions for their implementation should be taken into account (Fig. 3.4). One of the key criteria is the type of platform on which measurements are taken. They are grouped as follows:

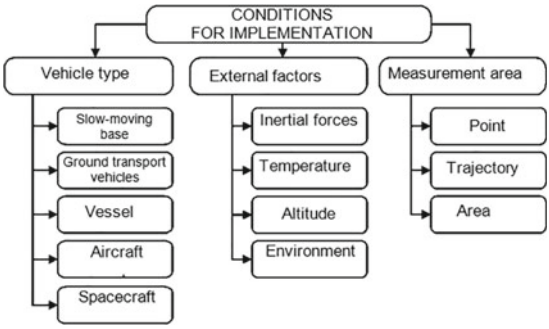

Fig. 3.4 Classification of DOV determination methods based on implementation conditions

- slow-moving platforms (e.g., drifting ice) characterized by low speeds and very low accelerations;
- ground-based vehicles, which can be stopped at certain points for observation and data correction (a conventionally mobile platform);
- marine vehicles characterized by large linear and angular accelerations; or a submarine with much smaller accelerations;
- aircraft (airplanes, helicopters, dirigibles) best suited for inaccessible mountainous areas. They have high linear speeds and accelerations due to atmospheric turbulence;
- space vehicles with low accelerations and lack of gravity, but very distant from the Earth's surface.

An interrelated classification criterion partly determined by the type of the vehicle covers a variety of typical levels of external factors directly affecting the DOV measuring equipment after all protection measures have been taken. These factors include inertial forces (vibration, impacts, overloading due to turning cycles) not compensated by the shock absorption system, the temperature, the altitude above the Earth's surface (the readings should be reduced), and the environment (air, water, vacuum). All these factors require consideration and special analysis before starting the design of instrumentation.

The last criterion determines the type of the geometric set of points of the measurement area where DOV values are determined. This is essential for selecting a DOV determination method. For example, astronomic methods are most effective for measurements at a point (or isolated points); inertial methods using INS should preferably be used for trajectory measurements during the vehicle motion (if a model is used to specify DOV variability along the motion path); gravimetric methods are applied in aerial measurements to achieve the desired DOV accuracy.

3.1.4 Qualitative Comparative Analysis of the Methods

A method for determining DOV on a moving base is selected based on the problem statement, requirements for the measured parameters, and availability of high-precision equipment. The requirements for the measured parameters usually include the achievable DOV accuracy, resolvable wavelength, and the ability to determine relative or absolute values.

For long-wavelength measurements, there exist global DOV maps based on the data obtained in the space missions mentioned above. For wavelengths over 10 km, mainly global models obtained by satellite missions or airborne gradiometry can be used. Short-wavelength real-time measurements should be taken by gravity gradiometry or astrogeodetic methods.

Implementation of a particular method depends on the performance of the instrumentation. DOV determination systems should be designed with account for the technological potential and feasibility of creating or using systems to improve the accuracy.

Zenith telescope or astronavigation system on a moving platform is able to determine DOV absolute values, but this requires the development of a precision gyroscopic stabilization system, which is a nontrivial problem taking into consideration the dimensions of the zenith telescope. Besides, such a system would require a comfortable environment for its operation: small motion angles and scattered clouds.

Using the inertial-geodetic method to determine relative DOV values requires an INS with high-accuracy gyroscopes. To set the initial conditions of INS operation, it is required to determine exact astronomical coordinates, for example, using astronomical measuring instruments. In addition, to determine DOV by the inertial-geodetic method with the use of Kalman filtering, it is necessary to specify a preliminary statistical mathematical model of the gravity field along the motion path (Anuchin 1992; Staroseltsev and Yashnikova 2016).

Despite all of its advantages, gravity gradiometry requires unique instrumentation such as FTG. It should be noted that it took about 30–40 years to design FTGs able to operate on a moving base. Only a small number of companies owning or having rights to use this technology can apply this method. To be able to use an FTG on a moving base, it is necessary to ensure high-precision gyro stabilization and apply all possible, both hardware and algorithmic, means of improving the accuracy.

3.1.5 Conclusion

Various methods to determine DOV on a moving base have been considered, and the potential for their hardware implementation has been estimated. It is shown that the comparative analysis of these methods requires that their specific application on a moving base be taken into account. Then it should be remembered that all DOV measurements are taken by indirect methods, and DOV values are calculated

in real time or during postprocessing. It is very important to provide stable operating conditions for the measuring equipment and to apply various error reduction methods, both hardware and software.

A structured system of classification criteria of DOV determination methods is proposed. The following three main classification criteria are selected: procedures for real-time or a posteriori DOV determination; methods for improving DOV accuracy, including instrumental, algorithmic, and combined ones; conditions for the practical application of DOV determination methods. A comparative qualitative analysis of the methods and fundamental solutions that implement various requirements for the instruments being developed has been carried out.

3.2 DOV Determination with the Use of an Automated Zenith Telescope

As mentioned in Sect. 3.1, DOV components can be determined with high precision by various methods. However, the methods based on the use of gravimetric or satellite data make it possible to determine DOV components with a specified error only if a significant amount of work was done previously and there is a detailed survey of the area of interest. In poorly studied areas, as well as in the case of more stringent requirements for the accuracy of determining DOV components, the astro-geodetic method based on a comparison of the astronomical and geodetic coordinates can be used (Table 3.1). Modern satellite equipment allows geodetic coordinates to be determined with accuracy of a few centimeters. Thus, DOV determination accuracy is limited by the error in determining astronomical coordinates, the reduction of which is an urgent task.

This section considers the basic principles of determining astronomical coordinates and DOV components by observing stars, as well as the instruments used to solve this problem in Russian and international geodetic astronomy. The emphasis is placed on the automated zenith telescope (AZT), the main parameters of its components and the algorithms for processing the observation results; also discussed is estimation of the AZT accuracy characteristics.

3.2.1 General Principles of Determining Astronomical Coordinates in Geodetic Astronomy

Astronomical latitude φ and the local sidereal time s at observation time T at some point on the Earth's surface can be determined if the zenith position on the celestial sphere is determined for this time and this point. Indeed, declination of the zenith is numerically equal to the observer's latitude $\delta_Z = \varphi$, and its right ascension to the local sidereal time $\alpha_Z = s$ (Fig. 3.5).

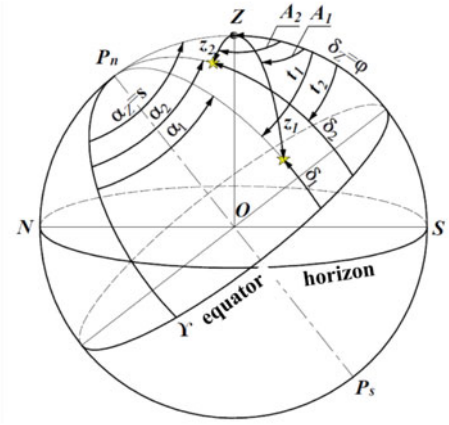

Fig. 3.5 Determination of the zenith position on the celestial sphere. P_n is the celestial north pole; P_s is the celestial south pole; ϒ is the vernal equinox; N is the north point; S is the south point; Z is the zenith (P_nZS is the celestial meridian); t is the horary angle; α is the right ascension; δ is the declination; A is the azimuth; z is the zenith distance

At any given moment of time T, the position of the zenith on the celestial sphere Z (α_Z, δ_Z) can be defined by

- zenith distances of at least two stars with known equatorial coordinates (α_1, δ_1) and (α_2, δ_2);
- the intersection of at least two verticals passing through these stars, i.e., azimuths of stars A_1 and A_2.

Thus, depending on the measurands, the methods for determining astronomical coordinates are divided into two main groups: zenithal and azimuthal.

In the zenithal methods, the time and latitude of the instrument position are determined from the measured zenith distances of stars or the differences in the zenith distances of stars, or from observations of groups of stars at the same zenith distance.

Azimuthal methods of astronomical determinations make it possible to determine the time and latitude based on the azimuths of two stars or using the measured differences in azimuths of stars or from observations of groups of stars in the same vertical (Uralov 1980).

As is known, the longitude of a point relative to the initial meridian is numerically equal to the difference between the local times of the same kind (Kulikov 1969) determined simultaneously (or with reference to the same moment) both at the observation point and at the point located at the first meridian, i.e.,

$$\lambda = s - S = m - \mathrm{UT1},$$

where

s is the local sidereal time;

S is the Greenwich sidereal time;

m is the local mean solar time;

UT1 is the mean Greenwich meridian universal time (Brumberg et al. 2004).

Thus, the problem of determining the longitude of a point consists in

- determining the local time s or m at a time T based on the measurements of the zenith distances of the stars or their azimuths;
- determining the time of the first meridian S or UT1 at the same moment of time T, for example, using the transmission of exact time signals over a radio link.

In geodetic astronomy, the horizontal coordinates of stars (A, z) are considered measurable, the equatorial coordinates of stars (α, δ) are considered known, and the geographical coordinates of point (φ, λ) are considered determinable. The relations between the determinable, known, and measurable parameters are obtained through the solution of the parallactic triangle (Kulikov 1969). The formulas for the relations of parameters used in the zenithal and azimuthal methods of astronomical determinations take the following form, respectively:

$$\cos z = \sin\varphi \sin\delta + \cos\varphi \cos\delta \cos t; \tag{3.2.1}$$

$$\operatorname{ctg} A = \sin\varphi \operatorname{ctg} t - \operatorname{tg}\delta \cos\varphi / \sin t. \tag{3.2.2}$$

In (3.2.1) and (3.2.2), t is the horary angle ($t = s - \alpha$).

From the above description of methods for determining astronomical coordinates, it is possible to formulate the following problems to be solved using astronomical equipment:

- measurement of zenith distances of stars and horizontal directions to stars;
- recording of moments of these measurements in a given time measurement system;
- recording of moments of the passage of stars through specified ertical circles or almucantar (a small circle of the celestial sphere whose plane is parallel to the plane of the horizon (Kulikov 1969)).

In Russia, astronomical field observations are conducted with the use of measuring systems that are capable of providing solutions to the above problems. Such systems consist of the following interrelated parts:

- an astronomical tube used as a sighting device. It turns around two mutually perpendicular axes; the vertical axis is set in the direction of the plumb line using levels;
- divided circles connected with the axes of rotation, vertical and horizontal, with readout devices;
- devices for pointing at a star, allowing for simultaneous measurement of small angular distances within the field of view and recording the moments of observations of stars—eyepiece micrometers (conventional, contact, photoelectric ones);

- astronomical clock that serves as a scale for measuring time when recording the moments of star observations;
- chronographs—devices for recording observation results;
- radio receiving equipment connected to the clock and the chronograph used to receive the time signals transmitted by time service radio stations.

The first three parts of the system are combined in one unit—the astronomical instrument, which has a communication channel with the clock and the recording devices.

The following astronomical instruments have been used in Russia for high-precision astronomical determinations of latitude and longitude: AU 2/10 (USSR, since the 1930s), Wild T-4 (Wild, Switzerland, since the 1940s, Fig. 3.6), DKM3-A (Kern-Aarau, Switzerland), AU01 (Russia, TsNIIGAiK, since the mid-1980s) (Rukovodstvo 1984).

When conducting high-precision astronomical determinations of coordinates using astronomical instruments (with visual recording of objects), it is necessary to take into account the influence of various components of the instrumental error: collimation error, tilting of the horizontal axis, lateral flexure of the telescope tube, errors in the pivot shapes, etc. (Uralov 1980; Rukovodstvo 1984). With this aim in view, the instrument is thoroughly examined before observations. For the above reasons, the requirements for the observers' qualifications are higher, and the duration of observations significantly increases (as a rule, to ensure high precision in determining astronomical coordinates, observations are conducted for three months).

In addition, the fact that the readings of the chronometer or the clock may be perceived by ear at the moments of star sighting, explains the observer's significant personal error, as well as a great random error of observations. To reduce the influence

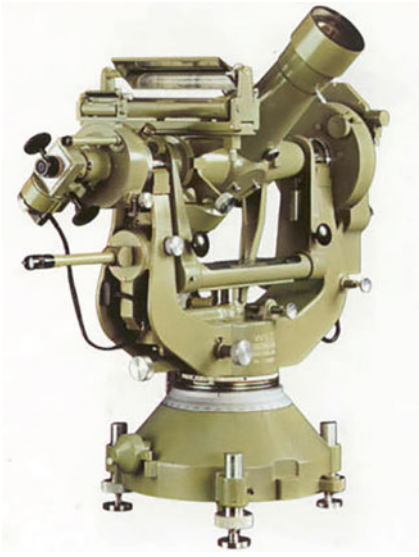

Fig. 3.6 Wild T-4 astronomical instrument

of these factors, as well as to improve performance, semi-automatic and automatic methods are used for star observation using special devices, primarily photodetector devices (e.g., CCD and CMOS image sensors) as radiation detectors. CCD- and CMOS image sensors make it possible to ensure observation of faint objects, as well as a digital representation of the observation material, which allows the results to be processed using a computer directly in the observation process, which improves both the performance and accuracy of determinations. Reference of observations to the precise time scale can also be carried out automatically using GNSS receivers.

Thus, the use of automated devices significantly improves the accuracy and efficiency of determining astronomical coordinates and, as a consequence, DOV components.

Work on the creation of such automated devices has been carried out over the past three decades. In the 1990s, a prototype of an automated prismatic astrolabe was created at Concern CSRI Elektropribor (Vasiliev et al. 1991b).

Digital zenith telescopes were created in a number of European universities (Hannover, Zurich) to quickly determine DOV components. They allow obtaining values with an accuracy of 0.2–0.3 arcsec and higher within less than an hour of observation (Hirt and Bürki 2002; Hirt et al. 2010). Work on creating such devices is also under way in Austria (Gerstbach and Pichler 2003), Turkey (Halicioglu et al. 2012), China (Tian et al. 2014).

In 2017 Concern CSRI Elektropribor completed the development of the prototype of an AZT designed for quick determination (about an hour) of DOV components from observations of the circumzenithal area of the stellar sky in the field of view. This Section describes the principle of operation of this device, the main parameters of its component parts, and the algorithms for processing observation results.

3.2.2 Description of the AZT and Its Principle of Operation

The AZT is an optoelectronic system, the sight axis of which is directed to the zenith. The objective connected to the camera and inclination sensors is mounted on a platform that can turn around a vertical axis (Fig. 3.7). A precise leveling mechanism is provided for horizontal leveling.

The AZT consists of an optoelectronic device, control device, and a power supply system containing a power supply device, battery packs, and chargers.

A general view of the AZT is presented in Fig. 3.8.

The optoelectronic device is intended

- to form images of stars in the field of view of the objective and record them in the plane of the digital camera photodetector;
- to determine the geodetic coordinates (latitude and longitude) of the observation point;
- to form the UTC scale based on the GNSS data;
- to determine the astronomical coordinates of the observation point.

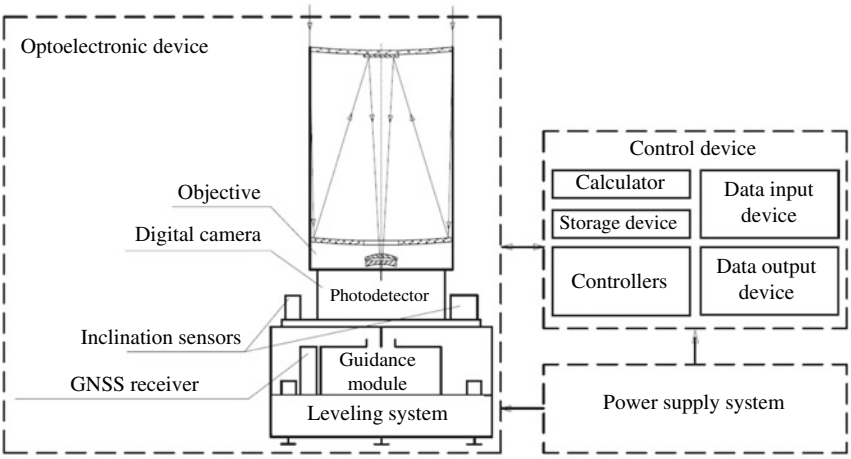

Fig. 3.7 AZT functional diagram

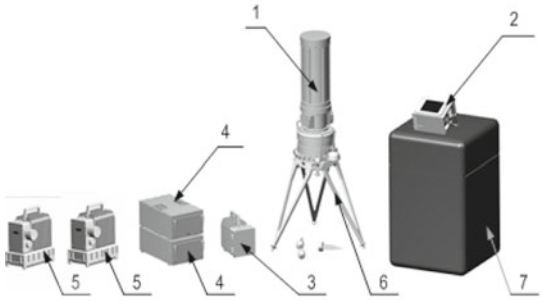

Fig. 3.8 General view of the AZT: 1—optoelectronic device; 2—control device; 3—power supply device; 4—battery pack; 5—charger; 6—tripod; 7—package

The optoelectronic device includes

- a catadioptric objective with the pupil diameter of 200 mm, the angular field of view 1.1 × 1.5°, and the relative aperture ratio of 1:6;
- a digital camera built on the basis of a thermally stabilized 20-megapixel CMOS image sensor (the size of the image sensor's sensitive area is 36.8 × 24.6 mm (5120 × 3840 pixels));
- GNSS receiver;
- guidance module;
- leveling system;
- inclination sensors.

The control device contains computational units of functional parts combined by exchange channels into a uniform information and control system. It is intended.

- to control AZT components (guidance drives, leveling drives, inclination sensors);

- to organize information exchange between the AZT components;
- to process observation data;
- to present the observation data on the display and record them to storage media.

The power supply device and battery packs provide the equipment with a stabilized voltage of autonomous power supply for 6 h.

During operation, the AZT is installed at a required point, whereupon its component parts are assembled. The AZT is controlled by the operator through the control device. The activation command initiates the preparation mode—leveling of the optoelectronic device platform. Next, the mode of DOV component determination is switched on, after which (within an hour) the values of astronomical and geodetic coordinates, as well as DOV components are displayed on the control device.

As shown in Sect. 3.1, the DOV components are determined using the following relations:

$$\begin{aligned} \xi &= \varphi - B; \\ \eta &= (\lambda - L)\cos\varphi, \end{aligned} \tag{3.2.3}$$

where

ξ is the DOV projection on the meridian plane;

η is the DOV projection on the prime vertical plane;

B, L are the geodetic coordinates of the location (latitude and longitude);

φ, λ are the astronomical coordinates of the location.

The astronomical coordinates are determined by measuring the direction to stars with known equatorial coordinates (the right ascension α, the declination δ) using the equivalence of astronomical coordinates (φ, λ) of the observation point (AZT location) and equatorial coordinates of stars located directly in the zenith (Fig. 3.9). This equivalence is due to the validity of the following relations:

$$\begin{aligned} \varphi &= \delta; \\ \lambda &= \alpha - \theta, \end{aligned} \tag{3.2.4}$$

where θ is the Greenwich apparent sidereal time (the horary angle of the vernal equinox relative to the Greenwich meridian, Fig. 3.9) (Abakumov 1996; Avanesov et al. 2013; Brumberg et al. 2004).

It should be emphasized that the probability of finding stars directly at the zenith point is extremely small; therefore, the purpose of observation is to record a sequence of frames with star images in the circumzenithal area (within the field of view) using a photodetector; to measure the coordinates of the energy centers of all stars in each frame, identify them, and determine the equatorial coordinates of the zenith point. Concurrently with the frames recording, also fixed is the time needed to calculate θ.

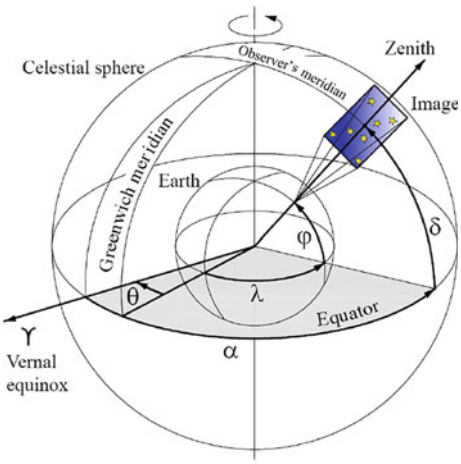

Fig. 3.9 Equivalence of astronomical and equatorial coordinates

3.2.3 Algorithm for Determining DOV Components Using the AZT and Error Analysis

A block diagram of the algorithm for determining DOV components is shown in Fig. 3.10.

After obtaining an image of the stellar sky, it is necessary to select areas containing images of objects, which is done with the help of a binary mask (Fig. 3.11a). To form it, the image is first filtered in order to eliminate the influence of background heterogeneity. In AZTs, this procedure is done with the use of a median filter (Andreev 2005). Then, related areas are identified using threshold filtering (Fig. 3.11a).

Objects are identified along the borders of the binary mask areas in the original image (Fig. 3.11b). The identified objects represent groups of photodetector elements, whose output signal values are used to determine the coordinates of the star image energy centers.

For highly accurate determination of astronomical coordinates, it is necessary to measure the star image position in the photodetector plane with an accuracy of hundredths of the decomposition element (pixel) of the photodetector, i.e., with subpixel resolution. This problem can be solved by different processing methods: for example, the weighted average method, the least squares method, the extreme correlation method, etc. (Berezin et al. 2004; Gonzalez et al. 2004; Mantsvetov et al. 2006; Yakushenkov and Solomatin 1986; Gaivoronsky et al. 2013). However, the weighted average method was chosen for the AZT being developed as the easiest one to implement.

Further, in order to reduce the time and amount of calculations needed to identify stars, it is necessary to determine the working area in the star catalogue based on the geodetic coordinates of the observation point and the image recording time.

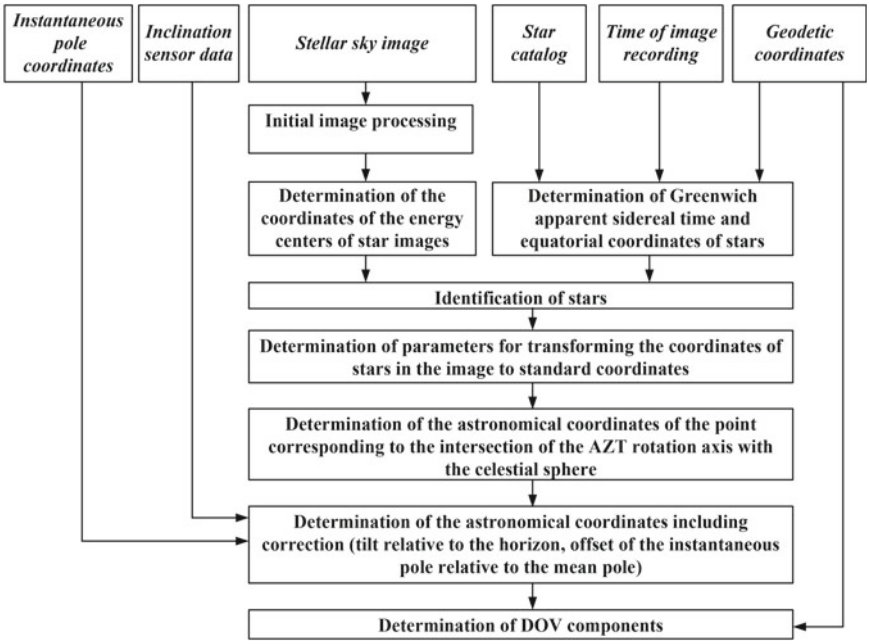

Fig. 3.10 Block diagram of the algorithm for determining DOV components

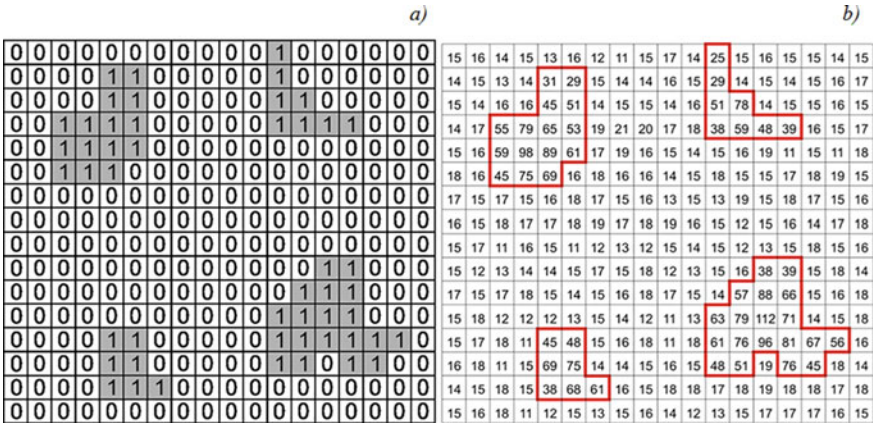

Fig. 3.11 Binary mask (**a**) and the identified objects (**b**)

Since the Earth rotates and the celestial sphere is stationary, it is necessary to know the Earth orientation relative to the celestial sphere for each moment of image recording, for which purpose Greenwich apparent sidereal time θ is used. The latter corresponds to the angle between the Greenwich meridian and the vernal equinox (see Fig. 3.9). The moment of frame recording is tied to the time recorded by a

GNSS receiver. Next, GNSS time is converted to the Greenwich apparent sidereal time (Brumberg et al. 2004; Kovalevsky 2004).

Equatorial coordinates of stars are determined from the star catalogue in the identified workspace. The AZT prototype makes use of a catalogue specially developed by the Institute of Applied Astronomy of the Russian Academy of Sciences. This catalogue contains information about stars whose equatorial coordinates are known with high accuracy. But it is also possible to use such catalogues as *Hipparcos*, *Tycho*, *UCAC*4 (Tsvetkov 2005a, b).

Star catalogues give the data for a certain epoch of observation (as a rule, it is J2000) and represent mean equatorial coordinates. To convert to the current values of the equatorial coordinates of objects, a reduction is made taking into account the proper motions of the stars, precession and nutation parameters, annual aberration, etc. (Brumberg et al. 2004; Astronomicheskii Ezhegodnik 2008). Next, an array is formed containing the equatorial coordinates of the stars (currently in the field of view) reduced to the observation epoch.

Thus, the initial data for the star identification algorithm are coordinates x^*, y^* of the energy centers of the object images in the photodetector plane and the equatorial coordinates of the stars currently in the field of view reduced to the observation epoch. To solve the identification problem, it is necessary to compare the objects in two areas (those in the image and from the catalogue). In AZT, this problem is solved using the method based on the combination of two algorithms: the algorithms for similar triangles and interstellar angular distances (Gaivoronsky et al. 2015).

Finally, an array is formed in which the coordinates of the stars in the image are compared with the equatorial coordinates of the stars from the catalogue. The next step in the algorithm for determining astronomical coordinates is transformation of the rectangular coordinates of the star image energy centers into the equatorial coordinates. First, spherical coordinates of stars are transformed to the so-called standard coordinates (Blazhko 1979). This transformation is performed by a conical projection from the center of the celestial sphere to the point with coordinates (α_0, δ_0). This point corresponds to the intersection of the AZT sight axis with the celestial sphere (Fig. 3.12a).

In the tangent plane, axes ζ and μ are tangent to the parallel and the celestial meridian, respectively. Axis ζ is directed towards the increase of the right ascensions and axis μ, to the north. This local system is called a standard coordinate system (Kovalevsky 2004). The transformation of equatorial coordinates of stars into standard coordinates is called the central projection; it is performed using the following expressions (Blazhko 1979):

$$\zeta^* = \frac{ctg\delta^* \sin(\alpha^* - \alpha_0)}{\sin\delta_0 + ctg\delta^* \cos\delta_0 \cos(\alpha^* - \alpha_0)}; \mu^* = \frac{\cos\delta_0 - ctg\delta^* \sin\delta_0 \cos(\alpha^* - \alpha_0)}{\sin\delta_0 + ctg\delta^* \cos\delta_0 \cos(\alpha^* - \alpha_0)},$$

where

α^*, δ^* are the equatorial coordinates of the star;

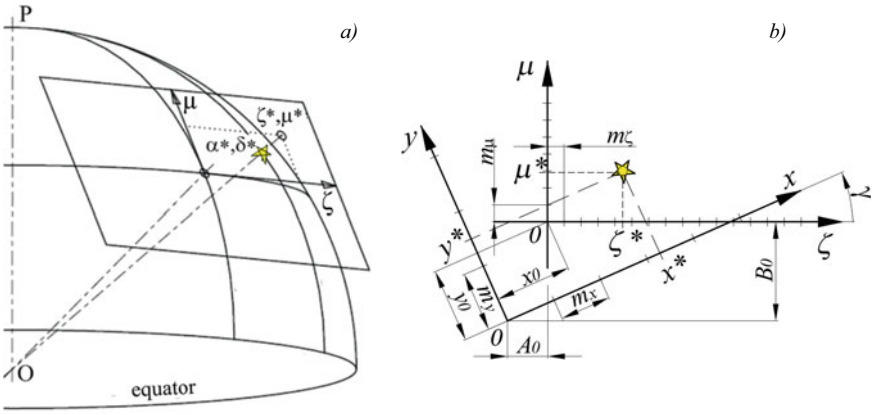

Fig. 3.12 Transformation of star coordinates: **a** is the transformation of equatorial coordinates of stars into standard coordinates; **b** is the transformation of rectangular coordinates determined in the photodetector plane into standard coordinates

α_0, δ_0 are the equatorial coordinates of the point corresponding to the intersection of the telescope sight axis with the celestial sphere (Fig. 3.12a):

$$\alpha_0 = L + \theta; \ \delta_0 = B.$$

Standard coordinates, in turn, are connected by the polynomial transformation with the coordinates of the star image energy centers determined in the photodetector plane. If there are no image distortions, a linear (affine) transformation is used, which is written as follows:

$$\begin{aligned} \zeta^* &= A_0 + A_1 x^* + A_2 y^*, \\ \mu^* &= B_0 + B_1 x^* + B_2 y^*, \end{aligned} \tag{3.2.5}$$

where

x^*, y^* are the coordinates of the star image energy center;

A_0, B_0 are the origin of the coordinate system x, y in the coordinate system ζ, μ (Fig. 3.12b).

Under the condition that the x-, y-axes are orthogonal, the transformation parameters are described as follows (Kiselev 1989):

$$\begin{aligned} A_0 &= -M_x \cdot x_0 \cdot \cos\gamma + M_y \cdot y_0 \sin\gamma; \\ A_1 &= M_x \cdot \cos\gamma; \\ A_2 &= -M_y \cdot \sin\gamma; \\ B_0 &= -M_x \cdot x_0 \cdot \sin\gamma - M_y \cdot y_0 \cos\gamma; \end{aligned}$$

$$B_1 = M_x \cdot \sin\gamma;$$
$$B_2 = M_y \cdot \cos\gamma,$$

where

x_0, y_0 are the coordinate origin ζ, μ in the coordinate system x, y (Fig. 3.12b);

γ is the angle between the axes $+x$ and $+\zeta$ (Blazhko 1979);

M_x, M_y are image scales on the x-axis and y-axis, respectively:

$$M_x = \frac{m_\zeta}{m_x};\ M_y = \frac{m_\mu}{m_y}.$$

The transformation parameters A_0, A_1, A_2, B_0, B_1, B_2 are determined for each image from measurements, representing a set of formulas (3.2.5) for all identified stars. This problem is solved by the least-squares method or the generalized least-squares method (Stepanov 2010; Motorin and Tsodokova 2016).

To compensate for the tilt of the objective's sight axis relative to the axis of rotation of the optoelectronic device and eliminate the influence of the offset of the inclination sensors, observations are made in two diametrically opposite positions (I and II), with the instrument turning by 180°.

Figure 3.13 shows a block diagram of the algorithm for determining the astronomical coordinates of the point corresponding to the intersection of the axis of rotation of the optoelectronic device with the celestial sphere. To determine the astronomical coordinates (φ_Z, λ_Z), it is necessary to transform rectangular coordinates in the photodetector plane into standard coordinates using expressions (3.2.5) and the transformation parameters $A_0, A_1, A_2, B_0, B_1, B_2$ obtained at the previous stage. After that, it is necessary to determine the equatorial coordinates using the following formulas (Blazhko 1979):

$$\alpha = \alpha_0 + arctg\left(\frac{\zeta}{\cos\delta_0 - \mu\sin\delta_0}\right);\ \delta = arctg\left(\frac{(\mu + tg\delta_0)\cos(\alpha - \alpha_0)}{1 - \mu tg\delta_0}\right).$$

Further, the astronomical coordinates are determined, with regard to the Greenwich apparent sidereal time, in accordance with (3.2.4).

The final astronomical coordinates of the point corresponding to the intersection of the axis of rotation of the optoelectronic device with the celestial sphere are obtained by averaging the astronomical coordinates determined in two diametrically opposite positions:

$$\varphi_Z = \frac{\varphi_I + \varphi_{II}}{2};\ \lambda_Z = \frac{\lambda_I + \lambda_{II}}{2}.$$

After obtaining astronomical coordinates based on the observation data in two positions, it is necessary to make a correction for the tilt relative to the horizon

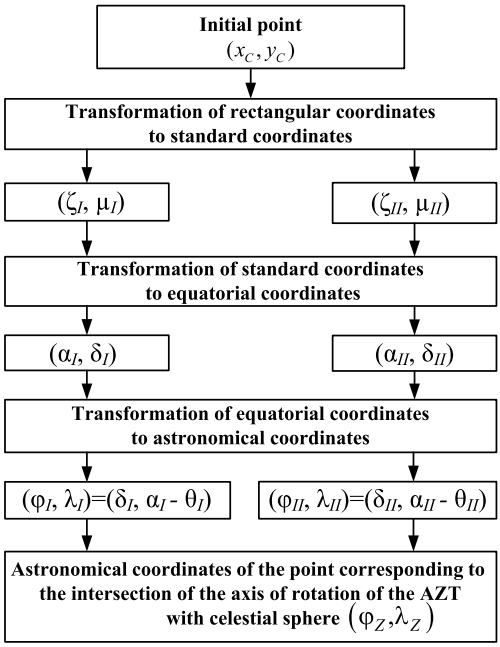

Fig. 3.13 Block diagram of the algorithm for determining the astronomical coordinates of the point corresponding to the intersection of the axis of rotation of the optoelectronic device with the celestial sphere

according to the inclination sensors:

$$\Delta\varphi_n = n_\varphi; \;\; \Delta\lambda_n = n_\lambda \sec\varphi_Z.$$

Here,

$$n_\varphi = n_1 \cos(A_{ph}) - n_2 \sin(A_{ph}),$$
$$n_\lambda = n_1 \sin(A_{ph}) + n_2 \cos(A_{ph}),$$

where n_1, n_2 are data of the 1st and 2nd inclination sensors, respectively, calculated according to the expressions:

$$n_1 = \frac{n_{1I} - n_{1II}}{2}; n_2 = \frac{n_{2I} - n_{2II}}{2},$$

where n_{1I}, n_{1II} are the data of the 1st sensor in the I and II positions, respectively; n_{2I}, n_{2II} are the data of the 2nd sensor in the I and II positions, respectively; A_{ph} is the azimuth of the photodetector row (Fig. 3.14):

$$A_{ph} = \frac{3\pi}{2} - \gamma.$$

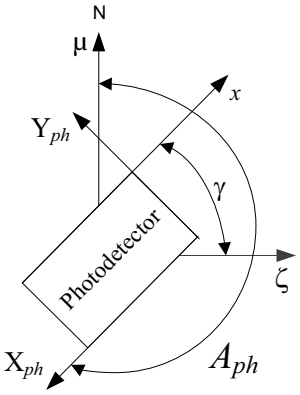

Fig. 3.14 The azimuth of the photodetector row

In addition, it is necessary to compensate for the offset of the instantaneous pole relative to the mean pole:

$$\Delta\varphi_p = -x_p \cos L + y_p \sin L;$$
$$\Delta\lambda_p = -(x_p \sin L + y_p \cos L) \cdot tgB,$$

where (x_p, y_p) is the offset of the instantaneous pole relative to the mean pole (Brumberg et al. 2004) ($x_p, y_p = const$).

Thus, the values of astronomical coordinates are calculated using the formulas:

$$\varphi = \varphi_Z + \Delta\varphi_n + \Delta\varphi_p; \ \lambda = \lambda_Z + \Delta\lambda_n + \Delta\lambda_p.$$

Further, DOV components are determined using expressions (3.2.3), taking into account the geodetic coordinates obtained with GNSS equipment.

The error in determining DOV components with AZT depends on the accuracy of determining the geodetic and astronomical coordinates. The error in determining geodetic coordinates is determined by the characteristics of the GNSS receiver and is at a level of 2–3 m (≤0.1arcsec). The error of astronomical coordinates, in turn, depends on

- error in the image fix to the time scale;
- error in determining the equatorial coordinates of stars;
- error due to an inaccurate choice of the point corresponding to the intersection of the sight axis of the celestial sphere;
- error in determining the coordinates of the star image energy centers in the photodetector plane;
- error in the rotation of the optoelectronic device around the vertical axis;
- error of inclination sensors;
- error in determining the offset of the instantaneous pole relative to the mean pole.

The error in determining the coordinates of the star image energy centers in the photodetector plane and the error of the inclination sensors have the greatest influence on the accuracy of determining DOV components. According to preliminary estimates obtained by computer simulation, the error in determining DOV components using AZT does not exceed 0.3 arcsec.

3.2.4 Field Studies of the AZT Prototype

The AZT prototype was created to test and checkout the developed data processing algorithms (Fig. 3.15).

The AZT prototype contained the following equipment:

- a *Meade LX-90-ACF* (USA) catadioptric objective with a 2000 mm focal length and 200 mm entrance pupil diameter;
- a CMOS 20-megapixel camera *JAI SP-20000-PMCL* (JAI Ltd. Japan) built on a CMOS image sensor; the size of the sensitive area of the image sensor is 32.77 × 24.58 mm (5120 × 3840 pixels); the pixel size is 6.4 × 6.4 μm. The camera allows synchronization of the image by an external pulse with accuracy of 25 μs;
- *JAVAD ALPHA* GPS/GLONASS receiver (to generate a second marker fixed to the *UTC* scale and determine geodetic coordinates);
- *Wyler Zerotronic Type* 3 inclination sensors with the angle measurement range of ±0.5°.

The AZT prototype provided for a series of stellar sky images in two diametrically opposite positions. Observations were carried out at one point on different dates. Processing of the observation data was carried out using the developed algorithms.

The following results were obtained after processing the data of all observation series: the values of the DOV components determined in the field studies are close to the real values; the RMSD between the series does not exceed 1 arcsec, which is an acceptable result for the prototype, given the unequal effect of temperature fields on different structural elements, as well as changes in illumination because the observations were conducted in urban conditions.

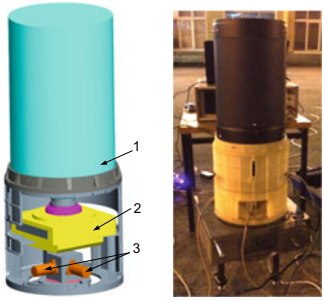

Fig. 3.15 The AZT prototype: 1—objective; 2—digital camera; 3—inclination sensors

3.2.5 Conclusion

A description is given of the AZT developed at Concern CSRI Elektropribor, JSC. The telescope is intended to determine DOV components in real time from field observations of the ircumzenithal area of the stellar sky.

The AZT principle of operation, the main parameters of its component parts, as well as the algorithms for processing the observation data have been discussed, and the telescope accuracy characteristics are given.

The results of the AZT prototype field studies clearly show the effectiveness of the proposed technical solutions and algorithms for processing observation data, as well as the feasibility of using the AZT under consideration to determine DOV with high accuracy.

3.3 Inertial Geodetic Method for DOV Determination

As mentioned in Sect. 3.1, the idea of the inertial geodetic method is based on using data from a precision INS and a GNSS receiver (Nash and Jordan 1978; Anuchin et al. 1982; Peshekhonov et al. 1989; Dmitriev 1997; Salychev et al. 1999; Nassar, 2003; Li and Jekeli, 2008). At the same time, unlike the classical astrogeodetic method, the INS used in the implementation of the inertial geodetic method produces not only astronomical coordinates but also their derivatives. This makes it possible to solve the DOV estimation problem using differential measurements, based on external information on the components of the linear speed vector and the acceleration of the vehicle in the local navigation frame. Section 3.3 is devoted to the features of the inertial geodetic method. In this case, it is assumed that a strapdown inertial measurement unit (SIMU) acts as an INS.

3.3.1 Inertial Geodetic Method Using Positional and Velocity Measurements

When DOV is determined using the inertial geodetic method, in general, the following velocity and positional differential measurements can be used (taking into account the features of the satellite navigation equipment in determining navigation parameters, including synchronization of velocity measurements) (Emel'yantsev and Stepanov 2016):

$$
\begin{aligned}
z_{V_j}(t_{k+1}) &= \left[\nabla S_{j\_INS}(t_{k+1}) - \nabla S_{j\_GNSS}(t_{k+1})\right]/Tz, \quad (j = E, N, H),\\
z_{\varphi}(t_{k+1}) &= \varphi_{INS}(t_{k+1}) - \varphi_{GNSS}(t_{k+1}),\\
z_{\lambda}(t_{k+1}) &= \lambda_{INS}(t_{k+1}) - \lambda_{GNSS}(t_{k+1}),
\end{aligned}
$$

$$z_h(t_{k+1}) = h_{INS}(t_{k+1}) - h_{GNSS}(t_{k+1}),$$

where

$\nabla S_{j\_GNSS}(t_{k+1})$ are the increments of the Cartesian coordinates of a vehicle in projections onto the geographic axes measured in a GNSS receiver with a discreteness of $Tz = t_{k+1} - t_k$ (for most modern GNSS receivers, interval Tz is in the range between 0.1 and 1 s);

$\nabla S_{j\_INS}(t_{k+1}) = \int_{t_k}^{t_{k+1}} V_{j\_pr}(\tau)d\tau$ are the increments of Cartesian coordinates on the interval Tz calculated according to the INS data on the vehicle speed.

Taking into account the data synchronization of the INS and the GNSS receiver, we can write:

$$z_{V_j}(t_{k+1}) = \Delta V_j(t_{k+1}) + \nu_{V_j}(t_{k+1}), \tag{3.3.1}$$

where

ΔV_j is the error of the linear-speed vector components produced by the INS;

$\nu_{V_j}(t_{k+1}) = -\left[\Delta V_j(t_{k+1}) - \Delta V_j(t_k + Tz/2)\right] - \delta\nabla S_{j\_GNSS}(t_{k+1})/Tz$ is the reduced noise. Here, $\delta\nabla S_{j\_GNSS}(t_{k+1})/Tz$ is the error of the linear-speed vector components. While deducing the above expression, the following should be borne in mind. In the GNSS receiver, the speed is generated as an integral of the phase in the Doppler channel over the time interval Tz. Thus, in practice, it can be assumed that the obtained speed corresponds to its average value on the interval Tz. To ensure synchronization during the formation of differential measurements, the components of the INS speed are generated in a similar way. To form measurements, it is important to go to the current time for determining the speed by the INS and its error while taking into account the difference in speed errors related to the middle of the interval Tz and the time it is finished and attributing this difference to the measurement noise. It should also be noted that, since the difference in the errors of the INS speed components generated by INS within the interval Tz is small, the fact that the measurements correlate with their errors can be neglected.

For positional measurements, the following is true:

$$\begin{aligned} z_\varphi(t_{k+1}) &= \Delta\varphi - \delta\varphi_{GNSS}, \\ z_\lambda(t_{k+1}) &= \Delta\lambda - \frac{1}{\cos\varphi}\delta W_{GNSS}, \\ z_h(t_{k+1}) &= \Delta h - \delta h_{GNSS}, \end{aligned} \tag{3.3.2}$$

where $\Delta\varphi, \delta\varphi_{GNSS}, \Delta\lambda, \delta W_{GNSS} = \delta\lambda_{GNSS}\cos\varphi, \Delta h, \delta h_{GNSS}$ are the errors of the INS and GNSS (in the differential mode), correspondingly, with respect to the observer's coordinates.

Assume that speed measurements (3.3.1) are used to effectively damp the natural (Schuler and diurnal) variations of SIMU errors. Then, according to the analytical solutions given in Emel'yantsev and Stepanov (2016), in the conditions of a quasi-stationary vehicle (i.e., at stops, when it is not required to get information about the change in the DOV), at some i-th point of the route for smoothed time values of positional measurements (3.3.2), we will have the following:

$$\tilde{z}_{\varphi i} = -\frac{1}{\Omega}(-\Delta\overline{\omega}_{bH}\cos\varphi_i + \Delta\overline{\omega}_{bN}\sin\varphi_i) + \frac{\Delta\overline{a}_{bN}}{g} - \xi_i - \delta\tilde{\varphi}_{GNSS}, \tag{3.3.3}$$

$$\tilde{z}_{\lambda i}\cos\varphi_i = -\tilde{\alpha}_*(t_k)\cos\varphi_i + (\Delta\overline{\omega}_{bH}\sin\varphi_i + \Delta\overline{\omega}_{bN}\cos\varphi_i)\cos\varphi_i \cdot \Delta t - \frac{1}{\Omega}\Delta\overline{\omega}_{bE}\sin\varphi_i + \frac{\Delta\overline{a}_{bE}}{g} + \eta_i - \delta\tilde{W}_{GNSS}, \tag{3.3.4}$$

where $\tilde{\alpha}_*(t_k)$ is the smoothed value of the SIMU error in longitude accumulated due to the gyroscope drifts; $\Delta t = t - t_k$, where t_k is the moment of the last SIMU correction in longitude; $\Delta\overline{\omega}_{bj}$, $\Delta\overline{a}_{bj}$ $(j = E, N, H)$ are low-frequency components of the gyroscope drifts and accelerometer errors in projections onto the geographical axes due to instability of their zeros with respect to the values during the calibration time; Ω is the angular velocity of the diurnal rotation of the Earth; g is the value of the normal gravity acceleration at the equator; ξ_i, η_i are the values of DOV components at the observer's meridian and in the prime vertical plane, respectively; $\delta\tilde{\varphi}_{GNSS}, \delta\tilde{W}_{GNSS}$ is the level of the smoothed noise of the GNSS receiver.

Note that in the case of the SIMU longitudinal correction generated by the GNSS, the expression for error $\tilde{\alpha}_*(t_k)$, according to Emel'yantsev and Stepanov (2016), can be written as:

$$-\tilde{\alpha}_*(t_k)\cos\varphi = \frac{1}{\Omega}\Delta\overline{\omega}_{bE}(t_k)\sin\varphi_i - \frac{\Delta\overline{a}_{bE}(t_k)}{g} - \eta(t_k). \tag{3.3.5}$$

It is also pertinent to note that due to the presence of the term $\tilde{\alpha}_*(t_k)$, i.e., accumulation of the INS error in longitude, it is impossible to determine the total value of the DOV component η in the prime vertical plane during the correction, even if the longitude is known exactly. That is, with the specified scope of measurements, the DOV component η cannot be observed fully. For a quasi-stationary vehicle, the frequency of longitudinal corrections does not affect the accuracy of DOV estimation. A similar situation takes place during motion, since the errors in (3.3.5) are not separated. They can be separated due to maneuvering, which is undesirable for DOV estimation because this dramatically complicates the description of the DOV model and causes difficulties in estimation (separation of DOV spectra and drifts of gyroscopes and accelerometers, which will be discussed later).

Substituting (3.3.5) into Eq. (3.3.4), we derive:

$$\tilde{z}_{\lambda i}\cos\varphi_i = (\Delta\overline{\omega}_{bH}\sin\varphi_i + \Delta\overline{\omega}_{bN}\cos\varphi_i)\cos\varphi_i\cdot\Delta t - \frac{1}{\Omega}\Delta\tilde{\omega}_{bE}\sin\varphi_i + \frac{\Delta\tilde{a}_{bE}}{g} + \nabla\eta_i - \delta\tilde{W}_{GNSS}, \tag{3.3.6}$$

where $\nabla\eta_i = \eta_i - \eta(t_k)$ is the increment of the DOV component η with respect to the SIMU update point; $\Delta\tilde{\omega}_{bE}$, $\Delta\tilde{a}_{bE}$ are the variations of the corresponding errors over the interval $\Delta t = t - t_k$.

According to (3.3.3), (3.3.6), the DOV estimates at the i-th route point are calculated as follows:

$$\begin{aligned}\hat{\xi}_i &= -\tilde{z}_{\varphi i},\\ \nabla\hat{\eta}_i &= \tilde{z}_{\lambda i}\cos\varphi_i,\end{aligned} \tag{3.3.7}$$

and the errors of their determination are described by the following expressions:

$$\begin{aligned}\delta\tilde{\xi}_{gi} &= \frac{1}{\Omega}(-\Delta\overline{\omega}_{bH}\cos\varphi_i + \Delta\overline{\omega}_{bN}\sin\varphi_i) - \frac{\Delta\overline{a}_{bN}}{g} + \delta\tilde{\varphi}_{GNSS},\\ \delta\nabla\tilde{\eta}_i &= (\Delta\overline{\omega}_{bH}\sin\varphi_i + \Delta\overline{\omega}_{bN}\cos\varphi_i)\cos\varphi_i\Delta t - \frac{1}{\Omega}\Delta\tilde{\omega}_{bE}\sin\varphi_i\\ &\quad + \frac{\Delta\tilde{a}_{bE}}{g} - \delta\tilde{W}_{GNSS}.\end{aligned} \tag{3.3.8}$$

Assume that bias instabilities of the SIMU's gyroscopes and accelerometers are at a level of $\Delta\tilde{\omega} \le 3\cdot 10^{-5}$°/h, $\Delta a \le 10^{-5}$ m/s^2. The level of smoothed values $\delta\tilde{\varphi}_{GNSS}$, $\delta\tilde{W}_{GNSS}$ of the GNSS receiver noise does not exceed 3 m. Then in middle latitudes, approximately, we have $\tilde{\xi}_i \le 0.6$ arcsec, $\nabla\tilde{\eta}_i \le 0.7$ arcsec. Note that the time between SIMU longitudinal corrections should not exceed 3 h, which characterizes the allowable interval between the reference points for η.

It should be noted that to improve the accuracy of DOV determination, it is advisable to carry out initial measurements both on forward and reverse courses. In this case, SIMU gyroscope drifts and accelerometer errors will be autocompensated in the axes of the local navigation frame with the North, East and Earth ellipsoid orthogonal axes with the origin at the point of the navigation solution (Groves 2013), which results in a sharp decrease in the accumulated error in coordinates and, accordingly, increase in the accuracy of DOV determination. Assuming that their variation has a low-frequency character, their effect, as well as the effect of misalignment between the sensitive axes of the gyro and accelerometer, can be critically mitigated.

When the problem of DOV estimation is solved by the inertial geodetic method while the vehicle is moving, it is required to take into account the DOV variation along the motion path using, in particular, the corresponding statistical models, for example, those given in Nash and Jordan (1978). However, it should be taken into consideration

that the accuracy of DOV determination can be improved only if there is a significant difference between the spectra of gyro drifts and accelerometer errors and the DOV spectrum in the process of the vehicle motion. In addition, the inconsistency of the calculated DOV models used in the filtering problem with their real changes in the survey area may result in additional errors in their estimation.

As follows from the above reasoning, when DOV are determined by the inertial geodetic method using data even from a precise INS, it is necessary to have reference points of exact DOV values, which is a significant disadvantage of this method.

3.3.2 Using ZUPT Technology

Another variant of the method under consideration is based on the use of differential velocity and acceleration measurements only. For land vehicles, it is implemented using so-called ZUPT corrections (zero velocity update). In marine and airborne gravimetry, this method can also make use of GNSS data (Dmitriev 1997; Mangold 1995; Salychev et al. 1999; Nassar 2003; Li and Jekeli 2008).

It was mentioned above that the use of differential position measurements provides observability of only the DOV full meridional component. It should be emphasized that in this case, when using ZUPT velocity measurements, it is only possible to measure the increments of both DOV components along the motion path, which follows from the specific features of the formation of differential measurements as increments of the value to be analyzed at a given time interval (see (3.3.13), (3.3.15)).

The initial information for DOV estimation during ZUPT corrections (INS) is a measurement, for example, for component ξ:

$$z_\xi = \Delta\tilde{\tilde{V}}_N,$$

which represents the output signal of the corresponding "horizontal" accelerometer smoothed over time $\tilde{T}$ of a stop (here, ΔV_N is the INS error in the north component of the linear speed vector). For SIMU, this is the projection of the data from the triad of accelerometers on the axis N. According to Dmitriev (1997), this measurement for the $(i-1)$-th stop can be represented as follows:

$$z_{\xi(i-1)} = g\tilde{\beta}_{(i-1)} + \Delta\overline{a}_{bN(i-1)} - g\xi_{(i-1)}, \tag{3.3.9}$$

where $\tilde{\beta}_{(i-1)}$ is the $(i-1)$-th stopping time-averaged error of the vertical construction, determined mainly by its Schuler oscillations; $\Delta\overline{a}_{bN(i-1)}$ is the zero drift of the "horizontal" accelerometer taking into account the assumption that the accelerometer noises are effectively smoothed over interval $\tilde{T}$.

The variability of error $\beta(t)$ in the i-th interval of motion is described by two equations for the northern channel of the vertical analogue (Anuchin and Emel'yantsev

2003). Reduce them to the form (Dmitriev 1997), given that the interval of motion between stops is $T << 2\pi/\nu$:

$$\ddot{\beta} + \nu^2\beta = \Delta\tilde{\omega}_{m_2} - \frac{1}{R}(\Delta\overline{a}_{bN} - \dot{V}_E\Delta K + \dot{V}_N\Delta M_a) + \nu^2\xi, \tag{3.3.10}$$

where, according to Emel'yantsev and Stepanov (2016), $\Delta\tilde{\omega}_{m_2} = -\Omega\tau_*(t_0) + \Delta\omega_{bm_2}$ is the equivalent drift of the gyro unit around the eastern axis (here, Ω is the angular velocity of the Earth diurnal rotation; τ_* is the SIMU error in the construction of the celestial axis in a plane orthogonal to the plane of the observer's meridian); ν is the Schuler frequency; ΔM_a is the accuracy of the accelerometer scale factor; ΔK is the INS heading error.

At the stop, provided that $\Delta V_N(t_0) = 0$, from (3.3.9) it follows:

$$\beta(t_0) = \tilde{\beta}_{(i-1)} = -\frac{1}{g}\Delta\overline{a}_{bN(i-1)} + \xi_{(i-1)}, \dot{\beta}(t_0) = \Delta\tilde{\omega}_{m_2 i}. \tag{3.3.11}$$

Following (Dmitriev 1997), assume that the INS operation time includes intervals of motion with a length T and stops with a length $\tilde{T}$. The vehicle acceleration on each interval $[0, T]$ can be described by the following model:

$$\dot{V}(t) = V\delta(t) - V\delta(T - t), \tag{3.3.12}$$

where $\delta(t)$ is a delta function. This model defines a uniform motion on the interval $[0, T]$ with an instantaneous stop and the speed acceleration to a value equal to V.

The solution to Eq. (3.3.10) for $t = T$ of the beginning of the i-th stop, taking into account (3.3.12), and for $t_0 = 0$, $\nu << 1$, has the form:

$$\beta(T) = \tilde{\beta}_{(i-1)} + \Delta\tilde{\omega}_{m_2 i}T - \frac{1}{R}(-\Delta K \cdot S_E + \Delta M_a S_N) - \nu^2\int_0^T\left[\frac{1}{g}\Delta a_{bN}(\tau) - \xi(\tau)\right](T - \tau)d\tau, \tag{3.3.13}$$

where S_E, S_N are the lengths of the path traveled by the vehicle on the i-th section of the motion path in geographic axes; $\Delta a_{bN}(\tau)$, $\xi(\tau)$ refer to time Δa_{bN} and spatial ξ variability on the intervals T and S.

Based on the solutions given in (Dmitriev 1997; Emel'yantsev and Stepanov 2016), it can be shown that, when using a medium accuracy-grade SIMU ($\Delta\tilde{\omega} \leq 5 \cdot 10^{-3}$°/h, $\Delta a \leq 3 \cdot 10^{-5}$ m/s^2, $\Delta M_a \leq 10^{-5}$) and the lengths of intervals between vehicle stops $T = 2\ldots5$ min, formula (3.4.13), with regard to smoothing during formation of measurements (3.3.9), can be presented in the following form:

$$\tilde{\beta}_i = \tilde{\beta}_{(i-1)} + \Delta\tilde{\omega}_{m_2 i} T + \Delta_i, \tag{3.3.14}$$

where error Δ_i does not exceed 0.1 arcsec (Markley and Crassidis 2014).

By analogy with (3.3.9), taking into account (3.3.14), measurement z_ξ for the i-th stop is represented as follows:

$$\begin{aligned} z_{\xi i} &= g\tilde{\beta}_i + \Delta\overline{a}_{bNi} - g\xi_i \\ &= -g\nabla\xi_i + \Delta\overline{a}_{bNi} - \Delta\overline{a}_{bN(i-1)} + g\Delta\tilde{\omega}_{m_2 i} T + g\Delta_i, \end{aligned} \tag{3.3.15}$$

where $\nabla\xi_i = \xi_i - \xi_{(i-1)}$.

Then, the following formula is used to obtain the estimate of increment ξ:

$$\delta\hat{\xi}_i = -z_{\xi i}/g; \tag{3.3.16}$$

at the same time, the error in estimating increment ξ is defined as follows:

$$\delta\nabla\tilde{\xi}_i = -\left(\frac{\Delta\overline{a}_{bNi} - \Delta\overline{a}_{bN(i-1)}}{g} + \Delta\tilde{\omega}_{m_2 i} T + \Delta_i\right). \tag{3.3.17}$$

For the error in determining increment ξ relative to the reference point, we have:

$$\delta\nabla\tilde{\xi}_i = \sum_{j=1}^{i} \delta\nabla\tilde{\xi}_j = -\left[\frac{\Delta\overline{a}_{bN}(t_i) - \Delta\overline{a}_{bN}(t_0)}{g} + \sum_{j=1}^{i} \Delta\tilde{\omega}_{m_2 j} T + \sum_{j=1}^{i} \Delta_j\right]. \tag{3.3.18}$$

The analysis of (3.3.18) shows that the accuracy of determining DOV increments relative to the reference point with the use of the ZUPT INS correction is affected only by the instability of accelerometer biases, while the error of their initial calibration does not play a significant role. At the same time, calibration errors of the gyro drifts and their time instability are fully reflected in the errors of DOV estimation.

The effect of the gyroscope drift can be reduced by processing a sequence of measurements of the type (3.3.15) generated at stops with the aim to filter relatively high-frequency signals $\nabla\xi_i, \nabla\eta_i$ against the background of slowly varying sequences $\Delta\tilde{\omega}_i T$. For this purpose, it is necessary to develop appropriate statistical models of DOV and gyro drifts. This makes it possible to obtain (Dmitriev 1997) DOV determination errors of about $\sigma_{\tilde{\xi}(\tilde{\eta})} \leq 1$ arcsec using the data from the INS of the considered accuracy grade over the interval $T_\Sigma = 1$ h. Obviously, a significant increase in the accuracy of DOV determination $\sigma_{\tilde{\xi}(\tilde{\eta})} << 1$ arcsec can be achieved if the DOV values are known exactly not only at the starting point but also at the end $t = T_\Sigma$ point of the route.

3.3.3 DOV Determination in High Latitudes

Consider a possible variation of the inertial geodetic method which can be used to determine the full DOV while maintaining the accuracy of DOV determination in high latitudes. For this purpose, it is proposed to additionally include a specially designed precision GNSS compass with an antenna baseline from 6 to 10 m into the integrated system and replace the differential measurement of longitude with the corresponding heading measurement:

$$z_K(t_{k+1}) = K_{INS}(t_{k+1}) - K_{GNSS}(t_{k+1}) = \Delta K - \delta K_{GNSS}, \tag{3.3.19}$$

where δK_{GNSS} are the errors of the multi-antenna GNSS receiver that are determined mostly by phase measurement noise provided that the reference frames of the SIMU and GNSS antenna module of the receiving equipment are matched in azimuth. Note that the error level of δK_{GNSS} does not practically depend on the latitude of the vehicle location.

Assume that in this case as well, velocity measurements (3.3.5) are used to damp the natural variations of SIMU errors. Then, according to the solutions given in (Emel'yantsev and Stepanov 2016), in the conditions of a quasi-stationary vehicle at an *i*-th route point, the heading measurements (3.3.19) smoothed on the final time interval can be represented as follows:

$$\tilde{z}_{Ki} \cos\varphi_i = -\frac{1}{\Omega}\Delta\overline{\omega}_{bE} + \sin\varphi_i \frac{\Delta\overline{a}_{bE}}{g} + \sin\varphi_i \cdot \eta_i - \delta\tilde{K}_{GNSS}\cos\varphi_i. \tag{3.3.20}$$

From Eqs. (3.3.3) and (3.3.20), it follows that $\hat{\xi}_i = -\tilde{z}_{\varphi i}$, $\hat{\eta}_i = \tilde{z}_{Ki} ctg\varphi_i$, where for the DOV estimation errors, we have:

$$\begin{aligned}
\delta\tilde{\xi}_i &= \frac{1}{\Omega}(-\Delta\overline{\omega}_{bH}\cos\varphi_i + \Delta\overline{\omega}_{bN}\sin\varphi_i) - \frac{\Delta\overline{a}_{bN}}{g} + \delta\tilde{\varphi}_{GNSS}, \\
\delta\tilde{\eta}_i &= -\frac{1}{\Omega\sin\varphi_i}\Delta\overline{\omega}_{bE} + \frac{\Delta\overline{a}_{bE}}{g} - \delta\tilde{K}_{GNSS} ctg\varphi_i.
\end{aligned} \tag{3.3.21}$$

From the solutions obtained, it follows that the proposed method makes it possible to estimate the total values of DOV components, so that there is no need in making reference points at sea, and also the fact that the effect of errors δK_{GNSS} in heading measurements on the accuracy of DOV determination is significantly reduced because the level of these errors does not depend on the latitude.

With the accepted values of SIMU and GNSS receiver errors in position coordinates, as well as the level of the smoothed noise of the precision GNSS compass (which includes the errors in matching the reference frames of the SIMU and GNSS antenna module) of the order of $\delta\tilde{K}_{GNSS} = 5$ arcsec at a latitude of 80°, we have $\tilde{\xi}_i \leq 0.6$ arcsec, $\tilde{\eta}_i \leq 1.06$ arcsec.

3.3.4 Simulation Results

To study the errors of the integrated system in solving the problem under consideration, a simulation model of the SIMU operation was used with discrete recursive algorithms similar to the model given in (Emel'yantsev and Stepanov 2016).

To form the virtual units of SIMU gyros and accelerometers, the following values of the parameters of their error models projected on the axes $x_b y_b z_b$ of the measurement unit were used.

Gyro errors:

- ΔM_{gx}, ΔM_{gy}, ΔM_{gz}—instability of scale factors—random values with RMSE of $10^{-5}\%$;
- $\Delta\overline{\omega}_{xb}$, $\Delta\overline{\omega}_{yb}$, $\Delta\overline{\omega}_{zb}$—systematic error components of the gyroscopes characterizing gyro bias stability from run to run—random values with an RMSE of $3 \cdot 10^{-5}$°/h;
- $\Delta\omega_{xb}$, $\Delta\omega_{yb}$, $\Delta\omega_{zb}$—gyro random error components characterizing in-run bias stability—the first-order Markov processes $\sigma 1_g = 10^{-5}$°/h, $\mu_g = 1/20\ \mathrm{h}^{-1}$;
- the gyro fluctuation error components—discrete white noise with an RMSE of $\sigma 2_g = 10^{-3}$°/h at a frequency of 100 Hz.

Errors of linear accelerometers:

- ΔM_{ax}, ΔM_{ay}, ΔM_{az}—instability of scale factors—random values with an RMSE of $10^{-4}\%$;
- $\Delta\overline{a}_{xb}$, $\Delta\overline{a}_{yb}$, $\Delta\overline{a}_{zb}$—bias stability from run to run—random values with an RMSE of 10^{-5} m/s^2;
- Δa_{xb}, Δa_{yb}, Δa_{zb}—in-run bias stability—first-order Markov processes $\sigma 1_a = 3 \cdot 10^{-6}$ m/s^2, $\mu_a = 1/1\,h^{-1}$;
- fluctuation error components—discrete white noise at the operating frequency with an RMSE of $\sigma 2_a = 10^{-4}$ m/s^2 at a frequency of 100 Hz.

DOV components were represented by Markov processes similar to those in (Nash and Jordan 1978), with $\sigma_\xi = \sigma_\eta = 5$ arcsec, $d = 20$ nm.

The GNSS errors:

- velocity errors —discrete white noise $\sigma_{V_{GNSS}} = 0.01$ m/s at 10 Hz;
- position errors—discrete white noise $\sigma_{S_{GNSS}} = 3$ m at 10 Hz;
- heading errors—deviation $\delta\overline{K}_{GNSS} = 5$ arcsec and discrete white noise $\sigma_{\delta K_{GNSS}} = 3$ arcmin at 10 Hz.

As is known, the majority of currently available GNSS compasses have an accuracy of about $0.2° \cdot 1/L$ (1σ), where $1/L$ is the ratio of the 1-m antenna baseline to the length L of the antenna baseline. This level of errors is primarily due to the noise of phase measurements generated in the GNSS receiver [Novatel].

To set the level of errors of the specialized GNSS compass with an antenna baseline of about 6 m shown in Fig. 3.16, the results of the sea trials of the Vega GNSS compass (developed at the CSRI Elektropribor) with an about 19 m-long antenna

baseline were used (Emel'yantsev et al. 2011). From this research, it follows that the heading fluctuation errors of the stable course were about 3 arcmin (1σ). The angular offset in the heading error is due to the misalignment in the reference frames of the GNSS compass and FOG-based IMU-120 (IXblue, France) used as a reference SIMU.

In the simulation, it is assumed that the reference frames of the precision SIMU and the GNSS compass antenna module are matched with an accuracy of 5 arcsec before going to sea at a point with known DOV components, and that in the process of DOV determination, the position of antenna phase centers is periodically updated, for example, using the procedure described in (Blazhnov et al. 2014).

The following differential measurements are used:

$$
\begin{aligned}
z_{V_j}(t_{k+1}) &= [\nabla S_{j\_INS}(t_{k+1}) - \nabla S_{j\_GNSS}(t_{k+1})]/Tz, \quad (j = E, N, H),\\
z_{\varphi}(t_{k+1}) &= \varphi_{INS}(t_{k+1}) - \varphi_{GNSS}(t_{k+1}),\\
z_{\lambda}(t_{k+1}) &= \lambda_{INS}(t_{k+1}) - \lambda_{GNSS}(t_{k+1}),\\
z_{h}(t_{k+1}) &= h_{INS}(t_{k+1}) - h_{GNSS}(t_{k+1}),\\
z_{K}(t_{k+1}) &= K_{INS}(t_{k+1}) - K_{GNSS}(t_{k+1}).
\end{aligned}
\tag{3.3.22}
$$

These measurements were processed using the Kalman filter with feedback at each measurement epoch.

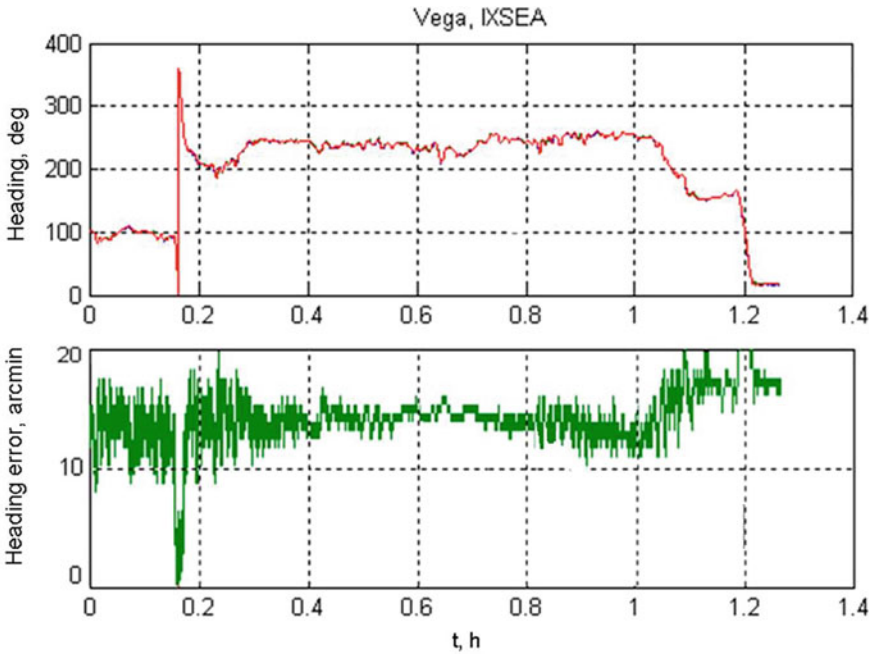

Fig. 3.16 Heading error (arcmin) of Vega GNSS compass as compared with IMU-120

The following approximations were used to describe the error model of the integrated system:

- gyro $\Delta\overline{\omega}_i$ and accelerometer $\Delta\overline{a}_i (i = x_b, y_b, z_b)$ run-to-run and in-run bias stability were approximated by the relevant Wiener processes;
- the DOV components ξ_i, η_i at the i-th point of the path were described by random values with known variances.

Under the assumptions made, the state vector of the simulation model of the system is represented as follows:

$$x^T = \big[\, \alpha\ \beta\ \gamma\ \Delta V_E\ \Delta V_N\ \Delta V_H\ \Delta\varphi\ \Delta\lambda\ \Delta h\ \Delta\overline{\omega}_{xb}\ \Delta\overline{\omega}_{yb}\ \Delta\overline{\omega}_{zb}\ \Delta\overline{a}_{xb}\ \Delta\overline{a}_{yb}\ \Delta\overline{a}_{zb}\ \xi\ \eta\,\big],$$

and the dynamics matrix $F = \big[f_{i,j}\big]$, $\big(i, j = \overline{1, 17}\big)$ is similar to the models given in (Emel'yantsev and Stepanov 2016), taking into account the assumptions made.

The measurement matrix H_{k+1} corresponds to Eq. (3.3.22), whose non-zero elements are the following:

$$H_{1,4} = 1;\ H_{2,5} = 1;\ H_{3,6} = 1;\ H_{4,7} = 1;\ H_{5,9} = 1;\ H_{6,1} = 1. \tag{3.3.23}$$

The simulation was carried out with the following initial data:

- characteristics of the Earth and gravitational field:

  $R = 6371000$ (m) is the mean radius of the Earth;

  $\Omega = 7.2921151467 \cdot 10^{-5}$ (rad/s); $S_{gr}(t_0) = 0$;

  $\mu_g = 3.98603 \cdot 10^{14}$ (m^3/s^2) is the gravitational constant of the Earth;

  $\varepsilon = 2.634 \cdot 10^{25} (m^5/s^2)$ and $\chi = 6.773 \cdot 10^{36} (m^7/s^2)$ are the coefficients of the gravity potential decomposition;
- $\varphi = 80°$; $V_o = 0$ m/s; $K = 0°$ or $K = 180°$, pitching angles are small.

The simulation results are presented in Fig. 3.17:

From the above data, it follows that averaged errors in DOV determination at the i-th point of the path obtained on the forward and reverse courses are ≤ 0.1 arcsec for $\tilde{\xi}_i$ and ≤ 0.75 arcsec for $\tilde{\eta}_i$.

In conclusion, it should be noted that a precision multi-antenna satellite orientation system with two antenna baselines, the one that determines the vehicle's pitching angles, may be an alternative to a GNSS compass. In this case, differential measurements formed on the basis of pitching angles can be used instead of heading measurements. This will completely eliminate the need to use positional measurements (3.3.2) and significantly reduce the accuracy requirements for the SIMU gyroscopes. The proposed version of the method also allows determining the full DOV values in different regions of the World Ocean with no limitations on the observer's latitude.

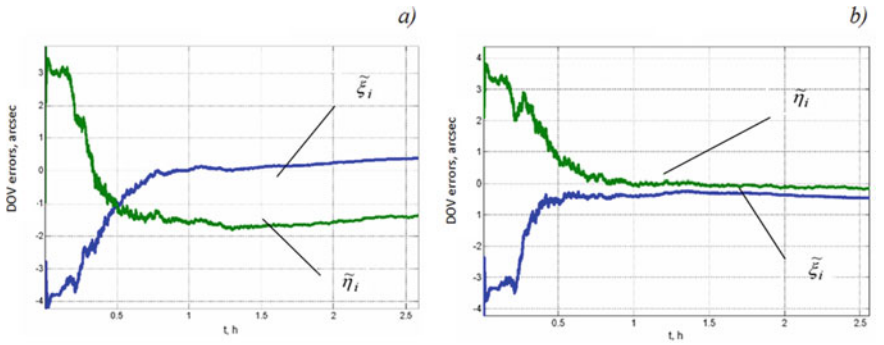

Fig. 3.17 Errors (arcsec) in DOV estimates at $K = 0°$ (**a**) and at $K = 180°$ (**b**)

3.4 Conclusion

Features of the inertial geodetic method for DOV determination have been considered.

It is noted that the use of only velocity and positional differential measurements cannot provide full observability of DOV components since it allows determining only one—the full value—of the DOV component, in the plane of the observer's meridian. As for ZUPT technology, it does not allow determination of full DOV components.

A modified inertial geodetic method, proposed and considered in this section, makes it possible to determine full DOV components in all latitudes, including high latitudes. The modified method is implemented through the use of a precision INS and a specialized GNSS compass with an antenna baseline of about 6 m.

It is shown that in order to achieve an acceptable accuracy in DOV determination, it is necessary to ensure the accuracy of determining the heading angle of about 6 arcsec. It should be noted that the error in determining the heading angle also includes the error in matching the reference frames of the INS and the antenna module of the GNSS compass. Such matching must be carried out with an error of no more than 6 arcsec every time before the vessel leaves the port at a point with known DOV value, and also periodically in the process of DOV determination to precisely determine the position of the phase centers of the GNSS compass receiving antennas.

References

Abakumov VM (1996) Features of the measurement of the angular coordinates of stars by precision optoelectronic systems. J Opt Technol 63(7)

Albertella A, Migliaccio F, Sansó F (2002) GOCE: The Earth gravity field by space gradiometry. Celest Mech Dyn Astron 83(1–4):1–15

Andreev AL (2005) Avtomatizirovannye televizionnye sistemy nablyudeniya (Automated television surveillance systems). Part II, Arifmetiko-logicheskie osnovy i algoritmy (Arithmetic-logic fundamentals and algorithms). St. Petersburg University of Information Technologies, Mechanics and Optics, St. Petersburg

Anuchin ON (1992) Inertial methods for determining the parameters of the Earth's gravity field at sea. Dr. Sci. (Engineering) Dissertation, St. Petersburg

Anuchin ON, Emel'yantsev GI (2003) Integrirovannye sistemy orientatsii i navigatsii dlya morskikh podvizhnukh ob"ektov (Integrated orientation and navigation systems for marine vehicles). CSRI Elektropribor, St. Petersburg

Anuchin ON, Karakashev VA, Emel'yantsev GI (1982) Influence of geodetic uncertainties on the errors of inertial systems. Sudostroenie za Rubezhom 5(185)

ARKeX (2013) eFTG instrument. Next generation gravity gradiometer. http://arkex.com/technology/eftg-instrument/

Astronomicheskii Ezhegodnik na 2009 God (2008) (Astronomical almanac for the year 2009). Nauka, St. Petersburg, p 2008

Avanesov GA, Bessonov RV, Kurkina AN, Lyudomirskii MB, Kayutin IS, Yamshchikov NE (2013) Autonomous strapdown stellar-inertial navigation systems: design principles, operating modes and operational experience. Gyrosc Navig 4(4):204–215

Berezin VB, Berezin VV, Sokolov AV, Tsitsulin AK (2004) Adaptive image reading in an astronomical system on a matrix CCD. Izvestiya vysshykh uchebnykh zavedenii. Radioelektronika (4)

Blazhko SN (1979) Kurs prakticheskoi astronomii (A course in practical astronomy). Nauka, Moscow

Blazhnov BA, Koshaev DA, Petrov PY (2014) Adjusting the data of a two-antenna GNSS system to the IMU-fixed coordinate frame. In: 21st International conference on integrated navigation systems. Elektropribor, St. Petersburg

Bolshakov DV (1997) Development and research of methods for determining the deflections of the vertical in the world ocean based on gravimetric data. Cand. Sci. (Engineering) Dissertation, Moscow

Bouman J (2012) Relation between geoidal undulation, deflection of the vertical and vertical gravity gradient revisited. J Geodesy 86(4):287–304

Brumberg VA, Glebova NI, Lukashova MV, Malkov AA, Pityeva EV, Rumyantseva LI, Sveshnikov ML, Fursenko MA (2004) Trudy Instituta prikladnoi astronomii RAN, no. 10 (Detailed explanation to the astronomical almanac)

Carraz O, Siemes C, Massotti L, Haagmans R, Silvestrin P (2014) Measuring the Earth's gravity field with cold atom interferometers. In: 5th International GOCE user workshop, Paris, France, Nov 2014

Ceylan A (2009) Determination of the deflection of vertical components via GPS and leveling measurement: A case study of a GPS test network in Konya, Turkey. Scien Res Essay 4(12):1438–1444

Chelpanov IB, Nesenyuk LP, Braginskii MV (1978) Raschet kharakteristik navigatsionnykh giropriborov (Calculation of characteristics of navigation gyrodevices). Sudostroenie, Leningrad

DiFrancesco D (2007) Advances and challenges in the development and deployment of gravity gradiometer systems. In: EGM 2007 international workshop innovation in EM, grav and mag methods: a new perspective for exploration, Capri, Italy, April 15–18, 2007

DiFrancesco D, Meyer T, Christensen A, FitzGerald D (2009) Gravity gradiometry—today and tomorrow. In: 11th SAGA biennial technical meeting and exhibition, Swaziland, September 2009, pp 80–83

Dmitriev SP (1991) Vysokotochnaya morskaya navigatsiya (High-precision marine navigation). Sudostroenie, St. Petersburg

Dmitriev SP (1997) Inertsial'nye metody v inzhenernoi geodezii (Inertial methods in engineering geodesy). CSRI Elektropribor, St. Petersburg

Drobyshev NV, Koneshov VN, Papusha IA, Popelensky MY, Rozhkov YE (2006) Recurrent algorithm for determining the vertical deflection using the gravity survey data based on stochastic approach. Giroskopiya i Navigatsiya 2:75–84

Emel'yantsev GI, Stepanov AP (2016) Integrirovannye inertsial'no-sputnikovye sistemy orientatsii i navigatsii (Integrated INS/GNSS orientation and navigation systems). Concern CSRI Elektropribor, St. Petersburg

Emel'yantsev GI, Blazhnov BA, Stepanov AP (2011) Using phase measurements for determining a vehicle's attitude parameters by a GPS-aided inertial system. Gyrosc Navig 2(4)

Emel'yantsev GI, Blazhnov BA, Stepanov AP (2015) Vertical deflection determination in high latitudes using precision IMU and two-antenna GNSS system. Gyrosc Navig 6(4):305–309

Evstifeev MI (2017) The state of the art in the development of onboard gravity gradiometers. Gyrosc Navig 8(1):68–79

Featherstone WE, Lichti DD (2009) Fitting gravimetric geoid models to vertical deflections. J Geodesy 83(6):583–589. https://doi.org/10.1007/s00190-008-0263-4

Forsberg R, Olesen AV, Einarsson I (2015) Airborne gravimetry for geoid determination with Lacoste Romberg and Chekan gravimeters. Gyrosc Navig 6(4):265–270

Gaivoronsky S, Rusin E, Tsodokova V (2013) A comparative analysis of methods for determining star image coordinates in the photodetector plane, Automation & Control: Proceedings of the International conference of young scientists. St. Petersburg State Polytechnical University, St. Petersburg, pp 54–58

Gaivoronsky SV, Rusin EV, Tsodokova VV (2015) Identification of stars in the determination of astronomical coordinates using an automated zenith telescope. Nauchno-Tehnicheskii Vestnik Informatsionnykh Tekhnologii, Mekhaniki i Optiki 15(1)

Gerber MA (1978) Gravity gradiometry: something new in inertial navigation. Astronaut Aeronaut 16:18–26

Gerstbach G, Pichler H (2003) A small CCD zenith camera (ZC-G1)—developed for rapid geoid monitoring in difficult projects. Publications of the Astronomical Observatory of Belgrade 75:221–228

Gonzalez RC, Woods RE, Eddins SL (2004) Digital image processing using MATLAB. Pearson Education

Groves PD (2013) Principles of GNSS, inertial, and multisensor integrated navigation systems, 2nd edn. Artech House

Guo J, Liu X, Chen Y, Wang J, Li C (2014) Local normal height connection across sea with shipborne gravimetry and GNSS techniques. Marine Geophys 35:141–148. https://doi.org/10.1007/s11001-014-9216-x

Halicioglu K, Deniz R, Ozener H (2012) Digital zenith camera system for astro-geodetic applications in Turkey. J Geodesy Geoinf 1(2):115–120

Hirt C (2010) Prediction of vertical deflections from high-degree spherical harmonic synthesis and residual terrain model data. J Geodesy 84:179–190

Hirt C, Bürki B (2002) The digital zenith camera—a new high-precision and economic astrogeodetic observation system for real-time measurement of deflections of the vertical. In: Tziavos I (ed) Proceedings of 3rd Meeting International gravity and geoid commission of the International Association of Geodesy, Thessaloniki, pp 161–166

Hirt C, Bürki B (2006) Status of geodetic astronomy at the beginning of the 21st century. https://www.ife.uni-hannover.de/fileadmin/ife/pdf/events/hirt8.pdf

Hirt C, Seeber G (2008) Accuracy analysis of vertical deflection data observed with the Hannover digital zenith camera system TZK2-D. J Geodesy 82:347–356. https://doi.org/10.1007/s00190-007-0184-7

Hirt C, Bürki B, Somieski A, Seeber G (2010) Modern determination of vertical deflections using digital zenith cameras. J Surv Eng 136(1):1–12

http://www.novatel.com

Jekeli C (1999) An analysis of vertical deflections derived from high-degree spherical harmonic models. J Geodesy 73:10–22

Jekeli C (2011) Accuracy requirements in position and attitude for airborne vector gravimetry and gradiometry. Gyrosc Navig 2(3):164–169
Jekeli C (2012) Geometric reference systems in geodesy, Ohio State University
Karpik AP, Kanushin VF, Ganagina IG, Goldobin DN, Mazurova EM (2015) Analyzing spectral characteristics of the global Earth gravity field models obtained from the CHAMP, GRACE and GOCE space missions. Gyrosc Navig 6(2):101–108
Kim J, Tapley BD (2002) Error analysis of a low–low satellite-to-satellite tracking mission. J Guid Control Dyn 25(6):1100–1106
Kiselev AA (1989) Teoreticheskie osnovaniya fotograficheskoi astrometrii (Theoretical foundations of photographic astrometry). Nauka, Moscow
Koneshov VN, Nepoklonov VB, Stolyarov IA (2012) Using modern geopotential models in studying vertical deflections in the Arctic. Gyrosc Navig 3(4):298–307
Koneshov VN, Nepoklonov VB, Sermyagin RA, Lidovskaya EA (2013) Modern global Earth's gravity field models and their errors. Gyrosc Navig 4(3):147–155
Koneshov VN, Nepoklonov VB, Sermyagin RA, Lidovskaya EA (2014) On the estimation of accuracy for global models of gravitational field of the Earth. Izvestiya. Phys Solid Earth 50(1):127–136
Koneshov VN, Boyarsky EA, Stepanova IE, Afanas'eva LV, Raevskii DN (2015) A new method for calculating the plumb line deflection based on S- and R-approximations: testing in the Atlantics. Izvestiya. Phys Solid Earth 51(1):124–133
Koneshov VN, Evstifeev MI, Chelpanov IB, Yashnikova OM (2016a) Methods for determining deflections of the vertical on a moving base. Gyrosc Navig 7(4):326–336
Koneshov VN, Nepoklonov VB, Pogorelov VV, Solov'ev VN, Afanas'eva LV (2016b) Arctic gravity exploration: State of the art and prospects. Izvestiya. Phys Solid Earth 52(3):443–451
Kovalevsky Zh (2004) Sovremennaya astrometriya (Modern astrometry). Vek 2, Fryazino
Krasnov AA, Sokolov AV, Evstifeev MI, Starosel'tseva IM, Elinson LS, Zheleznyak LK, Koneshov VN (2014) A new generation of gravimetric sensors. Meas Techniques 57(9):967–972
Kudrys J (2009) Automatic determination of the deflections of the vertical—first scientific results. Acta Geodynamics et Geomaterialia 6(3(155)):233–238
Kulikov KA (1969) Kurs sfericheskoi astronomii (A course in spherical astronomy). Nauka, Moscow
LaCoste L, Ford J, Bowles R, Archer K (1982) Gravity measurements in an airplane using state-of-the-art navigation and altimetry. Geophysics 47(5):832–838
Li X, Jekeli C (2008) Ground-vehicle INS/GPS vector gravimetry. Geophysics 73(2):I1–I10
Li F, Fu G-Y, Li Z-X (2001) Plumb line deflection varied with time obtained by repeated gravimetry. Acta Seismol Sin 14(1):66–71
Loparev AV, Yashnikova OM (2012) Application of the method of rectified logarithmic characteristics to smoothing problems. In: Materialy XIV konferentsii molodykh uchenykh "Navigatsiya i upravlenie dvizheniem" (Proceedings of the 14th Conference of young scientists "Navigation and motion control"). Elektropribor, St. Petersburg, pp 257–263
Loparev AV, Stepanov OA, Chelpanov IB (2012a) Using frequency approach to time-variant filtering for processing of navigation information. Gyrosc Navig 3(1):9–19
Loparev AV, Stepanov OA, Yashnikova OM (2012b) On using the method of rectified logarithmic characteristics in smoothing problems. Nauchno-Tehnicheskii Vestnik Informatsionnykh Tekhnologii, Mekhaniki i Optiki 5:151–152
Mangold V (1995) Rate bias INS augmented by GPS: To what extent is vector gravimetry possible. In: Proceedings of the 3rd International workshop High precision navigation, Stuttgart, Germany, pp 169–179
Mantsvetov AA, Sokolov AV, Umnikov DV, Tsytsulin AK (2006) Measurement of coordinates of specially formed optical signals. Voprosy Radioelektroniki 2
Markley FL, Crassidis JL (2014) Fundamentals of spacecraft attitude determination and control. Springer
Maslov IA (1983) Dinamicheskaya gravimetriya (Dynamic gravimetry). Nauka, Moscow

McBarnet A (2013) Gravity gradiometry has graduated! OE Digital Edition. http://www.oedigital.com/geoscience/item/3201-gravity-gradiometry-has-graduated

Medvedev PP, Nepoklonov VB, Lebedev SA, Zueva AN, Pleshakov DI, Rodkin MV (2010) Satellite altimetry. In: Brovar BV (ed) Gravimetriya i geodeziya (Gravimetry and geodesy). Nauchnyi mir, Moscow

Menoret V, Vermeulen P, Landragin A, Bouyer P, Desruelle B (2016) Quantitative analysis of a transportable matter-wave gravimeter. In: 4th IAG Symposium on terrestrial gravimetry: Static and mobile measurements (TG-SMM2016). Elektropribor, St. Petersburg

Mikhailov NV (2014) Avtonomnaya navigatsiya kosmicheskikh apparatov pri pomoshchi sputnikovykh radionavigatsionnykh sistem (Autonomous navigation of spacecraft using satellite radio navigation systems). Politekhnika, St. Petersburg

Moritz H (1980) Advanced physical geodesy. Wichmann, Karlsruhe

Motorin AV, Tsodokova VV (2016) Calculation of accuracy characteristic in the estimation of parameters for the star coordinates transformation. Izvestiya Tul'skogo gosudarstvennogo universiteta, pp 129–141

Mumaw G (2004) Marine 3D full tensor gravity gradiometry. The first five years. Hydro International, September 2004, pp 38–41

Murphy C (2004) The air-FTG™ airborne gravity gradiometer system. In: ASEG-PESA Airborne gravity 2004 workshop, pp 7–14

Nash RA, Jordan SK (1978) Statistical geodesy—An engineering perspective. Proc IEEE 66:532–550

Nassar S (2003) Improving the inertial navigation system (INS) error model for INS and INS/DGPS applications. UCGE Reports, Number 20183, 2003

Nepoklonov VB (2009) On using the new models of the Earth's gravity field in automated survey and design technologies. Avtomatizirovannye Tekhnologii Izyskanii i Proektorovaniya (2, 3)

Nepoklonov VB (2010) Methods to determine deflections of the vertical and quasigeoid heights using gravimetric data. In: Brovar BV (ed) Gravimetriya i geodeziya (Gravimetry and Geodesy). Nauchnyi mir, Moscow, pp 455–464

Nesenyuk LP, Starosel'tsev LP, Brovko LN (1980) Determination of deflections of the vertical using inertial navigation systems. Voprosy Korablestroeniya. Series Navigatsiya i Giroskopiya 46:16–22

Ogorodova LV (2006) Vysshaya geodeziya (Higher geodesy), Part III, Teoreticheskaya geodeziya (Theoretical geodesy). Geodezkartizdat, Moscow

Paturel Y, Honthaas J, Lefevre H, Napolitano F (2014) One nautical mile per month FOG-based strapdown inertial navigation system: A dream already within reach? Gyrosc Navig 5(1):1–8

Pavlis NK (2010) The global gravitational model EGM 2008: Overview of its development and evaluation. In: 10th International IGeS geoid school the determination and use of the geoid, St. Petersburg, Russia, 28 June–2 July, 2010

Peshekhonov VG (2003) Gyroscopes at the beginning of the 21st century. Giroskopiya i Navigatsiya 4:5–18

Peshekhonov VG (2011) Gyroscopic navigation systems: Current status and prospects. Gyrosc Navig 2(3):111–118

Peshekhonov VG, Nesenyuk LP, Starosel'tsev LP, Elinson LS (1989) Sudovye sredstva izmereniya parametrov gravitatsionnogo polya Zemli (Shipborne aids measuring the parameters of the Earth's gravity field). Rumb, Leningrad

Peshekhonov VG, Vasiljev VA, Zinenko VM (1995) Measuring vertical deflection in ocean combining GPS, INS and star trackers. In: Proceedings of the 3rd International workshop High precision navigation, Stuttgart, Germany, pp 180–185

Peshekhonov VG, Sokolov AV, Elinson LS, Krasnov AA (2015) A new air-sea gravimeter: development and test results. In: 22nd International conference on integrated navigation systems. Elektropribor, St. Petersburg

Peshekhonov VG, Sokolov AV, Stepanov OA, Krasnov AA, Stus' YF, Nazarov EO, Kalish EN, Nosov DA, Sizikov IS (2016) Concept of an integrated gravimetric system to determinate the

absolute gravity value aboard vehicles. In: 4th IAG Symposium on terrestrial gravimetry: Static and mobile measurements (TG-SMM 2016). Elektropribor, St. Petersburg, pp 61–67
Revnivykh SG (2012) Development trends in global satellite navigation. Gyrosc Navig 3(4):215–222
Rezo M, Markovinović M, Šljivarić M (2014) Influence of the Earth's topographic masses on vertical deflection. Tehnički Vjesnik 4(21):697–705
Richeson JA (2008) Gravity gradiometer aided inertial navigation within non-GNSS environments. PhD Thesis, University of Maryland, Washington, USA
RMG 29-2013. State system for ensuring the uniformity of measurements. Metrology. Basic terms and definitions
Rukovodstvo po astronomicheskim opredeleniyam: Geodezicheskie, kartograficheskie instruktsii, normy i pravila (A guide on astronomical determinations: Geodetic, cartographic instructions, norms, and rules) (1984) Nedra, Moscow
Rummel R, Balmino G, Johannessen J, Visser P, Woodworth P (2002) Dedicated gravity field missions—Principles and aims. J Geodyn 33(1):3–20
Rummel R, Yi W, Stummer C (2011) GOCE gravitational gradiometry. J Geodesy 85(11):777–790
Salychev O, Voronov V, Lukianov V (1999) Inertial navigation systems in geodetic application: L.I.G.S. experience. In: International conference on integrated navigation systems
Schultz OT, Winokur JA (1969) Shipboard or aircraft gravity vector determination by means of a three-channel inertial navigator. J Geophys Res 74(20):4882–4896
Seeber G (2003) Satellite geodesy: foundations, methods and applications, 2nd edn. de Gruyter, Berlin, New York
Semenov IV (2012) Control system of gyrostabilized platform of the mobile vertical gradiometer. Cand. Sci. (Engineering) Dissertation, St. Petersburg
Shimbirev BP (1975) Teoriya figury Zemli (Theory of the Earth's figure). Nedra, Moscow
Smith DA, Holmes SA, Li X, Guillaume S, Wang YM, Bürki B, Roman DR, Damiani TM (2013) Confirming regional 1 cm differential geoid accuracy from airborne gravimetry: The geoid slope validation survey of 2011. J Geodesy 87(10–12):885–907. https://doi.org/10.1007/s00190-013-0653-0
Sokolov AV, Stepanov OA, Krasnov AA, Motorin AV, Koshaev DA (2016) Comparison of stationary and nonstationary adaptive filtering and smoothing algorithms for gravity anomaly estimation on board the aircraft. In: 4th IAG Symposium on terrestrial gravimetry: Static and mobile measurements (TG-SMM 2016). Elektropribor, St. Petersburg, pp 53–60
Soroka AI (2010) Development of onboard meters of the geopotential second derivatives. In: Brovar BV (ed) Gravimetriya i geodeziya (Gravimetry and geodesy). Nauchnyi mir, Moscow, pp 300–310
Šprlák M, Novák P (2014) Integral transformations of deflections of the vertical onto satellite-to-satellite tracking and gradiometric data. J Geodesy 88:643–657
Staroseltsev LP (1995) Analysis of requirements for the gyroscopic stabilization system of a gravity gradiometer. Giroskopiya i Navigatsiya 3:30–33
Staroseltsev LP, Yashnikova OM (2016) Estimation of errors in determining the parameters of highly anomalous Earth's gravitational field. Nauchno-Tehnicheskii Vestnik Informatsionnykh Tekhnologii, Mekhaniki i Optiki 16(3):533–540
Stepanov OA (2010) Osnovy teorii otsenivaniya s prilozheniyami k zadacham obrabotki navigatsionnoi informatsii (Fundamentals of the estimation theory with applications to the problems of navigation information processing). Part 1, Vvedenie v teoriyu otsenivaniya (Introduction to the estimation theory). Concern CSRI Elektropribor, St. Petersburg
Stepanov OA (2012) Osnovy teorii otsenivaniya s prilozheniyami k zadacham obrabotki navigatsionnoi informatsii (Fundamentals of the estimation theory with applications to the problems of navigation information processing). Part 2, Vvedenie v teoriyu fil'tratsii (Introduction to the filtering theory). Concern CSRI Elektropribor, St. Petersburg
Stepanov OA, Loparev AV, Chelpanov IB (2014) Time-and-frequency approach to navigation information processing. Autom Remote Control 75(6):1090–1108

Sugaipova LS (2015) Planned satellite gravimetric projects. Izvestiya vuzov. Geodeziya i Aerofotos"emka 6:3–8
Tian L, Guo J, Han Y, Lu X, Liu W, Wang Z, Wang B, Yin Z, Wang H (2014) Digital zenith telescope prototype of China. Chin Sci Bull 59(17):1978–1983
Timochkin SA (2013) Methodical errors in constructing the astronomical vertical in an inertial navigation system damped by the meter of speed over ground. In: Materialy XV konferentsii molodykh uchenykh "Navigatsiya i upravlenie dvizheniem" (Proceedings of the 15th Conference of young scientists "Navigation and motion control"). Elektropribor, St. Petersburg, pp 38–45
Torge W (2001) Geodesy, 3rd edn. de Gruyter, Berlin
Troitskii VV (1994) Determination of deflections of the vertical at sea using near-zenith stars. Cand. Sci. (Engineering) Dissertation, St. Petersburg
Tse CM, Baki Iz H (2006) Deflection of the vertical components from GPS and precise leveling measurements in Hong Kong. J Surv Eng 123(3):97–100. https://doi.org/10.1061/_ASCE_0733-9453_2006_132:3_97
Tsodokova VV, Gaivoronsky SV, Tarasov SM, Rusin EV (2014) Determination of astronomical coordinates with an automated zenith telescope. In: Materialy XVI konferentsii molodykh uchenykh "Navigatsiya i upravlenie dvizheniem" (Proceedings of the 16th Conference of young scientists "Navigation and motion control"), St. Petersburg: Elektropribor, pp 269–276
Tsvetkov AS (2005a) Rukovodstvo po prakticheskoi rabote s katalogom Hipparcos (Instructions for using the Hipparcos catalog), St. Petersburg
Tsvetkov AS (2005b) Rukovodstvo po prakticheskoi rabote s katalogom Tycho-2 (Instructions for using the Tycho-2 catalog), St. Petersburg
Uralov SS (1980) Kurs geodezicheskoi astronomii (A course in geodetic astronomy). Nedra, Moscow
Vasiliev VA, Zinenko VN, Kogan LB, Savik VF, Peshekhonov VG, Troitskii VV, Yanushkevich VE (1991a) Shipborne astrogeodetic system for determining deflections of the vertical. Sudostroitel'naya promyshlennost' (Shipbuilding Industry), Series Navigatsiya i giroskopiya (Navigation and Gyroscopy) 2:51–56
Vasiliev VA, Zinenko VM, Kogan LB, Peshekhonov VG, Savik VF, Romanenko SK (1991b) High-latitude automatic astrolabe. Kinematika i Fizika Nebesnykh Tel 7(3)
Vitushkin LF (2015) Absolute ballistic gravimeters. Gyrosc Navig 6(4):254–259
Volfson GB (1997) Methods to solve the problem of creating an onboard gravity variometer. D.Sci. (Engineering) Dissertation, St. Petersburg
Volgyesi L (2005) Deflections of the vertical and geoid heights from gravity gradients. Acta Geodaetica et Geophysica Hungarica 40(2):147–157
Watts AB, Horai K, Ribe NM (1984) On the determination of the deflection of the vertical by satellite altimetry. Mar Geodesy 8(1–4):85–127
Yakushenkov YG, Solomatin VA (1986) Comparison of some methods for determination of the image coordinates using multielement radiation detectors. Izvestiya vysshikh uchebnykh zavedeniy. Priborostroenie 9:62–69
Yole Development Report (2012) Gyroscopes and IMUs for defense, aerospace & industrial
Zahzam N, Bonnin A, Theron F, Cadoret M, Bidel Y, Bresson A (2016) New advances in the field of cold atom interferometers for onboard gravimetry. In: 4th IAG Symposium on terrestrial gravimetry: Static and mobile measurements (TG-SMM2016). Elektropribor, St. Petersburg
Zheleznyak LK, Koneshov VN (2007) Studying the gravitational field of the world ocean. Her Russ Acad Sci 77(3):217–226

Chapter 4
Studying the Gravity Field in Hard-to-Reach Areas of the Earth

V. Koneshov, V. Pogorelov, V. Solov'ev, A. Krasnov, A. Sokolov, A. Golovan, Yu. Smoller, and S. Yurist

Abstract This chapter provides a historical overview of gravimetric surveys in the Arctic. Findings from modern airborne gravimetric surveys in the Arctic carried out by Russian and international companies are analyzed. Marine and airborne gravimetric surveys using the Chekan gravimeters in hard-to-reach areas of the Earth, such as the Geographic North Pole, the Greenland shelf, coastal seas of the Antarctic, and the Himalayas are addressed. Polar versions of the GT-2A gravimeter with the necessary modifications of equipment and software for all-latitude applications are covered. Application of multi-antenna GNSS receivers in these areas is analyzed, and the method of transition to quasi-geodetic coordinates is described.

Keywords Arctic gravimetric surveys · Gravimetric surveys in hard-to-reach areas · Gravimeter Chekan · Gravimeter GT-2A

V. Koneshov · V. Pogorelov · V. Solov'ev
Schmidt Institute of Physics of the Earth under the Russian Academy of Sciences, Moscow, Russia

A. Krasnov (✉) · A. Sokolov
Concern CSRI Elektropribor, St. Petersburg, Russia
e-mail: anton-krasnov@mail.ru

A. Sokolov
ITMO University, St. Petersburg, Russia

A. Golovan
Lomonosov Moscow State University, Moscow, Russia

Yu. Smoller · S. Yurist
Gravimetric Technologies, Moscow, Russia

V. G. Peshekhonov and O. A. Stepanov (eds.), *Methods and Technologies for Measuring the Earth's Gravity Field Parameters*, Earth Systems Data and Models 5,
https://doi.org/10.1007/978-3-031-11158-7_4

Introduction

This Chapter is devoted to the study of the gravity field in remote areas of the Earth. It includes three sections.

Section 4.1 provides a historical overview of gravimetric surveys in the Arctic. Measurements conducted on drifting ice, onboard submarines and icebreakers are described. The results of modern airborne gravimetric surveys in the Arctic carried out by Russian and international companies are analyzed.

Section 4.2 presents the results of marine and airborne gravimetric surveys using the Chekan-series gravimeters in hard-to-reach areas of the Earth, such as the Geographic North Pole, the Greenland shelf, coastal seas of the Antarctic, and the Himalayas. The methodological features of surveys using Chekan gravimeters, estimation of the accuracy and resolution of measurements are discussed.

Section 4.3 is devoted to the versions of the GT-2A gravimeter designed to conduct airborne gravimetric measurements in polar regions of the Earth. The experience in using multi-antenna GNSS receivers in these areas is analyzed, and the method of transition to quasi-geodetic coordinates used in the solution of this problem is described. The test results for the GT-2AQ gravimeter with a four-antenna GNSS receiver installed on a pickup truck are presented.

4.1 State of Knowledge of the Gravity Field in the Arctic

The data on the Earth's gravity anomalies in the Arctic were very fragmented and obtained using various methods by different authors and in various years (using diverse instruments with different errors). Moreover, the coordinate provision of these studies in the Arctic imposed its specifics and introduced errors. For these reasons, the errors of the GA models are present most of all in the polar cap of the Arctic. Due to the ice cover and remoteness from the bases, the detailed gravimetric area surveys in high latitudes can only be conducted onboard an aircraft.

4.1.1 Brief Historical Overview of Russian Gravimetric Surveys in the Arctic

To discuss the current state of knowledge of the Arctic gravity field and the potential for further research, a few words should be said about the historical sequence of gravimetric surveys in the Arctic and the significance of their results.

Measurements on drifting ice. In the mid-1950s, the USSR Ministry of Defense approached the Main Department of Geodesy and Cartography (GUGK) and the Academy of Sciences with a proposal to perform the gravimetric area survey of the Soviet sector of the Arctic Ocean. Extremely short performance time—only two years—was imposed. Because of the Arctic meteorological conditions, the

survey could be conducted only in spring (from March to May), when the polar night had already ended, but the ice was still strong enough to land heavy aircraft. This kind of work had never been carried out in the global practice of gravimetric surveys. GUGK refused to perform the studies for some reason, and it was decided to employ the Geophysical Institute of the USSR Academy of Sciences and the Military Topographic Service of the Soviet Army.

In a short time the methodology was developed, the required gravimetric instrumentation and auxiliary equipment for gravity measurements on drifting ice were prepared. By the Order of the Council of Ministers of the USSR No. 645 dated February 3, 1955, and the Resolution of the Council of Ministers of the USSR No. 383–232 dated March 3, 1955, it was "proposed to arrange a High-latitude airborne expedition of 1955 to conduct gravimetric and magnetic observations on drifting ice in the area north of Spitsbergen, Franz Josef Land, and Severnaya Zemlya, including the strip above the underwater Lomonosov Ridge and the area of the North Pole." This expedition was named the High-Latitude Airborne Expedition Sever-7.

The geophysical party had to conduct the area gravimetric survey with a density of 1 observation point per 10,000 km^2. The plan included the gravity determination at 105 points more or less uniformly distributed in the western part of the Central Arctic, including the North Pole. Gravimetric measurements were taken with the SN-3 pendulum gravimeters, and the geodetic referencing of gravity stations was performed with the OT-02 theodolite.

The expedition Sever-7 worked from March 20 to June 10, 1955, and, despite the harsh conditions of the Arctic, the geophysical party successfully completed the planned works. A total of 117 gravimetric stations were determined in the western sector of the Polar Basin. The accuracy of gravity survey was about 1.2 mGal. The station coordinates were obtained with RMS errors (RMSE) of 0.1 arcmin by planets and stars and 0.6 arcmin by the Sun.

By the Order of the Council of Ministers of the USSR No. 6410 dated September 1, 1955, the surveys were continued in the eastern sector of the Soviet Arctic. One hundred and sixty-four main gravity stations and a number of additional gravity stations were determined within 45 days, from April 4 to May 18, 1956, during the next Sever-8 expedition. The error of gravity survey was of the same order as in 1955. That is how the first gravimetric 1:1,000,000 map of the Soviet sector of the Arctic Ocean was obtained.

Underwater surveys of the Arctic. Regular underwater surveys in the World Ocean started in 1955 following the Resolution of the USSR Council of Ministers on the studies of the gravity field, the figure and structure of the Earth, for which purpose the Navy regularly provided combatant submarines. In the same year, the Sternberg Astronomical Institute (SAI MSU) organized an expedition to measure gravity in the Barents, Kara, and Pechora Seas (Stroyev et al. 2007). Thirty-eight stations were determined accurate to ±6–8 mGal. The next year, the survey profile ran in the Bering Sea with going out to the Chukchi Sea. The survey was conducted with the same gravimeters SZ-1 and SZ-2, and the GAK land gravimeter to reference the berthing measurements to the stations of the USSR reference gravimetric network. To estimate the effect of rolling, the measurements were taken at 30–120 m depths,

during the submarine motion and grounding. Despite the stormy weather, the Faye anomalies were calculated accurate to ±4 and ±6.2 mGal for pendulum instruments and gravimeters, respectively. The study of the dependence of the Brown correction for the effect of disturbing acceleration on depth showed that the depth of 60 m is sufficient for observations in stormy weather, whereas it can be half as large in good weather (Stroyev et al. 2007).

In 1957, the expedition jointly organized by the SAI MSU, the Central Research Institute of Geodesy, Airborne Survey and Cartography (TsNIIGAiK) with the participation of VNIIGeofizika conducted research in the Barents, Norwegian, Greenland Seas, and in the Atlantic Ocean. The route passed from Murmansk to the equator bypassing Iceland, making a 2.5-month independent transit. Pendulum instruments and auxiliary long-period pendulums developed by TsNIIGAiK were used during the expedition. Most of measurements were carried out at a depth of 100 m; specific features of measurements at depths from 30 to 120 m were investigated. To more accurately determine the submarine geographic coordinates, the behaviour of the main currents was studied, which helped to analyze their influence on the determination of the Eotvos correction (Stroyev et al. 2007). During the survey, the submarine passed all the climatic zones, took measurements at 119 stations with a gravity error of ±4–5 mGal and estimated 24 stations obtained by Vening Meinesz, Girdler, and TsNIIGAiK.

Underwater marine surveys were conducted by both Russian and international scientists in almost all latitudes of the World Ocean. International companies have gained positive experience in underwater research, the results of which are partially open for the scientific community. Among these initiatives, the SCICEX project (Science Ice Expedition) (Pyle et al. 1997) is worth mentioning.

Gravimetric measurements using icebreakers. Considering the potential of marine shipborne gravimetry, effective survey methods were developed to be applied onboard above-water carriers, such as icebreakers. As noted in (Litinsky 1972), gravimetric surveys onboard icebreakers can be quite widely applied, since a great number of mid-latitude seas freeze in winter along with polar water areas. Surveys onboard icebreakers can provide measurements with almost any resolution and can be supported by high-precision positioning using radio navigation and satellite systems. The first gravity measurements in the Arctic using the pendulums were carried out as early as in 1893–1896 by Nansen's expedition during the Fram's drift from the New Siberian Islands to the Svalbard Archipelago. The obtained measurements suffered from rather high systematic errors due to the structural imperfection of the measuring instruments. In 1937–1940 the Russian marine surveys were conducted onboard the icebreakers Georgy Sedov and Sadko drifting in the high Arctic latitudes, using three-pendulum instruments designed by Vening Meinesz (Zhonglovich 1950). The measurements were performed with errors comparable to those of submarine gravimetric observations.

With the development of marine survey practice, the first measurements onboard ice class ships were conducted by the First Soviet Antarctic Expedition (1955) and the High-Latitude Greenland Expedition (1956) onboard the diesel-electric vessel Ob (Gaynanov 1961; Chesnokova and Grushinsky 1961). The measurements were

taken with pendulum instruments (Cambridge and Askania Werke) and provided satisfactory results. It was shown that due to the strong vibration of the engines, observations onboard such vessels should be carried out in drift with the diesel generators off and under favorable weather conditions, or when the vessel enters the ice to avoid the influence of high swell in open waters.

The first high-precision marine gravimetric survey in the North Pole area was conducted in the central part of the Arctic Ocean using two similar gravimetric systems, Chekan-AM and Shelf-E developed by Concern CSRI Elektropribor (Blazhnov et al. 2002; Krasnov et al. 2014b). It was integrated with seismic and bathymetric surveys using a single grid of survey lines (Kazanin et al. 2016). As a result, 36 gravimetric lines were obtained and the catalog of 71,179 gravimetric stations was created. The estimated RMSE at the intersection points of survey lines was 0.28 mGal for Shelf-E and 0.72 mGal for Chekan-AM (Sokolov et al. 2016b). The results of this survey are discussed in detail in Sect. 4.2.

In gravimetric surveys, icebreakers can be applied as convoying and basing ships for complex expeditions and groups conducting airborne surveys onboard helicopters. Direct gravimetric observations are recommended onboard drifting icebreakers, mainly for organization of floating gravity reference stations to support airborne surveys.

4.1.2 Modern Russian Arctic Airborne Gravimetry

Several solutions have been recently implemented in Russia in the sphere of airborne gravimetry in the Arctic.

The GT-2A gravimeter has been upgraded based on the airborne survey experience in the Arctic (see Sect. 4.3 for details). The gravimeter software has been improved by the Laboratory of Control and Navigation of the Department of Mechanics and Mathematics of the Lomonosov Moscow State University. The Institute of Physics of the Earth RAS has proposed a number of improvements to the measuring system (see (Koneshov et al. 2016), and Sect. 1.3) and experimentally studied the gravimeter operability in latitudes up to 78°N using modern high-precision positioning technologies. In addition, Aerogeophysica has refined the surveying techniques, which allowed area survey with a scale of no worse than 1:1,000,000 in the North of the Kara Sea up to 81°N (Mogilevsky et al. 2015).

Chekan series gravimeters developed by Concern CSRI Elektropribor (see Sect. 1.2) and widely used in marine gravimetry are also applied to modern airborne area measurements, though less often than GT-2A gravimeters.

To support the Russian Federation claims to extend the Russian continental shelf in the Arctic, VNIIOkeangeologia conducted airborne magnetic and gravity surveys above the Lomonosov Ridge and Mendeleev Rise in 2005 and 2007 (Ekspeditsionnye issledovaniya 2006).

Airborne gravimetric studies of 2005 were carried out with the airborne gravimetric system including three string gravimeters GAMS, GSD-M and a string barometer (developed by VNIIGeophyzika, Russia). Airborne surveys above the Mendeleev Rise were carried out over an area of 240 × 640 km between 75° and 78°N using a system of submeridional lines with 10 km spacing and orthogonal crosslines with an interval of 20–30 km. A number of additional submeridional survey lines that shortened the distance between the survey lines to 5 km were passed to ensure a more detailed study of the central part of the area.

The airborne gravimetric survey by VNIIOkeangeologiya in 2007 was conducted using a more modern gravimeter Chekan-AM. The 100 × 720 km survey area was located along the Arctic-2007 geotraverse in the junction zone of the Lomonosov Ridge with the adjacent shelf between ~78° and 84°N (Palamarchuk et al. 2008; Russian Arctic Geotraverses 2011). The Chekan-AM gravimeter demonstrated stable performance in high latitudes, and a 1:1,000,000 map of EGF anomalies was constructed (Fig. 4.1). The details of conducting this survey are discussed in Sect. 4.2.

In 2006–2013, IPE RAS Graviinertial Measurements Laboratory successfully completed aerogravimetric surveys above the southern, central and north-western parts of the Novaya Zemlya Archipelago and the adjacent water areas of the Barents and Kara Seas. The measurements were conducted using GT-1A/2A airborne gravimetric systems installed onboard an airborne laboratory based on Antonov AN-26 BRL (Drobyshev et al. 2008, 2009, 2011). The total area of 180,000 km^2 was surveyed at a scale of 1:200,000, and relevant maps were constructed.

In 2011–2013, the IPE RAS conducted an area survey with a scale of 1:200,000 over 60,000 km^2 in the central part of the Kara Sea.

The most recent Russian airborne gravimetric surveys in the Arctic have been conducted by Aerogeophysica. The objective of the surveys was to solve prospecting problems and compile individual sheets of the new edition of the state geological map.

In 2011–2013, Aerogeophysica prepared nine survey maps at the scale 1:1,000,000 for the eastern coast of the Russian sector of the Arctic within 132°E to 174°W, 68°N to 72°N: R-53…R-01. Surveys with GT-2A gravimeters were integrated with airborne magnetic studies onboard AN-26 and AN-30 aircraft. By comparing the aerogravimetric measurements with the results of 1:200,000 land surveys conducted in 1970–1990s, and based on internal convergence, the accuracy of the aerogravimetric survey was estimated at 0.6–0.7 mGal (Mogilevsky and Kontarovich 2015). Aerogeophysica has also completed high-latitude surveys in the northern part of the Kara Sea (up to 81°N), in the western part of the Laptev Sea, north of the New Siberian Islands and in the south-east of the East Siberian Sea within a number of licence areas with promising hydrocarbon fields.

Airborne gravimetric survey in the Arctic is a very difficult task. This is not only due to the specific operation of gravimetric systems in this region and the refinement of the surveying methodological techniques, but also due to the lacking base airfields in a number of Arctic regions. For this reason, 1:200,000 maps have not yet been obtained for the junction areas of the Lomonosov and Mendeleev ridges and the shelf zone of Russia.

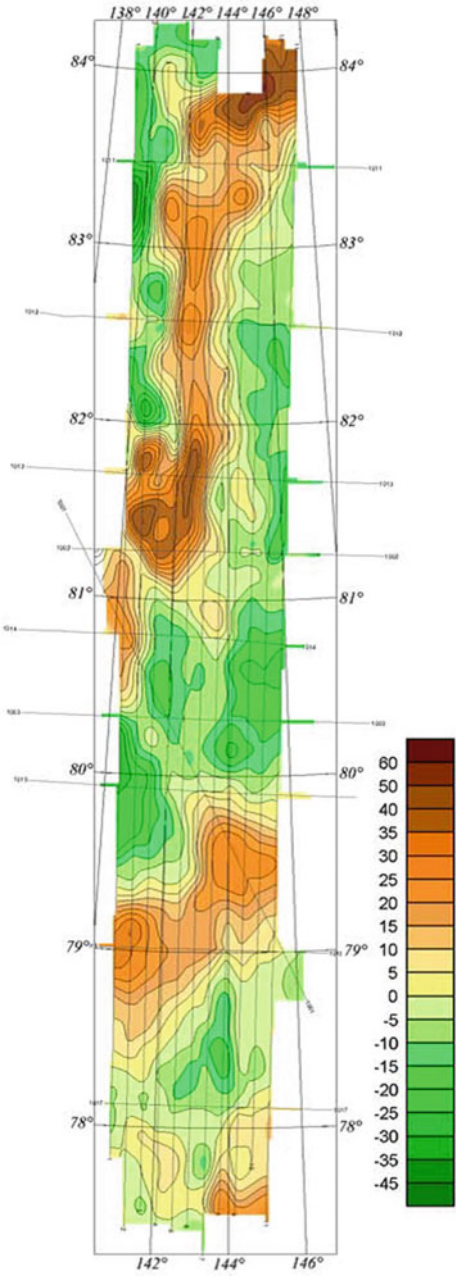

Fig. 4.1 EGF anomaly map based on Chekan-AM data

4.1.3 Modern International Arctic Airborne Gravimetry

About 30 years ago, airborne gravimetry began to be commonly used in international gravity field studies. During this time, the western researchers have carried out a significant amount of airborne gravimetric surveys in the Arctic.

For example, the Naval Research Laboratory, Washington, DC, USA, has surveyed more than 210,000 linear km covering almost 2/3 of the Arctic Ocean within the Arctic Airborne Gravity Measurement Program (Fig. 4.2) (Brozena and Salman 1996). The results of these studies, along with other gravity data available at the time, were applied to develop EGF integrated models using satellite measurements of projects ERS 1 and 2 that ensured data coverage up to 81.5°N.

To determine the resolution of aerogravimetric studies and the accuracy of the ERS 1998 integrated global model of the Earth's gravity field, a comparative analysis was performed for two groups of long lines, and the correlation was determined between them, airborne gravity surveys of 1996, and the Canadian ice surveys along these lines. Airborne gravimetric studies were conducted with LaCoste & Romberg gravimeters (USA). The first group of three lines of about 600 km oriented NNW between 71° and 75°N in the area of the Beaufort Sea demonstrated a good qualitative agreement between the measurements obtained by all three methods. Despite the fact that the standard deviation (SD) between ice observations and airborne survey data is about one-third lower than with the ERS 1998 model (1.86 and 2.64 mGal,

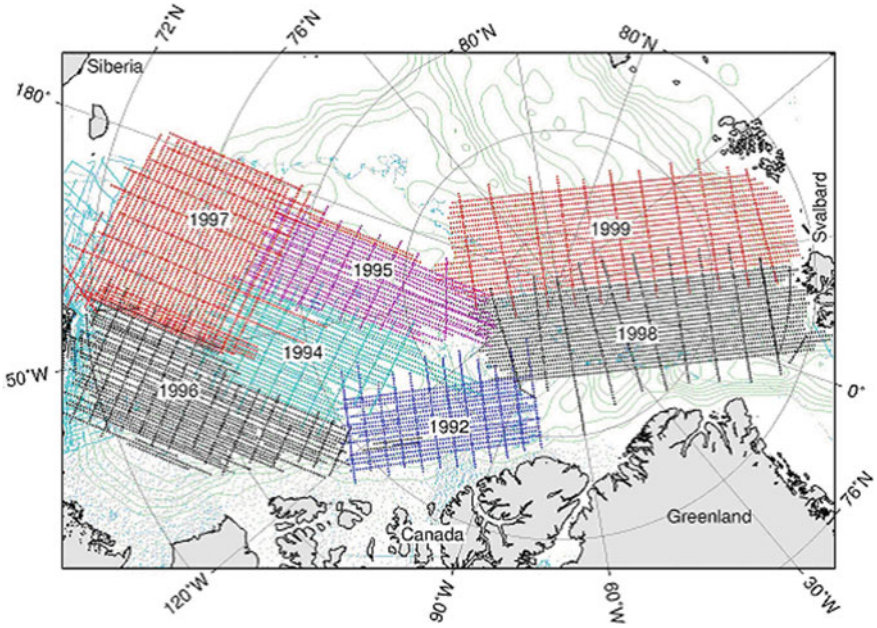

Fig. 4.2 Airborne gravimetric measurements by the Naval Research Laboratory

respectively), the SD between the model data and airborne survey data was 2.55 mGal. This indicates that when creating the global EGF model based on satellite data, the detailed ice and marine survey data could greatly contribute to the refinement of the final model values in the survey area. This assumption is also confirmed by the short-period anomalies in the values of the ERS model with the resolution of the gravimetric data estimated at 15 km. In this regard, airborne and marine and ice survey data (with a grid density of one station per 3–10 km^2) can be considered as independent measurements, and deviations of the ERS 1998 model can be considered as regional features. For details on estimating the accuracy of global EGF models in the Arctic, see Sect. 6.1 of this monograph.

In 1999–2001, Rene Forsberg and his colleagues carried out airborne surveys offshore Greenland with the RMSE reaching ~2 mGal for the spatial resolution of about 6 km (Forsberg et al. 2011). This exceeded the accuracy of earlier measurements greatly (RMSE ~5 mGal with a spatial resolution of ~20 km). In 1999–2001, measurements were also carried out near the Svalbard Archipelago. The new airborne gravimetric data well correlated with the results of marine surveys of the 1990s. The studies were applied to check and refine the earlier surveys conducted on various carriers during the ArcGP-2002 (Arctic Gravity Project) creating a detailed global free air EGF $5 \times 5'$ model (Fig. 4.3) (Forsberg and Keyon 2004).

Due to the unique opportunity to use airborne gravimetric data of the large-scale Arctic Airborne Gravity Measurement Program, as well as other available gravimetric data, the ArcGP-2002 project covered the area above 81.5°N not covered by the ERS mission data. The model first version was supplemented with the icebreaker gravimetric survey data, detailed gravimetric data for the Russian sector of the Arctic shelf, land measurements for Siberia (VNIIOkeangeologia, PMGRE, TsNIIGAiK), ICESat satellite mission data extending the satellite coverage to 86°N, and CryoSat data to create the improved EGF model ArcGP Ver. 2.0.

The second revision of the Arctic gravity field model mentioned above became the basis for the global EGF model EGM2008. This global model created using GOCE data showed a significantly increasing correlation of the digital geoid models for the Arctic and Antarctic polar caps above 83°N (Forsberg et al. 2011). To solve this problem in the South Pole area, R. Forsberg's group proposed to conduct an airborne gravimetric survey which, along with satellite data, would improve the quality of the global field model EGM2008 for high latitudes.

Due to the relevance of redefining the outer border of the continental shelf in the Arctic and studying the structure of the Earth's crust near the Lomonosov Ridge, the western researchers carried out airborne gravity and magnetic surveys over an area of over 550 thousand square km within the Lomgrav-09 project. The 2009 survey also covered the North Pole area claimed by Russia, Canada, the USA, Norway, and Denmark.

Airborne gravimetric measurements were carried out with the improved LaCoste & Romberg S99 and SL1 airborne gravimeters using a system of lines located subparallel to the Lomonosov Ridge on the Norwegian side of the Arctic Ocean with a 12–15 km spacing and three crosslines. The survey grid was chosen so that to cover a rather large area in the vicinity of the Lomonosov Ridge, as well

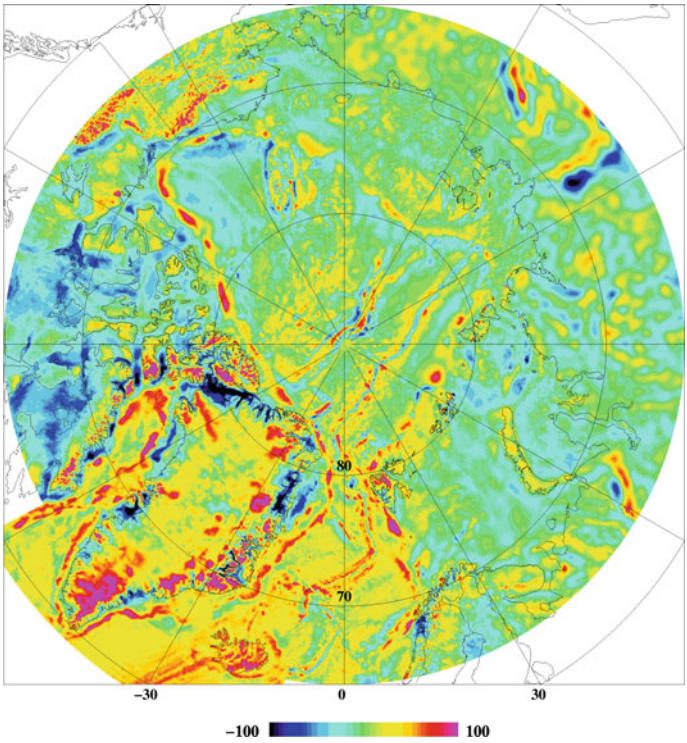

Fig. 4.3 Arctic gravitational field based on ArcGP project data

as due to the location of airports provided with sufficient amounts of fuel. The same factors probably explain the small number of crosslines (3 survey lines across the Alpha and the Lomonosov ridges). The survey RMSE of 2.4 mGal was obtained in the office processing of the airborne gravimetric data. The data from this airborne survey were compiled with the earlier measurements carried out on land, ice, and moving vehicles to create a new free-air GA map with a resolution of 2.5 km and 18 km correlation length. The use of earlier data in the final model of free-air gravity anomalies sometimes led to discrepancies in the anomaly amplitudes of more than 15 mGal compared with the LOMGRAV-09 measurements. The authors also note that the maximum discrepancies reached about 80 mGal and related to the airborne gravity surveys of 1998–1999 and to the Danish-Canadian ice surveys. This resulted in the need to remove these data from further analysis.

Based on the results obtained in the Greenland sector of the high-latitude Arctic (between 80° and 89°N), dense systems of linear positive anomalies were detected running along the central part of the Lomonosov Ridge, some of which were up to 300 km long. Some linear anomalies not represented in the modern seabed terrain were interpreted by the authors—based on the obtained seismic data—as presumably rift structures buried under Cenozoic sediments. New gravimagnetic data, according

to the authors, do not confirm the existence of a significant strike-slip or transform fault between the Lomonosov Ridge and the polar margin of the Lincoln Sea. The above-discussed EGF studies were used along with available seismic and other geological and geophysical data to determine the origin and tectonic structure of the Amundsen Basin and to redefine the position of the continental margin near Greenland.

4.1.4 Conclusions

Analysis of gravimetric surveys in hard-to-reach Arctic areas has shown that the conducted research is not extensive enough to adequately estimate the errors in the modern models of the gravitational field of the planet polar cap, and more detailed surveys are recommended in these areas. For this specific remote area of the Earth, airborne gravimetric surveys should be considered as the main method of gravimetric studies. Studying the field of the region will help solve one of the most important fundamental problems: refining the Earth's figure in the Arctic.

4.2 The Results of the Gravimetric Surveys with Chekan Gravimeters in Hard-to-Reach Areas

To date, polar areas, mountain ranges, as well as transit zones at the boundary of sea and land remain the least studied areas of the Earth in terms of GAs. The development of gravimetric systems and satellite technologies stimulated active industrial and scientific gravimetric surveys in such hard-to-reach areas at the beginning of the twenty-first century. Yet, the main method of measurement is, as before, determination of gravity increments on survey lines carried out with relative gravimeters installed onboard marine and airborne carriers, since other gravimetric methods do not provide the required spatial resolution.

The main surveys using the Chekan-AM gravimeter are traditionally conducted as a secondary geophysical method used in explorations for hydrocarbons on the sea shelf (Krasnov et al. 2014a). However, gravimeters of the Chekan series have recently been used to study the EGF in hard-to-reach areas. Section 4.2 discusses the results of such works and the methodological features of their implementation.

4.2.1 Marine Gravimetric Surveys in the Polar Regions

As part of the Russian Antarctic Surveys, the Polar Marine Geosurvey Expedition annually conducts gravimetric surveys of the marginal seas of the Antarctic onboard

the Akademik A. Karpinsky research vessel. In the period from 2005 to 2015, the surveys were conducted using two systems, Chekan-AM and Cheta-AGG, and since 2016, two Chekan-AM gravimeters have been used.

An overview map of the surveys conducted over these years is shown in Fig. 4.4. The total length of the survey lines is more than 70,000 km. Gravimetric studies are integrated with seismic and magnetic surveys.

A significant difference in gravity (over 2.5 Gal) relative to the gravity reference station (GRS) in the port of Cape Town and a long duration of work with no port calls are specific features of gravimetric measurements. In this regard, more stringent requirements are imposed on the calibration quality of the gravity sensor and stability of the gravimeter drift.

In the marginal seas of the Antarctic, surveys are usually conducted in severe meteorological and ice conditions. During hurricanes, the wind speed reaches 20 m/s and the sea state reaches 5–6 on the Douglas scale. When moving along most of the geophysical lines, it is necessary to sail around icebergs and ice fields, sometimes deviating from the survey line by 10 km or more, and in some cases, changing the direction of the line.

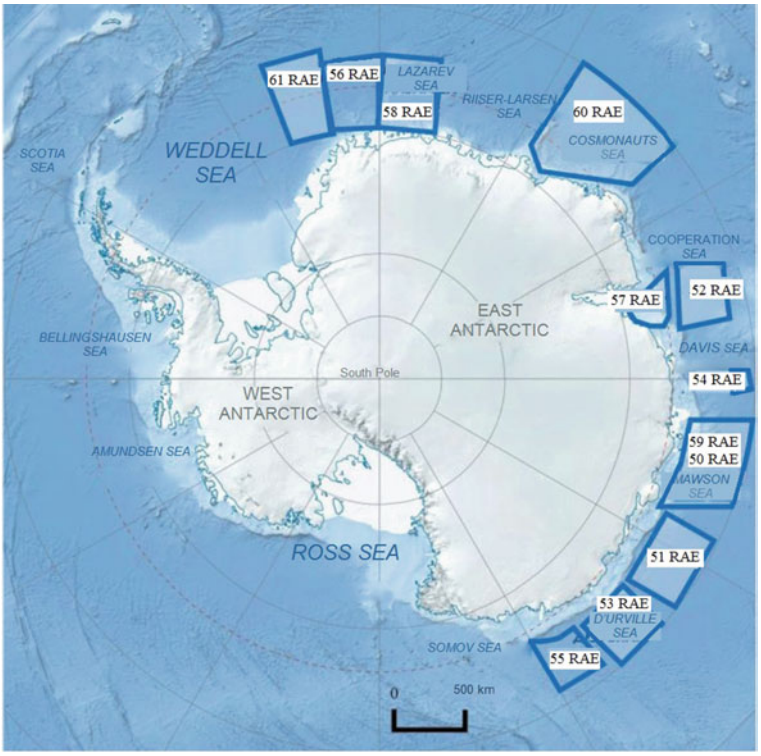

Fig. 4.4 Overview map of gravimetric surveys in the marginal seas of the Antarctic (RAE—Russian Antarctic Expedition)

As a result of the conducted surveys, 1:2,500,000-scale EGF maps were compiled for marginal seas of the Antarctic, such as the Weddell Sea, the Cooperation Sea (also called the Commonwealth Sea), the Riiser-Larsen Sea, the Cosmonauts Sea, and the Davis Sea. The RMS error of the gravimetric surveys was less than 1 mGal for all Antarctic surveys carried out over 11 years.

The first high-precision marine gravimetric survey near the North Pole was conducted in 2014 within the Arctic-2014 survey, which was coordinated by the Marine Arctic Geological Expedition (MAGE) as part of integrated geophysical surveys of the Arctic Basin (Kazanin et al. 2015; Sokolov et al. 2016b). Surface gravimetric survey was a secondary method; it was conducted in conjunction with the seismic and bathymetric surveys at a single grid of lines.

The survey was carried out with two gravimeters, Chekan-AM and Shelf-E, which were installed onboard the Akademik Fedorov research vessel (Fig. 4.5).

The following areas were defined as spatial boundaries of the survey area: the Arctic Ocean, the Podvodnikov Basin, the Vilkitsky Trough, the Amundsen Basin, the Nansen Basin, the Makarov Basin, the outer shelf of the Laptev Sea and the East Siberian Sea. The total survey area was about 350,000 km^2. A map of the survey lines is shown in Fig. 4.6.

Initial and final reference gravimetric observations were carried out at the port of Kiel (Germany) on July 14 and October 9, 2014, respectively. Measurements on the survey lines were carried out for two months from July 28 to September 27, 2014, with no port calls.

Taking into account the difficult ice conditions, two vessels were used to carry out the survey: the Yamal icebreaker was making a channel, while the Akademik

Fig. 4.5 Chekan-AM (*left*) and Shelf-E (*right*) gravimeters onboard the Akademik Fedorov research vessel

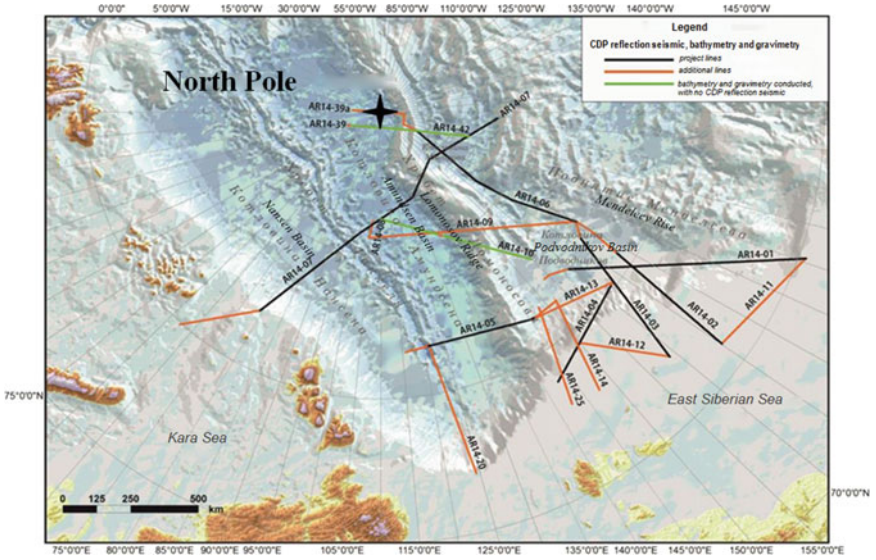

Fig. 4.6 Map of survey lines in the Arctic Basin

Fedorov, an ice-reinforced research vessel, followed the icebreaker conducting the survey.

In the polar regions, the solid ice was 4 m thick. In those conditions, the Akademik Fedorov could not keep on moving steadily and continuously. During the measurements, the vessel performed regular stops and changed tacks. Of 10,200 km of the survey, 7500 km were conducted in solid ice and only 2700 km in relatively open water. The average speed of the vessel through the ice was 3.8 kn (with a minimum of 2.1 kn) and 5.1 kn in open water.

Thirty-six gravimetric profiles were derived as a result of the complex research. The compiled catalog of the gravimetric sites comprises 71,179 independent measurements. The main criterion for the measurement accuracy was the RMS error of a single GA determination at repeated control points, which was 0.28 mGal for the Shelf-E gravimeter and 0.72 mGal for the Chekan-AM gravimeter. The results obtained correspond to the current level of high-precision marine surveys.

Figure 4.7 shows values of the depths, Bouguer and free-air anomalies for Line AR1409-07. The plot shows a high degree of correlation of the free-air anomalies with the seabed terrain as well as high-frequency EGF anomalies.

The processing of the results of the whole survey made it possible to detect EGF anomalies with a spatial resolution of less than 1 km and amplitude of 1–5 mGal, which can be measured only from a marine vessel. This is also confirmed by the comparison (Fig. 4.8) of the survey results with the values of the EGF anomalies from the EGM2008 global model and the data from the Arctic Gravimetric Project (ArcGP), which is presented by the results of the 1999 airborne gravimetric survey in this region.

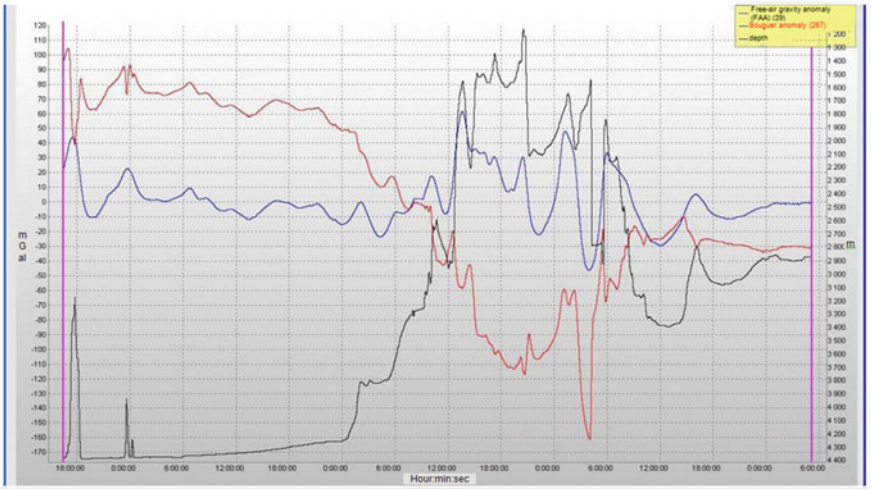

Fig. 4.7 Plots of depth, Bouguer and free-air anomalies on Line AR1409-07

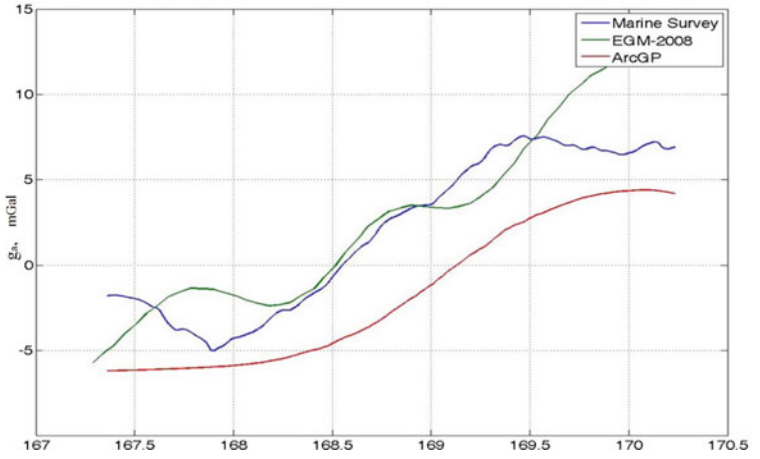

Fig. 4.8 Comparison of the gravimetric survey results with the data of the EGF models for Line AR1409-08

It can be seen that marine measurements have higher spatial resolution and are free from the systematic errors of airborne surveys (ArcGP) as well as an additional displacement of the local maxima of the calculated model (EGM-2008).

The results of the marine gravimetric survey carried out in the area of the North geographical pole have confirmed the undoubted priority of this method in the study of the high-frequency component of EGF anomalies. The unsteady motion of the vessel along the survey lines because of difficult ice conditions has little or no

impact on the accuracy of EGF measurements. The Chekan-AM gravimeter software and hardware allow for conducting high-accuracy gravimetric surveys in the Arctic latitudes up to the geographic pole of the Earth.

4.2.2 Regional Airborne Gravimetric Surveys

In 2007–2011, TGS-NOPEC Geophysical Company (Norway) used a Chekan-AM gravimeter to conduct five regional surveys in the northern, north-eastern, and southwestern parts of the Greenland shelf (Krasnov et al. 2010). Gravimetric measurements were carried out onboard various types of light turboprop aircraft (Table 4.1). An overview map of the surveys is shown in Fig. 4.9.

One Chekan-AM gravimeter was used for each survey. The field work lasted about three months. Throughout the whole period, the gravimetric equipment needed continuous thermal regulation. During the survey period, the air temperature varied by up to 30 °C. Therefore, of vital importance in the surveys was to maintain a constant temperature in the aircraft cabin, where the gravimeter was installed.

Quality control of temperature stabilization during the survey can be done using the reference observation database. Figure 4.10 shows a database of reference observations of the ULAG09 survey. Each point on the diagram represents the average value of the gravimeter readings for 1 h immediately before the flight. The data presented indicate that the standard deviation of the preflight measurements of the gravimeter for 33 days was about 0.3 mGal, which characterizes good temperature stabilization at the gravimeter location.

The aircraft speed on the survey lines of the Greenland shelf was about 70 m/s. A window filter with a cutoff frequency of 0.01 Hz was used in postprocessing. Thus, the resolution of the measurement results on the survey lines was about 7 km (half the wavelength). The surveys were carried out on a grid of primary and tie lines. The

Table 4.1 TGS-NOPEC airborne gravimetric measurements

Survey	Type of aircraft	Survey period	Duration, days	Total length of survey lines, km
NEGAG07	Piper Navajo PA 31 LN-NPZ	03.08.07—27.09.07	56	34,319
NEGAG08	Twin Otter DH-6	21.04.08—03.07.08	75	49,776
ULAG08	Piper Navajo LN-NPZ	25.08.08—25.10.08	62	50,684
ULAG09	Beechcraft King Air 90	06.07.09—21.09.09	78	39,897
SEGAG11	Beechcraft King Air 90	01.08.11—27.09.11	58	24,231

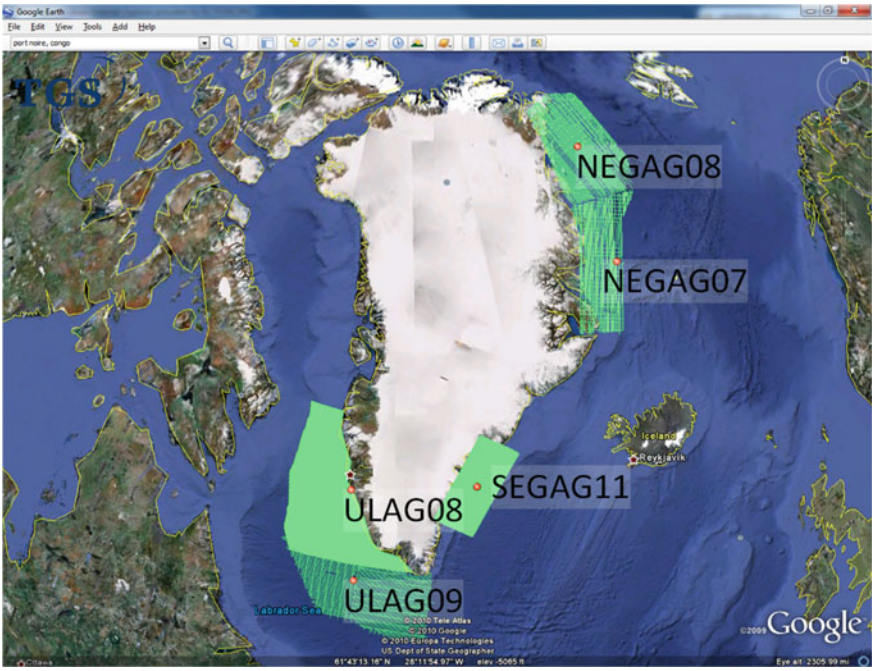

Fig. 4.9 Survey areas on the Greenland shelf

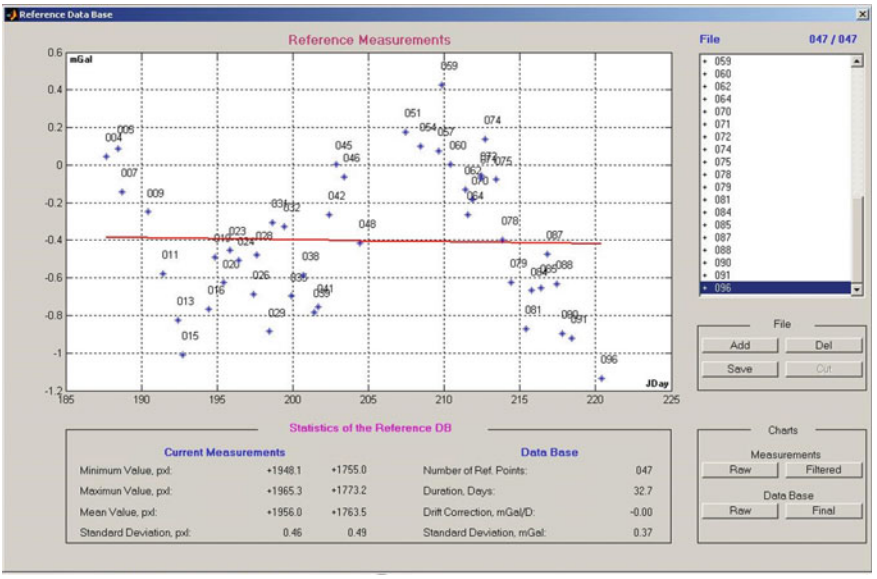

Fig. 4.10 Database of reference observations of the ULAG09 survey

Table 4.2 Parameters of surveys

Survey	Distance between lines, km	Total length of survey lines, km	Number of cross-points	Spatial resolution *L*/2, km	Survey RMSD, mgal
NEGAG07	4/20	34,319	1115	~7	0.87
NEGAG08	4/40	49,776	1079	~7	0.77
ULAG08	4/40	50,684	1082	~7	0.70
ULAG09	8/40	39,897	2120	~7	0.70
SEGA11	6/30	24,231	578	~7	0.85

distance between the primary lines was specified in accordance with the required scale of the final gravity anomaly map (Table 4.2).

Figure 4.11 shows the gravity anomaly for one of the tie lines of the ULAG08 project. The points on the diagram indicate the values of the anomalies at the primary lines. The figure also shows the gravity anomaly obtained with the use of satellite altimetry. It can be seen that the airborne gravity survey data have a higher resolution and provide a more detailed structure of the gravity field.

Office processing of the survey results carried out with special software validated the high quality of the data obtained. The total length of the lines of gravimetric surveys on the Greenland shelf exceeded 300 thousand km. The standard deviation of the error does not exceed 1 mGal at a spatial resolution of about 7 km. All the surveys were conducted in harsh conditions of the Arctic, with two of the surveys conducted in latitudes above 75°N. During the surveys, no gravimetric equipment failure was logged and the total amount of data rejected for various reasons was less than 5%.

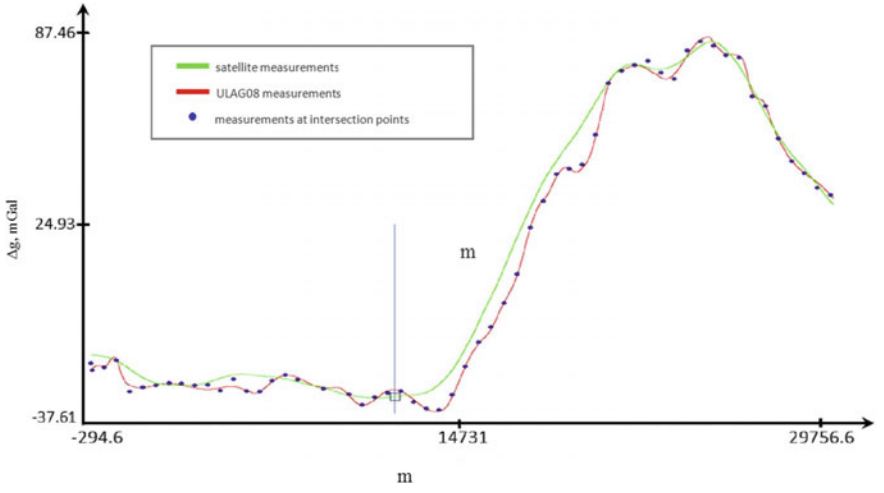

Fig. 4.11 Results of measurements on the tie line in comparison with satellite altimetry data

A geophysical survey conducted by the Russian company VNIIOkeangeologia in May 2007 is another example of production airborne surveys using the Chekan-AM gravimeter (Palamarchuk et al. 2008). Comprehensive gravimetric and magnetic studies were carried out in the Arctic Ocean in the zone of the Lomonosov Ridge in the area bounded by 75–84°N onboard an IL-18D aircraft. The plane flew at a speed of 100 m/s at an altitude of 500–1500 m along primary lines spaced by 10 km, and a series of tie lines.

The gravity field measured in the survey area turned out to be quite irregular. The average field gradient was ~0.7 mGal/km with maximum values up to 4 mGal/km. Figure 4.12, representing the primary line no. 2, also showing the seabed terrain, gives a clear idea of the field nature (Palamarchuk et al. 2008). It is easy to see a good correlation between the underwater terrain and the gravity anomaly. A comparison was made between the resulting field and the gravity anomaly map compiled in the ArcGP project. The comparison showed much greater detail of the first one as compared with the ArcGP map and a better correlation of the measured field with the seabed terrain.

Since the main objective was to conduct magnetic measurements, the weather conditions and flight mode were chosen mainly with consideration for the requirements of the magnetic survey; however, they were not always favorable for gravimetric measurements. As a result, the noise (vertical and horizontal accelerations of the aircraft) turned out to be as great as 25 Gal on average for the season, reaching 50–80 Gal at maneuvers.

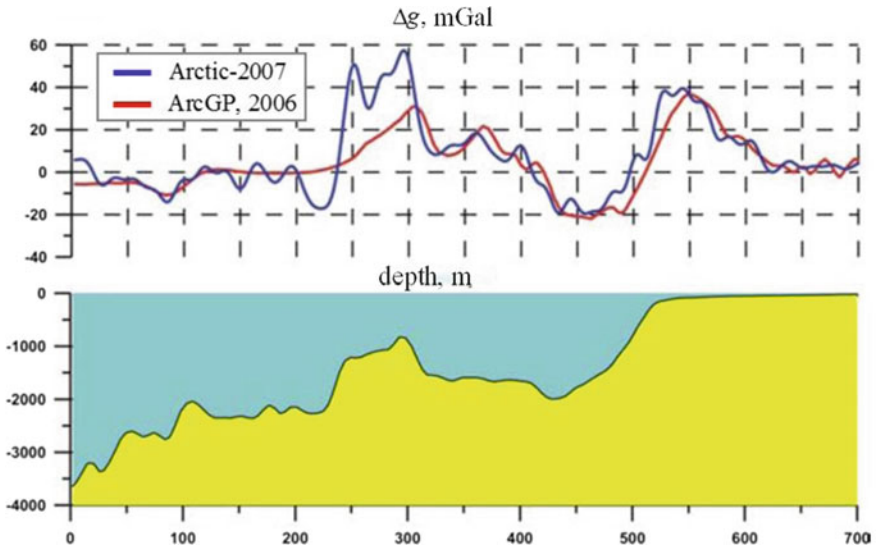

Fig. 4.12 Comparison of the airborne profile with the ArcGP Project Data and the underwater terrain

The RMS error of the survey estimated from the misties was 1.5 mGal, and after elimination of several points measured under high turbulence conditions, it became 0.8 mGal. The airborne survey resulted in a 1:1,000,000-scale map of the free-air gravity anomaly.

Another type of hard-to-reach areas in which it is necessary to perform gravimetric studies is mountain ranges. Due to the rugged terrain and the irregularity of the gravitational field, such measurements are needed to improve the geoid model. In December 2010, the Technical University of Denmark carried out an airborne gravimetric survey to map the geoid in Nepal (Forsberg et al. 2015). The airborne survey in the highest mountains of the Earth, the Himalayas, was carried out using Chekan-AM and L&R gravimeters from a Beech King Air aircraft.

The survey lines in Nepal were laid at a distance of about 6 nautical miles from each other (Fig. 4.13). Because of significantly different topographic conditions, the flights were conducted at altitudes from 4 km on the southern lines to 10 km on the northern lines. Flights along the tie lines were also conducted at an altitude of 10 km.

In the course of airborne gravimetric surveys in Nepal under difficult conditions of an irregular gravitational field and turbulence, the data on the Chekan-AM and L&R gravimeters employed in the surveys along with the new data from the GOCE mission and the topographic data were used to produce an improved national geoid model for Nepal. The accuracy estimate of the improved geoid model was about 10 cm over most of the country, which was confirmed by the GPS leveling data in the Kathmandu Valley.

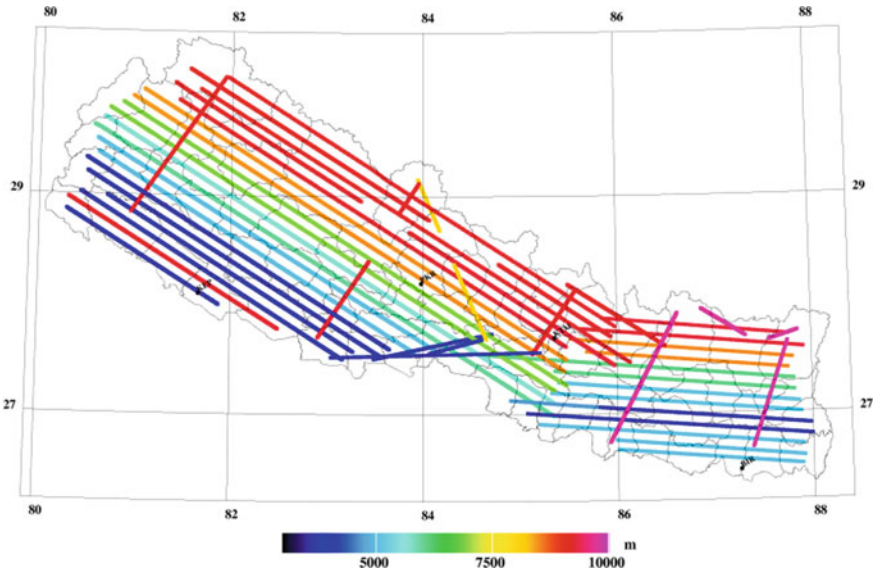

Fig. 4.13 Flight altitude (m) during the airborne gravimetric survey in Nepal

In addition, in 2015, it was for the first time that the work on integration of marine and airborne gravimetric measurements in the Arctic was done. Sevmorgeo, JSC, conducted their airborne gravimetric survey with the use of Chekan gravimeters. The survey was carried out in the northern part of the East Siberian Sea, from April 6 to August 31, 2015, with the aim to create a modern geological and geophysical basis for the poorly explored area with a high oil and gas potential (Peshekhonov et al. 2016).

Two Chekan-AM gravimeters and a Shelf-E gravimeter were used in the airborne gravimetric survey. The gravimeters were installed in the central part of the AN-30 aircraft fuselage. Flight measurements were carried out relative to the reference station at the airdrome of the town of Pevek.

The gravimetric survey was conducted at altitudes from 340 to 370 m. The distance between primary survey lines was 4 km; the distance between the tie survey lines was 25 km. The average flight speed during measurements varied from 75 to 100 m/s.

A distinctive feature of this survey is that the survey area is crossed by the lines of the marine survey that was previously carried out as part of the Arctic-2014 expedition (see Fig. 4.6). This allowed for a joint analysis of marine and airborne gravimetric data.

A map of airborne and marine survey lines is shown in Fig. 4.14.

The total length of airborne survey lines is more than 40,000 km. Data processing showed high accuracy in determining gravity acceleration. For example, the survey RMS error estimated for 1400 misties was as follows:

- for Chekan-AM gravimeters: 0.85 mGal and 0.83 mGal;

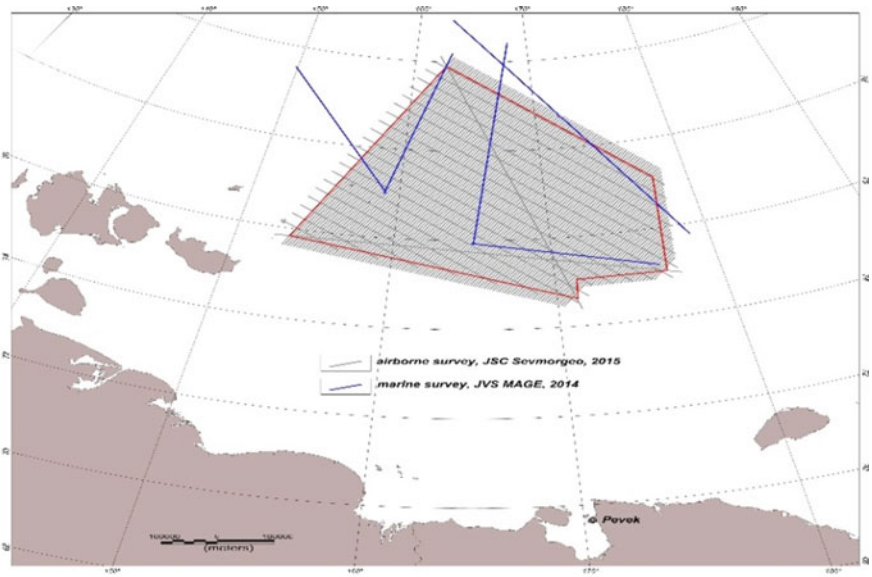

Fig. 4.14 Map of airborne and marine gravimetric survey lines

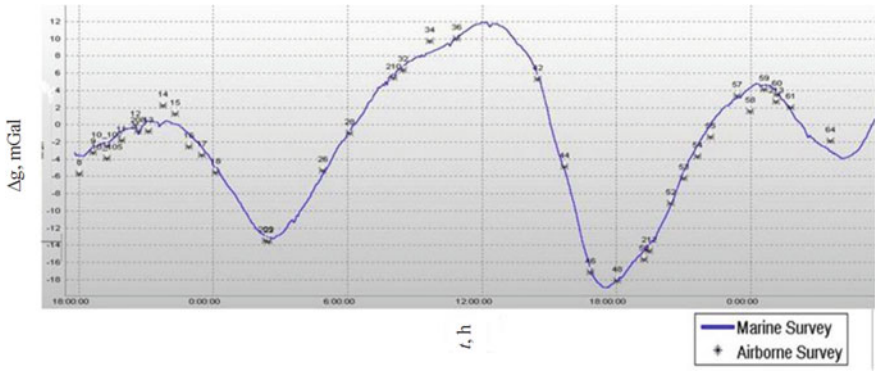

Fig. 4.15 Gravity anomaly curve on a marine survey profile and anomaly values from the airborne survey data

- for the Shelf-E gravimeter: 0.69 mGal.

For the comparative analysis, the marine and airborne gravimetric survey data were recalculated taking into account the absolute values of the gravity acceleration at reference stations. A station of Class 1 state grid was used for the Pevek aerodrome, and for the port of Kiel the absolute value was obtained from the AGrav international database (Wziontek et al. 2009).

The average correction for reduction of the airborne measurements to an ellipsoid was about 110 mGal. The difference with respect to the RGS was on average 0.5 Gal for airborne survey and 1.5 Gal for marine survey. At the same time, marine onboard measurements on the lines crossing the area of the airborne survey were taken 60–70 days after the reference observations in the port of Kiel.

Figure 4.15 shows an example of the gravity anomaly for one of the marine survey profiles, which also shows the values of the anomalies at the points of intersection with the airborne survey profiles.

Based on the analysis of 133 misties at the intersection points of marine and airborne survey lines, the following accuracy estimates were obtained:

- Systematic difference between surveys: 0.61 mGal;
- RMSD between marine and airborne surveys: 1.1 mGal.

Thus, the gravimetric lines of high-accuracy marine route survey up to the North Geographical Pole of the Earth can be considered as a reference grid for airborne gravimetric surveys. Such integration of data allows eliminating the methodological error of the recalculation of airborne gravimetric measurements to the ellipsoid surface, while the high performance of airborne gravimetric surveys, sufficient spatial resolution, and modern gravimetric equipment make it possible to successfully solve the problem of prospecting for hydrocarbons in the Arctic.

4.2.3 Carriers Used for Gravimetric Measurements

Airborne gravimetry is a crucial method to improve the knowledge about the Earth gravity field, especially in hard-to-reach regions. Its main advantage, compared to traditional marine and land surveys, is a relatively short period of time needed to obtain raw data. However, to date, it still remains a problem to increase the spatial resolution of the results of airborne gravimetric measurements. With this purpose in view, low-speed aircraft, such as light turboprop planes, helicopters, and airships, are considered attractive as carriers of gravimetric equipment.

The first experiment on conducting experimental methodological work using a Chekan-AM gravimeter onboard a light turboprop plane was performed in 2007 in cooperation with the Braunschweig Technical University (Krasnov and Sokolov 2009; Krasnov et al. 2007). The survey was carried out onboard a Dornier-128 aircraft with a flight height of about 300 m and a speed of 50–60 m/s.

The measurement accuracy was estimated by comparing the data with a high-resolution land map (Fig. 4.16).

The results of experimental methodological work have confirmed the feasibility of conducting airborne gravimetric surveys with an error of less than 1 mGal with a spatial resolution of 5–6 km. However, paths with satisfactory flight conditions turned out to be quite short. Nevertheless, those tests made it possible to work out a technique for conducting airborne surveys using the Chekan-AM gravimeter.

In January 2014, the first works were carried out using a Chekan-AM gravimeter onboard an AU-30 airship (Krasnov et al. 2015). The purpose of that experiment was to determine the possibility of using an airship as a carrier of gravimetric

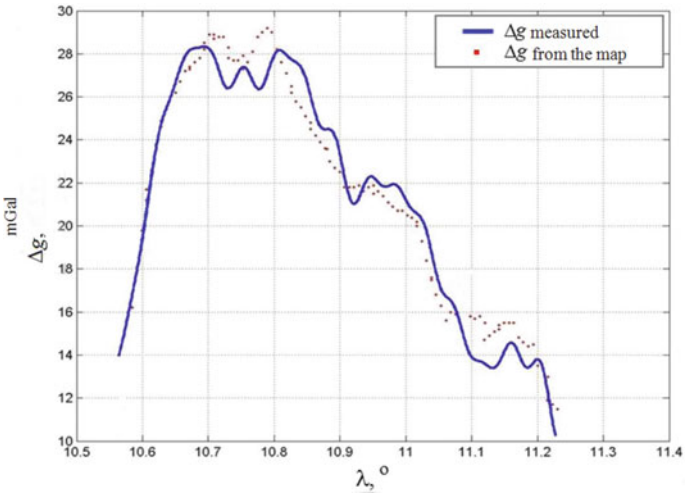

Fig. 4.16 Comparison of the data of an airborne survey and a land map

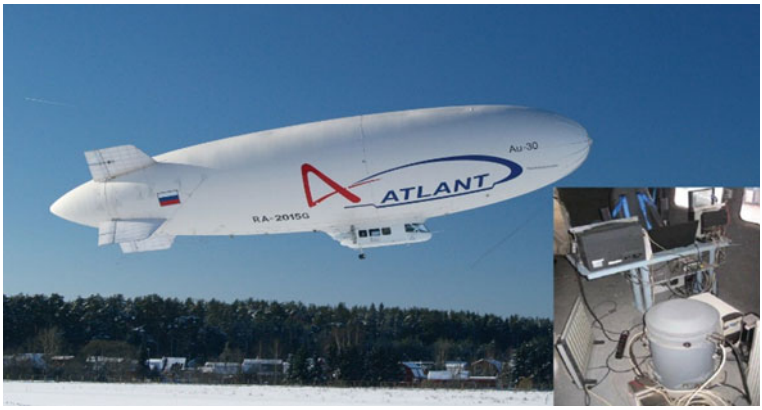

Fig. 4.17 Chekan-AM gravimeter onboard the AU-30 airship

equipment, to assess the level of induced perturbing accelerations, and to develop recommendations for creating an airship-based geophysical laboratory.

The Chekan-AM gravimeter was installed in the cabin of Augur Aeronautical Center's AU-30 airship (Fig. 4.17). The tests were conducted in the Vladimir Region.

A test line with a length of about 50 km was passed three times. The flights were conducted at an altitude of 330 m with an average speed of 17 m/s, corresponding to the cruising speed of the AU-30 airship. The airship was held at a specified altitude in the range of ±40 m, which is several times worse than the satisfactory conditions for airborne surveys (Sokolov et al. 2016a). Deviations from the specified trajectory reached significant values of 100–150 m, which is due to the fact that the airship speed was comparable to the wind speed, and it was impossible to ensure high-quality support for the carrier stable motion at the specified altitude and trajectory in such conditions. As a result, the value of inertial accelerations due to the unsteady motion of the carrier when running survey lines was 2–3 times higher as compared with similar measurements taken onboard light turboprop aircraft.

Despite the fact that the use of an airship as a carrier increased the spatial resolution of the gravimetric measurements 3–4 times, the accuracy obtained is approximately 2–3 times worse than the accuracy of measurements taken onboard aircraft that are less susceptible to the influence of dynamic perturbations.

Another urgent task of studying the EGF in remote areas is detailed gravity measurements in transit zones with depths starting at 0 m. Conventional marine surveys are carried out at safe depths of more than 5 m, approximately twice the draft of the vessel. In order to effectively solve the problem of conducting surveys in the conditions of extremely shallow waters, Yuzhmorgeologia has developed and successfully implemented a technology of surveys with the use of Chekan-AM gravimeters onboard hovercraft (Lygin 2013).

The technical specifications of the HIVUS-10 hovercraft provide for the surveys on lines more than 100 km long and at a distance of several tens of kilometers

from the base with a sea state not higher than 2. For gravimetric surveys in hard-to-reach areas, the hovercraft with gravimetric and navigation equipment installed in it is placed onboard a carrier vessel which is also supplied with all the necessary equipment for gravimetric surveys. Surveys using hovercraft have been conducted by Yuzhmorgeologia since 2007. They were carried out in the Sea of Azov and its estuaries, in the Pechora Sea, the Baydaratskaya Bay, the Yenisei Gulf, and the Khatanga Gulf.

Gravimeters of the Chekan series are also used to take measurements at land gravimetric stations, including those in hard-to-reach areas of the Earth, such as deserts and transit zones. In this case, Chekan gravimeters are used in much the same way as relative land gravimeters. Measurements are taken on a fixed base for 10 min after the carrier stops. As this takes place, the gravimeter equipment is not unloaded from the minivan. The advantages of using Chekan gravimeters for this type of measurements are an unlimited range of measurements, high performance and full automation of work (Zheleznyak et al. 2015).

Figure 4.18 shows the results of five routes with a Shelf-E gravimeter at the Leningrad gravimetric test site.

The RMS measurement error was 0.1 mGal. The test results characterize another way of studying the EGF; at the same time, they also show that it is possible in principle to use Chekan gravimeters for maintaining and developing Class 1 state gravimetric grid and creating Class 2 and Class 3 grids, provided that a Chekan gravimeter is transported to gravimetric stations by minivans.

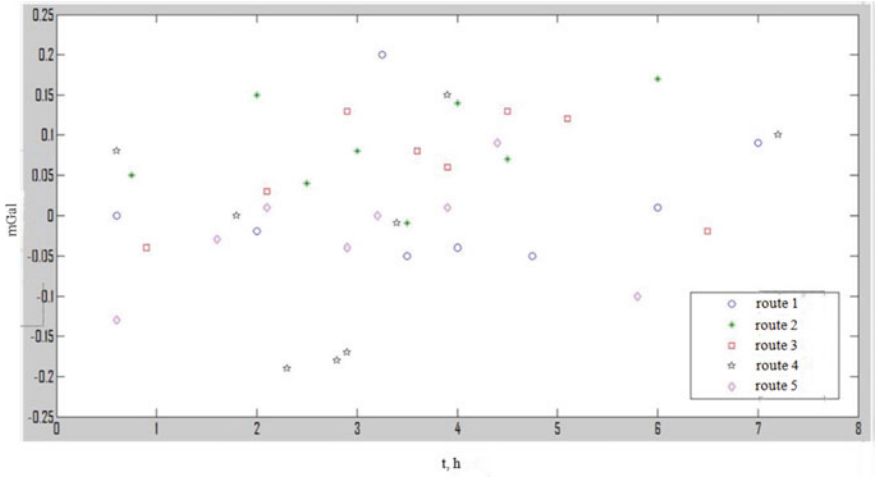

Fig. 4.18 Measurement errors at the gravimetric test site points in five test routes

4.2.4 Conclusions

Methodical features of gravimetric surveys in hard-to-reach areas of the Earth using Chekan gravimeters are described.

The results of marine and airborne geophysical surveys in the Arctic and the Antarctic are presented. It is shown that the survey error in airborne gravimetric measurements onboard light turboprop aircraft does not exceed 1 mGal with a spatial resolution of about 7 km.

The potential was discussed for studying hard-to-reach areas of the Earth using promising types of carriers such as hovercraft and airships, as well as using minivans for transporting gravimeters between land survey sites.

4.3 GT-2A Gravimeter All-Latitude Versions

Airborne gravimetric surveys in the polar regions of the Earth have recently been of particular interest to geophysics (Krasnov et al. 2011; Sokolov et al. 2016b; Koneshov et al. 2012; Drobyshev et al. 2011; Mogilevsky et al. 2015). Section 1.3 shows that Schuler oscillations of the GT-2A gravimeter gyro platform are damped in flight with the use of aiding information on the aircraft velocity projected on the free-azimuth coordinate system, in which inertial navigation equations are solved. The free-azimuth coordinate system is determined by the *XaYaZa* frame obtained from the local *ENZ* geodetic frame by turning about the vertical axis Z and having a zero absolute angular rate about its vertical axis Z_a. In the standard configuration of the GT-2A gravimeter, data on the eastern V_E^* and northern V_N^* components of the aircraft velocity, delivered by a single-antenna GNSS receiver, are used as aiding data. The specified velocity components are projected onto the instrument axes of the gyro platform using the current value of the compass heading generated by the navigation system of the gravimeter. It is known that the compass heading error increases as the aircraft approaches the pole and, as a result, the level of the gyro platform misalignment errors also increases, which makes it impossible to use GT-2A gravimeters in latitudes higher than $\pm 75^\circ$ in standard configuration.

The advent of multi-antenna GNSS receivers on the market provided conditions for creating polar versions of the GT-2A gravimeter. These modifications are discussed in the next section.

4.3.1 Using Multi-antenna GNSS Receivers

It was proposed to use a multi-antenna GNSS receiver as a source of information about the aircraft orientation for airborne gravimetric surveys conducted in the polar

areas with the use of GT-2A gravimeters. Three versions of the gravimeter with an extended latitudinal range of application were developed.

(1) The so-called **near-all-latitude** version of GT-2A gravimeter (Smoller et al. 2013, 2015a, b). The gravimeter uses the geodetic heading delivered by a two- or four-antenna GNSS receiver instead of the compass heading. The heading delivered by the multi-antenna GNSS receiver has no disadvantages of the compass heading discussed in Sect. 1.3; however, due to the degeneration of the geographical heading notion at a polar location, this version also leads to a latitude limitation $\pm 89°$. This version of the gravimeter firmware was created in 2011 and was given the code GT-2AP. Currently, GT-2AP gravimeters are used in airborne gravimetric surveys at high latitudes by the following companies: GNPP Aerogeophysica, the Schmidt Institute of Physics of the Earth of the Russian Academy of Sciences, Polar Research Institute of China, and Alfred-Wegener-Institut (AWI).

(2) The **all-latitude version** (Smoller et al. 2013, 2015a, b). In this version, the concept of a geodetic reference frame is not used in intermediate calculations of the four-antenna GNSS receiver. The orientation problem is solved based on the concepts of only two coordinate systems—the one associated with the aircraft body frame and the Greenwich coordinate system (or Earth Centered Earth Fixed (ECEF) reference frame). This version has no special features at polar locations, which made it possible to develop an all-latitude version of the gravimeter capable of operating even directly at the points of the geographic poles. However, this version required a thorough revision of the onboard software of the GT-2A gravimeter and a significant computation burden on its central processing unit (CPU). The latter has led to the need to introduce an additional processor into the gravimeter. In addition, in contrast to the near-all-latitude version discussed above, this version can be used *only* in the case of using a four-antenna GNSS receiver. This version of the gravimeter was developed in 2012 but it was not put into operation due to its disadvantages mentioned above.

(3) Further development of the proposed software solutions that helped to create an all-latitude version of the gravimeter was made possible owing to the use of quasi-geodetic coordinates known in inertial navigation and the notions of quasi-heading and quasi-track angle derived from them. The latter are the angles between the horizontal projections of the longitudinal axis of the aircraft, its relative velocity vector, and the direction to the quasi-north. The quasi-heading and the quasi-track angle do not have any special features in polar areas (Smoller et al. 2016). This version of the gravimeter allowed it to operate at all latitudes and, in addition, use the simplest and most reliable dual-antenna GNSS receiver. It is also important that this version does not cause any additional load on the gravimeter CPU in terms of the computation burden.

Let us describe this version in more detail.

4.3.2 Quasi-Geodetic Coordinates

Consider one of the possible options for the introduction of quasi-geodetic coordinates described, in particular, in (Belous et al. 2014; Yumanov 2013), taking a sphere as its reference surface.

First, recall the definition of the ECEF coordinate system $OX_GY_GZ_G$ (Fig. 4.19) used in the GNSS receiver. Point O is the geometric center of the Earth. The Z_G-axis coincides with the Earth's axis of rotation and is directed to the north, the OX_GZ_G plane is the plane of the Greenwich (zero) meridian, and the OX_GY_G is the equatorial plane.

The point of the Earth's surface with the geodetic coordinates $\varphi = 0°$, $\lambda = 180°$ is taken as the quasi-north pole *Nq*; the point with the coordinates $\varphi = 0°$, $\lambda = 0°$ is taken as the quasi-south pole *Sq*. A circle formed by the geodetic meridians $\lambda = 90°$W and $\lambda = 90°$E is taken as the quasi-equator (bold line in Fig. 4.19). The plane of the quasi-equator coincides with the plane of the zero meridian. The circle passing through the geodetic poles and the quasi-poles was taken as the initial (zero) quasi-meridian (double line in Fig. 4.19). The plane of the zero quasi-meridian coincides with the equatorial plane.

Multi-antenna GNSS receivers generate the following initial data:

1. X^*_G, Y^*_G, Z^*_G are the ECEF coordinates of the baseline antenna;
2. V^*_{XG}, V^*_{YG}, V^*_{ZG} are projections of the relative velocity vector of the baseline antenna in the ECEF coordinate system $OX_GY_GZ_G$;
3. d^*_{XG}, d^*_{YG}, d^*_{ZG} are projections of the baseline vector connecting the phase centers of the two antennas installed along the longitudinal axis of the aircraft in the ECEF coordinate system $OX_GY_GZ_G$.

Since the reference surface in the quasi-geodetic coordinate system—the sphere—almost coincides with the Earth ellipsoid for latitudes $|\varphi| > 89°$, quasi-track angle

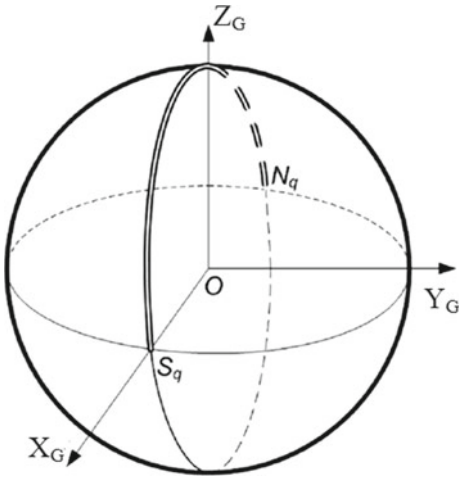

Fig. 4.19 Quasi-geodetic coordinates

GH^{q*} and quasi-heading K^{q*}can be calculated with sufficient accuracy using the following relations whose output is given in (Smoller et al. 2015a):

$$V_E^{q*} = -\frac{Y_G^*}{\sqrt{Y_G^* + Z_G^*}} V_Z^* + \frac{Z_G^*}{\sqrt{Y_G^* + Z_G^*}} V_Y^*; \tag{4.3.1}$$

$$V_N^{q*} = -\frac{Z_G^*}{\sqrt{Y_G^{*2} + Z_G^{*2}}} \frac{X_G^*}{\sqrt{X_G^{*2} + Y_G^{*2} + Z_G^{*2}}} V_{ZG}^* + \frac{Y_G^*}{\sqrt{Y_G^{*2} + Z_G^{*2}}} \frac{X_G^*}{\sqrt{X_G^{*2} + Y_G^{*2} + Z_G^{*2}}} V_{YG}^* + \frac{\sqrt{Y_G^{*2} + Z_G^{*2}}}{\sqrt{X_G^{*2} + Y_G^{*2} + Z_G^{*2}}} V_{XG}^*; \tag{4.3.2}$$

$$GH^{q*} = arctg\left(V_E^{q*} / V_N^{q*}\right); \tag{4.3.3}$$

$$d_E^{q*} = -\frac{Y_G^*}{\sqrt{Y_G^* + Z_G^*}} d_Z^* + \frac{Z_G^*}{\sqrt{Y_G^* + Z_G^*}} d_Y^*; \tag{4.3.4}$$

$$d_N^{q*} = -\frac{Z_G^*}{\sqrt{Y_G^{*2} + Z_G^{*2}}} \frac{X_G^*}{\sqrt{X_G^{*2} + Y_G^{*2} + Z_G^{*2}}} d_{ZG}^* + \frac{Y_G^*}{\sqrt{Y_G^{*2} + Z_G^{*2}}} \frac{X_G^*}{\sqrt{X_G^{*2} + Y_G^{*2} + Z_G^{*2}}} d_{YG}^* + \frac{\sqrt{Y_G^{*2} + Z_G^{*2}}}{\sqrt{X_G^{*2} + Y_G^{*2} + Z_G^{*2}}} d_{XG}^* \tag{4.3.5}$$

$$K^{q*} = arctg\left(d_E^{q*} / d_N^{q*}\right). \tag{4.3.6}$$

4.3.3 All-Latitude Version of the GT-2A Gravimeter

At the request of the developers of the airborne gravimeter GT-2A, the manufacturer, Javad Ltd., implemented the algorithms for calculating quasi-heading K^{q*} and quasi-track angle GH^{q*} in the software of the Javad DUO-G3D dual antenna GNSS receivers and the Javad QUATTRO-G3D four-antenna GNSS receivers in accordance with relations (4.3.1)–(4.3.6). As a result, an SY message was added to the Javad GNSS Receiver External Interface Specification (see Table 4.3). This message contains data that allows implementation of three modes in the gravimeter: the standard mode (using a compass heading), near-all-latitude mode (using the geodetic heading from a multi-antenna GNSS receiver), and the new polar mode using the new GH^{q*} and K^{q*} calculated in the software of the Javad multi-antenna GNSS receivers.

Table 4.3 Main parameters of the SY message

No	Parameter	Explanations
1	T_{GNSS}	UTC time
2	Flag of the GNSS velocity solution reliability	
	Flag of the GNSS heading reliability	
3	φ*	Geodetic latitude of the GNSS receiver baseline antenna
5	λ*	Geodetic longitude of the GNSS receiver baseline antenna
7	V*	Modulus of the horizontal component of the relative velocity
8	GH*	Geodetic track angle
9	Date	GNSS receiver date
10	K*	Geodetic heading
11	GH^{q*}	Quasi-track angle calculated from (4.3.1)–(4.3.3)
12	K^{q*}	Quasi-heading calculated from (4.3.4)–(4.3.6)

The software of the airborne gravimeter GT-2AQ (the code of the GT-2A gravimeter version that uses the concept of quasi-geodetic coordinates) was also modified to meet the new requirements.

The projections of the relative velocity of the aircraft onto its body frame V_x^*, V_y^* during the work using quasi-coordinates are calculated in the firmware of the GT-2AQ gravimeter using the following evident relations:

$$V_N^{q*} = V^* \cos GH^{q*}; V_E^{q*} = V^* \sin GH^{q*}; \tag{4.3.7}$$

$$V_y^* = V_N^{q*} \cos K_q^* + V_E^{q*} \sin K_q^*; \tag{4.3.8}$$

$$V_x^* = V_E^{q*} \cos K_q^* - V_N^{q*} \sin K_q^*. \tag{4.3.9}$$

The values of the projections of the aircraft relative velocity on the axes of the free-azimuth coordinate system V_{xa}^*, V_{ya}^* needed to damp Schuler oscillations of the gyro platform (see Sect. 1.3) are calculated using the following relations:

$$V_{ya}^* = V_y^* \cos(C + ASz) - V_x^* \sin(C + ASz); \tag{4.3.10}$$

$$V_{xa}^* = V_x^* \cos(C + ASz) + V_y^* \sin(C + ASz); \tag{4.3.11}$$

where C is the angle between the platform coordinate system and the free-azimuth one;

ASz are the readings of the angle sensor on the external axis of the gimbal suspension (see Fig. 1.3.4 in Sect. 1.3).

The GT-2AQ gravimeter software implements formulas for recalculating the relative velocity components from the aircraft body frame to the free-azimuth coordinate system taking into account not only the readings of the angle sensor on the external axis of the gimbal suspension ASz but also the readings of ASx and ASy of the angle sensors on the internal axes of the gimbal suspension X and Y. For simplicity, relations (4.3.10), (4.3.11) imply that the roll and the pitch of the aircraft are zero, and the terms containing the readings ASx and ASy equal to zero are not shown.

As mentioned above, the methodic errors in calculating the angles of the quasi-heading and the quasi-track angle using relations (4.3.1)–(4.3.6) are negligible when flights are carried out at latitudes $|\varphi| > 89°$, where the sphere is a good approximation of the Earth's ellipsoid. Therefore, in this case, the methodic errors in calculating the projections of the aircraft velocity on the axes of the free-azimuth coordinate system according to relations (4.3.7) and (4.3.11) are also negligible.

Taking into account the preceding, the GT-2AQ all-latitude gravimeter has two operation modes, standard and polar, to be chosen by the operator.

As with the GT-2A gravimeter, the compass heading is used in the standard mode for factory and routine calibrations. The standard mode can be used for flights at latitudes of $|\varphi| < 75°$ with both multi-antenna and single-antenna GNSS receivers. It should be recalled (see Sect. 1.3) that it is in this mode that the gravimeter gyro platform is stabilized in the geodetic coordinate system.

The geodetic heading from the multi-antenna GNSS receiver (SY message) is used in the polar mode up to the latitude of $|\varphi| < 89°$, as is the case with the GT-2AP near-all-latitude version described above. When crossing the latitude $|\varphi| = 89°$ towards the geographic pole, the gravimeter software automatically switches to using the values of the quasi-heading and the quasi-track angle. In the polar mode, the gravimeter gyro platform is stabilized in the free-azimuth coordinate system. Thus, the GT-2AQ gravimeter version is an all-latitude version capable of functioning even directly at the points of the geographic poles.

4.3.4 Method for Calibration of Instrumental Errors of the Gimbal Suspension Angle Sensor

It follows from (4.3.10), (4.3.11) that, in contrast to the standard-configuration GT-2A gravimeter, the readings of the gimbal suspension angle sensors take part in the damping process of the gyro platform. Since the errors of the angle sensors mainly consist of the first and second harmonics from a complete turn, as practice shows, the leveling accuracy of the gyro platform depends mainly on the ASz error.

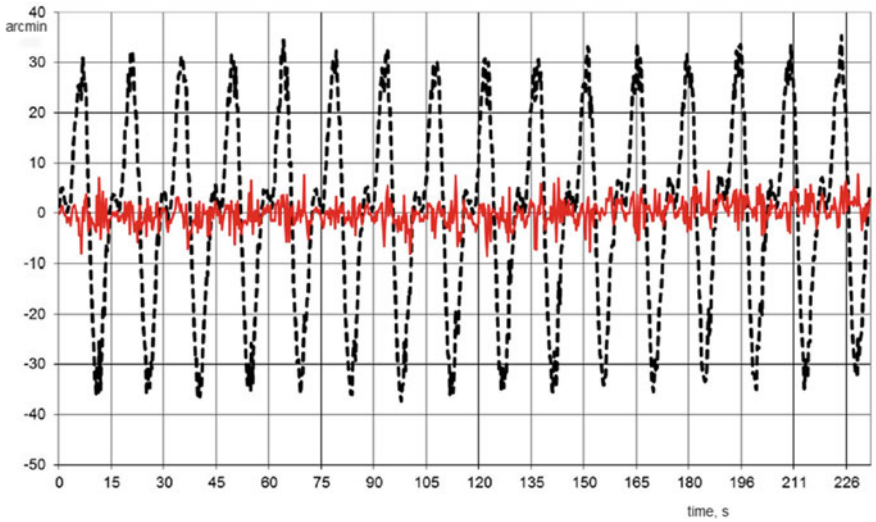

Fig. 4.20 *ASz* error estimate

The gravimeter developers proposed the procedures and a program to estimate the parameters of the approximating function of the *ASz* instrumental error.

For this, the gyro platform is rotated about the vertical axis. Based on the difference between the *ASz* readings and the integral of the readings of the gravimeter FOG, the program estimates the *ASz* error and four coefficients of its approximation by the first and second harmonics of the *ASz* readings. The coefficients obtained are entered in the gravimeter as constants and are used in real time to compensate for the *ASz* error.

The dotted curve in Fig. 4.20 is an estimate of the *ASz* error. It was obtained by processing sixteen rotations of the gyro platform. The solid curve is the *ASz* residual error after taking into account the approximating functions. From this curve, it follows that the error has decreased about 4–5 times.

4.3.5 Test and Operation Results

The first GT-2AQ gravimeter prototype was road tested prior to the installation on an aircraft. It was installed in the cargo tray of a Mitsubishi Triton pickup truck (Fig. 4.21). A Javad QUATTRO-G3D four-antenna GNSS receiver was also installed on the pickup truck. Its output information stream had a new SY message containing the values of the quasi-track angle and the quasi-heading.

The tests were conducted on September 21, 2015. The test route was located 80 km south of Perth, Western Australia (Fig. 4.22, left). Prior to the tests, initial reference measurements were made at a point located in the vicinity of the test route.

Fig. 4.21 GT-2AQ gravimeter with Javad QUATTRO-G3D GNSS antennas in the cargo tray of a pickup truck

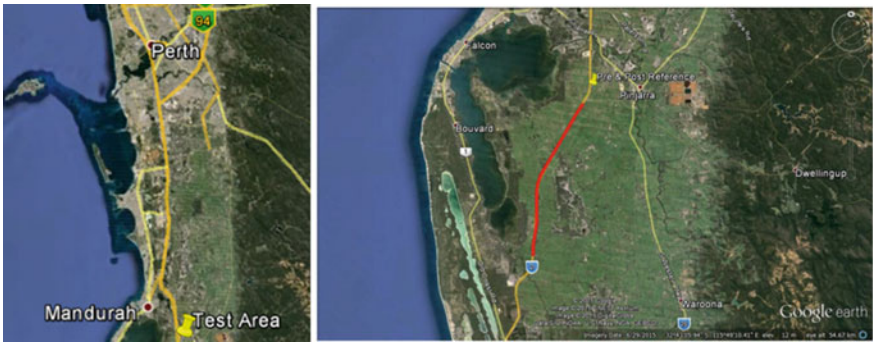

Fig. 4.22 Road test area and the route

The average speed of the vehicle was approximately 97 km/h. First, the truck was moving southward along the Forrest Highway. The route was approximately 14 km long (the red line on the right side of Fig. 4.22). At the end of the route, the truck made a U-turn and continued moving in the opposite direction. The motion cycle was repeated: two runs southward, and two northward, following the same route.

Then, the truck returned to the starting point for final reference measurements.

The GNSS base station was installed on the roof of a building in the city of Perth.

The test results for the four survey lines are presented in Fig. 4.23. The red line shows the average value of the gravity anomaly for four survey lines.

Average measurement time was 100 s.

Table 4.4 shows the estimated RMS deviation of the measured gravity anomaly value from its average value obtained for four survey lines.

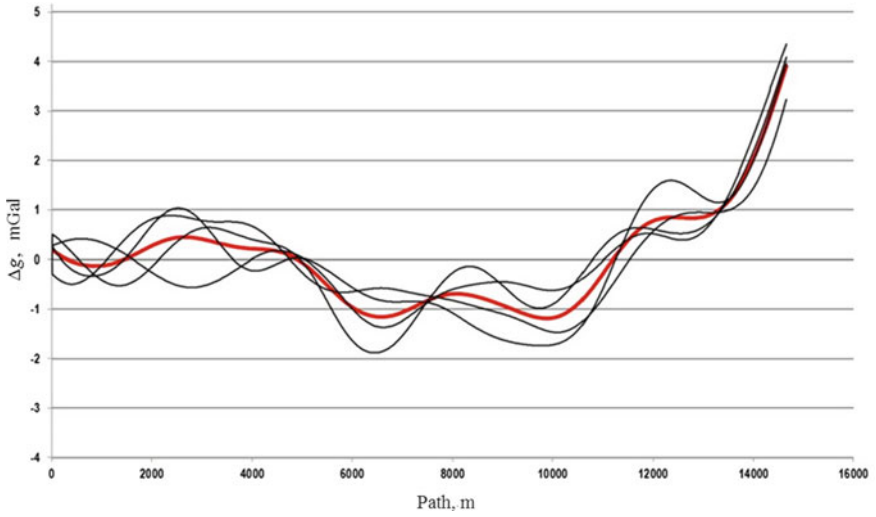

Fig. 4.23 Road test results

Table 4.4 Statistics of the road test results

Survey line number	1	2	3	4	Average RMSD, mGal
RMSD, mGal	0.37	0.42	0.39	0.36	0.39

The results presented in Table 4.4 are not inferior to the typical results of airborne gravimetric measurements with a GT-2A gravimeter, which confirms the fact that this gravimeter version is ready for surveys in high latitudes. The test results presented in Fig. 4.23, once again confirmed the imperturbability of the gyro platform of the GT-2 gravimeter by the vehicle maneuvering.

The road tests confirmed the effectiveness of the gravimeter version under consideration; however, they are of interest in themselves. The point is that some road tests carried out with the first prototypes of the GT-2A gravimeter having a dynamic measurement range of ± 0.5 g showed unacceptable results because of the GSE saturation during the tests.

It was for the first time that the road tests confirmed the feasibility of taking gravimetric measurements with the use of a GT-2A gravimeter installed on a truck (dynamic measurement range ± 1 g) while the truck was moving along an asphalt road.

Fig. 4.24 Bastler aircraft and GT-2AP gravimeter in the aircraft cabin

4.3.6 Polar Versions of the GT-2A Gravimeter

GNPP Aerogeophysica has been using near-all-latitude versions of the GT-2AP gravimeter (latitude range of application: ±89°) since 2013 to conduct airborne gravimetric measurements from AN-30 aircraft in different areas of the world, including polar regions.

Versions of the GT-2AP gravimeter were installed onboard three Bastler planes of polar aviation to carry out gravimetric measurements in the Antarctic. Figure 4.24 shows photos of an aircraft and a gravimeter in the aircraft cabin.

The GT-2AP gravimeter version was used in the Antarctic by the University of Texas (USA) in 2012–2015 (Richter et al. 2013), Alfred-Wegener-Institut (Germany) in 2014–2016, and the Polar Research Institute of China in 2014–2015.

After the road tests, the GT-2AP gravimeter used by the University of Texas was modified to the GT-2AQ all-latitude version that worked in the Antarctic in 2015–2016.

4.3.7 Conclusions

It has been shown that the latitudinal limitations (±75°) on using the GT-2A gravimeter in its single-antenna GNSS configuration are explained by the fact that the so-called compass heading has special features in high latitudes, which makes it impossible to damp Schuler oscillations of the gyro platform. Three versions of the GT-2A gravimeters with multi-antenna GNSS receivers have been described. All the gravimeters have extended latitude ranges of application. The experimental work has confirmed the effectiveness of the technical solutions implemented in the polar versions of the GT-2 gravimeter.

References

Belous Y, Peshekhonov V, Rivkin B (2014) Mapping support for navigation in high latitudes. Control Eng Russia 3(51):34–36

Blazhnov BA, Nesenyuk LP, Peshekhonov VG, Sokolov AV, Elinson LS, Zheleznyak LK (2002) Integrated mobile gravimetric system. Development and test results. In: Peshekhonov VG (ed) Primenenie graviinertsial'nykh tekhnologii v geofizike (gravity-inertial technologies in geophysics). CSRI Elektropribor, St. Petersburg, pp 33–44

Brozena JM, Salman R (1996) Arctic airborne gravity measurement program. In: Segawa J, Fujimoto H, Okubo S (eds) Gravity, geoid and marine geodesy, IAG series vol 117. Springer Verlag, pp 131–139

Chesnokova TS, Grushinsky NP (1961) Gravimetric measurements in the Greenland Sea in 1956 on the Ob diesel-electric vessel. In: Fedynsky VV (ed) Morskie gravimetricheskie issledovaniya (Marine Gravimetric Studies). Collection of articles. Moscow University Publishing House, Moscow, pp 37–41

Drobyshev NV, Koneshov VN, Klevtsov VV, Soloviev VN, Lavrentieva EY (2008) Development of an aircraft laboratory and a procedure for Arctic airborne gravimetric surveys. Seismicheskie Pribory 44(3):5–19

Drobyshev NV, Koneshov VN, Pogorelov VV, Rozhkov YE, Solov'ev VN (2009) Specific features of the technique of airborne gravity surveys at high latitudes. Izvestiya. Phys Solid Earth 45(8):656–660

Drobyshev NV, Koneshov VN, Koneshov IV, Soloviev VN (2011) Development of an aircraft laboratory and a procedure for Arctic airborne gravimetric surveys. Vestnik Permskogo Universiteta. Geologiya Series 3:37–50

Ekspeditsionnye issledovaniya VNIIOkeangeologii v Arktike, Antarktike i Mirovom okeane v 2005 godu (VNIIOkeangeologiya Survey Studies in the Arctic, Antarctic, and World Ocean in 2005). VNIIOkeangeologiya, St. Petersburg

Forsberg R, Kenyon S (2004) Gravity and geoid in the arctic region—the northern gap now filled. In: Proceedings of the second international GOCE user workshop, Italy

Forsberg R, Olesen AV, Yildiz H, Tscherning CC (2011) Polar gravity fields from GOCE and airborne gravity. In: Proceedings of 4th international GOCE user workshop, ESA SP–696

Forsberg R, Olesen AV, Einarsson I (2015) Airborne gravimetry for geoid determination with Lacoste Romberg and Chekan gravimeters. Gyroscopy and Navigation 6(4):265–270

Gaynanov AG (1961) Gravimetric measurements on the Ob diesel-electric vessel in the first Antarctic project. In: Fedynsky VV (ed) Morskie gravimetricheskie issledovaniya (Marine Gravimetric Studies). Collection of articles. Moscow University Publishing House, Moscow, pp 23–36

Kazanin GS, Ivanov GI, Kazanin AS, Vasilyev AS, Makarov ES (2015) Arctic 2014 survey: integrated geophysical research at the North Pole. In: Vesti gazovoy nauki (Gas Science News). Collection of Articles 2:92–97

Kazanin GS, Zayats IV, Ivanov GI, Makarov ES, Vasiliev AS (2016) Geophysical exploration at the North Pole. Oceanology 56(2):311–313

Koneshov VN, Nepoklonov VB, Stolyarov IA (2012) Using modern geopotential models in studying vertical deflections in the Arctic. Gyroscopy and Navigation 3(4):298–307

Koneshov VN, Klevtsov VV, Solov'ev VN (2016) Upgrading the GT-2A aerogravimetric complex for airborne gravity measurements in the Arctic. Izvestiya. Phys Solid Earth 52(3):452–459

Krasnov AA, Sokolov AV (2009) Studying the gravity field of hard-to-reach Earth areas using the Chekan-AM mobile gravimeter. Trudy Instituta Prikladnoi Astronomii RAN 20:353–357

Krasnov AA, Nesenyuk LP, Sokolov AV, Stelkens-Kobsch TH, Heyen R (2007) The results of the new airborne gravimeter tests. In: IAG international symposium on terrestrial gravimetry: static and mobile measurements (TG-SMM2007), St.Petersburg, Russia, pp 73–78

Krasnov AA, Sokolov AV, Usov SV (2010) Results of regional aerogravimetric surveys conducted in the Arctic with the use of gravimeter Chekan-AM. In: IAG international symposium on terrestrial gravimetry: static and mobile measurements (TG-SMM2010), St. Petersburg, Russia, pp 27–32

Krasnov AA, Sokolov AV, Usov SV (2011) Modern equipment and methods for gravity investigation in hard-to-reach regions. Gyroscopy and Navigation 2(3):178–183

Krasnov AA, Sokolov AV, Elinson LS (2014a) Operational experience with the Chekan-AM gravimeters. Gyroscopy and Navigation 5(3):181–185

Krasnov AA, Sokolov AV, Elinson LS (2014b) A new air-sea shelf gravimeter of the Chekan series. Gyroscopy and Navigation 3:131–137

Krasnov AA, Sokolov AV, Rzhevskiy NN (2015) First airborne gravity measurements aboard a dirigible. Seismic Instruments 51(3):252–255

Litinsky VA (1972) Experience of using gravimetric observations on an icebreaker. In: Fedynsky VV (ed) Morskie gravimetricheskie issledovaniya (Marine Gravimetric Studies). Collection of articles. Moscow University Publishing House, Moscow, pp 127–142

Lygin VA (2013) Gravimetric survey in the Arctic transit zones. In: IAG international symposium on terrestrial gravimetry: static and mobile measurements (TG-SMM2013), St. Petersburg, Russia, pp 63–65

Mogilevsky VE, Kontarovich OR (2015) Airborne gravimetric studies in the Arctic. Neft'. Gaz. Novatsii 2:36–40

Mogilevsky VE, Pavlov SA, Kontarovich OR, Brovkin GI (2015) Features of airborne geophysical surveys in high latitudes. Razvedka i Okhrana Nedr 12:6–10

Palamarchuk VK, Poselov VA, Glinskaya NV, Kirsanov SN, Makarov VM, Pryalukhina LA, Subbotin KP, Mishchenko ON, Lokshina VA, Demina IM, Sharkov DV, Kalinin VA (2008) Airborne geophysical survey in the junction zone of the Lomonosov Ridge with the shelf of the Laptev and East Siberian Seas (Arctic-2007). In: Ekspeditsionnye issledovaniya VNIIOkeangeologiya v 2007 godu (VNIIOkeangeologiya Survey Studies in 2007), VNIIOkeangeologia, St. Petersburg, pp 21–30

Peshekhonov VG, Sokolov AV, Krasnov AA, Atakov AI, Pavlov SP (201) Joint analysis of high-accuracy marine and airborne gravity surveys with Chekan-AM gravimeters in the Arctic basin. In: 4th IAG international symposium on terrestrial gravimetry: static and mobile measurements (TG-SMM2016), St. Petersburg, Russia, pp 26–32

Pyle TE, Ledbetter M, Coakley B, Chayes D (1997) Arctic ocean science. Sea Technol 38(10):10–15

Richter TG, Greenbaum JS, Young DA, Blankenship DD, Hewison WQ, Tuckett H (2013) University of Texas airborne gravimetry in Antarctica, 2008 to 2013. In: IAG international symposium on terrestrial gravimetry: static and mobile measurements (TG-SMM2013), St. Petersburg, Russia

Russian Arctic geotraverses (2011) In: Poselov VA, Avetisov GP, Kaminsky VD (eds) Trudy NIIGA-VNIIOkeangeologia (Proceedings of VNIIOkeangeologiya), vol 220, pp 21–25

Smoller YL, Yurist SS, Fedorova IP, Bolotin YV, Golovan AA, Koneshov VN, Hewison W, Richter T, Greenbaum J, Young D, Blankenship D (2013) Using airborne gravimeter GT2A in polar areas. In: IAG international symposium on terrestrial gravimetry: static and mobile measurements (TG-SMM2013), St.Petersburg, Russia

Smoller YL, Yurist SS, Golovan AA, Yakushik LY (2015a) Using a multiantenna GPS receiver in the airborne gravimeter GT-2a for surveys in polar areas. Gyroscopy and Navigation 6(4):299–304

Smoller YL, Yurist SS, Golovan AA, Yakushik LY (2015b) Using a multiantenna GPS receiver in the airborne gravimeter GT2a for surveys in polar areas. 22nd St. Petersburg international conference on integrated navigation systems, St. Petersburg: Elektropribor

Smoller YL, Yurist SS, Golovan AA, Iakushyk LY, Hewison W (2016) Using quasicoordinates in software of multi-antenna GPS receivers and airborne gravimeter GT-2A for surveys in polar areas. In: 4th IAG international symposium on terrestrial gravimetry: static and mobile measurements (TG-SMM2016), St.Petersburg, Russia

Sokolov AV, Krasnov AA, Konovalov AB (2016a) Measurements of the acceleration of gravity on board of various kinds of aircraft. Meas Tech 59(6):565–570

Sokolov AV, Krasnov AA, Koneshov VN, Glazko VV (2016b) The first high precision gravity survey in the North Pole region. Izvestiya. Phys Solid Earth 52(2):254–258

Stroyev PA, Panteleev VL, Levitskaya ZN, Chesnokova TS (2007) Podvodnye ekspeditsii GAISh (Iz istorii nauki) (Underwater Expeditions by Sternberg Astronomical Institute. History of Science). KDU, Moscow

Wziontek H, Wilmes H, Bonvalot S (2009) AGrav—an international database for absolute gravity measurements. IAG 2009 General Assembly, Buenos Aires, Argentina, Aug 31–Sept 4, 2009

Yumanov VS (2013) Algorithm for the transformation of quasigeographic coordinates for using various ellipsoids. In: 15 konferentsiya molodykh uchenykh "Navigatsiya i upravlenie dvizheniem" (15th Conference of Young Scientists "Navigation and Motion Control), St. Petersburg: Elektropribor

Zheleznyak LK, Koneshov VN, Krasnov AA, Sokolov AV, Elinson LS (2015) The results of testing the Chekan gravimeter at the Leningrad gravimetric testing area. Izvestiya. Phys Solid Earth 51(2):315–320

Zhonglovich ID (1950) Gravimetric stations in the Arctic determined on the Sadko and G. Sedov icebreakers in 1935–1940. In: Trudy dreifuyushchei ekspeditsii Glavsevmorputi na ledokol'nom parokhode "G. Sedov", 1937–1940 (Proceedings of the Glavsevmorput Drifting Expedition on the G. Sedov Icebreaker, 1937–1940). Glavsevmorput Publishing House, Moscow–Leningrad

Chapter 5
Advanced Gravity Field Survey Methods

Yu. Bolotin, A. Golovan, V. Vyazmin, M. Evstifeev, and A. Vershovskii

Abstract This chapter considers some of the promising methods for studying the Earth's gravity field. It deals with the vector gravimetry method based on application of strapdown inertial navigation systems, which obtain information on the gravity disturbance vector rather than only its vertical component. Integrated data processing in its inertial, satellite, and gravimetric aspects is discussed. The chapter also covers the scalar airborne gravimetry method based on the introduction of a stochastic gravity model in time; the method based on decomposition of the vector gravimetry problem into estimation of the systematic errors of inertial sensors and estimation of the gravity disturbance vector from the Kalman filter residuals; a new method based on the spherical wavelet decomposition of the gravity disturbance vector. Extensive information is provided on gravity gradiometers, in particular, full tensor gradiometers. The section on cold atom gravimeters discusses the main methods for laser cooling of atoms, controlling atomic ensembles using dual-frequency laser light, labeling atomic states and optical detection of interference signals of de Broglie waves. A review of the existing cold-atom gravimeters is provided.

Keywords Vector gravimetry · Gravity gradiometers · Full tensor gradiometers · Cold atom gravimeters

Yu. Bolotin · A. Golovan · V. Vyazmin
Lomonosov Moscow State University, Moscow, Russia

M. Evstifeev (✉)
Concern CSRI Elektropribor, St. Petersburg, Russia
e-mail: mevstifeev@eprib.ru

A. Vershovskii
Ioffe Institute of Physics and Technology, St. Petersburg, Russia

M. Evstifeev
ITMO University, St. Petersburg, Russia

V. G. Peshekhonov and O. A. Stepanov (eds.), *Methods and Technologies for Measuring the Earth's Gravity Field Parameters*, Earth Systems Data and Models 5,
https://doi.org/10.1007/978-3-031-11158-7_5

Introduction

This chapter considers some of the promising methods for studying the Earth's gravity field (EGF).

Section 5.1 is devoted to vector gravimetry based on strapdown inertial navigation systems, the purpose of which is to obtain information about the gravity disturbance vector rather than only its vertical component. It gives a description of different implementations of the vector gravimetry method and discusses the features of integrated data processing in its inertial, satellite, and gravimetric aspects. The inertial part describes possible forms of the inertial navigation system error equations taking into account the gravity disturbance vector for different versions of mechanization equations. The satellite part highlights the features of designing processing algorithms for raw satellite measurements and the problems of integration of inertial and satellite navigation systems as applied to the vector gravimetry problem. The gravimetric part compares some known methods used to directly determine the gravity disturbance vector based on airborne data. In addition, this section considers the method which is common to scalar airborne gravimetry and is based on the introduction of a stochastic gravity model in time; the method based on the decomposition of the vector gravimetry problem into estimation of the systematic errors of inertial sensors and then, estimation of the gravity disturbance vector from the Kalman filter residuals; a new method based on the spherical wavelet decomposition of the gravity disturbance vector and using the harmonicity of the anomalous gravity field in the Earth's outer space.

Section 5.2 describes the current state of development of tools for measuring the second derivatives of the geopotential, among which the main ones are gravity gradiometers (GG). It describes the use of gradiometers in the search for minerals and in space missions and discusses the results of their testing and operation. The Section analyzes the features of tensor GGs designed to determine all the components of the tensor of second derivatives of the geopotential and considers options for building GGs using atomic interferometry and cold atoms. The potential for the development of gravity gradiometry for various, including new, applications are discussed.

Section 5.3 provides an overview of gravimetric methods and devices using the wave properties of atomic ensembles cooled to ultra-low temperatures by interaction with resonant laser light. This section discusses the main methods for laser cooling of atoms, methods of controlling atomic ensembles (splitting, reflection, recombination of an atomic beam) using dual-frequency laser light, methods of "labeling" atomic states and optical detection of interference signals of de Broglie waves. It also presents a review of the existing cold-atom gravimeters, analyzes their inherent limitations and promising ways of developing such systems; in particular, interferometers based on a combination of various types of cold atoms, as well as on a condensate or a combination of Bose–Einstein condensates.

5.1 Airborne Vector Gravimetry Based on Strapdown Inertial Navigation Systems

This section is focused on airborne vector gravimetry based on strapdown inertial navigation systems. Studies in this area have been conducted by various authors since the 1990s (Schwarz et al. 1992; Jekeli and Kwon 1999). The term 'airborne vector gravimetry' is used to mean determination of all three components of the gravity disturbance (GD) vector. It should be noted that the vertical component of the GD vector coincides with the free-air gravity disturbance with accuracy of up to the height correction (Yelagin 2012). As it is known, a substantially more accurate element base is needed to determine the horizontal GD components than for traditional (scalar) airborne gravimetry, which only determines GA. The main difficulty in estimating the GD vector is to separate the horizontal GD components from the instrumental, geometrical errors of inertial sensors. For example, an orientation error of one arcsecond (~$4.85 \cdot 10^{-6}$ rad) leads to an error in the horizontal components of ~5 mGal (Bolotin et al. 2002). It should be noted that airborne vector gravimetry is closely related to the so-called inertial-geodetic method described in Sect. 3.4 and in (Emel'yantsev et al. 2015), the main purpose of which is to determine deflections of the vertical (DOV). The parameters to be determined in the GD model in use, for example, a stochastic or finite-dimensional model, serve, in addition to the instrumental errors of inertial sensors, as state vector components in the aiding problem of inertial navigation (Jekeli and Kwon 1999; Bolotin et al. 2002). Satellite navigation system (GNSS) data serve as external aiding information.

In accordance with the above, the description of the models of the airborne vector gravimetry problem in its inertial part includes:

- reference, ideal equations of inertial navigation, sometimes referred to as equations of the ideal operation of an inertial navigation system (INS) (Golovan and Parusnikov 2011);
- equations used in inertial navigation system algorithms, sometimes referred to as model equations which, unlike ideal equations, use sensor readings containing errors;
- equations of sensor readings (instrument equations) written in the axes of the INS instrument frame or, in the case of a strapdown inertial navigation system (SINS), in the axes of the so-called quasi-instrumental frame, sometimes referred to as a virtual gyro platform.

The use of notions about ideal, mechanization, and instrument equations of inertial navigation makes it possible to design relevant models of airborne vector gravimetry in a simple and clear form.

In the GNSS part, a common approach is the use of positional carrier phase (phase-differential) solutions (Golovan and Vavilova 2007) provided by off-the shelve software produced by the developer of satellite navigation equipment or companies specializing in processing of raw satellite measurements. At the same time, other trajectory parameters of the vehicle motion used in airborne gravimetry, such as

velocity, acceleration of a vehicle are determined by numerical differentiation of the mentioned positional solutions. As the experience in developing software for the GT-2A airborne gravimeter (Bolotin and Golovan 2013) shows, it is advisable to have proprietary GNSS software focused specifically on the airborne gravimetry problem and directly providing GNSS-derived velocity and acceleration from carrier-phase measurements.

Let us make a few general remarks on the inertial and GNSS aspects of airborne vector gravimetry.

1. The airborne gravimetry problem is solved in postprocessing mode. In this regard, SINS is not required to operate in the inertial, Schuler's operation mode as it does. SINS can only be considered as a recorder of measurements of inertial sensors synchronized with satellite data (Smoller et al. 2012).
2. The airborne gravimetry problem assumes that high-precision position and velocity solutions of the GNSS are always available. For this reason, when deriving the model equations, one can use the mentioned satellite information to the maximum, which allows for a significant simplification of the aiding equations in airborne gravimetry. A special example of such use is the GT-2A airborne gravimeter.
3. Traditionally, SINS algorithms use a numerical frame associated with a model geographic vertical, a particular azimuthal orientation law. Similarly, the SINS algorithms can be implemented in the axes of other frames, for example, in an inertial frame, in whose axes the algorithms have no singularities in Polar Regions unlike models that use the concepts of longitude and true heading.
4. The airborne vector gravimetry problem can be solved using both SINS and gimballed INS. There are no fundamental differences at the level of mathematical models. The only difference is that, in the case of the SINS, the instrumental errors of the SINS inertial sensors are projected from the "fast" body frame axes to the axes of the "slow" geodetic or fixed inertial-centered frame.

The gravimetric part deals with some approaches to estimating the GD vector. It should be recalled that in scalar airborne gravimetry, measurement processing is carried out in two stages (Bolotin and Golovan 2013) (see Sects. 5.1.3 and 5.2.2): first, the misalignments of the vertical axis of the 'virtual platform' frame relative to the navigation frame and the azimuthal error are estimated (the GD is ignored), and then, the basic airborne gravimetry equation (2.2.1) projected onto the vertical axis of the navigation frame is considered. In contrast to this, in airborne vector gravimetry, the attitude errors and the GD vector should be considered jointly, using some additional information for their separation. A common approach to separation is based on introducing a hypothesis of the stochastic nature of the GD and introducing the stochastic model of the GD in time. However, this approach raises the problem of choosing a correct model. According to recent publications, the use of the EGM2008 model for estimating low-frequency GD components (Cai et al. 2013), the use of the platform orientation star correction system (Dai et al. 2014) and others are other examples of introducing additional information or hypotheses about the GD characteristics.

An interesting heuristic approach, which does not require a stochastic GD model proposed in (Kwon and Jekeli 2001), suggests using repeated survey lines which provides additional information for the above separation. The approach is based implicitly on the hypothesis about the low-frequency nature of the GD vector. It consists in obtaining rough GD vector estimates on each repeated line as the Kalman filter residuals in the problem of INS aiding neglecting the GD vector in the INS error equations, and the subsequent decorrelation of the estimates obtained at the repeated survey lines (in what follows, the method is referred to as PDD—proximate decomposition and decorrelation). The algorithm is essentially nonlinear. Processing of the experimental data has given rather encouraging results.

Section 5.1 also analyzes the new approach (Bolotin and Vyazmin 2016) that does not require any stochastic hypotheses about the GD vector but uses harmonicity of the anomalous field. It makes use of local deterministic harmonic gravity models based on spherical scaling and wavelet expansion of gravity (Freeden and Michel 2004) described in this section. The problem of airborne vector gravimetry is formulated as a problem of estimating scaling coefficients along with the parameters of instrumental errors of inertial sensors. GNSS velocity solutions are used as aiding information. The assumption of the harmonic nature allows taking into account the correlation between the data on adjacent lines without introducing stochastic hypotheses about the GD. We use the abbreviation LHM—local harmonic modeling—for this method. The effectiveness of the method is checked by processing simulated data.

The traditional approach in geodesy consists in determining the DOV of the GD vector from its vertical component provided by scalar airborne gravimetry. In this case, DOV is determined with the use of the Vening–Meinesz formula. In what follows, the method based on this formula is called VCT—vertical component transformation. The drawback of the method is the need to know the GD vertical component within the vast survey area, for which data from global models are usually used.

Thus, at present, researchers have accumulated a substantial set of airborne vector gravimetry algorithms. Unfortunately, these algorithms are difficult to compare using experimental data, as the latter are often unavailable or not suitable for the analysis of a specific algorithm. For this reason, the development of an analytical methodology for such a comparison is of crucial importance. This Section attempts to develop such a methodology. It is the authors' opinion that the conventional comparison of covariance analysis along the trajectory lacks informativity since it depends on a specific trajectory. Therefore, the method of spectral analysis was used to compare various algorithms. The difficulties associated with its implementation are due to the nonstationary nature of the problem. A special averaging procedure was developed to transform this nonstationary problem into a stationary one. After averaging, the comparison is carried out in terms of the power spectral density (PSD) of the GD estimation errors.

Finally, the above-mentioned PDD, LHM, and VCT methods for determining the GD vector based on airborne survey data are described in detail and compared. The results of their qualitative comparison using spectral analysis methods are discussed; also considered are the results of the study of the spatial field correlation influence

on the quality of separation of the GD horizontal components and SINS systematic errors.

5.1.1 Airborne Vector Gravimetry Equations

An adequate choice of a coordinate system or a frame in which equations are written is very important for solution of inertial navigation and inertial gravimetry problems (Golovan and Parusnikov 2011). In this Section, the mechanization equations of airborne gravimetry are first written in geodetic and inertial frame, and then, the computed mechanization equations are written in the same frame. The so-called quasi-instrumental frames are introduced as a result of solving computed mechanization equations, and the ideal mechanization equations of airborne gravimetry are written in this frame. Finally, the computed and ideal mechanization equations in the quasi-instrumental frame are used to introduce error equations with the separation of errors into the so-called dynamic and kinematic ones.

Recall the standard definitions. The geodetic frame Mx is a frame defined as the right orthogonal coordinate system with its origin at a given point, one of the axes of which coincides with the outer normal to the surface of the reference ellipsoid; the second one is directed to the north, and the third one to the east. The instrument frame Mz is a frame whose axes are oriented along the sensitivity axes of sensors (accelerometers). The inertial frame Oξ is a frame with its origin at the center of the Earth and whose axes retain their direction in space.

Reference equations of airborne vector gravimetry in the geodetic frame. Let us write the basic equation of airborne vector gravimetry (ideal equation)—the equation of motion of the sensitive mass M of the gravimeter sensing element—in the projections on the geodetic frame (Golovan and Parusnikov 2011):

$$\dot{V}_x = \left(\omega_x^{\times} + u_x^{\times}\right) V_x + L_{xz} f_z + \gamma_x + \Delta g_x. \tag{5.1.1}$$

Here, Δg_x is the GD vector; $V_x = (V_E, V_N, V_{UP})^{\mathrm{T}}$ is the velocity vector of the aircraft relative to the earth (eastern, northern, vertical components); f_z is the external specific force in the projections on the axes of the frame Mz of the INS (body frame); L_{xz} is the matrix of transition from the body frame to the geodetic frame; $\boldsymbol{\gamma}_x$ is the normal gravity vector calculated using the known formula; ω_x is the vector of the absolute angular velocity of the frame Mx calculated using the known formulas; u_x is the vector of the angular velocity of the Earth's rotation in the Mx axes; $u_x^{\times}$ is a skew-symmetric matrix composed of vector components u_x.

The kinematic equation for the transition matrix is as follows (Golovan and Parusnikov 2011):

$$\dot{L}_{zx} = \boldsymbol{\omega}_z^{\times} L_{zx} - L_{zx} \boldsymbol{\omega}_x^{\times}.$$

Here, ω_z is the vector of the absolute angular velocity of the frame Mz.

Reference equations of airborne vector gravimetry in the inertial frame. For definiteness, let us assume that the axes of the inertial frame Oξ coincide with the axes of the Earth-centered Earth-fixed coordinate system at the initial moment of time. We have

$$\begin{aligned} \dot{\boldsymbol{\xi}} &= v_\xi, \qquad \dot{v}_\xi = L_{\xi z} f_z + \boldsymbol{\gamma}_\xi + \Delta g_\xi, \\ \boldsymbol{\gamma}_\xi &= L_{\xi x} \boldsymbol{\gamma}_x, \; \Delta g_\xi = L_{\xi x} \Delta g_x. \end{aligned} \tag{5.1.2}$$

Here, $\boldsymbol{\xi}$, v_ξ are the coordinates of point M and the vector of its absolute velocity in Oξ; $L_{\xi z}$ is the matrix of the transition from the body frame to the inertial frame satisfying the equation $\dot{L}_{z\xi} = \boldsymbol{\omega}_z^\times L_{z\xi}$; $L_{\xi x}$ is the matrix of the transition from the geodetic frame to the inertial frame. It should be noted that this version of the mechanization equations is often used in airborne vector gravimetry (Kwon and Jekeli 2001).

As a result, the problem of vector inertial gravimetry, airborne gravimetry in particular, is described as follows. The following trajectory parameters of the vehicle (gravimetric system carrier) are known: the coordinates (geodetic λ, φ, h, or $\boldsymbol{\xi}$), the vector of the linear velocity (relative V_x or absolute v_ξ). The vectors of absolute angular velocity ω_z and the specific force f_z in Mz are measured. A model for the normal gravity $\boldsymbol{\gamma}_x$ is known. It is required to determine the GD vector Δg_x (or Δg_ξ) based on the given reference models.

Computed mechanization equations of airborne vector gravimetry. The computed mechanization equations of vector gravimetry are defined from the above ideal equations by using the readings $\omega_z' = \omega_z - v_z, f_z' = f_z + \Delta f_z$ of inertial sensors. Here: $\boldsymbol{v}_z$ is the vector of measurement errors of gyroscopes; the minus sign is chosen in order to match the error equations of the platform and strapdown INS; Δf_z is the vector of measurement errors of accelerometers.

Below are only the versions of the computed mechanization equations that are based on the full use of the available high-precision satellite navigation solutions. It should be recalled that modern carrier phase differential satellite navigation makes it possible to determine locations with, at least, submeter accuracy and the velocity vector with an accuracy of a few cm/s.

First, let us provide some estimates. A positioning error of the order of 30 m leads to an angular error in determining the orientation of the geodetic frame at the level of 1 arcsec. The submeter accuracy means that the accuracy in calculating the orientation of the "satellite" geodetic frame will be of the order of 10^{-2} arcsec, which undoubtedly makes it an ideal geodetic frame. In addition, there is no need to use the positional group of mechanization equations of inertial navigation.

Mechanization equations of airborne vector gravimetry in the geodetic frame. Mechanization equations in the geodetic frame are written as follows (Golovan and Parusnikov 2011):

$$\dot{V}_x' = \left(\omega_x^\times + u_x^\times\right) V_x' + \gamma_x + L_{xz}' f_z',$$

$$\dot{L}'_{zx} = \omega_z'^{\times} L'_{zx} - L'_{zx}\omega_x^{\times}$$

where V'_x is the computed relative linear velocity. Matrix L'_{zx} defines and specifies the orientation of the computed body frame Mz' with respect to the geodetic frame. The values ω_x, u_x, γ_x are assumed to be calculated with high precision using GNSS solutions.

Mechanization equations of airborne vector gravimetry in the inertial frame. Mechanization equations in the inertial frame are written as follows:

$$\dot{v}'_\xi = L'_{\xi z} f'_z + \gamma_\xi.$$

Here, v'_ξ is the vector of the computed absolute velocity; $L'_{\xi z}$ is the matrix of transition from the computed body frame My to the inertial frame $O\xi$ satisfying the equation $L'_{z\xi} = \omega_z'^{\times} L'_{z\xi}$.

Quasi-instrumental frames Mz^x, $M\xi^x$. The concepts of quasi-instrumental frames Mz^x, Mz^ξ can be introduced based on the results of solving the corresponding computed mechanization equations (Golovan and Parusnikov 2011) (as shown in Fig. 5.1 for the frame Mz^x):

- the orientation matrix of the frame Mz^x relative to Mz is L'_{zx};
- the orientation matrix of the frame Mx relative to My is L'_{zx}.

The orientation matrix $L'_{z\xi}$ of the frame $M\xi^x$ relative to Mz is also introduced. If the computed mechanization reference equations are integrated with high precision, then Mz^x coincides with Mx, and Mz^ξ coincides with $M\xi$. Let us introduce the vector of infinitesimal rotation α_y which characterizes the closeness of two frames: the computed My and the body-fixed Mz frames. In the linear approximation, their

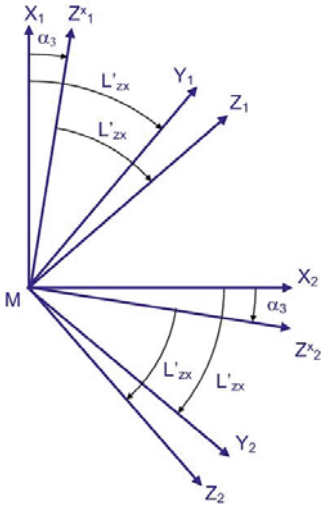

Fig. 5.1 Orientation of the geodetic Mx, quasi-instrumental Mz^x, computed My and body-fixed Mz frames

orientation matrix L_{zy} has the form $L_{zy} = I + \alpha_y^{\times}$, where $\alpha_y^{\times}$ is the skew-symmetric matrix corresponding to vector α_y (Golovan and Parusnikov 2011).

Similarly, let us introduce the vector of infinitesimal rotation $\alpha_x = (\alpha_1, \alpha_2, \alpha_3)^{\mathrm{T}}$ characterizing the orientation of the geodetic frame Mx and the quasi-instrumental frame Mz^x, and the vector of infinitesimal rotation $\boldsymbol{\alpha}_\xi$ characterizing the orientation of the inertial frame $M\xi$ and the quasi-instrumental frame Mz^ξ. It can be shown that the following relations are true in the linear approximation (Golovan and Parusnikov 2011):

$$L_{z^x x} = I + \alpha_x^{\times}, \quad L_{z^\xi \xi} = I + \alpha_\xi^{\times}, \quad \alpha_x = L'_{xz}\alpha_y, \quad \alpha_\xi = L'_{\xi z}\alpha_y.$$

Reference equations of airborne vector gravimetry in the quasi-instrumental frames. The reference equations in the quasi-instrumental frames Mz^x, Mz^ξ are needed for the subsequent derivation of the error equations in the case where the total errors of the navigation solutions are represented as a sum of the so-called kinematic and dynamic errors. They reflect the contribution of the errors of two different types of inertial sensors, gyroscopes and accelerometers, to the total error. Such a separation was first described in the classical monographs written by Andreev (1966, 1967), where they were referred to as errors of the first and second kind.

Reference equations in the quasi-instrumental frame Mz^x. We have

$$\dot{V}_{z^x} = \left(\omega_{z^x}^{\times} + u_{z^x}^{\times}\right)V_{z^x} + L'_{xz} f_z + \gamma_{z^x} + \Delta g_{z^x},$$
$$V_{z^x} = L_{z^x x} V_x, \quad u_{z^x} = L_{z^x x} u_x, \quad \gamma_{z^x} = L_{z^x x}\gamma_x, \quad \Delta g_{z^x} = L_{z^x x}\Delta g_x,$$

and the relations $\omega_{z^x} = \omega_x + v_x$, $v_x = L'_{xz} v_z$ are true.

Reference equations in the quasi-instrumental frame Mz^ξ. We have

$$\dot{v}_{z^\xi} = v_\xi^{\times} v_{z^\xi} + L'_{\xi z} f_z + \gamma_{z^\xi} + \Delta g_{z^\xi},$$
$$v_{z^\xi} = L_{z^\xi \xi} v_\xi, \quad \gamma_{z^\xi} = L_{z^\xi \xi}\gamma_\xi, \quad \Delta g_{z^\xi} = L_{z^\xi \xi}\Delta g_\xi, \quad v_\xi = L'_{\xi z} v_z.$$

5.1.2 *Airborne Vector Gravimetry Error Equations*

Error equations in the geodetic frame. Let us introduce the total errors of velocity solution $\Delta V_x = V'_x - V_x$. Thus, the equations in variations can be written as follows:

$$\Delta\dot{V}_x = \left(\omega_x^{\times} + u_x^{\times}\right)\Delta V_x + \alpha_x^{\times} f'_x + \Delta g_x + \Delta f_x, \quad f'_x = L'_{xz} f'_z, \quad \Delta f_x = L'_{xz}\Delta f_z.$$

A special feature of this form is the appearance of vector f'_x in the right side of the differential equation. Accordingly, in the simulation, it is necessary either to simulate

the value of f'_x based on the differentiation of the model velocity vector V'_x or to use noisy measurements f'_z of accelerometers when they are available.

To eliminate this feature, it is advisable to use the expansion of the total error ΔV_x into the so-called dynamic and kinematic components:

$$\Delta V_x = \delta V_x + \alpha_x^{\times} V'_x, \delta V_x = V'_x - V_{z^x}.$$

The dynamic error satisfies the equation:

$$\delta \dot{V}_x = \left(\omega_x^{\times} + u_x^{\times}\right)\delta V_x + \gamma_x{}^{\times}\alpha_x - \Delta g_x + \Delta f_x + V_x^{'\times} v_x, \tag{5.1.3}$$

and the kinematic component $\hat{\alpha}_x V'_x$ is defined by the vector of infinitesimal rotation α_x referred to as the kinematic error which satisfies the equation:

$$\dot{\alpha}_x = \omega_x^{\times}\alpha_x + v_x,\ v_x = L'_{xz} v_z. \tag{5.1.4}$$

As is the convention in inertial navigation, Eqs. (5.1.3)–(5.1.4) are obtained in a linear approximation. Model (5.1.3) does not contain the parameter f'_x, which is convenient for its simulation.

Error equations in the inertial frame. Let us introduce the total error of velocity $\Delta v_\xi = v'_\xi - v_\xi$. Thus, the equations in variations can be written as follows:

$$\Delta \dot{v}_\xi = \alpha_\xi^{\times} f'_\xi + \Delta g_\xi + \Delta f_\xi, \quad f'_\xi = L'_{\xi z} f'_z, \quad \Delta f_\xi = L'_{\xi z}\Delta f_z.$$

As above, the right side of these equations includes vector f'_ξ. To eliminate this feature, it is also advisable to use the expansion of the total error Δv_ξ to the dynamic and kinematic components:

$$\Delta v_\xi = \delta v_\xi + \alpha_\xi^{\times} v'_\xi, \quad \delta v_\xi = v'_\xi - v_{z^\xi};$$

moreover, the dynamic error δv_ξ satisfies the equation:

$$\delta \dot{v}_\xi = \alpha_\xi^{\times}\gamma_\xi + \Delta g_\xi + \Delta f_\xi - v_\xi^{\times} v'_\xi, \tag{5.1.5}$$

and the small rotation vector α_ξ also referred to as the kinematic error satisfies the equation $\dot{\alpha}_\xi = v_\xi$.

5.1.3 Models of Aiding Measurements

The airborne vector gravimetry problem can be considered as a problem of correcting the solution of mechanization equations using GNSS measurements. As noted in

Sect. 2.2.2, it is advisable to use phase-frequency GNSS solutions in the differential mode (Bolotin and Golovan 2013); relative velocities are used when the equations are written in the geodetic frame, and absolute velocities in the inertial frame.

When considering errors "in the small", the problem can be treated as the problem of correcting the solution of error equations using GNSS measurements "in the small".

Let us write down the equation for aiding velocity measurements "in the small". Let us use V_x^{GNSS} to denote the relative velocity vector defined by its projections on the axes of the geodetic frame based on the GNSS position solution. In the geodetic frame Ox we have the following relation (Golovan and Vavilova 2003; Golovan and Vavilova 2007; Wei et al. 1991):

$$y_x = V_x^{'} - V_x^{GNSS} = \Delta V_x - \Delta V_x^{GNSS} = \delta V_x + \alpha_x^{\times} V_x^{GNSS} - \Delta V_x^{GNSS}, \quad (5.1.6)$$

where ΔV_x^{GNSS} is the GNSS velocity error.

For the inertial frame $O\xi$, we have:

$$y_\xi = \mathrm{v}_\xi^{'} - \mathrm{v}_\xi^{GNSS} = \Delta \mathrm{v}_\xi - \Delta \mathrm{v}_\xi^{GNSS} = \delta \mathrm{v}_\xi + \alpha_\xi^{\times} \mathrm{v}_\xi^{GNSS} - \Delta \mathrm{v}_\xi^{GNSS}.$$

Let us present a model of aiding measurements of specific force. Let us use f_ξ^{GNSS} to denote the vector of specific force obtained by processing satellite measurements, $f_\xi^{GNSS} = \ddot{\xi}^{GNSS} - \gamma_\xi$, where the value $\ddot{\xi}^{GNSS} = \dot{v}_\xi^{GNSS}$ is estimated using satellite measurements. Thus, to measure.

$$y_\xi^{'} = f_\xi^{'} - f_\xi^{GNSS} = L_{\xi z}^{'} f_z^{'} - f_\xi^{GNSS},$$

the following model is valid:

$$y_\xi^{'} = \alpha_\xi^{\times} f_\xi^{'} - \Delta g_\xi + L_{\xi z}^{'} \Delta f_z - \Delta f_\xi^{GNSS}, \quad (5.1.7)$$

where Δf_ξ^{GNSS} is the error in determining the value f_ξ^{GNSS}. Note that (Kwon and Jekeli 2001) use in essence a similar model.

Error equations (5.1.3), (5.1.4) along with the aiding measurement equations (5.1.6) (when the problem is presented in the geodetic frame) or (5.1.5) along with (5.1.7) (when the problem is presented in the inertial frame) are used to determine the GD vector at the flight path of the aircraft. As already shown, these equations cannot be solved without using additional hypotheses about the nature of noise and the GD.

It should also be noted that both equations (in the geodetic and inertial frame) have their advantages and disadvantages (Golovan and Parusnikov 2011). For example, if the equations are written in the inertial frame, inertial corrections completely disappear, but the normal gravity becomes variable. In the case of the geodetic frame, the situation is quite the opposite.

5.1.4 Selected Approaches to the Solution of the Airborne Vector Gravimetry Problem

In airborne vector gravimetry, separation of GD horizontal components and errors requires either additional measurements (for example, stellar correction (Dai et al. 2014)) or the introduction of additional hypotheses.

Application of the stochastic GD model. The approach based on the introduction of the stochastic GD model in time is similar to that often used in scalar airborne gravimetry (Jekeli and Kwon 1999; Bolotin et al. 2002; Bolotin and Golovan 2013). However, similar to the scalar case, the problem of choosing the correct model is still open. It is shown (Jekeli and Kwon 1999) that the method is very sensitive to the choice of model.

Application of proximate decomposition and decorrelation method. K. Jekeli proposed a simple and original approach (Kwon and Jekeli 2001), which, for brevity sake, will be referred to as the method of proximate decomposition and decorrelation (PDD) which does not require a stochastic hypothesis for gravity. The method assumes a repeat flight along the same survey line, which gives additional information. It consists in a priori separation of the problem for each flight into estimation of the instrumental error parameters, ignoring the GD, and subsequent determination of GD from the Kalman filter residuals. The residual systematic errors of the SINS in the two GD estimates obtained in two flight paths are removed based on the mutual correlations found in them.

Let us describe the PDD algorithm in more detail. Calculations are carried out in the inertial frame. The algorithm actually includes the following stages (Kwon and Jekeli 2001):

1. transformation of the basic gravimetry equation and sensor readings into an inertial reference frame similar to (5.1.5);
2. calculation of the accelerations of the antenna of the onboard GNSS receiver as a smoothed double difference of GNSS coordinates;
3. smoothing of the obtained estimates of accelerations and measurements of accelerometers with a finite impulse-response filter with a window width of 60 s and decimation;
4. estimation of the parameters of SINS instrumental errors in (5.1.5) using the KF from measurements (5.1.7) without taking into account the GD vector in (5.1.5);
5. calculation of GD estimates on survey lines as residuals of measurements $\Delta\tilde{g}_\xi = y'_\xi - \tilde{y}'_\xi$, where $\tilde{y}'_\xi$ is the measurement estimate obtained from the KF;
6. removal of trends from the estimates $\Delta\tilde{g}_\xi$ due to known GD values at the ends of survey lines;
7. filtering of the residual systematic errors in the estimates $\Delta\tilde{g}_\xi$ due to the decorrelation (removal of uncorrelated spectral components) $\Delta\tilde{g}_\xi$ on the repeat survey lines (wavenumber correlation filter).

Since the algorithm includes smoothing which removes the high-frequency part of the information, it implicitly makes an assumption about the low-frequency nature of

the GD in the time domain. This smoothing can also be interpreted as the "whitening" of the noise of the double difference in positional GNSS measurements for the KF to be applied. Since the sensor errors on repeat survey lines are independent, the components caused by the errors in determining the platform orientation are expected to be partially removed from GD estimates due to the decorrelation. In general, the algorithm is clearly heuristic in its nature but it provided good results from real data processing (Kwon and Jekeli 2001).

Application of the local harmonic model. In the new approach proposed in (Bolotin and Vyazmin 2016), the solution of airborne gravimetry equations is based on simultaneous GD estimation along several adjacent airborne survey lines with the use of the local harmonic model for gravity. This automatically takes into account the mutual correlation of GD components and the cross-correlation of GD values on adjacent survey lines. The expansion of the gravity field in terms of the Abel–Poisson scaling functions is used in (Bolotin and Vyazmin 2015) as a local GD model (Freeden and Michel 2004; Bolotin and Vyazmin 2015). The problem is reduced to the joint estimation of constant scaling coefficients of the disturbing potential defined in the survey area and the instrumental errors of the SINS (for the reader's convenience, a brief mathematical description of the algorithm is given in a separate section below). It should be noted that here, similarly to the above, we use assumptions about the low-frequency nature of the GD, the maximum frequency of which is determined by the maximum resolution level of the GD scaling function expansion. It should also be noted that by taking into account the harmonic nature of the disturbing potential, it is possible to separate the GD and the platform orientation errors.

Application of the VCT method. It is relevant to pose a question whether airborne vector gravimetry is needed at all. Indeed, the GD vector can be obtained using a map of the vertical GD component and applying a suitable transformation method to this map, e. g., the Khotin kernel convolution (Jekeli 2009), or the Vening-Meinesz method for determining the DOV (see Formula (5.3.1) in Sect. 5.3.1). In order to try to answer the question asked, let us compare the PDD and LHM methods with the VCT method. At the same time, of course, one should be aware that the VCT method requires a map of a large survey region, which is not always feasible in practice, even when integrating airborne gravimetric data with global model data.

Simplified block diagrams of the methods are shown in Fig. 5.2.

5.1.5 Spectral Analysis of the Airborne Vector Gravimetry Accuracy

Spectral methods are used in gravimetry both in calculations and in the qualitative analysis of algorithms (Schwarz et al. 1990). The latter is considered here. The PDD, LHM, and VCT approaches are compared on the basis of spectral analysis.

This comparison brings about two problems. First, the equations of vector airborne gravimetry are nonstationary, and, strictly speaking, the spectral analysis is not

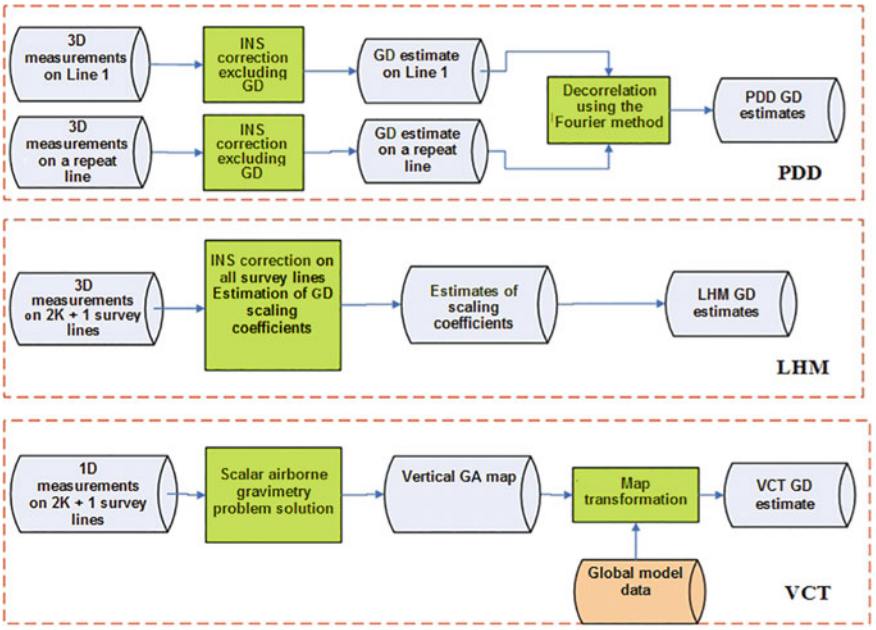

Fig. 5.2 Simplified block diagrams of the approaches to determining the GD vector

applicable to them. This problem is solved using a special averaging procedure which is based on a certain heuristic ergodic hypothesis. The Fourier transform, one-dimensional along survey lines (for PDD) and two-dimensional in the flight plane (for LHM and VCT), is applied to the resulting stationary system. Thus, the comparison problem is transferred to the frequency domain.

The second problem is that the hypotheses for the GD, on which the approaches are based, are different. To make a comparison, it is necessary to introduce a common hypothesis. A stochastic model of the GD will be used, the introduction of which allows the errors of the methods to be characterized in terms of the PSD of the Wiener optimal error estimate. The Wiener filtering formulas are used to derive formulas for the optimal GD vector estimates and PSD estimate error—for the PDD approach in one-dimensional version and for the LHM and VCT approaches in the two-dimensional version. Each of these PSDs gives a lower bound for the PSD of true error of gravity estimation. Finally, the PSDs for the LHM and VCT approaches are integrated in the direction of the frequencies across the survey lines and the obtained estimates of the one-dimensional PSD and the corresponding variances (integrals of the PSD over the frequency along the survey lines) are compared.

The analysis is based on the well-known formulas for the optimal (by the criterion of the minimum variance of the estimate error) Wiener estimate $\tilde{x}$ of a stationary signal x from the measurements $y = Hx + r$, where r is the noise, and for the PSD $S_{\delta x}$ of the error δx (Kailath et al. 2002):

$$S_{\delta x}^{-1} = S_x^{-1} + H^T S_r^{-1} H, \quad \tilde{x} = S_{\delta x}^{-1} H^T S_r^{-1} y.$$

It should be emphasized that the stochastic hypothesis introduces additional information into the problem; therefore, all the obtained accuracy estimates are inevitably too optimistic.

Assumptions in spectral analysis. Let us formulate assumptions that allow conversion of the airborne vector gravimetry problem into the frequency domain. Let us consider airborne measurements along a flight path (or a path of several flights), consisting of a fairly large set of survey lines and turns between them. The PDD and LHM approaches will be compared in the geodetic reference frame. Let us make the following simplifying assumptions for the spectral analysis of the approaches:

1. the orientation matrix L_{xz} is close to an identity matrix; the flight altitude is approximately constant;
2. the length L_1 of each survey line is much greater than the gravity correlation radius L_g; the distance ΔL_2 between the survey lines is much shorter than L_g;
3. variations of the aircraft measured speed $V_x^{GNSS}(t)$ are small on survey lines, and it can be represented in the form of $V_x^{GNSS}(t) = V_0 + V_1(t)$, where $V_0 =$ const, V_1 is a random process with zero mean and the correlation period T_V, which is much smaller that T_g, where $T_g = L_g / V_0$ is the GD correlation period, $V_0 = |V_0|$. The V_1 process is assumed to be stationary with the PSD $S_V(u)$, where u is the angular frequency in rad/s, and ergodic properties (P_V is a constant 3×3 covariance matrix of $V_1(t)$):

$$E\left[V_1 V_1^T\right] = P_V \approx \frac{1}{T_V} \int_0^{T_V} V_1(t) V_1^T(t) \mathrm{d}t;$$

4. the orientation and velocity errors, α_x and δV_x, are slowly varying functions with a typical period T_α, which is much greater than T_V (this implicitly assumes high accuracy of gyroscopes, at least 0.01°/h)
5. the errors of scale factors and the nonorthogonality of the sensitivity axes of accelerometers and gyroscopes are negligible after laboratory or flight calibration;
6. the errors in measuring the velocity with GNSS, accelerometers, and gyroscopes are stationary random processes with the PSDs:

$$S_{\Delta V}(u) = \frac{\sigma_P^2}{2\pi} u^2 I, \; S_f(u) = \frac{\sigma_f^2}{2\pi} I, \; S_v(u) = \frac{\sigma_v^2}{2\pi} I,$$

where I is the 3×3 identity matrix; σ_P, σ_f, σ_v are the standard deviations of the measurement errors of GNSS positions, accelerometers, and gyroscopes, respectively;

7. the reference ellipsoid in the vicinity of the survey area can be considered flat, with Cartesian coordinates $x_1,\ x_2$, where axis x_1 is directed along the survey lines, and axis x_2 lies across the lines, the GD in space is a stationary random process of $x_1,\ x_2$ with a known PSD $S_{\Delta g}(u_1,\ u_2)$, where $u_1,\ u_2$ are spatial frequencies in the directions along and across the survey lines respectively.

Reducing gravimetry equations to a stationary form and transition to the frequency domain. Airborne gravimetry equations (5.1.3)–(5.1.4) are not stationary along the trajectory but they can be brought to a stationary form under the above conditions using the following technique: applying a low-pass filter "cutting off" nonstationary terms. It should be emphasized that this filter is speculative and it is in no way part of the data processing algorithm.

We introduce a linear ideal low-pass filter with a finite impulse response with no phase shift $\Theta[\cdot]$ applied to functions of time, with a transfer function in time $\Theta[s]$ (s is the Laplace transform argument) and a cutoff frequency close to $2\pi/T_V$ with the following properties: $\Theta[V_1] \approx 0$, $\Theta[\Delta g_x] \approx \Delta g_x$, $\Theta[\alpha_x] \approx \alpha_x$, $\Theta[\delta V_x] \approx \delta V_x$. Due to the assumption of the ergodicity of $V_1(t)$, the low-pass filter determines the sample covariance matrix of $V_1(t)$, namely:

$$\Theta\left[V_1(t)V_1^T(t)\right] \approx E\left[V_1(t)V_1^T(t)\right] = P_V.$$

By applying the filter $\Theta[\cdot]$ to the terms in the error Eqs. (5.1.3)–(5.1.4) and the aiding measurement Eqs. (5.1.6), we obtain "smoothed" equations (hereinafter, subscript x on $\delta V,\ \alpha$, etc., is omitted):

$$\begin{aligned} \delta\dot{V} &= \left(\omega^{\times} + u^{\times}\right)\delta V + \gamma^{\times}\alpha - \Delta g + q_4 + V_0^{\times} q_3, \\ \dot{\alpha} &= \omega^{\times}\alpha + q_3, \end{aligned} \tag{5.1.8}$$

$$y_1 = \delta V - V_0^{\times}\alpha + q_1, \tag{5.1.9}$$

where the notations $q_1 = \Theta\left[\Delta V^{GNSS}\right]$, $q_3 = \Theta[v]$, $q_4 = \Theta[\Delta f]$ are introduced, and $V_0^{\times}$ is a skew-symmetric matrix corresponding to the vector V_0 (Golovan and Parusnikov 2011).

The PSDs of the noise introduced are defined by the formulas:

$$S_{q_1}(u) = \frac{\sigma_P^2}{2\pi} u^2 |\Theta(iu)|^2 I, \quad S_{q_4}(u) = \frac{\sigma_f^2}{2\pi} |\Theta(iu)|^2 I, \quad S_{q_3}(u) = \frac{\sigma_v^2}{2\pi} |\Theta(iu)|^2 I.$$

Equations (5.1.8)–(5.1.9) are stationary, but they lost some of the information associated with the redesign of errors in the process of aircraft evolutions. At the same time, small aircraft evolutions during the survey can improve the quality of the estimation (Becker et al. 2016). For a qualitative analysis of the influence of evolutions, let us introduce a "modulated" measurement y_2 which is additional to (5.1.9) and can be obtained by multiplying (5.1.6) on the left by the matrix $V_1^{\times}(t)$

and averaging with the filter Θ:

$$y_2 = Q_V \alpha + q_2. \tag{5.1.10}$$

Here, $y_2 = \Theta[V_1^{\times} y]$, $q_2 = \Theta\left[V_1^{\times} \Delta V^{GNSS}\right]$, $Q_V = tr\,(P_V)\, I - P_V$, where P_V, as above, is the covariance matrix of the process V_1, I is an identity matrix, tr is the trace of a matrix. The processes q_2 and q_1 are not correlated. Let us write an expression for the PSD of the process $q_2(t)$. Let us assume that V_1 is a bandpass white noise with a spectrum focused in the vicinity of the frequency $u_V = 2\pi/T_V$. Thus, the PSD of $q_2(t)$ can be approximately written as follows:

$$S_{q_2}(u) = \frac{\sigma_P^2}{4\pi^2} |\Theta(iu)|^2 \left[u^2 Q_V - \frac{1}{2} \frac{d^2}{dt^2} \left(Q_V + Q_V^T \right)\Big|_{t=0} \right].$$

To perform the spectral analysis (Schwarz et al. 1990), let us consider airborne gravimetry equations reduced to the stationary form (5.1.8) to (5.1.10), taking the coordinate x_1 as an independent variable. By substituting $x_1 = V_0 t$ in (5.1.8), making the survey line length tend to infinity, and performing the Fourier transform $x_1 \to u_1$, where u_1 is the spatial frequency along the survey line ($u_1 = u / V_0$), we obtain (while keeping the designation of each function for its Fourier transform):

$$\begin{aligned} iu_1 V_0 \delta V(u_1) &= \gamma^{\times} \alpha(u_1) - \Delta g(u_1) + q_4(u_1) + V_0^{\times} q_3(u_1), \\ iu_1 V_0 \alpha(u_1) &= q_3(u_1). \end{aligned} \tag{5.1.11}$$

Hereinafter, we neglect the small terms $\left(\omega^{\times} + u^{\times}\right)\delta V$, $\omega^{\times}\alpha$. By applying the Fourier transform in (5.1.9), substituting (5.1.11) into it, and introducing a new measurement $\boldsymbol{y'}_1 = iu_1 V_0\, \boldsymbol{y}$, we obtain:

$$y_1'(u_1) = -\Delta g(u_1) + \boldsymbol{\gamma}^{\times} \alpha(u_1) + q_4(u_1) + iu_1 V_0 q_1(u_1). \tag{5.1.12}$$

Finally, after making the Fourier transform in (5.1.9), we obtain:

$$y_2(u_1) = Q_V \alpha(u_1) + q_2(u_1). \tag{5.1.13}$$

In should be noted that, in the spatial frequency u_1, the PSD of noise is $S_{q_i}(u_1) = V_0\, S_{q_i}(u_1 / V_0)$, and the GD PSD on a survey line is defined by formula:

$$S_{\Delta g}(u_1) = \int S_{\Delta g}(u_1, u_2)\, du_2.$$

The errors of the PDD approach. Let us write the PDD errors in the frequency domain, ignoring measurement (5.1.13) for the sake of analytical formulas and assuming that the variation of V_1 is much smaller than that of $|V_0|$, i.e., assuming a "smooth" flight (a general case is considered in the calculations). First, let us consider

one survey line. According to stage 4 of the methodology, let us temporarily assume that there is no anomaly in measurement (5.1.12):

$$y_1' \approx \gamma^{\times}\alpha + q_4 + iu_1V_0q_1. \tag{5.1.14}$$

In the PDD approach, the optimal (according to the criterion of the variance minimum) estimate of the vector of the orientation errors α and the PSD of the estimate error according to (5.1.14) are as follows:

$$\tilde{\alpha} = -S_\alpha\gamma^{\times}S_{y_1'}^{-1}y_1',\ S_\alpha = (u_1V_0)^{-2}S_{q_3},\ S_{y_1'} = -\gamma^{\times}S_\alpha\gamma^{\times} + \tilde{S}_{q_4} + (u_1V_0)^2\tilde{S}_{q_1}. \tag{5.1.15}$$

The PSDs of the noise included in (5.1.15) take the following form:

$$\tilde{S}_{q_n}(u_1) = |N_3(iu_1V_0)|^2|N_5(iu_1V_0)|^2S_{q_n}(u_1),\ n = 1-4,$$

where $N_m(iu) = \sin c(uT/2)^m$ is the m-th order B-spline transfer function (TF) (the filter weight function is an m-fold convolution of a rectangular window with itself, $m = 3.5$) with the width of the window T applied in stages 2, 3 of the PDD approach. It should be noted that the smoothed accelerometer measurement errors and GNSS accelerations may nevertheless remain correlated in time after resampling. This is not taken into account in the PDD and can lead to methodological errors.

Let us define the GD vector estimate on a survey line as a residual (stage 5)

$$\Delta\tilde{g} = -y_1' + \gamma^{\times}\tilde{\alpha}. \tag{5.1.16}$$

Let us write the expression for the PSD of the orientation estimation error $\delta\alpha = \alpha - \tilde{\alpha}$ and the GD estimation error $\delta g = \Delta g - \Delta\tilde{g}$:

$$\begin{aligned} S_{\delta\alpha} &= S_\alpha + S_\alpha\gamma^{\times}\left(S_{y_1'}^{-1} - S_{y_1'}^{-1}S_{\Delta g}S_{y_1'}^{-1}\right)\gamma^{\times}S_\alpha, \\ S_{\delta g} &= -\gamma^{\times}S_{\delta\alpha}\gamma^{\times} + S_\zeta - \gamma^{\times}S_\alpha\gamma^{\times}S_{y_1'}^{-1}S_\zeta - S_\zeta S_{y_1'}^{-1}\gamma^{\times}S_\alpha\gamma^{\times}, \end{aligned} \tag{5.1.17}$$

where, for brevity, $S_\zeta = S_{q_4} + (u_1V_0)^2S_{q_1}$.

At stage 7, the last one, estimate (5.1.16) and the estimate obtained in a similar way for the repeat flights are decorrelated by the Fourier method. The PDD method is difficult to apply in the classical spectral analysis because of its nonlinear nature. In order to determine its accuracy approximately, let us calculate the variance of the optimal Wiener GD estimate error according to (5.1.17) within the stochasticity hypothesis for gravity (assuming that the GD vector PSD is known) and take into account the fact that this variance is lower than the variance of the PDD error since the filter is optimal. Thus, we obtain the lower bound of the PDD error. It is evident that

as the length of a survey line tends to infinity, when the sample covariance estimates become consistent, the resulting lower bound tends to the true one.

Formulas for the PSD of the GD Wiener estimation error obtained from processing of two survey lines require, in addition to expressions (5.1.17), for the PSD of the GD estimation error for each survey line, the calculation of the cross PSD of the estimation errors for these lines. The calculations are not given here because they are too cumbersome. Let us confine ourselves to giving only the cross PSD of estimation errors on survey lines. Let $\delta\alpha_1$, $\delta\alpha_2$ be the errors of the estimates of α obtained for two survey lines. Thus, the cross PSDs of the specified errors and the GDs are as follows:

$$S_{\Delta g\delta\alpha_1} = S_{\Delta g\delta\alpha_2} = -S_{\Delta g} S_{y_1'}^{-1} \gamma^{\times} S_{\alpha}, \quad S_{\delta\alpha_1\delta\alpha_2} = -S_{\alpha}\gamma^{\times} S_{y_1'}^{-1} S_{\Delta g} S_{y_1'}^{-1} \gamma^{\times} S_{\alpha}.$$

The errors of the LHM approach. Let us carry out a qualitative analysis of the LHM approach in the coordinate plane $x_1,\ x_2$ or in the plane of the corresponding frequencies $u_1,\ u_2$. To do this, it is necessary to write Eqs. (5.1.8)–(5.1.9) in the variables $x_1,\ x_2$. Suppose that the survey lines with numbers $-K \le k \le K$ are directed along the x_1 axis and have the length L_1, which is much longer than the correlation radius of the processes under consideration. Then, we can assume for the analysis that $-\infty < x_1 < \infty$. When using $t_{(k)}$ to denote the time on the k-th survey line, with no loss of generality, it can be assumed that $t_{(k)} = 0$ corresponds to the value $x_1 = 0$. Let us use $\alpha_{(k)} t_{(k)}$ to denote the dependence of the variable α (or another function) of time on the k-th survey line. Let us denote the variables as $x_1 = V_0 t_{(k)}$, $x_2 = \Delta L_2 k$ and perform the two-dimensional Fourier transform for α (continuous in x_1 and discrete in x_2) according to the formula (let us save the function designation for its Fourier transform for brevity)

$$\alpha\,(u_1, u_2) = \sum_{k=-K}^{K} \Delta L_2 \int\limits_{x_1=-\infty}^{\infty} dx_1\ \alpha_{(k)}(x_1/V_0)\ e^{-iu_1x_1 - iu_2\Delta L_2 k}. \tag{5.1.18}$$

Here, the spatial frequencies $u_1,\ u_2$ correspond to $x_1,\ x_2$. By performing the specified transformation for each term in (5.1.8), we obtain:

$$\begin{aligned} iu_1V_0\delta V(u_1,u_2) &= \gamma^{\times}\alpha(u_1,u_2) - \Delta g(u_1,u_2) + q_4(u_1,u_2) + V_0^{\times} q_3(u_1,u_2), \\ iu_1V_0\alpha(u_1,u_2) &= q_3(u_1,u_2). \end{aligned} \tag{5.1.19}$$

By applying transformation (5.1.18) to (5.1.9), substituting (5.1.19) into it, and introducing a new measurement $y_1' = iu_1V_0\, y$, we obtain:

$$y_1'(u_1,u_2) = -\Delta g(u_1,u_2) + \gamma^{\times}\alpha(u_1,u_2) + q_4(u_1,u_2) + iu_1V_0 q_1(u_1,u_2). \tag{5.1.20}$$

By applying (5.1.18) to (5.1.10), we obtain:

$$y_2(u_1, u_2) = Q_V \alpha(u_1, u_2) + q_2(u_1, u_2). \tag{5.1.21}$$

It should be noted that in (5.1.19), $\Delta g(u_1, u_2)$, the result of applying continuous-discrete Fourier transform (5.1.18) to the GD and its PSD, strictly speaking, differs from $S_{\Delta g}(u_1, u_2)$. However, this difference is small in the assumption of $\Delta L_2 \ll L_g \ll K\Delta L_2$. It should also be noted that the two-dimensional PSD of noises, taking into account that they are uncorrelated at different survey lines, is defined by the formula:

$$S_{q_n}(u_1, u_2) = \frac{\Delta L_2}{2\pi} S_{q_n}(u_1), \quad n = 1, 2, 3, 4.$$

Taking into account the PSD of the GD vector, consider the variance of the optimal Wiener estimation error in order to evaluate the LHM accuracy.

From (5.1.19), (5.1.21) we obtain the optimal estimate of α and the PSD of the error of its estimation provided that the flight is dynamic:

$$\begin{aligned} \tilde{\alpha} &= S_\alpha Q_V \left(S_{q_2} + Q_V S_\alpha Q_V\right)^{-1} y_2 = S_{\delta\alpha} Q_V S_{q_2}^{-1} y_2, \\ S_{\delta\alpha}^{-1} &= S_\alpha^{-1} + Q_V S_{q_2}^{-1} Q_V, \quad S_\alpha = (u_1 V_0)^{-2} S_{q_3}. \end{aligned} \tag{5.1.22}$$

Equation (5.1.20) can be rewritten taking into account estimate (5.1.22) as follows:

$$y_1' - \gamma^\times \tilde{\alpha} = -\Delta g + \gamma^\times \delta\alpha + q_4 + i u_1 V_0 q_1. \tag{5.1.23}$$

The processes δα, q_1 are uncorrelated since q_2, q_1 are uncorrelated. Thus, the optimal estimate of the anomaly in space for a given GD PSD $S_{\Delta g}$ and the PSD of the estimation error in space are as follows:

$$\begin{aligned} \Delta\tilde{g} &= S_{\delta g}\left[-\gamma^\times S_{\delta\alpha}\gamma^\times + S_{q_4} + (u_1 V_0)^2 S_{q_1}\right]^{-1}\left(y_1' - \gamma^\times \tilde{\alpha}\right), \\ S_{\delta g}^{-1} &= S_{\Delta g}^{-1} + \left[-\gamma^\times S_{\delta\alpha}\gamma^\times + S_{q_4} + (u_1 V_0)^2 S_{q_1}\right]^{-1}. \end{aligned} \tag{5.1.24}$$

The PSD of the GD estimation error on a survey line is determined by integrating the PSD $S_{\delta g}(u_1, u_2)$ over u_2, similarly to the above transformation of the two-dimensional GD PSD to the one-dimensional GD PSD.

The errors of the VCT approach. The VCT method estimates the vertical GD component Δg_3 first, after which the estimates of the horizontal components are determined using the formulas of the corresponding transformations (Jekeli 2009). Based on (5.1.24), let us write the optimal estimate of the vertical GD component $\Delta\tilde{g}_3(u_1, u_2)$ in the frequency domain and the PSD of the estimation error while assuming that Δg_3 in (5.1.24) is not correlated with the horizontal GD components with the known PSD Δg_3:

$$\begin{aligned}\Delta\tilde{g}_3 &= S_{\delta g_3} H^T \left[-\gamma^{\times} S_{\delta\alpha} \gamma^{\times} + S_{q_4} + (u_1 V_0)^2 S_{q_1}\right]^{-1} \left(y_1' - \gamma^{\times}\tilde{\alpha}\right),\\ S_{\delta g_3}^{-1} &= S_{\Delta g_3}^{-1} + H^T \left[-\gamma^{\times} S_{\delta\alpha} \gamma^{\times} + S_{q_4} + (u_1 V_0)^2 S_{q_1}\right]^{-1} H\,,\end{aligned} \tag{5.1.25}$$

where the designation $H = (0, 0, 1)^T$ is introduced. The estimates of the horizontal components in the frequency domain and the PSD of the estimation errors are then calculated using the transformation formulas in the frequency domain in the flat Earth approximation:

$$\begin{aligned}\Delta\tilde{g}_1 &= iu_1|u|^{-1}\Delta\tilde{g}_3,\ S_{\delta g_1} = u_1^2|u|^{-2} S_{\delta g_3},\\ \Delta\tilde{g}_2 &= iu_2|u|^{-1}\Delta\tilde{g}_3,\ S_{\delta g_2} = u_2^2|u|^{-2} S_{\delta g_3},\end{aligned} \tag{5.1.26}$$

where the designation $|u| = \sqrt{u_1^2 + u_2^2}$ is introduced.

Numerical example for the spectral analysis of estimation. Formulas (5.1.25), (5.1.24), and (5.1.17) serve as the basis for comparing the PDD, LHM, and VCT approaches. It should be noted that for a smooth flight in (5.1.24) we can use S_α instead of $S_{\delta\alpha}$, and assume that $\tilde{\alpha} = 0$.

Let us compare the spectral composition of the GD estimation errors in the PDD, LHM, and VCT approaches using true GD vector PSD and noise parameters. Let us introduce a stochastic model of the anomalous gravity field in the form of a single-layer mass model (Bolotin et al. 2002):

$$S_T(u_1, u_2, h) = \pi L_g^2 \sigma_g^2 |u|^{-2} e^{-2(h+L_g)|u|}, \tag{5.1.27}$$

where T is the potential of the anomalous field, h is the altitude above the "flat" surface of the ellipsoid, σ_g is the standard deviation of gravity, L_g is the gravity correlation radius. The expression for the true GD PSD is as follows (Bolotin et al. 2002):

$$S_{\Delta g}(u_1, u_2, h) = \begin{bmatrix} u_1^2 & u_1 u_2 & -u_1|u| \\ u_1 u_2 & u_2^2 & -u_2|u| \\ -u_1|u| & -u_2|u| & |u|^2 \end{bmatrix} S_T(u_1, u_2, h). \tag{5.1.28}$$

Let us consider different flight conditions and models:

- *Smooth flight.* In this case, the high-frequency component of velocity V_1 is close to zero and its covariance matrix P_V is equal to zero (note that in this case, airborne gravimetry Eqs. (5.1.3)–(5.1.4) can be considered stationary without introducing filter Θ);
- *Dynamic flight.* Here, the PSD S_V and the covariance matrix P_V of the variations of velocity V_1 are calculated from the data of one real flight and are equal to

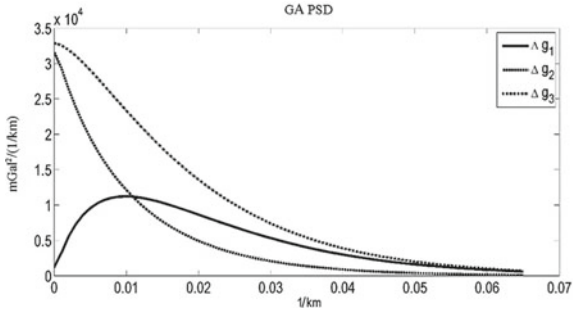

Fig. 5.3 PSD of horizontal Δg_1, Δg_2 and vertical Δg_3 components of the a priori GD model on a survey line

$$P_V = \begin{bmatrix} 8.2 & 0 & 0 \\ 0 & 3.4 & 0 \\ 0 & 0 & 3.8 \end{bmatrix} (\text{m/s})^2; \tag{5.1.29}$$

- A priori *low-intensity GD model.* The chosen parameters of the GD model correspond to the typical survey regions. It is assumed that $L_g = 5000$ m, $\sigma_g = 20$ mGal (Fig. 5.3).

- A priori *high-intensity GD model.* The comparison of accuracy for an intensive stochastic GD model with a large standard deviation and a wide spectrum simulates the lack of information on the GD while maintaining the property of the harmonic nature of the anomalous field. It is assumed that $L_g = 70$ m, $\sigma_g = 1400$ mGal.

For calculations, let us assume that the distance between the survey lines $\Delta L_2 = 1000$ m, the aircraft speed on a survey line $V_0 = 50$ m/s, the flight altitude $h = 1000$ m. Let us apply an ideal low-pass filter Θ with a cutoff frequency in time $u_V = 2\pi/T_V$, $T_V = 20$ s. The standard deviation values of the measurement errors of accelerometers, gyroscopes, GNSS coordinates are assumed to be the following:

$$\sigma_f = 0.2 T_f^{1/2} \text{mGal s}^{1/2}, \quad \text{where} \quad T_f = 60\text{s};$$

$$\sigma_\nu = 0.01^\circ \, T_\nu^{-1/2} \text{s}^{-1/2}, \quad \text{where} \quad T_\nu = 3600\text{s if } \nu_s \text{ is white noise};$$

$$\sigma_P = 0.005 \, T_{\Delta V}^{1/2} \text{m s}^{1/2}, \quad \text{where} \quad T_{\Delta V} = 1\text{s}.$$

Since the GD vertical component is usually well-estimated, let us focus on the horizontal components.

(abc) *Smooth and dynamic flight with a low-intensity GD.* The PSD of the GD estimation errors on a survey line (after integrating the PSD over u_2) obtained using the PDD and LHM approaches are shown in Figs. 5.4, 5.5, 5.6 and 5.7 for the frequency range u_1 from 0 to the cutoff frequency of the ideal filter $u_V V_0$. The accuracy of estimating the horizontal GD components in the LHM approach is significantly higher

than that in the PDD for smooth and dynamic flights and in VCT in the case of a dynamic flight (standard deviations of the estimation errors are given in Table 5.1). VCT is almost independent of the type of flight and, for the case of a smooth flight, the LHM and VCT provide similar results.

(abd) *Smooth and dynamic flight with an intensive* a priori *GD model.* In this case, S_g^{-1} is close to zero. Figures 5.8, 5.9 and 5.10 show the PSDs of the horizontal GD component estimation errors. The PDD and VCT approaches have a *greater* methodical error than the LHM over the entire frequency range in the estimation of the horizontal GD components in both smooth and dynamic flights (Table 5.2).

Thus, with the simulation parameters chosen, the LHM algorithm provides significantly more accurate estimates of the GD than the PDD algorithm; and these estimates

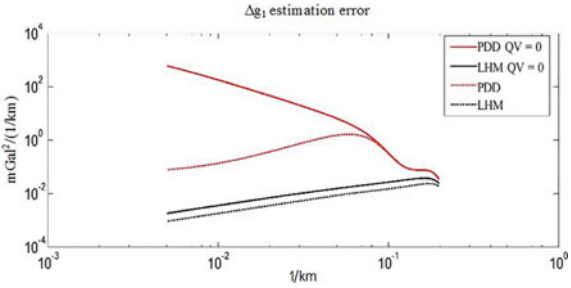

Fig. 5.4 PSD of estimation errors of the east GD component obtained in the PDD and LHM in smooth ($Q_V = 0$) and dynamic ($Q_V > 0$) flights with the low-intensity a priori GD model

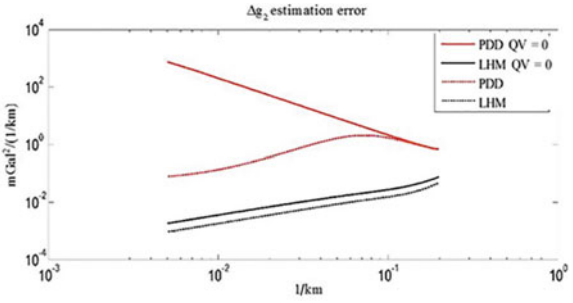

Fig. 5.5 The PSD of estimation errors of the north GD component obtained in the PDD and LHM in smooth ($Q_V = 0$) and dynamic ($Q_V > 0$) flights with the low-intensity a priori GD model

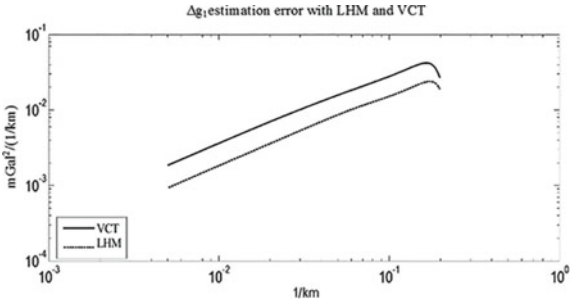

Fig. 5.6 PSD of estimation errors of the east GD component obtained in the LHM and VCT approaches in a dynamic flight

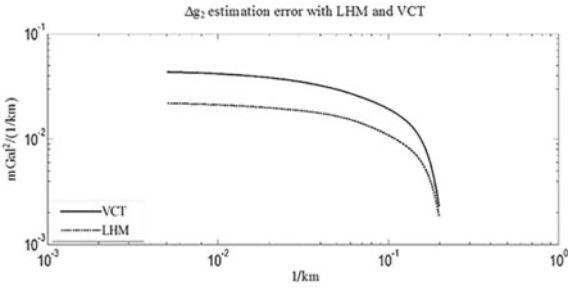

Fig. 5.7 PSD of estimation errors of the northern GD component obtained in the LHM and VCT approaches in a dynamic flight

Table 5.1 Standard deviations of GD estimation errors for the case of a low-intensity a priori GD model

GD component	Flight type	GD estimate error SD, mGal		
		PDD	LHM	VCT
East	Smooth	4.51	0.10	0.10
	Dynamic	0.45	0.08	
North	Smooth	10.59	0.09	0.09
	Dynamic	0.62	0.07	

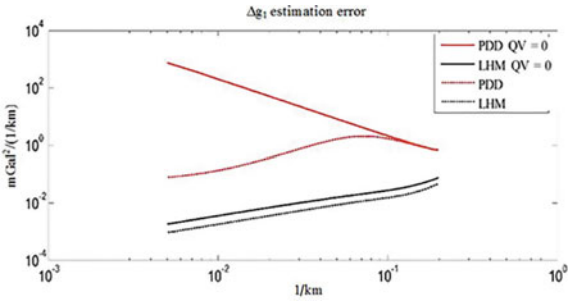

Fig. 5.8 PSD of estimation errors of the east GD component obtained in the PDD and LHM approaches in smooth ($Q_V = 0$) and dynamic ($Q_V > 0$) flights with the high-intensity a priori GD model

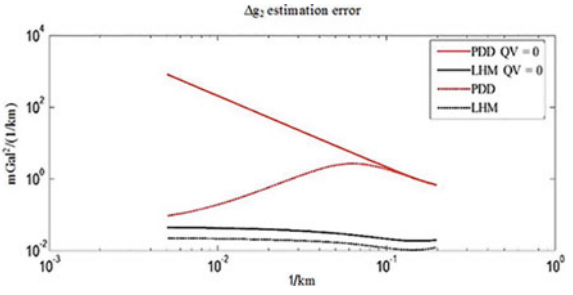

Fig. 5.9 PSD of estimation errors of the north GD component obtained in the PDD and LHM approaches in smooth ($Q_V = 0$) and dynamic ($Q_V > 0$) flights with the high-intensity a priori GD model

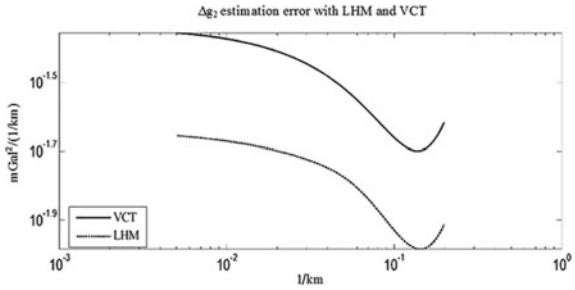

Fig. 5.10 PSD of estimation errors of the north GD component obtained in the LHM and VCT approaches in a dynamic flight

Table 5.2 Standard deviations of GD estimation errors for the case of a high-intensity a priori GD model

GD component	Flight type	GD estimate error SD, mGal		
		PDD	LHM	VCT
East	Smooth	5.22	0.11	0.12
	Dynamic	0.68	0.08	
North	Smooth	20.07	0.10	0.10
	Dynamic	0.74	0.07	

are comparable in accuracy with the VCT method. At the same time, unlike the VCT method, this approach does not require knowledge of the vertical GD component map in a large region. If the high-resolution vertical GD component is known in a smaller region, the accuracy of the VCT method will certainly be lower.

An important condition that has a significant impact on the accuracy of the estimates of the GD horizontal components is the requirement for a dynamic flight on survey lines. The latest result confirms these findings (Becker et al. 2016). It should be noted, of course, that for final conclusions, it is necessary to carry out simulation in a wide range of parameter changes and calculations using real data.

5.1.6 Algorithm for Gravity Disturbance Vector Estimation Based on a Local Harmonic Model

This Section briefly describes the LHM algorithm for solving the basic airborne vector gravimetry equations (5.1.3)–(5.1.4) based on parameterization of the GD vector using the Abel–Poisson scaling functions proposed in (Bolotin and Vyazmin 2016). By assuming that the potential of the anomalous field T is a harmonic function in the outer space of the Bjerhammer sphere, we can introduce a representation of T as an integral convolution of the scaling function and the scaling coefficients (SC) of a maximum resolution level J (in a discrete form) (Freeden and Michel 2004):

$$T(r_x) = \sum_s w_s \, \Phi_J(r_x, y_s) a_J(y_s) \tag{5.1.30}$$

where $a_J(y_s)$ is the SC of the anomalous field potential at $y_s$nodes of the equiangular grid on the Bjerhammer sphere Ω_R with a radius R; w_s are the integration weights; $\Phi_J(r_x, y_s)$ is the Abel–Poisson scaling function with the resolution level J introduced in Sect. 2.5.1. The choice of radius R of the Bjerhammer sphere is discussed in Sect. 2.5.1.

Expression (5.1.30) gives a representation for the GD vector defined as a potential gradient $\Delta g_x(r_x) = \nabla_r T(r_x)$ in the projections on the axes of the geodetic coordinate system:

$$\Delta g_x(r_x) = \sum_s w_s \, a_J(y_s) \, \nabla_r \Phi_J(r_x, y_s) \tag{5.1.31}$$

Consider airborne gravimetric measurements on the trajectory $r_x(t)$ of a single survey flight. Due to the properties of the scaling function described in Sect. 2.5.1, it is sufficient to take into account the y_s nodes only from a certain vicinity of point $r_x(t)$ in the summation in (5.1.30).

Let us introduce $N \times 1$-vector a_J composed of the potential SCs determined at N nodes generated by all measurement points $r_x(t)$ of one survey flight (Fig. 5.11). Thus, expression (5.1.31) for the GD vector can be rewritten as follows:

$$\Delta g_x(r_x(t)) = \Pi(t) \mathrm{a}_J, \tag{5.1.32}$$

where $\Pi(t)$ is a $3 \times N$ matrix consisting of the products of the integral weight values w_s and the values of the Abel–Poisson scaling function at the y_s nodes:

$$\Pi(t) = (\, w_1 \nabla_r \Phi_J(r(t), y_1), \ldots, w_N \nabla_r \Phi_J(r(t), y_N)).$$

Unknown SCs of the potential are assumed to be time invariant:

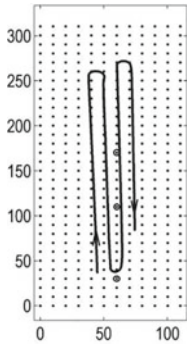

Fig. 5.11 The flight path of the aircraft and the set of nodes of the disturbing potential SC on the longitude latitude plane [km × km]

$$\dot{a}_J = 0. \tag{5.1.33}$$

Let us substitute representation (5.1.32) of the GD vector into error Eq. (5.1.3). Assume that the accelerometer error Δf_z in (5.1.3)–(5.1.4) is white noise with zero mean and the standard deviation σ_f; the gyroscope error v_z is assumed to be representable as $v_z = v_z^0 + v_z^s$, where v_z^0 is a constant bias:

$$\dot{v}_z^0 = 0 \tag{5.1.34}$$

and v_z^s is white noise with mean and the standard deviation σ_v.

The error ΔV_x^{GNSS} of the GNSS velocity is represented as the time-derivative of the GNSS position error Δr_x^{GNSS}, which is assumed to be white noise with a zero mean and the standard deviation σ_P.

Let us represent (5.1.3)–(5.1.5), (5.1.33), and (5.1.34) in discrete time and use a shaping filter for the velocity measurement errors; then, ΔV_x^{GNSS} can be written as

$$\Delta V_x^{GNSS}(t_k) = \frac{1}{\Delta t}(\zeta_k - \zeta_{k-1}) \tag{5.1.35}$$

Here, ζ_k is discrete white noise with a zero mean and the standard deviation $\sigma_q = \sigma_P \, \Delta t^{-1/2}$, where Δt is the sampling time step of GNSS data. Under the assumptions made, the PSD of ΔV_x^{GNSS} is represented as

$$S_{\Delta V}(u) = \frac{1}{2\pi \ \Delta t^2}\left|e^{iu\Delta t} - 1\right|^2 \sigma_P^2 \approx u^2 \sigma_P^2 / 2\pi. \tag{5.1.36}$$

Let us formulate the problem of estimating the potential SC and the parameters of the INS instrumental errors as a standard Kalman filtering problem with constraints (5.1.3), (5.1.4), (5.1.33), (5.1.34), (5.1.35) and aiding measurement Eqs. (5.1.5). The state vector $x(t_k)$ includes a 3×1-vector of the dynamic velocity error $\delta V_x(t_k)$, a 3×1-vector of the orientation errors $\alpha_x(t_k)$, a 3×1-vector of the constant biases of the gyroscopes v_z^0, an $N \times 1$-vector of the disturbing potential SC a_J, a 3×1-vector of fictitious noise $\boldsymbol{\zeta}_k$.

The estimation of the state vector is determined using the KF algorithm for the given initial conditions for the state vector and the covariance matrix of the estimation error. To obtain the potential SC estimates that are assumed to be constant, smoothing (KF in reverse time) is not necessary. Since the initial values of the SC vector and the error covariance matrix are completely unknown, the KF information form (Kailath et al. 2000) with zero information for the SC at the initial time is used.

5.1.7 Conclusions

Some approaches to the data fusion of vector gravimetry are described in the inertial, satellite and gravimetric aspects. The following conclusions can be drawn.

The airborne gravimetry problem is solved in postprocessing mode. Therefore, the SINS is not required to operate in the full operation mode. The SINS can be considered as a recorder of inertial sensor measurements. High-precision position and velocity GNSS solutions are always available. For this reason, when computing INS mechanization equations, one can use the mentioned satellite information to the maximum, which leads to a significant simplification of the aiding models in airborne gravimetry.

Traditionally, the SINS algorithms use a navigation frame associated with a geodetic vertical. Similarly, the SINS algorithms can be implemented in the axes of other frames, for example, in the inertial frame. It is advisable to represent INS error equations using the so-called dynamic errors, which simplifies the calculations.

When estimating the GD vector, it is necessary to use additional information. Two types of additional information and, accordingly, two methods are considered: measurements at repeat flights and the harmonicity of the disturbing potential. A comparison of these methods is given using spectral analysis. At the same time, bringing the nonstationary error equations to stationary form required the introduction of a special averaging procedure. Numerical results have shown significant advantages of the second approach. The improved quality of the estimation seems to be due to the harmonicity of the disturbing potential.

The GD vector can be obtained without the use of a vector gravimeter by transforming the vertical GD component obtained using a scalar gravimeter. As compared with the method of transformations, airborne vector gravimetry provides an improvement in the accuracy of DOV estimation by 10–30 % depending on the accuracy of the sensors. Besides, the method of transformations requires a map of the vertical GD in a wide area for the determination of the DOV, which is not always feasible in practice.

The obtained accuracy estimates for different methods of airborne vector gravimetry are given under the general assumption of the validity of the stochastic GD hypothesis. This assumption introduces additional information, the result of which is that numerical estimates of accuracy might be too optimistic. For this reason, they should be interpreted only as *relative* estimates of accuracy.

An important condition that has a significant impact on the accuracy of the estimates of the GD horizontal components is the requirement for a dynamic flight on survey lines. The requirements for the “dynamic” characteristics of the flight call for a further study.

5.2 Current State and Outlook for the Development of Instruments for Onboard Measurements of Second Derivatives of Geopotential

In recent years, considerable progress has been achieved in the development of instruments for measuring the components of second derivatives of the geopotential (SDGP) with the dimension of angular acceleration (s^{-2}). The components of SDGP second-rank tensor are measured in Eotvos (1 Eo = 10^{-9} s^{-2} = 10^{-4} mGal/m). On the Earth's surface, different SDGP tensor components have the order of 100–3000 Eo, and SDGP anomalies to be determined are several orders of magnitude lower.

The need to measure the SDGP stems from the fact that the anomalous tensor field of SDGP is very informative for identification of parameters used, for example, in gravity surveys and navigation. Onboard SDGP measurements help to effectively solve the current and prospective problems in basic research, geophysics, geology, and geodesy (Nerem et al. 1995; Volfson 2002; DiFrancesco et al. 2009; Vasin and Popkov 2010).

Gravity gradiometers (GG) are most commonly used to measure SDGP. Their principle of operation is based on measuring the gravity accelerations of at least two proof masses separated by a certain distance in chosen directions (Evstifeev 2017). The difference between the accelerations divided by the distance determines the components of the gradient of the Earth's gravity field or SDGP components. In geophysics, instruments for measuring the SDGP are traditionally divided into gravity variometers of the 1st and 2nd types and gravity gradiometers, depending on the tensor components to be determined. In this section, all onboard instruments are qualified as GG due to the arbitrary (but measurable) angular positions of their sensitivity axes.

The history of GG development covers more than a century. The first GG was proposed and designed by the Hungarian physicist R. Eotvos at the end of the 19th century for studying the Earth's gravity field. Based on the principle of torsion balance, his instrument recorded the difference between the gravity vector projections for the centers of gravity of two proof masses of a dumbbell. Eotvos' ideas were embodied in stationary gravity variometers and gradiometers developed in the 1950s for geological exploration (Jekeli 2007; Nabighian et al. 2005).

The need for onboard measurements of the Earth's gravity field parameters emerged in the 1980s, and the new solutions were mainly intended to aid autonomous inertial navigation systems (INS) in defense applications. Onboard GGs for measuring SDGP tensor components were designed by various companies both in Russia and abroad (DiFrancesco et al. 2009; Soroka 2010).

GG performance data for priority application areas are shown in Fig. 5.12.

The major GG applications are described below.

Autonomous navigation. Using GG for underwater navigation has become less relevant due to the development of satellite navigation systems and precision gyroscopes (see Peshekhonov 2020; Dzhandzhgava and Avgustov 2007, and Sects. 6.3

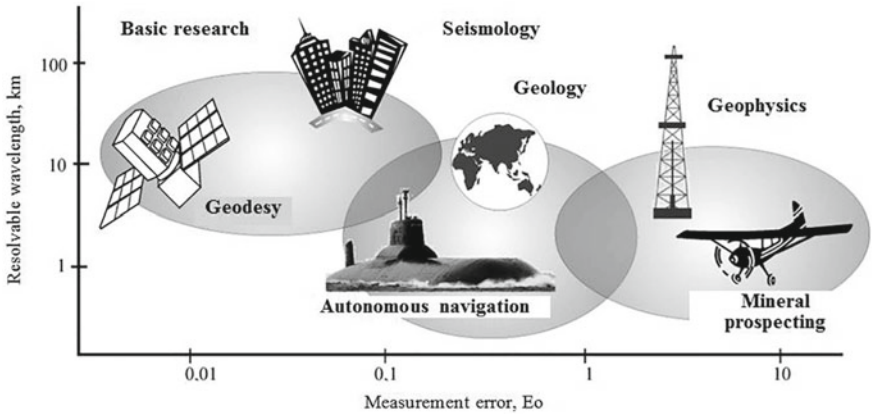

Fig. 5.12 Application areas of gravity gradiometers

and 6.4). However, to meet the requirements for autonomous systems, particularly in military applications, it is needed to use a GG unit measuring all SDGP components.

Geophysics and geology. This area includes the studies of the geological structure of the Earth's crust and deep distribution of masses under the Earth's surface. Gravity gradiometers are extensively used in exploration and oilfield geophysics in the search for mineral deposits (Dransfield 2007; DiFrancesco 2007).

Geodesy. Possible applications to geodesy include the study and refinement of the Earth's figure, detection and mapping of gravity anomalies during terrestrial and satellite surveys. GG data helps determine long-term, very slow fluctuations in the ocean level and can be employed in various physical studies. Space agencies of Europe and the USA develop various global projects on designing GG for oceanography, meteorology, and climate studies aimed at the Earth's surface mapping (Albertella et al. 2002; Rummel et al. 2002; Freeden et al. 2002; Touboul et al. 2012).

Basic research. Gravity gradiometers are applied in various studies to verify the fundamental equivalence principle, measure the gravity constant, search for new physical interactions, and record the gravity waves. The measurements can be performed both on a fixed base and onboard spacecraft (Paik 1989; Iafolla et al. 2003; Kasevich et al. 2014).

For the majority of SDGP dynamic measurements, noise error components should be normalized in addition to static and dynamic characteristics. The required spectrum of the random component of the measured SDGP useful signal should not exceed 1–10 Eo/$\sqrt{}$Hz; and for basic physical research, 0.1–0.001 Eo/$\sqrt{}$Hz. These values cannot be achieved at a normal temperature, since the thermal noise is much higher. The requirement can be met using the cryogenic technology providing lowered sensitivity threshold and enhanced potential accuracy of sensors, however, then the development costs will significantly increase.

At present, high sensitivity and noise spectra of 0.02–5 Eo/$\sqrt{}$Hz have been achieved for onboard GG, which makes it possible to use them in a wide range of problems.

5.2.1 Principles and Challenges of Measuring the Second Derivatives of Geopotential

The set of SDGPs is one of the characteristics of the Earth's gravity and centrifugal fields; it forms a symmetric second-rank tensor *W,* which mathematically is a derivative of the gravity vector to the radius vector of arbitrary direction. For each point in space, the tensor W defines a triad of mutually orthogonal eigenvectors, the orientation of which relative to the Earth can be measured. According to the general principle of map-aided navigation, the magnitude and direction of these vectors along the motion path can be determined by measuring the components of the tensor W in order to refine the vehicle position and orientation. Each component of the tensor W has a normal component corresponding to the accepted gravity field model and an anomalous component. It is the anomalous parts of the components that carry useful information, and the problem lies in measuring them.

As noted above, special devices—gravity variometers and gradiometers—are used to measure SDGP tensor components. According to the accepted terminology (Ogorodova 2006), variometers determine the individual components of the tensor W, while GGs determine only the gradients of gravity module W_{xz}, W_{yz}, W_{zz} characterizing the change in all three gravity components with altitude changes (z coordinate) or, equivalently, the change in the vertical component along three axes. Hereinafter, the first index refers to the component of the vector on which differentiation is performed, and the second index, to the coordinate, with respect to which the derivative is taken. The following types of instruments are classified: first type gravity variometers determining the components of the vector of difference between the curvatures of the geoid sections $W_{\Delta} = W_{xx} - W_{yy}$ and W_{xy}, second type variometers determining W_{Δ}, W_{xy}, W_{xz}, W_{yz}, horizontal GG determining W_{xz}, W_{yz}, and vertical GG determining W_{zz}. The tensor W is represented by components in a horizontal coordinate system with geographically oriented axes (OX to the East, OY to the North, OZ up) at the point of the common Earth ellipsoid.

The SDGP tensor contains six unknown (five independent) components W_{xx}, W_{yy}, W_{zz}, W_{xy}, W_{xz}, W_{yz}. The first invariant I_1 of the SDGP tensor, which is the sum of the components of the main diagonal, has an important feature: the condition $I_1 = W_{xx} + W_{yy} + W_{zz} = 2\omega_e{}^2$, where ω_e is the Earth's angular velocity, is satisfied for SDGP components driven by centrifugal forces. The first invariant I_1 can be appropriately used to check the gradiometer accuracy. Due to the potential properties of the gravity field, the gravitational parts of SDGP diagonal components are related by the Laplace (or Poisson) equation; therefore, this condition is also satisfied for the elements of the combined field of gravitational and centrifugal forces.

The tensor GG measures all components of the tensor W to determine the Earth's gravity field anomalies by integrating the gradients of gravity acceleration (Peshekhonov et al. 1989; Mumaw 2004). This gradiometer can have four proof masses located at the vertices of a tetrahedron. Each proof mass is held in an equilibrium position with a special elastic suspension, and the readout system measures the changes in their positions caused by external forces.

Several dozen GG designs have been proposed so far. They can be divided into two groups: those using accelerometers or dumbbells. In accelerometer GG, the difference between specific forces (with account for inertial forces) is determined by two accelerometers, whereas in dumbbell GG, this difference shows itself as a torque that is applied to the dumbbell and is to be determined by the device.

To construct a device measuring all SDGP components—a tensor GG, four three-axis linear accelerometers (by the number of proof masses of the tetrahedron), twelve uniaxial accelerometers, or six measuring dumbbells (by the number of faces of the tetrahedron) are needed.

Dumbbell and accelerometer GGs can be of static type, when the axes of accelerometers or dumbbells are fixed in a specified frame, or of modulation (rotating) type, when GGs are forced to rotate in a space with a constant angular velocity. Uniform rotation allows gravity effects to be modulated by the double rotation frequency, then the resonant properties of the mechanical system—high mechanical Q-factor, synchronous detection during conversion of displacement signals, etc—are used to detect the useful signal. Inertial accelerations of the base perpendicular to the rotation axis are modulated by the single rotation frequency, and gravity gradients are modulated by the double rotation frequency, so they can easily be distinguished.

The following challenges in the development of onboard SDGP measuring instruments should be outlined:

1. Detection of SDGP tensor components against the background of much larger acceleration gradients of inertia at the GG location. The measurement error of 1 Eo corresponds to the gravity acceleration change of 10^{-10} m s^{-2} (10^{-11} g) on a 0.1 m base, comparable with the actual size of an onboard GG. Many vehicles undergo intensive linear vibrations with amplitudes of up to 1 g and slowly varying motion accelerations up to 10^{-1} to 10^{-2} g. Thus, the measurement error should be 11 orders of magnitude lower than the measured value. From the above it follows that inertial effects should be reduced at least to 10^{-2} g through the use of effective antivibration system.
2. Using a high-precision GG angular stabilization system to reduce apparent changes in tensor components while minimizing dynamic errors. For example, dynamic errors of the stabilized platform with an amplitude of angular oscillations of 2 arcsec at 10 Hz provide an additional 400 Eo signal at GG input, under these oscillations the platform undergoes angular accelerations with an amplitude of $4 \cdot 10^7$ Eo. With the required measurement accuracy of 1 Eo, such errors are unacceptable (Staroseltsev 1995).
3. Measurement of the full SDGP tensor, including the vertical gradient, under inertial disturbances. For accelerometer GG, this requires accelerometers with

a unique sensitivity of 10^{-11} g and relevant parameters such as scale factors, alignment of sensitivity axes, etc.; for dumbbell GG, it is necessary to develop a set of dumbbells in elastic suspensions with static and dynamic balancing of 10^{-11} (in relative units) (DiFrancesco et al. 2009).

4. Provision of stable thermal measurement mode at the GG location. For metal dumbbells with the thermal expansion coefficient of about 10^{-5} K^{-1}, temperature variations in the structure shall not exceed 10^{-6} K, which requires the development of a unique thermal stabilization system. It is the main impediment to the development of static GG. Application of superconducting technology would greatly simplify the solution of this problem; however, operation of cryogenic systems onboard small vehicles, such as a light aircraft, also involves a lot of complications.
5. Development of high-precision transducers to measure displacements of proof masses under the action of gravity gradients at the level of hundredths and thousandths of an angstrom ($10^{-12} - 10^{-13}$ m). For GG with two orthogonal dumbbells to be able to measure SDGP tensor components accurate to 1 Eo, a device measuring antiphase angular oscillations of dumbbells with sensitivity of $10^{-5} - 10^{-6}$ arcsec should be developed.
6. Development of a low-speed driver with a rotation rate instability of about $10^{-6} - 10^{-7}$ for the rotational mode of both accelerometer and dumbbell schemes. Special requirement is to provide a uniform velocity at double frequency, which will decrease GG errors and lower the requirements for identity of accelerometer parameters or natural frequencies of dumbbell suspensions.
7. Development of metrological and calibration equipment for GG calibration, testing, and adjustment with setting the test signals accurate to 0.1 Eo or better.

Creation of gravity gradiometers for onboard SDGP measurements is a real challenge; in fact, the problem solution is on the verge of the present-day instrument engineering potential.

5.2.2 Gradiometers for High-Precision Autonomous Navigation

High-precision marine navigation involves application of various facilities, among which inertial navigation systems are of prime importance. The Earth's gravity field anomalies, first of all deflections of the vertical (DOV), cause additional methodological errors, which are comparable with INS instrumental errors and present a serious impediment to their accuracy increase (Peshekhonov et al. 1989; Koneshov et al. 2016). The permissible methodological errors for perspective INS are characterized by limiting DOV errors of 1 arcsec, which requires measurement of all SDGP tensor components with max 1 Eo error (Nesenyuk et al. 1980). This can be achieved by including a tensor GG in the navigation equipment. Apart from real-time DOV determination, GG data are used to measure the vertical components of Coriolis

acceleration, correct the Schuler error components of the INS velocity, and detect local anomalies of the bottom relief (Maleev and Kapustin 2007).

In the 1970s, the US Department of Defense initiated the development of GG to be used onboard submarines and to aid Trident II missile systems (Gerber 1978). A number of US companies, such as Bell Aerospace, Hughes Aircraft and the Draper Laboratory of Massachusetts Institute of Technology, participated in the creation of GG prototypes. Below we provide brief descriptions of their developments, which have become classics, especially as they have laid the basis for certain trends in the development of future projects.

Bell Aerospace/Textron Inc. proposed a rotating GG with four identical accelerometers at the periphery of a rotating platform. Each pair of accelerometers had parallel differently directed sensitivity axes arranged tangentially in the plane of the platform; with the accelerometers installed with the radius of 10 cm, and the signal of 1 Eo the difference in their readings was expected to be 10^{-11} g. The stability of the constant rotation rate of 5–10 Hz was at the level of 10^{-7}.

Hughes Aircraft developed a rotating gradiometer with two orthogonally arranged dumbbells in an elastic suspension. It is known as a Forward gravity gradiometer named after Robert L. Forward, its designer. The dumbbells are connected by a torsion bar with a built-in piezotransducer measuring the angular twist of dumbbells relative to each other. The amplitude of the measured angle is 10^{-5} arcsec at 1 Eo. The natural frequency of the elastic suspension is 35 Hz; it is equal to the double rotation frequency for resonance signal amplification. Two dumbbells and the elastic suspension were made from a single solid aluminum workpiece; as a result, the Q-factor exceeded 9000 (without regard for the piezotransducer losses).

The Draper Laboratory succeeded in creating a static GG to measure the vertical gradient (Trageser 1984). The beryllium dumbbell shaped as a sphere with tungsten weights was placed in a special liquid to ensure neutral buoyancy. The sphere was centered with the use of electrostatic sensors and balancing was carried out by metal deposition onto the sphere. The need to maintain balance in the presence of liquid required the development of a unique system providing thermal stabilization of about (10^{-6}–10^{-7}) °C, which, despite certain progress, made the whole project impracticable.

Development and accuracy of the onboard GG are considered in the publications of Russian scientists (Krasovsky 1983; Peshekhonov and Volfson 1996; Volfson 1997; Soroka 2010).

In Russia, a considerable research was conducted by the CSRI Elektropribor. The developed shipborne GG was built as a first type gravity variometer and had a sensor greatly outperforming the traditional geophysical gradiometric devices (Volfson 1997). The gradiometer weighed 16 kg and measured Ø270 × 170 mm (Fig. 5.13a). The GG sensitivity to variations of gravity gradients determined in the tests on a rocking base was 0.4 Eo.

Since 2001, Ramenskoye Design Company and Zhukovsky Air Force Engineering Academy have been jointly working on the development of rotating gradiometers, both with accelerometers and dumbbells. The dumbbells made of a nonmagnetic heavy alloy rotate at a rate of 2.3 Hz. The readout system comprises fiber-optic

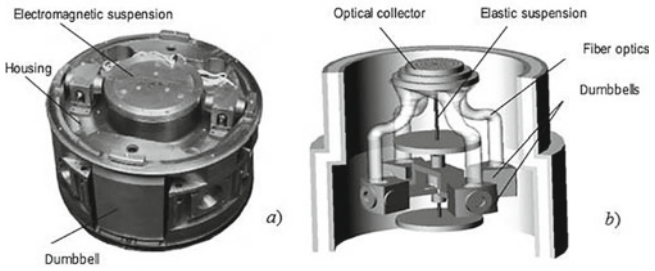

Fig. 5.13 Russian developments: **a** static GG by CSRI Elektropribor; **b** rotating GG by Ramenskoye Design Company and Zhukovsky Air Force Engineering Academy

channels and a three-ring fiber optical collector measuring microdisplacements up to 10^{-4} μm. Some prototypes based on Forward gravity gradiometer (Fig. 5.13b) have been manufactured; their errors from the bench tests were 13−16 Eo, which is insufficient for autonomous navigation (Avgustov and Soroka 2009).

The gradiometer designed by Bell Aerospace, which was later incorporated into Lockheed Martin, served as a basis for the tensor GG used onboard the Ohio-class submarines for autonomous navigation. It should be noted that the development and application of gravity gradiometers is included in the Militarily Critical Technologies List of the US Department of Defense (Korchak et al. 2013).

DARPA Research Center (USA) plans to create an autonomous noise-free precision inertial navigation system featuring positioning accuracy close to that of GPS-aided systems. This system is supposed to use GG for real-time measurements of the full SDGP tensor and DOV.

Further publications on GG intended for autonomous navigation are rather scarce for obvious reasons; they are mainly concerned with integrated systems comprising GG, INS, and GPS (Richeson 2008; DeGregoria 2010; Welker et al. 2013; Lee et al. 2015). At the end of the 20th century, the tensor GG technology was declassified and the conditions for its commercialization were created (Bell 1998).

5.2.3 Gradiometers for Mineral Exploration

GG development projects for military applications started in the 1970–80s and provided the gradiometers demonstrating good performance in tests onboard satellites, aircraft and ships. Gravity gradiometers were especially actively applied to exploration geophysics and mineral exploration.

The interest in GG application was due to the fact that gravity gradients (see Sect. 6.4) were more informative than gravity anomalies measured by gravimeters. Moreover, measurement of SDGP components provides a more contrasting anomaly map and a clearer detection of higher-density areas for mineral prospecting (salt domains for oil and gas prospecting, kimberlite pipes for diamond prospecting, etc.),

which greatly reduces the cost of drilling and production (Annecchione et al. 2007; McBarnet 2013; Mims et al. 2009).

Lockheed Martin significantly enhanced the accuracy of the gradiometers, and in 1994, Bell Geospace gained commercial rights to manufacture the 3D FTG (full tensor gradiometer) intended for marine surveys. This gradiometer consists of three orthogonally arranged GGs, each containing four high-precision accelerometers on a rotating platform with a diameter of 15 cm (DiFrancesco 2003). The rotation frequency is 0.25 Hz. The arrangement of gradiometers with orthogonal sensitivity axes allows all SDGP tensor components to be determined on a moving base. The noise level of such a gradiometer is ~10 Eo/$\sqrt{}$Hz.

Bell Geospace conducted the first SDGP surveys in the Gulf of Mexico (Mumaw 2004). In 2003, Bell Geospace modernized the equipment and developed the Air-FTG for airborne applications (Murphy 2004).

Under an agreement with Lockheed Martin, BHP Billiton (Australia) designed an airborne gravity gradiometer Falcon AGG (Airborne Gravity Gradiometer) for exploration surveys. The gradiometer has an enlarged 30 cm diameter rotating platform with 8 accelerometers, equally spaced along the edge of the platform. This enhances the gradiometer resolution and allows surveys onboard an aircraft at a height of about 100 m, which improves the efficiency of geophysical surveys (Dransfield et al. 2010; Dransfield and Christensen 2013; Christensen et al. 2015). The platform rotation axis is vertical, which allows determining the components of the tensor W_{Δ} and W_{xy}. Due to a larger size and more convenient operating conditions the noise level is as low as 2–3 Eo/$\sqrt{}$Hz.

In airborne surveys, it is desirable to achieve a resolvable wavelength of less than 50 m. In practice, the resolution of 200–300 m was obtained, which is associated with the lower limits of speed and the safe altitude. In addition account should be taken of the gradiometer displacement relative to the aircraft, the crew motion during the flight, the need to occasionally refine measurement results and introduce corrections at preformed zero points (reference points) in order to obtain corrected SDGP values (Jekeli 2006, 2011).

However, due to large size and weight the gradiometer could not be applied on light airplanes. These parameters were significantly reduced due to compact digital electronics. The new gradiometer HeliFalcon can be placed onboard a helicopter in order to provide the desired wavelength measurements (Dransfield 2010). Fugro Airborne Surveys, which is a part of Compagnie Générale de Géophysique holds exclusive rights to surveying with the Falcon gradiometer technology.

ARKeX (Cambridge, UK) commissioned by the European Space Agency (ESA) developed a vertical cryogenic exploration gravity gradiometer (EGG), operating at a temperature of 4 K. This gradiometer was specially designed to measure the component W_{zz} in highly dynamic conditions (DiFrancesco 2007; Lumley et al. 2001). The designers used the Meissner effect, allowing for contactless suspension of proof masses, and superconductivity, allowing for using a SQUID magnetometer to provide high-accuracy and stable measurements of proof mass displacements. The EGG comprises two vertically-spaced accelerometers with vertical sensitivity axes. The gradiometer comprises two proof masses with H-shaped cross section

(shaped as hollow cylinders with a flange in the middle), suspended in a contactless suspension. The proof masses with a diameter of 50 mm and weights of 100 g are made of niobium. The proof masses are arranged one over the other at a distance of 150 mm. The construction with the proof masses is installed in a cryostat, which is mounted on a gyrostabilized platform. The desired noise level was 1 Eo/$\sqrt{}$Hz, the actual measurements showed 7 Eo/$\sqrt{}$Hz.

This gradiometer was used by ARKeX in a range of geophysical surveys throughout the world; in 2008, the company announced its revenue from gravity surveys of about $30 million. Later, the company made an agreement with Lockheed Martin on using its FTG technology, probably because of the difficulties in operating cryogenic equipment onboard the aircraft and higher informativeness of FTG signal as compared with EGG signal. The technology was adapted for the ARKeX needs to create an FTGeX gradiometer. Together they developed the eFTG (Enhanced FTG) with improved accuracy, shock absorption and thermal stabilization, which reduced the noise level 3–4 times down to 2 Eo/$\sqrt{}$Hz.

In November 2015, ARKeX ceased to function for financial reasons.

The University of Western Australia (UWA) and Gedex Inc. (Canada) have jointly developed an airborne cryogenic dumbbell GG for mineral exploration, the key customer being Rio Tinto Ltd. (Australia) (Matthews 2002; Van Leeuwen 2003; Tryggvason et al. 2004).

The superconducting GG comprises two orthogonally arranged dumbbells in elastic suspension. This elastic system was called an orthogonal quadrupole responder. Each dumbbell of the niobium bar with a size of 30 × 30 × 90 mm has special elastic variable cross-section elements 0.03 × 0.2 × 20 mm in size functioning as elements of the elastic suspension. The design natural frequency of dumbbells in the suspension was 1 Hz, but in practice it was about 3 Hz due to technological limitations in manufacturing. The Q-factor of the dumbbell suspensions was 1500−2500, and it was about 80 for the whole construction. Dumbbells have special coils mounted on them needed to pick off signals with the use of a highly sensitive SQUID. The coils also function as magnetic springs allowing adjustment of the dumbbell mechanical frequencies since the manufacturing tolerances are very broad.

To improve thermal insulation, the dumbbells are placed in a vacuum chamber with a residual pressure of 10^{-11} atm. The dumbbell system is installed in a cryogenic chamber (dewar), with the temperature stability of about several μK. The whole construction is mounted onto a gyrostabilized platform with fiber optic gyroscopes.

Vibration control technology for this GG was developed by the Canadian Space Agency. It protects the gradiometer both from linear and angular vibrations. Without vibration control, the gradiometer error was 150 Eo at 1 Hz; with the control the error was reduced to 1 Eo. With the use of the vibration control system, linear accelerations $10^{-2}-10^{-3}$g were acting on the gradiometer. This cryogenic gradiometer was named VK1 after UWA physicist Dr Frank Van Kann, who invented the technology (Anstie et al. 2010).

Gedex Inc. (Canada) developed and patented a cryogenic high definition airborne gravity gradiometer (Gedex HD-AGG) consisting of three orthogonally arranged

pairs of angular accelerometers to measure the full tensor of SDGP. It is based on the principles proposed by the University of Maryland (Chan and Paik 1987). Each pair of accelerometers measures in-phase oscillations caused by the base angular accelerations (common mode) and antiphase oscillations caused by SDGP (differential mode) about the coincident sensitivity axes. This allows determining the components $W_{xx} - W_{yy}$ and W_{xy}, $W_{yy} - W_{zz}$ and W_{yz}, $W_{xx} - W_{zz}$ and W_{xz} depending on the angular position of sensitivity axes.

The angular accelerometers are carefully adjusted and calibrated to ensure identity of their characteristics. The residual static and dynamic imbalances, misalignment of sensitivity axes and other technological imperfections are measured and taken into account in the gradiometer error model during the calculation of SDGP components. To reduce the effect of the base motion, the accelerometer unit is placed on a six-degree-of-freedom antivibration platform. The temperature stability in the cryostat is provided at $\pm$ 20 μK. The gradiometer noise does not exceed 1 Eo/$\sqrt{\text{Hz}}$ at 0.001–1 Hz (Carroll et al. 2010).

Despite the rapid development of GG gravity surveying, the number of companies engaged in their design and operation has not increased in recent years. Note that the conference Airborne Gravity (2016) included the presentations by Lockheed Martin, Compagnie Générale de Géophysique, Gedex, Rio Tinto, Bell Geospace on the products described above.

5.2.4 Gradiometers for Space Missions

The development of satellite geodesy and the need to refine the global models of the Earth's gravity field require tools for determining the parameters of the anomalous gravity field, particularly SDGP. One of the first cryogenic GG for space missions was developed in the 1980s by the research group led by Dr. H.J. Paik from the University of Maryland (Chan and Paik 1987). Initially, this gradiometer was created under a contract with the NASA and was intended for space research in geodesy and fundamental Earth science. After the NASA stopped funding the project, Oxford Instruments (UK) continued the development of this gradiometer under a contract with the ESA. Both GG designs represent an analog of the accelerometer GG with two proof masses, but in the second case, the mechanical elastic suspension of the proof mass is replaced by a contactless magnetic suspension.

The GG design accuracy should be 10^{-4} Eo over the measurement time of 1 s. A group of researchers from Oxford Instruments suggests that their gradiometer can be used in geophysical explorations, but the claimed accuracy can be achieved only onboard an unperturbed satellite, where inertial acceleration is much lower than that on an aircraft. For aircraft conditions this yields the noise level of about 100 Eo, which is hardly suitable for airborne geophysical equipment. However, its design principles were applied in development of other GG versions such as EGG by ARKeX.

Dr. Paik proposed to develop a three-axis GG with 9 accelerometers (6 linear and 3 angular ones) for physical experiments in space. Such a gradiometer would

determine diagonal SDGP tensor components and measure the acceleration of the foundation in all six degrees of freedom (linear and angular). The gradiometer noise is estimated to be 0.02 Eo/$\sqrt{}$Hz (Moody et al. 2002).

ESA gravity mission GOCE focusing on geodetic explorations used two key technologies: satellite-to-satellite tracking and electrostatic gravity gradiometer. The tensor GG specially developed for this project has three pairs of orthogonally arranged precision electrostatic triaxial accelerometers (Albertella et al. 2002; Rummel et al. 2002, 2011). The components of the full SDGP tensor are determined by measuring the differences between the accelerations of the paired accelerometer proof masses. The accelerometers spaced 50 cm apart are mounted on a base of a highly-stable reinforced carbon/carbon with a honeycomb structure and isotropic elasticity in all directions. The distance between the proof masses is determined accurate to 0.01 angstrom over 3 min. The angular position of the base was strictly controlled: linear and angular accelerations were measured by all nine accelerometers. The base is fixed to a special equistiff suspension. The center of mass of the accelerometer unit is close to that of the satellite in order to reduce the influence of linear accelerations. Stability of the base temperature is maintained at about 10 mK within 200 s. The platform assembly with three pairs of accelerometers weights 150 kg, the whole satellite, about a ton. The power consumption of the GG electronics is 75 W.

The accelerometers were designed by Alcatel Space Industries (France), and the structure of six accelerometers with electronics was assembled by ONERA (France). The measuring range of the tensor GG is 0.005–0.1 Hz. The noise of one accelerometer is 2×10^{-13} g/$\sqrt{}$Hz, which, on the 50 cm base, provides the resolution of 0.002 Eo. By the space mission data, the noise achieved 0.01−0.02 Eo/$\sqrt{}$Hz for W_{xx}, W_{yy}, and 0.02 Eo/$\sqrt{}$Hz for W_{zz}, W_{xz}. Such high precision was obtained at minimum inertial perturbations of the satellite and in zero-gravity conditions.

Each accelerometer comprises a rectangular proof mass made of platina-rhodium alloy $4 \times 4 \times 1$ cm in size, weighing 320 g. The proof mass is suspended in a noncontact electrostatic suspension; its position is controlled by eight pairs of electrodes. Accelerometers with the similar design and proof mass dimensions were applied in the previous CHAMP and GRACE missions (STAR and SuperSTAR accelerometers, respectively). Comparative characteristics of these sensors are given in Table 5.3.

The difference in the electronics between the GOCE and cryogenic GG such as VK1 is that electrostatic GG measure capacities (i.e., voltage at the electrodes) in order to measure the displacement of the proof mass, whereas the superconducting GG measure inductance (i.e., current). This reduces potential sources of disturbances to the minimum and increases the stability of tensor GG accelerometers similarly to the superprecision electrostatic gyroscope.

Table 5.3 Comparative characteristics of accelerometers used in various missions

Mission	*CHAMP*	*GRACE*	*GOCE*
Material of the proof mass	TA6V	TA6V	PtRh10
Weight of the proof mass, g	72	72	320
Gap X, μm	60	60	32
Gap Y, Z, μm	75	175	299
Voltage, V	20	10	7.5
Measurement range Y, Z, g	$\pm 10^{-5}$	$\pm 5 \cdot 10^{-6}$	$\pm 6.5 \cdot 10^{-7}$
Noise level Y, Z, g/$\sqrt{\text{Hz}}$	$<10^{-9}$	10^{-11}	$2 \cdot 10^{-13}$
Bandwidth, Hz	0.0001–0.1	0.0001–0.1	0.005–0.1

5.2.5 *Promising Gravity Gradiometers*

As the range of GG applications is getting wider and the demands for high-precision measurements of SDGP tensor components are growing, designers come up with new methods and techniques to create novel tools based on various physical principles. Using superconductivity provides ultra-high threshold sensitivity; at the same time, it imposes special requirements for design.

Further increase in accuracy will be possible due to atom interferometry technologies. AOSense Inc. (USA) and Stanford University are working on the new generation of gravity gradiometers based on atom interferometry. In a Trapped Atom Interferometer the proof masses are individual atoms that have very stable dimensions and weights as compared with mechanical bodies, even precisely machined. The relative accelerations of the two free-falling atoms are measured by an atom interferometer. In 1998, this kind of GG was successfully used to measure gravity gradients. In principle, atom interferometry GG may have a very low noise component, 0.001 Eo/$\sqrt{\text{Hz}}$ (the potential resolution of an individual accelerometer being 10^{-15} g), but the goal has not been reached yet. The experimental studies of the prototype on a 1 m base showed a noise of about 38 Eo/$\sqrt{\text{Hz}}$ (Yu et al. 2005; Mahadeswaraswamy 2009; Wu 2009; McGuirk 2001; Brown et al. 2012). The immediate objective is to reduce the weight and dimensions and decrease the noise to 2 Eo/$\sqrt{\text{Hz}}$ so that the GG could be used onboard a submarine.

To increase GG resolution and enhance interferometer accuracy, special techniques are applied that slow down the atoms such as magneto-optical traps and laser cooling. The slowed-down atoms are called cold ones; their temperature is 2 μK and their speed is reduced to 2 cm/s while the standard speed is 300 m/s (Yu et al. 2010). This extends the time needed to measure the positions of the atoms (proof masses) and thus enhance the gradiometer accuracy.

The Jet Propulsion Laboratory (JPL) develops a quantum gravity gradiometer measuring the distance between individual cold atoms using an atom interferometer (Griggs et al. 2013; Carraz et al. 2014; Yu et al. 2005, 2010; Kohel et al. 2006). A prototype with a 10 m base has been designed and tested. Each interferometer is

an accelerometer, and a pair of them makes up a GG. Potentially such a quantum GG is millions of times more sensitive than a conventional GG. NASA spends about $400 million a year on this triennial JPL program on a quantum GG.

The advantages of atom interferometry GG are the following:

- free-falling atoms are ideal proof masses with identical characteristics;
- GG has no moving mechanical parts;
- laser cooling of atomic proof masses provides low temperatures of several μK without expensive cryogenic equipment;
- GG involves the technology and measurement techniques used in high-precision atomic clocks to ensure unique stability;
- measuring accelerations of free-falling atoms makes it possible to measure the absolute values of SDGP components. Therefore, quantum GGs are perspective for space missions studying the gravity fields of different satellites and planets, such as the Moon, Mars, and others (Griggs et al. 2013).

Another absolute GG was proposed by Micro-g Solutions Inc. (USA). The device consists of two absolute gravimeters FG5 spaced 60 cm apart. It measures the difference between the accelerations of two simultaneously falling bodies using a laser interferometer. It is calibrated with the help of standards of length and time. The development results are not published because of business considerations, but according to the promotional materials, the device accuracy is expected to be 20 Eo over the integration time of 1 min on a fixed base. The stated sensitivity is insufficient for the instrument to be used onboard space- or aircraft. In 2006 Micro-g Solutions Inc. merged with LaCoste Romberg and now it is known as Micro-g LaCoste. Now, no data on absolute GG is available at the company's website.

The gradiometer designed by Gravitec Instruments (UK) is based on an original principle proposed by Dr. Alexey Veryaskin in New Zealand in 1996. It is a prolate bar–a ribbon or a string–the cross-sectional dimensions of which are much smaller than its length. This GG is called a Gravitec Ribbon Sensor or a String Gravity Gradiometer. Under accelerations, the string performs vibrations that can be represented as the normal mode of vibrations. The first (primary) mode (C-mode) is a string bending under the base linear acceleration; the second mode (S-mode) is proportional to the gravity gradients along the string. The second mode is measured by differential transducers of the readout system, which makes it possible to calculate SDGP.

The gradiometer sensitivity can be enhanced by applying forced vibration of the string, similarly to the modulation principle used in rotating GG. Ideally, the readout system is sensitive only to the amplitude of the second harmonic and is insensitive to the amplitude of the primary mode. High requirements for the frequency and scale factor control are provided by the string uniformity along its length and symmetry of the sensors, which causes some difficulties in the new design.

The GG is designed for military, airborne and exploration applications, and mainly for monitoring of wells in mineral explorations, where it is included as a part of a borehole GG.

The sensitive element of the string GG has the following characteristics (Veryaskin 2003; Golden et al. 2007): dimensions 400 × 30 × 30 mm; weight 500 g; modulation frequency 5–10 Hz; and the desired noise 5 Eo/$\sqrt{\text{Hz}}$ at 1 Hz. The device measures the tensor components W_{xy}, W_{xz}, W_{yz}. The estimated instrumental noise of the prototype is about 8 Eo/$\sqrt{\text{Hz}}$ at 77 K (boiling point of liquid nitrogen).

The team from the University of Twente (Netherlands) proposed a MEMS GG for future satellite missions. The sensor consists of two linear accelerometers with proof masses moving in the plane of a silicon wafer. The advantage of such a device is the high precision fabrication of the proof masses and elastic suspensions (up to 0.1 μm accuracy). Using low temperatures further reduces the noise.

The proof masses weighing 1.34 g are suspended with four elastic elements with dimensions 0.05 × 0.5 × 60 mm. The proof masses and their suspensions are made by deep reactive ion etching technology. Additional gold weights of 1 cm^3 on each proof mass located 3.5 cm away from the sensor center are intended to increase their sensitivity. With the Q-factor of suspension loops of 10^5 and a temperature of 77 K, the noise may be expected to be 0.1 Eo/$\sqrt{\text{Hz}}$ (Flokstra et al. 2009; Liu et al. 2014).

In conclusion, Table 5.4 summarizes the performance data of gravity gradiometers both in operation and under development.

5.2.6 Expanding the Scope of Gradiometer Applications

Advances in modern technologies, theoretical and applied research as well as the interests of some economic sectors stimulate the development of gravity gradiometry. Various problems in geology, geodesy, geophysics, navigation, and fundamental physics require more detailed information on the anomalous gravity field of the Earth and other planets. The most challenging prospective GG application areas are outlined below.

1. Fundamental research on specification of the gravitational constant, the main provisions of the theory of relativity, and detection of gravitational waves (Paik 1989; Iafolla et al. 2003; Kasevich et al. 2014).
2. Studies of the planetary structure and figure of the Earth, detection of gravity anomalies and mapping of the Earth's gravity field in terrestrial and satellite surveys. For MicroSCOPE and GRACE Follow-On space missions, ONERA (France) has created a new MicroSTAR accelerometer with a noise of about 10^{-13} g/$\sqrt{\text{Hz}}$, which is twice less compared to GOCE accelerometers (Lenoir et al. 2011).
3. Exploration and industrial gravity measurement. GG application for mineral exploration was described above. This line will continue developing at an accelerated pace. Suffice it to say that the total length of GG survey lines increased by 20 times within 10 years (from 1999 to 2008) (Nerem et al. 1995).

Table 5.4 Current state and stages of GG development

Gravity gradiometer	Designer	Noise, Eo/$\sqrt{}$Hz	Stage of development
Rotating accelerometer	Bell Aerospace (USA)	10	Completed
Rotating dumbbell	Hughes Aircraft (USA)	5	Completed
Static Floated	Draper Laboratory (USA)	1	Completed
FTG	Lockheed Martin (USA)	3–5	In operation
3D FTG	BellGeospace (USA)	5	In operation
Falcon AGG	Lockheed Martin (USA) BHP Billiton (Australia)	3	In operation
EGG	ARKeX (UK)	7	Completed
eFTG, FTGeX	Lockheed Martin (USA) ARKeX (UK)	2	Completed
VK1	UWA/Rio Tinto (Australia) Gedex (Canada)	1–2	Prototype
HD-AGG	Gedex (Canada)	1	Prototype
Cryogenic	University of Maryland/Oxford Instruments Device (USA)	0.02 (estimate)	Laboratory
Electrostatic ESA/GOCE	Alcatel/ONERA (France)	0.02	In operation
Atom interferometer	AOSense/Stanford University/JPL (USA)	10^{-3} (estimate)	Laboratory
Two gravimeters	Micro-g Solutions (USA)	20	Completed
String	Gravitec (UK)	5	Prototype
MEMS	Universityof Twente (Netherlands)	0.1 (estimate)	Project

4. Detection of underground structures. Within the Gravity Anomaly for Tunnel Exposure (GATE) program, DARPA signed a $4.8 million contract with Lockheed Martin to develop GG-based equipment to be installed onboard helicopters to detect underground structures, bunkers and fortifications of terrorists (Lockheed Martin 2010).
5. Borehole gravity gradiometry. The demand for GG for borehole logging is associated with monitoring of ore deposits using the new hydromining technology, which displaces the traditional mining methods using mines, pits, etc., due to significant economic, environmental, and social advantages. In this case, there is no alternative to gravity gradiometry (because of acoustic and electromagnetic shielding of rather thick casing pipes), especially when it comes to the development of diamond bearing ores, which excludes the application of seismic exploration methods (Volfson et al. 1999; Neill 2010).

6. Identification of internal configurations of closed containers. Since it is impossible to shield the gravitational effects, GG is an ideal tool for determining the mass distribution within premises, carriages, containers, and so on. It can be applied to improve the security and customs inspection systems when looking for heavy items and substances, such as plutonium. It is possible to detect a 15 cm^3 high-density alloy in a shipping cargo container with a 1 Eo GG (Kirkendall et al. 2007).
7. Early prediction of severe earthquakes. A properly adjusted GG can generate a detected response to the low-frequency microseisms and detect seismic centers at distances of up to 11 thousand km, thus offering great advantages over seismometers (Kalinnikov et al. 1992; Volfson et al. 2010).
8. Development of new generation gravity gradiometers for measuring the third derivatives of the geopotential (Nerem et al. 1995). Such GGs are able to provide data for a more detailed gravity anomaly mapping and for determining the Earth's structure. The devices for measuring the third derivatives can be constructed as a combination of GGs (by analogy with GG comprising two or more gravimeters) or may have an original design.

5.2.7 Conclusions

The state of the art in the development of gravity gradiometers used to measure the second derivatives of the geopotential has been discussed. Though the history of GG development is rather long, their onboard operation involves severe difficulties. In recent years, a breakthrough has been made in this technology, and several onboard GGs were created within 15 years, from 1980 to 1995.

GG applications to mineral exploration and space missions have been described, their operation and test results have been discussed. It has been shown that design, manufacture and operation of GG are among the most complicated technologies in modern instrument engineering. Despite the impressive results obtained in gravity surveys and global modeling of the Earth gravity fields based on satellite data, gravity gradiometry still remains a unique and expensive method for measuring SDGP. So far only 11 gravity gradiometers have been manufactured for airborne gravity surveys (Zlotnikov 2011).

The design of a tensor GG determining all the components of the SDGP tensor has been analyzed. Difficulties in reducing external inertial and thermal effects have been considered.

GG designs based on atom interferometry and cold atoms have been discussed. Their merits have been described. It has been shown that they are the most promising devices for achieving the fantastic accuracies of about 10^{-4} Eo/$\sqrt{\text{Hz}}$. These gradiometers are now passing laboratory tests, and their characteristics are still far from their potential.

Prospects for the development of gravity gradiometry for various applications have been outlined.

5.3 Current State and Outlook for the Development of Cold-Atom Gravimeters

Modern absolute ballistic gravimeters (ABG) measure spatial positions of a moving mass using laser interferometers, the devices in which the change in the distance to an object is determined with an accuracy of a fraction of the light wavelength by the signal of laser light interference.

The natural way of increasing the sensitivity and accuracy of the interferometer is to reduce the wavelength of the electromagnetic radiation used. However, the wavelengths of the visible light lie within a relatively narrow range between 400 and 800 nm; then comes the ultraviolet light, which is followed by X-ray radiation. Though it is possible to create coherent radiation sources in these ranges (for example, see (Minogin 2010)), their implementation has been problematic so far. Yet, an alternative to an electromagnetic radiation interferometer does exist. As is known, any particles, including the atoms that make up the mass moving in a ballistic gravimeter, have wave properties and, accordingly, under certain conditions, they are able to interfere. The wavelength of a wavetrain (de Broglie wavelength) corresponding to a heavy particle is $\lambda = h/mv$, where $h = 2\pi\hbar$ is Planck's constant ($h = 6.62607 \times 10^{-34}$ J s), m is the particle mass, and v is the velocity. The lower is the atom velocity, the longer is the wavelength. Nevertheless, even for the atoms cooled to temperatures of the order of 10^{-3} K and, accordingly, having an average thermal velocity $v \approx 1$ m/s, the de Broglie wavelength is significantly smaller than the wavelength of the light: for example, for ^{87}Rb atom, which is most often used in laser cooling experiments, it is 4.5 nm at a velocity of 1 m/s.

In 1963, E.B. Aleksandrov demonstrated in his experiments that it is possible to observe interference of atomic states (Aleksandrov 1963). Nine years later, Yu.L. Sokolov built an interferometer of states of hydrogen atoms (Sokolov 1972). In 1991, some new different schemes of atomic interferometers (AI) were successfully demonstrated. Diffraction and interference of helium atoms on slits cut in thin gold foil were carried out at the University of Konstanz (Germany) (Carnal and Mlynek 1991); an interferometer on sodium atoms with a thermal velocity of about 10^3 m/s was built at Massachusetts Institute of Technology (MIT, USA) (Keith et al. 1991; Lenef et al. 1997). The novelty was that diffraction nanolattices with a period of 100 nm were used as semitransparent "mirrors". The first lattice split the beam into two beams; the second one turned the split beams, and the third one brought them together, resulting in interference of wavetrains that passed along different arms of the interferometer. Detection was carried out using a hot-wire detector (similar to that used in beam frequency standards).

As will be shown below, depending on the configuration, AIs have inherent sensitivity both to rotation and acceleration, and, accordingly, they can be used both as gyroscopes and accelerometers or gravimeters. The MIT interferometer, in which the atomic beam propagated in the horizontal plane, was tested as a gyroscope, wherein its sensitivity to rotation was $3 \cdot 10^{-6}$ rad/s/$\sqrt{\text{Hz}}$ or 0.004 °/$\sqrt{\text{h}}$.

Though the innovative research showed significant potential of AIs, the epoch of thermal-atom AIs came to an end soon since novel interferometric schemes were developed at the same time using the latest methods of the light interaction with matter. It was in the same year, 1991, that new schemes were developed at Physikalisch-Technische Bundesanstalt (PTB)—the National Metrology Institute of Germany (Riehle et al. 1991), and Stanford University (USA) (Kasevich and Chu 1991). They used coherent laser beams as semitransparent and nontransparent mirrors. We cannot but recognize the beauty of the idea: while in a conventional laser interferometer, photons move between mirrors consisting of atoms; in AIs, the approach is just the opposite, i.e., atoms move between mirrors consisting of photons.

Before proceeding to the physical methods used to create the interferometer-gravimeter with free-falling cold atoms, let us formulate the basics of its operation algorithm:

1. Preparation of an ensemble of atoms in a certain "internal" (e.g., hyperfine) state so that they are characterized by extremely small velocities and their uncertainty (laser trapping and cooling of atoms).
2. Switching off the trapping and cooling fields and the beginning of free fall. Atoms can start falling at a zero vertical velocity, or they may have a low fixed velocity in the upward direction ("atomic fountain" configuration).
3. Longitudinal splitting of an atomic cloud on a semitransparent laser "mirror", i.e., a change in the momentum of half the atoms by $2\Delta k$, where Δk is the photon momentum. As will be shown later, such a change in the momentum is always accompanied by a change in the internal state of the atom, i.e., its transition from one hyperfine state to the other one or to a superposition of two states.
4. Free fall over time T.
5. Reflection of an atomic cloud on a laser "mirror": a change in the momentum of the "slow" half of the atoms by $+ 2\Delta k$, and the "fast" half by $-2\Delta k$ accompanied by a change in their internal state.
6. Free fall over time T.
7. Recombination of an atomic cloud on a semitransparent laser "mirror".
8. Measurement of the phase, that is, of the relative number of atoms in each internal state. The end result is phase incursion $\Delta\varphi = k_{eff} \cdot g \cdot T^2$, where k_{eff} is the effective wave vector of the laser light forming "mirrors".

5.3.1 Basic Physical Principles of Cold-Atom Gravimeters

Consider the basic physical principles of AIs in more detail; we assume here that the readers have some idea of the atom energy structure (for example, see Elyashevich 2012). In what follows, we focus on alkali atoms with one electron in the outer shell. Such atoms have a similar energy structures: their ground state, i.e., the state with the lowest energy, is split into two so-called hyperfine states or sublevels (|1> and |2>) which differ in the projections of the electron angular momentum, or spin, on the direction of the nuclear momentum (Fig. 5.14). The spectroscopic notation for these

levels for the ^{87}Rb atom is $|5^2S_{1/2}, F = 1>$ and $|5^2S_{1/2}, F = 2>$, respectively; here, F is the total momentum of the atom representing the vector sum of the electronic and nuclear moments.

A significant feature of these states is that the difference in their energies is small compared with both the thermal energy of the atom and the energies of optical transitions (frequency $\omega^0{}_{12}$ of transition $|1> \leftrightarrow |2>$ lies in the HF or UHF (MW) range, and for ^{87}Rb, it is 6834.681 MHz). Their lifetimes are very long and can exceed tens of seconds for an isolated atom; therefore, the slow relaxation that causes transitions between these states is neglected in the subsequent discussion.

For the tasks of optical pumping and cooling of atoms, it is also essential that each hyperfine level in a magnetic field splits into $2F + 1$ Zeeman sublevels $m_F = -F...+F$, the energy gap between which, in the first approximation, is proportional to the field strength.

In addition to the ground state, an atom has an infinite number of excited states; special selection rules are used to determine the possibility of transition from one state to another under the effect of the resonant light. Assume that |3> is the nearest excited state of an alkali atom (for ^{87}Rb, this state is $|5^2P_{1/2}>$); frequencies $\omega^0{}_{13}$ and $\omega^0{}_{23}$ of $|1> \leftrightarrow |3>$ and $|2> \leftrightarrow |3>$ transitions lie in the optical range, and the typical lifetime of an atom in state |3> is 30 ns. From states |1> and |2>, the atom can be transferred to state |3> by applying the resonant light with a frequency of $\omega_{13} \approx \omega^0{}_{13}$ and/or $\omega_{23} \approx \omega^0{}_{23}$.

If an atom in state |1> is affected by the light with a frequency of ω_{13}, it can absorb one photon and transit to excited state |3>, from where it will transit very quickly (instantly as compared with the lifetime of the ground state) to one of the lower states, i. e., |1>, |2>. This process is accompanied by spontaneous emission of a photon in an arbitrary direction (Fig. 5.14a). If the excitation cycles with the frequency ω_{13} are repeated many times, all atoms will eventually gather in state |2>. This process is referred to as optical pumping to the level |2>. Similarly, it is possible to bring atoms from |2> into |1> by exposing them to the light with frequency ω_{23}. Thus, resonant radiation can be used to "prepare" atoms in states |1> or |2>.

During a cycle that comprises excitation and spontaneous emission, the momentum of an atom will change first by one momentum of an absorbed photon

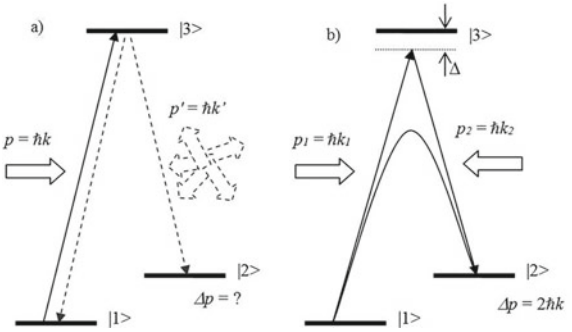

Fig. 5.14 Simplified energy structure of an alkali atom and its interaction with the resonant light: **a** forced absorption and spontaneous emission; **b** Raman excitation

directed along the axis of the light propagation and then by one momentum of a spontaneously emitted photon directed arbitrarily. Obviously, if the momentum of an atom is to be changed in doses, spontaneous light emission must be completely removed from the system. This is possible by using the so-called Raman excitation, that is, simultaneous excitation of an atom by two beams, the frequency difference of which $\omega_{12} = \omega_{13} - \omega_{23}$ is equal to the intrinsic frequency $\omega^0{}_{12}$ of the transition between the levels |1> and |2> (Fig. 5.14b). The simultaneous effect of these beams can be considered as a single process of the stimulated absorption of radiation with frequency ω_{13} and forced emission with the second frequency ω_{23} or vice versa, depending on the original state of the atom.

In contrast to spontaneous emission, under the action of Raman excitation, an atomic momentum changes strictly by the value $\boldsymbol{\Delta k_{eff}}$, where $\boldsymbol{k_1}$ and $\boldsymbol{k_2}$ are the wave vectors of the Raman beams, and $\boldsymbol{k_{eff} = k_1 - k_2}$. In the case when the beams are directed towards each other, $\Delta k_{eff} = \Delta(k_1 + k_2) \approx 2\Delta k_1$. Choosing a rather large common detuning $\Delta = \omega_{13} - \omega^0{}_{13} = \omega_{23} - \omega^0{}_{23}$ of Raman beam frequencies from the frequencies of the corresponding optical transitions (see Fig. 5.14b), it is possible to minimize the role played by the processes of ordinary single-photon excitation and the processes of spontaneous emission associated with them as compared with Raman excitation processes.

Such a system can be considered a two-level system with resonant frequency $\omega^0{}_{12}$ of the transition between levels |1> and |2>. The pair of Raman beams in this representation is regarded as a single light wave with frequency ω_{12} and the wave vector $\boldsymbol{k_{eff}}$.

Consider the probability of transition of such a quasi-two-level system "prepared" in state |1> to state |2> under the action of the Raman light (Fig. 5.15). After the "effective" light with frequency ω_{12} is switched on at the moment of time $t = 0$, the system populations start oscillating with a characteristic frequency Ω_R, which is determined by the energy of interaction of the resonant light with a dipole moment d of the transition and is referred to as the Rabi frequency: $\Omega_R = (d \cdot E)/\hbar$, where E is the electric field intensity. If the light is switched off at a moment of time τ such that $\Omega_R \cdot \tau = \pi$ (so-called π pulse), then almost all the atoms (or, in the absence of relaxation, all the atoms) will be transferred to state |2> and take an additional momentum $2\Delta k$. If $\Omega_R \cdot \tau = \pi/2$ (so-called $\pi/2$ pulse), then one might expect that half of the atoms shall be in state |2> and take an additional momentum $2\Delta k$, and the state of the second half shall not change at all.

However, quantum mechanics offers a different interpretation of this event, namely: under the action of the $\pi/2$ pulse, each atom finds itself in a coherent superposition of states |1> and |2> and each atom moves simultaneously along two trajectories: with the original and modified values of the momentum and, accordingly, velocity. Here, the difference between the quantum-mechanical interpretation and the classical one is that, from the standpoint of quantum mechanics, these two parts of the atomic beam can interfere with each other. It should be noted that the so-called $\pi/2$ pulse (the time interval of the resonant light with duration $\tau = (\pi/2)/\Omega_R$) acts on atoms in the same way as a semitransparent mirror acts on photons.

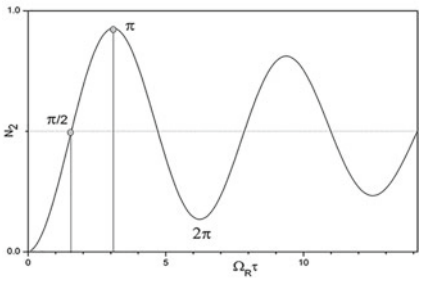

Fig. 5.15 Rabi oscillations: the dynamics of the populations of a two-level system when the resonant light is switched on

A simplest AI is built according to the scheme of the Mach–Zehnder interferometer (Fig. 5.16): an atomic cloud is split by π/2 pulse *A* into parts *a* and *b* that have different vertical projections of velocity. After the trajectories *a* and *b* diverge at a sufficient distance, they are subjected to π-pulse *B* which causes an "exchange" of states: the part of the atoms that had an additional pulse $2\Delta k$ will lose it and vice versa. Diverging trajectories begin to converge; the second π/2 pulse *C* brings trajectories together. In its impact zone (as shown in the inset in Fig. 5.16b), each of the two beams *a* and *b* splits into two, the halves of the beams merge and two atomic beams *c* and *d* go out of the interferometer, each containing atoms that have passed along both of its arms.

Note the factor the significance of which was first realized by the French physicist Borde (1989): in the AI scheme described above, there is a one-to-one relation between the "external" state of an atom, that is, the value of its momentum, and its "internal" state, which therefore may be used as a kind of a "label" for the external state (the so-called state labeling method). In particular, the interference of de Broglie waves shows itself in the form of oscillations of the populations of states |1> and |2> in beams *c* and *d*, which makes it possible to detect the interference pattern using high-performance optical methods.

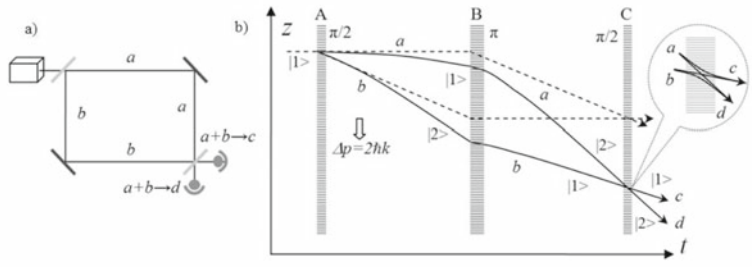

Fig. 5.16 **a** Optical Mach–Zehnder interferometer; **b** atomic interferometer: the shaded areas are Raman beams; the dotted lines are trajectories of atoms in the absence of gravity; the solid lines are the trajectories of atoms in the gravitational field

5.3.2 Sensitivity and Accuracy of the Cold-Atom Gravimeter

Hereinafter, let us distinguish between the absolute accuracy and the relative sensitivity (also known as resolution, variational sensitivity, or just sensitivity) of measurements. In accordance with the standards adopted in metrology (for example, see RMG 29-99 GSI), accuracy is a characteristic of the measurement quality that shows how close to zero the measurement error is, and relative sensitivity is a characteristic determined by the smallest change in the measured value which can be recorded with a certain device. Accordingly, it is conventional to divide measuring devices into two classes: absolute devices, that is, devices whose error (including systematic errors) does not exceed a certain level, and non-absolute devices. The latter often have high variational sensitivity and are referred to as variometers.

In physics, a distinction can also be made between the concepts of accuracy and absolute accuracy. In this case, absoluteness is understood as the ability to take measurements based only on fundamental constants and on the variables that are measured using fundamental constants, such as frequency. It may also be expressed as follows: absolute measurement does not require taking into account parameters that depend on the design of the measuring device and need to be calibrated. As can be seen later, ballistic AIs belong to the class of absolute devices in exactly this strict sense.

An AI signal, i.e., a phase difference in the two arms of the interferometer, is the sum of two terms (de Angelis et al. 2009): the first one is the inherent de Broglie wave phase difference. In the case of the free fall of atoms in a uniform field, it is equal to zero. The second term, which is the actual AI signal, is the sum $\Delta\Phi$ of phase differences that appear (and are "imprinted" in atoms) when interacting with the light and are equal to the local (i.e., measured directly at the points of interaction with atoms) light wave phases. The position of atoms in relation to the light wave in the gravitational field varies according to the law:

$$z(t) = gt^2/2. \tag{5.3.1}$$

Thus, the laser light phase

$$\mathrm{f_i} = k_{eff} \cdot z(t_i), \tag{5.3.2}$$

"imprinted" in the atoms during the pulses i = A, B, C, is summed up into the total phase incursion:

$$\Delta\Phi = \phi_A - 2\phi_B + \phi_C \tag{5.3.3}$$

Taking the time of the first pulse as a reference and designating the time between pulses as T, we obtain: $\phi_A = 0$, $\phi_B = \mathrm{k}_{\mathit{eff}} \cdot gT^2/2$, and $\phi_C = \mathrm{k}_{\mathit{eff}} \cdot g\ (2T)^2/2$. Thus,

$$\Delta\Phi = k_{eff} \cdot g \cdot T^2, \tag{5.3.4}$$

and, at the output of the interferometer, the population of state |2>, with regard to the total number of atoms, is given as

$$N_2 = 1/2[1 - \cos(\Delta\Phi)] = 1/2\left[1 - \cos(k_{eff} \cdot g \cdot T^2)\right]. \quad (5.3.5)$$

The reader may notice that formula (5.3.4) includes the effective wave vector of the Raman light rather than the de Broglie wavelength of atoms; therefore, it is the Raman wavelength that determines the period of the interference pattern. But, on the other hand, formula (5.3.4) does not include the terms that describe the position of the atomic mass (of the incident mirror in the classical gravimeter) and the perturbations associated with them are not included in (5.3.4). This is due to the fact that the de Broglie wavelength is substantially shorter than the wavelength of the light under these conditions.

In general, the ultimate spatial sensitivity of the interferometer can be estimated by dividing the period of the interference pattern by the signal-to-noise ratio. Considering that the maximum value of the signal-to-noise ratio when measuring on an incoherent ensemble of $N = N_1 + N_2$ atoms is $\sqrt{N}$ (quantum atomic projection noise), for one measurement with an AI, we obtain:

$$\Delta g_{min} \approx 2\pi / (N^{1/2} \cdot k_{eff} \cdot T^2) = (1/2) \cdot N^{-1/2} \cdot T^{-2}. \quad (5.3.6)$$

By substituting $N = 10^8$, $\lambda = 0.8 \cdot 10^{-6}$, $T = 1$ s, we obtain $\Delta g_{min} \approx 4 \cdot 10^{-11}$ m/s^2 = 4 nGal. Thus, the potential sensitivity of AIs is extremely high, but it is difficult to implement from the technical standpoint, which makes it impossible to go beyond hundreds of nGal so far. The difficulties are primarily associated with the formation of a dense homogeneous atomic cloud and particularly with the generation of Raman beams with perfectly flat and stable fronts, because, as follows from the above, error $\delta\varphi$ of the Raman wave phase is directly summed with signal (5.3.4) of the interferometer.

In addition to the limitations of the AI sensitivity, there are some factors that lead to its systematic errors. Formulas (5.3.4)–(5.3.5) are obtained under the assumption that the interferometer is fixed and its actual area S, bounded by trajectories a and b, is equal to zero. If this is not the case, AI obtains a rotational sensitivity which makes it possible to create highly sensitive gyros based on them. In the general case, the phase incursion in AIs is expressed by the formula:

$$\Delta\Phi = 4\pi m \boldsymbol{\Omega} \cdot S + k_{eff} \times gT\_k_{eff}(\boldsymbol{\Omega} \times g) \cdot T^3. \quad (5.3.7)$$

Here, $\boldsymbol{S}$ is a vector that is numerically equal to the interferometer area and directed perpendicular to the AI plane; $\boldsymbol{\Omega}$ is a pseudovector of angular velocity; the first term is responsible for the sensitivity of the device to rotation. The second term describes gravimetric sensitivity. The third member is a cross term. It zeroes only when there is no rotation or the axis of rotation is parallel to the gravity vector, i.e., at the poles of the planet.

The contribution of the second term is the main source of errors in AI-based gyroscopes; its influence is zeroed by launching two atomic beams towards each other and subtracting their signals. The first term may contribute to the gravimeter error in a similar way; to prevent this, the wave vectors of the Raman beams must be perfectly parallel to the gravity vector, and the atoms in the cloud must on average have a zero horizontal velocity projection. The third term is a source of errors both in gyroscopes and gravimeters. It cannot be compensated for but can be taken into account. At the equator, at $T = 1$ s, it gives a relative measurement error of $0.7 \cdot 10^{-5}$ or 7 mGal.

The gravity gradient is another source of systematic errors in the interferometer. On the Earth's surface, it is ~$3 \cdot 10^{-6}$ s^{-2}; its presence leads to a relative measurement error at the level of $3 \cdot 10^{-8}$ or 30 nGal.

In this section it was also assumed that Raman pulses are short as compared with the time of flight through the interferometer and that the resonant frequency of the falling atoms does not change as they accelerate, i.e., the Doppler effect was neglected. In (Kasevich and Chu 1991), it is mentioned that the use of a $\pi/2–\pi–\pi/2$ sequence of pulses ensures that the total phase shift does not depend on the initial velocity; therefore, the phase shift is the same for all atoms of the atomic cloud. Nevertheless, any difference in the vertical projection of the velocity of an atom from the average value leads to a decrease in the efficiency of its interaction with Raman beams, and the difference of the horizontal projection of velocity from zero leads to spreading of the atomic cloud. Both deteriorate the signal contrast. In this regard, creation of a deep-cooling system is a prerequisite for the creation of an AI.

5.3.3 Laser Cooling of Atoms

S. Chu, C. Cohen-Tannoudji and W.D. Phillips received the Nobel Prize in 1997 for their work on atom cooling with the laser light (see, e.g., Phillips 1998). However, the ideas on which the laser cooling methods are based were put forward by Hänsch and Schawlow (1975) and Letokhov and Minogin (1981). Successful experiments on controlling the velocity of atoms using the light were carried out by A.M. Shalagin, V.P. Chebotaev, and others.

The most probable velocity of atoms at room temperature is 200–500 m/s. If a chamber containing atoms is irradiated with the light, the frequency ω of which is slightly lower than the frequency of one of the resonant transitions $|1\rangle \leftrightarrow |3\rangle$ or $|2\rangle \leftrightarrow |3\rangle$ (see Fig. 5.14), the probability of photon absorption by an atom will be low. But if an atom moves with velocity v towards the laser beam, then, due to the Doppler effect, frequency ω' of the light perceived by the atom increases according to the following formula:

$$\omega' = \omega[1 - (v/c) \times \cos(\alpha)], \tag{5.3.8}$$

where c is the velocity of the light, α is the angle between the direction of motion of the atom and the light beam. Thus, the frequency detuning of the light decreases for such an atom and the probability that it will absorb a photon increases. Absorbing a photon, an atom receives a momentum in the direction opposite to the direction of its motion, after which it emits a photon in an arbitrary direction, as shown in Fig. 5.14a. Thus, if atoms are affected by the low-frequency detuned light coming from all sides at the same time, they can be slowed down and cooled to very low temperatures. If the cooling beams interact with the transition $|1\rangle \leftrightarrow |3\rangle$, all the atoms will gather at the level $|2\rangle$ after several cycles of excitation and decay, and vice versa. To prevent this process, the cooling beams are mixed with so-called repumping beams tuned to resonance with the transition $|2\rangle \leftrightarrow |3\rangle$.

Such a cooling method is limited by the fact that the absorption line of an atom is not infinitely narrow: it is limited by the lifetime of the excited state and is approximately 5 MHz; thus, the atom does not "distinguish" the detuning values of the laser light that are significantly smaller than this value. If we use formula (5.3.8) to transform the frequency detuning into the atom velocity, and the velocity into temperature, the limit of the Doppler cooling method will be $\sim 2 \cdot 10^{-4}$ K. Since the motion of atoms in the deceleration zone is described by the equations similar to the viscosity equation, this cooling scheme is referred to as optical molasses. The optical molasses slows down the movement of atoms but does not hold them in place. Due to gravity and residual velocities of atoms, the lifetime of atoms in the optical molasses does not exceed several tens of milliseconds.

In the 1980s, Phillips (1998) suggested combining laser cooling with laser trapping of atoms in a magneto-optical trap (MOT). The MOT uses the above-mentioned effect of splitting the energy levels of atoms in a magnetic field (the Zeeman effect).

The atoms being cooled (Fig. 5.17) are placed between the coils of the so-called anti-Hemholtz configuration that create a strong nonuniform magnetic field B such that the minimum of the field modulus ($B = 0$) is in the center of the trap. The distance between the Zeeman sublevels is proportional to the magnetic field induction and is also zero at the center of the trap; the atomic magnetic sublevels diverge in the shape of a fan towards the edges of the trap. As the distance from the center of the trap increases, the frequencies of the optical transitions for which the Zeeman shift is negative decrease so much that the laser light becomes resonant with it and the atoms begin interacting with it intensively.

By choosing the polarization of the laser beams (circular arrows in Fig. 5.17), it is possible to ensure that an atom flying up to the edge of the trap will interact with the beam that will give it a pulse directed towards the center of the trap. In such a pattern, all atoms move to the minimum field zone and accumulate in a dense cloud with a typical diameter of several tenths of a millimeter.

The first experiments on cooling of atoms in a MOT showed that an ensemble of atoms could be cooled to a temperature that was substantially lower than the Doppler limit (tens and even less than ten microkelvins). In 1989, J. Dalibard and C. Cohen-Tannoudji explained that result by creating the theory of Sisyphus cooling (Dalibard and Cohen-Tannoudji 1989). This effect can be briefly described as follows: counter-propagating laser beams of different polarizations form a standing wave in the trap.

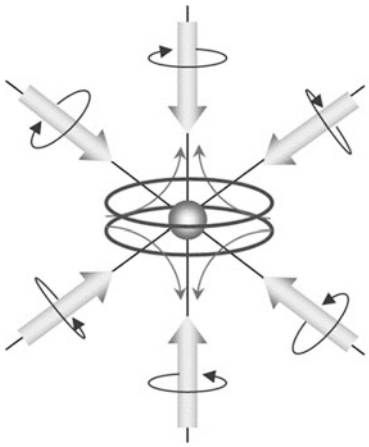

Fig. 5.17 Schematic diagram of a magneto-optical trap. Two coils carrying a current form a spherical magnetic quadrupole. The optical field is generated by three pairs of counter-propagating, circularly polarized laser beams

This wave spatially "modulates" the energy of an "atom + light field" system by replacing the flat levels of the system with alternating "ups" and "downs". When an atom moves along the trap, it travels up to the top of the potential, thus losing kinetic energy, then it falls down. It was found that an atom is more likely to interact with a photon when it is at the top of the potential; therefore, as a result of continuous repetition of this process, the atom is cooled significantly below the Doppler limit.

Subsequently, new limitations on atom cooling were discovered that were associated with stochasticity of the process of emitting photons by an atom and, hence, with unpredictability of the momentum recoiled by an atom. The corresponding "recoil" limit is a few microkelvins. Various methods have been developed to overcome this limit, among which are Raman cooling, cooling in a strong magnetic field, polarization gradient, evaporation method, etc. As a result, temperatures of the order of nanokelvin and even hundreds of picokelvins were achieved, which correspond to the atom velocities of less than 1 mm/s.

5.3.4 Physical Design of the Atomic Interferometer-Gravimeter

In the gravimetric configuration, an AI is a vertical vacuum chamber with transparent windows for cooling, Raman, and detecting beams.

In the standard AI configuration (Fig. 5.18a), the MOT chamber is located at the top. A cloud of atoms gathers in its center, after which the cooling beams and the magnetic fields are deactivated and the atoms start falling freely. At the beginning and at the end of their fall, they are subjected to the Raman $\pi/2$ pulse; and when they reach the midpoint, they are subjected to π pulse. The "fountain" configuration (Fig. 5.18b) is different in that the MOT is at the bottom and, at the end of the cooling process, the atoms "shoot" upward. For this purpose, the frequency of the

beams directed downwards is detuned relative to the beams directed upwards, so that the standing wave formed by these beams begins to move upwards at a velocity of several meters per second. In so doing, the cooling process continues, but now in a moving coordinate system, so that the width of the atomic velocity distribution does not grow.

After cooling, the atoms are prepared in a certain internal state (e.g., $|5^2S_{1/2}, F = 1, m_F = 0\rangle$). This is achieved by deactivation of cooling and repumping beams in a certain sequence. Besides, additional beams are used to "blow" away all atoms except those that are in the desired state. All the lasers used should be stabilized to atomic transitions or frequency-locked to the stabilized lasers. All manipulations with their frequencies and amplitudes are performed using acoustic and electro-optical modulators.

The interaction of atoms with π pulse in this configuration takes place at the upper point of the trajectory; the detection zone can be located either above or below the MOT. Special requirements are imposed on lasers that generate Raman frequencies: the wave fronts generated by them must be stable relative to each other with a sub-angstrom error. For this, their differential frequency is locked to the frequency of an ultra-stable generator (atomic frequency standard) having a frequency of ~6834 MHz. A typical width of the beat spectrum signal of two Raman lasers is 10 kHz with a power of 0.5 W. In order to compensate for the Doppler shift of the resonant frequency of accelerated atoms, the differential frequency should vary linearly with time. When the frequency rate exactly corresponds to the acceleration of atoms, the phase incursion of the AI is equal to zero.

The interferometer signal is detected by optical methods. First, the number of atoms in one hyperfine state (for example, $|2\rangle$) is measured, then all atoms in state $|1\rangle$ are transferred to state $|2\rangle$ by the π pulse and measurement is repeated,

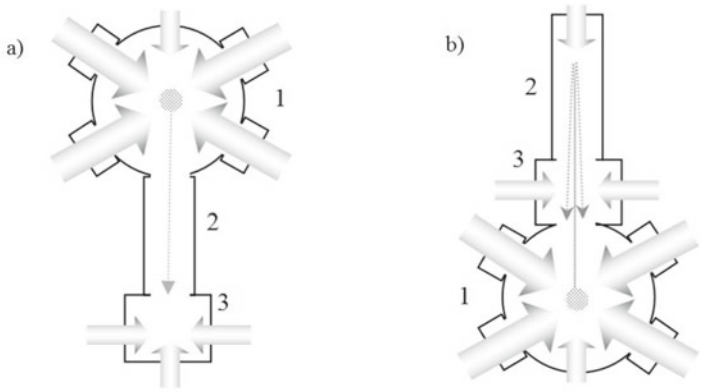

Fig. 5.18 **a** AI-based gravimeter in the standard configuration; **b** AI-based gravimeter in the "atomic fountain" configuration. (1) MOT; (2) ballistic tube; (3) detection chamber. Inclined, vertical and horizontal beams are cooling, Raman and detecting beams, correspondingly

following which, the background level of luminescence is measured. The procedure for measuring the number of atoms is based on the use of so-called cyclic transitions, i.e., transitions to the excited states from which spontaneous decay is possible only to the initial state. Exciting an atom repeatedly during a cyclic transition and recording the luminescence during spontaneous decay, it is possible to record many thousands of photons emitted by a single atom. This method allows the amplitude of the signals to be increased so that the level of atomic projection noise begins to exceed the level of shot noise of the light, thus ensuring the maximum sensitivity of the AI.

5.3.5 Modern Designs of Atomic Interferometers

To date, there are several dozen cold-atom gravimeters in the world. An example of AI for space applications is the interferometer based on two rubidium isotopes (^{85}Rb and ^{87}Rb) built as a result of cooperation among 16 laboratories from 7 European countries (Schuldt et al. 2015). In this device, designed to work on a satellite, the working atoms are cooled to the state of Bose–Einstein condensate (see Sect. 5.3.7). The use of two working substances makes it possible not only to eliminate some systematic errors of the AIs but also conduct various scientific experiments to study fundamental laws, such as the equivalence law. Semiconductor lasers with external cavities, laser amplifiers, acoustic and electro-optical modulators can be controlled remotely from the Earth. Bose–Einstein condensate takes 9 s to prepare; the result is $n_a \approx 10^6$ atoms of each substance at a temperature of 70 pK. The atom sampling time is 10 s with a travel length of 12 cm. The surfaces of the reflecting mirrors are made with an accuracy of $\lambda/50$. The whole device comprises 9 units, the total weight of which is 221 kg, power consumption—608 W, and the volume—470 l.

Consider the setup assembled at the Wuhan University, China, as an example of a modern stationary gravimeter (Hu et al. 2013; Zhou et al. 2015). In this setup, the atoms are cooled down sequentially in two traps, which allows obtaining a cloud of $n_a \approx 3 \cdot 10^9$ atoms cooled down to 7 μK. These atoms are shot upwards at a velocity of 3.83 m/s, which corresponds to a distance of 0.75 m from the highest point of the trajectory. When the atoms approach the interferometer inlet, a speed-selective π-pulse is activated; it "cuts out" a relatively small fraction of atoms ($\sim 5 \cdot 10^7$) that have a longitudinal temperature of 300 nK from the velocity distribution and transfers them to the initial state $|5^2S_{1/2}, F = 1, m_F = 0\rangle$, after which a standard π/2–π–π/2 pulse sequence affects the atoms. The gravimeter sensitivity shown in those experiments was 4.2 μGal/$\sqrt{\text{Hz}}$; such devices reach the resolution of about 0.1 μGal at an averaging time of 1000 s or more.

5.3.6 *Gravimeter Based on Cold Atoms Trapped in an Optical Dipole Trap*

We have not yet considered cold-atom gravimeters whose schemes are fundamentally different from ballistic gravimeters, such as gravimeters on cold atoms trapped in an optical dipole trap (Poli et al. 2011; Beaufils et al. 2011; Zhou et al. 2013). In their simplest form, these devices are analogs of the classic spring gravimeter, as well as of the superconducting levitating-mass gravimeter. As distinct from these instruments built on the principles of classical mechanics and, therefore, lacking the property of absolute accuracy, the cold atom gravimeter built at the University of Florence (Italy) has demonstrated (Poli et al. 2011) the ability to measure g with a relative error of 10^{-7}, which is also made possible owing to the use of pure quantum effects.

The design philosophy principles of the gravimeter based on cold atoms trapped in an optical dipole trap can be briefly described as follows: atoms are subjected to multi-stage laser cooling to a temperature of <1 μK. In addition to the usual cooling fields, atoms are affected by the field of a strong standing wave formed by two vertical beams of a solid-state laser with a power of about 1 W. The light wavelength of this laser is detuned very far (hundreds of nanometers) from the resonant frequencies of atomic transitions; therefore, this light is not absorbed by atoms and does not affect the cooling processes. But as the cooling fields are deactivated, part of the atoms is trapped, due to the nonzero polarizability of their electron shells, in the antinodes of the standing wave (Fig. 5.19a).

According to the Bloch theorem (Bloch 1928), the wave functions of such a system are described by a quasiperiodic relation that has the same period as the lattice. The gravitational contribution to the interaction potential of an atom with a standing wave results in a situation where the potentials of atoms in neighboring antinodes

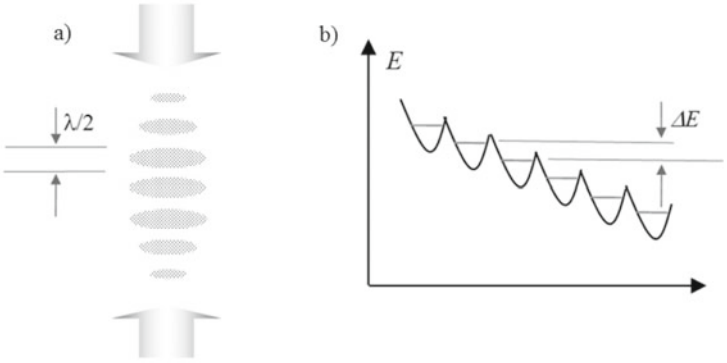

Fig. 5.19 **a** A cloud of cold atoms distributed over the antinodes of a standing light wave; **b** potentials and lower energy levels corresponding to different antinodes of a light wave (Wannier–Stark ladder)

spaced by λ/2, differ by exactly $\Delta E = mg\lambda/2$ (the so-called Wannier–Stark ladder, Fig. 5.19b) and, thus, the system has a resonant frequency (Bloch frequency) equal to

$$\omega_B = \Delta E/ = \mathrm{m}g\lambda/2. \tag{5.3.9}$$

If such a system is subjected to perturbation with a frequency of $\omega = \omega_B$, its transitions from one state to another one are initiated, i.e., the transitions of atoms to neighboring antinodes of a standing wave. This process can be recorded by measuring the vertical size of the atomic cloud: when it enters the resonance, it increases. The value of g can be calculated using formula (5.3.9). In (Poli et al. 2011), to excite Bloch resonances, the authors used periodic modulation of the depth of the dipole trap potential at the fifth harmonic of the Bloch frequency $\omega = 5\omega_B$, which corresponds to the transition of an atom through four antinodes. The relative measurement error of 140 ppb (parts per billion) is due to the instability of the wavelength of a high-power laser. According to the authors, stabilization of the laser will reduce the error by two orders of magnitude.

In (Beaufils et al. 2011; Zhou et al. 2013), the scheme described above was complemented with Raman beams that transfer atoms into coherent superpositions of states distributed over different antinodes of a standing wave and then bring them together again. In essence, the setup is an AI, in which separation of atoms by trajectories is replaced by their distribution over the antinodes of the standing wave, and the introduction of Raman beams allows the state labeling method (see Sect. 5.3.2) to be used to detect the interference signal of atoms and thereby increase sensitivity. In this case, as in the previous work, the signal is modulated at the Bloch frequency and its harmonics. However, in (Zhou et al. 2013), the sensitivity and the accuracy were limited at the level of $\Delta g/g \approx 10^{-5}$ by a small number of atoms, $n_a \approx 4 \cdot 10^4$, remaining in the optical dipole trap after their interaction with Raman pulses. A natural way to improve the characteristics of such a system is to increase the number of atoms cooled in a MOT and trapped in a dipole trap.

5.3.7 Outlook for the Development of Cold-Atom Gravimeters

The sensitivity of AIs is limited not only by technical factors, such as the level of vibrations, the uniformity of magnetic and electric fields in the path of the interferometer, the stability of the wave fronts of Raman beams, but also by fundamental factors, among which the number of simultaneously cooled atoms ($n_a = 10^7$–10^9 in ballistic schemes and $n_a = 10^4$–10^6 in optical dipole traps). These values are 8–12 orders of magnitude smaller than the number of photons n_{ph} usually recorded in 1 s in an optical interferometer (OI). Thus, the limiting signal-to-noise ratio in AIs in $\sqrt{n_{ph}/n_a} = 10^4$–10^6 is lower than that in OIs. However, such a great advantage of the OI is, firstly, not fully used because of the limitations inherent in the OI itself and, secondly, it is partially compensated by the advantages of the AI that were discussed

above, so that today, the sensitivity of AI-based ballistic gravimeters is not inferior to the classic counterparts. Nevertheless, a further increase in sensitivity will require the use of fundamentally new methods at some point. Below is the list of the most promising lines of research as we see it at present.

1. Using Bose–Einstein condensate. Such a condensate is an ensemble of atoms cooled to such an extent that their wave functions overlap and all atoms coalesce into a single quantum mechanical entity. A great number of experiments have already been conducted on separation and mixing of Bose–Einstein condensate, as well as on the interference of parts of one or more condensates prepared independently, e.g., the AI for space applications described in Sect. 5.3.5 (Schuldt et al. 2015).
2. Quantum non-demolition measurement. Quantum mechanics has limitations on the accuracy with which the product of noncommuting quantities can be measured. This means that in each pair of such quantities, the measurement uncertainty of one quantity can be reduced by increasing the measurement uncertainty of the second one. In the case of AI, such quantities are amplitude and phase. Earlier, methods for reducing phase uncertainty by increasing amplitude uncertainty were developed for laser cooling schemes (for example, see (Oblak et al. 2005). In the limit, for measurements on N atoms, this method allows for the signal-to-noise ratio increase from $\sqrt{N}$ to N.
3. Large momentum transfer. The effect of the Raman light causes a change in the atom momentum by $2\Delta k$, i.e., by two photon momentums. Multi-photon excitation methods provide multifold increase of one-time momentum transfer. Thus, if we choose Raman frequency ω_{12} so that $\omega_{12} = \omega^0{}_{12}/3$, the atom will be able to absorb no more and no less than three pairs of Raman photons at a time. Thus, each π pulse will change the photon momentum by $6\Delta k$. Applying three π-pulses to atoms instead of one, it is possible to increase the velocity separation in the interferometer to $18\Delta k$. To date, the transfer of 102 photon momentums to an atom has been successfully implemented (Chiow et al. 2011).

5.3.8 Conclusions

Several versions of cold-atom gravimeters have been created so far, the most accurate and sensitive of which use the de Broglie interference effects. In particular, gravimeters-interferometers on free-falling cold atoms are counterparts of classical devices, except for the fact that they use a cloud of cold atoms as a falling mass, and the signal is the result of interference of particles that followed two different time-space trajectories. They inherited the absoluteness of measurements from classical ABGs, the feature that significantly distinguishes them from other modern promising schemes, such as the superconducting levitating-mass gravimeter. At the same time, AI-based gravimeters are currently superior to classical ballistic gravimeters in sensitivity, which continues to increase each year. For example, in (Gillot et al. 2014), the authors present the results of comparative testing of the AI developed in

the laboratory LNE-SYRTE (Paris) and a classical Micro-g LaCoste FG5-X ABG (Luxembourg). It is shown that an error of 1 μGal is achieved by averaging FG5-X readings over 86 s, while the AI requires only 36 s. Also, gravimeters based on cold atoms trapped in an optical dipole trap are currently under development. They are expected to surpass classical devices in their basic metrological characteristics in future. Taking into account the fact that AI-based gravimeters are in principle free from many errors to which their classical counterparts are subject, their development is undoubtedly justified despite their high cost and sophistication.

References

Airborne Gravity 2016 (W10) Adelaide, Australia, August 2016. http://adelaide2016.aseg.org.au/PDF/W10.pdf

Albertella A, Migliaccio F, Sansó F (2002) GOCE: the earth gravity field by space gradiometry. Celest Mech Dyn Astron 83(1–4):1–15

Aleksandrov EB (1963) Quantum beats of resonance luminescence under excitation with modulated light. Opt Spektrosk 14(3):436–438

Andreev VD (1966) Teoriya inertsial'noi navigatsii. Avtonomnye sistemy (Theory of Inertial Navigation. Autonomous Systems). Nauka, Moscow

Andreev VD (1967) Teoriya inertsial'noi navigatsii. Korrektiruemye sistemy (Theory of Inertial Navigation. Aided Systems). Nauka, Moscow

Annecchione MA, Moody MV, Carroll KA, Dickson DB, Main BW (2007) Benefits of a high performance airborne gravity gradiometer for resource exploration. In: Exploration 07: fifth decennial international conference on mineral exploration, pp 889–893

Anstie J, Aravanis T, Johnston P, Mann A, Longman M, Sergeant A, Smith R, Van Kann F, Walker G, Wells G, Winterflood J (2010) Preparation for flight testing the VK1 gravity gradiometer. Airborne Gravity 2010, Abstracts from the ASEG-PESA Airborne Gravity 2010 Workshop: Australia, pp 5–12

Avgustov LI, Soroka AI (2009) Onboard gravity variometer. Experience in development and bench test results. Mekhatronika Avtomatizatsiya Upravlenie 3:51–56

Beaufils Q, Tackmann G, Wang X, Pelle B, Pelisson S, Wolf P, Dos Santos FP (2011) Laser controlled tunneling in a vertical optical lattice. Phys Rev Lett 106:213002

Becker D, Becker M, Leinen A, Zhao Y (2016) Estimability in strapdown airborne gravimetry. International Association of Geodesy Symposia, vol 144. Springer

Bell RE (1998) Gravity gradiometry. A formerly classified technique used to navigate ballistic-missile submarines now helps geologists search for resources hidden underground. Sci Am 74–79

Bloch F (1928) Über die Quantenmechanik der Elektronen in Kristallgittern. Z Phys 52:555–600

Bolotin YV, Golovan AA (2013) Methods of inertial gravimetry. Moscow Univ Mech Bull 68(5):117–125

Bolotin YV, Vyazmin VS (2015) Gravity anomaly estimation by airborne gravimetry data using LSE and minimax optimization and spherical wavelet expansion. Gyroscopy Navig 6(4):310–317

Bolotin YV, Vyazmin VS (2016) Gravity anomaly vector determination along flight trajectory and in terms of spherical wavelet coefficients using airborne gravimetry data. In: 4th IAG symposium on terrestrial gravimetry: static and mobile measurements (TG-SMM2016), St. Petersburg, Russia, pp 83–86

Bolotin YV, Golovan AA, Parusnikov NA (2002) Uravneniya aerogravimetrii. Algoritmy i rezul'taty ispytanii (Airborne Gravimetry Equations. Test Algorithms and Results. Publishing House of the Faculty of Mechanics and Mathematics of the Moscow State University, Moscow

Borde CJ (1989) Atomic interferometry with internal state labelling. Phys Lett A 140(1):2

Brown D, Mauser L, Young B, Kasevich M, Rice HF, Benischek V (2012) Atom interferometric gravity gradiometer system. In: 2012 IEEE/ION Position, location and navigation symposium, PLANS-2012, pp 30–37

Cai W, Zhang K, Wu M (2013) Improving airborne strapdown vector gravimetry using stabilized horizontal components. J Appl Geophys 98:79–89

Carnal O, Mlynek J (1991) Young's double slit experiment with atoms: a simple atom interferometer. Phys Rev Lett 66:2689

Carraz O, Siemes C, Massotti L, Haagmans R, Silvestrin P (2014) A spaceborne gravity gradiometer concept based on cold atom interferometers for measuring Earth's gravity field. Microgravity Sci Technol 26(3):139–145

Carroll KA, Hatch D, Main B (2010) Performance of the Gedex high-definition airborne gravity gradiometer. Airborne Gravity 2010, Abstracts from the ASEG-PESA Airborne Gravity 2010 Workshop, Australia, 2010, pp 37–43

Chan HA, Paik HJ (1987) Superconducting gravity gradiometer for sensitive gravity measurements. I. Theory. Phys Rev D 35(12):3551–3571

Chiow S-W, Kovachy T, Chien H-C, Kasevich MA (2011) 102 ℏk large area atom interferometers. Phys Rev Lett 107(13):130403

Christensen AN, Dransfield MH, Van Galder C (2015) Noise and repeatability of airborne gravity gradiometry. First Break 33:55–63

Dai D, Wang X, Zhang D, Huang Z (2014) An improved method for dynamic measurement of deflections of the vertical based on the maintenance of attitude reference. Sensors 14(9):16322–16342

Dalibard J, Cohen-Tannoudji C (1989) Laser cooling below the Doppler limit by polarization gradients: Simple theoretical models. J Opt Soci America B 6(11):2023–2045

de Angelis M, Bertoldi A, Cacciapuoti L, Giorgini A, Lamporesi G, Prevedelli M, Saccorotti G, Sorrentino F, Tino G (2009) Precision gravimetry with atomic sensors. Meas Sci Technol 20:022001

DeGregoria, A (2010) Gravity gradiometry and map matching: and aid to aircraft inertial navigation systems. MS degree thesis, Air Force Institute of Technology

DiFrancesco D (2007) Advances and challenges in the development and deployment of gravity gradiometer systems. EGM 2007 international workshop innovation in EM, Grav and Mag methods: a new perspective for exploration, Capri, Italy, April 15–18

DiFrancesco D (2003) Gravity gradiometry developments at Lockheed Martin, EGS-AGU-EUG Joint Assembly, Nice, France, April 2003, abstract #1069

DiFrancesco D, Balmino G, Johannessen J, Visser P, Woodworth P (2009) Gravity gradiometry—today and tomorrow, 11th SAGA Biennial Technical Meeting and Exhibition, Swaziland, September 2009, pp 80–83

Dransfield M (2007) Airborne gravity gradiometry in the search for mineral deposits. In: Exploration 07: fifth decennial international conference on mineral exploration, 2007, pp 341–354

Dransfield M (2010) Advances in airborne gravity gradiometry at Fugro Airborne Surveys. EGM 2010 International Workshop. Adding new value to Electromagnetic, Gravity and Magnetic Methods for Exploration, Capri, Italy, April 11–14, 2010

Dransfield M, Christensen AN (2013) Performance of airborne gravity gradiometers. Lead Edge 32(8):908–922

Dransfield M, Le Roux T, Burrows D (2010) Airborne gravimetry and gravity gradiometry at Fugro Airborne Surveys. Airborne Gravity 2010, Abstracts from the ASEG-PESA Airborne Gravity 2010 Workshop, Australia, 2010, pp 49–57

Dzhandzhgava GI, Avgustov LI (2007) Map-aided navigation problems. Research results. In: Proceedings of the 6th Russian Scientific and Technical Conference "Sovremennoe sostoyanie i problemy navigatsii i okeanografii" (Current State and Problems in Navigation and Oceanography) NO-2007, St. Petersburg, 2007, pp 43–49

Elyashevich MA (2012) Atomnaya i molekulyarnaya spektroskopiya: Obshchie voprosy spektroskopii (Atomic and Molecular Spectroscopy: General Issues of Spectroscopy). URSS, Moscow

Emel'yantsev GI, Blazhnov BA, Stepanov AP (2015) Vertical deflection determination in high latitudes using precision IMU and two-antenna GNSS system. Gyroscopy Navig 6(4):305–309

Evstifeev MI (2017) The state of the art in the development of onboard gravity gradiometers. Gyroscopy Navig 8(1):68–79

Flokstra J, Cupurus R, Wiegerink RJ, van Essen MC (2009) A MEMS based gravity gradiometer for future planetary missions. Cryogenics 49:665–668

Freeden W, Michel V (2004) Multiscale potential theory (With Applications to Geoscience). Birkhäuser Verlag

Freeden W, Michel V, Nutz H (2002) Satellite-to-satellite tracking and satellite gravity gradiometry. J Eng Math 43:19–56

Gerber MA (1978) Gravity gradiometry: something new in inertial navigation. Astronaut Aeronaut 16:18–26

Gillot P, Francis O, Landragin A, Pereira Dos Santos F, Merlet S (2014) Stability comparison of two gravimeters: Optical versus atomic interferometers. Metrologia 51(5):L15–L17

Golden H, McRae W, Veryaskin A (2007) Description of and results from a novel borehole gravity gradiometer. ASEG Extended Abstracts, pp 1–3

Golovan AA, Parusnikov NA (2011) Matematicheskie osnovy navigatsionnykh sistem (Mathematical Foundations of Navigation Systems) Part 1, Matematicheskie modeli inertsial'noi navigatsii (Mathematical Models of Inertial Navigation). Maks Press, Moscow

Golovan AA, Vavilova NB (2003) Determining the vehicle acceleration by GNSS raw measurements. Vestnik Moskovskogo Unversiteta. Seriya 1: Matematika. Mekhanika 5:5–13

Golovan AA, Vavilova NB (2007) Satellite navigation. Raw data processing for geophysical applications. J Math Sci 146(3):5920–5930

Griggs CE, Paik HJ, Moody MV, Han S-C, Rowlands DD, Lemoine FG, Shirron PJ, Gustavson T (2013) Cold atom gyros. IEEE Sensors 2013 Tutorial, AOSense, Inc., 11.3.2013

Hänsch TW, Schawlow AL (1975) Cooling of gases by laser radiation. Opt Commun 13(1):68–69

Hu Z-K, Sun B-L, Duan X-C, Zhou M-K, Chen L-L, Zhan S, Zhang Q-Z, Luo J (2013) Demonstration of an ultrahigh-sensitivity atom-interferometry absolute gravimeter. Phys Rev A 88:043610

Iafolla V, Nozzoli S, Fiorenza E (2003) One axis gravity gradiometer for the measurement of Newton's gravitational constant G. Phys Lett A 318(3):223–233

Jekeli C (2006) Airborne gradiometry error analysis. Surv Geophys 27(2):257–275

Jekeli C (2007) 100 years of gravity gradiometry, Lecture presented in Geological Science 781, Gravimetry, 27 November 2007

Jekeli C (2009) Potential theory and static gravity field of the earth. Treatise Geophys 3:11–42

Jekeli C (2011) Accuracy requirements in position and attitude for airborne vector gravimetry and gradiometry. Gyroscopy Navig 2(3):164–169

Jekeli C, Kwon J (1999) Results of airborne vector (3D) gravimetry. Geophys Res Lett 26(23):3533–3536

Kailath T, Sayed AH, Hassibi B (2000) Linear estimation. Prentice-Hall

Kalinnikov II, Matyunin VP, Nyunina NA, Getmanskaya VV (1992) Real-time earthquake prediction in teleseismic zone—a reality. Dokl Akad Nauk SSSR 232(6):1068–1071

Kasevich M, Chu S (1991) Atomic interferometry using stimulated Raman transitions. Phys Rev Lett 67(2):181–184

Kasevich M, Donnelly C, Overstreet C (2014) Prospects for improved accuracy in the determination of G using atom interferometry. Depts. of Physics, Applied Physics and EE Stanford University

Keith DW, Ekstrom CR, Turchette QA, Pritchard D (1991) An interferometer for atoms. Phys Rev Lett 66:2693–2696

Kirkendall B, Li Y, Oldenburg D (2007) Imaging cargo containers using gravity gradiometry. IEEE Trans Geosci Remote Sens 45(6):1786–1797

Kohel JM, Yu N, Kellogg JR, Thompson RJ, Aveline DC, Maleki L (2006) Quantum gravity gradiometer development for space, Jet Propulsion Laboratory, California Institute of Technology. https://trs.jpl.nasa.gov/handle/2014/39706

Koneshov VN, Evstifeev MI, Chelpanov IB, Yashnikova OM (2016) Methods for determining deflections of the vertical on a moving base. Gyroscopy Navig 7(4):326–336

Korchak V, Tuzhikov E, Bocharov L (2013) American program on militarily critical technologies. Characteristics and content analysis, Elektronika. Nauka. Tekhnologiya. Biznes 5:134–148

Krasovsky AA (1983) Methods of creating onboard rotating gravity gradiometers. Oboronnaya Tekhnika 6:52–57

Kwon JH, Jekeli C (2001) A new approach for airborne vector gravimetry using GPS/INS. J Geodesy 74:690–700

Lee J, Kwon JH, Yu M (2015) Performance evaluation and requirements assessment for gravity gradient referenced navigation. Sensors 15:16833–16847

Lenef A, Hammond T, Smith E, Chapman M, Rubenstein R, Pritchard D (1997) Rotation sensing with an atom interferometer. Phys Rev Lett 78:760

Lenoir B, Levy A, Foulon B, Christophe B, Lamine B, Reynaud S (2011) Electrostatic accelerometer with bias rejection for gravitation and Solar System physics. Adv Space Res 48(7):1248–1257

Letokhov VS, Minogin VG (1981) Laser radiation pressure on free atoms. Phys Rep 73(1):1–65

Liu H, Pike WT, Dou G (2014) Design, fabrication and characterization of a micro-machined gravity gradiometer suspension. In: Proceedings of IEEE SENSORS 2014, Valencia, 2–5 Nov. 2014, pp 1611–1614

Lockheed Using Gravity to Spot 'Subterranean Threats'. https://www.wired.com/2010/07/lockheed-using-gravity-to-spot-subterranean-threats/

Lumley JM, White JP, Barnes G, Huang D, Paik HJ (2001) A superconducting gravity gradiometer tool for exploration. In: Proceedings of the society of exploration geophysics meeting, San Antonio, September 2001

Mahadeswaraswamy C (2009) Atom interferometric gravity gradiometer: disturbance compensation and mobile gradiometry. PhD dissertation, Stanford University

Maleev PI, Kapustin IV (2007) Navigation aids of international strategic submarines. In: Proceedings of the 6th Russian scientific and technical conference "Sovremennoe sostoyanie i problemy navigatsii i okeanografii" (Current State and Problems in Navigation and Oceanography) NO-2007, St. Petersburg, pp 132–139

Matthews R (2002) Mobile gravity gradiometry. PhD dissertation, University of Western Australia

McBarnet A (2013) Gravity gradiometry has graduated! OE Digital Edition. http://www.oedigital.com/geoscience/item/3201-gravity-gradiometry-has-graduated

McGuirk JM (2001) High precision absolute gravity gradiometry with atom interferometry. PhD dissertation, Stanford University

Mims J, Selman D, Dickinson J, Murphy C, Mataragio J, Jorgensen G (2009) Comparison study between airborne and ship-borne full tensor gravity gradiometry (FTG) data. SEG Houston 2009 international exposition and annual meeting, pp 942–946

Minogin VG (2010) Fizika lazerov (Laser Physics). MIPT, Moscow

Moody M, Paik H, Canavan E (2002) Three-axis superconducting gravity gradiometer for sensitive gravity experiments. Rev Sci Instrum 73(11):3957. https://doi.org/10.1063/1.1511798

Mumaw G (2004) Marine 3D full tensor gravity gradiometry. The first five years, Hydro International, September 2004, pp 38–41

Murphy C (2004) The Air-FTG™ airborne gravity gradiometer system. ASEG-PESA Airborne Gravity 2004 Workshop, pp 7–14

Nabighian MN, Ander ME, Grauch VJS, Hansen RO, LaFehr TR, Li Y, Pearson WC, Peirce JW, Phillips JD, Ruder ME (2005) 75th Anniversary. Historical development of the gravity method in exploration. Geophysics 70(6):63ND–89ND

Neill F (2010) Potential of downhole gravity gradiometry for reservoir management. World Oil

Nerem R, Jekeli C, Kaula W (1995) Gravity field determination and characteristics: retrospective and prospective. Geophys Res 100(B8):15053–15074

Nesenyuk LP, Starosel'tsev LP, Brovko LN (1980) Determination of deflections of the vertical using inertial navigation systems. Voprosy Korablestroeniya. Series Navigatsiya i Giroskopiya 46:16–22

Oblak D, Petrov PG, Garrido Alzar CL, Tittel W, Vershovski AK, Mikkelsen JK, Sorensen JL, Polzik ES (2005) Quantum-noise-limited interferometric measurement of atomic noise: Towards spin squeezing on the Cs clock transition. Phys Rev A 71:043807

Ogorodova LV (2006) Vysshaya geodeziya (Higher Geodesy), Part III, Teoreticheskaya geodeziya (Theoretical Geodesy). Geodezkartizdat, Moscow

Paik H (1989) Tests of general relativity in Earth orbit using a superconducting gravity gradiometer. Adv Space Res 9:41–50

Peshekhonov VG (2020) Problem of the vertical deflection in high-precision inertial navigation. Gyroscopy and Navigation 11(1):255–262

Peshekhonov VG, Volfson GB (1996) Development of an onboard gravity variometer. Dokl Akad Nauk SSSR 351(6):766–768

Peshekhonov VG, Nesenyuk LP, Starosel'tsev LP, Elinson LS (1989) Sudovye sredstva izmereniya parametrov gravitatsionnogo polya Zemli (Shipborne Aids Measuring the Parameters of the Earth's Gravity Field). Rumb, Leningrad

Phillips WD (1998) Laser cooling and trapping of neutral atoms. Rev Mod Phys 70(3):721

Poli N, Wang F-Y, Tarallo MG, Alberti A, Prevedelli M, Tinox GM (2011) Precision measurement of gravity with cold atoms in an optical lattice and comparison with a classical gravimeter. Phys Rev Lett 107:038501

Richeson JA (2008) Gravity gradiometer aided inertial navigation within non-GNSS environments. PhD thesis, University of Maryland, Washington, USA

Riehle F, Kisters T, Witte A, Helmcke J, Borde CJ (1991) Optical Ramsey spectroscopy in a rotating frame—Sagnac effect in a matter-wave interferometer. Phys Rev Lett 67(2):177–180

Rummel R, Balmino G, Johannessen J, Visser P, Woodworth P (2002) Dedicated gravity field missions—principles and aims. J Geodyn 33(1):3–20

Rummel R, Yi W, Stummer C (2011) GOCE gravitational gradiometry. J Geodesy 85(11):777–790

Schuldt T et al (2015) Design of a dual species atom interferometer for space. Exp Astron 39(2):167–206

Schwarz KP, Colombo O, Hein G, Knickmeyer ET (1992) Requirements for airborne vector gravimetry. Proc IAG Symp 110:273–283

Schwarz KP, Sideris MG, Forsberg R (1990) The use of FFT techniques in physical geodesy. Geophys J Int 100(3):485–514

Smoller YL, Yurist SS, Bolotin YV, Golovan AA, Kozlov AV, Bogdanov ON (2012) Results of tests of the strapdown gravimeter GT-X on the yacht. In: 19th St. Petersburg international conference on integrated navigation systems, Elektropribor, St. Petersburg, pp 185–187

Sokolov YuL (1972) Interference of 2P1/2 state of hydrogen atoms. Zh Eksp Teor Fiz 63:461

Soroka AI (2010) Development of onboard meters of the geopotential second derivatives. Gravimetriya i geodeziya (Gravimetry and Geodesy), Brovar, B.V., Ed., Moscow: Nauchnyi mir, pp 300–310

Staroseltsev LP (1995) Analysis of requirements for the gyroscopic stabilization system of a gravity gradiometer. Giroskopiya i Navigatsiya 3:30–33

Touboul P, Foulon B, Christophe B, Marque JP (2012) CHAMP, GRACE, GOCE instruments and beyond, geodesy for planet earth. Int Assoc Geodesy Symp 136:215–221

Trageser M (1984) Floated gravity gradiometer. In: Proc IEEE Trans Aerosp Electron Syst 20(4)

Tryggvason B, Main B, French B (2004) A high resolution airborne gravimeter and airborne gravity gradiometer. In: Proceedings of airborne gravity 2004 Workshop, pp 41–47

Van Leeuwen E (2003) Three years of practical use of airborne gravity gradiometer. Geophys Res Abstr 5:22

Vasin MG, Popkov DI (2010) Modern problems in onboard gravity gradiometry. Gravimetriya i geodeziya (Gravimetry and Geodesy), Brovar, B.V., Ed., Moscow: Nauchnyi mir, pp 570–584

Veryaskin A (2003) String gravity gradiometer: noise, error analysis and applications. Geophys Res Abstr 5:01650

Volfson GB (1997) Methods to solve the problem of creating an onboard gravity variometer. D.Sci. (Engineering) dissertation, St. Petersburg

Volfson GB (2002) Development state and potential of gravity gradiometry. In: Primenenie graviinertsial'nykh tekhnologii v geofizike (Application of Graviinertial Technologies in Geophysics). CSRI Elektropribor, St. Petersburg, pp 90–105

Volfson GB, Evstifeev MI, Kazantseva OS, Kalinnikov II, Manukin AB, Matyunin VP, Shcherbak AG (2010) Gradiometric seismoreceiver with a magnetic suspension in the problems of operative earthquake forecasting. Seismic Instrum 46(3):265–274

Volfson GB, Evstifeev MI, Rozentsvein VG, Semenova MP, Nikolskii YuI, Rokotyan EV, Bezrukov SF (1999) New-generation gravity variometers for geophysical studies. Geofizicheskaya Apparatura 102:90–105

Wei M, Ferguson S, Schwarz KP (1991) Accuracy of GPS-derived acceleration from moving platform tests. In: Proceedings of IAG symposium, vol 110, pp 235–249

Welker TC, Pachter M, Huffman RE (2013) Gravity gradiometer integrated inertial navigation. In: Proceedings of 2013 European control conference (ECC), July 17–19, 2013, Zürich, Switzerland, pp 846–851

Wu X (2009) Gravity gradient survey with a mobile atom interferometer. PhD dissertation, Stanford University

Yelagin AV (2012) Teoriya figury Zemli (Theory of the Earth's Figure). Siberian State University of Geosystems and Technologies, Novosibirsk

Yu N, Kohel JM, Ramerez-Serrano J, Kellogg JR, Lim L, Maleki L (2005) Progress towards a space-borne quantum gravity gradiometer. Jet Propulsion Laboratory, California Institute of Technology

Yu N, Thompson RJ, Kellogg JR, Aveline DC, Maleki L, Kohel JM (2010) A transportable gravity gradiometer based on atom interferometry. NASA Tech Briefs, NASA's Jet Propulsion Laboratory, Pasadena, California, May 2010, pp 6–7

Zhou M-K, Duan X-C, Chen L-L, Luo Q, Xu Y-Y, Hu Z-K (2015) Micro-Gal level gravity measurements with cold atom interferometry. Chin Phys B 24(5):050401

Zhou M-K, Pelle B, Hilico A, Pereira Dos Santos F (2013) Atomic multiwave interferometer in an optical lattice. Phys Rev A 88:013604

Zlotnikov D (2011) Superior detective work: the promise of airborne gravity gradiometry. Earth Explorer, Energy Report, June 2011, pp 5–7

Chapter 6
Earth's Gravity Field Models and Their Application

V. Koneshov, V. Nepoklonov, V. Solov'ev, P. Mikhailov, L. Zheleznyak, A. Nosov, O. A. Stepanov, A. Toropov, and L. Avgustov

Abstract This chapter focuses on models of the Earth's gravity field, estimation of their accuracy, and use in applied problems. Various accuracy estimation approaches, including those based on the use of a priori and a posteriori estimates are presented. Gravimetric coverage of the Earth areas is considered. Quality monitoring of relative gravity measurements at sea with account for the global models is discussed. Using a large amount of survey data, EGM2008 is compared with marine gravity measurements by calculating the residuals. The widespread map-aided navigation method is addressed. The stochastic filtering algorithms for map-aided navigation within the Bayesian approach are reviewed and compared. Efficiency of the Earth's gravity field data use for navigation purposes is discussed.

Keywords Earth's gravity field models · Stochastic filtering algorithms for map-aided navigation

V. Koneshov · V. Solov'ev · P. Mikhailov · L. Zheleznyak
Schmidt Institute of Physics of the Earth under the Russian Academy of Sciences, Moscow, Russia

V. Nepoklonov
State University of Geodesy and Cartography and Schmidt Institute of Physics of the Earth of the Russian Academy of Sciences, Moscow, Russia

A. Nosov
Luxoft Professional LLC, St.Petersburg, Russia

A. Nosov · O. A. Stepanov (✉)
ITMO University, St.Petersburg, Russia
e-mail: soalax@mail.ru

O. A. Stepanov · A. Toropov
Concern CSRI Elektropribor, St.Petersburg, Russia

L. Avgustov
Ramenskoye Instrument Engineering Design Bureau, the Bauman Moscow State Technical University, Moscow, Russia

V. G. Peshekhonov and O. A. Stepanov (eds.), *Methods and Technologies for Measuring the Earth's Gravity Field Parameters*, Earth Systems Data and Models 5,
https://doi.org/10.1007/978-3-031-11158-7_6

Introduction

This chapter focuses on modern models of the Earth's gravity field (EGF), estimation of their accuracy, and use in applied problems. The Chapter contains four sections.

Section 6.1 discusses the estimation of accuracy of the EGF models. It describes the main approaches, including those based on the use of a priori and a posteriori accuracy estimates. The role of airborne EGF data is emphasized, which are especially useful in independent validation of the EGF models in the areas where other methods are barely applicable, such as the Arctic and Antarctic. Gravimetric coverage of the Earth areas is considered. The new results of experimental comparison of airborne gravimetric survey data and the modern global EGF models for the Russian Federation and the surrounding seas are analyzed.

Section 6.2 covers the monitoring of the quality of relative gravity measurements at sea with account for the global models. Using a large amount of survey data, EGM2008 is compared with marine gravity measurements by calculating the residuals. It is shown that the field harmonics with a wavelength over 50–100 km are reproduced by the model without distortions. The shorter the wavelength of the harmonics is, the more distorted they are; and the harmonics with a wavelength below 20 km are indistinguishable from noise. The obtained results enable the gravity model to be used to suppress the outliers in sensor output, refine the gravimeter zero-point drift and tie the measurements to the absolute gravity value without explicit reference measurements. These ideas have been validated in the field surveys in the Indian Ocean, and some examples are presented in this section.

Section 6.3 is devoted to the widespread map-aided navigation method using geophysical fields, a typical representative of which is the gravity field. The section discusses the current development of map-aided navigation algorithms, reviews and compares the filtering algorithms used for solving the navigation problem within the Bayesian framework. It is noted that with this framework, stochastic filtering methods traditionally used in navigation data processing can be applied, which help not only to design the algorithms, but also to correctly analyze their accuracy.

Section 6.4 focuses on the efficiency of EGF data use for navigation purposes. The field of deflections of the vertical (DOV) and the second derivatives of the perturbing potential are taken as examples to analyze the navigation informativity of the Earth's gravity field in the Sea of Okhotsk, using the EGM2008 global geopotential model to degree 2190.

6.1 Estimation of Accuracy of Modern Earth's Gravity Field Models

In a wide range of EGF-related problems in navigation, geodesy, and geophysics, the field data are specified using mathematical models (Avsyuk et al. 2010). The requirements for the model accuracy grow with the requirements for the accuracy of solutions to these problems. One of the widely used methods to estimate EGF

model accuracy is based on comparison with the reference data not used in the model development [GOST 18.101–76]. Over the past 20 years, the geoid heights obtained by satellite leveling have traditionally been used as the reference data. However, the effective use of this approach requires a sufficiently dense grid of leveling stations, which is not always available because, among other things, this estimation method can be only applied on land. For this reason, in recent years, as the airborne gravity surveys are becoming more widespread and accurate, the feasibility of EGF model accuracy estimation based on airborne gravity has been studied thoroughly (Nepoklonov 1998). This primarily refers to the areas where other methods for independent validation of EGF models are barely applicable, such as the Arctic and Antarctic. This section analyzes the modern approaches to estimating the accuracy of EGF models. The major a priori and a posteriori estimation methods are considered. The contribution of new space geodesy methods to improving the accuracy characteristics of global EGF models is noted. New estimates of the EGF models' accuracy are presented, based on the comparison of model gravity anomalies (GA) with airborne gravity survey data in the Arctic. Due to the need to shift to satellite leveling technology, special consideration is given to a posteriori estimation of the accuracy of global and regional EGF models based on geoid heights. Actual data are provided, which characterize the accuracy of modern regional and national digital models of geoid height, including the geoid models for the territory of Russia.

Considering the strategic importance of the Arctic regions, a special focus is made on a comparative study of modern global EGF models for high-latitude areas, including several Russian models.

Global models based on the expansion of geopotential in spherical harmonics (hereinafter referred to as global EGF models) are widely used for EGF description. Another widespread class of EGF models includes digital (grid) models in the form of an ordered set of discrete field values at the nodes of a uniform grid of meridians and parallels. Such models are used for describing the EGF on both global and regional (national) scales. Digital EGF models are widely applied because the method of spherical harmonics does not always meet the modern requirements for accuracy and detail in determining the EGF parameters. They are also computationally efficient and easy to implement. Detailed digital geoid height models (DGHM) in continental areas, based on gravimetric data are given priority in the class of digital EGF models. Such models are extensively applied in the development of elevation datums using satellite (GLONASS/GPS) leveling (Avsyuk et al. 2010).

In most cases, the construction of EGF models is reduced to linear approximation of geopotential and/or its linear functionals in a given system of basis functions. In practice, the following finite-dimensional approximations are used (Moritz 1976):

$$T(P) = \sum_{i=1}^{n} a_i f_i(P), \tag{6.1.1}$$

where P is the point to be determined; T is the quantity to be modeled (for definiteness, a disturbing potential); f_i are the basis functions; a_i are the coefficients (model parameters); n is the dimension of the model.

For global EGF models in the form of spherical harmonics of the geopotential, formula (6.1.1) is given as follows (Avsyuk et al. 2010):

$$T(\varphi, \lambda, r) = \frac{fM_\oplus}{a} \sum_{n=2}^{n_{\max}} \left(\frac{a}{r}\right)^{n+1} \sum_{m=0}^{n} (\overline{C}_{nm} \cos m\lambda + \overline{S}_{nm} \sin m\lambda) \overline{P}_{nm}(\sin \varphi), \tag{6.1.2}$$

where a is the semi-major axis of the reference ellipsoid; φ, λ, r are the spherical geocentric coordinates (latitude, longitude, radius vector) of a point; $fM_\oplus$ is the product of the gravitational constant by the Earth's mass; $\overline{P}_{nm}$ are the fully normalized Legendre functions; $\overline{C}_{nm}$, $\overline{S}_{nm}$ are the fully normalized coefficients of expansion of the disturbing potential in spherical harmonics that are the parameters of the model of the form (6.1.2).

Two main sources of model errors are known: the errors in determining the model parameters conditioned by the raw data and processing errors, and methodological approximation errors.

The accuracy characteristics of the EGF models can be estimated using various methods, including a priori and a posteriori estimation techniques.

6.1.1 A Priori Accuracy Estimates

A priori estimates are obtained analytically using real and/or hypothetical information on the statistical properties of the factors affecting the accuracy of the model to be created. As a rule, the results of a priori accuracy estimation are not associated with the actual values of the model parameters.

Assume D_M is the variance of the methodological error, D_P is the variance of the error in determining the model parameters. Taking these errors to be stationary, random, and statistically independent quantities, the total model error can be characterized by the variance

$$D = D_M + D_P. \tag{6.1.3}$$

A priori estimate of D_M can be obtained from the deviations of the model M under study in (6.1.1) from some reference model [GOST 18.101–76]:

$$M^* : T^*(P) = \sum_{i=1}^{m} a_j^* f_j^*(P), \tag{6.1.4}$$

where $\left\{f_j^*\right\}$ and $\left\{a_j^*\right\}$ are the basis functions and parameters of the model M^*, respectively; $j = 1, \ldots, m$. Often, a model of the same class as M but of higher resolution is used as M^*. For example, to estimate a model in the form of spherical harmonics of the geopotential to some degree N, the same model to degree $N^* \gg N$ is considered.

Assuming that the output values of the models M and M^* are random zero-mean values, the following formula can be used for the point estimation of D_M:

$$D_M(P) = \sum_{i=1}^{n}\sum_{k=1}^{n} \mathrm{E}(a_i a_k) f_i(P) f_k(P) + \sum_{j=1}^{m}\sum_{l=1}^{m} \mathrm{E}\left(a_j^* a_l^*\right) f_j^*(P) f_l^*(P)$$
$$- 2\sum_{i=1}^{n}\sum_{j=1}^{m} \mathbf{E}\left(a_i a_j^*\right) f_i(P) f_j^*(P), \tag{6.1.5}$$

where E is the expectation operator.

Obviously, to use formula (6.1.5), it is commonly needed to use the covariance matrices of M and M^* parameters, and the matrix of their mutual covariances as the source data.

A priori estimate of D_P can be obtained in two ways: by analyzing the model sensitivity to variations in its parameters [GOST 18.101–76] and by using the error variance equation of the linear function. In the latter case,

$$D_P(P) = \sum_{i=1}^{n}\sum_{j=1}^{n} \mathrm{E}\left(\delta a_i \delta a_j\right) f_i(P) f_j(P), \tag{6.1.6}$$

where δa_i is the error in the i-th parameter of the estimated model. To estimate D_P by (6.1.6), the error covariance matrix of M parameters is needed.

As the dimension of the studied model changes (i.e., the number n of its parameters increases or decreases), D_M and D_P vary in different ways. An increase in n commonly leads to decreasing D_M and increasing D_P, and vice versa. As a result, it becomes necessary to find n which minimizes the total variance D, or to select the minimum possible n with which D does not exceed the given tolerance D_0.

A priori estimates of the accuracy of EGF models in the form of spherical harmonics of the geopotential can be obtained using the formula (Nepoklonov 1998) which can be rewritten as

$$\sigma(N) = \sqrt{\delta(N)^2 + \varepsilon(N)^2}, \tag{6.1.7}$$

where σ is the root-mean-square (RMS) error of the model; δ and ε are the RMS values of the total contribution of errors in geopotential harmonic coefficients $\overline{C}_{nm}$, $\overline{S}_{nm}$ and methodological error due to truncation of geopotential expansion in spherical harmonics, respectively.

The values of δ and ε are estimated by the formulas in Table 6.1, where ζ is the geoid height; Δg is the gravity anomaly in free air; ξ, η are DOV components in the meridian and prime vertical planes; R is the average radius of the Earth, γ_0 is the average normal gravity on the reference ellipsoid; c_n^2 and δ_n^2 are the so-called degree variances of coefficients $\overline{C}_{nm}$, $\overline{S}_{nm}$ and their RMS errors $\delta\overline{C}_{nm}$, $\delta\overline{S}_{nm}$, respectively, determined by the following formulas (Moritz 1980; Nepoklonov 1998):

$$c_n^2 = \sum_{m=0}^{n} \left(\overline{C}_{nm}^2 + \overline{S}_{nm}^2\right), \tag{6.1.8}$$

$$\delta_n^2 = \sum_{m=0}^{n} \left(\delta\overline{C}_{nm}^2 + \delta\overline{S}_{nm}^2\right). \tag{6.1.9}$$

The truncation error is estimated using a suitable analytical model of degree variances. The GA degree variances Δg_n^2 are usually defined and the following ratio is used:

$$c_n^2 = \Delta g_n^2 / \gamma_0^2 (n-1)^2. \tag{6.1.10}$$

The applied models of GA degree variances (Pellinen 1970, 1992; Kaula 1966; Moritz 1976, 1980; Jekeli et al. 2009) and the corresponding a priori estimates of truncation errors are given in Tables 6.2 and 6.3. It is proposed to use the average value for several models (the bottom line in Table 6.3) as a final estimate of the truncation error.

Table 6.1 Analytical estimates of errors in global EGF models

Error	Parameter		
	ζ	Δg	$\vartheta = \sqrt{\xi^2 + \eta^2}$
δ^2	$R^2 \sum_{n=2}^{N} \delta_n^2$	$\gamma_0^2 \sum_{n=2}^{N} (n-1)^2 \delta_n^2$	$\sum_{n=2}^{N} n(n+1)\delta_n^2$
ε^2	$R^2 \sum_{n=N+1}^{\infty} c_n^2$	$\gamma_0^2 \sum_{n=N+1}^{\infty} (n-1)^2 c_n^2$	$\sum_{n=N+1}^{\infty} n(n+1) c_n^2$

Table 6.2 GA degree variance models

Item No	Model authors	Designation	Δg_n^2
1	Kaula (1966)	K	$\frac{96(n-1)^2(2n+1)}{n^4}$
2	Pellinen (1970)	P1	$166n^{-1.12}$
3	Pellinen (1992)	P2	$\begin{cases} 34(n-1)^2 n^{-2.68} & n \le 180 \\ 1559(n-1)^2 n^{-3.409} & n > 180 \end{cases}$
4	Tscherning, Rapp (1974)	TR	$\frac{425.28 s^{n+2}(n-1)}{(n-2)(n+24)}$, $s = 0.999617$, $n > 2$
5	Moritz (1976)	M	$(n-1)\left(\frac{3.405 s_1^{n+2}}{n+1} + \frac{140.03 s_2^{n+2}}{n^2-4}\right)$, $s_1 = 0.998006$, $s_2 = 0.914232$, $n > 2$
6	Jekeli (2009)	J	$161(n-1)^2 n^{-2.898}$

Table 6.3 Geoid height and gravity anomaly truncation errors versus the highest degree of spherical harmonics

Model Δg_n^2	$\varepsilon\zeta$, m					$\varepsilon\Delta g$, mGal				
	360	720	1440	1800	2160	360	720	1440	1800	2160
K	0.18	0.09	0.04	0.04	0.03	25.2	22.5	19.3	18.1	17.1
P1	0.11	0.05	0.03	0.02	0.02	26.1	25.1	24.0	23.7	23.5
P2	0.14	0.06	0.03	0.02	0.02	18.5	16.1	13.9	13.3	12.8
TR	0.22	0.10	0.04	0.03	0.02	25.2	20.1	14.5	12.7	11.2
M	0.30	0.12	0.04	0.02	0.01	28.7	20.1	9.8	6.8	4.8
J	0.22	0.11	0.06	0.05	0.04	34.0	30.8	26.9	25.4	24.2
Average	0.20	0.09	0.04	0.03	0.02	26.3	22.4	18.1	16.7	15.6

The contribution of errors in determining the coefficients $\overline{C}_{nm}$, $\overline{S}_{nm}$ is illustrated by the estimates obtained for several modern combined global EGF models, including ultrahigh-degree ones (Table 6.4). Judging by these estimates, the accuracy of determining the coefficients of spherical harmonics of the geopotential has been significantly increased since the mid-2000s. The accuracy of geoid height models has been increased 4–5 times, and that of gravity anomaly models, 2–3 times compared with the models of the mid-1990s and early 2000s. These improvements were achieved mainly due to the application of new space geodesy methods in the international projects, including satellite-to-satellite tracking (CHAMP and GRACE) and low-orbit satellite gravity gradiometry (GOCE) (Koneshov et al. 2013, 2014a).

The main advantage of a priori estimates is that they are relatively easy to obtain. However, this may be due to various simplifying assumptions. Therefore, the accuracy characteristics of global EGF models should be finally determined using a posteriori estimates.

Table 6.4 Influence of the errors in the geopotential spherical harmonics coefficients on the accuracy of geoid height and gravity anomaly models

EGF model	Country	Year	N	δ	
				Geoid height, m	GA, mGal
EGM96	USA	1996	360	0.36	8.5
PZ-2002	Russia	2002	360	0.45	10.8
EIGEN-GLO4C	Germany, France	2006	360	0.15	4.4
GAO-2008	Russia	2008	360	1.11	1.9
EIGEN-5C	Germany, France	2008	360	0.13	3.8
EGM2008	USA	2008	2190	0.08	4.2
GIF48	USA	2011	360	0.08	2.4
EIGEN-6C	Germany, France	2011	1420	0.10	3.6
EIGEN-6C2	Germany, France	2012	1949	0.08	3.3

6.1.2 A Posteriori Accuracy Estimates

A posteriori accuracy estimates are normally obtained for specific values of model parameters. Traditionally, the so-called internal and external estimates are distinguished in a posteriori estimates.

Internal accuracy estimates are based on internal convergence. They characterize the errors in the model parameters depending on the contents, accuracy, amount, and distribution of the source data based on the explicit functional relationships between these source data and the determined values, e.g., using the least squares method (Bol'shakov and Gaidaev 1977). This approach, however, fails to completely account for the methodological errors in the EGF modeling.

External accuracy estimates characterize the proximity of the tested model to independent (conditionally independent) reference data. Statistical characteristics of deviations are normally used as the measures of proximity: boundary values (min., max.), mean value μ, standard deviation σ. The proximity can also be analyzed using histograms of deviations between the model and reference values of EGF parameters. Depending on the type of reference data, a posteriori estimates can methodically be divided into three groups.

The first group includes the estimates, the reference data for which are the EGF characteristics (geoid height, GA, DOV, etc.) calculated using a model of higher accuracy, conditionally accepted as a reference. EGM2008 global EGF model to degree 2190 is commonly used as a reference (Pavlis et al. 2008). The estimates, i.e., the comparison of EGM2008 with other models, are listed in Table 6.4. The resulting deviations (Table 6.5) can be considered to be the errors of the model geoid height and GA with respect to EGM2008 reference model to degree 2190.

Comparison of EGF models in the form of spherical harmonics of geopotential in space domain can be complemented by analyzing the model differences in frequency domain. Here, the proximity of models at different frequencies can be estimated, for

Table 6.5 Statistical characteristics of deviations of EGF global models from EGM2008 reference model to degree 2190: geoid height and gravity anomaly

Model	n_{max}	Geoid height, m				Gravity anomaly, mGal			
		min.	max.	μ	σ	min.	max.	μ	σ
EGM96	360	–10.43	11.98	0.00	0.72	–478.8	461.1	0.2	29.9
PZ-2002	360	–10.66	10.60	0.01	0.74	–480.0	437.8	0.2	29.7
EIGEN-GLO4C	360	–6.01	7.22	0.01	0.36	–492.1	430.1	0.3	28.9
GAO-2008	360	–8.56	8.45	0.01	0.58	–491.3	400.8	0.3	32.8
EIGEN-5C	360	–6.31	7.04	0.00	0.33	–521.8	415.9	0.3	28.7
GIF48	360	–3.91	4.13	–0.01	0.19	–465.9	388.1	0.2	27.4
EIGEN-6C	1420	–2.51	3.49	0.00	0.14	–334.1	315.0	0.2	24.0
EIGEN-6C2	1949	–2.45	3.64	0.00	0.13	–220.5	231.4	0.2	23.0

example, by degree variances $\delta\zeta_n^2$ and δg_n^2 of the differences of model geoid heights ($\delta\zeta$) and gravity anomalies (δg), expressed as the differences between the coefficients $\overline{C}_{nm}$, $\overline{S}_{nm}$ of the first and second models. The examples for EGM96, GAO-2008 and GIF48 are presented in Fig. 6.1.

The comparison helps to detect the frequency range (values n), where $\delta\zeta_n(\delta g_n)$ characterizing the error spectrum of the studied model relative to the reference model do not exceed some significant limit.

The second group includes the estimates obtained by the orbital method using the ephemeris of artificial Earth satellites, calculated using the studied global model. The model accuracy is estimated by the residuals of trajectory measurements, and by the residuals of the measured sea levels at the crossover points of altimetry routes for satellites equipped with altimeters. High-precision laser and radio observation data

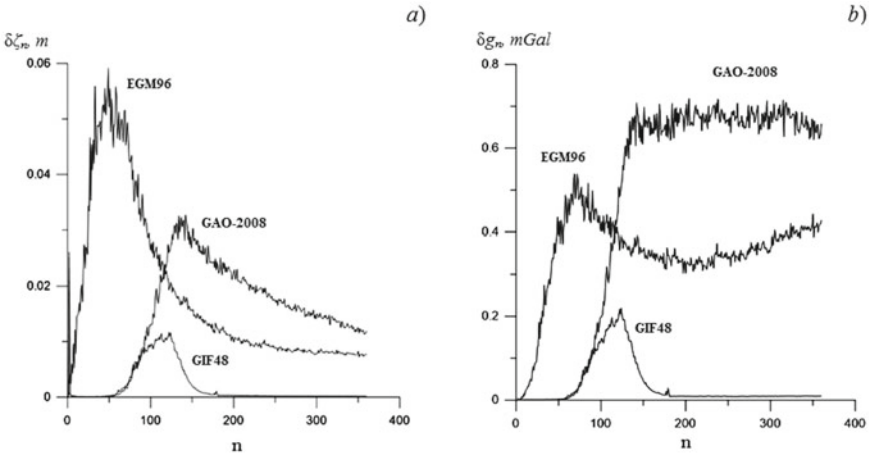

Fig. 6.1 Errors in model geoid height (**a**) and gravity anomaly (**b**) for different EGF models

Table 6.6 Standard deviations of satellite calculated ranges from the measured values averaged by orbital arcs, m

Satellite	Orbit altitude, km	EGM96	EIGEN-GLO4	EGM2008	EIGEN-5
Envisat	800	0.087	0.058	No data	No data
Jason-1	1340	0.042	0.041	No data	No data
Lageos-1	5900	0.015	0.046	0.015	0.014
Ajisai	1480	0.056	0.014	0.053	0.047
Starlette	810	0.050	0.031	0.046	0.031
Stella	810	0.091	0.026	0.029	0.026
ERS-2	800	No data	No data	No data	0.043

(DORIS, PRARE) obtained at terrestrial stations, and satellite orbit determination data obtained by space navigation systems can be used as the trajectory measurements. The orbital method application is illustrated in Table 6.6 with the accuracy estimates of global EGF models based on laser observations from artificial Earth satellites Envisat, ERS-2, Jason-1, Lageos-1, Ajisai, Starlette, and Stella (Foerste et al. 2008; Cheng et al. 2009; Gruber et al. 2011). These estimates characterize the model accuracy as the deviations of the calculated satellite orbit parameters from the measured ones, obtained using high-precision laser observations. The orbital method provides global information, however, it features relatively low sensitivity of satellite orbits to local gravity anomalies, and the need to exclude non-gravitational perturbations of the orbital motion (Gruber 2004).

The third group includes a posteriori estimates obtained by comparing the studied model with the reference values of the geoid height, GA, DOV components, and other functionals of the perturbing potential, obtained using various instrumental EGF survey methods such as the gravimetric and astrogeodetic methods, satellite altimetry, satellite gradiometry, and satellite leveling.

Such estimates are widely used for various global EGF models in modern publications. The differences between the model GAs and terrestrial gravimetric survey data in various parts of the Earth are listed in Table 6.7 compiled using the data of (Arabelos and Tscherning 2010). Over the past 20 years, geoid heights from satellite leveling have been extensively used for accuracy estimation and verification of EGF models. However, the effective use of this approach requires a sufficiently dense grid of leveling stations, which is not always available, among other things because this estimation method can be only applied on land. For this reason, in recent years, as the airborne gravity surveys become more widespread and accurate, the feasibility of EGF model accuracy estimation based on airborne gravity has been studied thoroughly. This primarily refers to the areas, where other methods for independent validation of EGF models are barely applicable, such as the Arctic region.

This section presents the new accuracy estimates for the global EGF models. They are based on comparing the model GAs with the data obtained in airborne gravimetric surveys in the Arctic in 2011 by the RAS Institute of Physics of the Earth (Russia), using Russian airborne gravimetric systems. Fourteen survey lines

Table 6.7 Statistical characteristics of differences between the model and gravimetric GA for various regions of the Earth

Model	n_{max}	Region	Number of stations	Differences, mGal			
				min	max	μ	σ
EGM96	360	Australia	1,117,054	–194.7	219.9	–0.3	12.1
		Arctic	56,878	–193.3	195.9	–1.0	18.0
		Antarctic	57,140	–355.5	279.9	4.3	22.1
		Canada	14,177	–124.9	114.2	–0.1	13.4
		Scandinavia	66,904	–47.4	76.7	–0.4	8.9
EIGEN-GLO4C	360	Australia	1,117,054	–192.1	218.3	0.3	12.1
		Arctic	56,878	–191.5	193.4	–1.2	15.9
		Antarctic	57,140	–356.4	282.2	4.4	23.2
		Canada	14,177	–124.1	105.9	–0.1	13.6
		Scandinavia	66,904	–50.9	83.9	–1.1	8.5
EGM2008	2190	Australia	1,117,054	–200.2	238.7	–0.3	5.4
		Arctic	56,878	–193.6	103.5	–1.0	10.9
		Antarctic	57,140	–349.9	268.3	4.3	18.6
		Canada	14,177	–100.7	85.7	–0.9	8.2
		Scandinavia	66,904	–47.8	49.4	–0.8	3.6

with a total length of over 2430 km were processed during the flights. A database containing over 23 thousand gravimetric stations was compiled. The accuracy and detail of measurements met the requirements for a 1:200,000 gravimetric survey. Statistical characteristics of differences between the model and measured GA values are presented in Table 6.8.

According to Tables 6.7 and 6.8, a posteriori accuracy estimates of modern global EGF models, obtained by comparing with gravimetric data, are consistent with the above a priori estimates. They illustrate the accuracy improvement through refining the harmonic coefficients of the geopotential and increasing the model resolution. A similar conclusion can be made from the published comparison of global EGF models with satellite altimetry data, including both the sea level (geoid height), and the gravity anomalies.

Table 6.8 Statistical characteristics of differences between model GA and Arctic airborne gravimetric survey data from IPE RAS

Model	n_{max}	Differences, mGal	
		μ	σ
EGM2008	2190	–2.58	2.01
EIGEN-6C	1420	–3.04	2.25
PZ-2002	360	–4.06	4.67

6.1.3 Estimation of Accuracy of Geoid Height Models

One of the main purposes of modern EGF models is to ensure the global coverage of the vertical datum, therefore, special attention is given to testing such models using geoid heights obtained by the inverse satellite leveling, i.e., as differences between the geodetic (satellite) and leveling heights.

The accuracy of the studied models is normally estimated using absolute heights only at individual geodetic points. Accuracy estimates of global EGF models using leveling geoid heights are given in Table 6.9.

To obtain more information on the accuracy characteristics, the model is tested not only by absolute heights, but also by relative ones, i.e., by geoid height differences at two stations grouped by the distances between the stations, e.g. 0–50 km, 50–100 km, etc. (Nepoklonov et al. 2007).

At present, obtaining similar external estimates of DGHM accuracies in continental areas is of particular importance, primarily in the context of studying the accuracy of the gravimetric geoid modeling. The estimates characterizing the dependence of DGHM accuracy and detail on the geographical location and national identity are presented in Table 6.10 (Nepoklonov and Abakushina 2016).

Two digital geoid height models have been constructed for the territory of the Russian Federation over the past 20 years. The first one is the Russian Gravimetric Geoid model developed in 2000 (RGG-2000) for experimental purposes with the support of the Russian Foundation for Basic Research (Fig. 6.2). Its main characteristics are as follows: the source data is EGM96 (up to degree 360), average GAs and heights in 5 × 5 arcmin trapezes (based on 1:1,000,000 gravimetric maps); the fixed interval is 5 arcmin; the borders are 40–80° in latitude, 26–192° in longitude. Nodal geoid heights are calculated using the Stokes formula. The average difference between the RGG-2000 and the similar European gravimetric geoid model EGG97 is 0.40 m and the standard deviation is 0.42 m. The errors of RGG-2000 in the leveling geoid heights are characterized by average values and standard deviations from 1 to 3–4 dm depending on the region (Nepoklonov and Abakushina 2016).

The second model was constructed by the Central Research Institute of Geodesy, Airborne Survey, and Cartography of Russia (TsNIIGAiK) in 2012 under the supervision of G.V. Dem'yanov. The following source information was used: the latest Russian global gravitational model GAO-2012; average values of GA and heights from 1:200,000 gravimetric maps. A specific feature of this model is that it consists of three units (schematically shown in Fig. 6.3).

In units 1 and 2, the geoid height grid has a grid size of 5 × 7.5 arcmin; and in unit 3, the grid size is 5 × 5 arcmin. The differences between the model and leveling geoid heights (835 stations of geodetic networks FAGS, VGS, and SGN-1 in Russia were used for reference) are schematically shown in Fig. 6.4. Statistically, these differences have the mean value of 0.15 m and the standard deviation of 0.42 m.

Table 6.9 Statistical characteristics of differences between model and leveling geoid heights

Model (N)	Region	Number of stations	Differences, m			
			min	max	μ	σ
EGM96(360)	Turkey	313	–2.19	0.82	–0.81	0.46
	Greece	1542	–1.06	1.58	–0.45	0.42
	Australia	1013	–2.44	3.54	0.02	0.50
	Poland	360	–0.54	0.57	–0.04	0.19
	Algeria	71	–0.90	0.78	–0.03	0.34
	Republic of South Africa	79	–0.95	0.68	–0.24	0.35
	South America	1190	–3.30	3.70	0.24	0.80
	Greenland	78	–0.52	2.62	0.71	0.52
	Belarus	196	–0.52	0.47	0.01	0.22
EIGEN-GLO4C(360)	Greece	1542	–1.17	1.77	–0.28	0.45
	Algeria	71	–0.63	0.64	–0.02	0.33
	South America	1190	–2.90	3.10	0.22	0.70
	China	652	–2.26	1.80	–0.25	0.43
EIGEN-5C(360)	Turkey	313	–3.33	0.75	–0.87	0.66
	Poland	360	–0.22	0.52	0.10	0.11
EGM2008(2190)	Turkey	313	–0.29	0.71	0.29	0.16
	Greece	1542	–0.44	0.54	–0.38	0.14
	South Korea	500	–0.54	1.17	0.10	0.18
	Poland	360	0.04	0.26	0.12	0.04
	The Czech Republic	1024	–0.52	–0.33	–0.42	0.04
	Italy	977	–0.33	0.34	0.00	0.10
	Algeria	71	–0.67	0.61	–0.08	0.21
	Republic of South Africa	79	–0.84	0.02	–0.42	0.24
	South America	1190	–3.30	3.40	0.22	0.68
	Greenland	78	–0.43	1.60	–0.19	0.40
	Canada	2579	–0.92	0.09	–0.38	0.13
	China	652	1.89	1.64	–0.12	0.26
	Belarus	196	–0.16	0.11	0.05	0.05

6.1.4 Estimation of Accuracy of the Global Models of the Earth's Gravity Field in the Arctic

Considering relatively low und uneven geophysical coverage of the Arctic and its planned exploration, it is interesting to find out how adequately the modern global

Table 6.10 Characteristics of modern digital geoid height models

Region, country	Model	Grid size (arcmin)	EGF reference model (order)	Accuracy characteristics	
				μ	σ
Europe	European gravimetric geoid 2008 (EGG08)	1 × 1.5	About 1.4 thousand	– 0.06	0.08
Africa	African geoid project 2007 (AGP2007)	5 × 5	No data	No data	0.21
South America	GEOID2014	5 × 5	About 1.8 thousand	0.17	0.52
Australia	AUSGeoid09	1 × 1	Over 6.5 thousand	No data	0.05
USA	US gravimetric geoid 2012 (USGG2012)	1 × 1	Over 18 thousand	0.01	0.06
Canada	Canadian gravimetric geoid 2013 (CGG2013)	2 × 2	Over 2.5 thousand	– 0.19	0.13
Mexico	Mexican gravimetric geoid 2005 (GGM05)	2.5 × 2.5	About 1.4 thousand	No data	0.20
China	National gravimetric geoid 2011 (CNGG2011)	2 × 2	650	– 0.16	0.13 (Tibet—0.22)
Kazakhstan	KazGM2010	5 × 5	20	No data	0.18
Mongolia	National gravimetric geoid 2007	5 × 5	58	– 1.14	0.20
Iran	Iranian quasigeoid 2009 (IRQG09)	1.5 × 1.5		No data	0.28
Turkey	Turkey geoid 2009 (TG09)	3 × 3	30	0.113	0.107
Ukraine	Ukrainian gravimetric geoid 2013 (UGG2013)	1.5 × 1.5	4	No data	0.10
Poland	Poland gravimetric quasigeoid 2013 (GDQM-PL13)	1.5 × 3.0	360	0.10	0.02
Hungary	Hungary gravimetric geoid 2013 (HGG2013)	1.5 × 1.5	18	0.01	0.04
Germany	Germany combined quasigeoid 2011 (GCG11)	1.0 × 1.5	675	<0.01	0.02

EGF models describe the EGF in high-latitude areas (from 70°N to the pole). Insight into this is offered by the available results of comparative analysis of the model geoid heights (ζ), gravity anomalies (Δg), and DOV components in the meridian (ξ) and the prime vertical (η) planes (Koneshov et al. 2012a, b). The calculations were made using various models with a 5 arcmin interval on the PZ-90.11 reference ellipsoid. To account for the geographical location of the Arctic regions, the models were analyzed

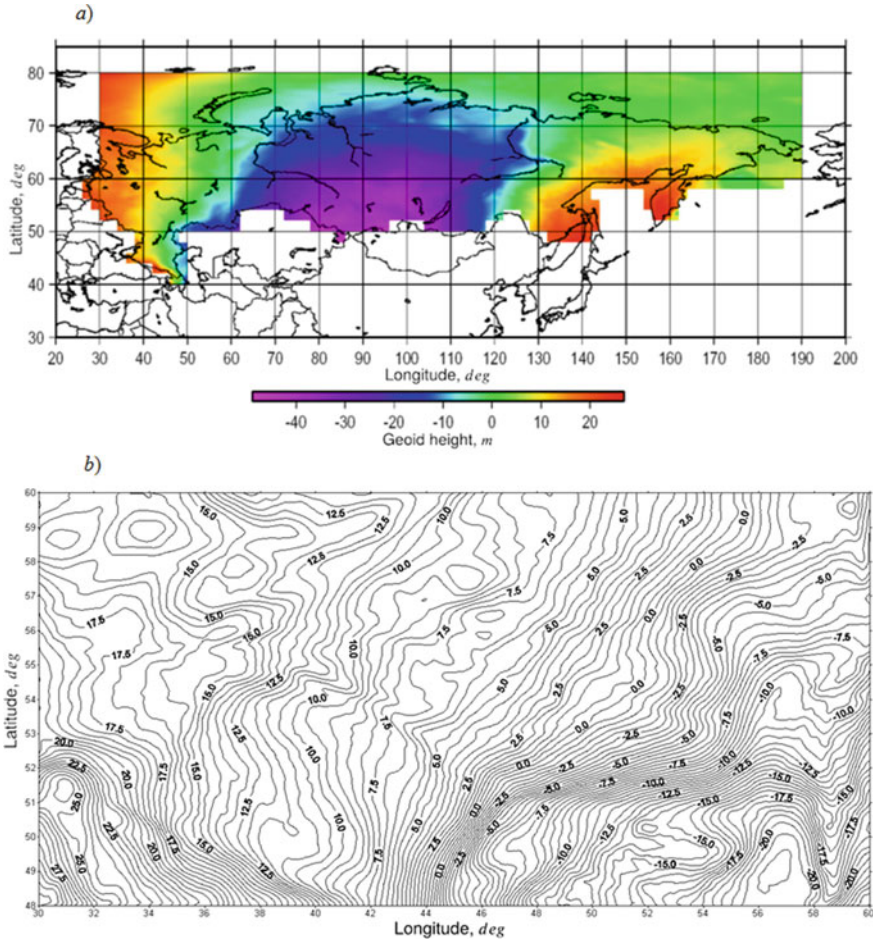

Fig. 6.2 Geoid heights in the territory of Russia according to RGG-2000: **a** general scheme; **b** European part of the country (enlarged); the lines of equal heights are plotted in 0.5 m intervals

separately for the polar cap sector Ω_0 ($B \geq 85°$) and for the remaining survey area Ω_1.

The list of the studied models (Table 6.11) adequately reflects the state of the art in the research of geopotential. On the one hand, it includes the models constructed by various developers (both Russian and international); on the other hand, there are the models differing in the source data (satellite, combined), methods to obtain them, and the degree N of spherical harmonics.

The study followed different lines: comparison of Russian and international models, of satellite and combined models, and the models obtained with and without the use of new space geodesy methods (inter-satellite measurements, satellite gradiometry).

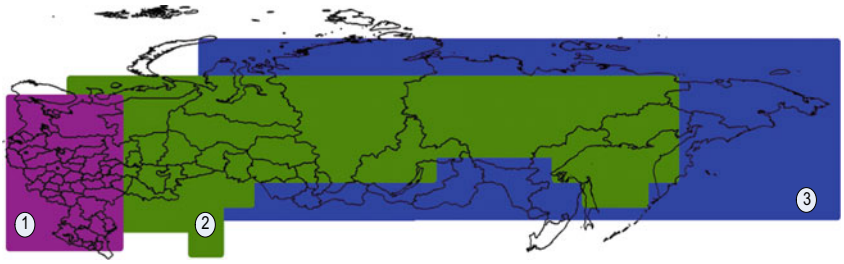

Fig. 6.3 The structure of the new DGHM (TsNIIGAiK) in Russia

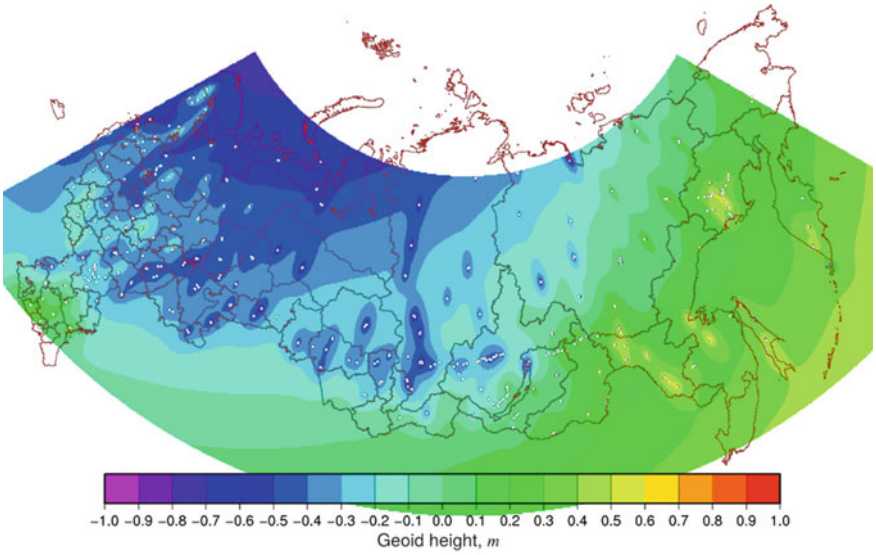

Fig. 6.4 Differences between leveling geoid heights and TsNIIGAiK model (2012)

In the course of analysis, statistical characteristics of the calculated ζ, Δg, ξ, η for each model and their deviations δζ, δg, δξ, δη from the reference values were estimated. EGM2008, initially considered to be a high-precision model, was taken as the reference (Pavlis et al. 2008). The mean value μ, standard deviation σ, minimum (min.) and maximum (max.) values were estimated.

Table 6.11 Global EGF models

Model	Year	Country (organization)	N	Source data
EGM96	1996	USA	360	S, G, A
GAO-98	1998	Russia (TsNIIGAiK)	360	S, G, A
GPM98	1998	Germany	1800	S, G, A
PZ-2002/360	2002	Russia (29 NII MO)	360	S, G, A
EIGEN-CG03C	2005	Germany	360	S (CHAMP, GRACE), G, A
EIGEN-GLO4C	2006	Germany, France	360	S (GRACE, LAGEOS), G, A
GAO-2008	2008	Russia (TsNIIGAIK, 29th Central Research Institute, Ministry of Defense)	360	S (CHAMP, GRACE), G, A
EGM2008	2008	USA	2190	S (GRACE), G, A
EIGEN-5C	2008	Germany, France	360	S (GRACE, LAGEOS), G, A
GGM-03C	2009	USA	360	S (GRACE), G, A
GOCE-DIR	2010	Germany, France	240	S (GOCE)
GOCE-TIM	2011	Germany, Austria	250	S (GOCE)
GOCO02S	2011	Austria, Germany, and Switzerland	250	S (GOCE, GRACE, CHAMP, etc.)
EIGEN-6C	2011	Germany, France	1420	S (GOCE, GRACE, LAGEOS), G, A
GIF48	2011	USA	360	S (GRACE), G, A
GAO-2012	2012	Russia (TsNIIGAiK)	360	S (GOCE), G, A

Note S—satellite; G—gravimetric; H—altimetric; N—maximum degree of geopotential spherical harmonics

Tables 6.12, 6.13, 6.14, 6.15, 6.16, 6.17, 6.18 and 6.19 present the estimates, including those averaged over the following groups: Russian and international models; satellite and combined models; low-degree ($N \leq 360$) and high-degree ($N \geq 1420$) models; and the models issued before and after 2005. The distinction in the latter two groups actually lies in the use of new space geodesy technology implemented in CHAMP, GRACE, and GOCE satellite missions.

The statistical characteristics of the model ζ, Δg, ξ, η first of all can be considered as the characteristics of anomalous EGF structure. It should be noted that the estimates obtained using different models are mostly consistent with each other and show that the Arctic as a whole can be classified as a region of medium anomalies. For geoid heights, long-wave changes are the most typical. For gravity anomalies, shortwave components are quite well visible. They are manifested mainly as meridional structures. Shortwave effects are also detected for DOV components, including

Table 6.12 Statistical characteristics of predicted geoid heights ζ, m

Model	Ω_0				Ω_1			
	min	max	μ	σ	min	max	μ	σ
EGM96	6.21	26.64	15.37	3.70	–28.19	60.04	10.72	16.84
GAO-98	7.61	25.05	14.88	3.13	–27.64	59.19	10.47	16.36
GPM98	5.97	25.70	15.48	3.73	–28.77	59.83	10.71	16.83
PZ-2002/360	7.25	27.58	15.87	3.70	–28.34	60.24	10.65	16.78
EIGEN-CG03C	7.01	26.27	15.58	3.77	–28.11	60.28	10.73	16.85
EIGEN-GLO4C	7.07	26.17	15.58	3.74	–28.17	60.33	10.73	16.85
GAO-2008	6.77	26.47	15.58	3.78	–28.26	61.01	10.72	16.86
EGM2008	6.83	26.86	15.55	3.75	–28.24	60.25	10.73	16.85
EIGEN-5C	7.15	26.25	15.56	3.74	–28.28	60.33	10.73	16.85
GGM-03C	7.16	26.24	15.49	3.74	–28.03	60.12	10.67	16.85
GOCE-DIR(3)	7.43	25.87	15.63	3.77	–28.37	59.98	10.72	16.85
GOCE-TIM(3)	7.46	26.02	15.38	3.90	–28.16	60.10	10.72	16.85
GOCO02S	7.50	26.94	15.53	3.74	–28.27	60.17	10.73	16.85
EIGEN-6C	7.22	26.53	15.55	3.74	–28.15	60.05	10.72	16.85
GIF48	7.25	26.17	15.49	3.74	–28.24	60.20	10.67	16.85
Russian	7.21	26.37	15.44	3.54	–28.08	60.15	10.61	16.67
International	7.50	26.30	15.52	3.76	–28.25	60.14	10.72	16.85
Satellite	7.46	26.28	15.51	3.80	–28.27	60.08	10.72	16.85
Combined	6.96	26.33	15.50	3.69	–28.20	60.16	10.69	16.80
Low-degree	7.16	26.31	15.50	3.70	–28.17	60.17	10.69	16.80
High-degree	6.67	26.36	15.53	3.74	–28.39	60.04	10.72	16.84
Before 2005	6.76	26.24	15.40	3.56	–28.24	59.82	10.64	16.70
After 2005	7.17	26.34	15.54	3.76	–28.21	60.26	10.72	16.85

those appearing as extended linear elements partly oriented in the meridian direction, partly in the transverse direction, which can be clearly observed, for example, in Greenland, Novaya Zemlya and Franz Josef Land.

The predicted geoid height and gravity anomaly values have a clearly pronounced positive trend both in Ω_0 and Ω_1 zones: from 10 to 16 m and from 3 to 9 mGal, respectively. At the same time, standard deviations and the spread of ζ and Δg in Ω_1 are noticeably (several times) larger than in Ω_0, which is probably caused by a significant difference in the areas of zones and increased disturbing potential in Ω_1. The difference in statistical characteristics of the Earth's gravity field (EGF) in Ω_0 and Ω_1 also shows itself in the fact that in Ω_0 the standard deviations and spread in the model ξ and η are normally much (several times) smaller than in Ω_1. This correlates with the relationship between similar characteristics of geoid heights and gravity anomalies and may also be partly due to the higher anomaly of disturbing potential, namely its horizontal gradients, in Ω_1.

Table 6.13 Statistical characteristics of predicted gravity anomalies Δg, mGal

Model	Ω_0				Ω_1			
	min	max	μ	σ	min	max	μ	σ
EGM96	–65.67	105.86	4.95	20.10	–142.30	147.87	3.14	26.45
GAO-98	–39.56	38.57	6.61	10.61	–126.97	100.76	3.04	21.74
GPM98	–88.45	130.51	5.20	24.50	–190.62	239.125	3.04	27.87
PZ-2002/360	–59.64	96.22	6.66	18.17	–132.46	137.80	2.96	24.40
EIGEN-CG03C	–60.44	79.21	7.63	17.19	–138.38	153.62	3.08	25.65
EIGEN-GLO4C	–58.25	79.04	7.69	16.99	–136.49	147.03	3.08	25.52
GAO-2008	–114.60	133.35	7.90	24.65	–211.52	248.97	3.03	34.38
EGM2008	–258.77	274.97	7.18	64.91	–270.82	293.44	3.08	50.94
EIGEN-5C	–57.00	78.04	7.35	16.26	–139.21	147.44	3.08	25.52
GGM-03C	–55.73	74.80	7.07	16.95	–130.99	143.56	3.08	25.24
GOCE-DIR	–47.06	65.07	9.20	18.88	–133.94	135.83	3.08	24.01
GOCE-TIM	–31.58	44.73	6.12	14.85	–127.03	138.16	3.07	24.24
GOCO02S	–48.96	61.95	6.70	15.62	–130.65	142.01	3.02	24.51
EIGEN-6C	–94.30	146.72	7.32	24.86	–191.50	236.64	3.07	29.65
GIF48	–62.66	76.71	6.93	17.22	–137.81	147.14	3.07	25.60
Russian	–71.27	89.38	7.06	17.81	–156.98	162.51	3.01	26.84
International	–77.41	101.47	6.94	22.36	–155.81	172.66	3.07	27.93
Satellite	–42.53	57.25	7.34	16.45	–130.54	138.67	3.06	24.25
Combined	–84.59	109.50	6.87	22.70	–162.42	178.62	3.06	28.58
Low-degree	–58.43	77.80	7.07	17.29	–140.64	149.18	3.06	25.60
High-degree	–147.17	184.07	6.57	38.09	–217.65	256.40	3.06	36.15
Before 2005	–63.33	92.79	5.86	18.34	–148.09	156.39	3.04	25.11
After 2005	–80.85	101.33	7.37	22.58	–158.94	175.80	3.08	28.66

It should be noted that the statistical characteristics of the EGF in the Arctic vary not only with the region but also with the global EGF model used. This is especially true for boundary values varying from about 1.1 to 2.5 m for ζ, from 144 to 236 mGal for Δg, from 27 to 30 arcsec for ξ, and from 26 to 35 arcsec for η. The discrepancies between the models slightly increase in Ω_0 zone, which can be attributed to insufficient coverage of EGF in the polar cap area.

From the point of view of intergroup differences, the greatest discrepancies in geoid heights are observed between Russian and international models, and between the models created before and after 2005. This is probably due to the success of international centers in determining the low-degree harmonics of the geopotential using new space geodesy methods. This factor is of fundamental importance, because in the Arctic region, space geodesy can compensate for the lack of traditional data (gravimetric, altimetric).

Table 6.14 Statistical characteristics of predicted DOV in meridian plane ξ, arcsec

Model	Ω_0				Ω_1			
	min	max	μ	σ	min	max	μ	σ
EGM96	–10.68	13.23	0.66	3.05	–27.25	21.40	–1.08	4.44
GAO-98	–6.00	6.52	0.07	2.38	–19.40	19.62	–0.97	3.92
GPM98	–13.23	15.20	0.65	3.72	–26.73	42.65	–1.08	4.59
PZ-2002/360	–9.44	10.85	0.41	2.98	–25.08	19.37	–1.10	4.10
EIGEN-CG03C	–8.94	11.81	0.09	3.22	–27.28	20.50	–1.06	4.40
EIGEN-GLO4C	–9.25	12.36	0.08	3.21	–27.13	20.71	–1.07	4.38
GAO-2008	–11.37	13.11	0.07	3.53	–38.40	32.21	–1.07	5.34
EGM2008	–35.42	37.36	0.20	9.50	–46.73	46.02	–1.07	8.00
EIGEN-5C	–9.21	11.48	0.16	3.09	–27.66	20.50	–1.07	4.36
GGM-03C	–10.32	11.41	0.24	3.23	–26.23	19.90	–1.07	4.36
GOCE-DIR(3)	–9.25	9.73	–0.28	3.74	–26.77	20.10	–1.05	4.18
GOCE-TIM(3)	–8.06	9.21	0.40	3.23	–27.36	19.82	–1.06	4.19
GOCO02S	–9.91	13.90	0.37	3.41	–27.45	20.46	–1.08	4.24
EIGEN-6C	–21.24	20.12	0.17	4.31	–37.43	35.35	–1.07	4.92
GIF48	–10.03	11.92	0.24	3.23	–26.71	21.52	–1.07	4.38
GAO-2012	–11.26	11.57	0.06	3.60	–32.27	26.23	–1.06	5.06
Russian	–9.52	10.51	0.15	3.12	–28.79	24.36	–1.05	4.61
International	–12.96	14.81	0.30	3.91	–29.56	25.74	–1.07	4.70
Satellite	–9.07	10.95	0.35	3.46	–27.19	20.13	–1.06	4.20
Combined	–12.98	14.48	0.20	3.83	–30.09	27.05	–1.06	4.82
Low-degree	–9.52	11.32	0.24	3.22	–27.61	21.72	–1.06	4.41
High-degree	–23.3	24.23	0.34	5.84	–36.96	41.34	–1.07	5.84
Before 2005	–9.84	11.45	0.45	3.03	–24.62	25.76	–1.06	4.26
After 2005	–12.86	14.50	0.20	3.94	–30.95	25.28	–1.07	4.82

The greatest discrepancies in the gravity anomalies are observed between high-degree and low-degree models, which is due to the significant contribution of the high-frequency part of the geopotential spectrum to Δg values; and between satellite and combined models, which is explained by the use of detailed gravimetric and altimetric information in constructing the combined models, even considering incomplete coverage of the Arctic regions with this information.

The greatest discrepancies in DOV are also revealed between low-degree and high-degree models, and between satellite and combined models. In both cases, these discrepancies are due to the extended use of detailed source information (gravimetric, altimetric) in the modeling, even taking into account the incomplete coverage of the Arctic with this information. The differences between the groups of models created

Table 6.15 Statistical characteristics of predicted DOV in prime vertical plane η, arcsec

Model	Ω_0				Ω_1			
	min	max	μ	σ	min	max	μ	σ
EGM96	–16.21	19.55	0.00	4.06	–21.37	29.59	0.00	4.98
GAO-98	–7.65	6.10	0.00	2.61	–17.96	21.09	0.00	4.38
GPM98	–17.70	20.49	0.00	4.48	–30.79	33.44	0.00	5.19
PZ-2002/360	–14.54	17.71	0.00	3.84	–21.49	28.10	0.00	4.80
EIGEN-CG03C	–10.86	14.25	0.00	3.73	–22.96	27.95	0.00	4.84
EIGEN-GLO4C	–11.25	14.05	0.00	3.61	–22.65	27.40	0.00	4.82
GAO-2008	–20.95	25.42	0.00	4.99	–31.22	43.91	0.00	6.13
EGM2008	–42.91	41.01	0.00	9.87	–44.90	46.16	0.00	8.00
EIGEN-5C	–10.81	13.74	0.00	3.56	–22.36	26.78	0.00	4.84
GGM-03C	–10.84	13.51	0.00	3.53	–21.84	27.72	0.00	4.78
GOCE-DIR	–8.86	10.58	0.00	3.41	–19.12	26.07	0.00	4.65
GOCE-TIM	–7.87	9.19	0.00	3.80	–19.14	26.89	0.00	4.69
GOCO02S	–8.39	9.40	0.00	2.93	–19.44	26.80	0.00	4.72
EIGEN-6C	–19.25	24.24	0.00	4.36	–33.79	33.54	0.00	5.32
GIF48	–10.38	13.83	0.00	3.67	–22.26	28.80	0.00	4.84
GAO-2012	–22.38	25.43	0.00	4.96	–32.07	40.14	0.00	5.77
Russian	–16.38	18.67	0.00	4.1	–25.69	33.31	0.00	5.27
International	–14.61	16.99	0.00	4.25	–25.05	30.1	0.00	5.14
Satellite	–8.37	9.72	0.00	3.38	–19.23	26.59	0.00	4.69
Combined	–16.59	19.18	0.00	4.41	–26.59	31.89	0.00	5.28
Low-degree	–12.38	14.83	0.00	3.75	–22.61	29.33	0.00	4.94
High-degree	–26.62	28.58	0.00	6.24	–36.49	37.71	0.00	6.17
Before 2005	–14.03	15.96	0.00	3.75	–22.9	28.06	0.00	4.84
After 2005	–15.40	17.89	0.00	4.37	–25.98	31.85	0.00	5.28

before and after 2005 are less significant. This is probably due to the limited capabilities of satellite data (including those obtained with new space geodesy methods) in refining the high-frequency spectrum of the geopotential, compared to the detailed gravimetry and altimetry data. As to the differences between the groups of Russian and international models, the use of a new Russian model GAO-2012 has helped to minimize them.

It should also be noted that significant discrepancies in the model EGF parameters in the Arctic are observed not only between the groups of models, but also within these groups. For example, the output characteristics of GAO-98 differ significantly from other models of its group. Both in the groups of Russian and combined global EGF models, it appears to be too smooth both in the range and in the variance of the model quasigeoid heights and gravity anomalies. For this reason, the use of the new

Table 6.16 Statistical characteristics of deviations of predicted geoid heights ζ from reference values, m

Model	Ω_0				Ω_1			
	min	max	μ	σ	min	max	μ	σ
EGM96	–3.12	4.99	–0.18	0.85	–4.66	4.83	0.00	0.78
GAO-98	–6.13	1.84	–0.67	1.05	–6.94	4.12	–0.26	1.07
GPM98	–3.32	4.90	–0.07	0.82	–5.06	3.96	–0.02	0.87
PZ-2002/360	–2.66	5.30	0.32	0.85	–4.45	4.10	–0.08	0.60
EIGEN-CG03C	–1.37	1.46	0.03	0.34	–2.12	2.08	0.00	0.25
EIGEN-GLO4C	–1.33	1.51	0.03	0.30	–2.22	1.83	0.00	0.23
GAO-2008	–2.12	2.84	0.03	0.48	–3.92	4.08	0.00	0.50
EIGEN-5C	–1.28	1.30	0.01	0.29	–1.74	1.92	0.00	0.22
GGM-03C	–1.47	1.25	–0.06	0.28	–1.67	1.59	–0.05	0.23
GOCE-DIR(3)	–2.26	2.46	0.08	0.71	–2.64	2.40	0.00	0.33
GOCE-TIM(3)	–2.78	3.41	–0.17	0.99	–2.58	2.56	0.00	0.33
GOCO02S	–2.53	2.11	–0.02	0.55	–2.53	2.52	0.00	0.35
EIGEN-6C	–0.79	0.76	0.00	0.19	–0.82	0.90	0.00	0.15
GIF48	–1.36	1.05	–0.06	0.27	–1.53	1.69	–0.05	0.20
Russian	–3.64	3.33	–0.11	0.79	–5.10	4.10	–0.11	0.72
International	–1.96	2.29	–0.04	0.51	–2.51	2.40	–0.01	0.36
Satellite	–2.52	2.66	–0.03	0.75	–2.58	2.56	0.00	0.34
Combined	–2.27	2.47	–0.06	0.52	–3.20	2.83	–0.04	0.46
Low-degree	–2.06	2.83	–0.04	0.50	–2.94	2.43	–0.01	0.51
High-degree	–2.37	2.46	–0.05	0.58	–3.08	2.81	–0.04	0.42
Before 2005	–3.81	4.26	–0.15	0.89	–5.28	4.25	–0.09	0.83
After 2005	–1.73	1.82	–0.01	0.44	–2.18	2.16	–0.01	0.28

Russian model GAO-2012 is of interest. According to the comparative estimates, it does not significantly differ from the previous Russian model GAO-2008, at least in terms of DOV. The differences between these models in zones Ω_0 and Ω_1 have almost zero mean values and standard deviations of 1.05 and 1.11 arcsec for ξ component, and 1.52 and 1.28 arcsec for η component, respectively.

The estimated statistical characteristics of $\delta\zeta$, δg, $\delta\xi$, and $\delta\eta$ can be considered as the accuracy characteristics of the global EGF models in terms of deviations of the model values ζ, Δg, ξ, η from the corresponding reference data.

Obviously, the estimates of these characteristics also depend on the region (the approximation errors of the reference data in Ω_0 zone are usually larger than in Ω_1 zone) and on the global EGF model used. The variation of the boundary values is especially significant: from about 3.9 to 6.1 m for $\delta\zeta$ and from 29 to 98 mGal for δg. This can be attributed to more frequent updates of the source data on low-degree harmonics of the geopotential due to the use of space geodesy methods. Low-degree

Table 6.17 Statistical characteristics of deviations of predicted gravity anomalies Δg from reference values, m Gal

Model	Ω_0				Ω_1			
	min	max	μ	σ	min	max	μ	σ
EGM96	–242.74	319.76	–2.23	65.05	–229.46	266.02	0.07	45.80
GAO-98	–258.24	260.44	–0.57	64.22	–274.18	237.81	–0.04	45.94
GPM98	–258.98	325.27	–1.98	66.41	–276.42	233.81	–0.04	47.30
PZ-2002/360	–240.89	313.01	–0.52	64.94	–236.62	256.15	–0.11	45.11
EIGEN-CG03C	–235.69	227.66	0.45	62.92	–224.34	232.57	0.00	44.34
EIGEN-GLO4C	–239.89	232.37	0.50	62.85	–222.62	233.73	0.00	44.32
GAO-2008	–262.42	228.72	0.71	64.31	–266.29	278.19	–0.05	46.74
EIGEN-5C	–240.34	231.87	0.16	62.85	–224.91	238.50	0.00	44.26
GGM-03C	–236.92	233.48	–0.12	62.76	–219.67	236.82	0.00	44.48
GOCE-DIR(3)	–264.30	249.91	2.02	65.98	–236.08	237.06	0.04	45.40
GOCE-TIM(3)	–262.22	256.75	–1.06	65.70	–240.87	242.76	0.00	45.39
GOCO02S	–263.74	277.84	–0.48	65.01	–237.57	241.00	–0.05	45.58
EIGEN-6C	–235.26	232.03	0.14	61.41	–210.35	227.23	–0.01	43.17
GIF48	–237.13	237.13	–0.26	62.75	–209.80	234.28	–0.01	44.15
Russian	–253.85	267.39	–0.13	64.49	–259.03	257.38	–0.07	45.93
International	–247.02	256.73	–0.26	63.97	–230.19	238.53	0.00	44.93
Satellite	–263.42	261.50	0.16	65.56	–238.17	240.27	0.00	45.46
Combined	–244.41	258.34	–0.34	63.68	–235.88	243.19	–0.02	45.06
Low-degree	–247.12	278.65	–0.92	63.91	–243.38	230.52	–0.02	45.24
High-degree	–248.71	255.74	–0.12	64.11	–235.20	244.57	–0.01	45.13
Before 2005	–250.21	304.62	–1.32	65.16	–254.17	248.45	–0.03	46.04
After 2005	–247.79	240.78	0.21	63.65	–229.25	240.21	–0.01	44.78

harmonics are the main contributors to the estimation of the quasi-geoid heights as compared to the satellite altimetry and gravimetric survey data that are mostly employed in the estimation of gravity anomalies.

The statistical characteristics of $\delta\xi$, $\delta\eta$ provide a better understanding of how well the lower-degree models including GAO-2012 approximate the ultrahigh-degree geopotential model EGM2008 in the Arctic regions.

Analysis of the obtained estimates reveals, first of all, a considerable improvement in the accuracy characteristics of models released after 2005, especially in quasi-geoid heights. Compared to the earlier models, the average discrepancies between post-2005 models and the reference quasi-geoid heights have decreased two or more times, with the RMS errors of the models considered to be the best in this respect not exceeding 0.3 m. In comparison, the improvement in GA and DOV is smaller: for gravity anomalies, the absolute deviations vary from a few mGal to a few dozen

Table 6.18 Statistical characteristics of deviations of predicted DOV component ξ from the reference values, arcsec

Model	Ω_0				Ω_1			
	min	max	μ	σ	min	max	μ	σ
EGM96	–36.21	36.10	0.46	9.16	–45.13	39.21	–0.01	6.96
GAO-98	–36.81	34.08	–0.13	9.15	–44.14	41.47	0.10	6.99
GPM-98	–37.73	39.16	0.45	9.42	–38.66	45.66	–0.01	7.26
PZ-2002/360	–36.21	35.39	0.21	9.17	–44.97	38.93	–0.03	6.85
EIGEN-CG03C	–36.66	34.51	–0.11	8.99	–44.22	39.74	0.00	6.75
EIGEN-GLO4C	–36.02	34.53	–0.11	8.98	–44.58	40.44	0.00	6.74
GAO-2008	–40.26	37.43	–0.12	9.12	–45.93	46.21	0.00	7.05
EIGEN-5C	–35.47	34.88	–0.04	8.98	–44.92	39.65	0.00	6.73
GGM-03C	–35.47	34.72	0.04	8.98	–44.77	40.40	0.00	6.80
GOCE-DIR(3)	–38.54	37.13	–0.48	9.45	–48.21	40.11	0.02	6.89
GOCE-TIM(3)	–35.71	34.70	0.20	9.38	–47.90	40.23	0.01	6.88
GOCO02S	–37.68	35.64	0.18	9.34	–48.04	40.22	–0.01	6.91
EIGEN-6C	–37.60	35.73	–0.02	8.68	–33.90	36.50	0.00	6.56
GIF48	–35.34	35.50	0.05	8.94	–43.84	38.65	0.00	6.70
GAO2012	–39.73	39.57	–0.14	9.14	–42.25	40.03	0.01	6.98
Russian	–38.25	36.62	–0.05	9.15	–44.32	41.66	0.02	6.97
International	–36.58	35.69	0.06	9.12	–44.02	40.07	0.00	6.83
Satellite	–37.31	35.82	–0.03	9.39	–48.05	40.19	0.01	6.89
Combined	–36.96	35.97	0.05	9.06	–43.11	40.57	0.01	6.86
Low-degree	–36.93	35.71	0.00	9.14	–45.3	40.41	0.01	6.86
High-degree	–37.67	37.45	0.22	9.05	–36.28	41.08	–0.01	6.91
Before 2005	–36.74	36.18	0.25	9.23	–43.23	41.32	0.01	7.02
After 2005	–37.13	35.85	–0.05	9.09	–44.41	40.20	0.00	6.82

mGal and the RMS errors are from about 1 to 1.5 mGal; and for the DOV, the absolute deviations are 1.5 arcsec and the RMS errors are 0.2 arcsec.

The improvement is mainly attributed to the use of international combined models, including EIGEN-GLO4C, EIGEN-5C, GIF48 to degree 360, and EIGEN-6C to degree 1420; the latter has expectedly become the leader in most parameters. This is due to not only its higher resolution, but also to the application of GOCE satellite gradiometry data. Among the above-mentioned combined models up to degree 360, GIF48 (USA) features the smallest deviations from the reference values.

The GAO-2012 model has slightly improved the rating of the Russian models; however, it can be hardly called a significant step in the DOV accuracy improvement in the Arctic, especially as compared to the latest international models. This

Table 6.19 Statistical characteristics of deviations of predicted DOV component η from reference values, arcsec

Model	Ω_0				Ω_1			
	min	max	μ	σ	min	max	μ	σ
EGM96	–40.78	43.38	0.00	9.71	–42.95	40.12	0.00	6.64
GAO-98	–40.25	40.65	0.00	9.49	–36.84	37.59	0.00	6.65
GPM98	–40.60	44.23	0.00	9.84	–39.96	41.31	0.00	6.77
PZ-2002/360	–39.66	43.48	0.00	9.69	–41.17	37.16	0.00	6.53
EIGEN-CG03C	–37.08	40.34	0.00	9.25	–37.64	36.75	0.00	6.40
EIGEN-GLO4C	–36.86	40.70	0.00	9.24	–37.33	37.00	0.00	6.40
GAO-2008	–38.85	42.10	0.00	9.53	–42.16	37.40	0.00	6.82
EIGEN-5C	–36.91	40.82	0.00	9.24	–37.42	37.32	0.00	6.39
GGM-03C	–37.34	40.53	0.00	9.21	–37.41	36.89	0.00	6.39
GOCE-DIR(3)	–38.73	41.62	0.00	9.67	–36.06	35.54	0.00	6.58
GOCE-TIM(3)	–41.00	42.58	0.00	9.81	–36.52	36.52	0.00	6.58
GOCO02S	–42.22	41.36	0.00	9.54	–36.54	36.03	0.00	6.61
EIGEN-6C	–37.19	39.82	0.00	9.09	–32.12	33.86	0.00	6.24
GIF48	–36.61	39.96	0.00	9.24	–38.32	37.01	0.00	6.39
GAO-2012	–38.46	40.79	0.00	9.59	–41.69	37.14	0.00	6.73
Russian	–39.31	41.76	0.00	9.58	–40.47	37.32	0.00	6.68
International	–38.67	41.39	0.00	9.44	–37.48	37.12	0.00	6.49
Satellite	–40.65	41.85	0.00	9.67	–36.37	36.03	0.00	6.59
Combined	–38.38	41.40	0.00	9.43	–38.75	37.46	0.00	6.53
Low-degree	–38.83	41.41	0.00	9.48	–38.62	37.11	0.00	6.55
High-degree	–38.90	42.03	0.00	9.47	–36.04	37.59	0.00	6.51
Before 2005	–40.32	42.94	0.00	9.68	–40.23	39.05	0.00	6.65
After 2005	–38.30	40.97	0.00	9.40	–37.56	36.50	0.00	6.50

model was developed with the use of satellite gradiometry data, which have relatively low resolution and could not significantly improve the determination of high-degree spherical harmonics of the geopotential, that are the main contributors to the estimation of model gravity anomalies and DOVs. On the other hand, GAO-2012 outperforms other Russian global EGF models in terms of the accuracy of the geoid heights approximation in high-latitude areas.

Now let us focus on the comparison of accuracies of satellite and combined global EGF models. Generally, the satellite models (GOCE-DIR, GOCE-TIM, GOCO02S), including low-degree ones, are inferior to the combined EGF models in terms of the accuracy of rapidly changing EGF parameters such as gravity anomalies and DOVs, especially in the polar cap area. This can be explained by insufficient completeness and sensitivity of satellite data to local gravity anomalies. In other regions, the difference between satellite and combined (low-degree) models is less pronounced. This

can also be interpreted as a result of the new space geodesy methods used in GRACE and GOCE low-orbit measurement missions.

In the group of satellite models, GOCO02S stands out in Ω_0 zone, and GOCE-TIM does in Ω_1 zone. The advantage of GOCO02S is that it is based on both GOCE (96.7° orbit inclination) and GRACE (89° orbit inclination) satellite data. As a result, it was possible to compensate for the lack of polar cap coverage by GOCE data, using the data from GRACE satellites moving in near-polar orbit.

6.1.5 Conclusions

Based on the analysis of the methods and results of estimating the accuracy of EGF models, the following conclusions can be made.

Among the EGF models, the main objective is to estimate the accuracy of models in the form of spherical harmonics of the geopotential and digital (grid) EGF models. The accuracy characteristics of modern EGF models should be estimated using the combination of methods, including a priori and a posteriori accuracy estimation. A priori estimates should be used in a preliminary analysis of the model accuracy, and final conclusions should be made using a posteriori estimates, including the external ones obtained by comparing the model with independent reference data.

The external estimates of EGF model accuracy can be obtained by the following methods: by comparing the studied model with a reference model conventionally accepted as a standard; by using the orbital method (based on the residuals of satellite measurements for the studied global model used for calculating the ephemeris of artificial Earth satellites); by comparing the studied model with the reference values of geoid heights, gravity anomalies, DOV components, and other functionals of perturbing potential, obtained using various methods of EGF study, such as gravimetric and astrogeodetic methods, satellite altimetry, satellite gradiometry, and satellite leveling.

At present, the accuracy of EGF models for geoid heights is of particular importance for geodetic applications. The accuracy of geoid height estimation on land can be improved by applying regional and national digital geoid height models constructed by refining the global EGF models in continental areas, using detailed gravimetric data. The geoid height models currently have the following characteristics: resolution (detail) from 5 to 1–2 arcmin; accuracy (RMS error) from a few decimeters (Africa, Asia, South America, Russia) to a few centimeters (Europe, USA, Canada).

The Arctic regions, especially the polar cap area, have always been problematic from the point of view of accuracy characteristics of EGF models. The best EGF models in terms of the proximity to the reference EGM2008 model to degree 2190 in the Arctic are EIGEN-6C ($N = 1420$) in the class of high-degree models and GIF48 ($N = 360$) in the class of low-degree models. The new Russian model GAO-2012 approaches the best international counterparts for the most part of the Arctic due to the use of satellite gradiometry.

6.2 Using the Earth's Gravity Field Model in Marine Gravity Measurements

A specific feature of marine gravity measurements is that the vessel is away from the reference stations at the ports of call for a long time. Under these conditions, it is important to monitor the reliability and accuracy of relative measurements, which depend on proper operation of the equipment, tying to reference stations, and the influencing physical factors that should be taken into account. To implement such monitoring, modern EGF models can be used for continuous real-time monitoring of the measurement process.

A new phase of the EGF studies began when space geodesy methods appeared (Rapp 1986). Since the gravity field anomalies define the figure of the geoid, they can be estimated using the heights of the geoid measured by satellite altimetry in the World Ocean along with other satellite-based measurements. Obviously, such measurements do not contain the high-frequency components of the gravity field. The frequency ranges of gravity anomalies (GAs) calculated from satellite data can be evaluated experimentally by comparing them with marine gravity measurements.

6.2.1 Comparison of Satellite Data with Marine Gravity Measurements

Based on altimetry measurements in the World Ocean from the GEOS-3 and SEASAT satellites, geoid heights with an error of 10 cm were obtained and further used in calculating the gravity anomalies on a 15 × 15 arcmin grid with an error of ±8 mGal. The leading role in the development of the methodology for GA estimation in water areas, using space data belongs to the National Geospatial-Intelligence Agency (NGA) (Yale and Sandwell 1999).

The RAS Institute of Physics of the Earth (IPE RAS) compared the GAs calculated from altimetry data with marine gravity measurements conducted in 1993 in the World Ocean (Zheleznyak and Koneshov 1995). Gravity anomalies were compared at two test sites: the Dacia Seamount in the Atlantic Ocean and the region of Kamchatka and Komandorskie Islands in the Pacific Ocean. The analysis confirmed that the data under study were highly consistent in terms of the long-wavelength components of the spectrum and the presence of outliers in the altimetric data, caused by the short-period components of the spectrum.

Similar comparison was made on long survey profiles in the Indian and the Pacific Oceans. The systematic difference between the GAs obtained using altimetry and marine measurements was calculated on 38 profile lines including a sample of more than 3000 gravimetric stations with an increment of 15 arcmin. Its average value was 0.02 mGal, which actually indicates that there is no systematic difference. On some individual profiles the difference varied from –2.9 to +3.5 mGal. The standard deviation on individual profiles varied from 4.1 to 11.3 mGal, and amounted to

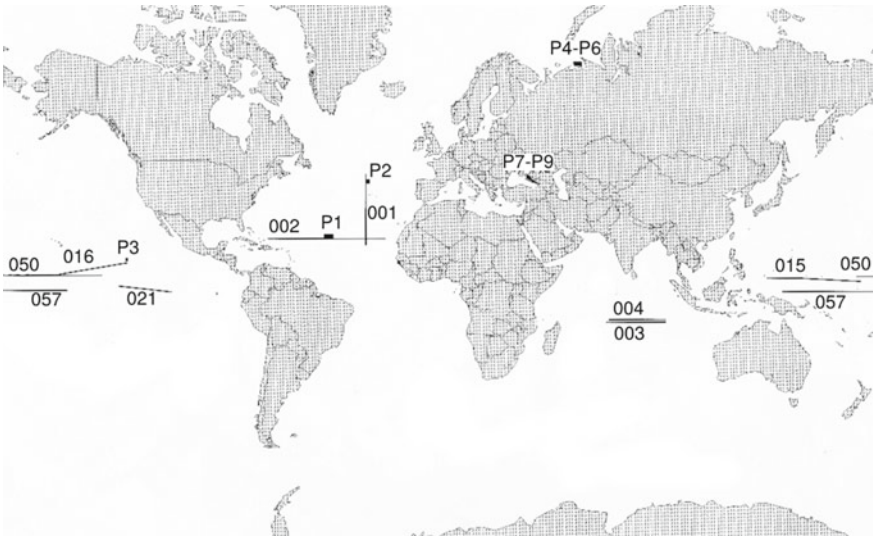

Fig. 6.5 Survey profiles and sites for GA comparison. Lines show survey profiles with their working numbers, and rectangles show survey sites

7.2 mGal over the entire sample set. The maximum error of marine measurements was 0.7 mGal for the random component and 1 mGal for the systematic one (Zheleznyak 1992; Zheleznyak and Koneshov 1992).

At the next stage (Drobyshev et al. 2005), the 1 arcmin grid of GAs calculated from the altimetric data, provided by the Scripps Institute of Oceanography of the University of California, San Diego, was compared to the results of the surveys using a Cheta-AGG marine gravimetric system, conducted with the participation of the IPE RAS on board the "17th S'yezd Profsoyuzov" research vessel in 1990–1993 (Fig. 6.5).

The data on more than 80,000 points on 10 profiles ranging from 2500 to 7000 km and more than 73,000 site survey points on 9 sites ranging from 400–60,000 km^2 were used for comparison. The random error of marine measurements was in the range of 0.25 to 0.7 mGal on survey routes and in the range of 0.10 to 0.4 mGal on survey sites after adjustment (Zheleznyak 1992; Zheleznyak and Koneshov 1992). Measurements did not contain systematic errors greater than 0.7 mGal. The distance between points ranged from 0.3–1 km and perturbing accelerations often exceeded 200 Gal.

Table 6.20 presents statistical characteristics of the differences between marine measurements and satellite-based estimation of GAs. The systematic discrepancy between the results, excluding the Black Sea, was about 1 mGal, and the random error varied from 2.1 mGal in low anomaly zones to 6.2 mGal in high anomaly zones, regardless of the location of the survey. The differences for outliers far exceeded the triple RMS value in high anomaly areas.

Table 6.20 Characteristics of discrepancies between GAs obtained using the two methods, mGal

Profiles or sites (P)	Survey area	Number of points	Systematic component	Random component	Minimum value	Maximum value
001	Atlantic Ocean	4700	1.51	5.72	–20.07	27.82
002	Atlantic Ocean	4862	1.17	3.97	–13.53	15.43
68 P1	Atlantic Ocean	427	–3.17	5.70	–19.94	4.72
80 P1	Atlantic Ocean	411	5.26	6.15	–4.83	22.55
P1	Atlantic Ocean	4700	1.51	5.72	–20.07	27.82
P2	Atlantic Ocean	9725	1.17	3.97	–13.53	15.43
004	Indian Ocean	4998	0.53	5.29	–37.97	17.15
003	Indian Ocean	5243	–0.02	4.75	–24.70	14.90
050	Pacific Ocean	10,510	1.89	5.04	–16.13	24.21
057	Pacific Ocean	14,440	0.52	4.48	–20.50	24.56
P3	Pacific Ocean	1656	2.12	2.83	–6.21	9.38
P4, P5, P6	Barents Sea	24,325	1.04	2.06	–11.39	7.54
502	Black Sea	816	–14.41	8.43	–17.86	2.44
503	Black Sea	956	–5.72	5.01	–21.20	4.84
P8	Black Sea	8663	–12.47	6.96	–51.84	1.92
P9	Black Sea	15,155	–17.88	16.16	–101.16	27.72

The greater discrepancies obtained in the Black Sea are apparently because these profiles are located near the Caucasus mountain system. This region is an isostatically uncompensated area where there are significant gravitating masses above the geoid equipotential surface, which is a violation of the Stokes theorem conditions (Morgunova et al. 2004).

Transatlantic Profile Line 002 (located at the latitude 23°N and intersecting two basins and the Mid-Atlantic Ridge, see the curves in Fig. 6.6) was investigated in most detail.

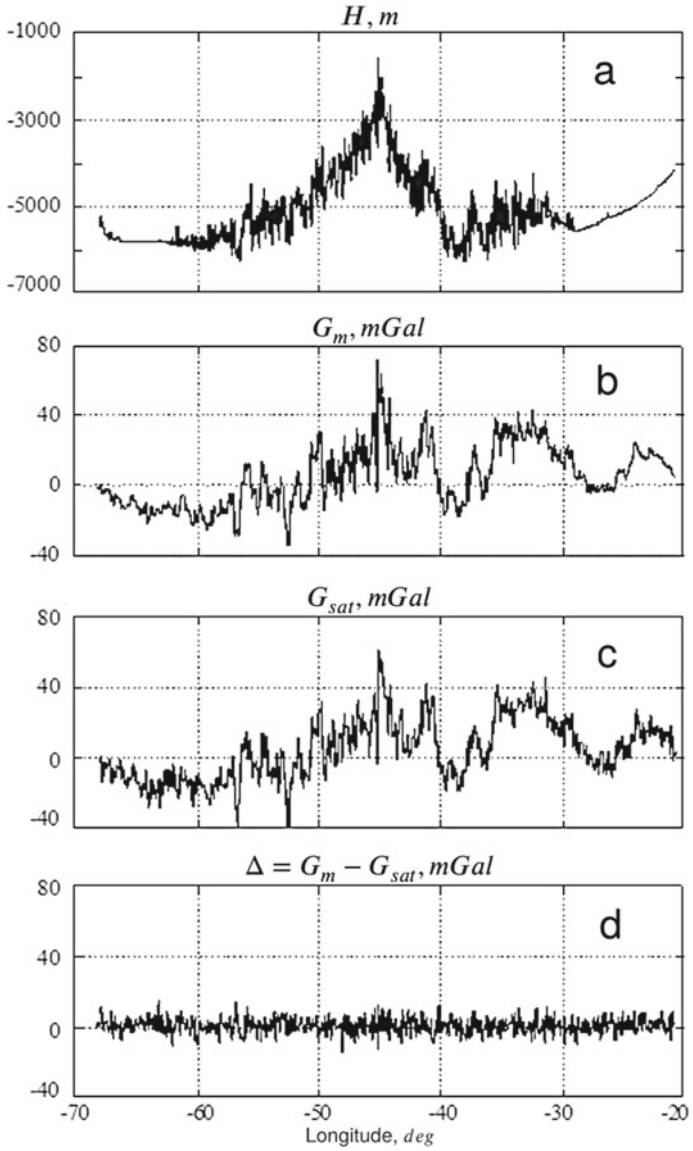

Fig. 6.6 Profile line 002, Atlantic Ocean: **a**—depth H; **b**—gravity anomaly measurements G_{m}; **c**—satellite-based estimate of gravity anomaly G_{sat}; **d**—difference $\Delta = G_{\mathrm{m}} - G_{\mathrm{sat}}$

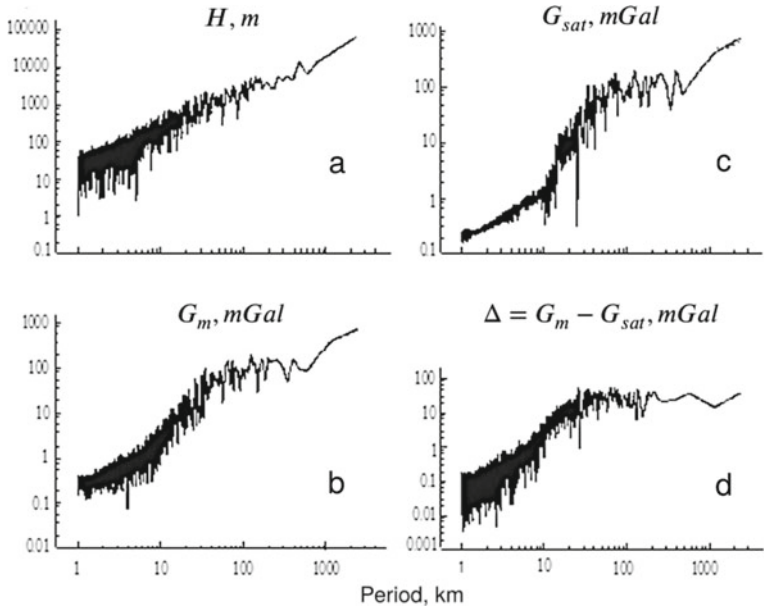

Fig. 6.7 Power spectra on Profile line 002, Atlantic Ocean (see also Fig. 6.6 caption)

Figure 6.7 shows the power spectra of the values presented above. These diagrams indicate that the difference between the satellite and marine gravity data contains only high-frequency components. Besides other factors they are caused by the numerical and methodological errors in satellite data processing. Similar spectra were obtained for other survey profiles. Thus, the spectra of marine and satellite GA estimates coincide only in their low-frequency part.

Squared modulus of the coherence spectrum between these two methods was calculated to quantitatively estimate the boundaries of the coincidence region (Brillinger 1975). The procedure allows one to identify the matching frequencies in these two data arrays. The curves of the squared modulus of the coherence spectrum for all the survey profiles are presented in Fig. 6.8. They are similar to one another in all areas of the World Ocean, except for the Black Sea.

The analysis of these graphs shows that the satellite-based GA estimates almost coincide with the marine measurements in the open ocean for the wavelength above 50 km, where the squared modulus of the coherence spectrum exceeds 0.9. All field harmonics with wavelengths less than 20 km derived from satellite measurements should be considered as noise due to the errors in the initial altimetry data. The distortion of the field harmonics in the range from 20 to 50 km increases with wavelength shortening.

Maps of gravity anomalies based on marine measurements and altimetry data on the same site P3 in the Pacific Ocean are presented below in Fig. 6.9. Field patterns do not match each other due to altimetry errors.

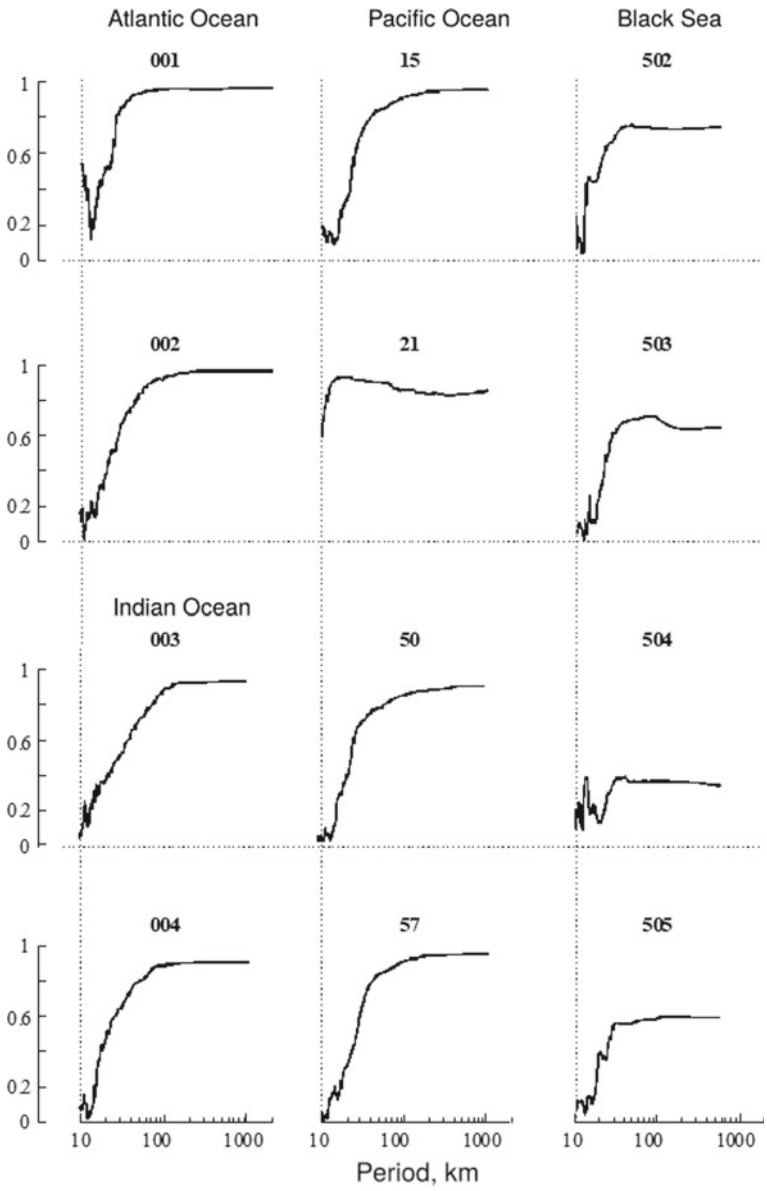

Fig. 6.8 Squared modulus of the coherence spectrum between marine and satellite data in the Atlantic (001–002), Indian (003–004), Pacific (15, 21, 50, 57) Oceans and in the Black Sea (502–505)

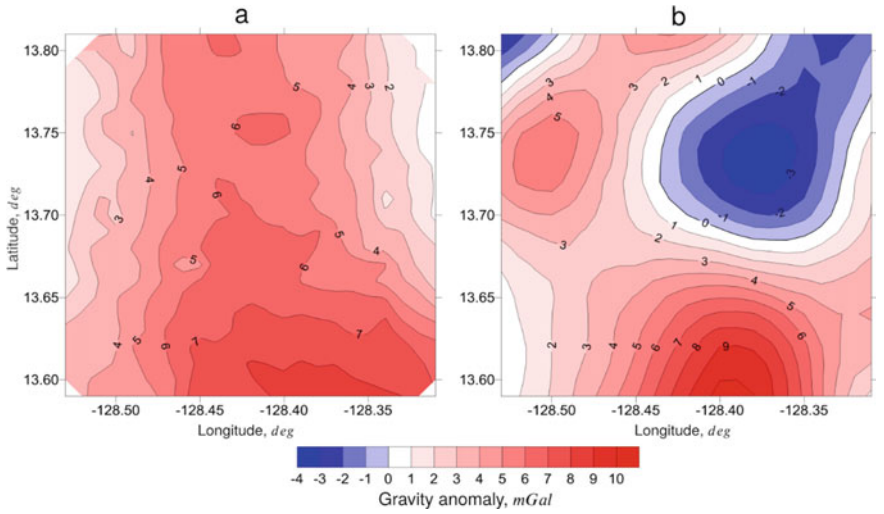

Fig. 6.9 GA maps based on the results of marine (**a**) and satellite altimetry (**b**) measurements, Site P3 (Table 6.20), Pacific Ocean

The profiles in Fig. 6.10, corresponding to the marine data and the EGM2008 model, also clearly show the difference in high frequencies where the smoother line belongs to the model.

The idea of using the satellite data instead of the onshore reference point to tie the marine measurements was expressed as early as in 1995 (Zheleznyak and Koneshov 1995). The practical use of this idea became possible when the EGF models were improved and their frequency characteristics were studied in detail. In recent years, international and Russian experts have created several new combined EGF models calculated using the satellite altimetry and gradiometry along with integrated land, marine, and airborne measurements. These models have improved characteristics in terms of accuracy in the estimation of geopotential harmonic coefficients, and increased spatial resolution (Koneshov et al. 2014b). A special place in the series of these models is occupied by the EGM2008 global ultrahigh-degree EGF model (Koneshov et al. 2014a, b), the materials of which are published by the NGA (Earth Gravitational Model 2008). The EGM2008 model is the most accurate and detailed global model as of today (Koneshov et al. 2012b).

A survey on a site in the Atlantic Ocean, located at the junction of the Mid-Atlantic Ridge and the Kane Transform Fault was conducted in 1991 using the Cheta-AGG marine gravimetric system to estimate the suitability of the EGM2008 model for solving the problem at issue. The area of 300 × 200 km^2 is covered with a grid of intersecting profiles with 5 km × 10 km pitch. The seabed terrain and GAs are very complex in this area and are strongly stratified within the range of 1000–6000 m and −65 mGal to +100 mGal, respectively.

Figure 6.11 shows a GA map based on marine measurements using a gravimetric system.

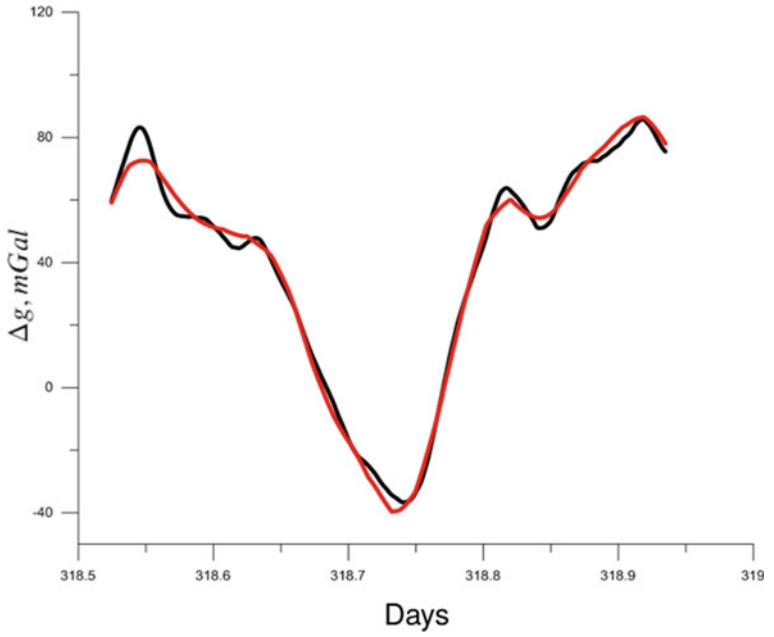

Fig. 6.10 Profiles of GA marine measurements (*black line*) and EGM2008 model (*red line*)

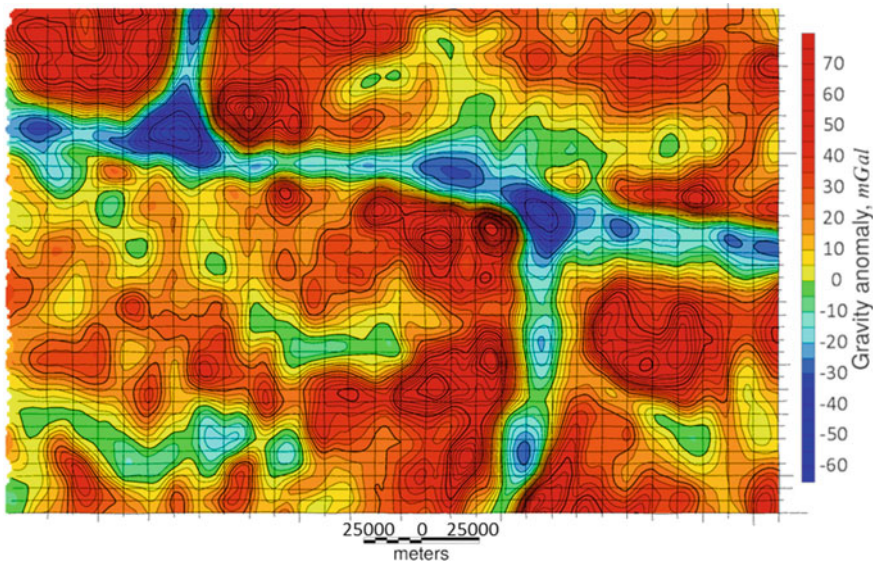

Fig. 6.11 GA map of the Kane Transform Fault. Lines show the site survey routes

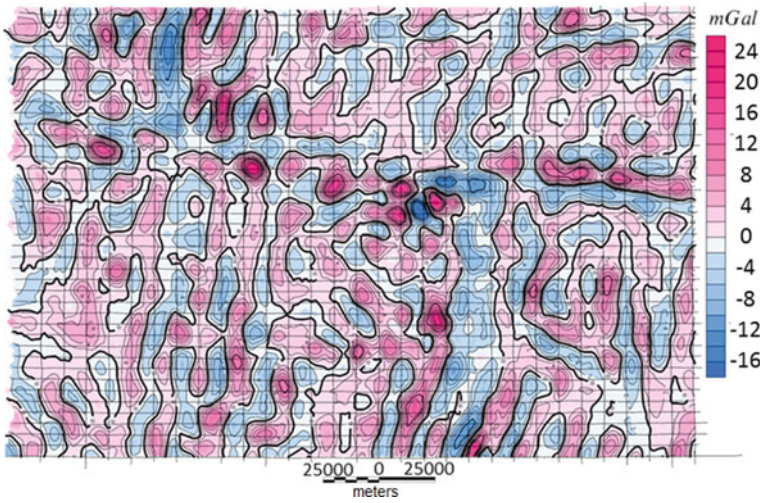

Fig. 6.12 Map of the differences between GA marine measurements and EGM2008 model for the Kane Transform Fault

The accuracy of the survey after adjustment is 0.35 mGal as estimated by residuals at 1230 crossover points. The accuracy of tying to the coastal point in Novorossiysk is not worse than 0.3 mGal as estimated by residuals between the output of marine gravimetric systems and the measurements at 5 reference stations in different ports. The differences between the GA measured values and the values of the EGM2008 model were calculated at all survey points with an interval of 1 min or 300 m. The mean value of this difference is 0.60 mGal, while the standard deviation is 3.97 mGal due to the strong stratification of the field.

Figure 6.12 shows a map of the differences between GA marine measurements and EGM2008 model, illustrating the model frequency distortion.

Experimental results show that the EGM2008 model can be used for monitoring the survey bias or tying the gravity survey to the model if there are no reliable reference values at the port of departure.

6.2.2 Method for Tying Marine Measurements to the Earth's Gravity Field Model

The method for tying the measurements to the EGF model at the post-processing stage involves several steps.

First, it is necessary to complete a cycle of gravimeter measurements processing. The initial knowledge of gravity in the port of departure can correspond to a normal field or another known value, and the value of the zero-point drift of the gravimeter is to be predicted.

Then, the difference Δ between the measured GAs and those taken from the EGM2008 model is calculated at all the site survey points. All the resulting residuals are sorted by time and approximated by a linear (or other) function which is then used to tie the measurements to the EGF model and to refine the zero-point drift rate.

The final step involves the survey adjustment and its accuracy estimation (Zheleznyak 2002).

The idea of monitoring the survey bias and tying the marine measurements to the EGM2008 model was tested during the fieldworks in the Indian Ocean, carried out in 2012–2013 using the Chekan-AM mobile gravimeter on three survey sites. Figure 6.13 shows the residuals between the measurements and the model on Site P1 located on the continental slope.

The normal gravity field value was used as the initial value at the reference point, and the processing was carried out without correcting the gravimeter zero-point drift. The coefficient for the linear term of the approximating function of these differences is +2.199 mGal/day. It has the physical meaning of the zero-point drift rate. The linear function obtained is used for tying the measurements to the GA values in the EGM2008 model, and for adjusting the gravimeter zero-point drift rate. The systematic difference between the survey lines and crosslines in this experiment was

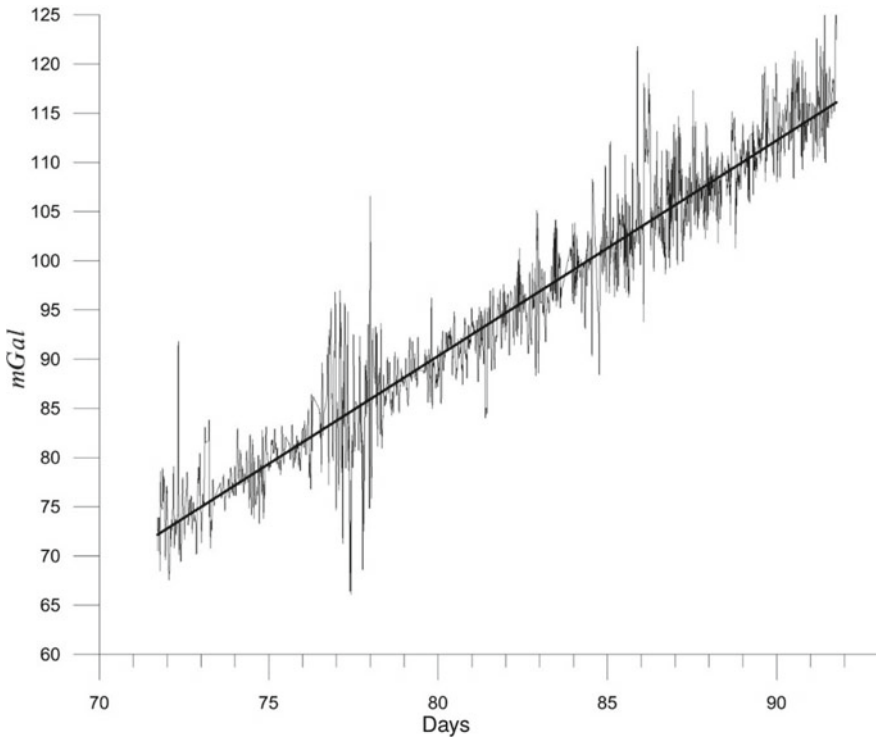

Fig. 6.13 Residuals between measurements and model on Site P1

0.08 mGal, and the random component was 0.25 mGal. After the crossover point adjustment, the random error was 0.17 mGal, and the average difference between the GAs and EGM2008 model values was –0.07 mGal.

According to the results of standard processing of measurements on Site P1 using the gravity values at the reference stations in the ports, the gravimeter zero-point drift rate was estimated at +2.184 mGal/day. The random error on Site P1 after adjustment was 0.17 mGal, and the average difference between the measured and model GA values was +2.12 mGal.

The parameters to be estimated in the experimental and standard versions of processing are almost the same except for the bias: –0.07 mGal and +2.12 mGal respectively. It may be both due to the errors in tying and due to the inaccuracy of the EGM2008 model on the continental slope.

Figure 6.14 shows a map of residuals between the measured and model GA values, illustrating the frequency distortions of the model on Site P1.

Site P2 of square shape with a side of 120 km was surveyed in the rift zone of the Mid-Ocean Ridge in the Indian Ocean. The residuals between the measured and model values for this site are shown in Fig. 6.15.

The residuals shown cannot be approximated by a linear function due to the nature of their occurrence. With an increase in perturbing accelerations above 200 Gal, a bias appeared in the gravimeter output, which was associated with its malfunction. A processing technique differing from the recommended one was used here. First, the

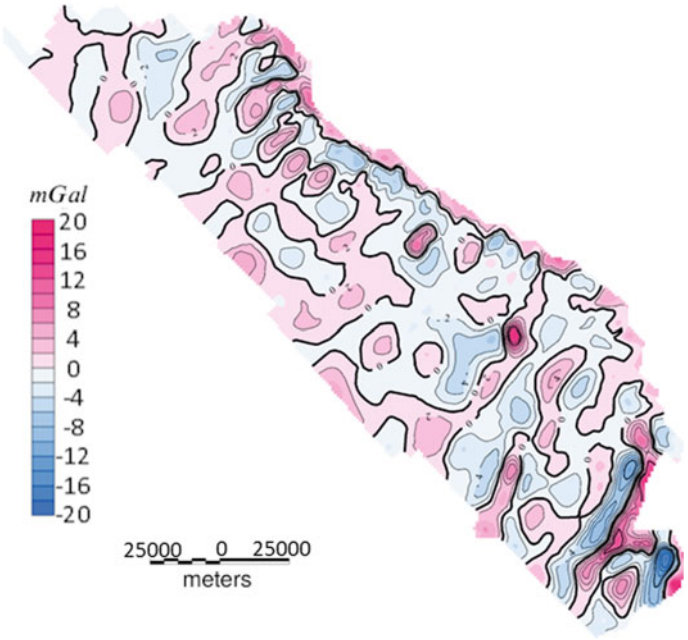

Fig. 6.14 Map of the residuals between measurements and model on Site P1

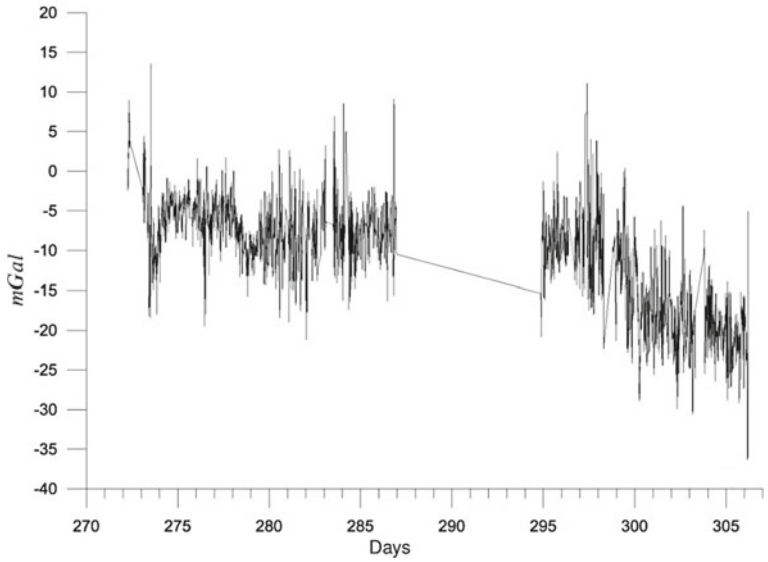

Fig. 6.15 Residuals between measurements and model on Site P2

site adjustment was performed. Then, the mean difference between the measurements and model was calculated for the entire site, after which it was used as a correction for all measurements. Table 6.21 shows the results of estimating the accuracy of measurements at different stages of data processing on Site P2.

The maps of the measured field values and their differences from the EGM2008 model on Site P2 are presented in Figs. 6.16 and 6.17.

It follows from the above processing results that it is possible to obtain satisfactory survey data using the EGM2008 model even under very adverse weather conditions and instrument malfunctions.

Another example of using the EGM2008 model to check the gravimeter operation is shown in Fig. 6.18.

It shows the difference between the measured and model GA values (black) on Site P3, and the results of the linear approximation of the recording intervals before and after the spike in the gravimeter output (red). Based on the plot of this difference, the time and magnitude of the spike could be determined. The spike occurred when

Table 6.21 Error estimates at different processing stages, mGal

Site P2	Number of crosslines	Systematic component	Random component	Deviation from the model
Primary processing	54	1.17	5.77	13.6
Adjustment and leveling	54	0.02	1.01	0.00

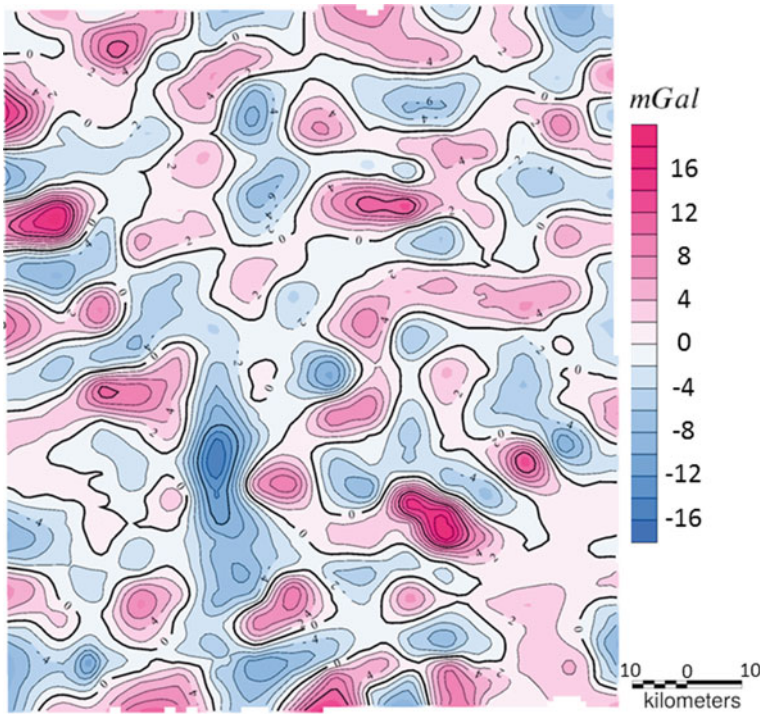

Fig. 6.16 Map of GA on Site P2, based on marine measurements

the vessel stopped for technical reasons and the measurements were suspended on Profile Line 34.

Figure 6.19 shows the position of Profile Line 34 (black line) and GA profile from the EGM2008 model (blue curve), Survey Line 34_1 before the spike (red curve), and Survey Line 34_2 after the spike (magenta curve).

A GA spike is observed in the zone of overlapping survey lines on Profile Line 34 which can be easily detected by comparing the measurements with the model. More precisely, the magnitude of this spike of +3.5 mGal corresponds to the crossover error. After correcting the spike, starting from Profile Line 34, the RMS error on Site P3 became equal to 0.15 mGal.

6.2.3 Conclusions

The use of the EGM2008 model makes it possible to conduct gravimetric surveys in remote waters of the World Ocean without tying to any onshore reference station; and to estimate and, if necessary, correct the data obtained in abnormal conditions.

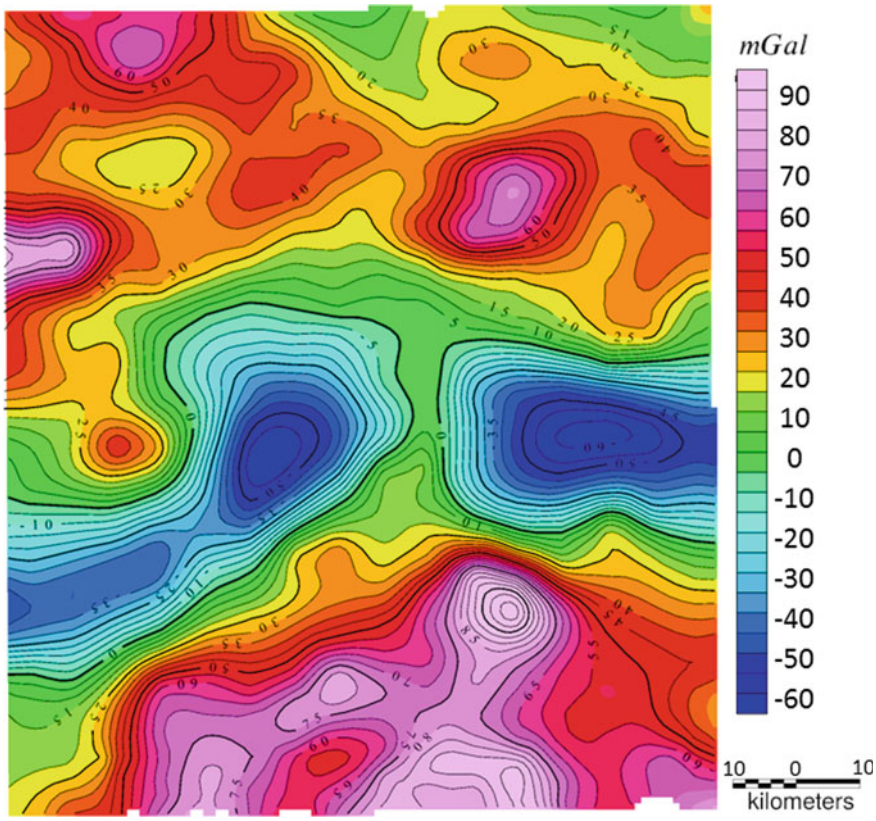

Fig. 6.17 Map of the residuals between measurements and model on Site P2

Using this survey method, the measurements can be processed offline directly on board the vessel in the absence of gravity reference stations in ports of call.

6.3 Map-Aided Navigation

The design of modern navigation systems generating the navigation parameters of moving vehicles, in particular, the coordinates and velocity components, is based on the integration of inertial and GNSS technologies [for example, see (Dmitriev et al. 1999; Stepanov 2002; Groves et al. 2006; Veremeenko et al. 2009; Grewal et al. 2013; Groves 2013; Emel'yantsev and Stepanov 2016)]. However, interest in navigation methods applicable to GNSS-denied environment has recently increased (Boreyko et al. 2008, 2010; Carreno et al. 2010; Adler et al. 2015; Vaman, 2014; Berkovich et al. 2016; Chernodarov 2016; Stepanov 2016). One of such methods is map-aided navigation based on the use of geophysical fields which, in particular,

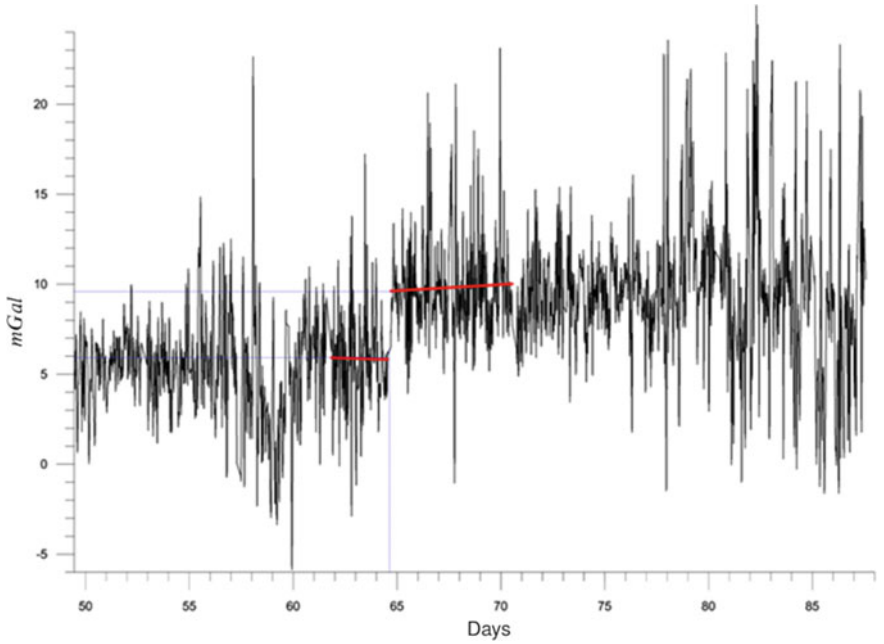

Fig. 6.18 Residuals between measurements and model on Site P3

include the gravity and the terrain fields (Lowrey and Shellenbarger 1997; Stepanov 1998; Bergman 1999; Berdyshev and Kostousov 2007; Nygren 2005; Karlsson and Gustafsson 2006; Teixeira 2007; Richeson 2008; Baklitski 2009; Veremeenko et al. 2009; Carreno 2010; Pavlov et al. 2010; Shcherbinin 2011; Afzal 2011; Meduna 2011; Shockley 2012; Beloglazov et al. 2012; Klyueva and Zav'yalov 2013; Toropov 2013; Dzhandzhgava et al. 2013; Vaman 2014; Avgustov et al. 2015; Stepanov and Toropov 2015, 2016; Karshakov et al. 2018; Klyueva 2016; Koneshov et al. 2016; Vyazmin et al. 2016; Melo and Matos 2017; Wu et al. 2017; Wei et al. 2017; Kiselev et al. 2017; Zhou et al. 2018; Dzhandzhgava and Avgustov 2018; Pasnani and Seto 2018; Kostousov and Tarkhanov 2019; González-García et al. 2020; Karshakov et al. 2018, 2021; Lee and Canciani 2020; Minligareev et al. 2020; Stepanov and Nosov 2020; Dunaevskaya et al. 2021). The idea of the method consists in the comparison of the field values measured by sensors installed on board a moving vehicle and the same values calculated using the available a priori information normally presented as a digital map or a field model.

Depending on the amount of information used, it is a common practice in Russia to classify systems in which the measurements are taken at a current time at a point, along a certain line, or from an area of a field, i.e., the measurements are actually presented as a frame or an image (Beloglazov et al. 1985; Stepanov et al. 2020). The specific feature of geophysical map-aided navigation is best manifested in the systems that use point information accumulating during the vehicle motion, which

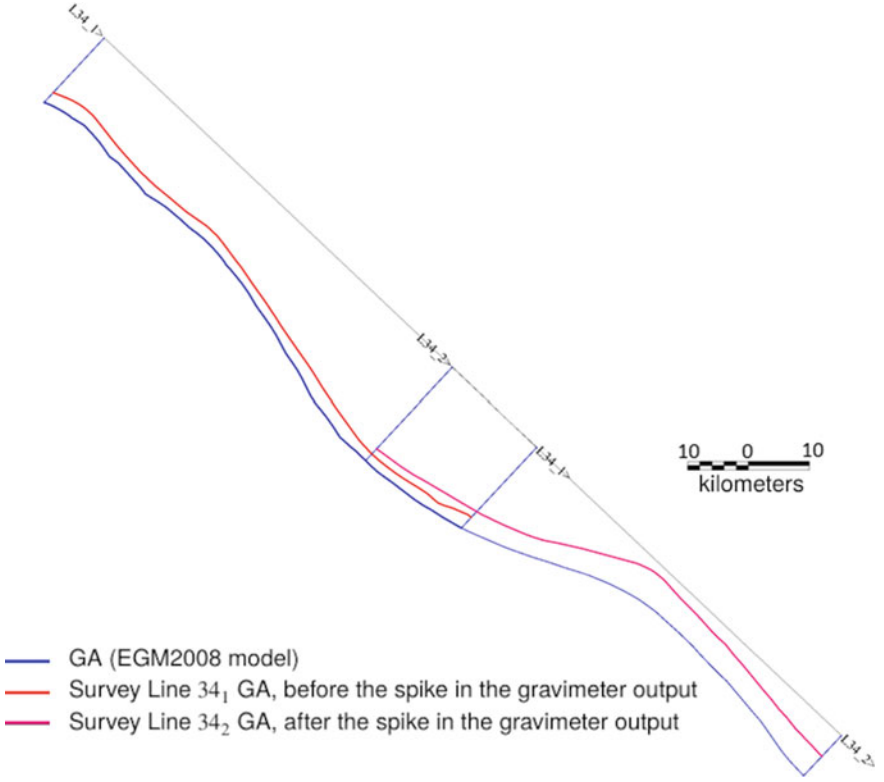

Fig. 6.19 GA plots based on the EGM2008 model and gravimeter measurements

means that the problem solution is a long-lasting process. This Section addresses the systems of this type.

Various approaches and methods have been applied to map-aided navigation. However, according to the authors of this Section, this problem appears to be considered most comprehensively within the Bayesian framework which is the basis for the stochastic estimation methods conventionally used in navigation data processing. Besides formulating and solving the problem of algorithm synthesis, these methods imply correct accuracy analysis.

The purpose of this Section is to review and compare Bayesian filtering algorithms used in solving the map-aided navigation problem based on geophysical fields. The Section relies heavily on the published studies in this area (Stepanov and Toropov 2015, 2016), with the focus made on illustrating the advantages and disadvantages of various algorithms.

6.3.1 Statement and General Solution of Map-Aided Navigation Problem Based on the Nonlinear Filtering Theory

Let us assume, without loss of generality, that the navigation parameters to be updated are the coordinates of a moving vehicle on a plane in a Cartesian coordinate system, and the problem is considered for the case of discrete time.

Thus, assume that on board the vehicle there is a navigation system (NS) that provides the estimates of its two-dimensional position in a plane $y_i^{NS} = \left[y_i^{(1)} \; y_i^{(2)} \right]^T$ at the i-th time points. There is also an additional sensor to measure the geophysical field (parameter) y_i, and the measurements can be written as

$$y_i^{NS} = X_i + \Delta y_i^{NS}, \tag{6.3.1}$$

$$y_i = \phi(X_i) + \Delta y_i, \tag{6.3.2}$$

where $X_i = \left[X_i^{(1)} \; X_i^{(2)} \right]^T$ is the true position of the vehicle in a Cartesian coordinate system; $\Delta y_i^{NS} = \left[\Delta y_i^{(1)} \; \Delta y_i^{(2)} \right]^T$ are the NS positioning errors; $\phi(X_i)$ is the function of the vector argument describing the dependence of the field used on coordinates; and Δy_i is the sensor error. These values are normally calculated using a function that allows calculating the field values at an arbitrary point in a given area with some error Δy_i^k relative to $\phi(X_i)$, i.e., $\phi^k(X_i) = \phi(X_i) + \Delta y_i^k$. As a rule, function $\phi^k(X_i)$ is formed using the available a priori information accumulated from the results of the preliminary field survey, and is given in the form of a digital map or using various analytical models, e.g. those described in Sect. 6.1. In view of the above, instead of (6.3.2), we can write:

$$y_i = \phi(X_i) + \Delta y_i = \phi^k(X_i) + \Delta y_i^{\Sigma}, \tag{6.3.3}$$

where $\Delta y_i^{\Sigma} = \Delta y_i - \Delta y_i^k$ is the cumulative error of the sensor and the field map.

The problem basically consists in obtaining the estimates of the NS errors $\Delta \hat{y}_i^{NS}$ and, if possible, the current characteristics of their accuracy, based on the available set of measurements (6.3.1), (6.3.3) with $i = 1, 2$. These estimates and characteristics could be further used for updating the NS output. In other words, it is necessary to solve the problem of the NS output correction using external nonlinear measurements (Stepanov 2017).

A general block diagram explaining the essence of the problem is given in Fig. 6.20 (Stepanov and Toropov 2015).

Let us consider the main features of the problem under discussion, which complicate the design of algorithms and their accuracy analysis.

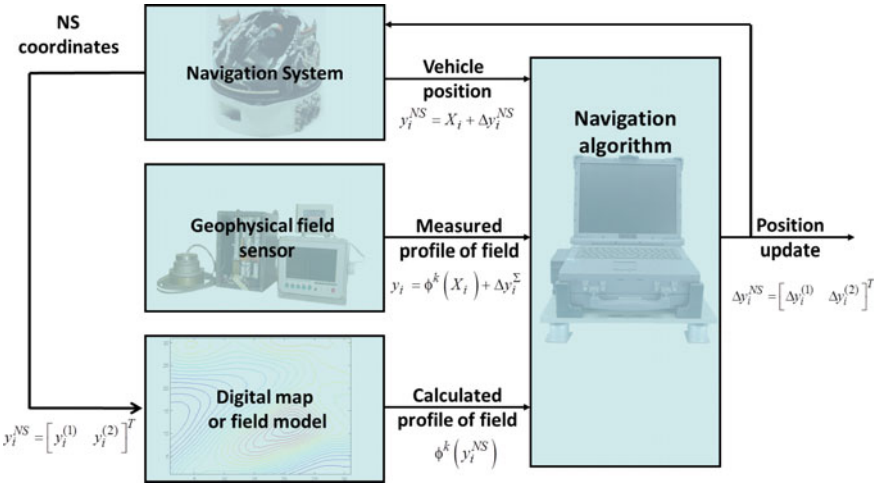

Fig. 6.20 Block diagram of a map-aided navigation system

1. The function $\phi^k(X_i)$ is nonlinear, and the area of a priori position uncertainty y_i^{NS} may be such that it is not always possible to accurately use the linearized representation for $\phi^k(X_i)$ obtained by applying Taylor series expansion with rejection of higher-order vanishing terms. This function can be formed with the use of preliminary survey data, or obtained analytically; to solve the problem, it is necessary, first, to build such a function and, second, to take into account the presence of errors of the field map along with those of the sensor.
2. Usually, to solve this problem, it is necessary to have an aided NS, and the map data are selected with respect to its output. Thus, in most cases only updating the output of this system is concerned.
3. To accumulate the information necessary for updating the position using a single scalar field, the vehicle is required to move in space, thus resulting in the long-term solution of the problem and, as a consequence, in the need to specify the models to take into account the time variability of the NS errors Δy_i^{NS} and Δy_i^{Σ}.
4. Positioning accuracy within a selected area of the field is essentially dependent on the length of the vehicle path, the field variation in its vicinity, the level of the map errors, the field sensor accuracy, and the level of a priori uncertainty of the position generated by the NS used. Thus, to improve the efficiency of NS correction, it is important that the paths are selected properly to ensure navigation with required accuracy. To do this, it is necessary to have a method for finding these paths, including a procedure for calculating the expected accuracy considering all the factors listed above.

Let us formulate the problem of map-aided navigation based on the Bayesian nonlinear filtering theory. For definiteness, we assume that the models of errors Δy_i^{NS} and Δy_i^{Σ} can be specified using two shaping filters for the vector sequences x_i^{NS}, x_i^{Σ} with dimensions n^{NS} and n^{Σ} (Stepanov and Toropov 2015):

$$x_i^{NS} = \Phi_i^{NS} x_{i-1}^{NS} + \Gamma_i^{NS} w_i^{NS}, \tag{6.3.4}$$

$$x_i^{\Sigma} = \Phi_i^{\Sigma} x_{i-1}^{\Sigma} + \Gamma_i^{\Sigma} w_i^{\Sigma}, \tag{6.3.5}$$

so that $\Delta y_i^{NS} = H_i^{NS} x_i^{NS}$, $\Delta y_i^{\Sigma} = H_i^{\Sigma} x_i^{\Sigma} + v_i^{\Sigma}$. In these equations, Φ_i^l, Γ_i^l, H_i^l are the known system matrix, noise matrix, and observation matrix; w_i^l is zero-mean system white-noise sequences with dimension p^l with covariance matrices Q_i^l, $l = NS,\ \Sigma$; v_i^{Σ} is the zero-mean white-noise component of the total errors of the map and the sensor with the covariance matrix R_i^{Σ}. For simplicity, it is assumed that these sequences are independent of each other and of the initial conditions. With the agreed notation, measurements (6.3.3) can be written as follows:

$$y_i = \phi^k\left(y_i^{NS} - H_i^{NS} x_i^{NS}\right) + H_i^{\Sigma} x_i^{\Sigma} + v_i^{\Sigma} = s_i\left(H_i^{NS} x_i^{NS}\right) + H_i^{\Sigma} x_i^{\Sigma} + v_i^{\Sigma}, \tag{6.3.6}$$

where $s_i\left(H_i^{NS} x_i^{NS}\right) = \phi^k\left(y_i^{NS} - H_i^{NS} x_i^{NS}\right)$.

Introducing the augmented vectors $x_i = \left[\left(x_i^{NS}\right)^T \left(x_i^{\Sigma}\right)^T\right]^T$, $w_i = \left[\left(w_i^{NS}\right)^T \left(w_i^{\Sigma}\right)^T\right]^T$, dimensions $n = n^{NS} + n^{\Sigma}$, $p = p^{NS} + p^{\Sigma}$ and functions $\tilde{s}_i\left(x_i^{NS}\right) = s_i\left(H_i^{NS} x_i^{NS}\right)$, $\tilde{\tilde{s}}_i(x_i) = \tilde{s}_i\left(x_i^{NS}\right) + H_i^{\Sigma} x_i^{\Sigma}$, it is possible to form the following equations for the state and the measurement vectors:

$$x_i = \Phi_i x_{i-1} + \Gamma_i w_i, \tag{6.3.7}$$

$$y_i = \tilde{\tilde{s}}_i(x_i) + v_i^{\Sigma}, \tag{6.3.8}$$

where Φ_i, Γ_i and w_i, v_i^{Σ} are formed according to (6.3.4), (6.3.5).

Now, after specifying the probability density functions (PDF) (hereinafter referred to as densities) $f\left(w_i^{NS}\right)$, $f\left(w_i^{\Sigma}\right)$, $f\left(v_i^{\Sigma}\right)$, $f(x_0)$, the nonlinear filtering problem can be formulated. Its purpose is to obtain, using the measurements $Y_i = [y_1, ..., y_i]^T$ collected by the current time i, a mean-square optimal estimate that minimizes the unconditional covariance matrix

$$G_i^{opt} = \iint \left\{\left(x_i - \hat{x}_i^{opt}(Y_i)\right)\left(x_i - \hat{x}_i^{opt}(Y_i)\right)^{\mathrm{T}}\right\} f(x_i, Y_i) dx_i dY_i, \tag{6.3.9}$$

where $f(x_i, y_i)$ is the joint PDF for vectors x_i and Y_i. Matrix minimization is understood in the sense that for any arbitrary estimate $\tilde{x}_i(Y_i)$ with a covariance matrix $\tilde{G}_i$, the inequality $G_i^{opt} \leq \tilde{G}_i$ holds true as an inequality for quadratic forms. It is well known that such an estimate and the current accuracy characteristic corresponding to it in the form of a conditional covariance matrix are determined using the following

formulas (Stratonovich 1968; Stepanov 1998; Bergman 1999; Yarlykov et al. 2004):

$$\hat{x}_i^{opt}(Y_i) = E_{x_i/Y_i}\{x_i\} = \int x_i f(x_i/Y_i)dx_i, \tag{6.3.10}$$

$$P_i^{opt}(Y_i) = E_{x_i/Y_i}\left\{\left(x_i - \hat{x}_i^{opt}(Y_i)\right)\left(x_i - \hat{x}_i^{opt}(Y_i)\right)^{\mathrm{T}}\right\}. \tag{6.3.11}$$

Here, $f(x_i/Y_i)$ is the a posteriori density, for which the following recurrence formula quite useful when solving the problem in consideration holds true:

$$f(x_i/Y_i) = \frac{f(y_i/x_i)f(x_i/Y_{i-1})}{\int f(y_i/x_i)f(x_i/Y_{i-1})dx_i}, \tag{6.3.12}$$

where $f(y_i/x_i)$ is the likelihood function obtained taking into account (6.3.8), and $f(x_i/Y_{i-1})$ is the prediction density determined as

$$f(x_i/Y_{i-1}) = \int f(x_i/x_{i-1})f(x_{i-1}/Y_{i-1})dx_{i-1}. \tag{6.3.13}$$

The transition density $f(x_i/x_{i-1})$ in this formula can be obtained using Eq. (6.3.7). In (6.3.10) and (6.3.11), integrals are understood as multiple ones with infinite limits, and E is an expectation sign with the subscript characterizing the probability density function for which it is taken.

Thus, the solution of the problem reduces to the calculation of multiple integrals (6.3.10), (6.3.11). Having the estimate x_i, the desired estimate Δy_i^{NS} and the corresponding accuracy characteristics can be easily found using the equality $\Delta y_i^{NS} = H_i^{NS} x_i^{NS}$.

Let us consider an example explaining the above equations.

Example 1 Assume that NS errors are described using Gaussian Wiener sequences, the field measurements are scalar, and the total errors of the map and the sensor are the sum of the slowly changing component, also specified as the Gaussian Wiener sequence, and the high-frequency component described by white Gaussian noise with the variances r_i^2. In other words, we assume that

$$\begin{aligned} x_i^{NS} &= x_{i-1}^{NS} + \Gamma^{NS} w_i^{NS}, \\ x_i^{\Sigma} &= x_{i-1}^{\Sigma} + q^{\Sigma} w_i^{\Sigma}, \\ y_i &= s_i\left(x_i^{NS}\right) + x_i^{\Sigma} + v_i^{\Sigma}, \end{aligned} \tag{6.3.14}$$

where $\Delta y_i^{NS} = x_i^{NS} = \left[x_{i,1}^{NS}\ x_{i,2}^{NS}\right]^T$, i.e., $H_i^{NS} = I_2$ (I_2 is an identity matrix with a dimension of 2×2), $s_i\left(x_i^{NS}\right) \equiv \tilde{s}_i\left(H_i^{NS} x_i^{NS}\right)$, $\Gamma_i^{NS} = q^{NS} I_2$, $\Delta y_i^{\Sigma} = x_i^{\Sigma} + v_i^{\Sigma}$, $\Phi_i^{HC} = I_2$, $\Phi_i^{\Sigma} = 1$, w_i^{NS}, w_i^{Σ} are two-dimensional and one-dimensional white noises with unit variances; q^{NS}, q^{Σ} are positive scalar values.

When refining the recurrence formulas (6.3.12), the likelihood function and the transition density under the assumptions made will be as follows:

$$f(y_i/x_i) = N\left(y_i; s_i(x_i), r_i^2\right), \;\; f(x_i/x_{i-1}) = N\left(x_i; x_{i-1}, diag\left\{q^{NS}, q^{NS}, q^{\Sigma}\right\}\right),$$

where $diag\left\{q^{NS}, q^{NS}, q^{\Sigma}\right\}$ is a diagonal matrix, on the main diagonal of which there are the elements indicated in brackets. It should be recalled that the notation $f(x) = N(x; \overline{x}, P)$ is used for the Gaussian vector with the expectation $\overline{x}$ and the covariance matrix P, i.e.,

$$f(x) = N(x; \overline{x}, P) = \frac{1}{(2\pi)^{n/2}\sqrt{\det P}} \exp\left(-\frac{1}{2}(x-\overline{x})^T P^{-1}(x-\overline{x})\right),$$

where n is the dimension of this vector.

The equation for the a posteriori density becomes much simpler if we assume that the NS position errors do not change while solving the problem, and there is no slowly changing component, i.e., $x_i^{NS} = x_{i-1}^{NS} = x^{NS}$, $x_i^{\Sigma} = 0$, $w_i^{NS} = 0$. Since $x_i^{\Sigma} = 0$, the state vector includes only NS errors, i.e., $x = x^{NS}$. Let us assume that a priori PDF for the initial state vector is a Gaussian one with independent components and variances σ^2, i.e., $f(x) = N\left(\begin{bmatrix} x_1 \\ x_2 \end{bmatrix}; \begin{bmatrix} 0 \\ 0 \end{bmatrix}, \begin{bmatrix} \sigma^2 & 0 \\ 0 & \sigma^2 \end{bmatrix}\right)$. In this case, we can write the following representation for the a posteriori density:

$$f(x/Y_i) = c \exp\left\{-\frac{1}{2}\left(\frac{x_1^2}{\sigma^2} + \frac{x_2^2}{\sigma^2} + \sum_{j=1}^{i} \frac{\left(y_j - s_j(x_1, x_2)\right)^2}{r_j^2}\right)\right\}, \qquad (6.3.15)$$

where c is a normalizing constant.

Figure 6.21 shows the behavior of the a posteriori density isolines when solving the navigation problem using a terrain field when the vehicle moves from the lower left to the upper right (Toropov 2013). It was assumed that the state vector included only NS errors, i.e. $x = x^{NS}$, and the formula for the a posteriori density was (6.3.15). The figure shows the isolines of the field and examples of isolines of a posteriori density (6.3.15) for different numbers of measurements. The "+" symbol indicates the true position of the vehicle, and the "∗" symbol indicates the position according to the NS output which was updated according to the results of the problem solution. Black lines indicate a posteriori confidence ellipses (Stepanov 2017).

Figure 6.22 shows the samples of a posteriori densities (6.3.15), the isolines of which are shown in Fig. 6.21.

It should be noted that the behavior of the a posteriori density for the first measurement corresponds to the behavior of the field isolines, the nonlinear nature of which in this area actually generates the nonlinearity of the problem under consideration.

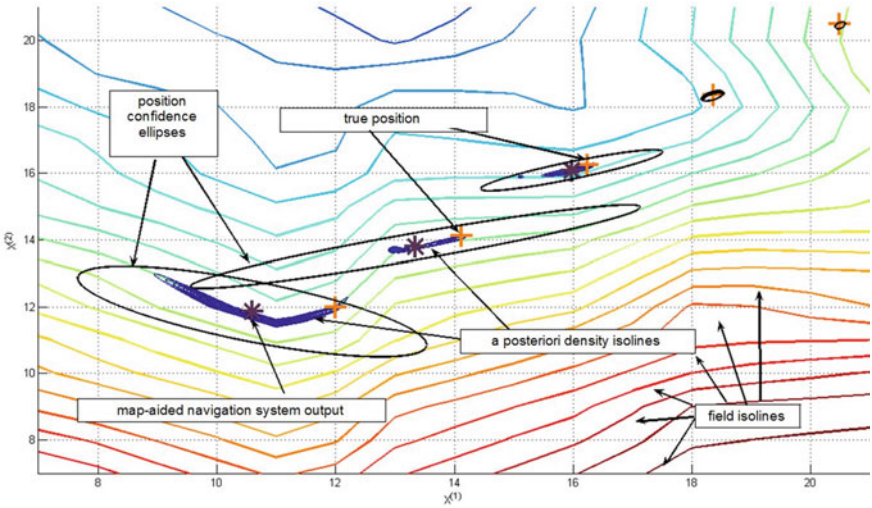

Fig. 6.21 Field isolines and an example of the solution to map-aided navigation problem

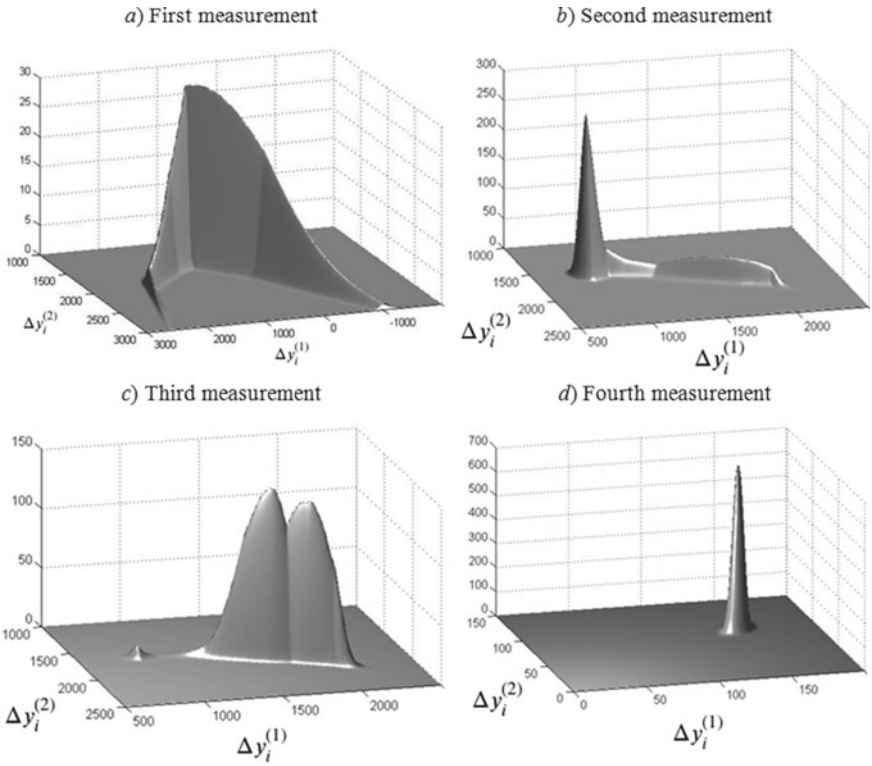

Fig. 6.22 Behavior of a posteriori density (15) with different numbers of measurements

When calculating the integrals (6.3.10), (6.3.11), it is necessary to specify the function $f(x_i/Y_i)$. To do so, various PDF approximations are used within the Bayesian framework. It should be noted that in addition to adequate representation of the function $f(x_i/Y_i)$, the chosen approximation should be convenient for the recursive solution of the problem.

According to (Stepanov and Toropov 2015), there are two main methods that can be distinguished among various approximation methods used, including in solving the problem under consideration. These two methods are defined by the following formulas:

$$f(x_i/Y_i) \approx \sum_{j=1}^{M} \omega_i^j N\left(x_i; \hat{x}_i^j, P_i^j\right), \tag{6.3.16}$$

$$f(x_i/Y_i) \approx \sum_{j=1}^{L} \mu_i^j \delta\left(x_i - x_i^j\right). \tag{6.3.17}$$

Here, μ_i^j, ω_i^j are the weights that ensure normalization of the densities on the left; $N\left(x_i; \hat{x}_i^j, P_i^j\right)$ are Gaussian densities with the expectations $\hat{x}_i^j$ and the covariance matrices P_i^j, $j = \overline{1.M}$; $\delta\left(x_i - x_i^j\right)$ is a set of delta functions for different grid nodes x_i^j, $j = \overline{1.L}$.

A special case of representation (6.3.16) for $M = 1$ corresponds to the Gaussian approximation of the a posteriori density generating the algorithms of the Kalman type. When $M > 1$, the density approximation is referred to as the Gaussian sum approximation of a posteriori density (Sorenson and Alspach 1971).

When points (grid nodes) x_i^j are selected deterministically in the (6.3.17) representation, the corresponding algorithm is called the point mass method (filter), or the grid method. If these nodes are chosen at random, various versions of the Monte Carlo method are obtained (Bucy and Senne 1971; Stepanov 1998; Bergman 1999; Toropov 2013; Stepanov and Toropov 2014).

Further we discuss the specifics of filtering algorithms based on the use of the above approximations.

6.3.2 *Algorithms Based on Gaussian Approximations*

Let us consider the algorithms generated by the density approximation using (6.3.16) for $M = 1$. Such a representation can be obtained, for example, based on linearization of a function describing a geophysical field $s_i\left(\Delta y_i^{NS}\right)$, i.e.,

$$s_i\left(\Delta y_i^{NS}\right) \approx s_i(0) + \left.\frac{\partial s_i\left(\Delta y_i^{NS}\right)}{\partial\left(\Delta y_i^{NS}\right)^T}\right|_{\Delta y_i^{NS}=0} \Delta y_i^{NS}, \tag{6.3.18}$$

where $s_i(0) = \phi^k\left(y_i^{NS}\right)$; $\left.\frac{\partial s_i\left(\Delta y_i^{NS}\right)}{\partial\left(\Delta y_i^{NS}\right)^T}\right|_{\Delta y_i^{NS}=0} = \left.\frac{\partial \phi^k\left(y_i^{NS}-\Delta y_i^{NS}\right)}{\partial\left(\Delta y_i^{NS}\right)^T}\right|_{\Delta y_i^{NS}=0}$.

and

$$\tilde{y}_i = y_i - s_i(0) \approx \left.\frac{\partial s_i\left(\Delta y_i^{NS}\right)}{\partial\left(\Delta y_i^{NS}\right)^T}\right|_{\Delta y_i^{NS}=0} \Delta y_i^{NS} + \Delta y_i^{\Sigma}. \tag{6.3.19}$$

The approximation of the nonlinear function in the form (6.3.18) makes it possible to use the linear Kalman filter for solving the problem of map-aided navigation. In the Russian literature these algorithms are often referred to as searchless estimation algorithms (Beloglazov et al. 1985).

Figure 6.23 illustrates two cases of the linearization procedure (6.3.18), (6.3.19) application in a one-dimensional problem. In the first case, the linearization point is chosen in such a way that the linear representation of the geophysical field profile reflects its real behavior around the true position of the vehicle. In this case, Kalman filter allows obtaining the correct estimate of the vehicle position. In the second case, the situation is different. Here, the linearization point is chosen improperly, and the resulting linear representation does not reflect the real behavior of the field near the true position, which results in algorithm divergence and significant estimation error.

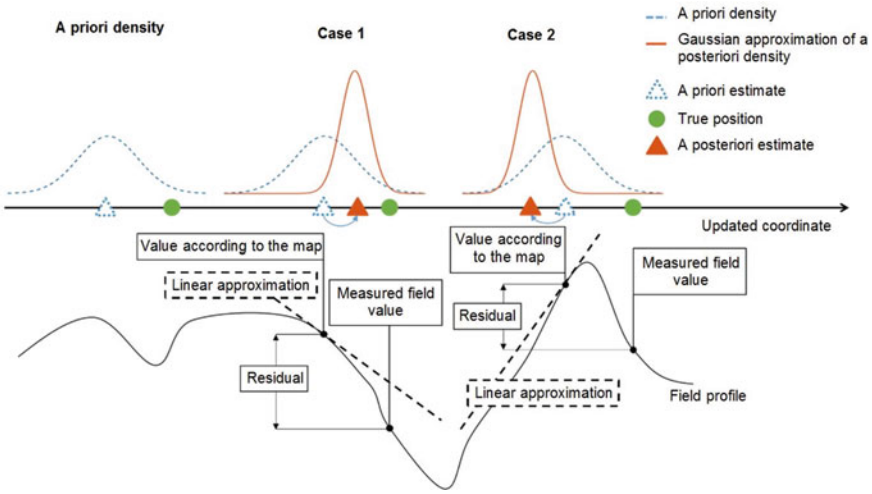

Fig. 6.23 Illustration of geophysical field linearization procedure

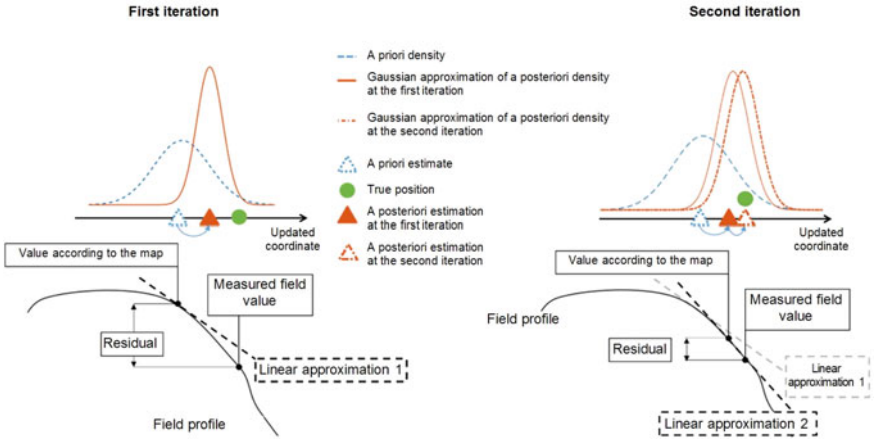

Fig. 6.24 Iterative linearization procedure

The diagrams presented in Fig. 6.23 show that the use of such algorithms in the case of nonlinear nature of the function $s_i\left(\Delta y_i^{NS}\right)$ is limited; the reason is that a linear field representation is inappropriate when there is a significant distance between the linearization point and the true value of the coordinate to be estimated.

The efficiency of approximation type (6.3.18) can be increased using various modifications of Kalman type filters, in particular, the so-called iterative algorithms that correct the linearization point (Yazwinski 1970; Dmitriev 1991; Simon 2006; Stepanov 2017). For this purpose, the same measurements are processed several times with the linearization point being changed at each iteration. The idea of an iterative algorithm is illustrated in Fig. 6.24. The left part of the figure shows the approximation of the function describing the behavior of the field (profile) used with conventional linearization (Linear approximation 1 in Fig. 6.24), and the right part shows the behavior after updating the linearization point based on the results of measurement processing at the first iteration.

In this case, such a procedure provides a more accurate description of the nonlinear function in the vicinity of the measurement point after adjusting the linearization point. At the same time, it should be noted that the use of an iterative procedure does not always result in a positive effect and, if the choice of the linearization point is improper, the filter may diverge, i.e., its error will increase with increasing number of measurements.

Filters using the so-called statistical linearization procedure were proposed in addition to the iterative algorithms (Gelb 1974). Such linearization differs from Taylor series expansion (6.3.18), (6.3.19) in that the derivative of the field is not used when a linear representation of a function describing the field is searched. The least squares method is used here for this purpose. It minimizes the difference between a nonlinear function and a linear counterpart in a priori uncertainty. The idea of this linearization method is explained in Fig. 6.25

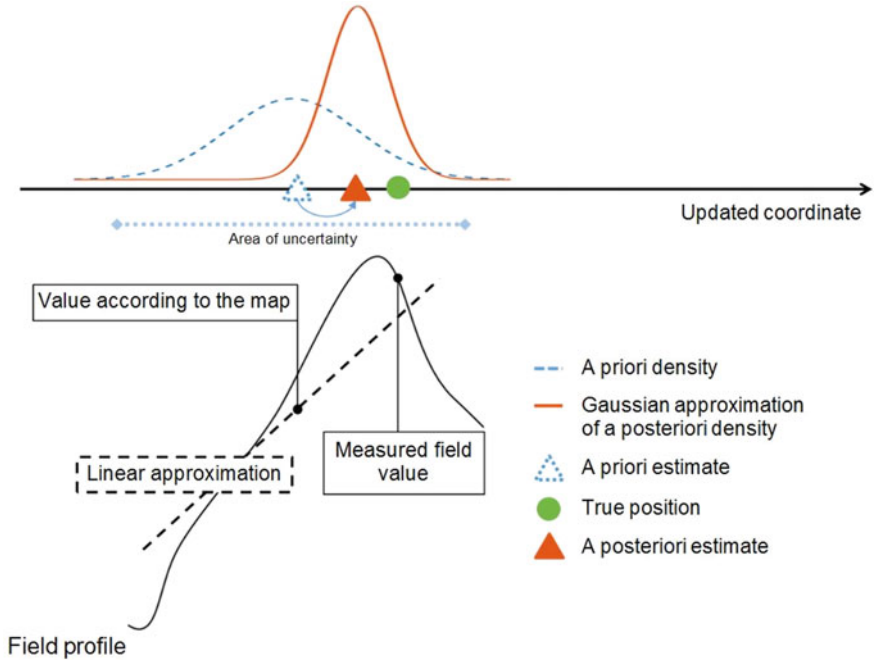

Fig. 6.25 Statistical linearization method

In addition to the aforementioned, a number of recently proposed "new" Kalman-type filters can be used to solve the problem under consideration, including the so-called Unscented Kalman Filter (UKF) and a number of other filters (Norgaard et al. 2000; Juiler and Uhlmann 2004; Li and Jilkov 2004; Metzger 2005; Simon 2006; Stepanov 2006; Ånonsen and Hallingstad 2007; Stepanov et al. 2007; Särkkä 2013; Candy 2016; Šimandl et al. 2016; Afshari et al. 2017), as well as filters similar to the above ones in terms of the design idea and based on the statistical linearization method (Gelb 1974; Lefebvre et al. 2005) and others (Luhtala et al. 2015; Stepanov et al. 2019, 2021a, b).

Example 2 As applied to Example 1 given above, Kalman filter-based algorithms are easy to obtain if the measurements in (6.3.14) are given as follows:

$$y_i \approx y_i^{KT} = H_i x_i + \overline{y}_i + v_i^{add} + v_i^{\Sigma},$$

where H_i is a three-dimensional row matrix, $\overline{y}_i$ is a known value, and v_i^{add} is a random quantity characterizing the error caused by the replacement of nonlinear measurements (6.3.8) by linear ones. Matrix H_i, value $\overline{y}_i$, and statistical characteristics v_i^{add} depend on the type of Kalman algorithm used. For example, when using an extended Kalman filter in which the prediction value of the state vector from the previous step is chosen as a linearization point (in this example, this value coincides with the

estimate from the previous step $\hat{x}_{i-1}^{NS}$), we have:

$$H_i = \left[\left. \frac{ds_i(x_i^{NS})}{dx_{i,1}^{NS}} \right|_{x_i^{NS}=\hat{x}_{i-1}^{NS}} \left. \frac{ds_i(x_i^{NS})}{dx_{i,2}^{NS}} \right|_{x_i^{NS}=\hat{x}_{i-1}^{NS}} 1 \right], \; v_i^{add} = 0, \; \overline{y}_i = s_i\left(\hat{x}_{i-1}^{NS}\right).$$

Using the standard procedures of the extended Kalman filter with the measurements $\tilde{y}_i = y_i - \overline{y}_i = H_i x_i + v_i^{add} + v_i^{\Sigma}$ and the model corresponding to the example in consideration, it is possible to find the desired estimate and covariance matrix.

The literature with more detailed description of the Kalman filter versions and their application to map-aided navigation can be found in (Stepanov and Toropov 2015, 2016).

6.3.3 *Algorithms Based on Gaussian Sum Approximations*

Kalman-type algorithms are easy to implement and do not require much calculations. Their main drawback is that all of them, in one way or another, are based on the Gaussian approximation of a posteriori density. It does not support possible multiextremal nature of the PDF associated with nonlinearity of the function $S_i\left(\Delta y_i^{NS}\right)$. To overcome this drawback, Gaussian sum approximation of a posteriori density, based on representation (6.3.16) with $M > 1$, can be used (Sorenson and Alspach 1971; Stepanov 1998). The parameters of partial Gaussian densities $N\left(x_i; \hat{x}_i^j, P_i^j\right)$ included in (6.3.16) can be found using a set of M Kalman filters (or their versions mentioned above) of the dimension $n = n^{NS} + n^{\Sigma}$ with corresponding linearization points. Rather simple formulas for the desired estimates and covariance matrices follow from (6.3.16):

$$\begin{aligned} \hat{x}_i^{opt}(Y_i) &\approx \hat{x}_i(Y_i) = \sum_{j=1}^{M} \omega_i^j \hat{x}_i^j, \\ P_i(Y_i) &\approx \sum_{j=1}^{M} \omega_i^j \left(\hat{x}_i^j \left(\hat{x}_i^j\right)^T + P_i^j \right) - \hat{x}_i(Y_i)\hat{x}_i^T(Y_i). \end{aligned} \tag{6.3.20}$$

Approximation (6.3.16) proved to be quite suitable for designing the map-aided navigation algorithms. A schematic illustration of the Gaussian sum approximation with several linearization points is shown in Fig. 6.26.

In contrast to conventional linearization, several linearization points are used here, each of which generates Gaussian approximation of a posteriori density in (6.3.16). This is exactly what determined the name of the corresponding algorithm proposed for solving the problem of map-aided navigation in (Dmitriev and Shimelevich 1978). The contribution of partial densities in representation (6.3.16) is determined by the weight which depends on the value of the likelihood function. Its value, in turn,

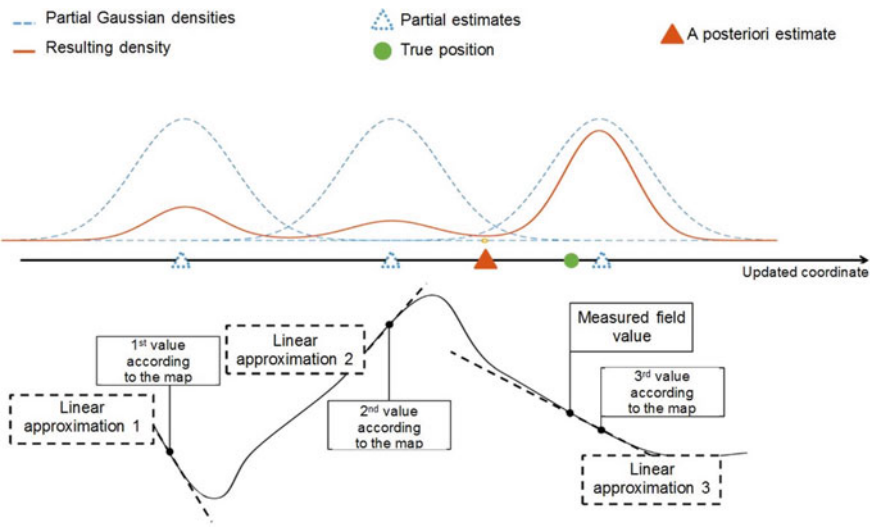

Fig. 6.26 Gaussian sum approximation example

depends on the residual between the measured and calculated field values. It is clear that in the case of several linearization points in the a priori uncertainty area, there is a high probability that one of the points will be chosen properly and the corresponding linear approximation will most likely show the actual behavior of the field in the vicinity of the measurement point. Figure 6.26 shows that the third linear approximation is the most apposite one.

The difficulty of implementing the algorithms arising from (6.3.16) is that the number of summands increases at each step when processing a recurrent measurement and presenting the likelihood function in a form similar to (6.3.16). Various methods based, for example, on occasional substitution of sum (6.3.16) with Gaussian density were proposed in order to limit them. More detailed information on the versions of these algorithms can be found in (Dmitriev 1991; Stepanov 1998).

6.3.4 Point Mass Method

The filtering algorithms based on approximation (6.3.16) do not always work effectively with high a priori uncertainty. In some cases, the filters converge to a single filter, and often to a point that does not correspond to the true position. This is what triggered the development of the algorithms based on approximation (6.3.17) which generated rather simple formulas for the estimate and the covariance matrix:

$$\hat{x}_i^{opt}(Y_i) \approx \hat{x}_i(Y_i) = \sum_{j=1}^{L} \mu_i^j x_i^j,$$

$$P_i^{opt}(Y_i) \approx P_i(Y_i) = \sum_{j=1}^{L} \mu_i^j \left(x_i^j \left(x_i^j \right)^T \right) - \hat{x}_i(Y_i)\hat{x}_i^T(Y_i), \tag{6.3.21}$$

where x_i^j, $j = \overline{1.L}$ are the grid nodes of vector x_i.

In the simplest case, when the vector $x_i = \left[\left(x_i^{NS}\right)^T \left(x_i^{\Sigma}\right)^T \right]^T = x$ is time-invariant, the point-mass filter makes it possible to find the weights in (6.3.17) according to the following equations:

$$\mu_i^j = \frac{\tilde{\mu}_i^j}{\sum_{j=1}^{L} \tilde{\mu}_i^j}, \quad \tilde{\mu}_i^j = f\left(y_i / x^j\right)\tilde{\mu}_{i-1}^j, \quad \tilde{\mu}_{i-1}^j = f\left(Y_{i-1} / x^j\right), \quad \tilde{\mu}_0^j = f\left(x^j\right), \tag{6.3.22}$$

where $f\left(y_i / x^j\right) = N\left(y_i; s_i\left(x^{NS\,j}\right) + H_i^{\Sigma}\left(x^{\Sigma}\right)^j, R^{\Sigma}\right)$. If the subvector x_i is time-varying, the weights are calculated using the below equations rather than (6.3.22) (Bucy and Senne 1971; Stepanov 1998):

$$\tilde{\mu}_i^j = f\left(y_i / x_i^j\right)\tilde{\mu}_{i,i=1}^j, \quad \tilde{\mu}_{i,i=1}^j = \sum_{k=1}^{L} \mu_{i-1}^k g_i^{jk}, \quad g_i^{jk} = \frac{f\left(x_i^j / x_{i-1}^k\right)}{\sum_{j=1}^{L} f\left(x_i^j / x_{i-1}^k\right)}.$$

These equations significantly increase the amount of computation due to double summation.

When designing the algorithms of the type discussed, it is very important that the density can be represented for the augmented vector $x_i = \left[\left(x_i^{NS}\right)^T \left(x_i^{\Sigma}\right)^T \right]^T$ as follows (Lainiotis 1976):

$$f(x_i / Y_i) = f\left(x_i^{NS} / Y_i\right) f\left(x_i^{\Sigma} / x_i^{NS}, Y_i\right). \tag{6.3.23}$$

It follows from models (6.3.7) that if the densities $f\left(w_i^{\Sigma}\right)$, $f\left(v_i^{\Sigma}\right)$, $f\left(x_0^{\Sigma}\right)$ are of Gaussian nature, it is generally possible to design efficient algorithms for optimal estimates and covariance matrices, based on a bank of Kalman filters of n^{Σ} dimension. This can be explained by the fact that for the fixed subvector x_i^{NS}, $i = 1, 2 \ldots$, the density $f\left(x_i^{\Sigma} / x_i^{NS}, Y_i\right)$ will be a Gaussian one, and its parameters can be found using Kalman filter.

Let us explain this by an example where the errors of the NS are time-invariant, i.e., $\Delta y_i^{NS} = x_i^{NS} = x_{i-1}^{NS} = x^{NS}$ (Stepanov 1998).

Example 3 We use approximation (6.3.17) for the subvector x^{NS}:

$$f\left(x^{NS}/Y_i\right) \approx \sum_{j=1}^{L} \mu_i^j \delta\left(x^{NS} - x^{NS\,j}\right).$$

Taking into account (6.3.23), we can write:

$$f(x_i/Y_i) \approx \sum_{j=1}^{L} \mu_i^j f\left(x_i^{\Sigma}/x^{NS\,j}, Y_i\right)\delta\left(x^{NS} - x^{NS\,j}\right). \tag{6.3.24}$$

Considering Gaussian-type densities $f\left(w_i^{\Sigma}\right)$, $f\left(v_i^{\Sigma}\right)$, $f\left(x_0^{\Sigma}\right)$, the densities

$$f\left(x_i^{\Sigma}/x^{NS\,j}, Y_i\right) = N\left(x_i^{\Sigma}, \hat{x}_i^{\Sigma}\left(x^{NS\,j}, Y_i\right), P_i^{\Sigma}\left(x^{NS\,j}\right)\right)$$

with different $j = 1, ..., L$ will also be Gaussian with the parameters $\hat{x}_i^{\Sigma}\left(x^{NS\,j}, Y_i\right)$ and $P_i^{\Sigma}\left(x^{NS\,j}\right)$. Thus, these parameters can be easily found with the use of a set (a bank) of recursive Kalman filters based on the measurements $\tilde{y}_i^j = y_i - s_i\left(x^{NS\,j}\right) = H_i^{\Sigma} x_i^{\Sigma} + v_i$ with the dimension n^{Σ}. As applied to model (6.3.14) in the absence of generating noise for the subvector x_i^{NS}, these formulas will be as follows:

$$\hat{x}_i^{\Sigma}\left(x^{NS\,j}, Y_i\right) = \hat{x}_{i-1}^{\Sigma}\left(x^{NS\,j}, Y_{i-1}\right) + K_i\left(\tilde{y}_i^j - \hat{x}_{i-1}^{\Sigma}\left(x^{NS\,j}, Y_{i-1}\right)\right), \hat{x}_0^{\Sigma} = \overline{x}_0^{\Sigma},$$

$$K_i = \frac{P_i^{\Sigma}\left(x^{NS\,j}\right)}{r_i^2}, P_i^{\Sigma}\left(x^{NS\,j}\right) = \frac{r_i^2 P_{i/i-1}^{\Sigma}\left(x^{NS\,j}\right)}{P_{i/i-1}^{\Sigma}\left(x^{NS\,j}\right) + r_i^2},$$

$$P_{i/i-1}^{\Sigma}\left(x^{NS\,j}\right) = P_{i-1}^{\Sigma}\left(x^{NS\,j}\right) + \left(q^{\Sigma}\right)^2, P_0^{\Sigma} = \left(\sigma_0^{\Sigma}\right)^2,$$

where $\overline{x}_0^{\Sigma}$, σ_0^{Σ} are a priori mathematical expectation and root-mean-square deviation for the vector x^{Σ}.

Having $\hat{x}_i^{\Sigma}\left(x^{NS\,j}, Y_i\right)$ and $P_i^{\Sigma}\left(x^{NS\,j}\right)$, it is possible to obtain recursive formulas for the weights as well:

$$\tilde{\mu}_i^j = \exp\left\{-\frac{1}{2}\frac{\left(y_i - s_i\left(x^{NS\,j}\right) - \hat{x}_{i-1}^{\Sigma}\left(x^{NS\,j}, Y_{i-1}\right)\right)^2}{r_i^2 + P_{i/i-1}^{\Sigma}\left(x^{NS\,j}\right)}\right\}\tilde{\mu}_{i-1}^j, \tilde{\mu}_0^j = f\left(x^{NS\,j}\right).$$

The method based on representation (6.3.23) was called the partitioning method in (Lainiotis 1976). A congenial method specifically developed for map-aided navigation is known in the Russian literature as the recurrence-search algorithm (Beloglazov et al. 1979).

6.3.5 Sequential Monte Carlo Methods

It should be noted that Monte Carlo method is widely used along with the point mass method in designing the algorithms using approximation (6.3.17). These methods are based on density approximation, where x_i^j, $j = \overline{1.L}$ is a set of samples of some independent random vectors. In particular, when using the simplest Monte Carlo method with a constant state vector $x_i = \left[\left(x_i^{NS}\right)^T \left(x_i^{\Sigma}\right)^T \right]^T = x$ the weights are determined using (6.3.22); however, the nodes x^j are formed by sampling the random vectors in accordance with the a priori density $f(x)$, and the formula for weights at the initial time point is defined as $\tilde{\mu}_0^j = 1/L$ (Stepanov 1998; Bergman 1999). When using the simplest Monte Carlo method with variable vector x_i, the relationships for the weights do not change, and the difference will be that the sample x_i^j, $j = \overline{1.L}$ is formed at each step in accordance with the density $f\left(x_i / x_{i-1} = x_{i-1}^j\right)$.

One of the advantages of the Monte-Carlo method is that it allows implementing a recursive approximation procedure (6.3.17) which is simpler than the point-mass method. The term *recursive* is taken to mean a procedure where density approximation like (6.3.17) at the i-th step is formed with the use of x_{i-1}^j sample and the weights are calculated using the data from the previous step.

Over the recent decades, the Monte Carlo method has developed rapidly in the form of its recursive versions called the sequential Monte Carlo methods or particle filters (Doucet et al. 2001). The main techniques that are used in the Monte Carlo method and increase its efficiency, including those applied to the map-aided navigation, are described below.

First, for approximation (6.3.17), it is important to choose a set of samples x_i^j to be used. These samples should be formed in the area where the values of a posteriori density are significantly above zero. To achieve this, the importance sampling method is widely used, which is aimed at exactly this way of samples formation (Stepanov 1998; Doucet et al. 2001). The technique that provides for importance sampling and recursive procedures for samples generation and weights calculation in Monte Carlo methods is called sequential importance sampling (Doucet et al. 2001).

Implementation of the sequential Monte Carlo methods brings up a problem of algorithm degeneration, which shows itself in the fact that only one weight will have a value close to one when time is increased, whereas the others will be close to zero (Doucet et al. 2001). This drawback is partially overcome by using a procedure referred to as sequential importance resampling or a bootstrap procedure. The essence of the bootstrap procedure as applied to the problem under consideration is that a new set of samples $\tilde{x}_i^j$, $j = \overline{1.L}$ is formed based on the set x_i^j ($j = \overline{1.L}$) in accordance with the discrete distribution (6.3.17), which allows for the following approximation instead of (6.3.17):

$$f(x_i / Y_i) \approx \frac{1}{L} \sum_{j=1}^{L} \delta\left(x_i - \tilde{x}_i^j\right). \tag{6.3.25}$$

It is important that the values $\tilde{x}_i^j$ are chosen from the previously generated set x_i^j, $j = \overline{1.L}$, which retains the possibility of recursive generation of samples x_i^j, $i = 1, 2...$ and, as a result, the capability of designing a recursive algorithm as a whole. An illustration of this procedure as applied to Example 1 discussed in Sect. 6.3.1 is shown in Fig. 6.27.

It is evident that this procedure allows a sample to be redistributed to the domain, where the a posteriori density is substantially different from zero, which determines its effectiveness.

A very important feature of the successive Monte-Carlo methods is that it is possible to use all the advantages of the a posteriori density representation as (6.3.23) not only for quasi-deterministic models for the vector x_i^{NS}, but also for models in the general form of Markov sequences (Doucet et al. 2001). This feature is successfully used in the development of map-aided navigation algorithms (Gustafsson et al. 2002; Gustafsson 2010; Stepanov and Toropov 2014).

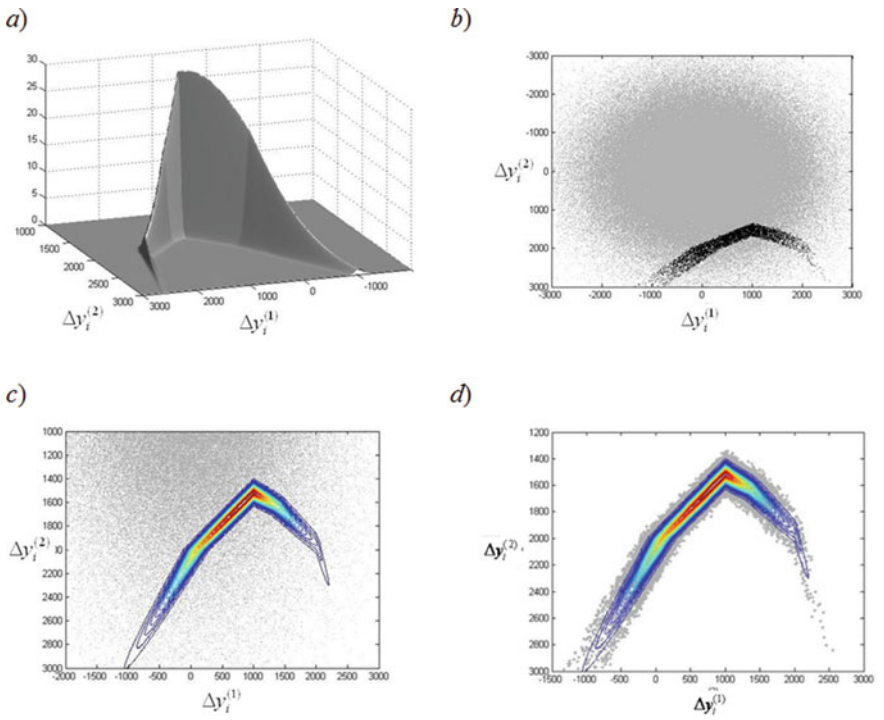

Fig. 6.27 Resampling procedure example: **a**—a posteriori density; **b**—gray and black: sampling before and after the resampling procedure; **c**—isolines of a posteriori density against the background of the sample prior to resampling; **d**—isolines of a posteriori density against the background of sampling after resampling

6.3.6 Analysis of the Accuracy of Filtering Algorithms

Unconditional covariance matrix (6.3.9) which quantitatively characterizes the potential estimation accuracy is normally used when analyzing the accuracy and comparing various estimation algorithms. This matrix can be calculated using the simulation as

$$G_i^{opt} \approx \tilde{G}_i^a = \frac{1}{L}\sum_{j=1}^{L}\left(x_i^j - \tilde{x}_i^j\left(Y_i^j\right)\right)\left(x_i^j - \tilde{x}_i^j\left(Y_i^j\right)\right)^{\mathrm{T}}, \tag{6.3.26}$$

where x_i^j, Y_i^j are the j-th samples ($j = \overline{1.L}$) of the estimated sequence and its corresponding measurements, obtained by modeling using (6.3.7), (6.3.8); $\tilde{x}_i^j\left(Y_i^j\right)$ is an estimate calculated using the algorithm under study. For unconditional covariance matrix (6.3.9), the formula $G_i^{opt} = \int P_i^{opt}(Y_i) f(Y_i) dY_i$ also holds true, from which it follows that it can be calculated using the formula

$$G_i^{opt} \approx \tilde{G}_i^b = \frac{1}{L}\sum_{j=1}^{L}\tilde{P}_i^j\left(Y_i^j\right), \tag{6.3.27}$$

where $\tilde{P}_i^j\left(Y_i^j\right)$ is the calculated covariance matrix of x_i^j estimation errors formed in the algorithm to be tested. The coincidence of $\tilde{G}_i^a$ and $\tilde{G}_i^b$ confirms the consistency of the results obtained.

Taking into account the fact that the described procedures require a significant amount of computation, the accuracy analysis in map-aided navigation often involves the Cramer–Rao inequality which makes it possible to calculate the theoretical lower bound (CRLB) for estimating the desired parameters (Stepanov 1998; Bergman 1999; Stepanov and Vasil'ev 2016). For model (6.3.7), (6.3.8), one of the versions of this inequality can be written as follows:

$$E_{x_i,Y_i}\left[\left(x_i - \hat{x}_i(Y_i)\right)\left(x_i - \hat{x}_i(Y_i)\right)^T\right] \geq J_i^{-1}, \tag{6.3.28}$$

where J_i is defined as

$$J_i = E_{x_i,Y_i}\left[\frac{d\ln f(x_i, Y_i)}{dx_i}\left(\frac{d\ln f(x_i, Y_i)}{dx_i}\right)^T\right]. \tag{6.3.29}$$

It is the diagonal elements of the matrix J_i^{-1} that determine the minimum possible variances for the parameters to be estimated. When using the Cramer–Rao inequality, it should be kept in mind that it allows finding only a theoretical bound which does

not have to be achieved by using an optimal algorithm. At the same time, the CRLB makes it easy to identify the areas of the geophysical field where it is impossible to obtain good navigation accuracy, which is of vital importance when choosing the paths that are recommended for NS position update (Stepanov 1998; Stepanov and Nosov 2021).

Example 4 Below is the explanation of the procedure for calculating the CRLB from the Example 1, assuming that the subvector x_i^{NS} does not change, i.e. $x_i^{NS} = x_{i-1}^{NS} = x = \left[x_1\ x_2\right]^T, x_i^{\Sigma} = 0$, the RMS error (RMSE) of measurements is constant $r_i = r_{i-1} = r$, and a priori functions of the density of the state vector and noise are Gaussian. In this case, matrix (6.3.29) is defined as

$$J_i = P_x^{-1} + \frac{1}{r^2}\int\left[\frac{dS_i^T(x)}{dx}\frac{dS_i(x)}{dx^{\mathrm{T}}}\right]f(x)dx, \tag{6.3.30}$$

where $S_i(x) = \left[s_1(x)\ \ldots\ s_i(x)\right]^T$; P_x is the a priori covariance matrix for the state vector; $\frac{dS_i^T(x)}{dx}$ is the derivative of the vector function of the vector argument (Stepanov 2017). The integrals $\int \frac{\partial s_j(x)}{\partial x_l}\frac{\partial s_j(x)}{\partial x_m}f(x)dx$, $j = 1, 2\ldots., l, m = \overline{1,2}$ in (6.3.30) can be found by Monte Carlo methods using the formula $\frac{1}{L}\sum_{k=1}^{L}\left.\frac{\partial s_j(x)}{\partial x_l}\right|_{x=x^k}\left.\frac{\partial s_j(x)}{\partial x_m}\right|_{x=x^k}$, where L is the number of samples, $x^k\ f(x)$, $k = \overline{1..L}$. With these data, the lower bound can be found by inversion of matrix J_i.

It is easy to notice that instead of (6.3.30), a convenient recursive equation can be used:

$$J_i = J_{i-1} + \frac{1}{r^2}\int\left[\frac{ds_i(x)}{dx}\frac{ds_i(x)}{dx^{\mathrm{T}}}\right]f(x)dx, \tag{6.3.31}$$

where $J_0 = P_x^{-1}$.

Based on (6.3.30), it is possible to derive a formula for approximate accuracy estimation using a certain geophysical field. Let us neglect the contribution of a priori information, i.e., the first term in (6.3.30), and assume that the scalar x is to be estimated, i.e., only one component of the coordinates is to be refined. We introduce a sample average gradient of the geophysical field:

$$\overline{h}_i = \sqrt{\frac{1}{i}\sum_{j=1}^{i}\int\left(\frac{\partial s_j(x)}{\partial x}\right)^2 f(x)dx}.$$

In this case, the following approximate formula for the RMSE corresponding to the CRLB can be written (Stepanov 1998):

$$\sigma_i^{lb} \approx \frac{r}{\overline{h}_i \sqrt{i}}, \tag{6.3.32}$$

from which it follows that the expected minimum possible positioning RMSE is determined by the ratio of the RMSE of the field measurement to its gradient.

6.3.7 Comparison of Filtering Algorithms

As an illustration, we present the simulation results that allow us to compare some of the above map-aided navigation algorithms based on the information about the seabed terrain field. The simulation uses a field with an average depth of 190 m and average gradients of 150 m/km and 100 m/km in two perpendicular directions. The field map was represented as a grid of field values in the nodes with a space Δ. The measurements were taken with the same interval during the simulation.

It was assumed that the NS errors did not change and there was no slowly changing component, i.e., $x_i^{NS} = x_{i-1}^{NS} = x^{NS}$, $x_i^{\Sigma} = 0$, $w_i^{NS} = 0$. The RMSE for the measurement noise was assumed to be 2% of the average depth of the sea.

The following algorithms were compared: the extended Kalman filter, the iterated Kalman filter, the unscented Kalman filter, the point-mass method, and the sequential Monte Carlo method.

Real and calculated covariance matrices of estimation errors in accordance with (6.3.26) and (6.3.27) were calculated to analyze the accuracy of these algorithms. The number of statistical tests for calculating these characteristics was chosen in the range of 10^4–10^6. The calculated RMSEs of the NS coordinates, which are the square roots of the matrix (6.3.27) diagonal elements, are denoted as $\tilde{\sigma}_{(1)}^{\mu}$ and $\tilde{\sigma}_{(2)}^{\mu}$, and the real RMSEs corresponding to matrix (6.3.26) are $\sigma_{(1)}^{\mu}$ and $\sigma_{(2)}^{\mu}$, where the superscript μ defines the algorithm, and subscripts (1), (2) are the components of the coordinates. Additionally, the CRLB was calculated.

The simulation results are presented in Table 6.22 (Toropov 2013). The table shows that for small areas of a priori uncertainty $\sigma_0 = 0.1\Delta$, the coordinate RMSEs for all algorithms almost coincide with each other and reach the CRLB. The accuracy coincidence for different algorithms is explained by the fact that the problem is almost linear in the given conditions.

As the area of a priori uncertainty ($\sigma_0 = 0.3 - 0.5\Delta$) increases, the difference in the RMSEs between the corresponding algorithms becomes noticeable. The difference in the estimation accuracy of coordinates components is due to the fact that the angles of the relief inclination along the route are different. With the assumptions made, the linearization-based algorithms (extended Kalman filter), in contrast to the unscented Kalman filter, do not allow obtaining a consistent accuracy characteristic. With the values $\sigma_0 \geq \Delta$, the a posteriori density becomes multi-extremal (as shown in Fig. 6.22). In this case, the difference between the RMSEs corresponding to the Kalman type algorithms and the RMSEs achieved using the point-mass method or

Table 6.22 Calculated and real RMSEs for various algorithms, in fractions of 0.1 Δ

σ_0 in fractions of Δ	RMSE	Algorithm used				
		Extended Kalman filter	Iterated Kalman filter	Unscented Kalman Filter	Point-mass method, Monte Carlo method	CRLB
0.1	$\sigma^{\mu}_{(1)}/\tilde{\sigma}^{\mu}_{(1)}$	7/7	7/7	7/7	7/7	7
	$\sigma^{\mu}_{(2)}/\tilde{\sigma}^{\mu}_{(2)}$	6/6	6/6	6/6	6/6	6
0.3	$\sigma^{\mu}_{(1)}/\tilde{\sigma}^{\mu}_{(1)}$	8/8	8/8	8/8	8/8	7
	$\sigma^{\mu}_{(2)}/\tilde{\sigma}^{\mu}_{(2)}$	10/9	10/9	10/10	9/9	8
0.5	$\sigma^{\mu}_{(1)}/\tilde{\sigma}^{\mu}_{(1)}$	9/8	8/8	8/8	8/8	7
	$\sigma^{\mu}_{(2)}/\tilde{\sigma}^{\mu}_{(2)}$	14/10	12/11	12/11	11/11	7
1	$\sigma^{\mu}_{(1)}/\tilde{\sigma}^{\mu}_{(1)}$	20/8	16/8	14/10	9/9	6
	$\sigma^{\mu}_{(2)}/\tilde{\sigma}^{\mu}_{(2)}$	33/12	25/12	19/18	13/13	10
1.4	$\sigma^{\mu}_{(1)}/\tilde{\sigma}^{\mu}_{(1)}$	40/8	33/9	24/16	10/10	8
	$\sigma^{\mu}_{(2)}/\tilde{\sigma}^{\mu}_{(2)}$	68/12	51/12	34/27	15/15	9

the Monte Carlo method is noticeable, and the calculated accuracy characteristic generated in the Kalman-type algorithms is not equal to the real value. Thus, the Kalman-type algorithms do not always provide an accurate solution to the problem. At the same time, the algorithms based on the point-mass method and Monte Carlo methods are effective in all the cases considered and produce a consistent accuracy characteristic.

When designing the algorithms for map-aided navigation, it is very important to take into account the variability of the vector x_i. For example, as shown in (Toropov 2013), if the variability of NS errors is neglected in NS error model, this can result in the algorithm divergence manifested in a significant difference between the calculated and real accuracy characteristics. This fact is illustrated in Fig. 6.28, where the results are shown for the case when a dead-reckoning system is used as NS. The positioning errors of this system are described as integrals of the speed errors defined by Markov processes of the first order. Figure 6.28a shows the dependence of the real and calculated RMSE for estimating the error by one of the coordinates taking into account variability using sequential Monte Carlo methods. Figure 6.28b shows the same without taking into account the variability. It is obvious that the difference between the calculated accuracy and the real accuracy is over 200% in the second case.

It should be noted that the point-pass method becomes more cumbersome when solving a problem with a variable vector x_i due to the need to perform double summation when calculating the weights, which is not required in the Monte Carlo method. In addition, the idea of representing the density in the form of (6.3.23) jointly with the point-pass method becomes difficult to implement (Stepanov and Toropov 2010).

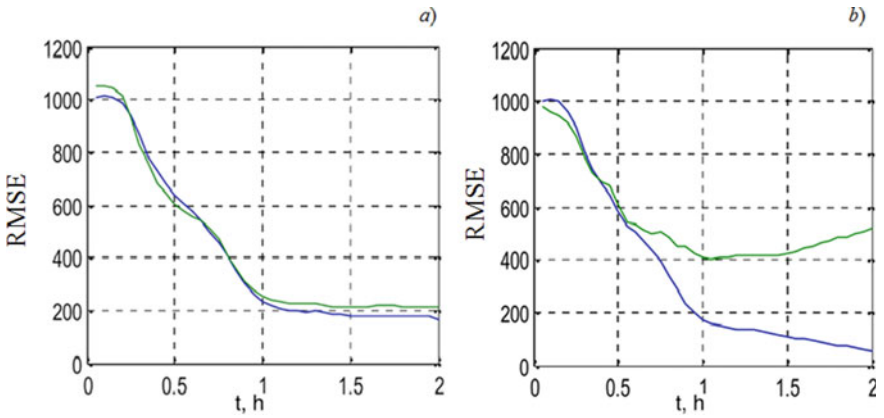

Fig. 6.28 The results of solving the map-aided navigation problem with (**a**) and without (**b**) consideration for the variability of the estimated vector. The blue curves show the calculated accuracy characteristics, the green curves show the real ones

Thus, the use of various versions of sequential Monte Carlo methods is preferable in this situation.

6.3.8 Conclusions

Within the Bayesian framework, the problem of map-aided navigation has been considered as a nonlinear filtering problem which takes into account all its specific features; in particular, its nonlinear and prolonged nature. A corresponding problem statement has been given, and an overview of filtering algorithms based on various types of a posteriori PDF approximation has been presented. The considered algorithms have been compared to each other.

It has been shown that the effectiveness of filtering algorithms depends directly on the level of a priori position uncertainty. When it is high, Kalman-type algorithms can lead to significant losses in accuracy and to inconsistent calculated accuracy characteristics. It has been stated that the most efficient algorithms for solving the problem of map-aided navigation are based on sequential Monte Carlo methods.

6.4 Estimating the Navigation Informativity of the Earth's Gravity Field

When solving the problem of map-aided navigation (Beloglazov et al. 1985; Dzhandzhgava et al. 2013; Avgustov et al. 2015; Stepanov and Toropov 2015), using the Earth's gravity field (EGF), it is important, as noted in the previous Section, to

choose the area of the field that is suitable for position updating. At the same time, a certain generalized factor characterizing its navigation informativity may correspond to each spatial domain of the EGF. Navigation informativity estimates can be used for plotting the traffic routes and removing the insufficiently informative areas from the solution of the navigation problem. The issues associated with the informativity estimation of the gravity field and other physical fields of the Earth were addressed in a number of Russian and international publications (Stepanov 1998; Richeson 2008; Dzhandzhgava et al. 2013; Wang et al. 2013; Stepanov and Nosov 2021; Kalinovskii et al. 2015). Obtaining relevant estimates generally involves the choice of characteristics and criteria of navigation informativity as well as an appropriate EGF model. As follows from the materials of Sect. 6.1, a number of new global EGF models with enhanced accuracy and spatial resolution have been created in recent years. This Section contains an analysis of potential use of these models for estimating the navigation informativity of EGF.

6.4.1 Choosing a Model of the Earth's Gravity Field

The factors determining an EGF model choice for the estimation of its navigation informativity include the geographical location, the area of the survey site or route, the height or the depth of the surface for which the navigation informativity is estimated; the scope of EGF parameters to be measured, the accuracy, the sample rate, the measurement data averaging interval, as well as acceptable accuracy characteristics of the model itself and the laboriousness of its numerical implementation.

Navigation problems can be solved in areas (on routes) of considerable lengths (up to several thousand kilometers), located in different parts of the globe and at different altitudes. The EGF parameters to be measured may include various functionals of the perturbing potential, such as gravity anomalies (GAs), deflections of the vertical (DOV), and second derivatives of the gravity potential (SDGP). The accuracy characteristics of measurement information have been steadily increasing. Therefore, the navigation informativity should be estimated with the use of modern EGF models in the form of spherical harmonics of the gravity potential, based on the combination of various geodetic data. Such models are global, universal, and can serve as a consolidated source of information on the EGF navigation properties in different parts of the globe. Special focus is made on the EGF informativity in the oceans, since in this part of the globe there are limited options of using other geophysical fields which may be more informative on land in comparison with the EGF, for example, radar contrast fields, surface relief fields, or optical fields (Beloglazov et al. 1985).

As shown in Sect. 6.1, due to the progress in space geodesy and gravimetric coverage of the globe in recent years, a number of new models of this class have been created abroad. The new models have much better accuracy and spatial resolution: EGM2008 ($N = 2190$), EIGEN-6C ($N = 1420$), EIGEN-6C2 ($N = 1949$), EIGEN-6C3 ($N = 1949$), EIGEN-6C4 ($N = 2190$), GECO-2014 ($N = 2190$), where N is the highest degree of the geopotential spherical harmonics. The international experience

shows that the EGM2008 model by the US National Geospatial-Intelligence Agency has received the widest international recognition (Pavlis et al. 2012). This is due to its fairly high accuracy and the formal status of a model which supports the world geocentric coordinate system WGS-84. Thus, EGM2008 can be considered as the basic option in choosing a computational model for estimating the EGF navigation informativity.

6.4.2 *Methods for Estimating the Navigation Informativity of the Earth's Gravity Field*

The analysis of the current situation with the application of gravity and other physical fields of the Earth to autonomous navigation has shown that there are no unified approaches to the estimation of navigation informativity of these fields today. Section 6.3 mentions that the expected accuracy of navigation which essentially characterizes the navigation informativity can be estimated using a value representing the ratio of the field measurement error to the value of this field gradient. The values of the variance D_z and the radius (interval) of correlation ρ_z which characterize the vertical and horizontal stratification of the parameter (z) under study, respectively, can also be used as indicators of the navigation informativity of the EGF parameters. It is these characteristics that will be used in this subsection. It should be noted that, given the values of D_z and ρ_z, it is possible to approximately estimate the value of the gradient using the expression $\sqrt{D_z}/\rho_z$, so the above-mentioned informativity characteristics are interrelated to some extent.

These values are determined through the autocorrelation function (ACF) of the parameter $Z - C_{zz}(P, Q)$, where P, Q are sample points of the studied area. Using the traditional approach to the correlation analysis of the EGF, distribution of the parameter z can be considered as a random field which is ergodic, stationary in a broad sense, and isotropic. Under these simplifying assumptions, the ACF can be interpreted as a function of one variable $C_{zz}(r)$, where r is the distance between the sample points. The correlation interval is the distance ρ_z, for which

$$C_{zz}(\rho_z) = \alpha D_z, \tag{6.4.1}$$

where α is some significance coefficient ($0 < \alpha < 1$). For commonly used exponential-type ACFs, it is normally assumed that $\alpha = 1/e \approx 0.37$ (Levitskaya 1988). Another fairly common option is $\alpha = 1/2$. In the general case, the interval from 0.3 to 0.5 is a suitable range of permissible values for the significance coefficient α.

In practice, determination of D_z and ρ_z is reduced to the calculation of the empirical ACF $C_{zz}(r)$ with $r \in [0, r_{\max}]$, based on specified model values of the parameter Z, the assignment of a value $C_{zz}(0)$ to D_z, and approximate solution of Eq. (6.4.1) using a set of discrete values of the empirical ACF.

The problem of building an empirical ACF is conveniently solved on a plane. This is done by choosing an appropriate system of planimetric rectangular coordinates x, y. The values of the parameter z specified at the nodes of a uniform grid of lines in this coordinate system are used as source data.

In the simplest case, D_z and ρ_z are estimated using the values of the empirical ACF on the route (or the route segment) oriented along one of the axes of the specified coordinate system. Assume that, for definiteness, the route coincides with axis x and the ACF is constructed using the values $z_1, z_2, ..., z_N$ of parameter z in N grid points, respectively, $x_0, x_1, ..., x_{N-1}$, where $x_k = k\Delta x$ ($k = 0, 1, ..., N-1$; Δx is the grid step along axis x). The ACF values for this route can be calculated by the following formulas (Pellinen and Neyman 1980):

$$C'_{zz}(x_k) = \frac{1}{N-k}\sum_{i=1}^{N-k}(z_i - \overline{z})(z_{i+k} - \overline{z}), \tag{6.4.2}$$

$$\overline{z} = \frac{1}{N}\sum_{i=1}^{N} z_i, \tag{6.4.3}$$

where $\overline{z}$ is a sample average of the initial values of the parameter z on the survey route segment. The index k takes values from 0 to n, where n is the integer part of the number $N/2$. Note that formulas (6.4.2), (6.4.3) make it possible to obtain values of a route ACF for any grid line that is parallel to axis x.

This example can be expanded to the construction of an areal ACF in the direction of axis x. The following formulas can be used for that:

$$C'_{zz}(x_k) = \frac{1}{(N-k)M}\sum_{j=1}^{M}\sum_{i=1}^{N-k}\left(z_{i,j} - \overline{\overline{z}}\right)\left(z_{i+k,j} - \overline{\overline{z}}\right), \tag{6.4.4}$$

$$\overline{\overline{z}} = \frac{1}{M}\sum_{j=1}^{M}\overline{z}_j, \tag{6.4.5}$$

where $z_{1,j}, z_{2,j}, ..., z_{N,j}$ are the values of the parameter z along the j-th line of the grid ($j = 1, 2, ..., M$); $\overline{z}_j$ is their average value determined by Eq. (6.4.3); M is the number of grid lines in the given direction. Obviously, formulas (6.4.2) and (6.4.3) are special cases of formulas (6.4.4), (6.4.5) for M = 1.

The resulting ACF values $C'_{zz}(x_0), C'_{zz}(x_1), ..., C'_{zz}(x_n)$ are used for the subsequent estimation of variance $D'_z = C'_{zz}(x_0)$ and correlation radius ρ'_z, assuming that N is sufficient to solve this problem, i.e. $C'_{zz}(x_n) > \alpha D'_z$.

Alternatively, the problem is solved along the grid lines parallel to axis y. The ACF values are calculated using the same formulas with x replaced with y, and Δx replaced with Δy, where Δy is the grid size along the axis y; and also with interchanges $N \leftrightarrow M$ and $i \leftrightarrow j$. Having them as an array $C''_{zz}(y_0), C''_{zz}(y_1), ..., C''_{zz}(y_m)$, where

m is the integer part of the number $M/2$, it is possible to find the corresponding values of the variance $D_z'' = C_{zz}''(y_0)$ and the correlation radius ρ_z''.

It is easy to verify that the variance estimates in two versions should coincide $\left(D_z' = D_z''\right)$. On the other hand, in the general case, the values of ρ_z' and ρ_z'' do not have to be the same, as evidenced by the results of experimental calculations. The discrepancy between the ρ_z' and ρ_z'' estimates may be due to the actual anisotropy of the field.

The integral estimate of the correlation radius over the area can be obtained either by weighted averaging of the ρ_z' and ρ_z'' values, for example, using the formula (with $\Delta x = \Delta y$)

$$\rho_z = \frac{N\rho_z' + M\rho_z''}{M+N}, \tag{6.4.6}$$

or by using the integral values of the ACF which can be obtained in different ways, either as the weighted average of $C_{zz}'(x)$ and $C_{zz}''(y)$ with the same values of the arguments, by generalizing formulas (6.4.2)–(6.4.5), or by using the spectral approach.

In the first method, assuming again that $\Delta x = \Delta y$ and $x_k = y_k = r_k$, the averaged ACF values can be obtained by the following formula (Pellinen and Neyman 1980):

$$C_{zz}(r_k) = \frac{(N-k)MC_{zz}(x_k) + (M-k)NC_{zz}''(y_k)}{(N-k)M + (M-k)N}. \tag{6.4.7}$$

In the second method, the following formula (Dem'yanov and Savel'yeva 2010) can be used as a generalized formula:

$$C_{zz}(r_k) \equiv \frac{1}{N_k}\sum_{i=1}^{N_k} z(P_{ik})z(Q_{ik}) - \frac{1}{N_k^2}\sum_{i=1}^{N_k} z(P_{ik})\sum_{i=1}^{N_k} z(Q_{ik}), \tag{6.4.8}$$

where P_{ik}, Q_{ik} is the i-th pair of points separated by a distance equal to the specified value r_k (within permissible deviations); N_k is the number of such pairs.

In the third case, the algorithm for calculating the ACF integral values can be formed on the basis of the following equations (Serkerov 1986):

$$C_{zz}(r_k) = \sum_{p=0}^{M-1}\sum_{\substack{q=0 \\ (p+q>0)}}^{N-1} Z_{pq}Z_{pq}^* J_0\left(r_k\sqrt{u_p^2+v_q^2}\right)\sqrt{u_p^2+v_q^2}, \tag{6.4.9}$$

$$Z_{pq} = \frac{1}{\sqrt{MN}}\sum_{m=0}^{M-1}\sum_{n=0}^{N-1} z(x_m, y_n)\exp\left[i2\pi\left(\frac{np}{N}+\frac{mq}{M}\right)\right], \tag{6.4.10}$$

where J_0 is the zero-order Bessel function of the first kind; u_p, v_q are the values of angular frequencies ($u_p = 2\pi p/N\Delta x$, $v_q = 2\pi q/M\Delta y$); $\{Z_{pq}\}_{M\times N}$ are Fourier coefficients of zero-mean values of the initial function (asterisked terms are their complex conjugated values); i is an imaginary unit.

The described methods for estimating the variance and the correlation radius in relatively large areas can provide the results that are not detailed enough for the navigation informativity awareness. In such cases, it is advisable to divide the initial area into smaller sections and estimate D_z and ρ_z for each of them, that is, to apply moving-average estimation of the variance and correlation radius (both for route and site survey estimates). To provide more detail, these areas can overlap.

Sections with $D_z \geq D_z^*$ and (or) $\rho_z \leq \rho_z^*$, where D_z^* and ρ_z^* are specified threshold values, can be considered informative. Thus, the sections for which these conditions do not hold should be considered unsuitable for map-aided navigation. The threshold values of variance should be sufficiently high because only the areas with high enough variability of the field can be considered informative. According to rough estimates that take into account the achieved accuracy characteristics of the EGF parameter measurements, D_z^* can be represented by the following values of the variance: 16 mGal^2 for GAs; 4 arcsec^2 for DOV; and 25 E^2 for SDGP.

The threshold values of the correlation radius should be sufficiently small because only the areas with relatively high roughness can be considered informative. Bearing in mind that the values of the EGF correlation radius vary from several kilometers to several tens of kilometers and also taking into consideration the requirements for the accuracy of navigation solutions, $\rho_z^* = 10$ km can be taken as a generalized threshold value of the correlation radius.

6.4.3 Results of Experimental Studies

Let us consider the results of an experimental study of the described approach to estimating the navigation informativity of EGF using the above-mentioned EGM2008 model to degree 2190. A test area located in the southern part of the Sea of Okhotsk was chosen for this study. This area is a strip ±100 km relative to the center line with the following geographic coordinates (latitude B, longitude L) of the boundary points: the initial point coordinates are 45.5330°N, 143.500°E; the endpoint coordinates are 49.7170°N, 150.000°E. The EGF structure in and around the survey area is illustrated in Fig. 6.29 which shows that within the area boundaries marked with thick black lines, sections with a relatively smooth field alternate with sections with increased roughness. The distribution of the sections acceptable for map-aided navigation over the whole area is not uniform. Note that the western part of the area is visually characterized by significant vertical segmentation, while the eastern part generally has significant horizontal segmentation.

To obtain the quantitative estimates of navigation informativity indicators, the following parameters of the EGF were used: horizontal components of the gravity disturbance vector, characterized by the DOV components in the meridian (ξ) and

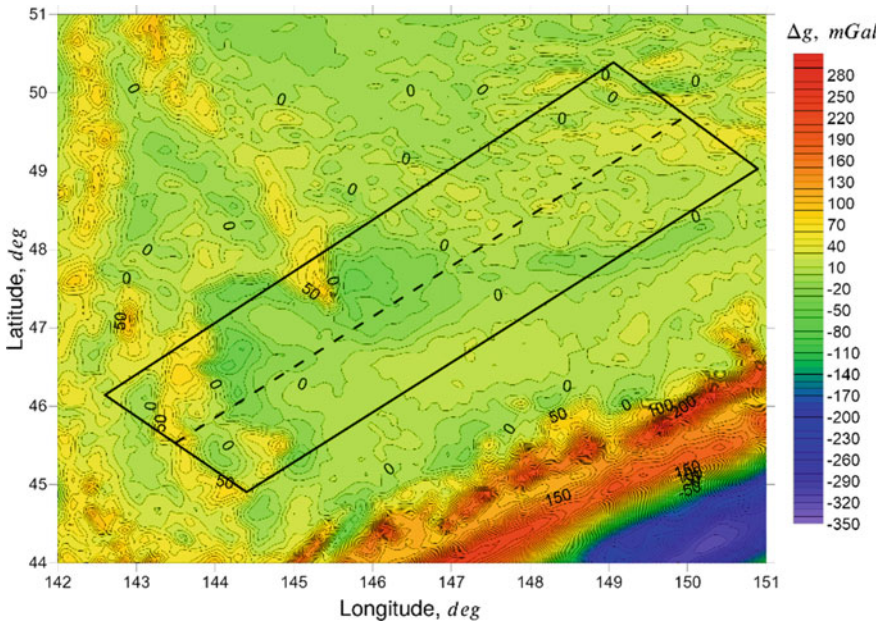

Fig. 6.29 GA areal distribution in the southern part of the Sea of Okhotsk and the survey area

the prime vertical (η), as well as the horizontal gradients of the gravity disturbance vector, characterized by the second derivatives T_{xx}, T_{yy} of the perturbing potential T along the axes of a planimetric rectangular coordinate system x, y. According to the EGM2008 model data, for the area as a whole, these parameters have the statistical characteristics shown in Table 6.23.

The parameters of EGF navigation informativity (variance and correlation radius) were estimated on the field route cross-sections parallel to the center line and spaced 10 km apart (including the center line) across the width of the area. Their values were calculated for each cross-section at 100 km intervals in the moving-average mode, with an increment of 20 km. The initial values of the EGF parameters at the route points were calculated with an increment of about 2 km (1 arcmin).

Table 6.23 Statistical characteristics of the EGF parameters in the survey area

Parameter	Value			
	min	max	Average	Standard deviation
ξ, arcsec	–9.3	13.7	1.5	3.0
η, arcsec	–7.6	20.8	1.1	4.0
T_{xx}, E	–52.3	53.9	0.3	8.9
T_{yy}, E	–91.5	55.5	0.5	11.9

The estimates of the navigation informativity parameters are presented in detail in Figs. 6.30, 6.31 as two-dimensional diagrams describing the areal distribution of D_z and ρ_z. The ordinal numbers of the moving-average intervals in determining the current values of the variance and the correlation radius are plotted on the horizontal axis. The linear measurement unit is a specified value of the moving interval shift (20 km). The shifts of cross-sections relative to the center line of the area are plotted on the vertical axis. The linear measurement unit is the specified interval of the cross-section shift (10 km). The values of shifts for all the diagrams are fixed in the interval from –10 to +10. The distribution of the values of each parameter is shown by isolines and coloring.

Analysis of the diagrams confirms the visual estimation of the EGF segmentation based on the gravity anomaly data in the survey area; generally, the highest values of variances predominate in the western part of the area, while the lowest values of the correlation radius are mainly concentrated in its eastern part.

General characteristics of the navigation informativity parameters for the whole area are summarized in Table 6.24. They present the range of fluctuations of variances and correlation radiuses of DOV and SDGPs, as well as the proportion of informative sections in relation to their total number, based on the threshold values of D_z^* and ρ_z^* given above. Comparison of the generalized navigation informativity indicators of different EGF parameters shows that an average of about 23% of the

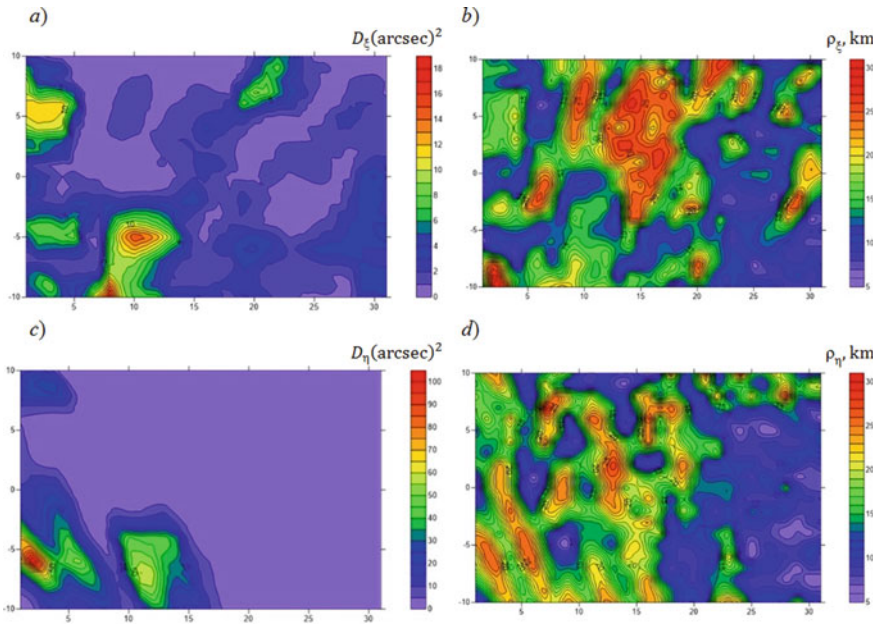

Fig. 6.30 Areal distribution of DOV informativity parameters: **a**, **b**—variance and correlation radius ξ; **c**, **d**—variance and correlation radius η

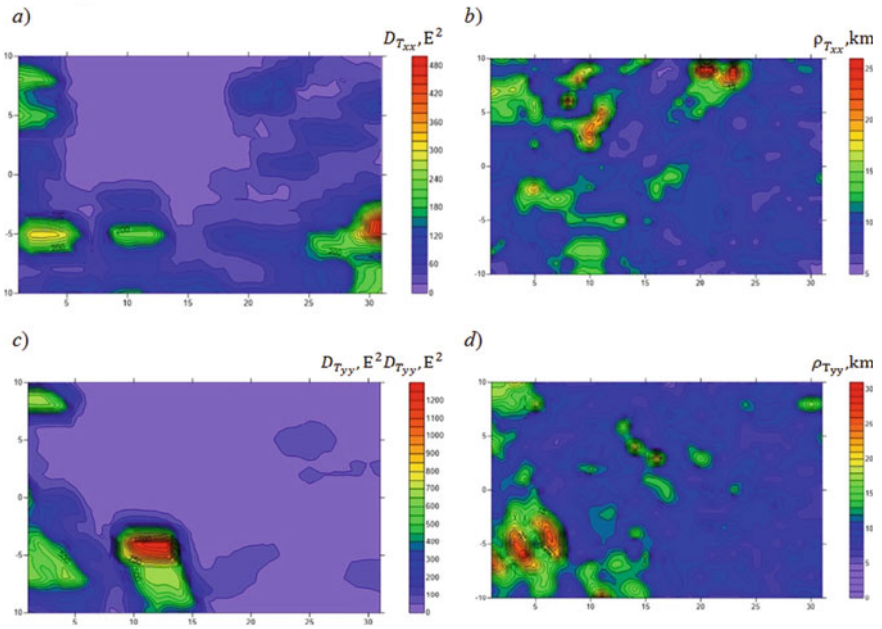

Fig. 6.31 Areal distribution of SDGP informativity parameters: **a**, **b**—variance and correlation radius T_{xx}; **c**, **d**—variance and correlation radius T_{yy}

area are informative (in the sense of the above definition of this term) for the gravity disturbance vector, and 65% are informative for the horizontal gradients.

It should be noted that in the general case, interpretation of EGF navigation informativity model parameters should take into account modeling errors, including the errors of geopotential harmonic coefficients and the errors due to the replacement of infinite series of spherical harmonics with finite sums (truncation errors). In this case, the variance of the total modeling error $D_{z,m}$ is defined as the sum of the variance $D_{z,c}$ which reflects the contribution of the errors of harmonic coefficients, and the

Table 6.24 Generalized characteristics of the navigation informativity parameters of the survey area

Parameter	Variance			Correlation radius, km		
	min	max	Informative sections (%)	min	max	Informative sections (%)
ξ, arcsec	0.04	16.77	20	6	28	21
η, arcsec	0.03	103.21	26	6	30	27
T_{xx}, E	2.31	473.89	70	6	26	66
T_{yy}, E	2.11	1261.75	57	4	29	68

variance $D_{z,r}$ of the truncation error. The value of $D_{z,c}$ is estimated using the available data on the RMSE of the geopotential harmonic coefficients determined from geodetic measurements. The value of $D_{z,r}$ is estimated using a suitable asymptotic model of degree variances of EGF (Nepoklonov 1998). For instance, the following estimates were obtained for GAs and DOV components (for the globe as a whole): 17.5 mGal^2 and 0.8 arcsec^2 for $D_{z,c}$; 11.2 mGal^2 and 2.5 arcsec^2 for $D_{z,r}$. Therefore, $D_{z,m}$ can be estimated with the following values (globally): 28.7 mGal^2 for the GA, and 3.3 arcsec^2 for the DOV components. For comparison, when using the EGM2008 model data, the variances of GAs and DOV over the globe as a whole are about 900 mGal^2 and 50 arcsec^2, respectively. As for detailed estimates of $D_{z,c}$, $D_{z,r}$, and $D_{z,m}$, they can vary significantly from area to area. The analysis of modeling errors effect on the correlation interval determined for the EGF parameters requires further study which goes beyond the scope of this book.

It should be emphasized that the obtained estimates characterize the EGF navigation informativity at the sea (geoid) level. In practice, navigation using the EGF is associated mainly with airborne and/or underwater vehicles. Accordingly, the characteristics of the EGF navigation informativity should be recalculated for flight altitudes in the first case, and for the vehicle's depth of immersion in the second case. In both cases, recalculation can be done on the basis of the same global EGF model in the form of spherical harmonics, using standard formulas for harmonic synthesis of perturbing potential and its functionals (Barthelmes 2009).

At the same time, it should be kept in mind that each of these options has its own features. When performing upward recalculation, one should remember that the effect of EGF smoothing with increasing height may result in weakening of some field features, which will make it necessary to improve the measurement accuracy. Recalculation, as such, is a correctly formulated problem to be solved by replacing the value r of the geoid geocentric radius-vector (reference ellipsoid) with $r + H$, where H is the geodetic height of the calculated point. In contrast to this, the problem of downward recalculation is incorrect in terms of its formulation, which can increase the errors in the model values of the EGF parameters. Elimination of the effect of this inconsistency can generally involve regularized harmonic synthesis algorithms (Neyman 1979) and taking into account the effect of underwater terrain.

6.4.4 Conclusions

The studies on the estimation of the EGF navigation informativity allow drawing the following conclusions.

EGF navigation informativity can be estimated with the use of variance (RMS value) and the radius (interval) of correlation of measured EGF parameters (gravity anomalies, deflections of the vertical, second derivatives of perturbing potential). The present level of EGF knowledge, including the availability of high-precision global geopotential models, makes it possible to estimate the parameters of the EGF navigation informativity with a resolution of a few kilometers.

We have considered the formulas that provide the estimation of the EGF navigation informativity both for individual routes and for areas. According to the experimental data obtained with these formulas and the modern EGM2008 geopotential model to degree 2190, the parameters of navigation informativity, i.e., the variance and correlation radius, may vary considerably depending on the area and the EGF parameter being studied.

Sufficiently informative (in terms of the above criteria) sections may alternate with the sections the information content of which is below an acceptable level. Keeping this in mind, it seems appropriate in the future to divide the water area of the World Ocean (which is a probable area of application of autonomous navigation systems based on the EGF) into zones based on the navigation informativity of various EGF parameters, using modern geopotential models.

Acknowledgements The research activities described in Sect. 6.3 were supported by the Russian Science Foundation (project № 18-19-00627, https://rscf.ru/project/18-19-00627/).

References

Adler S, Schmitt S, Wolter K, Kyas M (2015) A survey of experimental evaluation in indoor localization research. In: IEEE international conference on indoor positioning and indoor navigation (IPIN), Banff, Alberta, Canada, pp 1–10

Afshari HH, Gadsden SA, Habibi S (2017) Gaussian filters for parameter and state estimation: a general review of theory and recent trends. Signal Process 135:218–238

Afzal MH (2011) Use of earth's magnetic field for pedestrian navigation. PhD Thesis, University of Calgary, Canada, Calgary

Ånonsen KB, Hallingstad O (2007) Sigma point Kalman filter for underwater terrain-based navigation. Control Appl Marine Syst 7(1):106–110

Arabelos DN, Tscherning CC (2010) A comparison of recent earth gravitational models with emphasis on their contribution in refining the gravity and geoid at continental or regional scale. J Geodesy 84(11):643–660

Avgustov LI, Babichenko AV, Orekhov MI, Sukhorukov SY, Shkred VK (2015) Navigatsiya letatel'nykh apparatov v okolozemnom prostranstve (Vehicles Navigation in Near-Earth Space). Nauchtekhlitizdat, Moscow

Avsyuk YN, Bagramyants VO, Brovar BV et al (2010) Gravimetriya i geodeziya (Gravimetry and Geodesy), Brovar BV (ed). Nauchnyi mir, Moscow

Baklitskii VK (2009) Korrelyatsionno-ekstremal'nye metody navigatsii i navedeniya (correlation extreme methods of navigation and guidance). TO Knizhnyi Klub, Tver

Barthelmes F (2009) Definition of functionals of the geopotential and their calculation from spherical harmonic models. In: Scientific technical report STR 09/02, Deutsches GeoForschungsZentrum GFZ, Potsdam

Beloglazov IN, Ermilov AS, Karpenko GI (1979) Recursive searching estimation and design of algorithms for extremum correlation navigation systems. Autom Remote Control 40(7):1001–1010

Beloglazov IN, Dzhandzhgava GI, Chigin GP (1985) Osnovy navigatsii po geofizicheskim polyam (Fundamentals of map-aided navigation). Nauka, Moscow

Beloglazov IN, Kazarin SN, Kosyanchuk VV (2012) Obrabotka informatsii v ikonicheskikh sistemakh navigatsii, navedeniya i distantsionnogo zondirovaniya mestnosti (Data processing in the iconic systems of navigation, guidance, and earth remote sensing). Fizmatlit, Moscow

Berdyshev VI, Kostousov VB (2007) Ekstremal'nye zadachi i modeli navigatsii po geofizicheskim polyam (Extreme problems and models of map-aided navigation). UrO RAS, Ekaterinburg

Bergman N (1999) Recursive Bayesian estimation: navigation and tracking applications. PhD Thesis, Linkoping University, Sweden, Linkoping

Berkovich SB, Kotov NI, Sadekov RN, Sholokhov AV, Tsyshnatii VA (2016) Using information of visual systems and digital road maps to improve positioning accuracy of ground vehicles. In: 23rd St. Petersburg international conference on integrated navigation systems. Elektropribor, St. Petersburg, pp 506–513

Bol'shakov VD, Gaidaev PA (1977) Teoriya matematicheskoi obrabotki geodezicheskikh izmerenii (Theory of mathematical processing of geodetic observations). Nedra, Moscow

Boreyko A, Moun S, Scherbatyk A (2008) Precise UUV positioning based on images processing for underwater construction inspection. In: Proceedings of ISOPE Pacific/Asia offshore mechanics symposium, pp 14–20

Boreyko AA, Vorontsov AV, Kushnerik AA, Shcherbatyuk AF (2010) Image processing algorithms for solving some problems of control and navigation of autonomous underwater vehicles. Podvodnye Issledovaniya i Robototekhnika 1:29–39

Brillinger D (1975) Time series: data analysis and theory. Holt, New York

Bucy RS, Senne KD (1971) Digital synthesis of non-linear filters. Automatica 7(3):287–298

Candy JV (2016) Bayesian signal processing: classical, modern, and particle filtering methods, 2nd edn. Wiley, New Jersey

Carreno S, Wilson P, Ridao P, Petillot YR (2010) A survey on terrain based navigation for AUVs. In: Proceeding of OCEANS 2010 MTS/IEEE

Cheng M, Ries JC, Chambers DP (2009) Evaluations of the EGM-2008 gravity model. Newton's Bulletin 4:18–23

Chernodarov VA (2016) Integrated information processing in geoinertial navigation systems. In: 23rd St. Petersburg international conference on integrated navigation systems. Elektropribor, St. Petersburg, pp 563–567

Dem'yanov VV, Savel'eva EA (2010) Geostatistika: teoriya i praktika (Geostatistics: theory and practice). Nauka, Moscow

Dmitriev SP (1991) Vysokotochnaya morskaya navigatsiya (High-Precision marine navigation). Sudostroenie, St. Petersburg

Dmitriev SP, Shimelevich LI (1978) A generalized Kalman filter with repeated linearization and its use in navigation over geophysical fields. Autom Remote Control 39(4):505–509

Dmitriev SP, Stepanov OA, Koshaev DA (1999) Methods of data integration for INS and navigation satellite system. Giroskopiya i Navigatsiya 26(3):36–52

Doucet A, de Freitas N, Gordon NJ (2001) Sequential Monte Carlo methods in practice. Springer-Verlag, New York

Drobyshev NV, Zheleznyak LK, Klevtsov VV, Koneshov VN, Solov'ev VN (2005) Accuracy of satellite determinations of the gravity field at sea. Izvestiya, Phys Solid Earth 41(6):462–474

Dunaevskaya KV, Kostousov VB, Kiselev LV (2021) Study of a method for calculating the current accuracy in map-aided navigation problem. Gyroscopy and Navigation 12(1):50–60

Dzhandzhgava GI, Avgustov LI (2018) Navigatsiya po geopolyam (Map-aided navigation). Nauchtekhlitizdat, Moscow

Dzhandzhgava GI, Gerasimov GI, Avgustov LI (2013) Navigation and homing by spatial geophysical fields. Izvestiya YuFU, Tekhnicheskie Nauki 140(3):74–83

Emel'yantsev GI, Stepanov AP (2016) Integrirovannye inertsial'no-sputnikovye sistemy orientatsii i navigatsii (Integrated INS/GNSS navigation and orientation systems), Peshekhonov VG (ed). Concern CSRI Elektropribor, St. Petersburg

Foerste C, Schmidt R, Stubenvoll R, Flechtner F (2008) The GFZ/GRGS satellite-only and combined gravity field models: EIGEN-GL04S1 and EIGEN-GL04C. J Geodesy 82(6):331–346

Gelb A (1974) Applied optimal estimation. M.I.T. Press, Cambridge, MA
González-García J, Gómez-Espinosa A, Cuan-Urquizo E, García-Valdovinos LG, Salgado-Jiménez T, Escobedo-Cabello J-A (2020) Autonomous underwater vehicles: localization, navigation, and communication for collaborative missions. Appl Sci 10(4):1256. https://doi.org/10.3390/app10041256
GOST (National Standard) 18.101–76 (1980) Quantitative methods of optimization for parameters of standardization objects. basic provisions for construction of mathematical models
Grewal MS, Andrews AP, Bartone CG (2013) Global navigation satellite systems, inertial navigation, and integration. Wiley
Groves PD (2013) Principles of GNSS, inertial, and multisensor integrated navigation systems, 2nd edn. Artech House
Groves PD, Handley RJ, Runnalls AR (2006) Optimising the integration of terrain referenced navigation with INS and GPS. J Navig 59(1):71–89
Gruber T (2004) Validation concepts for gravity field models from satellite missions. In: Proceedings of the 2nd international GOCE user workshop GOCE, the geoid and oceanography, ESA SP-569, ESA
Gruber T, Viesser PN, Ackermann C, Hosse M (2011) Validation of GOCE gravity field models by means of orbit residuals and geoid comparisons. J Geodesy 85(11):845–860
Gustafsson F (2010) Particle filter theory and practice with positioning applications. IEEE Aerosp Electron Syst Mag 25(7):53–82
Gustafsson F, Gunnarsson F, Bergman N, Forssell U, Jansson J, Karlsson R, Nordlund P-J (2002) Particle filters for positioning, navigation, and tracking. IEEE Trans. Sig Process 50(2):425–437
Jekeli C, Yanh HJ, Kwon JH (2009) Evaluation of EGM08—globally and locally in South Korea. Newton's Bulletin 4:38–49
Julier SJ, Uhlmann JK (2004) Unscented filtering and nonlinear estimation. Proc IEEE 93(3):401–422
Kalinovskii AA, Kovalev VA, Dmitruk AA et al (2015) Search for invormative area on space images for UAV coordinates updating. In: Materialy 8-i Vserossiiskoi multikonferentsii v 3 tomakh (Proceedings 8th Russian national multiconference in 3 volumes), Southern Federal University Publisher, Rostov-on-Don
Karlsson R, Gustaffson F (2006) Bayesian surface and underwater navigation. IEEE Trans Sig Process 54:4204–4213
Karshakov EV, Tkhorenko MY, Pavlov BV (2018) Aeromagnetic gradiometry and its application to navigation. Autom Remote Control 79(5):897–910
Karshakov EV, Pavlov BV, Tkhorenko MY, Papusha IA (2021) Promising map-aided aircraft navigation systems. Gyroscopy and Navigation 12(1):38–49
Kaula WM (1966) Theory of satellite geodesy. Blaisdell, Waltham, MA
Kiselev LV, Medvedev AV, Kostousov VB, Tarkhanov AE (2017) Autonomous underwater robot as an ideal platform for marine gravity surveys. In: 24th St. Petersburg international conference on integrated navigation systems. Elektropribor, St. Petersburg, pp 1–4
Klyueva SF (2016) Clustering algorithms application to seabed navigation problems. Eurasian Scientific Association 1(4):26–30
Kostousov VB, Tarkhanov AE (2019) New method for estimating the errors in position updates by the geophysical field map. Tekhnicheskie Problemy Osvoeniya Mirovogo Okeana 8:347–351
Klyueva SF, Zav'yalov VV (2013) Sintez algoritmov batimetricheskikh sistem navigatsii (Synthesis of algorithms for bathymetric navigation systems). MSU, Vladivostok
Koneshov VN, Nepoklonov VB, Stolyarov IA (2012a) Using modern geopotential models in studying vertical deflections in the Arctic. Gyroscopy and Navigation 3(4):298–307
Koneshov VN, Nepoklonov VB, Stolyarov IA (2012b) Study of the anomalous gravity field in the Arctic based on modern geopotential models. Izvestiya, Phys Solid Earth 48(7–8):587–593
Koneshov VN, Nepoklonov VB, Sermyagin RA, Lidovskaya EA (2013) Modern global earth's gravity field models and their errors. Gyroscopy and Navigation 4(3):147–155

Koneshov VN, Nepoklonov VB, Sermyagin RA, Lidovskaya EA (2014a) On the estimation of accuracy for global models of gravitational field of the Earth. Izvestiya, Phys Solid Earth 50(1):127–136

Koneshov VN, Nepoklonov VB, Solov'ev VN (2014b) Comparison of global earth's gravity field models with the aerogravimetric data obtained during a transcontinental flight. Gyroscopy and Navigation 5(4):275–282

Koneshov VN, Nepoklonov VB, Avgustov LI (2016) Estimating the navigation informativity of the earth's anomalous gravity field. Gyroscopy and Navigation 7(3):277–284

Lainiotis DG (1976) Partitioning: a unifying framework for adaptive systems, I: estimation. II: control. In: Proceedings of the IEEE 64(8):1126–1140 and 1182–1198

Lee TN, Canciani AJ (2020) MagSLAM: aerial simultaneous localization and mapping using earth's magnetic anomaly field. Navigation 67(1)

Lefebvre T, Bruyninckx H, de Schutter J (2005) Nonlinear Kalman filtering for force-controlled robot tasks. Springer, Berlin

Levitskaya ZN (1988) Statistical models of anomalous characteristics of the earth's gravity field. In: Bulanzhe YuD, Sagitov MU (eds) Gravimetricheskie issledovaniya na more (Marine gravimetric surveys). Nauka, Moscow, pp 26–47

Li XR, Jilkov VP (2004) A survey of maneuvering target tracking: approximation techniques for nonlinear filtering. In: Proceeding of SPIE—conference on signal and data processing of small targets, vol 5428, pp 537–550

Lowrey J, Shellenbarger JC (1997) Passive navigation using inertial navigation sensors and maps. Nav Eng J 5(3):245–249

Luhtala JA, Särkkä S, Piché R (2015) Gaussian filtering and variational approximations for Bayesian smoothing in continuous-discrete stochastic dynamic systems. Signal Process 111:124–136

Meduna DK (2011) Terrain relative navigation for sensor-limited systems with application to underwater vehicles. PhD Thesis, Stanford University, USA, Stanford, CA

Melo J, Matos A (2017) Survey on advances on terrain based navigation for autonomous underwater vehicles. Ocean Eng 139:250–264

Metzger J, Wisotzky K, Wendel J, Trommer GF (2005) Sigma-point filter for terrain referenced navigation. In: Proceeding of AIAA guidance, navigation and control conference, San Francisco, CA

Minligareev VT, Sazonova TV, Kravchenok VL, Tregubov VV, Khotenko EN (2020) Geophysical support of magnetometric autonomous navigation systems. In: 27th St. Petersburg international conference on integrated navigation systems, Elektropribor, St. Petersburg

Morgunova EA, Saprykin YF, Uspenskaya ND (2004) Computer technology for building gravimetric maps by the geoid height conversion into gravity at sea. Rossiiskii geofizicheskii zhurnal 35/36

Moritz H (1976) Covariance functions in least-squares collocation. Report No. 240, Department of geodetic science, The Ohio State University

Moritz H (1980) Advanced physical geodesy. Wichmann, Karlsruhe

Nepoklonov VB (1998) Computer models of anomalous gravity field of the Earth. Izvestiya Vuzov. Geodeziya i Aerofotos'emka 6:104–106

Nepoklonov VB, Abakushina MV (2016) The current state of digital geoid model in continental areas. In: Geodeziya, kartografiya, kadastr, GIS—problemy i perspektivy razvitiya: tezisy dokladov Mezhdunarodnoi nauchno-prakticheskoi konferentsii (Proceedings of international research-to-practice conference "geodesy, cartography, land inventory and GIS: problems and prospects), Novopolotsk, 9–10 June, 2016. Polotsk State University, Novopolotsk, p 3

Nepoklonov VB, Zueva AN, Pleshakov DI (2007) The development and application of computer simulation systems for global studies of the Earth's gravity field. Izvestiya Vuzov. Geodeziya i Aerofotos'emka 2:79–97

Neyman YuM (1979) Variatsionnyi metod fizicheskoi geodezii (The Variational Method of Physical Geodesy). Nedra, Moscow

Norgaard M, Poulsen NK, Ravn O (2000) New developments in state estimation for nonlinear systems. Automatica 36(11):1627–1638
Nygren I (2005) Terrain navigation for vehicles. PhD Dissertation, Stockholm Royal Institute of Technology
Pasnani P, Seto ML (2018) Terrain-based localization and mapping for autonomous underwater vehicles using particle filters with marine gravity anomalies. IFAC-PapersOnLine 51(29):354–359
Pavlis NK, Holmes SA, Kenyon SC, Factor JK (2008) An earth gravitational model to degree 2160: EGM2008. EGU General Assembly 2008, Vienna, Austria
Pavlis NK, Holmes SA, Kenyon SC, Factor JK (2012) The development and evaluation of the earth gravitational model 2008 (EGM2008). J Geophys Res 117:B04406. https://doi.org/10.1029/2011jb008916
Pavlov BV, Volkovitskii AK, Karshakov EV (2010) Low frequency electromagnetic system of relative navigation and orientation. Gyroscopy and Navigation 1(3):201–208
Pellinen LP (1970) Estimation and application of degree variances of gravity. Stud Geophys Geod 14(2):168–173
Pellinen LP (1992) Calculation of smoothed gravity anomalies using altimetry and gravity data. In: Sbornik nauchnykh trudov TsNIIGAiK. Fizicheskaya geodeziya (Collected works of TsNIIGAiK. Physical Geodesy). TsNIIGAiK, Moscow, pp 3–39
Pellinen LP, Neyman YuM (1980) Fizicheskaya geodeziya (Physical geodesy). VINITI, Moscow
Rapp R (1986) Gravity anomalies and sea surface heights derived from a combined GEOS-3/SEASAT altimeter data set. J Geophys Res 94:4867–4876
Richeson JA (2008) Gravity gradiometer aided inertial navigation within non-GNSS environments. PhD Thesis, University of Maryland, USA, Washington
Särkkä S (2013) Bayesian filtering and smoothing. Cambridge University Press
Serkerov SA (1986) Korrelyatsionnye metody analiza v gravirazvedke i magnitorazvedke (Correlation methods of analysis in gravity and magnetic field surveys). Nedra, Moscow
Shcherbinin VV (2011) Postroenie invariantnykh korrelyatsionno-ekstremal'nykh sistem navigatsii i navedeniya letatel'nykh apparatov (Constructing invariant correlation-extreme systems of navigation and guidance for aircraft). Bauman State Technical University, Moscow
Shockley JA (2012) Ground vehicle navigation using magnetic field variation. PhD Thesis, Air Force Institute of Technology, Ohio, USA, Dayton, OH
Šimandl M, Straka O, Duník J (2016) Efficient adaptation of design parameters of derivative-free filters. Autom Remote Control 77(2):261–276
Simon D (2006) Optimal state estimation: Kalman, H-Infinity, and nonlinear approaches. John Wiley & Sons Inc., New York
Sorenson HW, Alspach DL (1971) Recursive Bayesian estimation using Gaussian sums. Automatica 7(4):465–479
Stepanov OA (1998) Primenenie teorii nelineinoi fil'tratsii v zadachakh obrabotki navigatsionnoi informatsii (Application of nonlinear filtering theory for navigation data processing), CSRI Elektropribor, St. Petersburg
Stepanov OA (2002) Integrated INS/GNSS navigation systems. Giroskopiya i Navigatsiya 1:23–45
Stepanov OA (2006) A linear optimal algorithm for nonlinear navigation problems. Giroskopiya i Navigatsiya 4:11–20
Stepanov OA (2016) Map-aided navigation, indoor navigation, and fingerprint-based positioning: common features and differences. In: 23rd St. Petersburg international conference on integrated navigation systems, Elektropribor, St. Petersburg, pp 568–571
Stepanov OA (2017) Osnovy teorii otsenivaniya s prilozheniyami k zadacham obrabotki navigatsionnoi informatsii (Fundamentals of the estimation theory with applications to the problems of navigation information processing), Part 1, Vvedenie v teoriyu otsenivaniya (Introduction to the estimation theory). Concern CSRI Elektropribor, St. Petersburg
Stepanov OA, Nosov AS (2020) A map-aided navigation algorithm without preprocessing of field measurements. Gyroscopy and Navigation 11(2)

Stepanov OA, Nosov AS (2021) Algorithm for planning an informative route for map-aided navigation. In: 28th St. Petersburg international conference on integrated navigation systems. Elektropribor, St. Petersburg

Stepanov OA, Toropov AB (2010) Comparison of point mass and particle filters in map-aided navigation. In: 17th St. Petersburg international conference on integrated navigation systems. Elektropribor, St. Petersburg, pp 381–384

Stepanov OA, Toropov AB (2014) Using sequential Monte-Carlo methods and analytical integration in navigation data processing, XII Vserossiiskoe soveshchanie po problemam upravleniya (12th Russian meeting on control problems). RAS Trapeznikov Institute of Control Problems, Moscow, pp 3324–3337

Stepanov OA, Toropov AB (2015) Nonlinear filtering for map-aided navigation. Part 1. An overview of algorithms. Gyroscopy and Navigation 6(4):324–337

Stepanov OA, Toropov AB (2016) Nonlinear filtering for map-aided navigation. Part 2. Trends in the algorithm development. Gyroscopy and Navigation 7(1):82–89

Stepanov OA, Vasil'ev VA (2016) Cramer-Rao lower bound in nonlinear filtering problems under noises and measurement errors dependent on estimated parameters. Autom Remote Control 77(1):81–105

Stepanov OA, Toropov AB, Amosov OS (2007) Comparison of Kalman-type algorithms in nonlinear navigation problems for autonomous vehicles. IFAC Proceedings Volumes 40(15):493–498

Stepanov OA, Vasiliev VA, Toropov AB, Loparev AV, Basin MV (2019) Efficiency analysis of a filtering algorithm for discrete-time linear stochastic systems with polynomial measurement. J Franklin Inst 356:5573–5591

Stepanov OA, Toropov AB, Nosov AS (2020) About classification of map-aided navigation algorithms. In: 28th St. Petersburg international conference on integrated navigation systems. Elektropribor, St. Petersburg

Stepanov OA, Litvinenko YA, Vasiliev VA, Toropov AB, Basin MV (2021a) Polynomial filtering algorithm applied to navigation data processing under quadratic nonlinearities in system and measurement equations. Part 1. Description and comparison with Kalman type algorithms. Gyroscopy and Navigation 12(3):205–223

Stepanov OA, Litvinenko YA, Vasiliev VA, Toropov AB, Basin MV (2021b) Polynomial filtering algorithm applied to navigation data processing under quadratic nonlinearities in system and measurement equations. Part 2. Solution examples. Gyroscopy and Navigation 12(4):314–328

Stratonovich RL (1968) Conditional Markov processes and their application to the theory of optimal control. Elsevier, New York

Teixeira F (2007) Terrain-aided navigation and geophysical navigation of autonomous underwater vehicles. PhD Thesis, Instituto Superior Tecnico, Universidade Tecnica de Lisboa

Toropov AB (2013) Filtering algorithms in problems of marine navigation system position error correction using nonlinear measurements. Cand. Sci. Dissertation. Concern CSRI Elektropribor, St. Petersburg

Tscherning CC, Rapp RH (1974) Closed covariance expressions for gravity anomalies, geoid undulations, and deflections of the vertical implied by anomaly degree variance models. Rep 208, Dept Geod Sci and Surv, Ohio State University, Columbus

Vaman DA (2014) GPS-inspired terrain referenced navigation algorithm. PhD Thesis, Delft University of Technology

Veremeenko KK, Zheltov SY, Kim NV, Sebryakov GG, Krasil'shchikov MN (2009) Sovremennye informatsionnye tekhnologii v zadachakh navigatsii i navedeniya bespilotnykh manevrennykh letatel'nykh apparatov (Modern information technologies in the navigation and guidance tasks of unmanned maneuverable aircraft), Krasil'shchikov MN, Sebryakov GG (eds). Fizmatlit, Moscow

Vyazmin VS, Golovan AA, Papusha IA, Popelensky MY (2016) Informativeness of vector magnetometer measurements and global geomagnetic field models in the aircraft INS aiding. In: 23rd St. Petersburg international conference on integrated navigation systems. Elektropribor, St. Petersburg, pp 397–401

Wang F, Wen X, Sheng D (2013) Observability analysis and simulation of passive gravity navigation system. J Comput 8(1):248–255

Wei E, Dong C, Yang Y, Shenquan T, Liu J, Gong G, Deng Z (2017) A robust solution of integrated SITAN with TERCOM algorithm: weight-reducing iteration technique for underwater vehicles' gravity-aided inertial navigation system. Navigation 64(1):111–122

Wu L, Wang H, Chai H, Zhang L, Hsu H, Wang Y (2017) Performance evaluation and analysis for gravity matching aided navigation. Sensors 17(4)

Yale MM, Sandwell DT (1999) Stacked global satellite gravity profiles. Geophysics 64(6):1748–1755

Yarlykov MS, Anikin AL, Bashaev AV et al (2004) Markovskaya teoriya otsenivaniya v radiotekhnike (Markov theory of estimation in radio engineering). Radiotekhnika, Moscow

Yazwinski AA (1970) Stochastic processes and filtering theory. Academic Press, New York

Zheleznyak LK (1992) Areal mapping in ocean by various-type gravimeters. Fizika Zemli 3:50–55

Zheleznyak LK (2002) Adjustment of large-scale geophysical survey data. Fizika Zemli 3:45–47

Zheleznyak LK, Koneshov VN (1992) Large-scale gravimetric survey at sea. Fizika Zemli 11:64–68

Zheleznyak LK, Koneshov VN (1995) Estimation of satellite altimetry data errors in comparison with gravimetric materials. Fizika Zemli 1:76–81

Zhou T, Peng D, Xu C, Zhang W, Shen J (2018) Adaptive particle filter based on Kullback-Leibler distance for underwater terrain aided navigation with multi-beam sonar. IET Radar Sonar Navig 12(4):433–441

Appendix

List of Contributors

Avgustov, Lev (Sect. 6.4), Candidate of Sciences (Engineering). He works at Ramenskoye Instrument Engineering Design Bureau (Moscow Region, Russia) and at the Bauman Moscow State Technical University. His area of interest is global autonomous map-aided navigation. He is the author of 28 scientific publications and has 13 copyright certificates for inventions and patents of the Russian Federation.

Blazhnov, Boris (Sect. 3.3), Candidate of Sciences (Engineering). He is employed at Concern CSRI Elektropribor (St. Petersburg, Russia). His research interests are integrated INS/GNSS orientation and navigation systems, inertial modules and their sensing elements, and gravimetry. He is the author of more than 70 scientific publications and has 20 copyright certificates for inventions and patents of the Russian Federation.

Bolotin , Yurii (Sects. 2.2, 2.4, 2.5, and 5.1), Doctor of Sciences (Physics and Mathematics), Professor. He works at Lomonosov Moscow State University (Moscow, Russia). He is a full member of the Academy of Navigation and Motion Control. His research interests include optimal control and estimation, inertial navigation, and inertial gravimetry. He has authored over 100 scientific publications.

Chelpanov, Igor' (Sect. 3.1), Doctor of Sciences (Engineering), Honored Scientist of the Russian Federation. He worked for Concern CSRI Elektropribor (St. Petersburg, Russia). His research fields included signal conversion in navigation devices and systems, testing, and robotic technologies. He authored more than 400 scientific publications, including three monographs and three study guides.

Elinson, Leon (Sect. 1.2), Candidate of Sciences (Engineering). He was a long-service employee of Concern CSRI Elektropribor (St. Petersburg, Russia). He received the Russian Federation Government Prize in the field of science and technology for the development and implementation of dual-purpose gravimeters operated onboard marine and air carriers. He was the author of more than 80 scientific

V. G. Peshekhonov and O. A. Stepanov (eds.), *Methods and Technologies for Measuring the Earth's Gravity Field Parameters*, Earth Systems Data and Models 5,
https://doi.org/10.1007/978-3-031-11158-7

publications, including one monograph and 53 copyright certificates of inventions and patents of the Russian Federation.

Emel'yantsev , Gennadii (Sect. 3.3), Doctor of Sciences (Engineering), Professor. He is employed at Concern CSRI Elektropribor (St. Petersburg, Russia). He has the title of Honored Scientist of the Russian Federation. Dr. Emel'yantsev is a full member of the Academy of Navigation and Motion Control. His areas of research are inertial navigation systems and integrated INS/GNSS systems. He has authored over 100 scientific publications, three monographs, and has 17 certificates of inventions and patents of the Russian Federation.

Evstifeev, Mikhail (Sects. 3.1, and 5.2), Doctor of Sciences (Engineering), Professor. He works at Concern CSRI Elektropribor and at ITMO University (St. Petersburg, Russia). He is a full member of the Academy of Navigation and Motion Control. His areas of research interests are sensing elements of navigation devices, micromechanical and geophysical devices, and the theory of elastic mechanical systems. He has authored more than 180 scientific publications. ORCID: 0000–0001-8785-767X.

Gaivoronskii, Stanislav (Sect. 3.2), Candidate of Sciences (Engineering). He is with Concern CSRI Elektropribor. He is a member of the Academy of Navigation and Motion Control. His research interests are precision optical electronic systems for astronomic and geodetic purposes, and periscope systems. He has authored more than 20 scientific publications.

Golovan, Andrei (Sects. 2.2, 4.3, and 5.1), Doctor of Sciences (Physics and Mathematics). He works at Lomonosov Moscow State University (Moscow, Russia), and is a full member of the Academy of Navigation and Motion Control. His current interests include integrated navigation systems, the theory and methods of estimation and their application to navigation and geophysical data processing. He has authored more than 50 scientific publications, including four monographs. ORCID: 0000–0001-5628-248X.

Koneshov , Vyacheslav (Sects. 3.1, 4.1, 6.1, 6.2, and 6.4), Doctor of Sciences (Engineering), Professor. He is employed at Schmidt Institute of Physics of the Earth under the Russian Academy of Sciences (IPE RAS) (Moscow, Russia). Dr. Koneshov is a corresponding member of the Russian Academy of Natural Sciences, and a full member of the Academy of Navigation and Motion Control. His research interests are gravi-inertial studies and airborne gravimetry. He is an awardee of the Russian Federation Government Prize in the field of science and technology for the development and implementation of dual-purpose gravimeters operated onboard marine and air carriers. He has more than 230 scientific publications, including two monographs and two study guides.

Krasnov, Anton (Sects. 1.2, 2.1, and 4.2), Candidate of Sciences (Engineering). He is with Concern CSRI Elektropribor (St. Petersburg, Russia). He is a full member of the Academy of Navigation and Motion Control. His fields of research include gravimetry, geodesy, and inertial navigation. He has authored more than 70 scientific publications and one patent of the Russian Federation. ORCID: 0000-0003-0298-2418.

Mikhailov, Pavel (Sect. 6.2), Candidate of Sciences (Engineering). He is employed at Schmidt Institute of Physics of the Earth under the Russian Academy of Sciences (IPE RAS) (Moscow, Russia). His research interests are gravity measurement, survey methods and data processing, and global models of potential fields. He is the author of more than 20 scientific publications.

Motorin, Andrei (Sect. 2.3), Candidate of Sciences (Engineering). He works for ITMO University and Concern CSRI Elektropribor (St. Petersburg, Russia). He is a full member of the Academy of Navigation and Motion Control. His fields of research are the theory and methods of linear and nonlinear processing of navigation and geophysical data, and integrated navigation systems. He is the author of more than 60 scientific publications. ORCID: 0000-0002-2093-5079.

Nepoklonov, Viktor (Sects. 6.1, and 6.4), Doctor of Sciences (Engineering). He is employed at Moscow State University of Geodesy and Cartography and Schmidt Institute of Physics of the Earth of the Russian Academy of Sciences (Moscow, Russia). His current interests are mathematical modeling of the Earth's gravity field, and the theory and methods of geodetic and navigation data processing. He is the author of more than 70 scientific publications, including four monographs.

Nosov , Aleksei (Sects. 2.3, and 6.3). He works at Luxoft Professional LLC and ITMO University (St. Petersburg, Russia). His fields of research include integrated navigation systems, methods of linear and nonlinear filtering, map-aided navigation systems, gravimetry and its navigation applications, and time series analysis. He has authored more than 30 scientific publications. ORCID: 0000-0002-0345-0862.

Parusnikov, Nikolai (Sect. 2.2), Doctor of Sciences (Physics and Mathematics), Professor, and a full member of the Academy of Navigation and Motion Control. He is employed at Lomonosov Moscow State University. His areas of research interests include integrated navigation systems, the theory and methods of estimation and their application to navigation and geophysical data processing. He received the Russian Federation Government Prize in the field of science and technology for the development and implementation of dual-purpose gravimeters operated onboard marine and air carriers. He is the author of more than 130 scientific publications, including four monographs.

Peshekhonov, Vladimir (Sect. 1.2), Doctor of Sciences (Engineering), Professor, Academician of the Russian Academy of Sciences. He is a Chief Scientific Officer at Concern CSRI Elektropribor, also working at ITMO University (St. Petersburg, Russia). He is the President of the Academy of Navigation and Motion Control. His field of research is high-precision autonomous navigation, including navigation and geodetic software. Academician Peshekhonov received the Lenin Prize and the State Prize of the Russian Federation in the field of science and technology; and the Russian Federation Government Prize in the field of science and technology for the development and implementation of dual-purpose gravimeters operated onboard marine and air carriers. He holds the title of the Hero of Labor of the Russian Federation. He has authored more than 300 scientific publications.

Pogorelov , Vitalii (Sect. 4.1), Candidate of Sciences (Physics and Mathematics). He works for Schmidt Institute of Physics of the Earth under the Russian Academy of Sciences (IPE RAS) (Moscow, Russia). His current interests are airborne gravimetry,

dependence of gravity anomalies on the stressed state of the Earth's crust, and satellite navigation technologies. He is the author of more than 50 scientific publications.

Smoller , Yurii (Sects. 1.3, and 4.3), Candidate of Sciences (Physics and Mathematics). He works at the Gravimetric Technologies (Moscow, Russia). He is a full member of the Academy of Navigation and Motion Control. He is an awardee of the State Prize of the Russian Federation. His field of research is gravimetry. He is the author of 23 scientific publications and has 12 copyright certificates of inventions and patents of the Russian Federation.

Sokolov , Aleksandr (Sects. 1.2, 2.1, and 4.2), Candidate of Sciences (Engineering). He is the General Director of Concern CSRI Elektropribor, and the Head of Applied Photonics Department at Peter the Great Polytechnic University (St. Petersburg, Russia). He received the Russian Federation Government Prize. Dr. Sokolov is a full member of the Academy of Navigation and Motion Control. His research interests include gravimetry, geodesy, and inertial navigation. He is the author of more than 80 scientific publications and has 10 copyright certificates of inventions and patents of the Russian Federation. ORCID: 0000-0002-6423-1591.

Solov'ev, Vladimir (Sects. 4.1, 6.1, and 6.2). He works for Schmidt Institute of Physics of the Earth under the Russian Academy of Sciences (IPE RAS) (Moscow, Russia). His areas of research interests are gravity determination methods, methods and techniques for processing the data obtained using the gravimeters on moving vehicles. He has developed a software package for marine and airborne measurement data processing. He has also authored and coauthored over 20 scientific publications.

Stepanov , Aleksei (Sect. 3.3), Candidate of Sciences (Engineering). He is employed at Concern CSRI Elektropribor and ITMO University (St. Petersburg, Russia). His current interests are integrated orientation and navigation systems, their errors, calibration and testing methods. He is the author of more than 60 scientific publications, including one monograph, and has more than 20 copyright certificates of inventions and patents of the Russian Federation.

Stepanov, Oleg (Introduction to the book and to Chapters 1–6, Sects. 2.3, and 6.3), Doctor of Sciences (Engineering), Professor, Corresponding Member of the Russian Academy of Sciences. He serves as the Vice-President of the Academy of Navigation and Motion Control. He is employed at Concern CSRI Elektropribor and ITMO University (St. Petersburg, Russia). His fields of research include integrated navigation systems, theory and methods of linear and nonlinear filtering and their application to navigation and geophysical data processing. He is the author of more than 250 scientific publications, including six monographs. ORCID: 0000-0003-3640-3760.

Toropov, Anton (Sect. 6.3), Candidate of Sciences (Engineering). He works for Concern CSRI Elektropribor (St. Petersburg, Russia). His areas of research interests are mathematical software for navigation systems, theory and methods of linear and nonlinear filtering and their application to navigation and geophysical data processing, and underwater vehicles positioning. He has authored over 60 scientific publications. ORCID: 0000-0001-6262-7691.

Tsodokova , Veronika (Sect. 3.2), Candidate of Sciences (Engineering). She works for Concern CSRI Elektropribor (St. Petersburg, Russia). Her research

interests are precision optical-electronic systems for astronomic and geodetic applications. She is the author of more than 30 scientific publications.

Vershovskii, Anton (Sect. 5.3), Doctor of Sciences (Physics and Mathematics). He is employed at Ioffe Institute of Physics and Technology (St. Petersburg, Russia). His fields of research include quantum optics and optical radiospectroscopy, in particular, quantum magnetometry and gyroscopy based on the effect of optically detectable magnetic resonance, quantum frequency standards, laser deceleration, and cooling of atoms. He is the author of more than 70 scientific publications, including two monographs. ORCID 0000-0002-9740-1104.

Vitushkin, Leonid (Sect. 1.1), Doctor of Sciences (Engineering). He works at Mendeleyev Institute for Metrology (St. Petersburg, Russia). His areas of interests are gravimetry, in particular, absolute gravimetry, frequency-stabilized lasers, laser interferometry, metrology, and nanometrology. He is the author of more than 120 scientific publications and has a number of copyright certificates for inventions and patents of the Russian Federation.

Vyazmin, Vadim (Sects. 2.5, and 5.1), Candidate of Sciences (Physics and Mathematics). He is employed at Lomonosov Moscow State University (Moscow, Russia). He is a full member of the Academy of Navigation and Motion Control. His research interests are airborne gravimetry, local models of the Earth's gravity field, and navigation systems. He has authored more than 30 scientific publications. ORCID: 0000-0003-3848-6045.

Yurist , Samuil (Sects. 1.3, 2.4, and 4.3), Candidate of Sciences (Engineering). He works at Gravimetric Technologies (Moscow, Russia). He is a full member of the Academy of Navigation and Motion Control, and an awardee of the State Prize of the Russian Federation. His area of research interest is gravimetry. He is the author of 27 scientific publications and has 20 copyright certificates of inventions and patents of the Russian Federation.

Yashnikova, Olga (Sect. 3.1). She is employed at Concern CSRI Elektropribor (St. Petersburg, Russia). Her areas of research interests are integrated navigation systems, geodetic and gravimetric systems. She has authored more than 30 scientific publications. ORCID: 0000-0003-4681-7537.

Zheleznyak, Leonid (Sect. 6.2), Doctor of Sciences (Engineering). He is employed at Schmidt Institute of Physics of the Earth under the Russian Academy of Sciences (IPE RAS) (Moscow, Russia). His areas of research interests are gravity measurements on moving vehicles: instrumentation, methods, and metrology. He is an awardee of the Russian Federation Government Prize in the field of science and technology for the development and implementation of dual-purpose gravimeters operated onboard marine and air carriers. He has authored over 150 scientific publications, including two monographs.

List of Contributors' Emails

Name, email
Krasnov, Anton anton-krasnov@mail.ru
Peshekhonov, Vladimir onti@eprib.ru
Stepanov, Oleg soalax@mail.ru
Yashnikova, Olga olga_evstifeeva@mail.ru